



Electrochemical properties of vanadium oxide-based cathode materials for Li/Na-ion batteries and aqueous rechargeable zinc batteries

Dauren Batyrbekuly

► To cite this version:

Dauren Batyrbekuly. Electrochemical properties of vanadium oxide-based cathode materials for Li/Na-ion batteries and aqueous rechargeable zinc batteries. Mechanics of materials [physics.class-ph]. Université Paris-Est Créteil Val-de-Marne - Paris 12; Nazarbayev University, 2021. English. NNT : 2021PA120034 . tel-04071118

HAL Id: tel-04071118

<https://theses.hal.science/tel-04071118>

Submitted on 17 Apr 2023

HAL is a multi-disciplinary open access archive for the deposit and dissemination of scientific research documents, whether they are published or not. The documents may come from teaching and research institutions in France or abroad, or from public or private research centers.

L'archive ouverte pluridisciplinaire **HAL**, est destinée au dépôt et à la diffusion de documents scientifiques de niveau recherche, publiés ou non, émanant des établissements d'enseignement et de recherche français ou étrangers, des laboratoires publics ou privés.



Thèse pour obtenir le grade de
Docteur de l'Université Paris Est Créteil Val de Marne
Ecole doctorale : SIE-Sciences, Ingénierie et Environnement
Spécialités « Sciences des Matériaux »

Présentée publiquement par
Monsieur Dauren BATYRBEKULY

Le 15 décembre 2021

Titre:

Electrochemical properties of vanadium oxide-based cathode materials for
Li/Na-ion batteries and Aqueous Rechargeable Zinc Batteries

Jury :

Thierry Djenizian, Professeur, EMSE
Sylvain Franger, Professeur, Univ. Paris Saclay
Vanessa Pereira Pimenta, Maître de conférence, ESPCI
Rita Baddour-Hadjean, Directrice de recherche CNRS,
Christine Cachet-Vivier, Professeur, UPEC
Zhumabay Bakenov, Professeur, Univ. Nazarbayev,
Jean-Pierre Pereira-Ramos, Directeur de recherche CNRS
Dr Barbara Laïk, Maître de conférence, UPEC

Rapporteur
Rapporteur
Examinatrice
Examinatrice
Examinatrice
Codirecteur de thèse
Directeur de thèse
Examinatrice



Acknowledgements

This thesis work was carried out in the Group of Electrochemistry and Spectroscopy of Materials – GESMAT (BATTion) of the Institute of Chemistry and Materials Paris Est Créteil (ICMPE-CNRS, Thiais, France) and National Laboratory Astana (NLA, Nur-Sultan, Kazakhstan).

This thesis work was directed by Professor Jean-Pierre Pereira-Ramos, CNRS Research Director at BATTion group. I would like to thank him for continuous support, guidance and valuable advice during my PhD study and allowing me to work in this team. I got a lot of knowledge in related to the structural investigation and electrochemical properties of cathode materials for M-ion batteries. I thank him for the strong impact on my thesis writing. I appreciated his encouragement as well as his vision of the research profession.

I would like to thank Dr. Rita Baddour-Hadjean, CNRS Research Director and Head of BATTion group, for their support, enthusiastic encouragement, valuable guidance, thoughtful suggestions and discussion as well as so much patience to teach me “How to use Raman equipment and how to analyze the obtained data”.

Moreover, I would express many thanks to Professor Jean-Pierre Pereira-Ramos and Dr. Rita Baddour-Hadjean for their support and much patience from both experimental part and many discussions for analyzing the data, for their support from the scientific part, technique part, and daily, harmonious and warm atmosphere in the laboratory.

I also would like to express thankfulness to the Professor Zhumabay Bakenov, Director of Center of Energy and Advanced Materials Science of National laboratory Astana, for his strong support and guidance from scientific part and strong help during my PhD and allowing me to make experiments in the laboratory in Nur-Sultan.

I would like to thank Dr. Barbara Laik, CNRS Researcher, for her help in experimental work, discussion, instruction how to properly make electrochemical investigation by using Biologic and how to KaleidaGraph to make a graph, how to make Impedance measurements.

Thank also Nicolas Emery, CNRS Researcher for his help on Rietveld refinement and thoughtful discussion and answers related to crystal structure aspects and the training in the GSAS software.

I would like to thank the Director of ICMPE-CNRS, Dr Daniel Grande for allowing me to work in the ICMPE institute.

I also thank Bernari Gladys, for administrative support during my stay in France.

I want to thank the PhD students in BATTion group, Ankush Bhatia and Yanlong Zhou, for their strong help, support and good time spent during my PhD.

I want to thank the thesis committee members: Professeur Thierry Djenizian, Professeur Sylvain Franger, Dr Vanessa Pereira Pimenta, Dr Rita Baddour-Hadjean, Professeur Christine Cachet-Vivier, Professeur Zhumabay Bakenov, Dr Jean-Pierre Pereira-Ramos, Dr Barbara Laïk.

This thesis work was supported by French Embassy in Kazakhstan, Campus France and National Laboratory Astana. I would like to thank Alexandra Thirciur-mens, Attachée de coopération (ex Attachée à la Science et la Technologie), for her support and help with visa and financial support from French Embassy in Kazakhstan.

In conclusion, I obviously want to thank my family, who make everything possible. I want thank my parents, my sisters for their support. I wouldn't be there where I am today, without their help. Finally, I want to thank my wife, my daughter and my son for their endless love, confidence, support and encouragement to me in my life.

CONTENTS

General Introduction	9
CHAPTER 1: Concise overview of the main positive electrode materials for Li- and Na-ion batteries.....	18
1.1 Introduction.....	18
1.2 Positive electrode materials for Li-ion batteries	20
1.3 Positive electrode materials for Sodium-ion batteries	24
1.4 Interest of the V_2O_5 cathode material and objectives of the thesis	35
References	39
CHAPTER 2: Electrochemical and structural study of γ'-V_2O_5 polymorph synthesized by a solution technique as cathode material for Li-ion and Na-ion batteries.....	43
2.1 Electrochemical and structural study of Li insertion in γ'-V_2O_5 polymorph synthesized by a solution technique	43
2.1.1 Introduction.....	43
2.1.2 Synthesis	44
2.1.3 Structural Characterization	46
2.1.4 Electrochemical Study	50
2.1.5 Structural investigation upon discharge-charge.....	53
2.1.6 Cycling properties2.1.7 Conclusion.....	56
Supporting Information	59
References	62
2.2 Improved electrochemical performances of γ'-V_2O_5 prepared by a solution technique as cathode material for Na-ion batteries	64
2.2.1 Introduction.....	64
2.2.2 Synthesis	66
2.2.3 Structural Characterization	67
2.2.4 Electrochemical Study	68
2.2.5 Structural investigation upon discharge-charge.....	69

2.2.6 Cycling properties	75
2.2.7 Kinetic study	76
2.2.8 Conclusion	81
Supporting Information	83
References	86

CHAPTER 3 : New $M_xV_2O_5$ bronzes as competitive cathode materials for sodium-ion batteries ($M = Na, K$).....88

3.1 Introduction.....88

3.2 The sodiated bronze γ - $Na_{0.96}V_2O_5$ as cathode material for Na-ion batteries.....89

3.2.1 Synthesis	90
3.2.2 Structural Characterization	91
3.2.3 Electrochemical study	95
3.2.4 Structural investigation upon discharge-charge.....	95
3.2.5 Cycling Properties.....	96
3.2.6 Conclusion	98
References	99
Publication	102

3.3 Bilayered Potassium Vanadate $K_{0.5}V_2O_5$ as Superior Cathode Material for Na-ion Batteries103

3.3.1 Introduction.....	103
3.3.2 Synthesis	103
3.3.3 Structural characterization	104
3.3.4 Electrochemical study	106
3.3.5 Structural investigation upon discharge-charge.....	109
3.3.6 Conclusion	111
References	113
Publication	114

CHAPTER 4: V₂O₅ polymorphs as cathode material in aqueous rechargeable Zinc batteries.....	115
4.1 Aqueous rechargeable Zinc batteries : a state of the art	115
4.1.1 Introduction.....	115
4.1.2 Aqueous Rechargeable Li-ion batteries	115
4.1.3 Rechargeable Aqueous Zinc-ion batteries	120
4.1.3-1 Mn-based cathode materials	122
4.1.3-2 V-based cathode materials.....	132
4.1.4 Rechargeable Aqueous hybrid-ion batteries	151
4.1.4-1 Water-in-salt hybrid electrolytes.....	154
References	161
4.2 Electrochemical and structural investigation of α-V₂O₅ in hybrid Li⁺/Zn²⁺ aqueous electrolyte for rechargeable aqueous Zn batteries.....	174
4.2.1 Introduction.....	174
4.2.2 Structural Characterization	175
4.2.3 Electrochemical study	178
4.2.4 Structural investigation upon discharge-charge.....	180
4.2.5 Cycling properties	185
4.2.6 Conclusion	188
Supporting Information.....	189
References	192
Publication	194
4.3 Electrochemical and structural investigation of γ'-V₂O₅ in hybrid Li⁺/Zn²⁺ aqueous electrolyte for rechargeable aqueous Zn batteries.....	195
4.3.1 Introduction.....	195
4.3.2 Synthesis	196
4.3.3 Structural characterization	197
4.3.4 Electrochemical study in the 1.6-1V voltage range	201

4.3.5 Structural investigation upon discharge-charge	203
4.3.6 Cycling properties in the 1.6-1V	207
4.3.7 Optimization of the specific capacity	210
4.3.8 Structural Investigation of Zn Li ₂ SO ₄ -ZnSO ₄ γ' -V ₂ O ₅ system at wide voltage range.....	212
4.3.9 Cycling properties at in the 1.6-0.7V	216
4.3.10 Conclusion	219
Supporting Information.....	220
References	226
Publication	228
5. General Conclusion.....	229

General Introduction

The renewable energy integration into the electric grids is one of the key factors for the global economy to continuously grow through “smart industrialization” even under difficult economic circumstances. Almost all the countries currently heavily rely on the fossil fuels for energy, which are non-renewable finite resources that will eventually dwindle, and will become too expensive in the near future. The Government of Kazakhstan supports and encourages the development and investments in this field. The Law “About support of use of renewable energy sources” (June 4, 2009) has been accepted to provide the support and preferences for the development of renewable energy in Kazakhstan. This project directly meets the requirements of this measure.

The major concern restricting a wider application of renewable energy is the energy storage systems (**Figure 1**). Renewable energy sources are intermittent sources and cannot be directly integrated to electric grids without using energy storage systems. However, so far there are no energy storage systems that can satisfy the requirements for renewable energy connection to the grids mainly because of low energy density, poor durability and high cost. Therefore, the high energy density and highly durable storage systems are indispensable. Rechargeable batteries are the promising candidates for such energy storage systems.

Lead-acid rechargeable batteries (LARBs) are mostly used currently in large energy storage (renewable sources). Among other commercialized systems, nickel-cadmium (Ni-Cd), nickel-metal hydride (Ni-MH), lithium-ion batteries (LIBs), and redox flow-cells (RFCs) have been applied. However, these technologies have serious drawbacks such as:

- Ni-Cd and LARBs batteries are toxic due to use of toxic metals, lead and cadmium; in addition, LARBs have low energy density due to the use of heavy lead electrodes and hence poor gravimetric energy density limiting its use to wheeled applications;
- Ni-MH system is expensive due to less available anode material;
- flow cells are complicated and of low energy densities (very large in size) and cannot be considered for the transportation use.
- Compressed air and pumped hydro are low efficient, complicated and have many difficulties to implement.

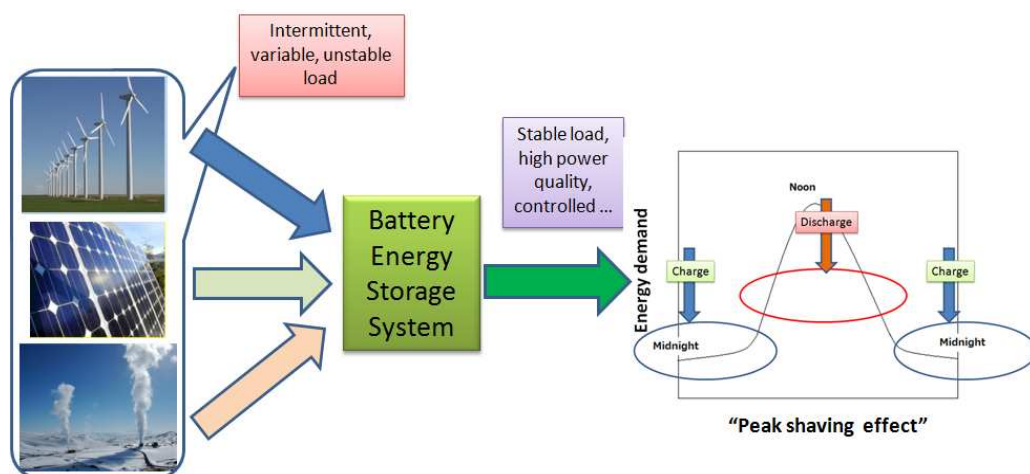


Figure 1. Role and place of Battery Energy Storage System in connecting grids with renewable resources.

One of the most prevalent rechargeable batteries in use today is the Lithium-ion battery (LIB). Lithium-ion batteries (LIBs) are leading power sources for various portable applications, such as laptops, cellular phones and even hybrid-electric and electric cars, due to their high energy density:

- 100 Wh/kg, conventional Graphite/LiCoO₂;
- 250 Wh/kg, Panasonic Hard Carbon/Li(Ni_{0.8}Co_{0.15}Al_{0.05})O₂, used for Nissan *Leaf*;
- 400 Wh/kg, Envia Si-C nanocomposite/Li(Ni_{1/3}Co_{1/3}Mn_{1/3})O₂-Li₂MnO₃, used for Tesla *Roadstar*.

However, the increasing demand for lithium associated with these large-scale applications is expected to increase the price of lithium, affecting reserves as well, as it is not a naturally abundant element in earth crust. For these reasons, other battery technologies are being explored around the world. The unlimited resources of sodium, an alkaline ion with chemical properties similar to lithium (**Table 1**), justify research into the chemistry of insertion of this element into various host networks.

Table 1. A comparison of different ions in the ionic radius, standard potential, theoretical gravimetric and volumetric capacity, crustal abundance and cost, adapted from [1]

Characteristics	Li ⁺	Na ⁺	K ⁺	Zn ²⁺
Ionic radius [Å]	0,76	1,02	1,38	0,74
Standard potential [V] vs SHE	-3,05	-2,71	-2,92	-0,76
Theoretical gravimetric capacity (mAh g ⁻¹)	3829	1165	685	820
Theoretical volumetric capacity (mAh cm ⁻³)	2044	1128	610	5854
Crustal abundance [ppm]	18	23000	21000	79

Cost of metal anode (USD) kg ⁻¹	19,2	3,1	13,1	2,2
---	------	-----	------	-----

Sodium-ion batteries (NIBs) were originally developed in the early 1980s, approximately over the same time period as LIBs [2]. In recent years, NIBs have drawn increasing attention for large-scale energy storage, because of the natural abundance, low cost, and environmental friendliness of sodium [3]. NIBs are considered to be one of the most appealing alternative rechargeable batteries to LIBs. Nonaqueous NIBs, such as the “18,650”-type battery developed within the French framework of RS2E, are characterized by high-energy density (90Wh kg⁻¹) and excellent cycling behavior for up to 2000 cycles [4]. The electrode materials in LIBs provide the best library for research on NIBs because many Na-ion insertion hosts have their roots in Li-ion insertion hosts. Layered Na_xCoO₂ is known as the oldest layered oxide studied as sodium insertion host. The early NIBs were demonstrated by Shacklette et al. with P2- and P3-type Na_xCoO₂ as positive electrode materials in 1988 [5]. Maximum reversible capacities of 140 mAh g⁻¹ for O3, 130 mAh g⁻¹ for a P3 phase sample, and 120 mAh g⁻¹ for P2 phases were observed. Other pioneering work on transition metal chalcogenides (Na_xTiS₂, Na_xTaS₂) has been reported by K.M. Abraham [6], with interesting voltages and reloadability.

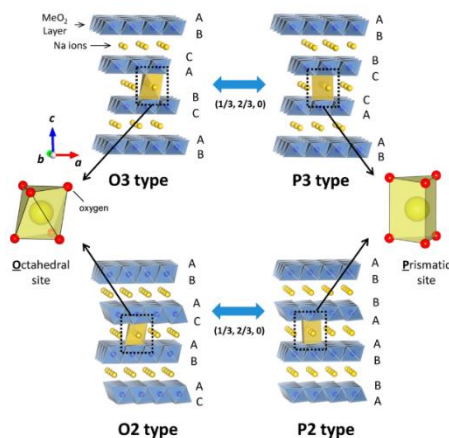


Figure 2. Classification of Na–Me–O layered materials with sheets of edge-sharing MeO₆ octahedra and phase transition processes induced by sodium extraction [7].

In 1993, J. P. Pereira-Ramos et al. studied the insertion of sodium into the layered manganese birnessite [8]. In 1989, the same group became interested in bronze Na_{0.33}V₂O₅ [9], showing interesting specific capacities, of the order of 80 mAh g⁻¹ but an unsatisfactory lifespan.

In 2011 Komaba et al. [10] demonstrated the NaNi_{0.5}Mn_{0.5}O₂ (120 mAh g⁻¹) / hard carbon (240 mAh g⁻¹) system in 1M PC/NaClO₄ electrolyte. The hard-carbon/NaNi_{0.5}Mn_{0.5}O₂ cell,

demonstrates steady cycling performance as next generation secondary batteries and an alternative to Li-ion batteries.

Today SIB technology represents the most serious alternative to lithium, as evidenced by research on this system which is now emerging again globally, with an exponential number of publications since 2010 [7], [11]. A wide variety of positive and negative electrode materials have been proposed. Many oxides have been studied as potential cathodes of SIBs: Na_xCoO_2 [12], $\text{Na}_{2/3}(\text{Fe}_{1/2}\text{Mn}_{1/2})\text{O}_2$ [13], NaMnO_2 [14], NaCrO_2 [15], Na_xVO_2 [16], [17], $\text{Na}_{1.5+y}\text{VO}_3$ [18], $\text{Na}_{0.33}\text{V}_2\text{O}_5$ [9], [19]. However, a good compromise between a satisfactory capacity, a good stability of this capacity in cycling and a high working voltage has not yet been reached.

Since LIBs and NIBs have very close insertion chemistry [7], [20], V_2O_5 has been regarded as a potential cathode material for sodium insertion. A few years ago, our group reported for the first time the structural changes of electrochemically formed $\text{Na}_x\text{V}_2\text{O}_5$ samples at room temperature. After the irreversible electrochemical formation of α' - NaV_2O_5 , 0.8 Na per mole of NaV_2O_5 could be reversibly inserted at a working potential of around 2.0 V, at room temperature (120 mAh g^{-1}), over several tens of cycles [21]. Results in literature suggest that nano-structuring the material is beneficial in terms of capacity and cycling. For instance, V_2O_5 hollow nanospheres exhibit a capacity about 150 mAh g^{-1} for cycling, at 20 mA g^{-1} , in the wide 1.0-4.2 V potential window [22]. Another way to increase V_2O_5 electrochemical performances is to consider polymorphs such as the ϵ' bilayered V_2O_5 [23], [24] or γ' - V_2O_5 . The γ' polymorph, characterized by a puckered layer stacking, has already been studied in our team as cathode material in LIBs [25] and more recently in NIBs [26]. Sodium insertion, occurring at c.a. 3.3 V vs. Na^+/Na ($\sim 0.6 \text{ V}$ vs. NHE), takes place practically at the same potential as lithium insertion. This suggests that Na^+ insertion is facilitated in the γ' polymorph due to its original puckered and flexible structure with a large interlayer spacing (5.02 \AA in γ' - V_2O_5 against 4.37 \AA in α - V_2O_5).

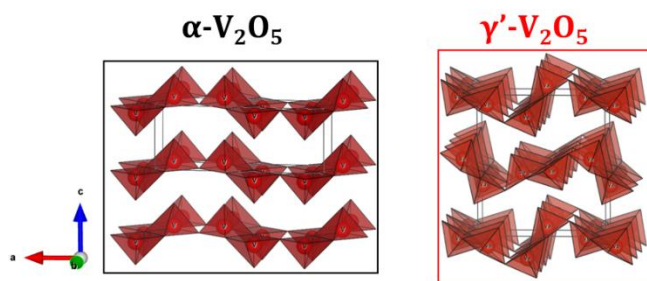


Figure 2. Crystal structure of α - V_2O_5 and γ' - V_2O_5

After a concise overview of the main positive electrode materials for Li- and Na-ion batteries developed in chapter 1, we propose a low temperature solution technique for preparing reduced sized γ' -V₂O₅ in order to optimize its cathode properties in Li-ion and Na-ion batteries (Chapter 2). The polymorph is obtained from a homemade α -V₂O₅ precursor produced through a polyol process, leading easily to an homogeneous pure fine **nanosized** powder. In addition to the evidence for improved electrochemical properties with the polyol γ' -V₂O₅ towards Li and Na, a detailed study by X-ray diffraction and Raman spectroscopy allows us to describe the structural response of the host material.

In Chapter 3 we decided to chemically synthesized the γ' NaV₂O₅ bronze in order to have a positive active material directly usable in Na-ion batteries with the hope of keeping the attractive performances known for the γ' -V₂O₅ oxide. Moreover, we extended our study to the investigation of K_{0.5}V₂O₅ (named KVO) as a potential candidate for cathode material of SIBs.

Lithium-ion technology is a serious contender for smart grids applications and large-scale stationary systems connected to renewable power plants. However, safety of LIBs is one of the major issues which is not solved as yet due to the high risk of flammability of organic electrolytes and the thermal runaway caused by the reactivity of electrode materials with electrolytes. In addition, the cost of LIBs is high. Adopting LIBs technology to aqueous system could solve the mentioned and disadvantages, providing a high performance inexpensive and very safe energy storage system. Therefore, aqueous rechargeable alkali-metal ion (Li⁺, Na⁺, Zn²⁺) batteries are promising alternatives for large scale applications, which could solve several challenges of LIB in terms of safety, low-cost manufacturing conditions, huge improvement of electrolyte conductivity, power improvement, environmentally friendliness, and recycling conditions. In particular, Zinc ion batteries are considered now as the most promising candidates for grid energy storage.

Vanadium oxide (V₂O₅) material was widely investigated for aqueous zinc ion batteries, however according to literature, only few papers can be found related to the Zn²⁺/Li⁺ hybrid electrolyte system (water in salts). Promising results reported for LiFePO₄ by Prof. Z. Bakenov from National Lab in Astana University, prompted us to investigate the V₂O₅ system in same conditions. In addition, little attention has been paid to the structural behavior of cathode materials. Therefore, in Chapter 4, our goal was to deeply examine the electrochemical properties of V₂O₅ polymorphs

(α and γ' phases) in aqueous hybrid electrolyte (Li^+ , Zn^{2+}) focusing on reaction mechanisms, structural evolution upon discharge/charge, and comparison with the obtained results in organic (non-aqueous) electrolyte.

REFERENCES

- [1] B. Tang, L. Shan, S. Liang, and J. Zhou, “Issues and opportunities facing aqueous zinc-ion batteries,” *Energy Environ. Sci.*, vol. 12, no. 11, pp. 3288–3304, 2019, doi: 10.1039/c9ee02526j.
- [2] G. H. Newman and L. P. Klemann, “Ambient Temperature Cycling of an Na - TiS₂ Cell,” *J. Electrochem. Soc.*, vol. 127, no. 10, pp. 2097–2099, Oct. 1980, doi: 10.1149/1.2129353.
- [3] D. Larcher and J.-M. Tarascon, “Towards greener and more sustainable batteries for electrical energy storage,” *Nat. Chem.*, vol. 7, no. 1, pp. 19–29, Jan. 2015, doi: 10.1038/nchem.2085.
- [4] “Research areas | Research | RS2E.” [Online]. Available: <https://www.energie-rs2e.com/en/research-areas>. [Accessed: 13-Oct-2021].
- [5] L. W. Shacklette, T. R. Jow, and L. Townsend, “Rechargeable Electrodes from Sodium Cobalt Bronzes,” *J. Electrochem. Soc.*, vol. 135, no. 11, pp. 2669–2674, 1988, doi: 10.1149/1.2095407.
- [6] K. ABRAHAM, “Intercalation positive electrodes for rechargeable sodium cells,” *Solid State Ionics*, vol. 7, no. 3, pp. 199–212, Oct. 1982, doi: 10.1016/0167-2738(82)90051-0.
- [7] N. Yabuuchi, K. Kubota, M. Dahbi, and S. Komaba, “Research Development on Sodium-Ion Batteries,” *Chem. Rev.*, vol. 114, no. 23, pp. 11636–11682, Dec. 2014, doi: 10.1021/cr500192f.
- [8] S. Bach, J. P. Pereira-Ramos, and N. Baffier, “Electrochemical sodium insertion into the sol-gel birnessite manganese dioxide,” *Electrochim. Acta*, vol. 38, no. 13, pp. 1695–1698, 1993, doi: 10.1016/0013-4686(93)85063-5.
- [9] S. Bach, N. Baffier, J. P. Pereira-Ramos, and R. Messina, “Electrochemical sodium intercalation in Na_{0.33}V₂O₅ bronze synthesized by a sol-gel process,” *Solid State Ionics*, vol. 37, no. 1, pp. 41–49, 1989, doi: 10.1016/0167-2738(89)90285-3.
- [10] S. Komaba *et al.*, “Electrochemical Na insertion and solid electrolyte interphase for hard-carbon electrodes and application to Na-ion batteries,” *Adv. Funct. Mater.*, vol. 21, no. 20, pp. 3859–3867, 2011, doi: 10.1002/adfm.201100854.
- [11] “Batterie sodium-ion: une révolution en marche | CNRS Le journal.” [Online]. Available: <https://lejournel.cnrs.fr/articles/batterie-sodium-ion-une-revolution-en-marche>. [Accessed:

- 10-Oct-2021].
- [12] R. Berthelot, D. Carlier, and C. Delmas, “Electrochemical investigation of the P2–Na_xCoO₂ phase diagram,” *Nat. Mater.*, vol. 10, no. 1, pp. 74–80, Jan. 2011, doi: 10.1038/nmat2920.
 - [13] N. Yabuuchi *et al.*, “P2-type Na_x[Fe_{1/2}Mn_{1/2}]O₂ made from earth-abundant elements for rechargeable Na batteries,” *Nat. Mater.*, vol. 11, no. 6, pp. 512–517, Jun. 2012, doi: 10.1038/nmat3309.
 - [14] X. Ma, H. Chen, and G. Ceder, “Electrochemical Properties of Monoclinic NaMnO₂,” *J. Electrochem. Soc.*, vol. 158, no. 12, p. A1307, 2011, doi: 10.1149/2.035112jes.
 - [15] S. Komaba, C. Takei, T. Nakayama, A. Ogata, and N. Yabuuchi, “Electrochemical intercalation activity of layered NaCrO₂ vs. LiCrO₂,” *Electrochem. commun.*, vol. 12, no. 3, pp. 355–358, Mar. 2010, doi: 10.1016/j.elecom.2009.12.033.
 - [16] M. Guignard, C. Didier, J. Darriet, P. Bordet, E. Elkaïm, and C. Delmas, “P2-Na_xVO₂ system as electrodes for batteries and electron-correlated materials,” *Nat. Mater.*, vol. 12, no. 1, pp. 74–80, 2013, doi: 10.1038/nmat3478.
 - [17] D. Hamani, M. Ati, J. M. Tarascon, and P. Rozier, “Na_xVO₂ as possible electrode for Na-ion batteries,” *Electrochem. commun.*, vol. 13, no. 9, pp. 938–941, 2011, doi: 10.1016/j.elecom.2011.06.005.
 - [18] G. Venkatesh, V. Pralong, O. I. Lebedev, V. Caignaert, P. Bazin, and B. Raveau, “Amorphous sodium vanadate Na_{1.5} + yVO₃, a promising matrix for reversible sodium intercalation,” *Electrochem. commun.*, vol. 40, pp. 100–102, 2014, doi: 10.1016/j.elecom.2013.11.004.
 - [19] H. Liu, H. Zhou, L. Chen, Z. Tang, and W. Yang, “Electrochemical insertion/deinsertion of sodium on NaV₆O₁₅ nanorods as cathode material of rechargeable sodium-based batteries,” *J. Power Sources*, vol. 196, no. 2, pp. 814–819, 2011, doi: 10.1016/j.jpowsour.2010.07.062.
 - [20] F. Li, Z. Wei, A. Manthiram, Y. Feng, J. Ma, and L. Mai, “Sodium-based batteries: from critical materials to battery systems,” *J. Mater. Chem. A*, vol. 7, no. 16, pp. 9406–9431, 2019, doi: 10.1039/C8TA11999F.
 - [21] D. Muller-Bouvet, R. Baddour-Hadjean, M. Tanabe, L. T. N. Huynh, M. L. P. Le, and J. P. Pereira-Ramos, “Electrochemically formed α'-NaV₂O₅: A new sodium intercalation

- compound,” *Electrochim. Acta*, vol. 176, pp. 586–593, 2015.
- [22] D. W. Su, S. X. Dou, and G. X. Wang, “Hierarchical orthorhombic V₂O₅ hollow nanospheres as high performance cathode materials for sodium-ion batteries,” *J. Mater. Chem. A*, vol. 2, no. 29, pp. 11185–11194, 2014, doi: 10.1039/C4TA01751J.
- [23] S. Tepavcevic *et al.*, “Nanostructured bilayered vanadium oxide electrodes for rechargeable sodium-ion batteries,” *ACS Nano*, vol. 6, no. 1, pp. 530–538, 2012, doi: 10.1021/nn203869a.
- [24] R. Baddour-Hadjean, M. Safrany Renard, N. Emery, L. T. N. Huynh, M. L. P. Le, and J. P. Pereira-Ramos, “The richness of V₂O₅ polymorphs as superior cathode materials for sodium insertion,” *Electrochim. Acta*, vol. 270, pp. 129–137, 2018, doi: 10.1016/j.electacta.2018.03.062.
- [25] M. Safrany Renard, R. Baddour-Hadjean, and J. P. Pereira-Ramos, “Kinetic insight into the electrochemical sodium insertion-extraction mechanism of the puckered γ' -V₂O₅ polymorph,” *Electrochim. Acta*, vol. 322, p. 134670, 2019, doi: <https://doi.org/10.1016/j.electacta.2019.134670>.
- [26] M. S. Renard, N. Emery, R. Baddour-Hadjean, and J. P. Pereira-Ramos, “ γ' -V₂O₅: A new high voltage cathode material for sodium-ion battery,” *Electrochim. Acta*, vol. 252, pp. 4–11, 2017, doi: 10.1016/j.electacta.2017.08.175.

CHAPTER 1

Concise overview of the main positive electrode materials for Li- and Na-ion batteries

1.1 Introduction

Energy-storage devices are now powering our world due to concerning the climate change. Sustainable energy resources such as solar and wind have entered the global spotlight, triggering the search for reliable, low-cost electrochemical energy storage. An ideal energy-storage device that is characterized by high capacity, fast charge/discharge capability, safety, environmental friendliness, and low cost is of vital important for today's society.

Due to their high energy density, Lithium-Ion Batteries (LIBs) are the best candidates among all batteries to power various portable equipment and large-scale applications like electric vehicle. In addition, the Lithium-ion technology is a serious contender for smart grids applications and large-scale stationary systems connected to renewable power plants.

Batteries convert chemical potential energy into usable electrical energy. Basically, battery have three main components: positive electrode (cathode) containing Lithium metal oxides, negative electrode (anode) comprised of graphite and the electrolyte (containing lithium ions) (**Figure 1**).

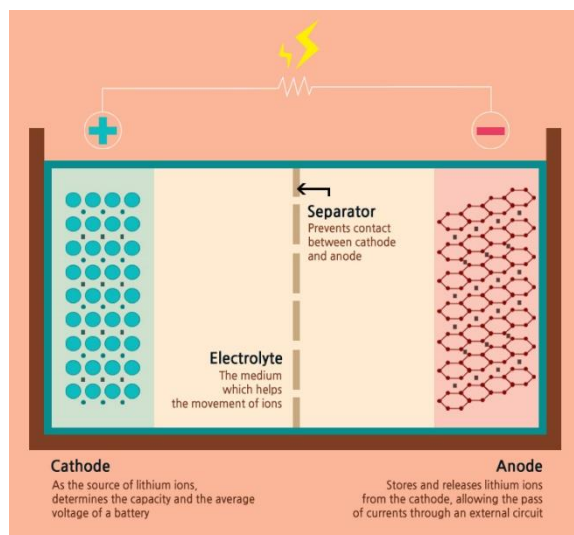


Figure 1. Schematic illustration of Li-ion battery

Lithium-ion batteries usually use lithium cobalt oxide (LiCoO_2) as positive electrode and graphite (C) as negative electrode. During the charge, lithium ions and electrons move from positive electrode to the negative electrode. During discharge, electrons go through the external circuit and lithium-ions moves through the electrolyte (**Figure 2**). The essential characteristic of this system is its operation ensured by a reversible transfer of lithium ions between the positive and negative electrodes by using of an ionic conductive electrolyte, this is the principle of so-called “rocking-chair” batteries. or "lithium-ion".

The electrochemical reaction follows below:

On positive side: $\text{LiCoO}_2 \leftrightarrow \text{Li}_{1-x}\text{CoO}_2 + x \text{Li}^+ + x \text{e}^-$

On negative side: $6\text{C} + x \text{Li}^+ + x \text{e}^- \leftrightarrow \text{Li}_x\text{C}_6$

Overall reaction: $\text{LiCoO}_2 + 6\text{C} \leftrightarrow \text{Li}_x\text{C}_6 + \text{Li}_{1-x}\text{CoO}_2$

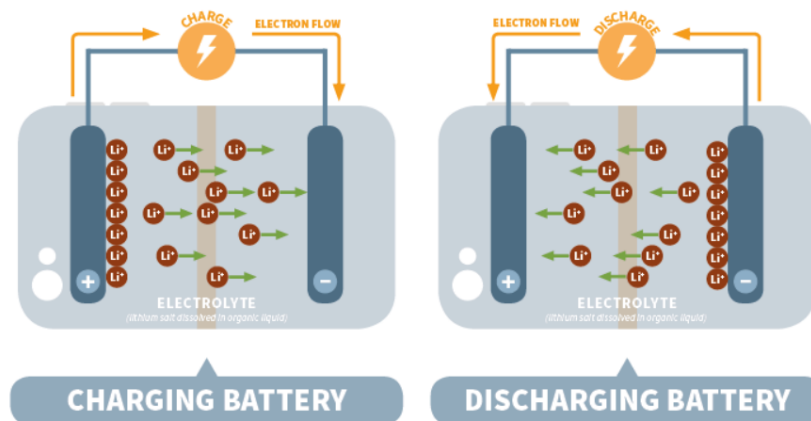


Figure 2. Schematic illustration of lithium insertion/extraction mechanism during discharge/charge process

The energy delivered by such a battery corresponds to the change in free enthalpy ΔG of this reaction. The operating voltage of the most popular LiCoO_2 / graphite system with an organic electrolyte is close to 3.8 V. Generally speaking, the stable form of the positive electrode material is its reduced form. Therefore, the battery must be charged before use.

In a lithium-ion battery, the choice of positive and negative electrode materials is critical to the energy and power density characteristics. The main criteria for electrode material: stable electrochemical and structural reversibility, high capacity and ionic conductivity. Furthermore, to

be integrated into marketable systems, the electrode materials must meet the following specifications: low cost, easy to use industrially non-toxic and safe. The voltage-capacity diagram in **Figure 3** illustrates the issue in solid-state chemistry of the appropriate choice of a redox couple and a structure in order to modulate the voltage and the capacity of lithium ions in the structure [1].

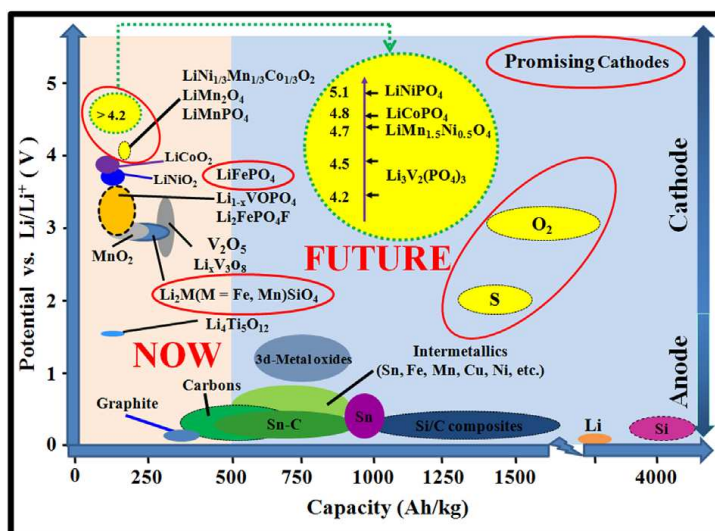


Figure 3. Electrode materials and electrochemical performance in LIB technology [1]. Copyrights reserved

1.2 Positive electrode materials for Li-ion batteries

The materials of positive electrodes have a solid host network, which can intercalate/deintercalate the guest ions (Li^+). Metal chalcogenides, transition metal oxides, and polyanion compounds were studied as intercalation cathode material for Li ion batteries. However, most of the research works are based on the transition metal oxides and polyanions, due to their high operating voltage and energy capability. Typically, these materials have specific capacity of 100-200 mAh/g and 3 – 5 V working voltage (vs. Li/Li^+). In Li-ion batteries, intercalation compounds can be classified by crystal structure: layered, spinel, olivine and tavorite (**Figure 4**).

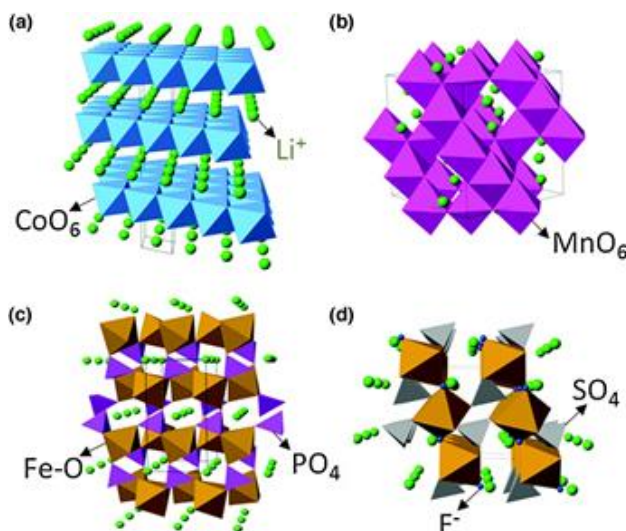


Figure 4. Crystal structure of intercalation cathodes: (a) layered (LiCoO_2), (b) spinel (LiMn_2O_4), (c) olivine (LiFePO_4) and (d) tavorite (LiFeSO_4F) [2]

Layered **LiCoO_2 (LCO)** is the first cathode material which widely used in portable electronics. Mizushima and Goodenough et al. introduced Li_xCoO_2 (LCO) with an ordered rock-salt structure as a new cathode material for batteries in the early 1980s. The advantages of LCO are high energy density, good electrical conductivity, high operating voltage (~ 4.0 V vs Li/Li^+) and low self-discharge. The octahedral array of edge-shared CoO_6 plays the main role in good conductivity. In addition, the LCO has high theoretical capacity (274 mAh/g) when 1 mol of Li^+ is extracted. However, the major limitations of LCO are high cost, toxicity, instability of the material at complete charged state and limited practical capacity (~ 135 mAh/g) have prevented its large-scale application in transportation.

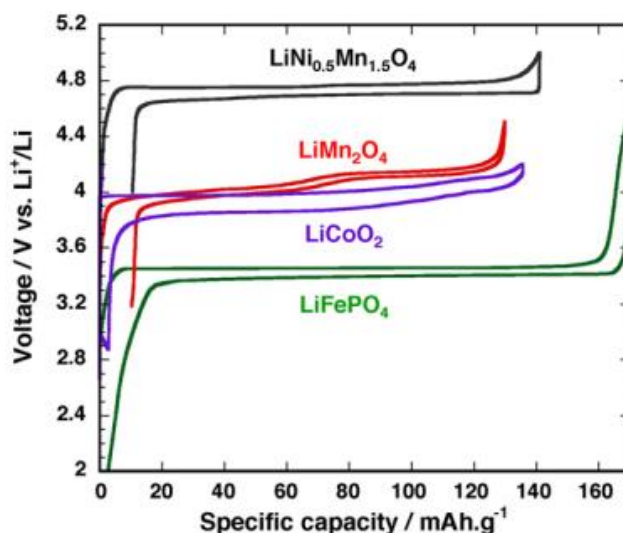


Figure 5. Discharge-charge profile of positive electrodes at C/5 [3]

LiNiO₂ (LNO) has same crystal structure with LCO, gains high theoretical capacity (275 mAh/g) and lower cost in comparison to Co. The main benefit of LNO from LCO, it doesn't undergo changes in the lattice oxygen at complete discharged state. However, the drawback of LNO is the synthesis of the material with pure Ni³⁺ element at high temperature, due to the instability of Ni³⁺ at high temperatures (>250 °C) leading to Ni²⁺ and disordering between Li and Ni sites. It was also found that LNO undergoes phase transformation at different state of charge. The LNO can be electrochemically activated when it exists as a trigonal structure, however, when 0.5 < x < 0.75, LNO transforms to monoclinic phase, which leads to fast capacity fading. The partial substitution of Ni and Co was to effective way to stabilize the structure.

LiNi_{0.8}Co_{0.15}Al_{0.05}O₂ (NCA) cathode was used in Panasonic batteries for Tesla EVs. The NCA has high specific capacity (~200 mAh/g) and long cycle life. However, it was reported that at elevated temperature (40 – 70 °C) capacity fading can be observed due to the solid electrolyte interphase (SEI) growth and formation of microcracks at grain boundaries [2].

LiMnO₂ (LMO) can replace the LCO due to the high theoretical capacity (~285 mAh/g). In addition, LMO is less expensive and environmentally benign compared to LCO and LNO. The structure of LMO is not identical to the layered O3-structure as it crystalizes in orthorhombic phase (*Pmmm* space group). However, LMO has a tendency to change crystal structure, from layered to spinel structure (LiMn₂O₄), resulting poor cyclability. In addition, Mn dissolution occurs when

Mn³⁺ undergoes disproportionation reaction to form Mn²⁺ and Mn⁴⁺, and this process is observed for all cathodes containing Mn.

LiNi_{0.5}Mn_{0.5}O₂ (NMO) could be attractive cathode material, due to the similar energy density to LCO. The presence of Ni allows higher Li extraction. However, cation mixing cause the low Li diffusion resulting on rate capability. The addition of Co in NMO can enhance the structural stability of material. **LiNi_{0.33}Co_{0.33}Mn_{0.33}O₂ (NCM or NMC)** has similar operating voltage and less cost due to the lower content of Co and widely used in battery market. It benefits from the high charge capacity of LiNiO₂, rate capability of LiCoO₂ and structural stability of Mn⁴⁺. The microporous NMC exhibits high specific capacity of 234 mAh/g and stable cyclability at 50 °C. On the one hand, the presence of Co³⁺ appears to be useful in suppressing the structural distortion stemming from the Ni³⁺ Jahn–Teller effect by disrupting the Ni²⁺/Mn⁴⁺ cation ordering to some extent.

Spinel **LiMn₂O₄ (also LMO)** has several benefits, like abundance, low cost and environmentally friendly. Li occupies tetrahedral (8a) sites and Mn located in octahedral (16a) sites of the cubic arrangement of O²⁻ lattice in spinel structure. Li ions can migrate through vacant tetrahedral (8a) and octahedral sites (16c), offers 3D diffusion network. LMO has two operating voltage plateau: at high voltage ~4.0 V Li intercalate/deintercalate from/into tetrahedral (8a) sites, maintaining the cubic structure, at lower voltage (~3.0 V) Li⁺ migrates from/into the vacant (16c) sites, which leads to the phase transition from cubic to tetragonal structure, resulting the capacity fading. On the other side, Mn disproportionation reaction ($2\text{Mn}^{3+} \rightarrow \text{Mn}^{2+} + \text{Mn}^{4+}$), causing the dissolution of the cathode into the electrolyte with LiPF₆ salt (contains HF traces).

Another class of cathodes is olivine type **LiFePO₄ (LFP)**. In 1997 by Padhi and Goodenough et al., demonstrated the reversible Li extraction/insertion with operating plateau ~3.45 V vs. Li/Li⁺. LFP is the polyanion material crystallized in orthorhombic system (*Pnma* space group) with slightly distorted hexagonally close-packed (HCP) oxygen arrangement. P is located in tetrahedral sites, whereas Li⁺ and Fe²⁺ occupy octahedral sites. The strong P–O bond in (PO₄)³⁻ is the key factor that stabilizes the whole olivine structure, reducing O₂ release during cycling. However, LFP suffers from low Li⁺ diffusion and electronic conductivity.

Other olivine structures include **LiMnPO₄ (LMP)** which offers ~0.4 V higher average voltage compared to olivine LFP (Table 1), reach higher specific energy, but it suffers from lower conductivity [4]. LiCoPO₄, LiNi_{0.5}Co_{0.5}PO₄, and LiMn_{0.33}Fe_{0.33}-Co_{0.33}PO₄ (LCP, NCP, MFCP) have also been developed and shown promising results, but further improvements in power, stability and energy density are required.

Novel materials like **Li₃V₂(PO₄)₃ (LVP)** or **LiFeSO₄F (LSF)** exhibits high operating voltage and specific capacity of 151 mAh/g. In comparison to LVP, LSF has better electronic/ionic conductivity and can be prepared from abundant resources. The characteristics of different cathode materials are shown in **Table 1**.

Table 1. Electrochemical characteristics of positive electrodes for Li-ion batteries, adapted from [2]

Crystal structure	Compound	Specific Capacity theoretical/ experimental (mAh/g)	Average voltage (V)	Level of development
Layered	LiCoO ₂	274/148	3.8	Commercialized
	LiNiO ₂	275/150	3.8	Research
	LiMnO ₂	285/140	3.3	Research
	LiNi _{0.33} Mn _{0.33} Co _{0.33} O ₂	280/160	3.7	Commercialized
	LiNi _{0.8} Co _{0.15} Al _{0.05} O ₂	279/199	3.7	Commercialized
	Li ₂ MnO ₃	458/180	3.8	Research
Spinel	LiMn ₂ O ₄	148/120	4.1	Commercialized
	LiCo ₂ O ₄	142/84	4.0	Research
Olivine	LiFePO ₄	170/165	3.4	Commercialized
	LiMnPO ₄	171/168	3.8	Research
	LiCoPO ₄	167/125	4.2	Research
Tavorite	LiFeSO ₄ F	151/120	3.7	Research
	LiVPO ₄ F	156/129	4.2	Research

1.3 Positive electrode materials for Sodium-ion batteries

As we have seen previously, Li-ion battery technology is the most efficient battery system, and its growth is explained by its ability to meet different applications from the smallest module for sensors, microelectronics to computers. and now to electric vehicles. However, the increasing

demand for lithium associated with these large-scale applications is expected to increase the price of lithium, affecting reserves as well, as it is not a naturally abundant element in earth crust (Table 2). Sodium resources are more globally available and include Na_2CO_3 , Na_2SO_4 and NaCl , which are all low-cost and highly abundant salts that can be obtained from minerals and brine (**Table 2**).

Table 2. A comparison of different ions in the ionic radii, abundance, price etc.

	Abundance /1000 ppm	Price (euros kg^{-1})	Mass/ e^- (g)	Ionic radii (\AA)	E° (V vs. Li^+/Li)
Li	0,01	6,40	6,94	0,76	0,00
Na	26	0,22	23	1,02	0,33

However, there are some main differences between these systems. Na^+ ions (1.02 \AA) are larger compared to Li^+ ions (0.76 \AA), which affects the phase stability, transport properties, and interphase formation [5]. Sodium is also heavier than lithium (23 g/mol compared to 6.9 g/mol) and has a higher standard electrode potential (-2.71 V vs. SHE as compared to -3.02 V vs. SHE for lithium); thus, SIBs will have less energy density. However, the weight of cyclable Li or Na is a small fraction of the mass of the components, and the capacity is determined primarily by the characteristics of the host structures that serve as electrodes. The research investigation in Na-ion batteries have been built and evaluated with hard-carbon anodes and cathode materials selected from layered transition metal oxides, transition metal fluorophosphates, and Prussian blue and its analogues (**Figure 6**).[6]–[10]

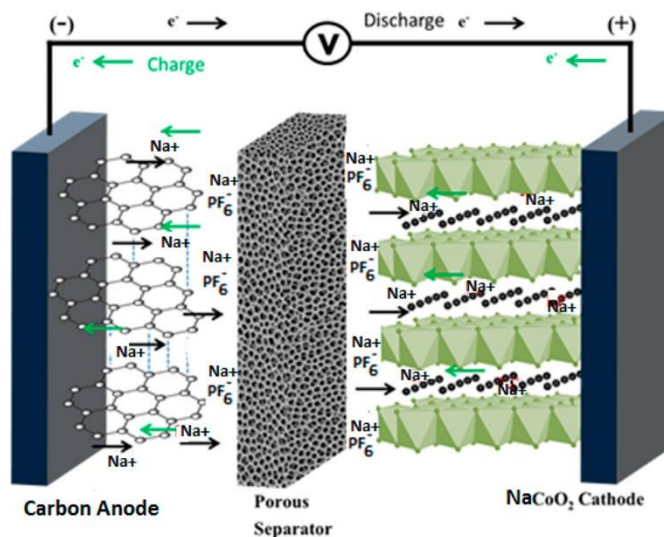
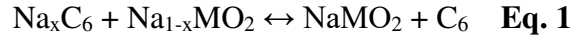


Figure 6. Schematic illustration of Na-ion battery

Layered transition metal dioxides, NaMO_2 , where $M = \text{Fe, Ni, Mn, Co}$ etc., exist in O3 and P2 crystallographic versions. In the O3- NaMO_2 phase, Na resides in octahedral sites, while in the P2-phase Na is in prismatic sites. The electrode reactions in a Na-ion battery utilizing hardcarbon (C_6) anode and a layered transition metal oxide, NaMO_2 , cathode is depicted in eq 1. The discharged electrodes are on the right-hand side of eq 1.



The positive electrode materials are mainly categorized into oxides, polyanions such as phosphates, pyrophosphates, fluorosulfates, oxychlorides, and NASICON (Na super ionic conductor) types, and organic compounds (**Figure 7**). These materials exhibit stable structural changes during deintercalation/intercalation of Na^+ ions with stable cyclability. However, sodiated transition metal materials are highly hygroscopic, even with brief exposure to air,[11] and caution is necessary to avoid hydration of the material, particularly the surface, which results in formation of NaOH that degrades electrode performance due to its insulating properties. Therefore, the preparation of sodiated cathode materials and batteries requires meticulous handling and moisture-free conditions.

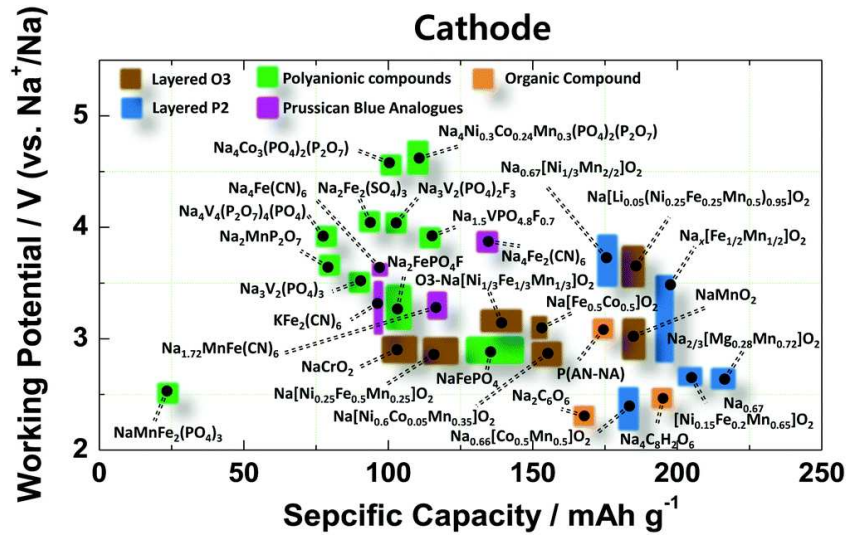


Figure 7. Positive electrode materials for Na-ion batteries [5]

The NaCoO_2 cathode, like LiCoO_2 , is initially brought into the Na-ion cell in the discharged state, and the cell is activated by charging first to form the Na intercalated anode and Na deintercalated cathode in the fully charged cell. The charge and discharge profile of $\text{Li/Li}_{1-x}\text{CoO}_2$ and

Na/Na_{1-x}CoO₂ half-cells compared in **Figure 8** reveals stepwise voltage profiles for the Na cell [12].

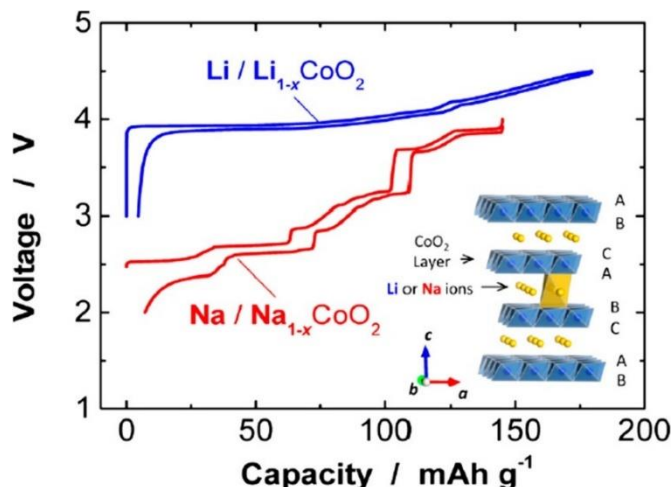


Figure 8. Comparison of discharge/charge curves of Li/LiCoO₂ and Na/NaCoO₂ half-cells.

Komaba et al. [13] have shown that the NaNi_{0.5}Mn_{0.5}O₂ (120 mAh g⁻¹) / hard carbon (240 mAh g⁻¹) system in 1M PC / NaClO₄ electrolyte (**Figure 9**). NaNi_{0.5}Mn_{0.5}O₂/hard carbon cells at current densities between 25 and 300 mA g⁻¹ over more than 80 cycles with specific capacities ranging between 150 and 200. mAh g⁻¹ [13]. The structural change and passivation for hard-carbon are investigated to study the reversible sodium insertion. The hard-carbon/NaNi_{0.5}Mn_{0.5}O₂ cell, demonstrates steady cycling performance as next generation secondary batteries and an alternative to Li-ion batteries.

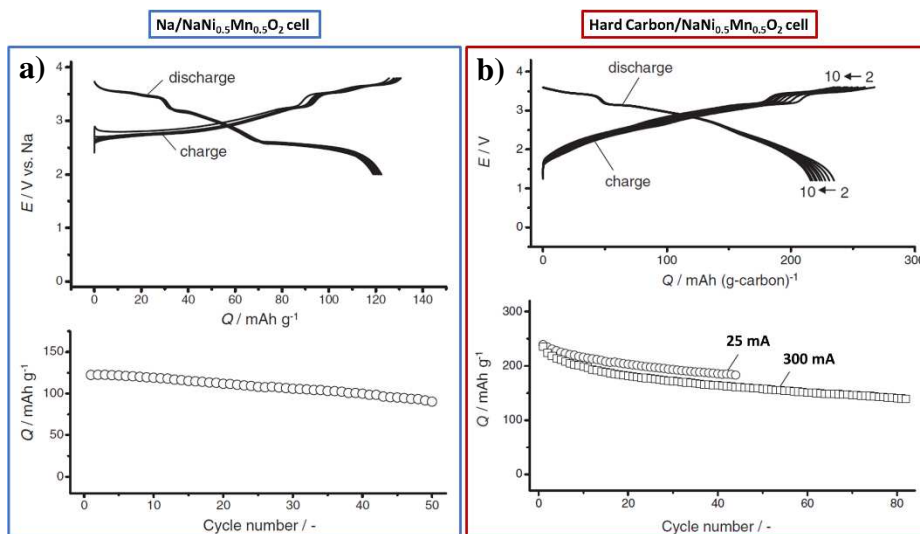


Figure 9. Discharge/charge profile and cyclability of Na/NaNi_{0.5}Mn_{0.5}O₂ and HC/ NaNi_{0.5}Mn_{0.5}O₂ cell at various C-rate

In the family of layered oxides, it is necessary to underline the performances of the compounds NaFeO_2 , NaCoO_2 , $\text{Na}_{2/3}\text{CoO}_2$, $\text{NaFe}_{1/2}\text{Co}_{1/2}$ and $\text{Na}_{2/3}\text{Fe}_{1/2}\text{Mn}_{1/2}\text{O}_2$ (**Figures 10 and 11**). Specific capacities between 80 and 150 mAh g^{-1} are obtained depending on the composition [6], [14]. These are already interesting capacities compared to lithium systems and available at high voltages. As illustrated in **Figure 10**, it is remarkable to note that significant capacities are still available at high C rate (120 mAh g^{-1} at 20C for the compound $\text{NaFe}_{0.5}\text{Co}_{0.5}\text{O}_2$ for example) [6], [14].

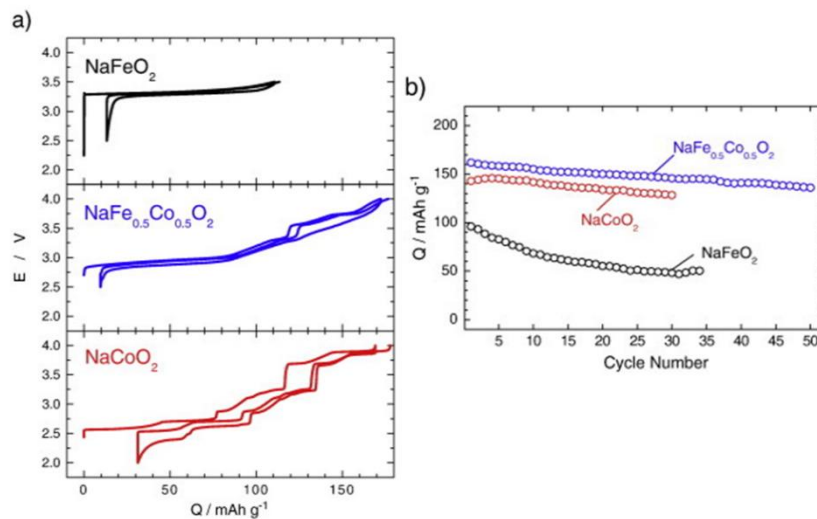


Figure 10. Comparison of the performances of Na/NaFeO₂, Na/NaCoO₂ and Na/NaFe_{1/2}Co_{1/2}O₂ cells [14].

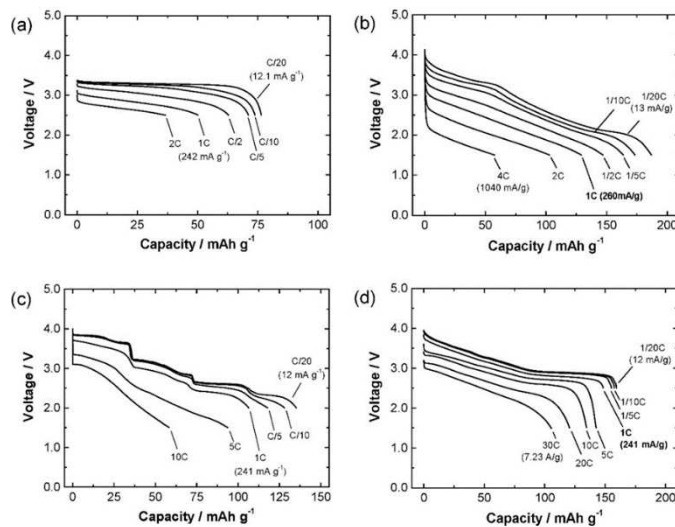


Figure 11. Comparison of the performances of (a) Na/NaFeO₂, (b) Na/Na_{2/3}Fe_{1/2}Mn_{1/2}O₂, (c) Na/Na_{2/3}CoO₂, et (d) Na/NaFe_{1/2}Co_{1/2}O₂ [6]

The layered $\text{NaNi}_{1/3}\text{Co}_{1/3}\text{Mn}_{1/3}$ (Na-NMC), isostructural of NaCoO_2 , and which corresponds to its Li-NMC analogue for the Li-ion battery, has also been studied [15]. Reversible extraction of 0.5

sodium ion per mole is possible, which provides capacity of 120 mAh g^{-1} in the voltage range of 3.75 V and 2 V with phase transformation (mono and two-phase) involving a reversible hexagonal-monoclinic transition for 30 cycles at C/10. In addition, this material exhibits good rate-capability with specific capacity of 80 mAh g^{-1} at 1C (Figure 12). The maximum voltage cannot exceed 4 V in an EC / DMC NaClO_4 electrolyte.

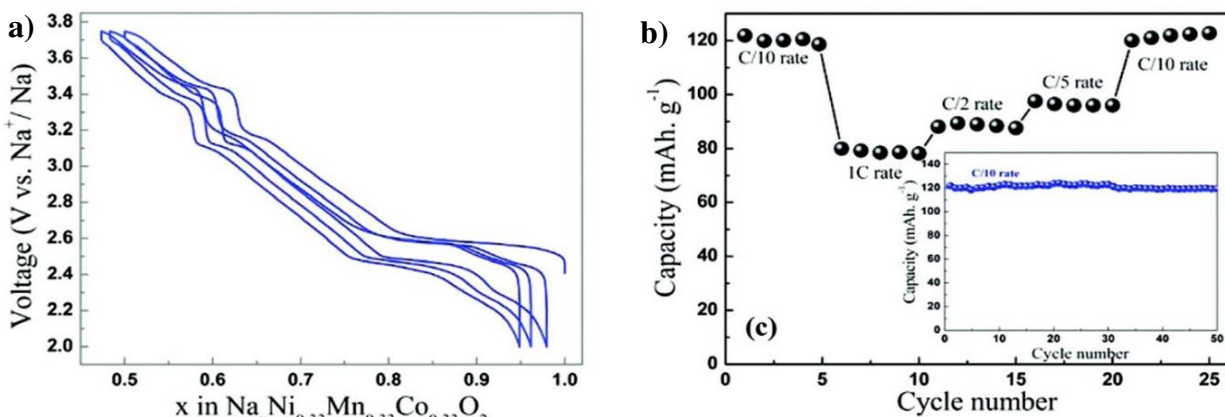


Figure 12. Discharge/charge profile of $\text{NaNi}_{1/3}\text{Co}_{1/3}\text{Mn}_{1/3}$ at 0.1C and rate-capability.

C. Johnson et al. [56] demonstrated attractive performance for a full Na-ion cell using hard carbon and the layered $\text{NaNi}_{1/3}\text{Fe}_{1/3}\text{Mn}_{1/3}\text{O}_2$: working voltage of 2.75 V vs. Na^+/Na for a capacity of 100 mAh g^{-1} over 150 cycles at 1C (Figure 12)

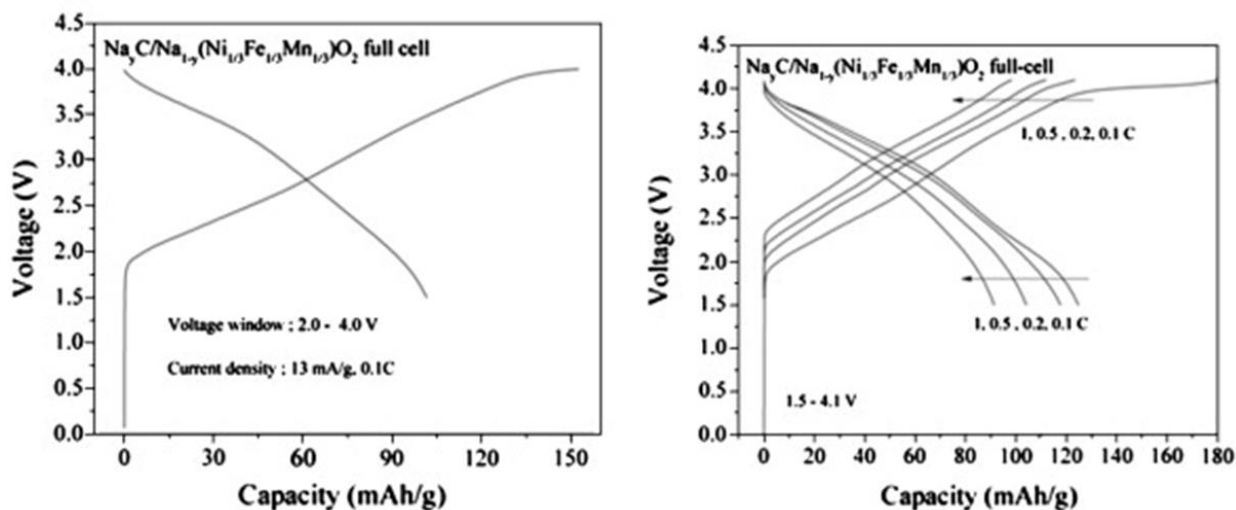


Figure 12. The performance of $\text{Na}_3\text{C}/\text{Na}_{1-y}(\text{Ni}_{1/3}\text{Fe}_{1/3}\text{Mn}_{1/3})\text{O}_2$; ($\sim 0 < y < 0.7$ (charge)) [16].

Vondrak et al. reported electrochemical sodiation at RT in γ -MnO₂ (tunnel structure) with a maximum ratio of Na/Mn = 0.16/0.17 [17]. Besides, interesting results were obtained with 3D λ -MnO₂ with spinel structure. Indeed, electrochemical investigation demonstrated that ≈ 0.6 Na⁺ ions can be inserted at RT. In addition, sol-gel prepared birnessite pointed big interest as intercalation material for Li, Na-ion batteries [18]. The main advantage of the material is low cost due to the manganese. Zhou et al. reported the electrochemical performance of Na_{0.33}MnO_{1.66} (dehydrated) treated at 200 °C [19]. However, Nam et al. underline the importance of inter-sheet water molecules for rate-capability of Na_{0.71}MnO₂ * 0.25H₂O with large interlayer space of 7.16 Å (Figure 13) [20]. The hydrated material exhibits higher capacity at C/15 over 30 cycles (Figure 13 a-b). At 2C/5 hydrated material reveals 120 mAh g⁻¹ and reaches 100 mAh g⁻¹ after 100 cycles (Figure 13c). The rate capability was improved in comparison to anhydrous compound (Figure 13d).

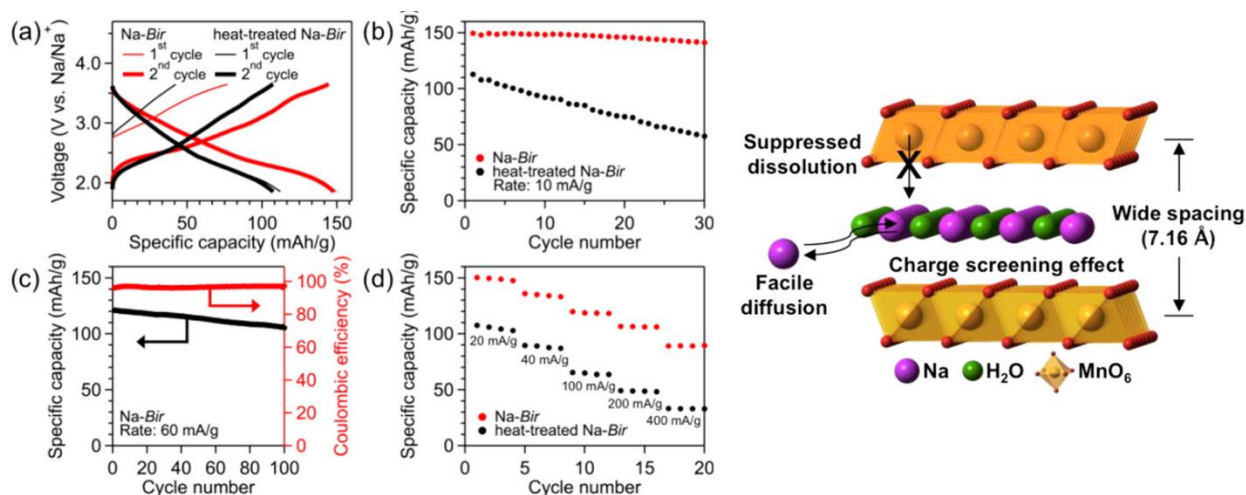


Figure 13. Cycle performance of hydrated and anhydrous Na-Bir (a), (b) at C/15; (c) at 2C/5; (d) rate-capability

Na₂FePO₄F is the promising cathode material has been studied for Na-ion batteries [21]–[23]. The synthesis carried out by solid-state with addition of carbon precursors for coating [23]. The electrochemical properties are illustrated in Figure 14. Na₂FePO₄F gains high working potential ≈ 3 V (vs. Na⁺/Na) with specific capacity 110 mAh g⁻¹, which corresponds to 90% of theoretical capacity (Fe²⁺/Fe³⁺ redox). Two well-defined plateaus can be observed at 3.06 and 2.91 V with low polarization (Figure 14).

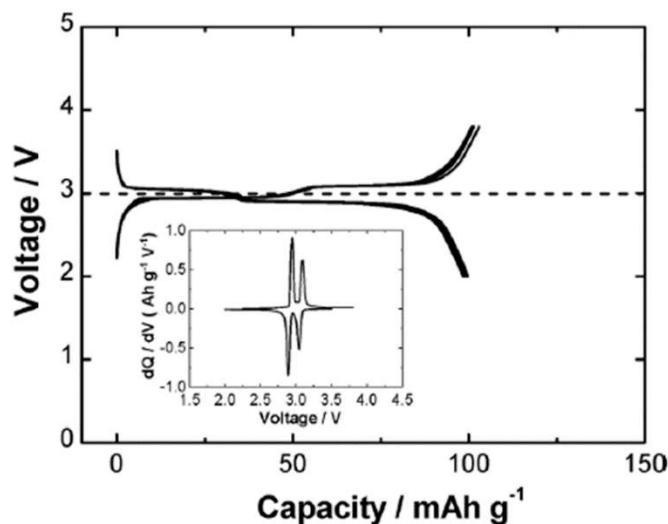


Figure 14. Discharge-charge profile of Na/ $\text{Na}_2\text{FePO}_4\text{F}$ at current density of 6.2 mA g^{-1} [23]

The attractive electrochemical characteristics was obtained with $\text{NaV}(\text{PO}_4)\text{F}$ by Barker et al. [24]. The material prepared by mixing NaF and VPO_4 with two polymorphs: monoclinic at low temperature and tetragonal phase at high temperature. The specific capacity of 100 mAh g^{-1} reached is based on $\text{V}^{4+}/\text{V}^{3+}$ redox couple with working voltage of 3.7 V . However, capacity decay of 50% after 30 cycles can be observed, due to the irreversible reactions on the surface of carbon anode. The cycling stability can be improved by substitution of vanadium with aluminum or chromium at low temperature.

Even more recently, $\text{Na}_3\text{V}_2(\text{PO}_4)_3$ (NASICON type) [25] and $\text{Na}_3\text{V}_2(\text{PO}_4)_2\text{F}_3$ [26] materials with polyanionic structure (**Figure 15**) were described. The electrochemical performance of $\text{Na}_3\text{V}_2(\text{PO}_4)_3$ exhibits good capacity retention at high C-rate, 50% of initial capacity still available after 30 000 cycles at 40°C (**Figure 16a**) [25]. The $\text{Na}_3\text{V}_2(\text{PO}_4)_2\text{F}_3$ exhibits specific capacity of 120 mAh g^{-1} with two working plateaus at 4.1 and 3.6 V (**Figure 16b**) [26].

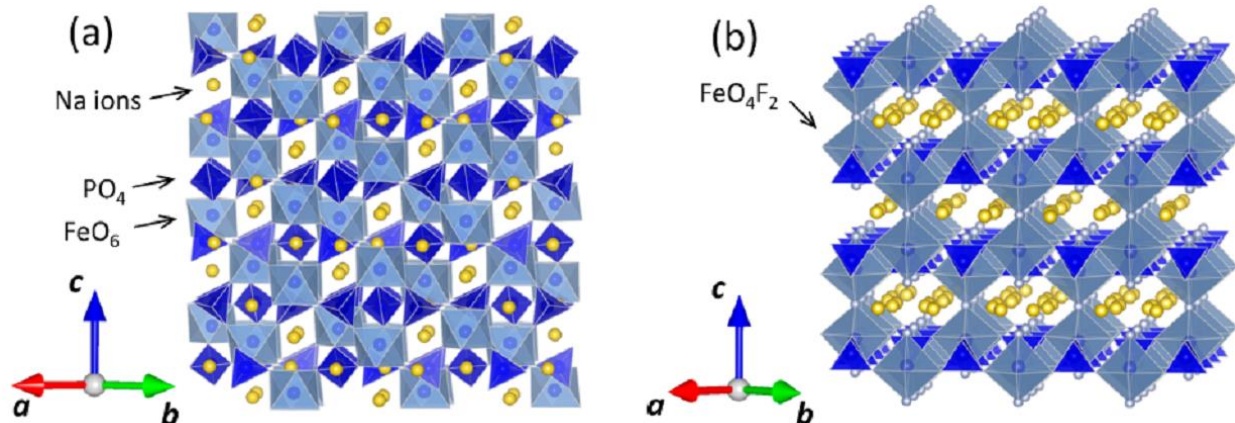


Figure 15. Structures of (a) $\text{Na}_3\text{V}_2(\text{PO}_4)_3$ (b) $\text{Na}_3\text{V}_2(\text{PO}_4)_2\text{F}_3$ [6].

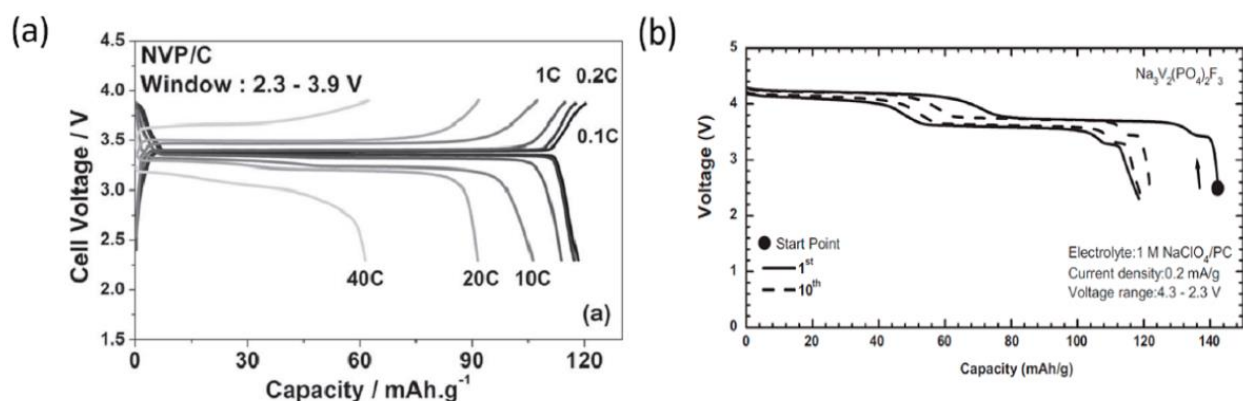


Figure 16. Comparison of performances of the (a) $\text{Na}_3\text{V}_2(\text{PO}_4)_3$ [25]; (b) $\text{Na}_3\text{V}_2(\text{PO}_4)_2\text{F}_3$ [26].

In 2015, a French team developed the first battery using sodium ions in the "18650" format delivering an energy density of 90 Wh kg^{-1} over 2000 cycles and fast recharging [27]. This announcement demonstrates the real potential offered by Na-ion batteries. In the prototype cited, the positive electrode would consist of $\text{Na}_3\text{V}_2(\text{PO}_4)_2\text{F}_3$.

J.P. Pereira-Ramos et al. reported $\beta\text{-Na}_{0.33}\text{V}_2\text{O}_5$ bronze prepared by sol-gel method as cathode material for Na-ion battery [28]. Sodium occupancy inside the $\sim \text{Na}_{0.33}\text{V}_2\text{O}_5$ lattice proceeds in a similar manner to that of Li intercalation, i.e., in the available sites of the tunnel structure of the bronze, which corresponds to a maximum uptake of about 1.6 Na^+ per mole of sodium bronze. The specific capacity of 80 mAh g^{-1} was obtained at $30 \mu\text{A/cm}^2$ in potential range of $3.6 - 2.4 \text{ V}$ (**Figure 17a**). Liu et al. reported $\text{NaV}_6\text{O}_{15}$ nanorods synthesized by low temperature hydrothermal method [29]. It was found that the $\text{NaV}_6\text{O}_{15}$ nanorods exhibited stable sodium-ion insertion/deinsertion reversibility and delivered 142 mAh g^{-1} sodium ions when worked at a current density of 0.02 A g^{-1} (**Figure 17b**).

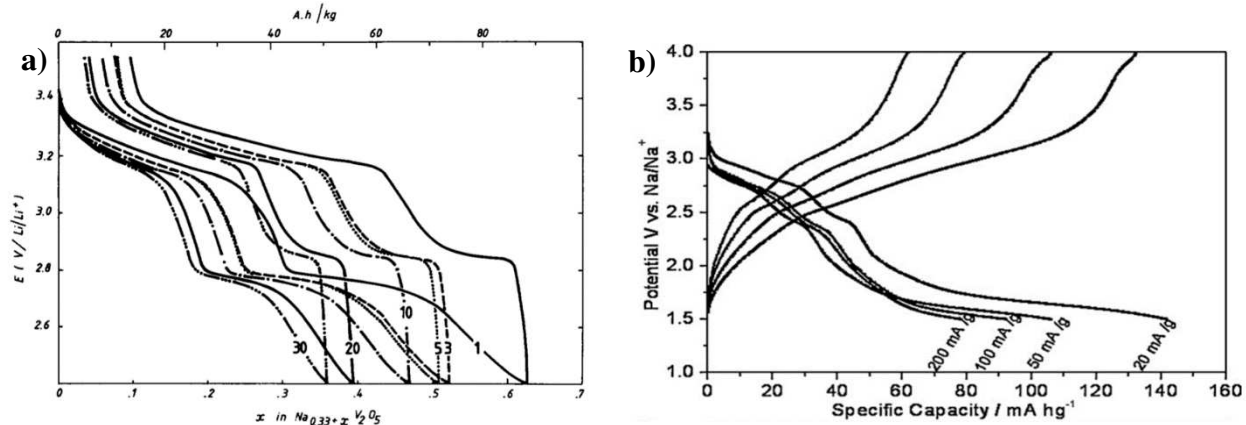


Figure 17. Discharge-charge profile of (a) $\text{Na}_{0.33}\text{V}_2\text{O}_5$ and (b) $\text{NaV}_6\text{O}_{15}$ nanorods

$\text{Na}_{1.5+x}\text{VO}_3$ [30] and Na_xVO_2 [31] bronze with specific capacity of 120 mAh g⁻¹ at C/10 – C/50 has been reported. However, operating voltage of the material is 1.8 V vs Na^+/Na for $\text{Na}_{1.5+x}\text{VO}_3$ [30] and cyclability was studied only for 8 cycles (**Figure 18a**). In the case of Na_xVO_2 [31] discharge/charge profile is more complex, which consist of several working plateaus with more than 50% of the capacity can be reached at 1.6/1.7 V vs Na^+/Na (**Figure 18b**).

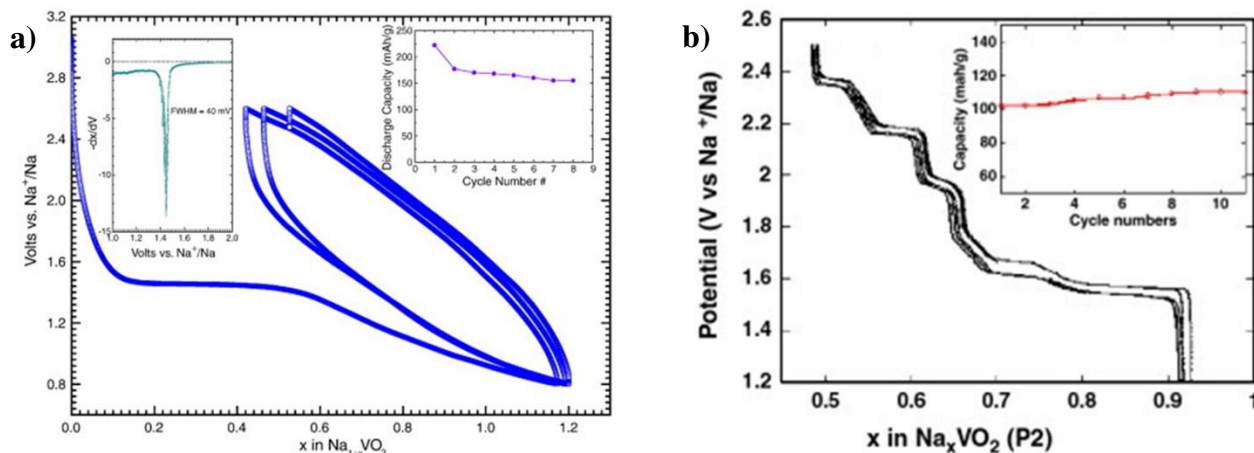


Figure 18. Discharge-charge profile of (a) $\text{Na}_{1.5+x}\text{VO}_3$ [30] at C/50 and (b) Na_xVO_2 [31] at C/20

On the other hand, the team of J.P. Pereira-Ramos very recently demonstrated that orthorhombic oxide V_2O_5 can be reversibly cycled in Na-ion battery at room temperature [32]. After electrochemical formation of NaV_2O_5 bronze, the orthorhombic structure exhibits inter-sheet spacing increased by 10% and cycled at voltage range of 4 – 1 V vs Na^+/Na . The material can intercalate/deintercalate 0.8 Na^+ which corresponds to the capacity of 120 mAh g⁻¹ (**Figure 19**). The working voltage of NaV_2O_5 is around 1.4 V (vs. Na^+/Na) in comparison to discharge potential

at 2V (vs. Li⁺/Li) as reported for α' -NaV₂O₅ in Li-ion battery [33]. The same value of discharge potential was reported by West et al. for insertion of sodium in V₂O₅ at 80 °C [34].

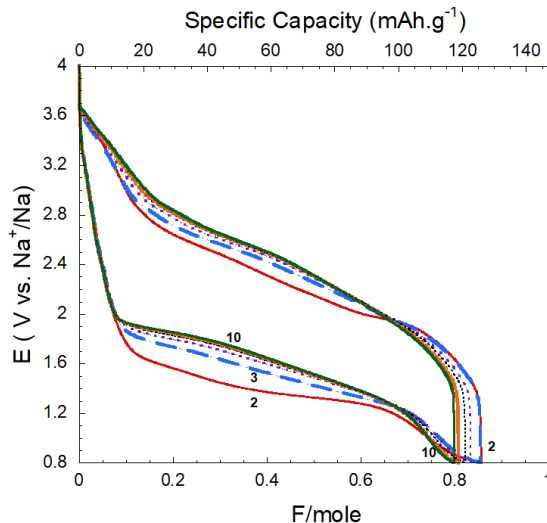


Figure 19. Discharge-charge profile of NaV₂O₅ bronze at C/10 in 1M NaClO₄/PC

Tepavcevic et al. reported vanadium pentoxide xerogel films by gaining specific capacity of 200 mAh g⁻¹ at current density of 20 mA g⁻¹ and working potential at 2.75 V [35]. Indeed, V₂O₅ xerogel nanoparticles synthesized by solvothermal method, reaches capacity of 230 mAh g⁻¹ with operating voltage of 2.05 V with stable cyclability (**Figure 20**) [36]. The obtained results can be explained due to the lamellar structure, which allows for easy sodium diffusion.

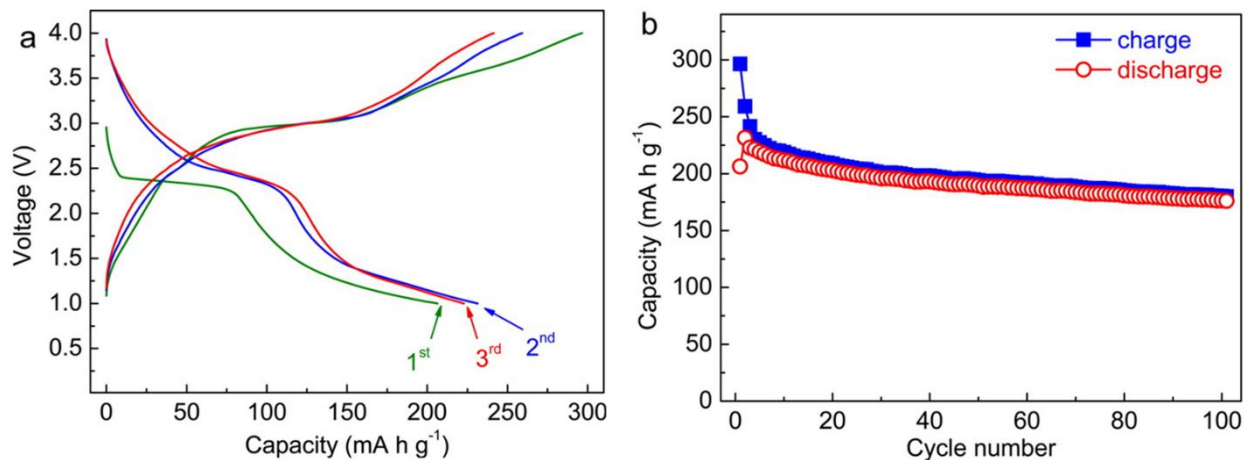


Figure 20. Cycling performance of Na/V₂O₅ Xerogel nanoparticles (bilayer structure) at current density of 80 mA g⁻¹ [36].

1.4 Interest of the V_2O_5 cathode material and objectives of the thesis

Vanadium-based cathodes sparked a great interest due to the rich redox chemistry of vanadium enabling high specific capacities to be reached, and to various open host structures promoting insertion reactions. High-valent oxides (V_2O_5 and V_2O_5 xerogel) as well as mixed-valence oxides (V_6O_{13} , LiV_3O_8) were extensively investigated as cathode materials in the 70-80s. This is why vanadium oxides were studied very early and participated to the birth of the rechargeable lithium battery [37].

Vanadium pentoxide is still the objective of many works as positive electrode. Its open structure (orthorhombic symmetry **Figure 21**) combined with a theoretical high specific capacity of 450 mAh g^{-1} has prompted a great effort to consider closely related forms like V_2O_5 xerogel [38], [39] and high surface area aerogels [40], [41] either to modify the discharge-charge profile, or to enhance the lithium insertion capacity and to improve the rate capability. One main feature of the system is the fairly complex structural behavior of the host material upon lithiation as illustrated by the phase diagram (**Figure 22**).

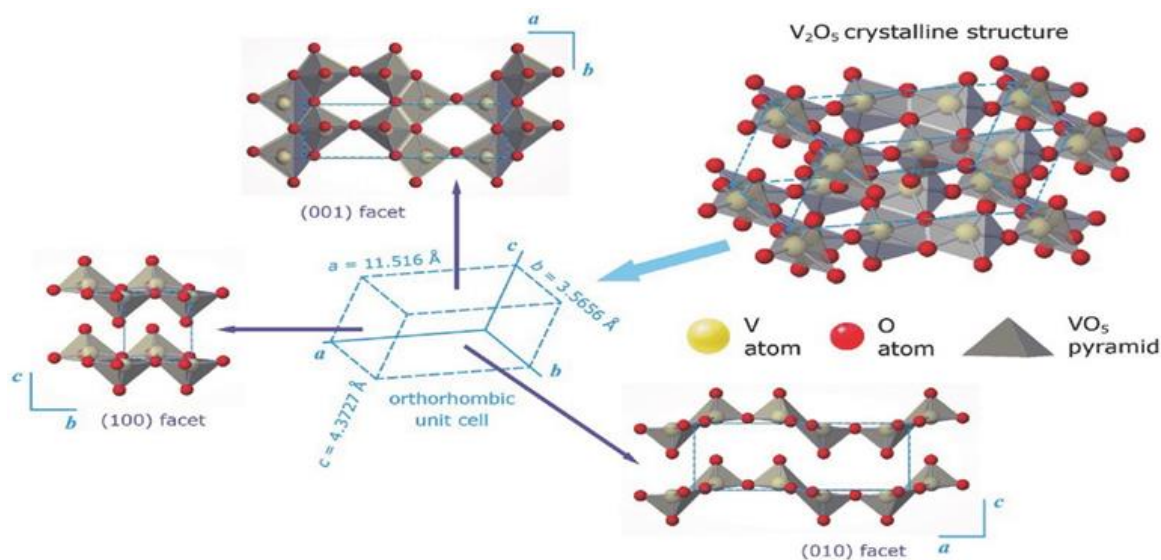


Figure 21. Crystal structure of V_2O_5

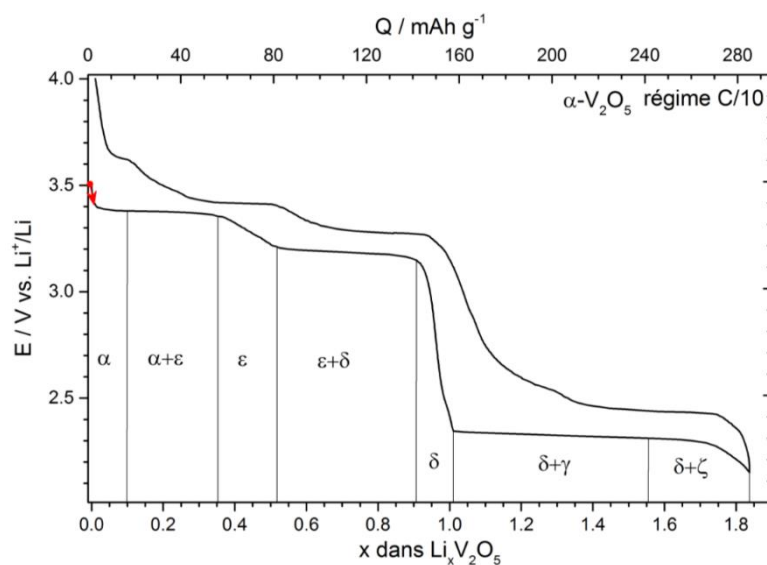


Figure 22. Discharge/charge profile of V_2O_5 and structural behavior of the host material upon lithiation

Nanosizing effect has been also evaluated by many groups to optimize the electrochemical properties especially by shortening the lithium diffusion pathway [42]–[44].

Another way was applied by using derivative forms of the orthorhombic V_2O_5 . For instance, divalent cations were incorporated in the V_2O_5 framework to give $\text{M}_{0.16}\text{V}_2\text{O}_5$ mixed oxides with $\text{M} = \text{Ni}^{2+}$, Cu^{2+} , Co^{2+} and Ba^{2+} respectively prepared by a solution technique and a sol–gel process [45]. These cathode materials were evaluated without any improvement in comparison with that known for the V_2O_5 parent oxide. However, our group reported the sol–gel chemistry offers a new approach to get new orthorhombic $\text{M}_{0.11}\text{V}_2\text{O}_{5.16}$ mixed oxides where M is a trivalent metallic ion ($\text{M} = \text{Al}^{3+}$, Fe^{3+} , Cr^{3+}) [46]–[48] with a structure very close to that of the parent oxide but characterized by original and improved electrochemical properties. Among them, the chromium–vanadium mixed oxide was reported to be the most attractive electrode material with a specific capacity of 260 mAh g^{-1} stable over 20 cycles at C/10 in the 3.8–2 V potential range. This corresponds to a gain in the range 10–15% in comparison with the pristine oxide.

An alternative way to identify new attractive stable V_2O_5 -based cathode materials consists in considering the chemical removal of metallic species from vanadium pentoxide bronzes $\text{M}_x\text{V}_2\text{O}_5$. Such approach allows benefiting from the availability of new types of structures combined with a low amount of metallic species, thus optimizing the possible specific capacity. This strategy has been successfully applied to synthesize the two-dimensional ϵ' - V_2O_5 [49], [50] and γ' - V_2O_5 polymorphs [51]. These polymorphs were obtained from the chemical removal of Cu or Li from

the ε - $\text{Cu}_{0.9}\text{V}_2\text{O}_5$ and γ - LiV_2O_5 bronzes respectively by means of strong oxidizing agents. The original structure of the bronze precursors is kept upon the removal of metallic species and as a result, original bilayered stacking was reported by Garcia-Alvarado et al. for the ε' - V_2O_5 polymorph [49], [50] and puckered layer stacking for γ' - V_2O_5 (Figure 23a) [51]. Promising performances for both materials were found toward lithium insertion: the ε' -polymorph was reported to reversibly accommodate up to 1.8 Li ions in the 4 V-1 V potential range [49], [50] whereas the electrochemical lithium insertion in γ' - V_2O_5 was shown to occur at a higher voltage (3.6/3.5 V vs. Li⁺/Li) (Figure 23b)[52], [53].

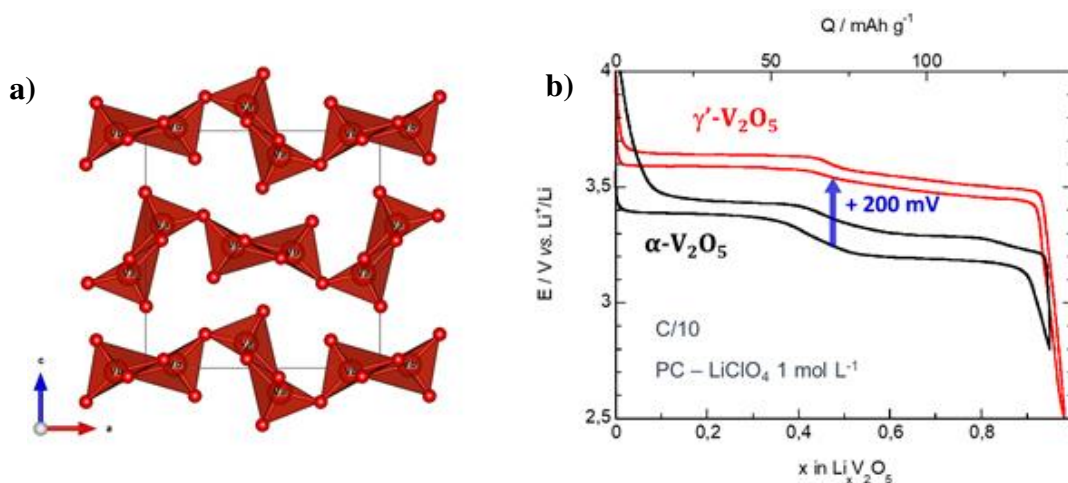


Figure 23. (a) Crystal structure of γ' - V_2O_5 and (b) discharge/charge of α and γ' - V_2O_5 in Li cell (1M LiClO₄ in PC at C/10)

The latter has been deeply investigated in the thesis of M. Safrany [54] who particularly described its electrochemical features and structural response as cathode material in a Li- and Na cell in the 3.8V-2.5V potential range.

However, this work revealed two major drawbacks

- 1- a low-rate capability towards Li and Na insertion
- 2- a low charge-discharge efficiency limited to 50% in the case of sodiation

The material was prepared via a solid-state reaction at high temperature and characterized by micrometric particles with heterogeneous sizes.

In the present work we will address these two aspects using an original solution technique producing homogeneous nanosized particle of the γ' - V_2O_5 polymorph with a notable improvement of electrochemical performance. The corresponding chapter, **Chapter 2**, is entitled

“Electrochemical and structural study of γ' -V₂O₅ polymorph synthesized by a solution technique as cathode material for Li-ion and Na-ion batteries”.

Our efforts to propose new cathode materials for Na-ion batteries will be summarized in **Chapter 3** where two different solution techniques will be used to produce a new sodiated γ NaV₂O₅ phase and a potassiated vanadium bronze (K_{0.5}V₂O₅). **Chapter 3** is entitled “New M_xV₂O₅ bronzes as competitive cathode materials for sodium-ion batteries (M = Na, K)”.

The last chapter will be a contribution to the research of new cathode materials for rechargeable aqueous zinc batteries. The growing demands for large-scale energy storage devices have put a spotlight on aqueous batteries which possess a number of highly desirable features such as low cost, safety over organic electrolytes, environment-friendly. In particular, Zinc ion batteries are considered now as the most promising candidates for grid energy storage. The low price, nontoxicity, and abundance of zinc make combined with good cycling properties in mild conditions (pH = 4) make it very attractive. A previous work performed by Professor Z. Bakenov from Nazarbayev University demonstrated the excellent cycling properties of a LiFePO₄//Zn battery using an hybrid ZnCl₂-LiCl aqueous electrolyte [55]. The Li ions were involved in intercalation reactions at the positive side while zinc cations ensure a good cycling behavior of Zn.

This finding prompted us to evaluate the electrochemical features of the α -V₂O₅ and γ' -V₂O₅ polymorphs in Zinc aqueous batteries using a Li⁺/Zn²⁺ hybrid electrolyte in the last chapter, (**Chapter 4**) entitled “V₂O₅ polymorphs as cathode material in aqueous rechargeable Zinc batteries”.

REFERENCES

- [1] J. Xu, S. Dou, H. Liu, and L. Dai, “Cathode materials for next generation lithium ion batteries,” *Nano Energy*, vol. 2, no. 4, pp. 439–442, Jul. 2013, doi: 10.1016/j.nanoen.2013.05.013.
- [2] N. Nitta, F. Wu, J. T. Lee, and G. Yushin, “Li-ion battery materials: present and future,” *Mater. Today*, vol. 18, no. 5, pp. 252–264, Jun. 2015, doi: 10.1016/j.mattod.2014.10.040.
- [3] S. Patoux *et al.*, “High voltage spinel oxides for Li-ion batteries: From the material research to the application,” *J. Power Sources*, vol. 189, no. 1, pp. 344–352, Apr. 2009, doi: 10.1016/j.jpowsour.2008.08.043.
- [4] C. Delacourt *et al.*, “Toward Understanding of Electrical Limitations (Electronic, Ionic) in LiMPO[sub 4] (M=Fe, Mn) Electrode Materials,” *J. Electrochem. Soc.*, vol. 152, no. 5, p. A913, 2005, doi: 10.1149/1.1884787.
- [5] J.-Y. Hwang, S.-T. Myung, and Y.-K. Sun, “Sodium-ion batteries: present and future,” *Chem. Soc. Rev.*, vol. 46, no. 12, pp. 3529–3614, 2017, doi: 10.1039/C6CS00776G.
- [6] N. Yabuuchi, K. Kubota, M. Dahbi, and S. Komaba, “Research Development on Sodium-Ion Batteries,” *Chem. Rev.*, vol. 114, no. 23, pp. 11636–11682, Dec. 2014, doi: 10.1021/cr500192f.
- [7] S. Mariyappan, Q. Wang, and J. M. Tarascon, “Will Sodium Layered Oxides Ever Be Competitive for Sodium Ion Battery Applications?,” *J. Electrochem. Soc.*, vol. 165, no. 16, pp. A3714–A3722, Dec. 2018, doi: 10.1149/2.0201816jes.
- [8] K. Kubota and S. Komaba, “Review—Practical Issues and Future Perspective for Na-Ion Batteries,” *J. Electrochem. Soc.*, vol. 162, no. 14, pp. A2538–A2550, 2015, doi: 10.1149/2.0151514jes.
- [9] J. MOLEND, C. DELMAS, and P. HAGENMULLER, “Electronic and electrochemical properties of Na_xCoO_2 —y cathode,” *Solid State Ionics*, vol. 9–10, no. PART 1, pp. 431–435, Dec. 1983, doi: 10.1016/0167-2738(83)90271-0.
- [10] L. Wang *et al.*, “Rhombohedral Prussian White as Cathode for Rechargeable Sodium-Ion Batteries,” *J. Am. Chem. Soc.*, vol. 137, no. 7, pp. 2548–2554, Feb. 2015, doi: 10.1021/ja510347s.
- [11] E. Monyoncho and R. Bissessur, “Unique properties of α - NaFeO_2 : De-intercalation of sodium via hydrolysis and the intercalation of guest molecules into the extract solution,” *Mater. Res. Bull.*, vol. 48, no. 7, pp. 2678–2686, Jul. 2013, doi: 10.1016/j.materresbull.2013.03.027.
- [12] K. M. Abraham, “How Comparable Are Sodium-Ion Batteries to Lithium-Ion Counterparts?,” *ACS Energy Lett.*, vol. 5, no. 11, pp. 3544–3547, 2020, doi: 10.1021/acsenergylett.0c02181.
- [13] S. Komaba *et al.*, “Electrochemical Na insertion and solid electrolyte interphase for hard-carbon electrodes and application to Na-ion batteries,” *Adv. Funct. Mater.*, vol. 21, no. 20, pp. 3859–3867, 2011, doi: 10.1002/adfm.201100854.
- [14] H. Yoshida, N. Yabuuchi, and S. Komaba, “ $\text{NaFe}_{0.5}\text{Co}_{0.5}\text{O}_2$ as high energy and power positive electrode for Na-ion batteries,” *Electrochem. commun.*, vol. 34, pp. 60–63, 2013, doi: 10.1016/j.elecom.2013.05.012.
- [15] M. Sathiya, K. Hemalatha, K. Ramesha, J.-M. Tarascon, and A. S. Prakash, “Synthesis, Structure, and Electrochemical Properties of the Layered Sodium Insertion Cathode Material: $\text{NaNi}_{1/3}\text{Mn}_{1/3}\text{Co}_{1/3}\text{O}_2$,” *Chem. Mater.*, vol. 24, no. 10, pp. 1846–

- 1853, May 2012, doi: 10.1021/cm300466b.
- [16] D. Kim, E. Lee, M. Slater, W. Lu, S. Rood, and C. S. Johnson, “Layered Na[Ni 1/3Fe 1/3Mn 1/3]O₂ cathodes for Na-ion battery application,” *Electrochem. commun.*, vol. 18, no. 1, pp. 66–69, 2012, doi: 10.1016/j.elecom.2012.02.020.
 - [17] J. Vondrák, J. Bludská, and I. Jakubec, “Sodium insertion in manganese dioxide electrodes,” *Electrochim. Acta*, vol. 37, no. 4, pp. 603–606, 1992, doi: 10.1016/0013-4686(92)80060-Y.
 - [18] S. Bach, J. P. Pereira-Ramos, and N. Baffier, “Electrochemical sodium insertion into the sol-gel birnessite manganese dioxide,” *Electrochim. Acta*, vol. 38, no. 13, pp. 1695–1698, 1993, doi: 10.1016/0013-4686(93)85063-5.
 - [19] S. Guo *et al.*, “A high-capacity, low-cost layered sodium manganese oxide material as cathode for sodium-ion batteries,” *ChemSusChem*, vol. 7, no. 8, pp. 2115–2119, 2014, doi: 10.1002/cssc.201402138.
 - [20] K. W. Nam *et al.*, “Critical role of crystal water for a layered cathode material in sodium ion batteries,” *Chem. Mater.*, vol. 27, no. 10, pp. 3721–3725, 2015, doi: 10.1021/acs.chemmater.5b00869.
 - [21] B. L. Ellis, W. R. M. Makahnouk, Y. Makimura, K. Toghill, and L. F. Nazar, “A multifunctional 3.5V iron-based phosphate cathode for rechargeable batteries,” *Nat. Mater.*, vol. 6, no. 10, pp. 749–753, 2007, doi: 10.1038/nmat2007.
 - [22] N. Recham, J.-N. Chotard, L. Dupont, K. Djellab, M. Armand, and J.-M. Tarascon, “Ionothermal Synthesis of Sodium-Based Fluorophosphate Cathode Materials,” *J. Electrochem. Soc.*, vol. 156, no. 12, p. A993, 2009, doi: 10.1149/1.3236480.
 - [23] Y. Kawabe *et al.*, “A comparison of crystal structures and electrode performance between Na₂FePO₄F and Na₂Fe_{0.5}Mn_{0.5}PO₄F synthesized by solid-state method for rechargeable na-ion batteries,” *Electrochemistry*, vol. 80, no. 2, pp. 80–84, 2012, doi: 10.5796/electrochemistry.80.80.
 - [24] J. Barker, M. Y. Saidi, and J. L. Swoyer, “A sodium-ion cell based on the fluorophosphate compound NaVPO₄F,” *Electrochem. Solid-State Lett.*, vol. 6, no. 1, pp. 4–7, 2003, doi: 10.1149/1.1523691.
 - [25] K. Saravanan, C. W. Mason, A. Rudola, K. H. Wong, and P. Balaya, “The first report on excellent cycling stability and superior rate capability of Na₃V₂(PO₄)₃ for sodium ion batteries,” *Adv. Energy Mater.*, vol. 3, no. 4, pp. 444–450, 2013, doi: 10.1002/aenm.201200803.
 - [26] K. Chihara, A. Kitajou, I. D. Gocheva, S. Okada, and J. I. Yamaki, “Cathode properties of Na₃M₂(PO₄)₂F₃ [M = Ti, Fe, V] for sodium-ion batteries,” *J. Power Sources*, vol. 227, pp. 80–85, 2013, doi: 10.1016/j.jpowsour.2012.10.034.
 - [27] “Batterie sodium-ion: une révolution en marche | CNRS Le journal.” [Online]. Available: <https://lejournel.cnrs.fr/articles/batterie-sodium-ion-une-revolution-en-marche>. [Accessed: 10-Oct-2021].
 - [28] S. Bach, N. Baffier, J. P. Pereira-Ramos, and R. Messina, “Electrochemical sodium intercalation in Na_{0.33}V₂O₅ bronze synthesized by a sol-gel process,” *Solid State Ionics*, vol. 37, no. 1, pp. 41–49, 1989, doi: 10.1016/0167-2738(89)90285-3.
 - [29] H. Liu, H. Zhou, L. Chen, Z. Tang, and W. Yang, “Electrochemical insertion/deinsertion of sodium on NaV₆O₁₅ nanorods as cathode material of rechargeable sodium-based batteries,” *J. Power Sources*, vol. 196, no. 2, pp. 814–819, 2011, doi: 10.1016/j.jpowsour.2010.07.062.

- [30] G. Venkatesh, V. Pralong, O. I. Lebedev, V. Caignaert, P. Bazin, and B. Raveau, "Amorphous sodium vanadate $\text{Na}_{1.5} + y\text{VO}_3$, a promising matrix for reversible sodium intercalation," *Electrochem. commun.*, vol. 40, pp. 100–102, 2014, doi: 10.1016/j.elecom.2013.11.004.
- [31] D. Hamani, M. Ati, J. M. Tarascon, and P. Rozier, "NaxVO₂ as possible electrode for Na-ion batteries," *Electrochem. commun.*, vol. 13, no. 9, pp. 938–941, 2011, doi: 10.1016/j.elecom.2011.06.005.
- [32] D. Muller-Bouvet, R. Baddour-Hadjean, M. Tanabe, L. T. N. Huynh, M. L. P. Le, and J. P. Pereira-Ramos, "Electrochemically formed α' -NaV₂O₅: A new sodium intercalation compound," *Electrochim. Acta*, vol. 176, pp. 586–593, 2015, doi: 10.1016/j.electacta.2015.07.030.
- [33] L. Bouhedja, S. Castro-Garcia, J. Livage, and C. Julien, "Lithium intercalation in α' -NaV₂O₅ synthesized via the hydrothermal route," *Ionics (Kiel)*, vol. 4, no. 3–4, pp. 227–233, May 1998, doi: 10.1007/BF02375950.
- [34] K. WEST, "Sodium insertion in vanadium oxides," *Solid State Ionics*, vol. 28–30, no. PART 2, pp. 1128–1131, Sep. 1988, doi: 10.1016/0167-2738(88)90343-8.
- [35] S. Tepavcevic *et al.*, "Nanostructured bilayered vanadium oxide electrodes for rechargeable sodium-ion batteries," *ACS Nano*, vol. 6, no. 1, pp. 530–538, 2012, doi: 10.1021/nn203869a.
- [36] D. Su and G. Wang, "Single-Crystalline Bilayered V₂O₅ Nanobelts for High-Capacity Sodium-Ion Batteries," *ACS Nano*, vol. 7, no. 12, pp. 11218–11226, Dec. 2013, doi: 10.1021/nn405014d.
- [37] M. S. Whittingham, "Lithium Batteries and Cathode Materials," *Chem. Rev.*, vol. 104, no. 10, pp. 4271–4302, Oct. 2004, doi: 10.1021/cr020731c.
- [38] R. BADDOUR, J. P. PEREIRA-RAMOS, R. MESSINA, and J. PERICHON, "ChemInform Abstract: A Thermodynamic, Structural and Kinetic Study of the Electrochemical Lithium Intercalation into the Xerogel V₂O₅×1.6 H₂O in a Propylene Carbonate Solution," *ChemInform*, vol. 23, no. 2, p. no-no, Aug. 2010, doi: 10.1002/chin.199202019.
- [39] S. Passerini, "XAS and electrochemical characterization of lithium intercalated V₂O₅ xerogels," *Solid State Ionics*, vol. 90, no. 1–4, pp. 5–14, Sep. 1996, doi: 10.1016/S0167-2738(96)00380-3.
- [40] F. Coustier, "V₂O₅ aerogel-like lithium intercalation host," *Solid State Ionics*, vol. 116, no. 3–4, pp. 279–291, Jan. 1999, doi: 10.1016/S0167-2738(98)00349-X.
- [41] S. Passerini, J. J. Ressler, D. B. Le, B. B. Owens, and W. H. Smyrl, "High rate electrodes of V₂O₅ aerogel," *Electrochim. Acta*, vol. 44, no. 13, pp. 2209–2217, Feb. 1999, doi: 10.1016/S0013-4686(98)00346-6.
- [42] V. M. Mohan, B. Hu, W. Qiu, and W. Chen, "Synthesis, structural, and electrochemical performance of V₂O₅ nanotubes as cathode material for lithium battery," *J. Appl. Electrochem.*, vol. 39, no. 10, pp. 2001–2006, Oct. 2009, doi: 10.1007/s10800-009-9910-6.
- [43] X. Li, W. Li, H. Ma, and J. Chen, "Electrochemical Lithium Intercalation/Deintercalation of Single-Crystalline V₂O₅ Nanowires," *J. Electrochem. Soc.*, vol. 154, no. 1, p. A39, 2007, doi: 10.1149/1.2374945.
- [44] C. K. Chan, H. Peng, R. D. Twisten, K. Jarausch, X. F. Zhang, and Y. Cui, "Fast, Completely Reversible Li Insertion in Vanadium Pentoxide Nanoribbons," *Nano Lett.*,

- vol. 7, no. 2, pp. 490–495, Feb. 2007, doi: 10.1021/nl062883j.
- [45] J. P. Pereira-Ramos, P. Soudan, R. Baddour-Hadjean, and S. Bach, “A kinetic study of lithium transport in the sol-gel $\text{Cr}_{0.11}\text{V}_{2}\text{O}_{5.16}$ mixed oxide,” *Electrochim. Acta*, vol. 56, no. 3, pp. 1381–1386, 2011, doi: 10.1016/j.electacta.2010.10.069.
 - [46] R. Baddour-Hadjean, J. Farcy, J. P. Pereira-Ramos, and N. Baffier, “A Kinetic Study of Lithium Transport in a New Li Intercalation Material $\text{Al}_{0.11}\text{V}_{2}\text{O}_{5.15}$ Synthesized via a Sol-Gel Process,” *J. Electrochem. Soc.*, vol. 143, no. 7, pp. 2083–2088, Jul. 1996, doi: 10.1149/1.1836962.
 - [47] J. Farcy, S. Maingot, P. Soudan, J. . Pereira-Ramos, and N. Baffier, “Electrochemical properties of the mixed oxide $\text{Fe}_{0.11}\text{V}_{2}\text{O}_{5.16}$ as a Li intercalation compound,” *Solid State Ionics*, vol. 99, no. 1–2, pp. 61–69, Aug. 1997, doi: 10.1016/S0167-2738(97)00196-3.
 - [48] P. Soudan, “Sol-gel chromium–vanadium mixed oxides as lithium insertion compounds,” *Solid State Ionics*, vol. 135, no. 1–4, pp. 291–295, Nov. 2000, doi: 10.1016/S0167-2738(00)00449-5.
 - [49] F. Garcia-Alvarado, J. M. Tarascon, and B. Wilkens, “Synthesis and Electrochemical Study of New Copper Vanadium Bronzes and of Two New V_{2}O_{5} Polymorphs: β' - and ϵ' - V_{2}O_{5} ,” *J. Electrochem. Soc.*, vol. 139, no. 11, pp. 3206–3214, Nov. 1992, doi: 10.1149/1.2069054.
 - [50] F. GARCIAALVARADO and J. TARASCON, “New vanadium bronzes $\text{M}_y\text{V}_2\text{O}_5$ ($\text{M}=\text{Cu}$ or Ag ; $0 < y < 0.85$): Structure and lithium intercalation,” *Solid State Ionics*, vol. 63–65, pp. 401–406, Sep. 1993, doi: 10.1016/0167-2738(93)90135-P.
 - [51] J. M. Cocciantelli, P. Gravereau, J. P. Doumerc, M. Pouchard, and P. Hagenmuller, “On the preparation and characterization of a new polymorph of V_2O_5 ,” *J. Solid State Chem.*, vol. 93, no. 2, pp. 497–502, 1991, doi: 10.1016/0022-4596(91)90323-A.
 - [52] J. COCCIANTELLI, M. MENETRIER, C. DELMAS, J. DOUMERC, M. POUCHARD, and P. HAGENMULLER, “Electrochemical and structural characterization of lithium intercalation and deintercalation in the γ - LiV_2O_5 bronze,” *Solid State Ionics*, vol. 50, no. 1–2, pp. 99–105, Jan. 1992, doi: 10.1016/0167-2738(92)90041-M.
 - [53] J. M. Cocciantelli, J. P. Doumerc, M. Pouchard, M. Broussely, and J. Labat, “Crystal chemistry of electrochemically inserted $\text{Li}_x\text{V}_2\text{O}_5$,” *J. Power Sources*, vol. 34, no. 2, pp. 103–111, Mar. 1991, doi: 10.1016/0378-7753(91)85029-V.
 - [54] “Propriétés électrochimiques et réponse structurale du polymorphe γ' - V_2O_5 vis-à-vis de l’insertion du lithium et du sodium - TEL - Thèses en ligne.” [Online]. Available: <https://tel.archives-ouvertes.fr/tel-01799564>. [Accessed: 10-Oct-2021].
 - [55] N. Yesibolati *et al.*, “High Performance $\text{Zn}/\text{LiFePO}_4$ Aqueous Rechargeable Battery for Large Scale Applications,” *Electrochim. Acta*, vol. 152, pp. 505–511, Jan. 2015, doi: 10.1016/j.electacta.2014.11.168.

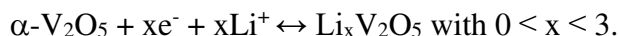
CHAPTER 2

Electrochemical and structural study of γ' -V₂O₅ polymorph synthesized by a solution technique as cathode material for Li-ion and Na-ion batteries

2.1 Electrochemical and structural study of Li insertion in γ' -V₂O₅ polymorph synthesized by a solution technique

2.1.1 Introduction

V₂O₅ is a model lithium intercalation compound and the α -form has been very early identified as a promising cathode material for secondary lithium batteries [1]. The electrochemical lithium insertion-extraction process corresponds to the following reaction:



The structural and electrochemical behavior of the Li_xV₂O₅ system has been studied in details [2–19]. For $0 < x \leq 2$, three successive (α/ϵ), (ϵ/δ) and (δ/γ) biphasic regions along the three well defined voltage plateaus at 3.4 V, 3.2 V and 2.3 V, respectively are described [2,7, 20-22], with a maximum lithium uptake of 1.8 Li per mol of oxide corresponding to a high specific capacity of 265 mAh g⁻¹. While the Li_xV₂O₅ system is highly reversible in the $0 \leq x \leq 1$ composition range (4 V- 2.3 V voltage window), cycling experiments in the extended $0 < x \leq 2$ composition range (4 V - 2.1 V) produce irreversible structural change due to the formation of the highly puckered γ -LiV₂O₅ phase [7, 22]. Therefore, the voltage profile is modified with additional plateaus occurring at higher voltage of 3.5 and 3.6 V [7]. The γ -LiV₂O₅ formation is governed by the temperature, the number of cycles, the depth of discharge, the grain size and crystallite size. For instance, it does not take place at 100°C [23] or by using a nanosized V₂O₅ [24].

Cocciantelli et al. identified the γ' -V₂O₅ polymorph as the irreversible charge product of the γ -LiV₂O₅ phase formed along the third potential plateau at 2.3 V, responsible for the voltage enhancement upon cycling [6].

Soon afterwards, the same team reported that γ' -V₂O₅ can also be obtained through the chemical oxidation of γ -LiV₂O₅ in a solution of bromine in acetonitrile [4]. In spite of its potential interest, the electrochemical lithiation mechanism in γ' -V₂O₅ had not been investigated before the

contribution of our laboratory. Indeed, most efforts were focused on the study of γ - LiV_2O_5 as a cathode for Li-ion batteries [6, 25-30]. The γ - LiV_2O_5 material is mostly prepared by carbothermal reduction at 600°C [25], precipitation techniques [26], hydrothermal [27] or solvothermal routes [28, 29] with controversial and scattered results showing that γ - LiV_2O_5 electrochemical features are not easy to control.

Therefore, the GESMAT team (now BATTion) deeply investigated for the first time the electrochemical lithium insertion in the micrometric γ' - V_2O_5 powder synthesized from chemical oxidation of the γ - LiV_2O_5 bronze obtained by carboreduction. A comprehensive structural study has allowed to establish the γ' - $\text{V}_2\text{O}_5/\text{Li}$ phase diagram up to 2 Li per mole of oxide while the corresponding kinetic behavior has been described in details [31]. The layered structure of γ' - V_2O_5 consists of infinite ribbons made of VO_5 edge-sharing distorted pyramids leading larger interlayer spacing than in α - V_2O_5 (5.02 Å in γ' - V_2O_5 against 4.37 Å in α - V_2O_5). It makes easier the accommodation of guest cations with a gain in working potential of around 200 mV vs α - V_2O_5 .

However, poor rate capability and cycling properties of micrometric γ' - V_2O_5 were found using this high temperature synthesis showing that additional efforts are required to optimize this new cathode materials for Li-ion batteries. To solve this drawback, a possible alternative could consist in mastering the particle size of γ' - V_2O_5 in order to benefit from the shortening of Li diffusion pathway leading an improvement of γ' - V_2O_5 insertion properties.

In this work we present a new synthesis way to achieve smaller and homogeneous particle size of γ' - V_2O_5 hoping to combine the higher working voltage of the cathode material for $0 < x < 1$ with an expected higher rate capability and cycling properties than in the case of the same oxide obtained from the carboreduction process at 600°C. The structural response of the cathode material is also investigated upon lithiation-delithiation.

2.1.2 Synthesis

The polyol synthesis of γ' - V_2O_5 consist from several steps which is illustrated in **Figure. 1**. First, the α - V_2O_5 the precursor is prepared by a solution technique in ethylene glycol promoting nanosized particles. This step is followed by a lithiation procedure and moderate heat treatment

leads to the γ - LiV_2O_5 bronze while the last step consists in the final oxidative reaction in acetonitrile as explained below.

Step 1. Synthesis of α - V_2O_5 . Ammonium metavanadate (NH_4VO_3) and ethylene glycol (EG) were used without purification. NH_4VO_3 (7 gr) was dispersed in 500 ml of EG under stirring. The resulting mixture was heated to 110 °C under continuous stirring to obtain yellow colored solution, then refluxed at 340 °C for 3 hr until solution become blue color and cooled to room temperature. At the end of the reaction excess EG was removed and precipitant (vanadium ethyleneglycolate) was washed with ethanol and dried at 110 °C for 2 hr. To synthesize α - V_2O_5 powder, vanadium ethyleneglycolate was annealed at 490 °C for 3 hr in air.

Step 2. Synthesis of γ - LiV_2O_5 . α - V_2O_5 was dispersed in 40 ml of acetonitrile under continuous stirring. Lithium iodide in excess (molar ratio 1:2) was slowly added to obtain δ - LiV_2O_5 and mixed for 4 hrs. The obtained powder was washed 4 times with acetonitrile and acetone to remove iodide. After drying at 70 °C powder was heat-treated at 300 °C for 3 hrs under vacuum in Buchi furnace to form distorted γ -type layers (δ - $\text{LiV}_2\text{O}_5 \rightarrow \gamma$ - LiV_2O_5).

Step 3. Synthesis of γ' - V_2O_5 . γ' - V_2O_5 is obtained by chemical oxidation of γ - LiV_2O_5 . Deinsertion of lithium from γ - LiV_2O_5 was performed with strong oxidizing agent NO_2BF_4 (molar ratio 1:1.5) in acetonitrile. The solution was stirred at room temperature for 4 hrs. The obtained powder was washed 4 times with acetonitrile and acetone and dried at 80 °C. The color of powder changed from dark green to orange, which confirms complete delithiation of the product.

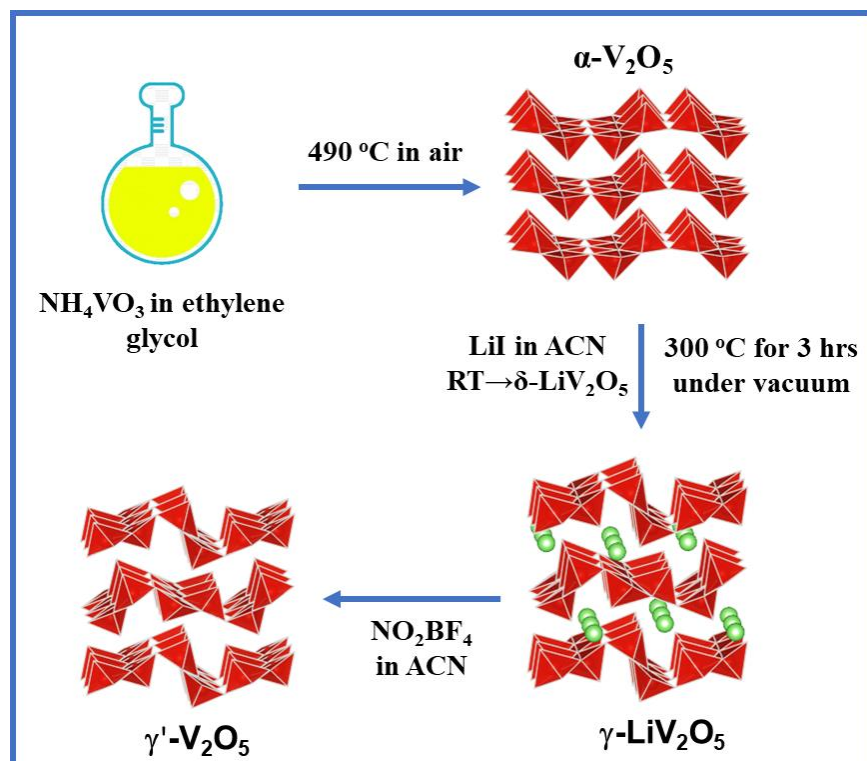


Figure 1. Scheme of polyol synthesis to obtain γ' - V_2O_5

2.1.3 Structural characterization

The obtained powder after oxidation of $\gamma\text{-LiV}_2\text{O}_5$ examined by XRD and Raman. All the reflection lines in **Figure 2** can be indexed with expected orthorhombic symmetry of $Pnma$ space group and calculated unit cell parameters using Bragg's law [$a=9.94\text{ \AA}$, $b=3.58\text{ \AA}$, $c=10.05\text{ \AA}$] are in a good agreement with the literature ⁴. Sharp and intense diffraction peaks illustrate high crystallization degree. The Rietveld refinement does not reveal the presence of impurity. (**Figure S1**)

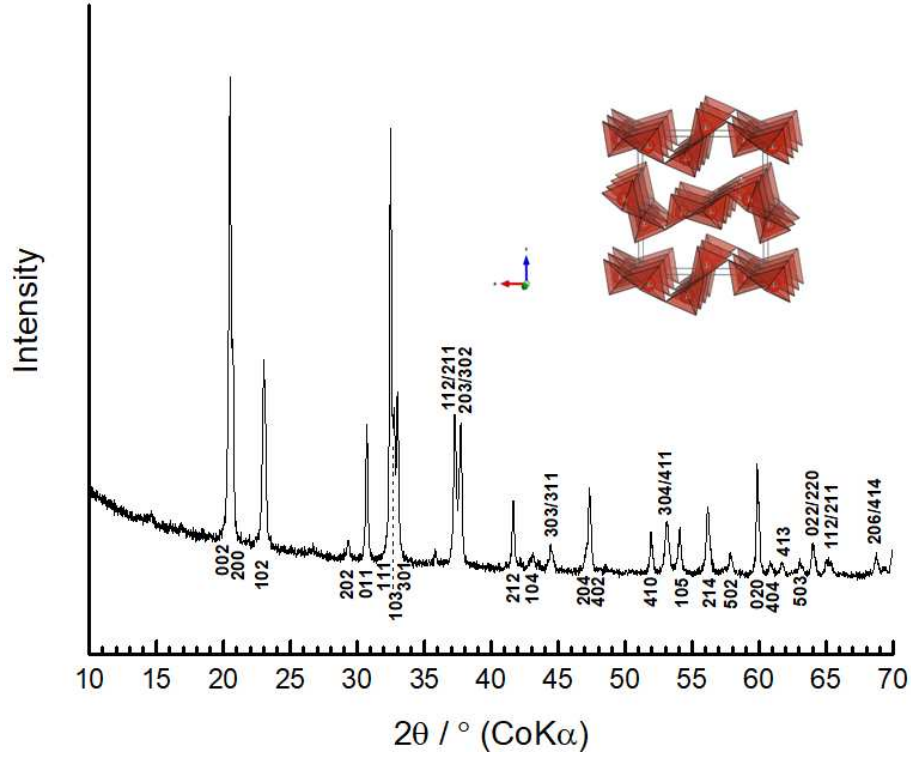


Figure 2. X-ray diffraction pattern of γ' - V_2O_5 powder

For the calculation of d -spacing, Bragg's law was used, $d = \frac{n\lambda}{2\sin\theta}$

where, $\lambda=1.7889 \text{ \AA}$ (wavelength of X-ray Co source), θ = Peak position ($^\circ$), $n=1$ (Order of diffraction), d = interplanar spacing (\AA); d values, Miller indices, and 2θ values of diffraction lines are gathered in **Table 1**.

Table 1. The calculation of Peak position, interplanar spacing, hkl indexes, FWHM, Crystallite size from XRD data of γ' - V_2O_5

No.	Peak position		Interplanar spacing $d \text{ (\AA)}$	Miller indices (hkl)	FWHM ($^\circ$)	Crystallite size nm
	2 Theta ($^\circ$)	Theta ($^\circ$)				
1	20,493	10,246	5,028	002	0,23984	39,085
2	20,727	10,363	4,972	200	0,13165	71,232
3	23,036	11,518	4,479	102	0,29284	32,148
4	29,323	14,661	3,533	202	0,16776	56,838
5	30,711	15,355	3,377	011	0,18548	51,575
6	32,476	16,238	3,198	111	0,14759	65,099
7	32,668	16,334	3,180	103	0,61662	15,589
8	33,018	16,509	3,147	301	0,14349	67,052
9	35,803	17,901	2,909	210	0,00632	37,040
10	37,286	18,643	2,798	112/211	0,26262	37,071

11	37,700	18,850	2,768	203/302	0,2633	37,020
12	41,636	20,818	2,516	212	0,22336	44,184
13	47,335	23,667	2,228	402	0,27842	36,175
14	51,938	25,969	2,042	410	0,22971	44,668
15	53,123	26,561	2,000	304/411	0,33246	31,021
16	54,055	27,027	1,968	105	0,27272	37,972
17	56,174	28,087	1,899	214	0,30788	33,962
18	59,888	29,944	1,791	020	0,25538	41,686

The calculation of lattice constant values $\frac{1}{d^2} = \frac{h^2}{a^2} + \frac{k^2}{b^2} + \frac{l^2}{c^2}$

As an example, to estimate a , b , c values the most intense hkl peaks will be chosen (002, 200, 011 peaks) in a first approach.

For calculation of lattice constant c (002 peak) $\frac{1}{5.028^2} = \frac{2^2}{c^2}$; $c = 10.05 \text{ \AA}$

For calculation of lattice constant a (200 peak) $\frac{1}{4.972^2} = \frac{2^2}{a^2}$; $a = 9.94 \text{ \AA}$

For calculation of lattice constant b (011 peak) $\frac{1}{3.378^2} = \frac{1^2}{b^2} + \frac{1^2}{10.05^2}$; $b = 3.586 \text{ \AA}$

The γ' -V₂O₅ has layered structure consist of infinite ribbons with VO₅ edge-sharing distorted pyramids oriented alternatively up and down. The following ribbons are connected each other along the a-direction by one pyramid corner oxygen, which leads to formation of puckered layers located perpendicular to the c-axis. (**Figure 3**)

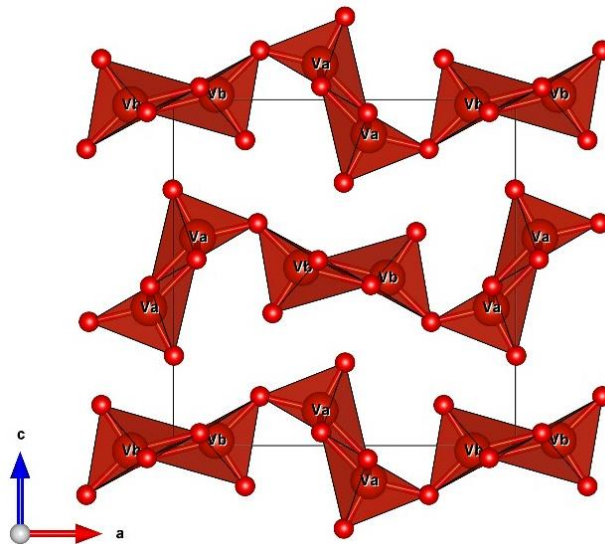


Figure 3. Crystal structure of γ' -V₂O₅

The average crystallite size of γ' -V₂O₅ is ~ 45 nm, which is calculated by Sherrer equation (see below).

The calculation of **crystallite size** and average crystallite size from XRD by using Sherrer equation (see **Table 1**)

$$D = \frac{k\lambda}{\beta \cos \theta}$$

where, D = crystallite size (nm), K = 0.9 (Sherrer constant), λ = 0.17889 nm (wavelength of Co X-ray source), β = FWHM, θ = Peak position

The Raman spectrum of synthesized powder fully agrees with typical fingerprint of γ' -V₂O₅, showing bands in the 90 – 1050 cm⁻¹ wavenumber range (**Figure 4**). All vibrations of the chains can be identified: stretching of shortest bonds V_a-O_{1a} and V_b-O_{1b} at 1037, 1021, 1003 cm⁻¹, bond stretching vibrations localized within V_a-O₃-V_b bridges at 752 and 603 cm⁻¹, V_a-O_{2a}-V_a and V_b-O_{2b}-V_b bridges at 722 and 694 cm⁻¹. Modes involving the V – O₂ ladder step bonds at 532 and 500 cm⁻¹. The lower frequency modes at 92, 126, 138, 153, 171, 190, 238, 266, 282, 299, 349, 390 cm⁻¹ are related to the complex distortions of ladders.

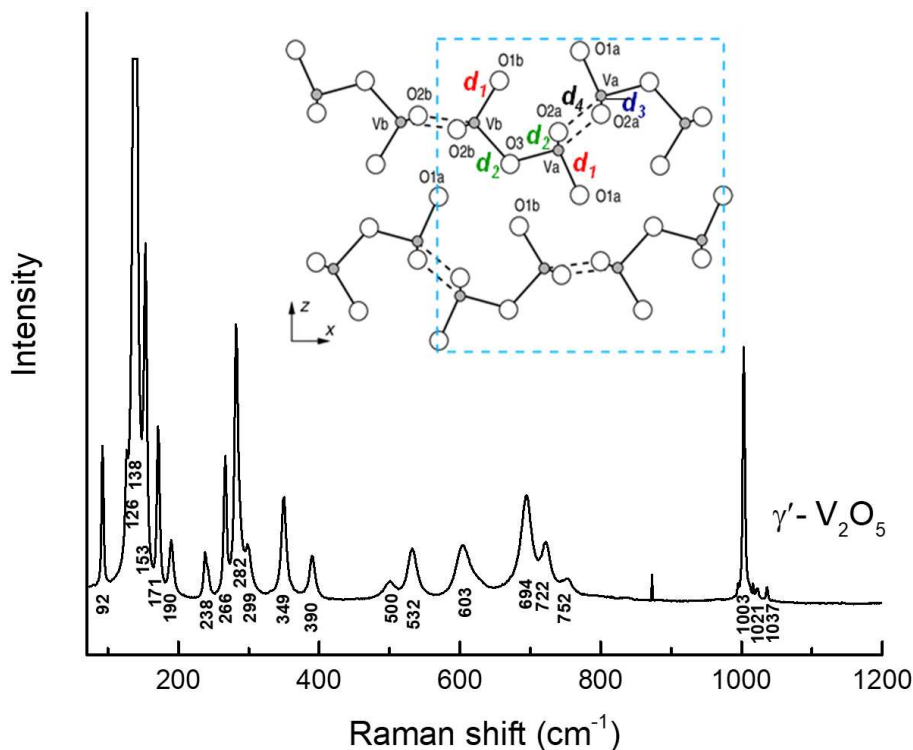


Figure 4 Raman spectrum of γ' -V₂O₅ powder

The morphology of the obtained powder was characterized by scanning electron microscopy (SEM) at different magnifications (**Figure 5**). It reveals that obtained product consists of agglomerated particles with uniform size. The average particles size is around 100~500 nm. The high sharp intensity from XRD indicates the good crystallinity of the γ' -V₂O₅ powder.

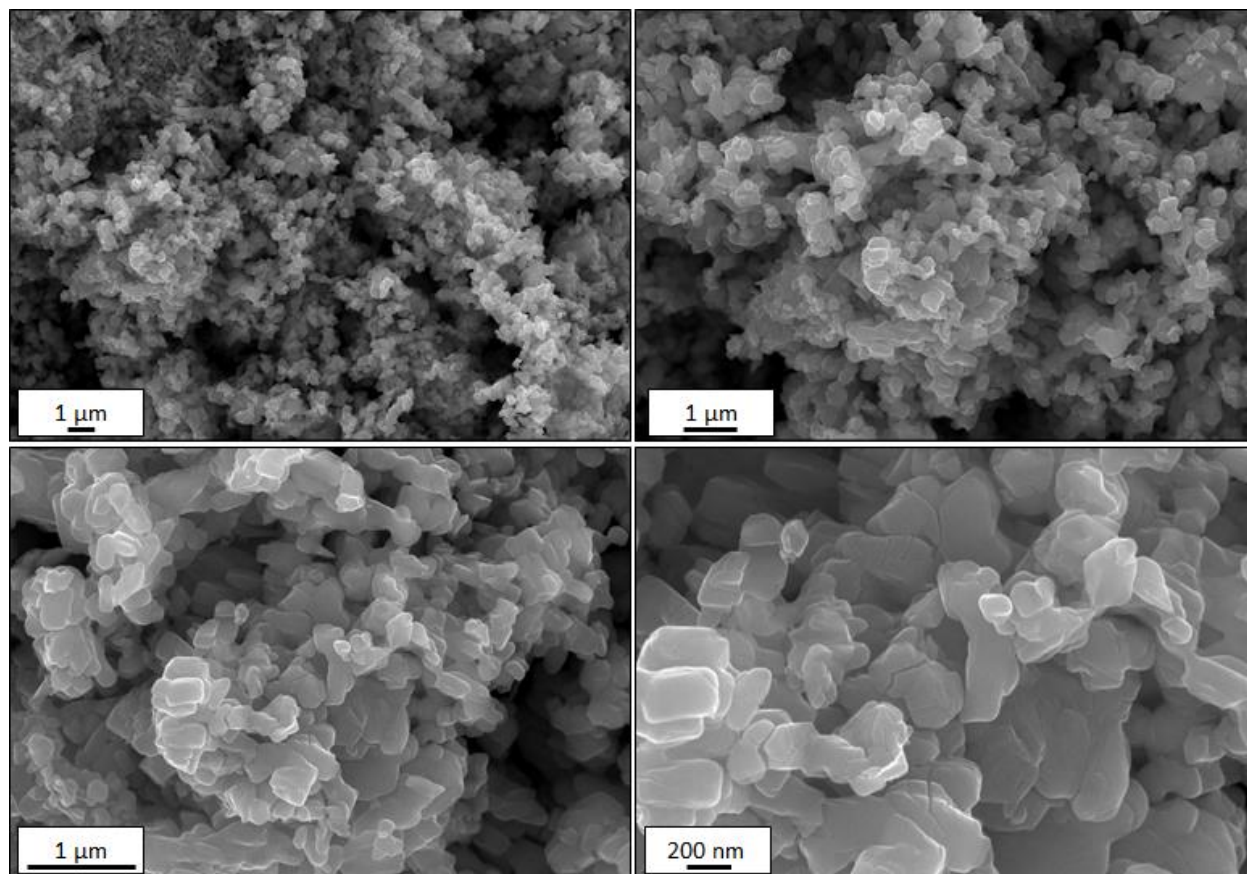


Figure 5. SEM micrographs of γ' -V₂O₅ powder at different magnifications.

2.1.4 Electrochemical study

Figure 6 clearly illustrates the main advantage provided by the puckered layers of γ' -V₂O₅ polymorph and its large interlayer spacing (5.02 Å). Indeed γ' -V₂O₅ allows reversible Li insertion in higher voltage window (3.6/3.5 V vs. Li⁺/Li) than α -V₂O₅ (3.4/3.2 V vs. Li⁺/Li) for the same specific capacity of 145 mAh/g. Therefore it attracts the current attention as cathode material for Li, Na-ion batteries in organic electrolyte.

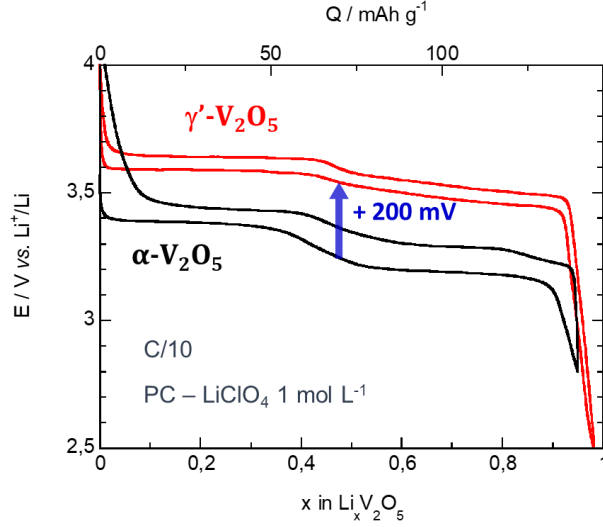


Figure 6. Discharge-charge curves of α - V_2O_5 and γ' - V_2O_5 in organic electrolyte at C/10

Cyclic voltammetric experiments were performed to determine the optimal battery voltage window at different scanning rate ($16 \mu\text{V/s} \rightarrow 0.196 \text{ mV/s}$). As seen from **Figure 7a**, the lithium insertion/extraction can be characterized by two separate highly reversible process with two well-defined cathodic peaks located at 3.55 V and 3.4 V and two anodic peaks at 3.54 V and 3.65 V. During the reduction, the sharp peak at 3.55V is probably related to a two-phase behavior ($0 \leq x < 0.4$), while the relatively broad peak at 3.4V could indicate a single-phase of the lithiation process ($0.4 \leq x \leq 1$). The intensities of anodic and cathodic peaks are nearly same showing the high reversibility of γ' - V_2O_5 as shown also from 1 cycle at C/50 (**Figure 7b**). It can be seen that the increase of scan rate leads to a higher polarization.

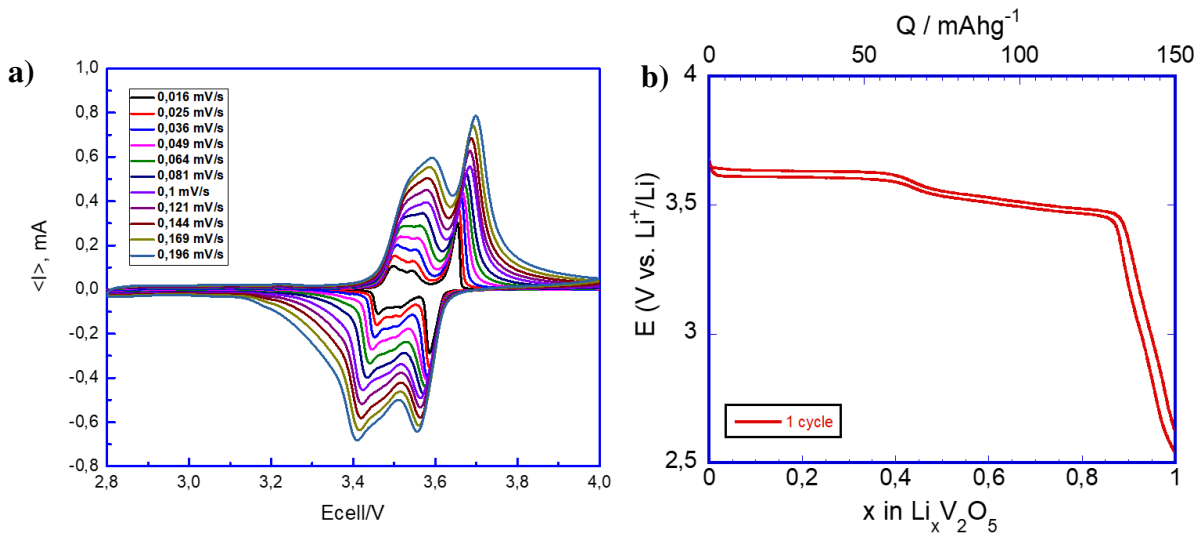
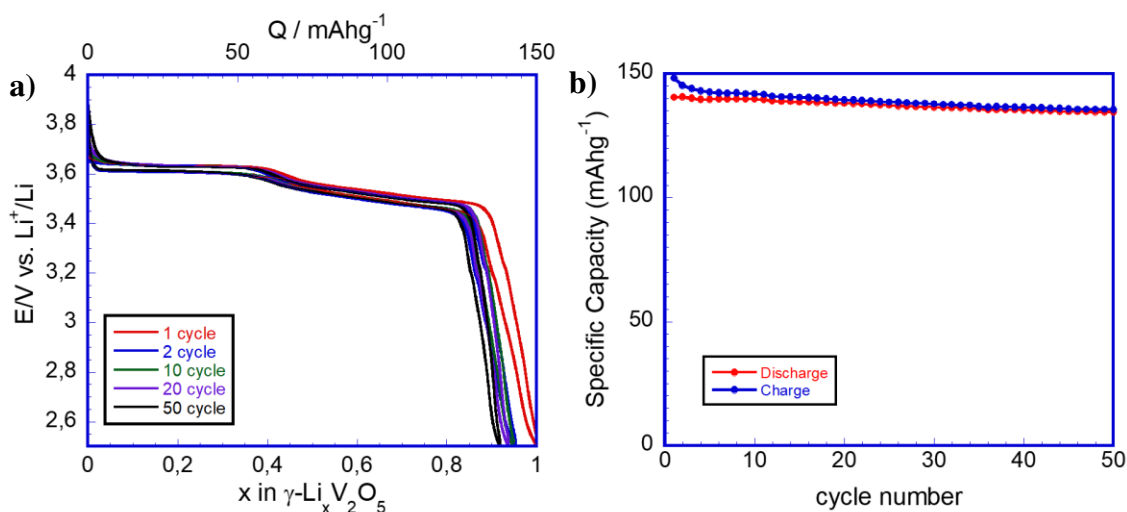


Figure 7. (a) Cyclic voltammetry at different scan rate and (b) 1st cycle at C/50

The discharge-charge cycle at low C rate nicely illustrates the maximum Li uptake is 1 for a cut off voltage of 2.5V and the two well defined steps also shown in **Figure 7a** at 3.6 V and 3.5V. The potential E-x dependence indicates a two-phase behavior for the first part of the process with a potential plateau at 3.6V followed from mid-discharge by a step with a decreasing potential suggesting a single phase region. This C/50 rate can be considered as an equilibrium curve due to the very symmetric shape and minimum hysteresis between reduction and oxidation curves.

The discharge/charge profile of γ' -V₂O₅ at C/10 in the 4.0-2.5 V voltage range is shown in **Figure 8a**. From discharge curve two plateaus can be observed at 3.6 and 3.5V with total faradic yield of 1 F/mol which is consistent with CV results. The discharge/charge capacity exhibits 150 mAh g⁻¹, indicating reversible insertion/extraction process. The initial discharge capacity slightly reduced to 138 mAh g⁻¹ after 50 cycles with a good capacity retention and keeping the same voltage profile shape without increasing hysteresis (~15 mV). By increasing the C-rate from C/10 to 1C (with pre-cycling at C/10) the discharge capacity reaches 141 mAh g⁻¹ with Faradic yield of 0.95 F mol⁻¹ with typical two working plateau (**Figure 8 c, d**). The polarization is slightly increased from ~15 mV to ~70 mV at C/10 and 1C respectively. The discharge capacity slightly decreases by 8% after 50 cycles, from 141 to 131 mAh g⁻¹ at 1C with stable polarization in discharge/charge shape (**Figure 8c**).



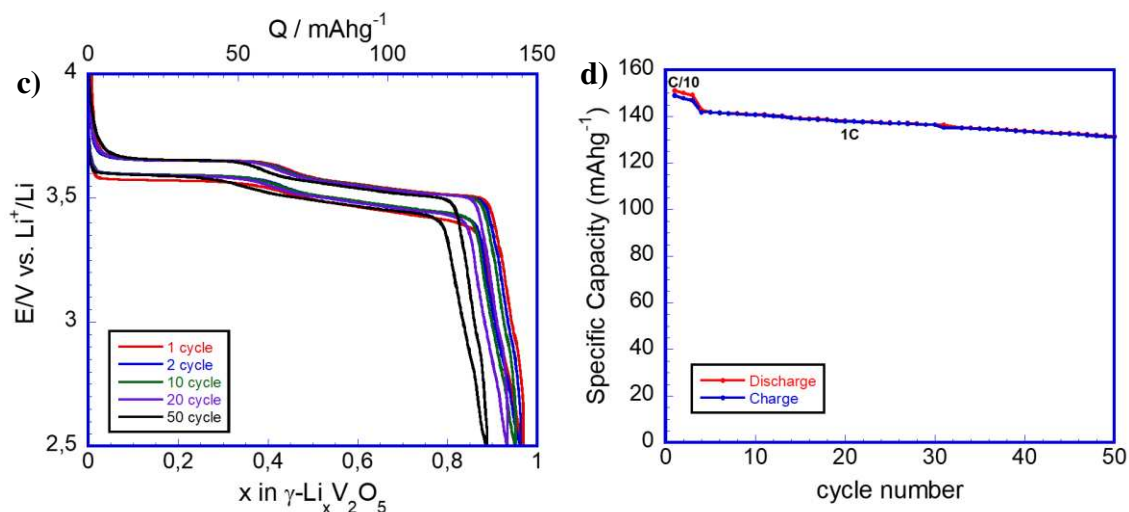


Figure 8. Discharge-charge and cycle performance of γ' - V_2O_5 at (a, b) C/10 at (c, d) 1C (with pre-cycling at C/10) in 4 – 2.5V voltage range

2.1.5 Structural investigation upon discharge-charge

Further, structural changes of γ' - V_2O_5 were examined during lithium insertion process on 1st discharge at C/10 at different value of x ($0 \leq x \leq 1$) (**Figure 9**). The XRD patterns and Raman spectra of γ' - V_2O_5 electrodes are shown in **Figure 10 and 11**. Before discharge, the pristine electrode indicates the typical XRD pattern of γ' - V_2O_5 , cell parameters [$a=9.94$ Å, $b=3.58$ Å, $c=10.04$ Å] are consistent with the orthorhombic structure of $Pnma$ space group.

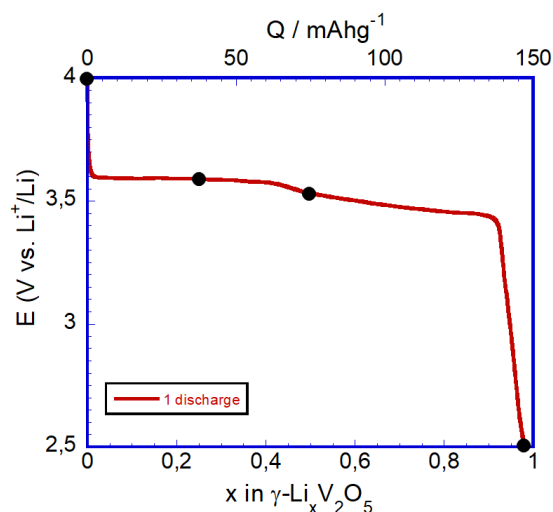


Figure 9. The first discharge of γ' - V_2O_5 at C/10 in 4 – 2.5V voltage range

From $x=0.2$, a new set of 002, 200, 102, 103, 214 diffraction lines at 19.9° , 20.95° , 22.5° , 31.9° and 55° appears and coexists with initial γ' - V_2O_5 material. This new set of lines, also indexed in

an orthorhombic cell with $Pnma$ space group, belongs to lithiated host lattice. The unit cell parameters for γ' - $\text{Li}_x\text{V}_2\text{O}_5$ is [$a=9.81 \text{ \AA}$, $b=3.6 \text{ \AA}$, $c=10.43 \text{ \AA}$] and for γ' - V_2O_5 [$a=9.91 \text{ \AA}$, $b=3.59 \text{ \AA}$, $c=10.05 \text{ \AA}$].

For $x=0.5$ diffraction patterns are indexed according to the orthorhombic lithiated single phase ($Pnma$ space group) with significant shift of the most reflections. This variation is typical to the solid solution behavior with progressive lithium enrichment into γ - $\text{Li}_x\text{V}_2\text{O}_5$. The unit cell parameters for the fully lithiated phase: $a=9.69 \text{ \AA}$, $b=3.60 \text{ \AA}$, $c=10.67 \text{ \AA}$ are in good agreement with reported data for synthesized γ - LiV_2O_5 [31].

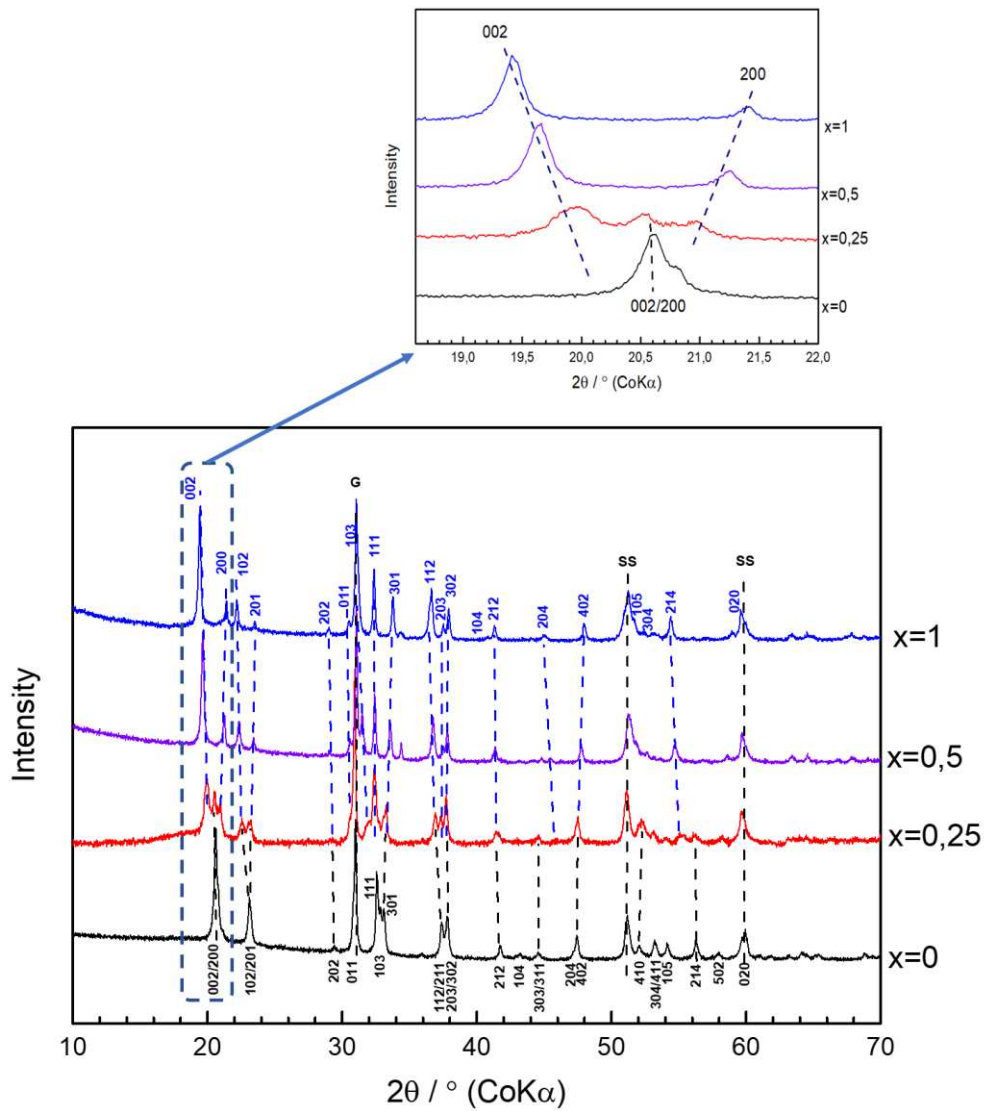


Figure 10. Ex-situ XRD of γ' - V_2O_5 at state of discharge at C/10

Ex-situ Raman spectra at different state of discharge ($x = 0.25, 0.5, 1$) are shown in **Figure 11**. The Raman spectrum of pristine electrode exhibits typical fingerprint of γ' - V_2O_5 showing 21 bands at 92, 126, 138, 153, 171, 190, 238, 266, 282, 299, 349, 390, 500, 532, 603, 694, 722, 752, 1003, 1021, 1037 cm^{-1} . During discharge the most intensive band at 138 cm^{-1} disappear at $x=0.25$, while intensity of γ' - V_2O_5 Raman features located at 153, 171, 190, 238, 282, 390, 532, 603, 1037 cm^{-1} gradually decreased with x . At the same time, additional bands arise at 160, 544, 625, 730 cm^{-1} . For $x=0.5$ a new band at several shifts toward lower wavenumber are observed: 349 cm^{-1} to 343 cm^{-1} , 390 cm^{-1} to 380 cm^{-1} , 1003 cm^{-1} to 990 cm^{-1} , 1015 cm^{-1} to 1010 cm^{-1} . For $x=1$ the Raman fingerprint of the new system, which bands are located at 101, 125, 171, 207, 272, 331, 374, 462, 531, 727, 966 and 990 cm^{-1} can be seen. The Raman spectrum of for fully discharged electrode matches with reported γ - LiV_2O_5 [32].

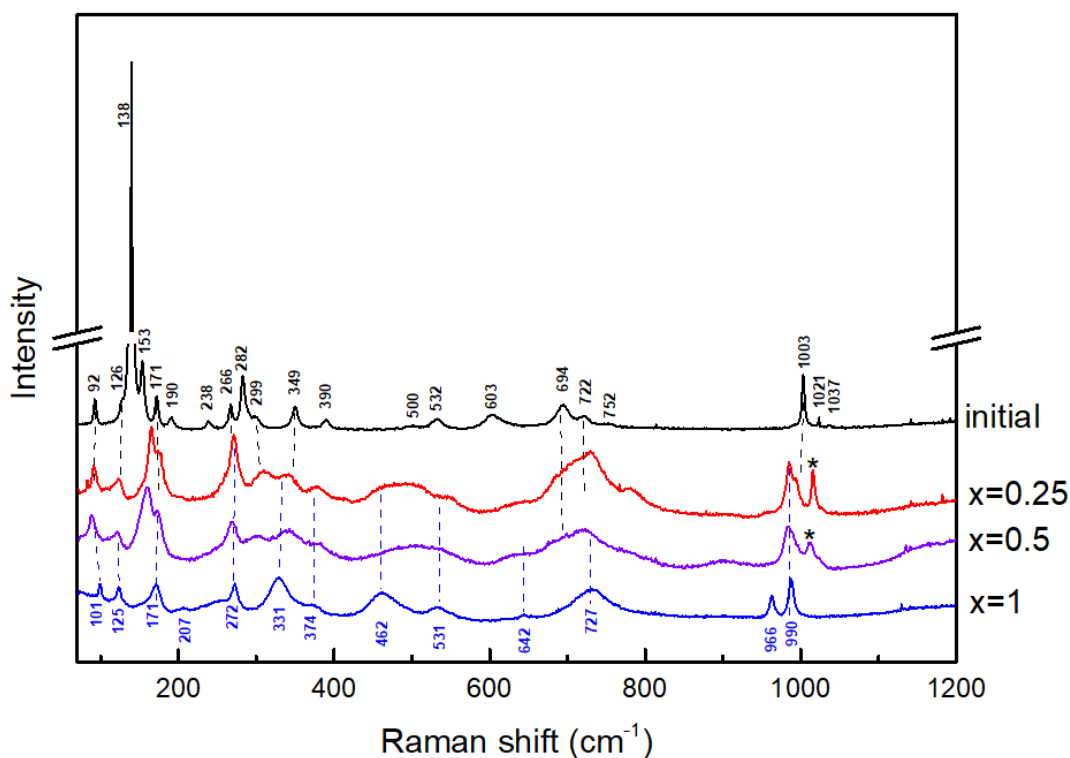


Figure 11. Ex-situ Raman spectra at different state of discharge of γ' - V_2O_5 at C/10

In addition, the structural reversibility of the γ' - V_2O_5 material was examined after 1 cycle. The Ex-situ XRD pattern and Raman spectrum of charged electrode in potential range 4 – 2.5V at C/10 is shown in **Figure 12**. The obtained results after 1 cycle correspond to the initial γ' - V_2O_5 , demonstrating the complete Li insertion/extraction from the γ' - V_2O_5 structure. The additional peak or band was not detected.

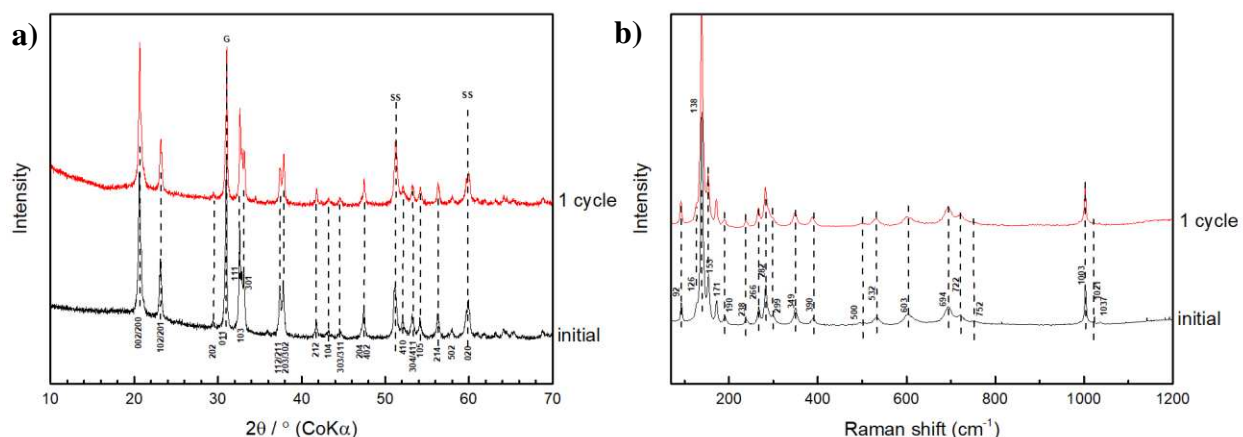


Figure 12. Ex-situ (a) XRD pattern and (b) Raman spectrum γ' -V₂O₅ electrode material after 1 cycle at C/5 in potential range of 4 – 2.5V.

2.1.6 Cycling properties

The cycling properties of the polyol nanosized γ' -V₂O₅ (~200nm) compound were determined at C/10 between 4V and 2.4V and compared with that of γ' -V₂O₅ (*carbo*, micrometric platelets), obtained through the carbothermal reduction. Such comparative study should provide information on the relationship of a possible size and morphology effects on electrochemical performance. The discharge-charge profiles and cycle performance of γ' -V₂O₅ compounds at C/10 are shown in **Figure. 13**. The both samples show same voltage shape during discharge with two steps at 3.6 and 3.5V vs Li⁺/Li, with initial discharge capacity of ~150 mAh g⁻¹. During the charge, symmetric profiles can be observed with small hysteresis values of ~40 mV. After 50 cycles both materials exhibit discharge capacity of 138 mAh g⁻¹ with Faradic yield of 0.92 F/mol. At C/10, both compounds exhibit the same cycling performance.

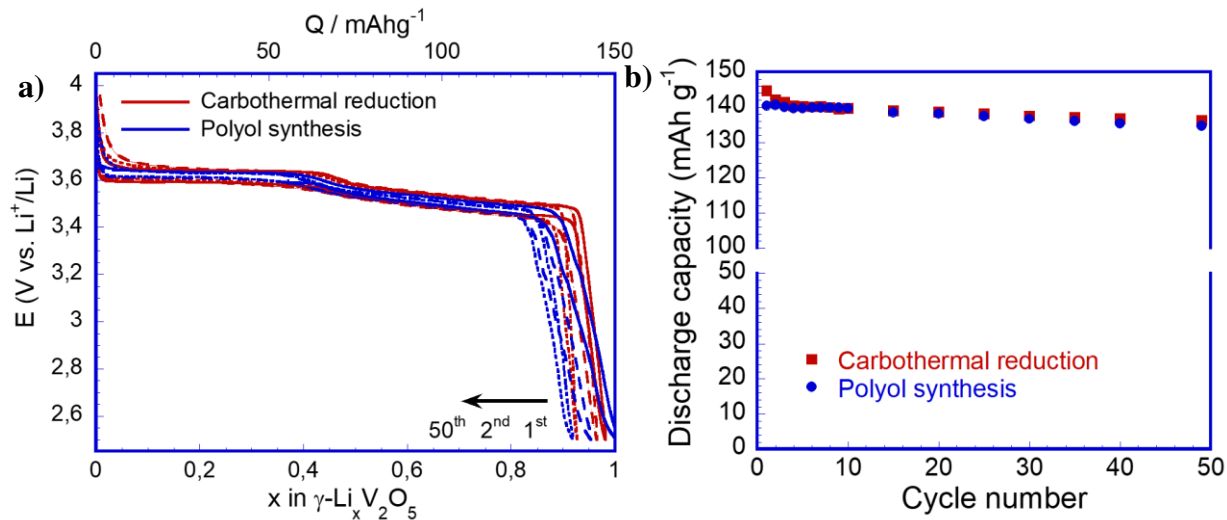


Figure 13. (a) Discharge-charge profile and (b) cycle performance of polyol and carboreduced γ' - V_2O_5 at C/10.

The electrochemical performance of the γ' - V_2O_5 was further investigated in terms of its rate capability (**Figure 14**). For γ' - V_2O_5 (carbo.), the initial discharge capacity exhibits 147 and 142 mAh g^{-1} at C/10 and C/5, with low hysteresis ($\sim 50\text{mV}$) while, at C/2 the discharge capacity of 134 mAh g^{-1} can be recovered. However, by increasing the C-rate in the range (1C – 10C) a huge increase of polarization can be observed. The hysteresis of 300 mV at 1C greatly increased to 540 mV at 2C and 1200 mV at 5C. In the same time, the discharge capacity decreased to 103, 79, 40, 5 mAh g^{-1} at 1C, 2C, 5C, 10 C (**Figure 14a**).

For γ' - V_2O_5 (pol.) the initial discharge capacity displays 144 and still 140 mAh g^{-1} at C/10 and C/5, respectively. The polarization for low C-rates (C10 – C/5) is only around 30 mV and slightly increases to 70 mV at C/2 (**Figure 14b**). The discharge capacities at C/2, 1C, 2C, 5C, 10C reach 136, 133, 129, 125 and 108 mAh g^{-1} , respectively (**Figure 15b**). In addition, the capacity is fully recovered upon charge with a symmetric profile at all C-rates which indicates a high reversibility in line with the highly reversible structural changes shown in our structural study. Compared with carboreduced- γ' - V_2O_5 , the hysteresis found for polyol oxide is limited to only 100 mV at 1C, 150 mV at 2C and 300 mV at 5C.

From **Figure 14 and 15**, the huge difference in the rate capability behaviour of both samples clearly reveals a positive nanosize effect promoting the electrochemical properties of the polyol γ' - V_2O_5 material from the 1C rate. Even after applying 20C (discharge capacity 47 mAh g^{-1}), the specific capacity is fully recovered when C-rate switched to C/5 (discharge capacity 133 mAh g^{-1}).

¹) with stable cyclability. The better rate capability found for the polyol material can be understood in terms of a faster and more efficient lithiation process due to a shortening of diffusion pathway for lithium ions. The electrochemical surface area of polyol oxide is probably enhanced compared to micro-sized material.

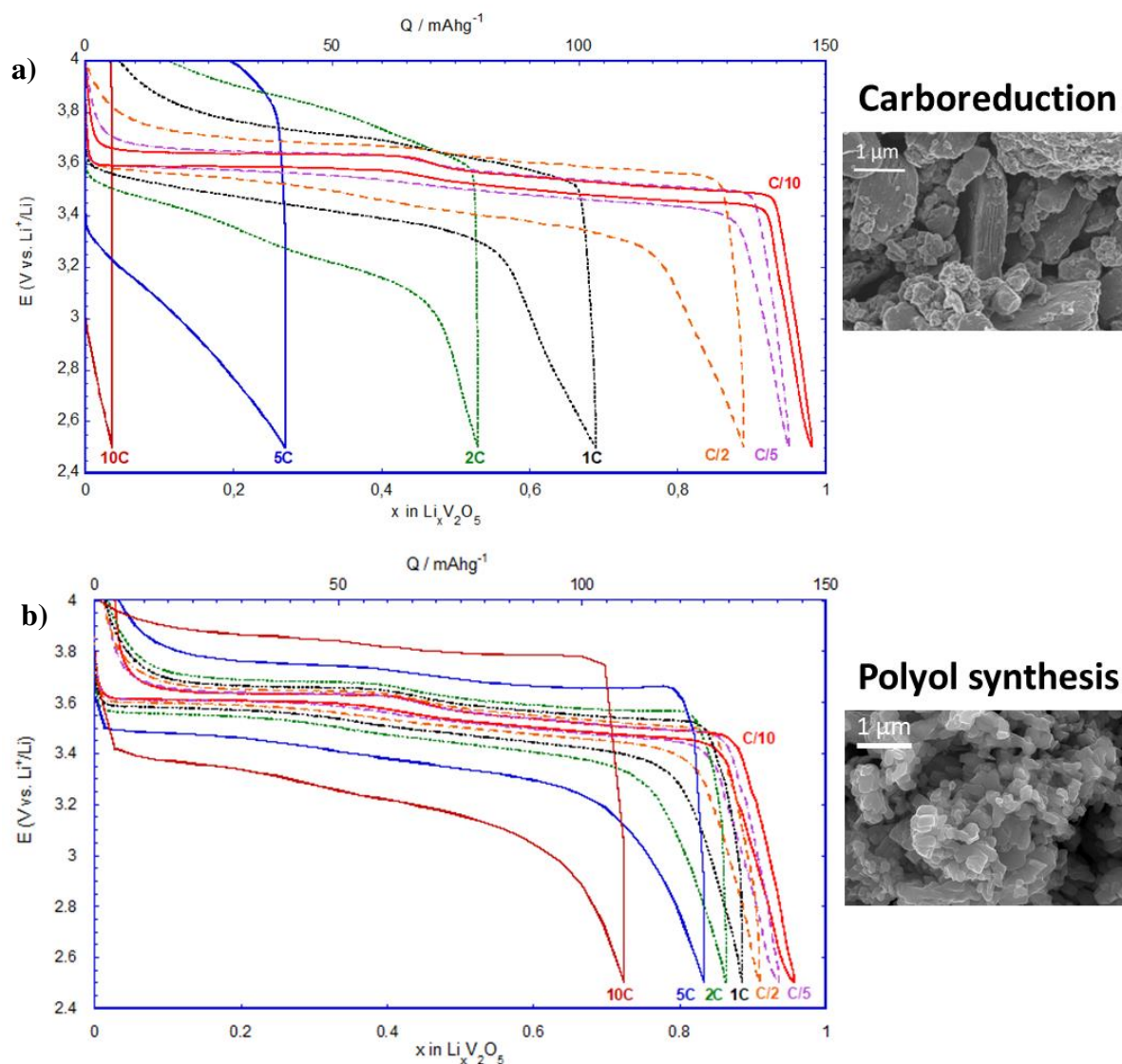


Figure 14. Discharge-charge profiles of γ' - V_2O_5 (*carbo.*) and γ' - V_2O_5 (*pol.*) at different C-rate

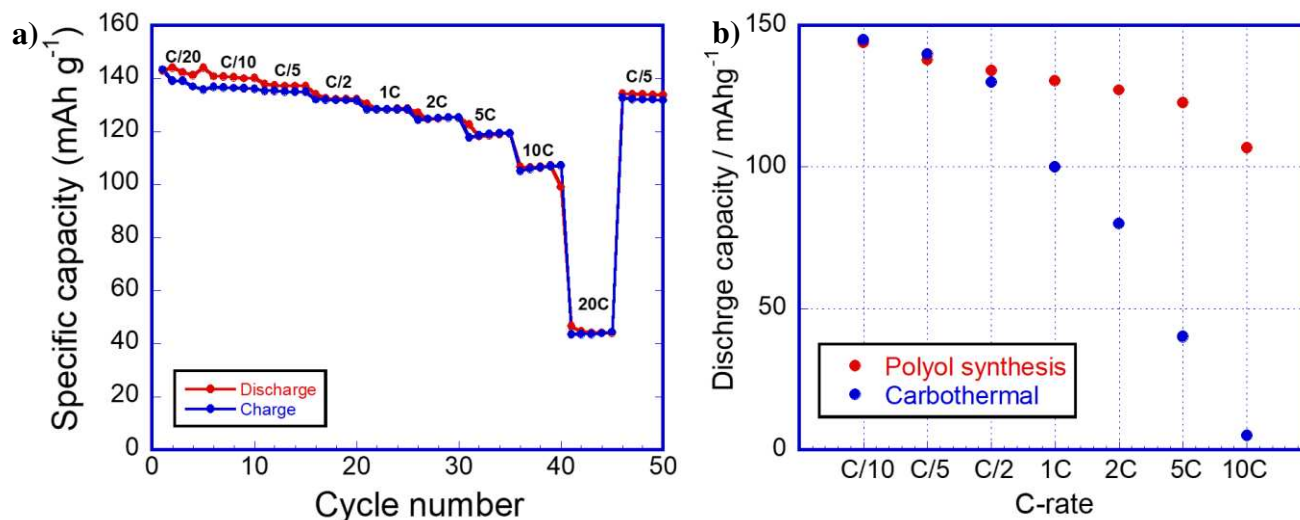


Figure 15. Rate-capability of γ' -V₂O₅ (*pol.*) and comparison of discharge capacities at different C-rates

2.1.7 Conclusion

The electrochemical properties of polyol synthesized γ' -V₂O₅ toward Li was investigated with high working potential in comparison to α -V₂O₅. This voltage enhancement, related to the specific structure, represents a key improvement in term energy density. The corresponding discharge capacity of 150 mAh g⁻¹ at C/10 was achieved, with well-defined two working plateaus at 3.6 and 3.5V with Faradic yield of 1 F/mole. A stable cyclability was achieved over 50 cycles at C/10 and 1C, with discharge capacity of 138 and 131 mAh g⁻¹, respectively. The structural evolution of γ' -V₂O₅ was investigated by Ex-situ XRD and Raman spectroscopy during first discharge and one complete cycle showing the existence of a diphasic region for the first half discharge while the second part corresponds to a single phase whose interlayer distance increases with Li content. The obtained results on the rate capability of *pol.* and *carbo.* synthesized γ' -V₂O₅ illustrate the correlation between particle size, morphology and electrochemical performance of the material. The smaller particle size (~200 nm) against micrometric pellets, leads to the enhancement of rate capability of material with minimized hysteresis. High specific capacities of 136, 133, 129, 125 and 108 mAh g⁻¹ are achieved at C/2, 1C, 2C, 5C, 10C. Even after 20C, by switching C-rate to C/5, discharge capacity gains 133 mAh g⁻¹ for over 5 cycles. Finally, polyol γ' -V₂O₅ has been proved to be is one of the best cathode materials among vanadium oxides due to its high performance even at 10C with 108 mAh g⁻¹ available at 3.2V upon cycling.

SUPPORTING INFORMATION

Electrochemical characterization

γ' -V₂O₅ positive electrodes were prepared by mixing 90wt% of active material, 6wt% polyvinylidene fluoride (PVDF, Kynar, HSV900) as a binder, 4wt% ketjen black (Ketjen Black International Co., Japan) as conductive agent dissolved in 1-methyl-2-pyrrolidinone (NMP, Sigma-Aldrich). The prepared slurry was casted on carbon paper (Alfa Aesar Co.), vacuum dried at 70 °C for 3hr and punched into the disks of 8 mm in diameter. The mass loading of active material was ~ 5 mg/cm² (2.7-2.8 mg of active material). Zinc foil (Goodfellow, USA) was used as negative electrode. The electrolyte was prepared by dissolving 4 mole L⁻¹ of ZnSO₄ and 3 mole L⁻¹ of Li₂SO₄ in distilled water and pH was adjusted to 4 by titration with 0.5 mole L⁻¹ of H₂SO₄. Prepared electrolyte was bubbled with nitrogen gas (N₂) to remove dissolved oxygen. AGM (Absorptive Glass Mat NSG Corporation) was used as separator. The structural investigation of Zn/Li₂SO₄-ZnSO₄/ γ' -V₂O₅ system was investigated by using two-electrode split cell (MTI company). The cells were discharged to the required composition by electrochemical reduction using VMP3 Biologic tester at C/5 rate. After reduction, cells were disassembled in air, electrodes were rinsed in distilled water in order to remove the traces of salt and separator. Cyclic voltammetry (CV) was performed with VMP3 potentiostat/galvanostat (Bio-Logic Science Instrument Co.)

Structural investigations

XRD measurements were carried out using a Panalytical X'pert pro diffractometer equipped with an X'celerator detector and a Co Ka radiation (wavelength 1.7889 Å). All the diffraction patterns were collected with a 2 θ step of 0.0167°. The Raman spectra were measured with a LaBRAM HR 800 (Jobin-Yvon-Horiba) Raman micro-spectrometer including Edge filters and equipped for signal detection with a back illuminated charge coupled device detector (Spex CCD) cooled by Peltier effect to 200 K. A He:Ne laser (632.8 nm) was used as the excitation source. The spectra were measured in back-scattering geometry. The resolution was about 0.5 cm⁻¹. A 50X LWD objective was used to focus the laser light on sample surface to a spot size of 1 μ m². To avoid local heating of the sample, the power of the laser beam was adjusted to 0.2–0.5 mW with neutral filters of various optical densities. Raman spectra were recorded on ten different spots of each electrode

to check the homogeneity. The powders were characterized by scanning electron microscopy (SEM), Zeiss, Merlin-type microscope.

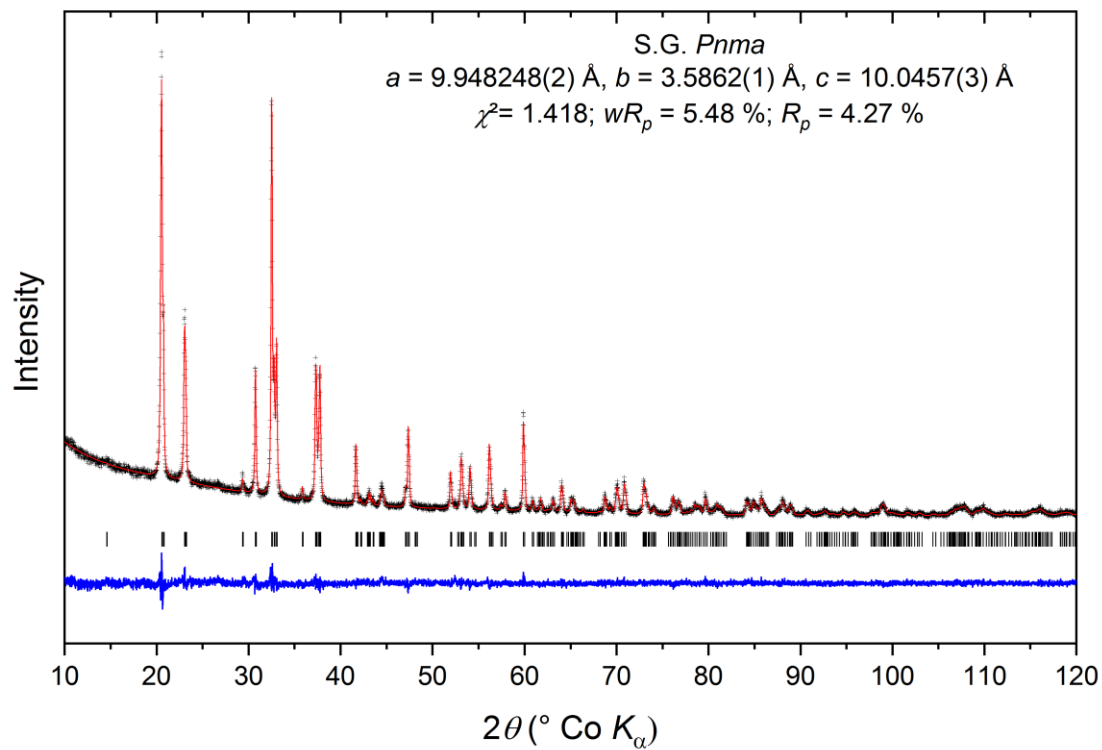


Figure S1. Rietveld refinement of γ' - V_2O_5 XRD pattern

REFERENCES

- [1] M.S. Whittingham, Lithium batteries and cathode materials, *Chem. Rev.* 104 (2004) 4271-4301.
- [2] D.W. Murphy, P.A. Christian, F.J. Disalvo, J.V. Waszczak, Lithium incorporation by vanadium pentoxide, *Inorg. Chem.* 18 (1979) 2800-2803.
- [3] J.P. Pereira-Ramos, R. Messina, C. Piolet, J. Devynck, A thermodynamic study of electrochemical lithium insertion into vanadium pentoxide, *Electrochim. Acta* 33 (1988) 1003-1008.
- [4] J.M. Cocciantelli, P. Gravereau, J.P. Doumerc, M. Pouchard, P. Hagenmuller, On the preparation and characterization of a new polymorph of V_2O_5 , *J. Solid State Chem.* 93 (1991) 497-502.
- [5] C. Delmas, S. Brethes, M. Menetrier, Omega- $Li_xV_2O_5$ - a new electrode material for rechargeable lithium batteries, *J. Power Sources* 34 (1991) 113-118.
- [6] J.M. Cocciantelli, M. Menetrier, C. Delmas, J.P. Doumerc, M. Pouchard, P. Hagenmuller, Electrochemical and structural characterization of lithium intercalation and deintercalation in the gamma- LiV_2O_5 bronze, *Solid State Ionics* 50 (1992) 99-105.
- [7] C. Delmas, H. Cognac-Auradou, J.M. Cocciantelli, M. Menetrier, J.P. Doumerc, The $Li_xV_2O_5$ system - an overview of the structure modifications induced by the lithium intercalation, *Solid State Ionics* 69 (1994) 257-264.
- [8] K. West, B. Zachau-Christiansen, T. Jacobsen, S. Skaarup, Lithium insertion into vanadium pentoxide bronzes, *Solid State Ionics* 76 (1995) 15-21.
- [9] B. Pecquenard, D. Gourier, N. Baffier, EPR identification of $Li_xV_2O_5$ phases generated by chemical and electrochemical lithium intercalation in V_2O_5 , *Solid State Ionics* 78 (1995) 287-303.
- [10] E. Prouzet, C.C.D. Moulin, F. Villain, A. Tranchant, Electrochemical intercalation of lithium into vanadium pentaoxide: an in situ X-ray absorption study, *J. Chem. Soc., Faraday Trans.* 92 (1996) 103-109.
- [11] P. Rozier, J.M. Savariault, J. Galy, A new interpretation of the $Li_xV_2O_5$ electrochemical behaviour for $1 < x < 3$, *Solid State Ionics* 98 (1997) 133-144.
- [12] P. Rozier, J.M. Savariault, J. Galy, C. Marichal, J. Hirschinger, P. Granger, epsilon- $Li_xV_2O_5$ bronzes ($0.33 \leq x \leq 0.64$) a joint study by X-ray powder diffraction and Li-6, Li-7 MAS NMR, *Eur. J. Solid State Inorg. Chem.* 33 (1996) 1-13.
- [13] E.A. Meulenkamp, W. van Klinken, A.R. Schlattmann, In-situ X-ray diffraction of Li intercalation in sol-gel V_2O_5 films, *Solid State Ionics* 126 (1999) 235-244.
- [14] Y. Sato, T. Asada, H. Tokugawa, K. Kobayakawa, Observation of structure change due to discharge/charge process of V_2O_5 prepared by ozone oxidation method, using in situ X-ray diffraction technique, *J. Power Sources* 68 (1997) 674-679.
- [15] J.M. Savariault, P. Rozier, Evidence of lithium ordering in epsilon- $Li_xV_2O_5$ phase, *Phys. B.* 234 (1997) 97-99.
- [16] R.J. Cava, A. Santoro, D.W. Murphy, S.M. Zahurak, R.M. Fleming, P. Marsh, R.S. Roth, The structure of the lithium-inserted metal-oxide delta- LiV_2O_5 , *J. Solid State Chem.* 65 (1986) 63-71.
- [17] H. Katzke, M. Czank, W. Depmeier, S. Van Smaalen, On the incommensurately modulated structure of epsilon'- $Li_xV_2O_5$ at room temperature, *Philos. Mag BPhys. Condens. Matter Stat. Mech. Electron. Opt. Magn. Prop.* 75 (1997) 757-767.

- [18] B. Garcia, M. Millet, J.P. Pereira-Ramos, N. Baffier, D. Bloch, Electrochemical behaviour of chemically lithiated $\text{Li}_x\text{V}_2\text{O}_5$ phases ($0.9 \leq x \leq 1.6$), *J. Power Sources* 81 (1999) 670-674.
- [19] C. Leger, S. Bach, P. Soudan, J.P. Pereira-Ramos, Structural and electrochemical properties of omega- $\text{Li}_{(x)}\text{V}_{(2)}\text{O}_{(5)}$ ($0.4 \leq x \leq 3$) as rechargeable cathodic material for lithium batteries, *J. Electrochem. Soc.* 152 (2005) A236-A241.
- [20] P.G. Dickens, S.J. French, A.T. Hight, M.F. Pye, Phase-relationships in the ambient temperature $\text{Li}_x\text{V}_2\text{O}_5$ system ($0.1 < x < 1.0$), *Mater. Res. Bull.* 14 (1979) 1295e1299.
- [21] J.M. Cocciantelli, J.P. Doumerc, M. Pouchard, M. Broussely, J. Labat, Crystalchemistry of electrochemically inserted $\text{Li}_x\text{V}_2\text{O}_5$, *J. Power Sources* 34 (1991) 103-111.
- [22] R. Baddour-Hadjean, A. Marzouk, J.P. Pereira-Ramos, Structural modifications of $\text{Li}_x\text{V}_2\text{O}_5$ in a composite cathode ($0 \leq x < 2$) investigated by Raman microspectrometry, *J. Raman Spectrosc.* 43 (2012) 153-160.
- [23] K. West, B. Zachau-Christiansen, T. Jacobsen, S. Skaarup, Lithium insertion into vanadium pentoxide bronzes, *Solid State Ionics* 76 (1995) 15-21.
- [24] D. Huo, A. Contreras, B. Laïk, P. Bonnet, K. Guérin, D. Muller-Bouvet, C. Cenac- Morthe, R. Baddour-Hadjean, J.P. Pereira-Ramos, Evidence for a nanosize effect on the structural and high performance electrochemical properties of V_2O_5 obtained via fluorine chemistry, *Electrochim. Acta* 245 (2017) 350-360.
- [25] A. Parija, D. Prendergast, S. Banerjee, Evaluation of multivalent cation insertion in single- and double-layered polymorphs of V_2O_5 , *Appl. Mater. Interfaces* 9 (2017) 23756-23765.
- [26] A. Parija, Y. Liang, J.L. Andrews, L.R. De Jesus, D. Prendergast, S. Banerjee, Topochemically de-intercalated phases of V_2O_5 as cathode materials for multivalent intercalation batteries : a first principle evaluation, *Chem. Mater.* 28 (2016) 5611-5620.
- [27] J. Barker, M.Y. Saidi, J.L. Swoyer, Performance evaluation of the electroactive material $\gamma\text{-LiV}_2\text{O}_5$ made by a carbothermal reduction method, *J. Electrochem. Soc.* 150 (2003) A1267-A1272.
- [28] J. Dai, S.F.Y. Li, Z. Gao, K.S. Siow, Novel method for synthesis of g-lithium vanadium oxide as cathode materials in lithium ion batteries, *Chem. Mater.* 11 (1999) 3086-3090.
- [29] W. Wang, H. Wang, S. Liu, J. Huang, Synthesis of $\gamma\text{-LiV}_2\text{O}_5$ nanorods as a high performance cathode for Li ion battery, *J. Solid State Electrochem.* 16 (2012) 2555-2561.
- [30] Y.W. Wang, H.Y. Xu, H. Wang, Y.C. Zhang, Z.Q. Song, H. Yan, C.R. Wan, Solvothermal synthesis and characterizations of $\gamma\text{-LiV}_2\text{O}_5$ nanorods, *Solid State Ionics* 167 (2004) 419-424.
- [31] Renard, Marianne. (2017). Propriétés électrochimiques et réponse structurale du polymorphe $\gamma'\text{-V}_2\text{O}_5$ vis-à-vis de l'insertion du lithium et du sodium.
- [32] R. Baddour-Hadjean, M. Safrany Renard, J.P. Pereira-Ramos Unraveling the structural mechanism of Li insertion in $\gamma'\text{-V}_2\text{O}_5$ and its effect on cycling properties, *Acta Materialia* 165 (2019) 183-191

2.2 Improved electrochemical performances of γ' -V₂O₅ prepared by a solution technique as cathode material for Na-ion batteries.

2.2.1 Introduction

Nowadays, lithium-ion batteries (LIBs) are widely used in portable equipment like smartphones, laptops, cameras, power tools, etc.. Moreover, they are gaining popularity in automotive, aerospace, marine, medical, etc., applications. This success is due to high-energy density, a tiny memory effect and low self-discharge. Global LIBs market is expected to reach USD 107.6 Billion by 2025 [1]. Despite these growth forecasts, considering the low natural presence of lithium in the upper crust and mining and refining expenses, the scientific community is moving towards the discovery of alternative systems to LIBs. This context prompted researchers to transfer the LIBs technology to sodium ion batteries (NIBs), because of sodium low cost, its abundant resource and environmental friendliness. Moreover, contrary to lithium, sodium does not alloy with aluminum, which enables its use as current collectors instead of copper that is heavier and more expensive, with the benefit of gravimetric cell energy and power density. Consequently, and despite a larger radius (0.102 nm vs. 0.076 nm for Na⁺ vs. Li⁺), a heavier molar mass (22.99 g mol⁻¹ vs. 6.94 g mol⁻¹ for Na⁺ vs. Li⁺) and a more positive potential (-2.71 V/ENH vs. -3.04 V/ENH for Na⁺ vs. Li⁺) causing loss of energy and power density, NIBs have recently gained commercialization status, and the market is expected to grow with an impressive annual growth rate of 24 % for the forecast period of 2017 to 2025 [2]. Based on the intended applications, including the stationary storage of intermittent clean energies, one of the most challenging problems remains the identification of suitable electrodes materials.

Among various candidates, the layered orthorhombic transition metal oxide V₂O₅, with high theoretical capacity (442 mAh g⁻¹ for three moles of lithium per mole of V₂O₅) and large abundance, has been intensively investigated as positive electrode in LIBs [3]. Lithium-ion intercalation capacity and cyclability can be optimized by playing on the structure, crystallinity, morphology, grain size of the material of the material thanks to different synthesis [4].

Since LIBs and NIBs have very close insertion chemistry [5,6], V₂O₅ has been regarded as a potential cathode material for sodium insertion. After the pioneering works of West [7] and Pereira-Ramos [8] carried out respectively at 80°C with a solid electrolyte and at 150°C in molten dimethylsulfone in the late 1980s, few papers have been devoted to the study of the Na

electrochemical insertion in this open structure material and no structural evolution under sodiation/desodiation was provided to explain the mechanism. A few years ago, our group reported for the first time the structural changes of electrochemically formed $\text{Na}_x\text{V}_2\text{O}_5$ samples at room temperature. After the irreversible electrochemical formation of α' - NaV_2O_5 , 0.8 Na per mole of NaV_2O_5 could be reversibly inserted at a working potential of around 2.0 V, at room temperature (120 mAh g^{-1}), over several tens of cycles [9]. Results in literature suggest that nano-structuring the material is beneficial in terms of capacity and cycling. For instance, V_2O_5 hollow nanospheres exhibit a capacity about 150 mAh g^{-1} for cycling, at 20 mA g^{-1} , in the wide 1.0-4.2 V potential window [10].

Another way to increase V_2O_5 electrochemical performances is to consider polymorphs such as the ϵ' bilayered V_2O_5 [11,12] or γ' - V_2O_5 . The γ' polymorph, characterized by a puckered layer stacking, has already been studied in our team as cathode material in LIBs [13] and more recently in NIBs [14]. It is noticeable, that 1 Li^+ is reversibly inserted per mole of oxide at a higher working potential than α - V_2O_5 , (3.55 V vs. Li^+/Li for γ' - V_2O_5 vs. 3.35 V vs. Li^+/Li for α polymorph) [13]. On the other hand, in the case of sodium insertion, the γ' polymorph exhibits one single reduction step with a plateau extending up to $\sim 1 \text{ Na}^+$ per mole of oxide [14]. Sodium insertion, occurring at c.a. 3.3 V vs. Na^+/Na ($\sim 0.6 \text{ V}$ vs. NHE), takes place practically at the same potential as lithium insertion. This suggests that Na^+ insertion is facilitated in the γ' polymorph due to its original puckered and flexible structure with a large interlayer spacing (5.02 \AA in γ' - V_2O_5 against 4.37 \AA in α - V_2O_5).

Synthesized by lithium removal from γ - LiV_2O_5 obtained by carbothermal reduction method requiring high-temperature treatment (2 hours at 600°C) [15], γ' - V_2O_5 exhibits a high discharge rate capability for sodiation with a slight decrease from 145 mAh g^{-1} at C/60 to 135 and 120 mAh g^{-1} at C/2 and 1C respectively. However, the charge process itself has a strong kinetic limitation since a low 60 % efficiency at RT (C/20) is observed while a full Na extraction is only achieved at higher temperature (50°C) combined with a lower C rate (C/60) [14]. To overcome this kinetic limitation probably due to the micrometric platelets size of pristine material, ball-milling has been firstly considered [12]. This strategy was proved to be successful with a clear improvement in the charge efficiency ($\approx 90 \%$) allowing a stable capacity about 120 mAh g^{-1} to be achieved upon cycling. Nevertheless, its implementation is done at the expense of an additional

step in the synthesis and a strong modification of the charge/discharge profile with a significant lower working potential.

Therefore, we decided to develop another way for mastering the grain size in order to benefit from i) the high available capacity of 145 mAh g^{-1} , ii) the high working potential about 3.2 V vs. Na^+/Na , iii) an enhanced kinetics of sodium insertion/deinsertion and iv) a high rate capability and good cycle life. We propose here a low temperature solution technique for preparing reduced sized γ' - V_2O_5 . The polymorph is obtained from a homemade α - V_2O_5 precursor produced through a polyol process, leading easily to an homogeneous pure fine powder, with a mean grain size of 100–200 nm [16]. Contrary to the γ' - V_2O_5 usually obtained via a high temperature synthesis, we show here this down-sizing approach enables an excellent sodium insertion / deinsertion efficiency. In addition to the evidence for improved electrochemical properties with the polyol γ' - V_2O_5 , a detailed study by X-ray diffraction and Raman spectroscopy allows us to describe the structural response of the host material. Finally, a kinetic study performed using electrochemical impedance spectroscopy reveals the great enhancement of the electroactive surface area as the key-point for explaining the optimized behavior of polyol γ' - V_2O_5 .

2.2.2 Synthesis

The synthesis of γ' - V_2O_5 developed in the laboratory is already described in literature [16]. The α - V_2O_5 precursor is synthesized according to the polyol method [17], whose characteristic is to lead to very fine powder with a narrow particle size distribution. By reaction with an excess of lithium iodide in acetonitrile, the intermediate δ - LiV_2O_5 phase is formed. After washing in acetonitrile and drying at 70 °C, the obtained powder is heat treated at 300 °C for 2 hours under dynamic primary vacuum in a Büchi® furnace to allow the phase transition towards γ - LiV_2O_5 . A chemical oxidation is then carried out in presence of an excess of NO_2BF_4 , at room temperature, in acetonitrile and under stirring. This step entails the removing of lithium ions from the interlayer structure of the γ phase without altering the distorted framework consequently kept in the final γ' - V_2O_5 product, labelled as γ' -polyol.

2.2.3 Structural characterization

Both γ' -V₂O₅ compounds that are compared in this work were synthesized in our lab. They were obtained by chemical oxidation of γ -LiV₂O₅, by addition of nitronium tetrafluoroborate (NO₂BF₄) at room temperature in acetonitrile. The only difference was in producing γ -LiV₂O₅. In one case it is prepared by carbothermal reduction method that consists in intimately mixing carbon, commercial micrometric alpha-pentoxide vanadium (α -V₂O₅) and lithium carbonate (Li₂CO₃) before a high temperature heat-treatment (2 hours at 600 °C under primary vacuum) [15]. In the other case, it is synthesized according to a polyol soft chemistry route described in the experimental section. For convenience, the resulting polymorphs will be referred to as γ' -carbo. and γ' -polyol in the following.

γ' -carbo. and γ' -polyol powders are presented with the same magnification on the SEM image in **Figure 1**. γ' -carbo. exhibits aggregates with various sizes up to several hundred nanometers in thickness and several micrometers in plane. In contrast, γ' -polyol presents porous aggregates made of grains with homogeneous size distribution in the 100 - 200 nm range. While both polymorphs have crystallite sizes (estimated from the Scherrer equation from the hkl diffraction peaks) of the same order of magnitude (about 100 – 150 nm), it is also pointed out that the synthesis way has a strong impact on the grain size and distribution.

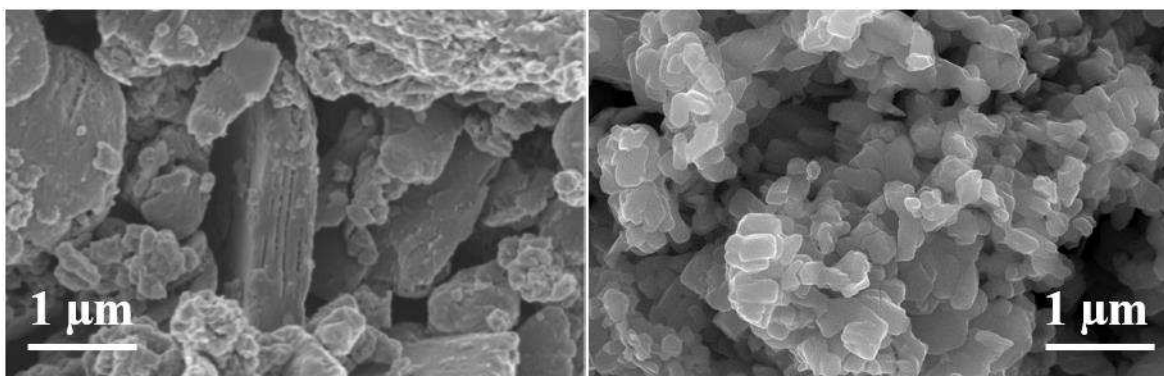


Figure 1. SEM images of γ' -V₂O₅ synthesized from commercial α -V₂O₅ (on left) and from α -V₂O₅ obtained by polyol process (on right).

The X-ray diffraction pattern of γ' -polyol (**Figure 2a**) exhibits the characteristics hkl reflections corresponding to an orthorhombic structure ($Pnma$ space group) with unit cell parameters $a = 9.9484(2)$ Å, $b = 3.5863(1)$ Å and $c = 10.0459(3)$ Å in agreement with previous

studies[18,19]. The structure of γ' -V₂O₅ (inset in **Figure 2a**) retains the layered V₂O₅ framework although puckering of the layers is observed. Besides, the Raman spectrum (**Figure 2b**) fully agrees with the previously reported fingerprint of γ' -V₂O₅ [19], composed of 21 peaks in the 90-1050 cm⁻¹ wavenumber range. All the vibrations of the chains can be identified: the stretching of the two vanadyl bonds at 1036, 1023, and 1001 cm⁻¹, the bond stretching vibrations localized within the V_a-O₃-V_b bridges at 753 and 602 cm⁻¹, and those of the V_a-O_{2a}-V_a and V_b-O_{2b}-V_b bridges forming the rails of the ladders at 721 and 694 cm⁻¹. Modes involving the V-O₂ ladder step bonds are observed at 530 and 497 cm⁻¹, while lower-frequency modes observed at 91, 126, 138, 152, 170, 190, 236, 266, 282, 297, 349, and 388 cm⁻¹ are related to the complex distortions of the ladders.

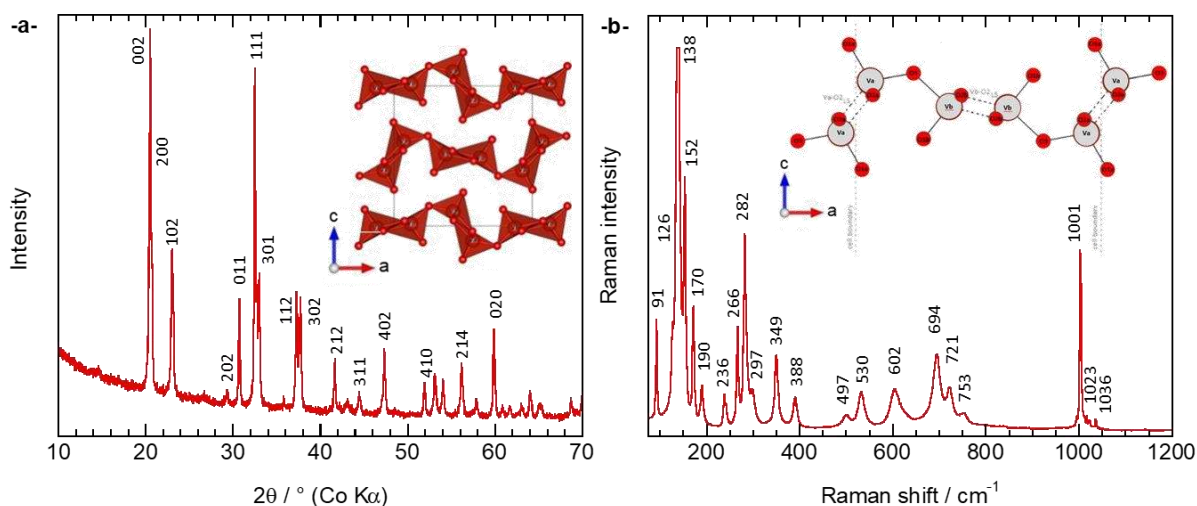


Figure 2. X-ray diffractogram (a) and Raman spectrum (b) of γ' -polyol V₂O₅. In inset: crystal structure and its projection along the *b*-crystallographic direction.

2.2.4 Electrochemical study

Figure 3, registered at C/10, illustrates the strong impact of the particle size and morphology on the electrochemical behavior of γ' -V₂O₅ in sodiated electrolyte. Indeed, while γ' -polyol- and γ' -carbo. show similar first discharge profile, i.e. one single step at c.a. 3.3 V vs. Na⁺/Na involving the insertion of 1 Na⁺ per mole of V₂O₅ (discharge capacity \approx 147 mAh g⁻¹), the charge reaction is greatly improved in the case of γ' -polyol. The poor charge efficiency limited at 51% during the

first cycle of γ' -carbo. was previously reported [14]. Conversely, γ' -polyol exhibits a fully symmetric first discharge-charge cycle with a charge efficiency close to 100 % and a low hysteresis (about 100 mV). This remarkable result suggests highly reversible structural changes upon sodiation/desodiation.

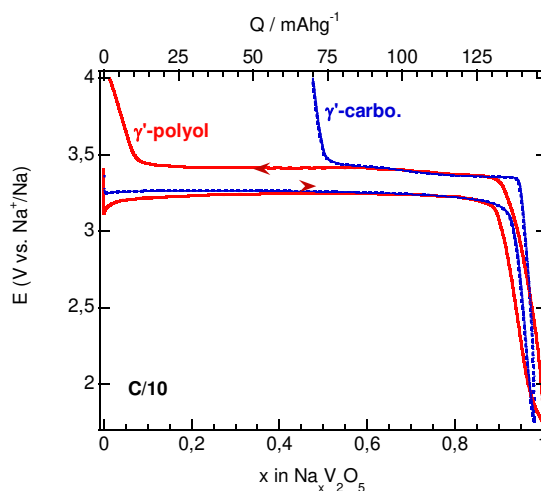


Figure 3. First discharge/charge cycles of γ' -polyol (red curve) and γ' -carbo. (blue dashed line) at C/10 in 1 mol L⁻¹ NaClO₄-PC-2 vol. % FEC in the 4.0V – 1.75 V potential range.

In the case of γ' -carbo., sodium ions trap in the structure was explained by a poor deinsertion kinetics [14]. This finding was confirmed by an increase of the charge efficiency when the cycling temperature was raised to 50 °C and/or when the C rate was lowered to C/60. Clearly, the high electrochemical reversibility achieved in the case of γ' -polyol confirms the benefit of the reduction in grain size shown in the SEM images (**Figure 1**) on the kinetics of the charging process. In order to understand the structural answer upon electrochemical sodiation of polyol- γ' -V₂O₅, *ex-situ* X-ray diffraction and Raman spectroscopy investigations were performed during the first discharge-charge cycle in the 4.00 V- 1.75 V potential range.

2.2.5 Structural investigation upon discharge-charge

The XRD patterns of discharged Na_xV₂O₅ electrodes in the $0 \leq x \leq 1$ composition range are gathered in **Figure 4**. The diffractogram of an electrode prior to reduction (in black, at the bottom) is indexed using the *Pnma* structure of γ' -V₂O₅. As soon as 0.1 Na is inserted in the γ' -V₂O₅ structure, a new set of peaks (highlighted in **Figure 4** by red vertical lines located at $2\theta = 17.3, 20.3, 21.2, 27.4, 28.2, 32.0, 34.0, 35.4, 36.5, 37.0, 40.1, 45.6, 46.7, 47.7$ and 48.0°) appears,

suggesting the emergence of a new phase. It can be noted that, for higher sodium contents, these peaks increase in intensity at the expense of peaks intensity of γ' -V₂O₅. This behavior is characteristic of a diphasic domain. When $x = 0.4$, the pristine phase has completely disappeared. The single sodiated phase, Na_{0.4}V₂O₅, can be indexed like the fully discharged electrode Na_{0.96}V₂O₅, with the same *Pnma* space group [14,16]. For $0 \leq x \leq 0.4$, the shifts of the 002 line towards lower angles (20.5° to 17.3°) and 200 peak towards higher angles (20.8° to 21.1°) in the diffractograms indicate a higher interlayer distance along the *c* axis, and a contraction along the *a* axis in the sodiated Na_{0.4}V₂O₅ compound. The subsequent patterns, i.e. for x varying from 0.5 to 1, do not exhibit new peaks and indicate a solid solution domain. In this composition range, very slight 002 and 200 peaks shifts are observed, indicating that both increase of the interlayer distance and contraction along the *a* axis are continuing but very mildly. To quantitatively illustrate these observations, the cell parameters and volume of both phases have been determined upon sodiation. They are gathered in **Figure 5**. The cell parameters of γ' -V₂O₅ ($a = 9.94$ Å, $b = 3.58$ Å, $c = 10.04$ Å) and Na _{x} V₂O₅ ($a = 9.79$ Å, $b = 3.61$ Å, $c = 11.91$ Å) are constant within the diphasic domain, ie for $0 \leq x \leq 0.4$. Then, for $x > 0.4$, the *a* parameter slightly decreases gradually (from 9.79 Å for $x = 0.4$ to 9.755 Å for $x = 1$) while *b* and *c* faintly increase (from $b = 3.61$ Å and $c = 11.91$ Å for $x = 0.4$ to $b = 3.63$ Å and $c = 11.94$ Å for $x = 1$). These evolutions, which are almost linear, confirm the existence of a solid solution domain for $0.4 < x \leq 1$. The volume expansion, about 17 %, mainly takes place in the diphasic domain. It is indeed very remarkable that the electroformed γ -Na _{x} V₂O₅ ($x \geq 0.4$) bronze does not undergo any significant lattice parameters variations in the $0.4 < x \leq 1$ composition domain. This sodiated phase is characterized by a highly expanded interlayer *c* parameter (+1.9 Å between γ' -V₂O₅ and γ -NaV₂O₅) which probably allows insertion of Na ions for $x > 0.4$ without any further structural changes. It is worth also noticing the lowering of the *a* parameter in γ -Na _{x} V₂O₅ (-0.2 Å between γ -NaV₂O₅ and γ' -V₂O₅). This trend reveals an extra folding of the V₂O₅ sheets as a consequence of the shortening of the vanadium-vanadium distances upon reduction. Besides, at the end of the reduction process, the obtained lattice constants are in excellent agreement with those reported for electrochemically and chemically formed Na_{0.96}V₂O₅ [14,16].

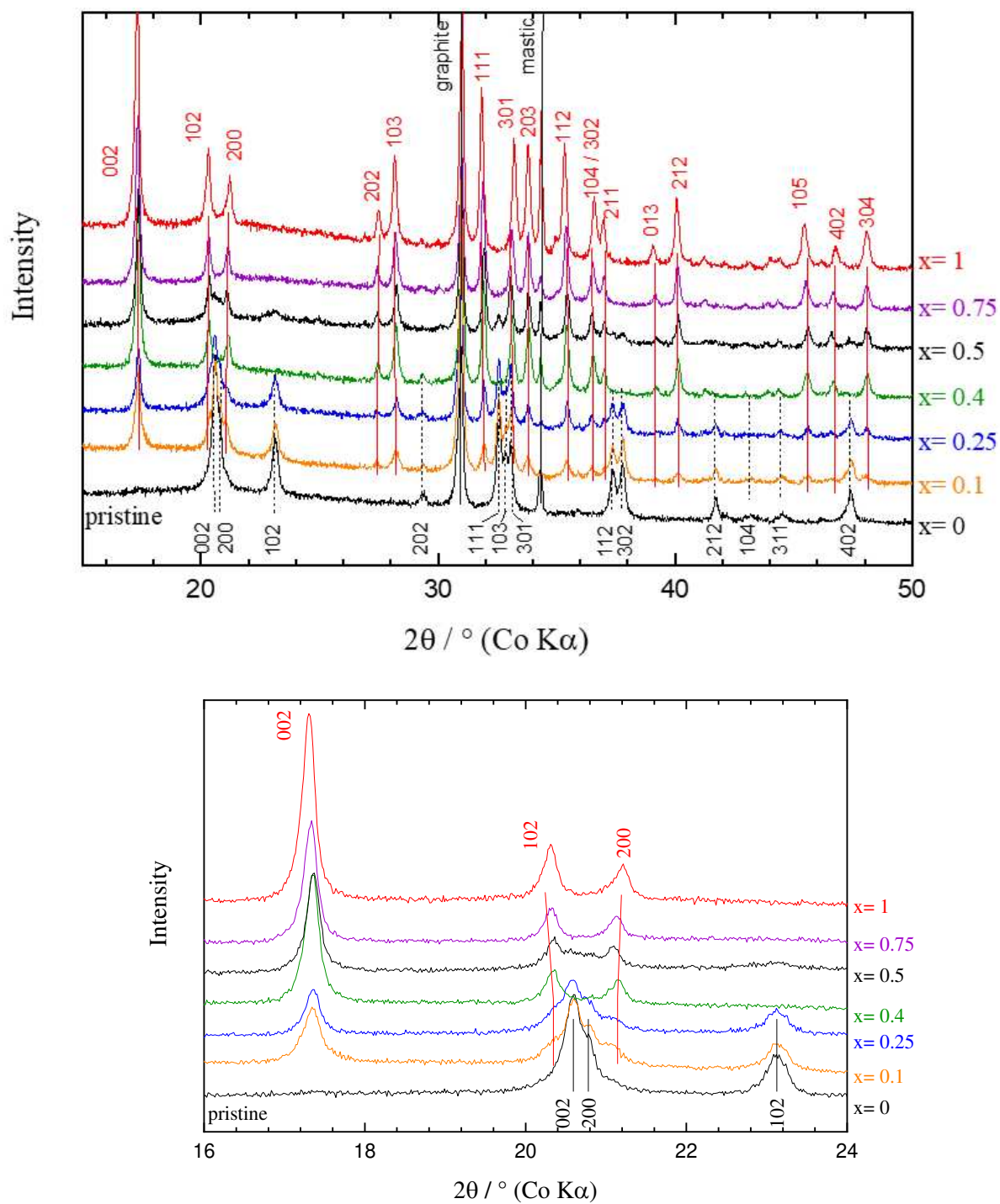


Figure 4. XRD patterns of discharged $\text{Na}_x\text{V}_2\text{O}_5$ electrodes in the $0 \leq x \leq 1$ composition range. Lower indexation (in black) is related to γ' - V_2O_5 while the upper one (in red) corresponds to the of γ - $\text{Na}_x\text{V}_2\text{O}_5$.

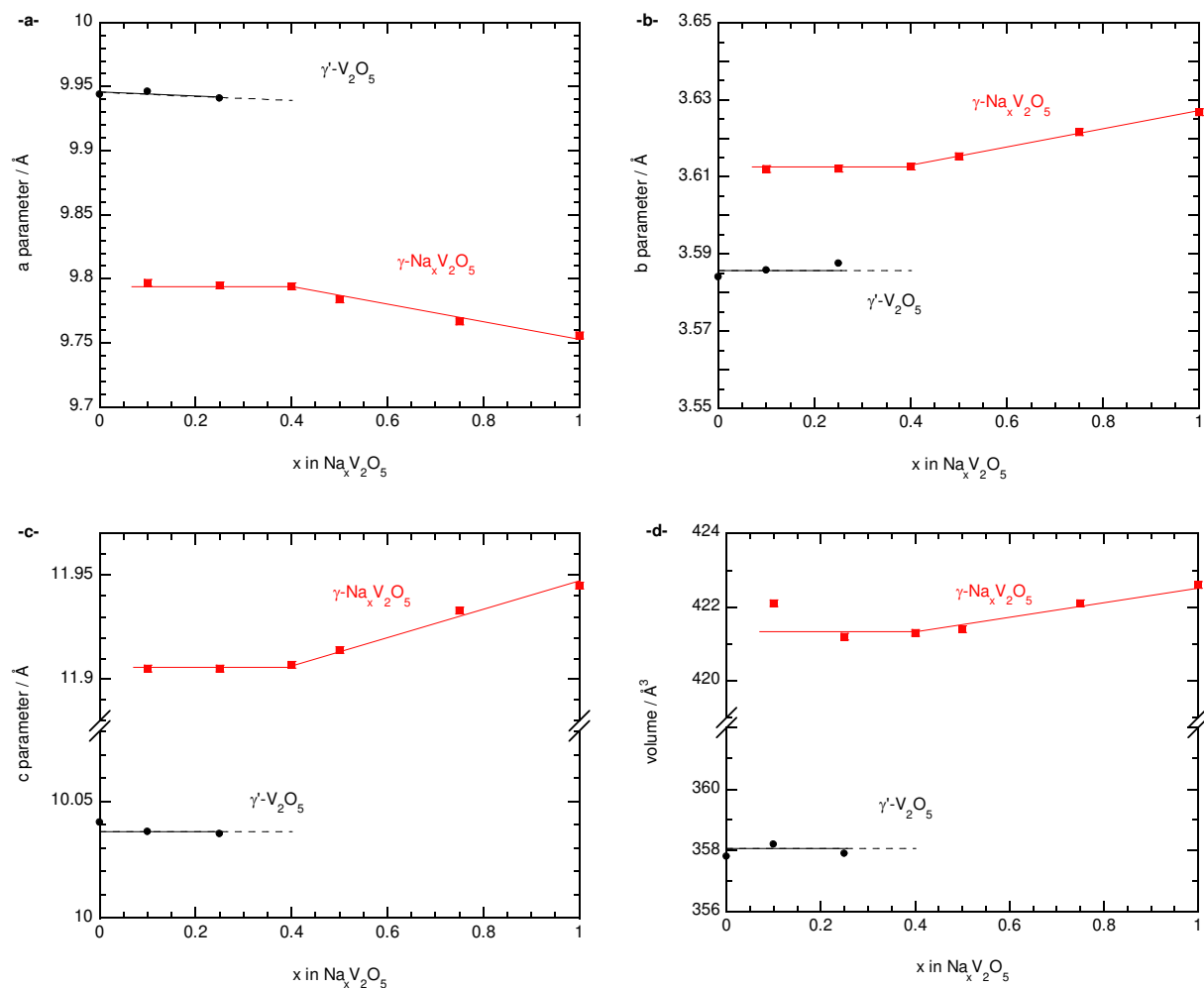


Figure 5: Evolution of the cell parameters and unit cell volume of the identified phases (• and ■ respectively for $\gamma'\text{-V}_2\text{O}_5$ and $\gamma\text{-Na}_x\text{V}_2\text{O}_5$) during the first discharge of γ' -polyol.

The Raman spectra of the $\gamma\text{-Na}_x\text{V}_2\text{O}_5$ ($0 \leq x \leq 1$) electrodes recorded during the first discharge process are shown in **Figure 6**. Note that for each Na uptake, similar spectra were found for the 10 investigated points, which indicates the good homogeneity of the electrode. Sodium insertion in polyol $\gamma'\text{-V}_2\text{O}_5$ leads to the following spectral changes. For $x = 0.1$, five new bands are seen (indicated by red circles), located at 86, 473, 960, 990 and 1015 cm^{-1} , that coexist with the Raman fingerprint of the pristine oxide (peaks indicated by black stars). For $x = 0.25$, the new bands are more intense and two additional peaks are observed at 110 and 323 cm^{-1} . For $x = 0.4$, the Raman spectrum is dominated by bands belonging to the new system while the presence of $\gamma'\text{-V}_2\text{O}_5$ is only revealed by small Raman features located at 92, 138, 170, 190 and 266 cm^{-1} . From $x = 0.5$ and up to the end of the discharge, the Raman signature of single phase $\gamma\text{-Na}_x\text{V}_2\text{O}_5$ phase is observed, with bands at 86, 110, 155, 195, 216, 248, 295, 323, 389, 473, 546, 670, 715, 736, 960, 977 and 1004

cm⁻¹. This Raman fingerprint is also in excellent agreement with that previously reported for electrochemically and chemically formed Na_{0.96}V₂O₅ [14,16].

In summary, the evolution of the Raman spectra indicates the appearance of a new sodiated phase from $x = 0.1$ which coexists with the pristine γ' -V₂O₅ in the $0.1 \leq x \leq 0.4$ composition range and is pure in the $0.4 < x \leq 1$ domain (**Figure 6**). These findings are in line with the XRD study and confirm also that the sodiated γ -Na_xV₂O₅ phase does not undergo any structural variation at the atomic scale, as revealed by its invariant signature in the $0.4 < x \leq 1$ composition range.

This structural study during the discharge process points to the existence of a two-phase mechanism involved during sodium insertion in polyol γ' -V₂O₅. A sodiated phase is produced from the early Na content ($x = 0.1$) that coexists with γ' -V₂O₅ up to $x = 0.4$. Then a single phase domain is observed in the $0.4 < x \leq 1$ composition range. Such mechanism exhibits a strong similarity with that previously reported for γ' -carbo., characterized by a two-phase mechanism for $0 < x \leq 0.7$ followed by a narrow single phase region for $0.7 \leq x \leq 0.97$ [14]. However, in the present case, the wider solid solution domain found for γ' -polyol V₂O₅ probably results from a downsizing effect. Such a finding should impact the electrochemical properties of γ' -polyol.

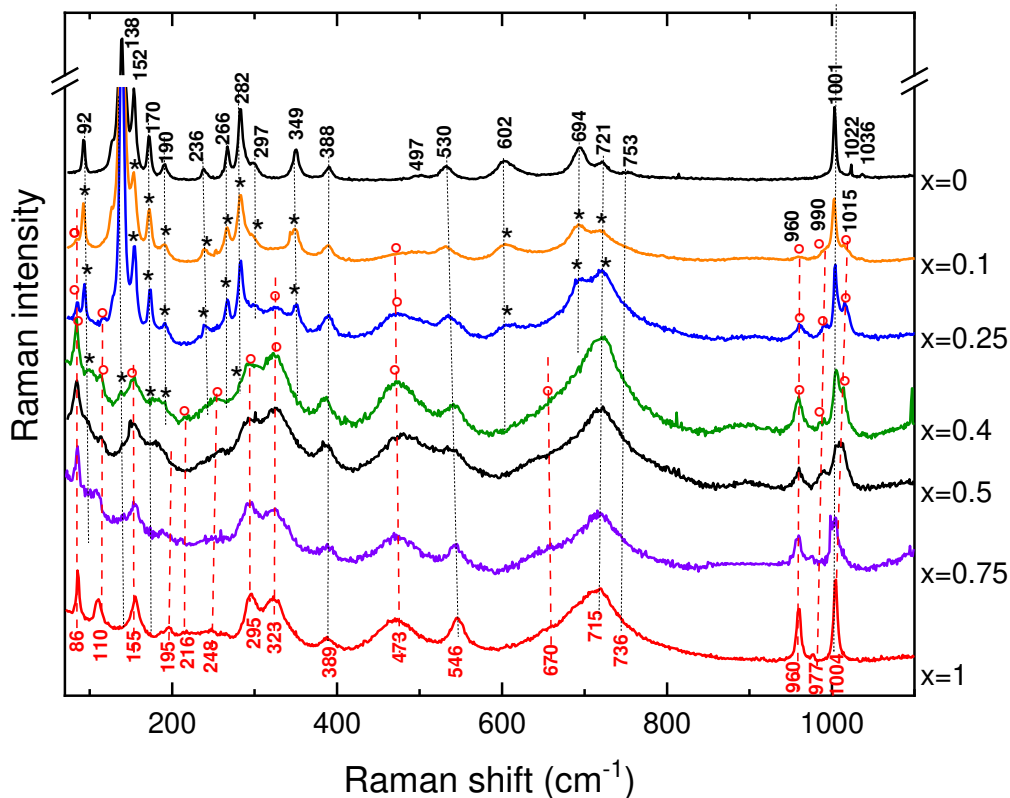


Figure 6. Raman spectra of discharged $\text{Na}_x\text{V}_2\text{O}_5$ electrodes in the $0 \leq x \leq 1$ composition range. *: Raman bands of γ' - V_2O_5 ; °: Raman bands of the sodiated phase

During the consecutive charge, both XRD and Raman spectroscopy indicate a complete reversible structural behavior since pristine γ' - V_2O_5 diffractogram and Raman spectrum are recovered at the end of a complete cycle (**Figure S1**). The first sodiation/desodiation cycle exhibits high electrochemical and structural reversibility. Clearly, the ability to restore the pristine material after one cycle indicates the sodiation/desodiation processes concern the whole electrode material in the case of γ' -polyol contrary to γ' -carbo., probably due to reduction in grain size and more homogenous distribution promoting electronic and ionic transfers.

2.2.6 Cycling properties

The rate performances of γ' -polyol has also been investigated. Various current densities varying from C/10 until 10 C have been applied. For each C rate, one typical cycle has been extracted and is reported in **Figure 7a**. Whatever the C rate, the shape of the curves is maintained with a single voltage plateau located at 3.36 V vs. Na^+/Na and an excellent electrochemical reversibility. When the applied current increases from C/10 to 2 C, the capacity decreases by less than 30 %, from 145 to 103 mAh g^{-1} . In the same time, the hysteresis doubles from 100 mV to ~ 320 mV, which represents much lower values than those observed with γ' -carbo. (173 mV at C/10 and 664 mV at 1 C) [14]. These findings and the absence of huge polarization indicate the sodium ions diffusion is favored in the case of smaller active material particles and is not drastically impacted in this current range. For higher C rates, gravimetric capacity rapidly decreases while hysteresis increases (70 and 34 mAh g^{-1} – 600 and 1180 mV respectively at 5 C and 10 C). The subsequent imposition of a lower current density (C/10-presented in dashed line in **Figure 7a**) leads to the typical curve shape obtained during first cycles. The material has not been impacted by the high C rates.

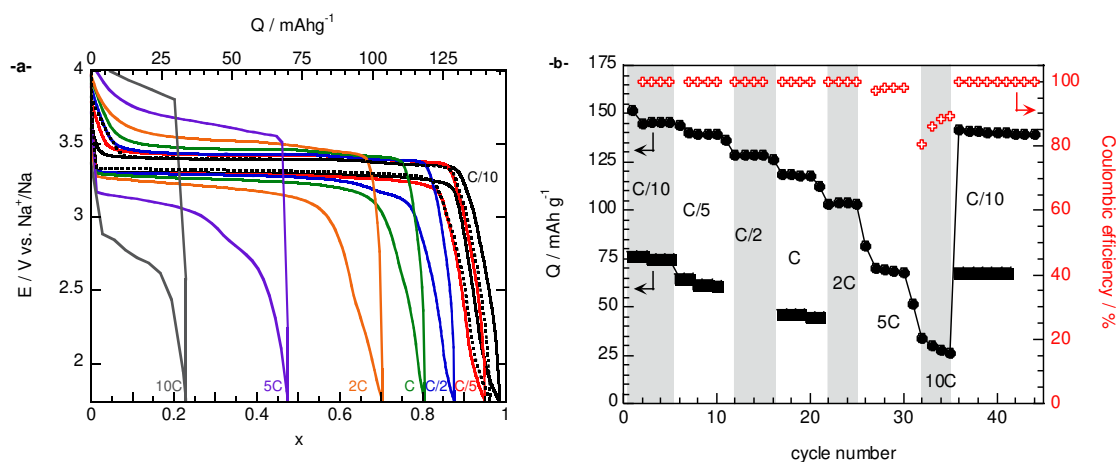


Figure 7. (a) Galvanostatic cycles registered for γ' -polyol at different C rates, in 1 mol L^{-1} NaClO_4 -PC-2 vol. % FEC in the 4V – 1.75 V potential range. (b) Charge rate capability performance of γ' -carbo. (black squares) and of γ' -polyol (black dots). Coulombic efficiency is presented on the right scale only for γ' -polyol (red empty markers).

Whatever the C rate, for all cycles, recovered capacities and corresponding coulombic efficiencies are reported as a function of cycle number in **Figure 7b**. Capacities higher than 100 mAh g^{-1} for C rates increasing from C/10 until 2 C with an excellent 100 % coulombic efficiency are confirmed. For higher C rates, lower capacities about 70 and 34 mAh g^{-1} respectively are achieved at 5 C and 10 C. Only these high current densities lead to coulombic efficiencies < 100 % due to

a high polarization. From comparison with the rate capability achieved for γ' -carbo, (**Figure 7b**), a huge improvement of capacity is allowed with γ' -polyol whatever the C rate. At C/10, the achieved capacity is twice than that found for γ' -carbo., while at 1 C, an enhancement factor of 3 is obtained.

2.2.7 Kinetic study of γ' -V₂O₅

In order to fully describe the electrochemical sodiation process, its kinetics has been examined during the first reduction. Typical impedance spectra of γ -Na_xV₂O₅ ($0 \leq x < 1$) electrodes are reported in **Figure 8**. These impedance diagrams are strongly dependent on sodium uptake. First, the sodium free pristine electrode exhibits a high impedance value (936 Ω), largely higher than for any sodiated one. As soon as a few sodium ions ($x = 0.02$) are inserted in the material, a huge decrease of impedance is observed, to reach $\sim 180 \Omega$. Then $|Z|$ slightly decreases up to $x = 0.2$ (60 Ω) before increasing to 185 Ω for $x = 0.8$. Such high $|Z|$ value for the sodium free host lattice could explain the overpotential observed at the very first beginning of discharge curve (**Figure 3**). In other respects, the electrode impedance variation vs. x in polyol-Na_xV₂O₅ is strongly limited compared to the tremendous growth by a factor 5 found for $|Z|$ in carbored γ -Na_xV₂O₅ [13].

Whatever the x value, the impedance spectra (**Figure 9a**) present a similar shape: two depressed semi-circles at high and medium frequencies, with characteristic frequencies about $f_1 \approx 1000$ -1500 Hz and $f_2 \approx 50$ -100 Hz. The first one, practically unchanged with x , is directly followed by a second one whose size is x dependent. This latter can be then safely ascribed to the charge transfer. At low frequencies, a straight line with a phase angle of 45° corresponding to the Warburg region (when $\omega \gg 2D_{Na}/L^2$, D_{Na} and L being respectively the apparent diffusion coefficient of sodium and the maximum length of the diffusion pathway) followed in some cases by a quasi-vertical line (when $\omega \ll 2D_{Na}/L^2$) at low frequency are observed. All the spectra can be fitted with the equivalent electrical circuit presented in **Figure 8b** [20]. The deduced characteristic parameters are discussed below, and R_2 and f_2 variations with sodium content are reported in **Figure 9b.v**

As expected with the three-electrode cell and such an electrolyte, the electrolyte resistance, R_0 , is low and stable around 2 Ω . The characteristic frequency (i.e. frequency at which the top of the semicircle is reached, f_1) and the resistance (i.e. the diameter of the fitted semi-circle, R_1) of the first semi-circle located at high frequency keep quite the same values in the whole composition

range, respectively 1.10^3 - $1.5.10^3$ Hz and 3.3Ω . Therefore this first x independent semi-circle can be attributed to the presence of a stable oxide film on the current collector.

The second semi-circle observed at medium frequency is x dependent and can be then ascribed to charge transfer. A moderate increase of the charge transfer resistance, R_2 , (R_{ct}) is observed with the sodium content from 10 to 28Ω (**Figure 8b** and **9b**) while at the same time, the characteristic frequency slightly decreases from 100 to 46 Hz for $x = 0.02$ to $x = 0.8$. The charge transfer resistance increases between $x = 0.02$ and 0.4 when γ' - V_2O_5 and γ - $Na_{0.4}V_2O_5$ coexist, and more significantly (80 %) in the monophasic domain ($0.4 \leq x \leq 0.8$). This slowdown in charge transfer kinetics can be related to the localized character of electrons in the fully sodiated phase [16]. The resulting double layer capacity ($C_{DL} = CPE_2$ here) is kept quite constant ($\sim 170 \mu F cm^{-2}$) for $x \leq 0.4$ and decreases by 30 %, to reach $128 \mu F cm^{-2}$ for $x = 0.8$. Hence the exchange current density j° is found to be $2.6 mA cm^{-2}$ for polyol γ' - V_2O_5 and still $1 mA cm^{-2}$ for $x = 0.8$. It is important to note the present C_{dl} values obtained are five-fold higher than in the case of γ' -carbo [11]. This finding reveals the effective electrochemical surface area is significantly higher than in the case of γ' -carbo. Such crucial difference explains the better behavior found with γ' -polyol in terms of charge efficiency and rate capability.

The moderate impedance variation upon sodiation (100 - 200Ω) compared to that observed with γ' -carbo. (100 - 700Ω) [13] may also indicate a better accommodation of volume change (17 %, **Figure 7d**) allowed by the lower particle size of polyol γ' . Hence the loss of inter-particles contact can be minimized.

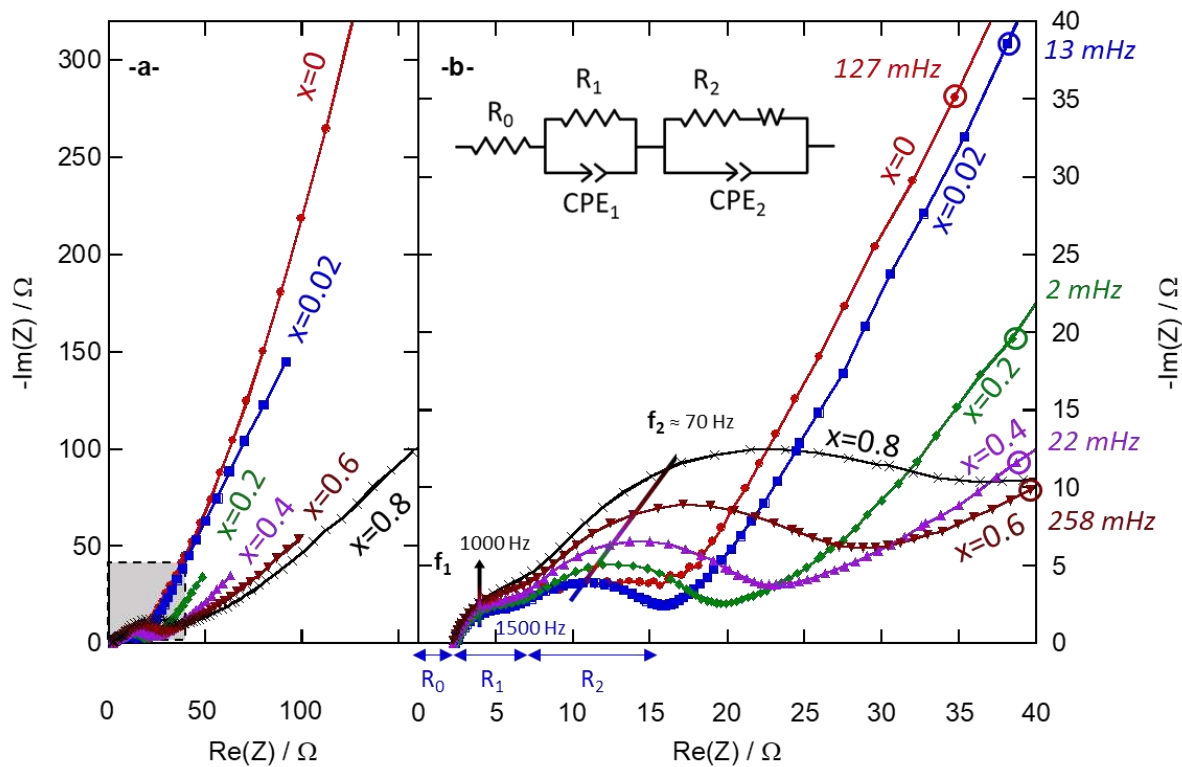


Figure 8. Impedance spectra for $\gamma\text{-Na}_x\text{V}_2\text{O}_5$ ($0 \leq x < 1$) (for $x = 0$, the spectrum is cut). Right graph is a magnification of left graph, corresponding to the grey part.

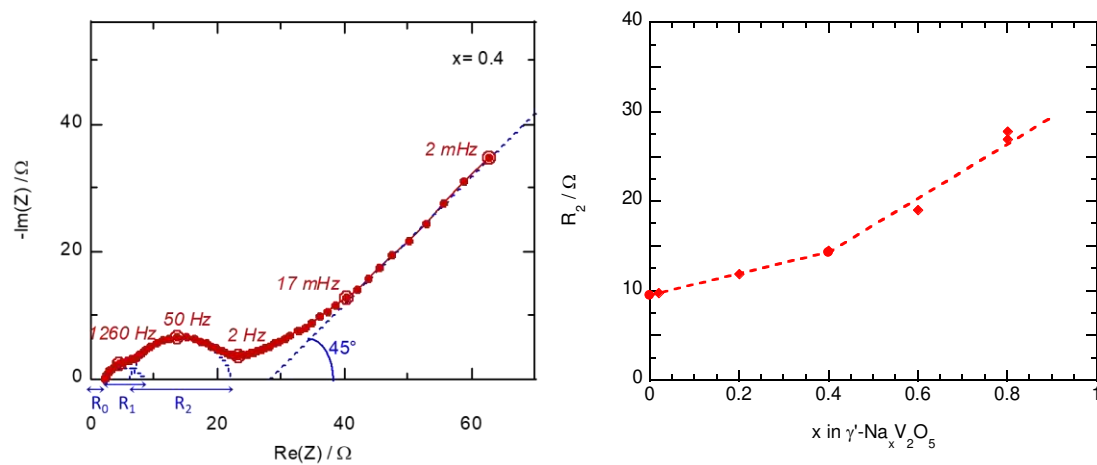


Figure 9. (a) Nyquist diagram for $\gamma\text{-Na}_{0.4}\text{V}_2\text{O}_5$ (b) Evolution of the charge transfer resistance (R_2).

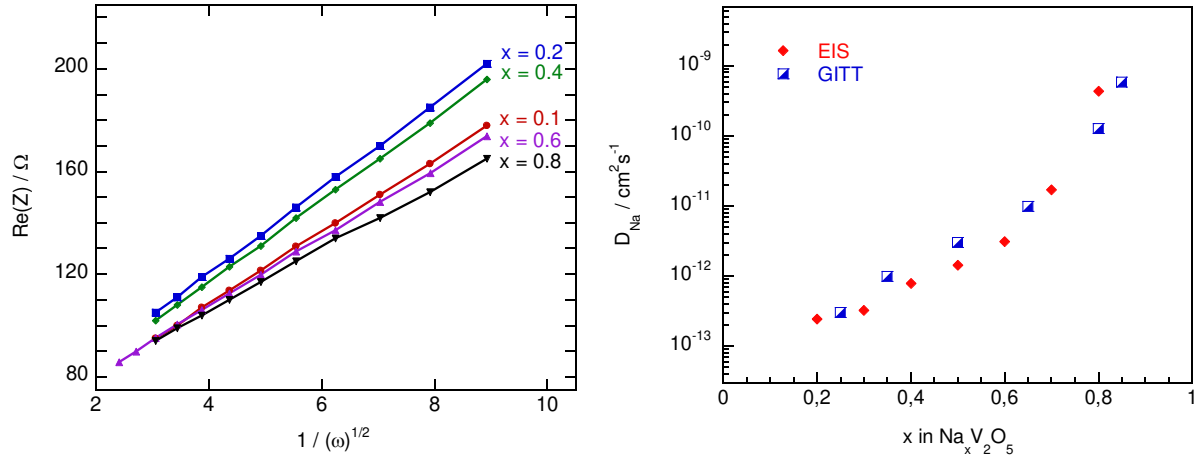


Figure 10. Evolution of (a) the Warburg prefactor and (b) D_{Na} sodium diffusion coefficient as a function of x ($0 < x < 1$).

From the Warburg domain present in all spectra (**Figure 9a**), the apparent Na chemical diffusion coefficient D_{Na} has been calculated according to **equation (1)**.

$$D_{\text{Na}} = \left(\frac{V_m}{\sqrt{2}nFS} \left(\frac{dE}{dx} \right)_x \frac{1}{A_w} \right)^2 \quad (1)$$

A_w is the Warburg prefactor (which was, for each x value, calculated based on the linear relation between $\left(\frac{1}{\sqrt{\omega}} \right)_x$ and $\text{Re}(Z)$), V_m is the molar volume of the compound ($V_m = 58.7 \text{ cm}^3$ for $\gamma'\text{-V}_2\text{O}_5$ and $V_m = 63.2 \text{ cm}^3$ for $\gamma\text{-Na}_x\text{V}_2\text{O}_5$ ($0.4 \leq x$) – a linear variation of the volume is considered in the sodium content varying from 0 to 0.4), n the electron number in the considered redox reaction ($n = 1$), F the Faraday's constant ($F = 96500 \text{ C mol}^{-1}$), S is the geometric surface area of the electrode (1 cm^2), $\left(\frac{dE}{dx} \right)_x$ the slope, at fixed x , of the equilibrium potential composition curve.

On the other hand, the galvanostatic intermittent titration technique (GITT) has been carried out and the different values of D_{Na} has been calculated according to the **equation (2)**:

$$D_{\text{Na}} = \frac{4}{\pi \tau} \left(\frac{m_B V_m}{M_B S} \right)^2 \left(\frac{\Delta E_s}{\Delta E_t} \right)^2 \quad (2)$$

In **equation (2)**, τ is the duration during which the current is applied (30 mn), m_B is the active material mass in the electrode, M_B is the molar weight of V_2O_5 , ΔE_s is the difference between the

equilibrium potential reached at the end of the relaxation scheduled after the galvanostatic step and the one obtained at the end of the previous relaxation (measured when $dE/dt < 0.1 \text{ mV h}^{-1}$), ΔE_t is the potential variation registered during the galvanostatic step after ohmic drop subtraction. As shown in **Figure 10b**, values from EIS measurements and from GITT are of the same magnitude order, increasing from $3 \cdot 10^{-13}$ and $10^{-9} \text{ cm}^2 \text{ s}^{-1}$ with x . In the sodium content range corresponding to biphasic domain ($x \leq 0.4$), the apparent chemical diffusion coefficient is roughly constant around $7 \cdot 10^{-13}$ while it significantly increases up to $10^{-9} \text{ cm}^2 \text{ s}^{-1}$ in the monophasic region ($0.4 < x \leq 0.8$). The high D_{Na} values found for the Na rich compounds indicate the typical interlayer space of puckered layers in γ' -polyol promotes a high mobility of sodium ions in spite of their size.

Cycling performance of γ' -polyol has been examined for an applied current density of 147 mA g^{-1} (1 C rate). Some of the first two hundred cycles are presented in **Figure 11**. The evolution of the gravimetric capacity as a function of cycle number is presented in inset. It slightly decreases by 9 % after 200 cycles, from 126 mAh g^{-1} to 115 mAh g^{-1} while galvanostatic cycles keep the same shape, without increased hysteresis. The electrochemical performances obtained with the γ' -polyol polymorph differ from those presented in the literature at various points. To begin, most of the studies on the $\text{Na}^+ / \text{V}_2\text{O}_5$ system presents a working voltage between 1.9 and 2.7 V [10,21,22] while it reaches a significantly higher value of 3.36 V in the case of γ' -polyol. Then, the achieved capacities are often less than 200 mAh g^{-1} , although the range of potential scanned is wider: for example D. Su *et al* obtain from 110 mAh g^{-1} to 150 mAh g^{-1} , respectively with V_2O_5 hollow nanospheres and bilayered V_2O_5 nanobelts, after 100 cycles for cycling between 4 and 1 V at 160 mA g^{-1} [10,22] while sponge-like V_2O_5 xerogel prepared by K. Zhu *et al* exhibit a capacity of $\sim 90 \text{ mAh g}^{-1}$ after 100 cycles for cycling between 4 and 1.25 V at 100 mA g^{-1} [21]. A more recent study reports 78 mAh g^{-1} at the 100th cycle for V_2O_5 single-crystalline nanowires cycled between 4 and 1 V at 100 mA g^{-1} (0.6 C) [23]. Finally, considering capacities reached by these different kinds of nanomaterials (nanospheres, nanobelts, nanosheets, nanowires), during the sodiation step at a potential of 1.75V, value which corresponds to the lower limit in the present study, and the working potential discussed above, specific energy densities delivered by those systems are less than the some 400 Wh kg^{-1} of the Na^+ / γ' -polyol V_2O_5 system. This characteristic constitutes an undeniable asset for the γ' polymorph prepared according to this synthesis route.

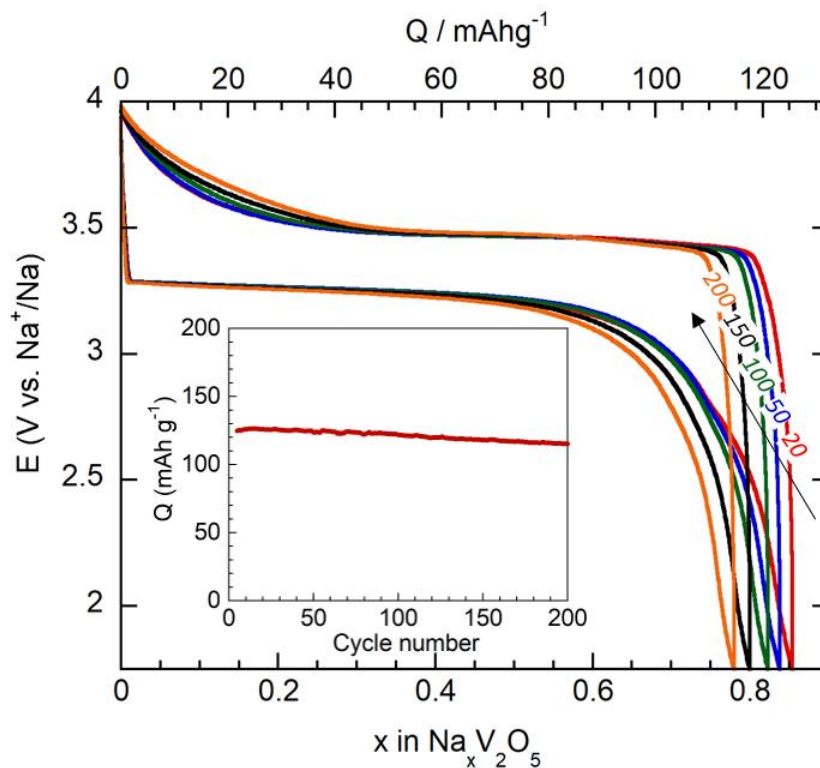


Figure 11. 20th, 50th, 100th, 150th and 200th cycles for γ' -polyol cycled in 1 mol L⁻¹ NaClO₄-PC-2 vol. % FEC in the 4V – 1.75 V potential range with a current density of 147 mA g⁻¹ (1 C). Evolution of the discharge capacity as a function of the cycle number in inset.

2.2.8 Conclusion

In this work, we have reported the electrochemical features of γ' -V₂O₅ polymorph, prepared by the polyol process, as negative electrode material for NIBs. This route to synthesize the α -V₂O₅ precursor allows to get the γ' -V₂O₅ polymorph made of nanoparticles 100-200 nm long against big platelets a few microns long and thick using the conventional carboreduction synthesis (carbored γ' -V₂O₅). The latter exhibited an appealing discharge capacity of 145 mAh g⁻¹ available at a high potential 3.3 V vs Na⁺/Na, but a charge efficiency limited to 50 % at C/10. We have demonstrated here this huge drawback limiting the effective capacity to only 70 mAh g⁻¹ is solved with the use of polyol γ' -V₂O₅ characterized by a quantitative charge process. We have provided evidence for enhanced electrochemical performance with a specific capacity of 145 mAh g⁻¹ at C/10, i.e. twice that found for carbored γ' -V₂O₅ and a superior rate capability allowing to benefit from a capacity of 100 mAh g⁻¹ at 2 C. A detailed picture of structure changes upon electrochemical sodiation has

been also provided by XRD and Raman spectroscopy. We show the nanosizing approach has induced a significant shortening of the diphasic region ($0 < x \leq 0.4$) and an expansion of the single-phase region $\gamma\text{-Na}_x\text{V}_2\text{O}_5$ ($0.4 < x \leq 1$). Impedance spectroscopy data reveal a moderate change in electrode impedance upon sodiation and a low decrease of charge transfer kinetics due to the highly localized character of electrons in the sodiated phase. A significant C_{DL} increase by a factor 4-5 vs micro-sized polymorph illustrates the significant nanosize effect on the electrochemical surface enhancement. The evolution of the chemical diffusion coefficient D_{Na} shows a faster diffusion in the single-phase region than in diphasic domain. The present work shows that optimized electrochemical properties can be achieved using polyol- $\gamma'\text{-V}_2\text{O}_5$: a high-performance cathode material working at high voltage 3.3 V vs Na^+/Na with a high capacity of 140 mAh g^{-1} , a high rate capability, an excellent charge efficiency and good cycle life.

SUPPORTING INFORMATION

Structural characterization. The morphology of the synthesized γ' -V₂O₅ powder is investigated by using a field-emission scanning electron microscope (SEM) (Zeiss, Merlin-type) operating at 5 keV. The X-Ray Diffraction (XRD) experiments are performed using a PANalytical X-Pert Pro diffractometer equipped with a X'celerator linear detector and Co K α source. Data are then processed on Eva software to identify peaks and adjusted the cell parameters of the identified phases. The Raman spectra are measured with a LaBRAM HR 800 (Jobin-Yvon-Horiba) Raman micro-spectrometer including Edge filters and equipped for signal detection with a back illuminated charge coupled device detector (Spex CCD) cooled by Peltier effect to 200 K. A He:Ne laser (632.8 nm) is used as the excitation source. The spectra are measured in back-scattering geometry. The resolution is about 0.5 cm⁻¹. A long distance 50X LWD objective is used to focus the laser light on sample surface to a spot size of 1 μ m². To avoid local heating of the sample, the power of the laser beam is adjusted to 0.2–0.5 mW with neutral filters of various optical densities. The structural study was performed on electrochemically formed γ -Na_xV₂O₅ samples prepared at C/10 discharge/charge rate. After 2 hours of equilibrium time, the positive electrode was removed from the cell in the Ar-filled glove box, rinsed with DMC, and placed in appropriate airtight sample holders to be analyzed by X-ray diffraction and Raman spectroscopy. Raman spectra have been recorded on 10 different spots of each electrode. This led to similar spectra for all the investigated points, whatever the Na uptake.

Electrochemical experiments. All the electrochemical measurements were performed with a VMP3 Biologic Multipotentiostat-Galvanostat apparatus. The electrolyte was a solution of 1 mol L⁻¹ NaClO₄ in propylene carbonate (PC) containing a fluoroethylene carbonate (FEC) additive (2 Vol %). The positive electrode was made of a mixture of active material (γ' -V₂O₅ 80 wt %), acetylene black (7.5 wt %), graphite (7.5 wt %) and teflon as binder agent (5 wt %) pressed on a stainless steel grid under a pressure of 5 tons per cm².

Cycling experiments and galvanostatic intermittent titration technique (GITT) were carried out in two-electrode coin cells (CR 2032) with sodium disk as reference and auxiliary electrodes. The separator consists of three glass Whatman microfiber filters and acts as an electrolyte tank. All the coin cells were assembled in the argon-filled glove box where water and oxygen concentrations are kept less than 1 ppm. The GITT measurement was programmed to supply a constant current

of 14.7 mA g^{-1} for 30 min followed by an open circuit stand until the deviation dE/dt reaches values lower than 0.1 mV h^{-1} .

A conventional three-electrode cell is used in the glove box for impedance measurements. Reference and counter electrodes were made of Li wires in separate compartments filled up with electrolyte during charge / discharge steps while a gold wire was used as reference electrode during impedance acquisition. EIS spectra (frequency range: $10^4 - 2 \cdot 10^{-3} \text{ Hz}$; excitation signal: 10 mV peak to peak) were measured on equilibrated working electrodes ($S = 1 \text{ cm}^2$) at different discharge / charge rates. Equilibrium was considered to be reached when the open circuit voltage remained stable (potential variations lower than 0.1 mV per hour) and the working electrode compositions were adjusted by coulometric titration using a low current density corresponding to a C/20 rate (7.4 mA g^{-1}).

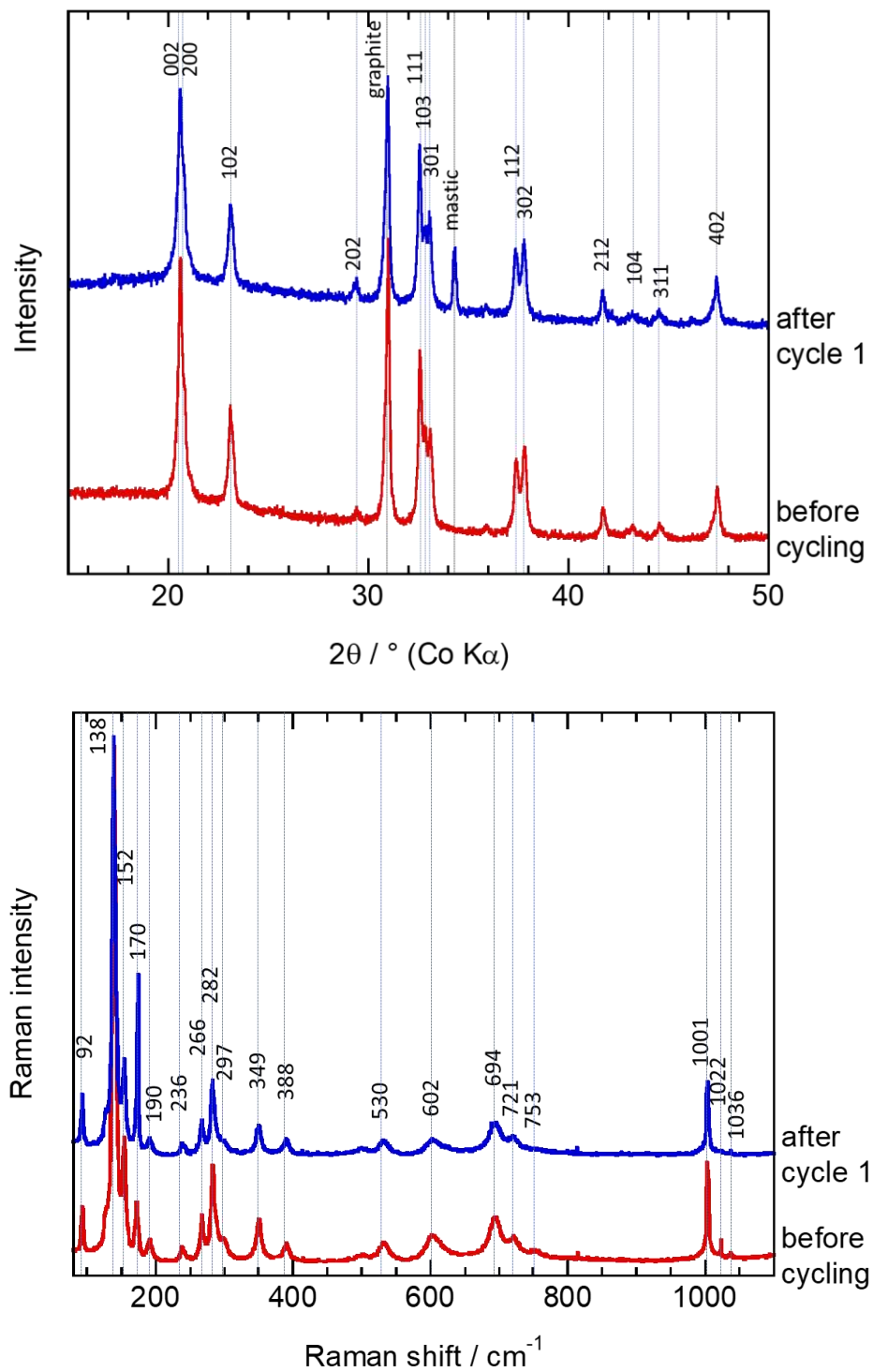


Figure S1. XRD patterns and Raman spectra of pristine γ' -V₂O₅ (red curves) and γ' -V₂O₅ electrode after 1 cycle (blue curves)

REFERENCES

- [1] Global Lithium Ion Battery - A Market by Type, (2019). <https://www.fiormarkets.com/report/global-lithium-ion-battery-market-by-type-cathode-material-376017.html#description> (accessed February 18, 2021).
- [2] Sodium-ion Batteries Market 2020| Analysis, Revenue, Price, Market Share, Growth Rate, Forecast to 2025 | Market Research Engine, (2021). <https://www.marketwatch.com/press-release/sodium-ion-batteries-market-2020-analysis-revenue-price-market-share-growth-rate-forecast-to-2025-market-research-engine-2021-03-05> (accessed March 18, 2021).
- [3] M.S. Whittingham, Lithium batteries and cathode materials, *Chem. Rev.* 104 (2004) 4271–4301. doi:10.1021/cr020731c.
- [4] J. Yao, Y. Li, R.C. Massé, E. Uchaker, G. Cao, Revitalized interest in vanadium pentoxide as cathode material for lithium-ion batteries and beyond, *Energy Storage Mater.* 11 (2018) 205–259.
- [5] N. Yabuuchi, K. Kubota, M. Dahbi, S. Komaba, Research development on sodium-ion batteries, *Chem. Rev.* 114 (2014) 11636–11682.
- [6] F. Li, Z. Wei, A. Manthiram, Y. Feng, J. Ma, L. Mai, Sodium-based batteries: from critical materials to battery systems, *J. Mater. Chem. A* 7 (2019) 9406–9431. doi:10.1039/C8TA11999F.
- [7] K. West, B. Zachau-Christiansen, T. Jacobsen, S. Skaarup, Sodium insertion in vanadium oxides, *Solid State Ionics*. 28 (1988) 1128–1131.
- [8] J.P. Pereira-Ramos, R. Messina, J. Perichon, Electrochemical Formation of Vanadium Pentoxide Bronzes $M_xV_2O_5$ in Molten Dimethylsulfone, *J. Electrochem. Soc.* 135 (1988) 3050.
- [9] D. Muller-Bouvet, R. Baddour-Hadjean, M. Tanabe, L.T.N. Huynh, M.L.P. Le, J.P. Pereira-Ramos, Electrochemically formed α' - NaV_2O_5 : A new sodium intercalation compound, *Electrochim. Acta.* 176 (2015) 586–593.
- [10] D.W. Su, S.X. Dou, G.X. Wang, Hierarchical orthorhombic V_2O_5 hollow nanospheres as high performance cathode materials for sodium-ion batteries, *J. Mater. Chem. A* 2 (2014) 11185–11194. doi:10.1039/C4TA01751J.
- [11] S. Tepavcevic, H. Xiong, V.R. Stamenkovic, X. Zuo, M. Balasubramanian, V.B. Prakapenka, C.S. Johnson, T. Rajh, Nanostructured bilayered vanadium oxide electrodes for rechargeable sodium-ion batteries, *ACS Nano*. 6 (2012) 530–538.
- [12] R. Baddour-Hadjean, M.S. Renard, N. Emery, L.T.N. Huynh, M.L.P. Le, J.P. Pereira-Ramos, The richness of V_2O_5 polymorphs as superior cathode materials for sodium insertion, *Electrochim. Acta.* 270 (2018) 129–137.
- [13] M. Safrany Renard, R. Baddour-Hadjean, J.P. Pereira-Ramos, Kinetic insight into the electrochemical sodium insertion-extraction mechanism of the puckered γ' - V_2O_5 polymorph, *Electrochim. Acta.* 322 (2019) 134670. doi:<https://doi.org/10.1016/j.electacta.2019.134670>.
- [14] M. Safrany Renard, N. Emery, R. Baddour-Hadjean, J.-P. Pereira-Ramos, γ' - V_2O_5 : A new high voltage cathode material for sodium-ion battery, *Electrochim. Acta.* 252 (2017) 4–11. doi:10.1016/j.electacta.2017.08.175.
- [15] J. Barker, M.Y. Saidi, J.L. Swoyer, Performance Evaluation of the Electroactive Material, γ - LiV_2O_5 , Made by a Carbothermal Reduction Method, *J. Electrochem. Soc.* 150 (2003) A1267–A1272. doi:10.1149/1.1600462.

- [16] N. Emery, R. Baddour-Hadjean, D. Batyrbekuly, B. Laik, Z. Bakenov, J.-P. Pereira-Ramos, B. Laik, Z. Bakenov, J.-P. Pereira-Ramos, γ -Na_{0.96}V₂O₅: A New Competitive Cathode Material for Sodium-Ion Batteries Synthesized by a Soft Chemistry Route, *Chem. Mater.* 30 (2018) 5305–5314. doi:10.1021/acs.chemmater.8b02066.
- [17] I. Mjejri, A. Rougier, M. Gaudon, Low-Cost and Facile Synthesis of the Vanadium Oxides V₂O₃, VO₂, and V₂O₅ and Their Magnetic, Thermochromic and Electrochromic Properties, *Inorg. Chem.* 56 (2017) 1734–1741. doi:10.1021/acs.inorgchem.6b02880.
- [18] J.M. Cocciantelli, P. Gravereau, J.P. Doumerc, M. Pouchard, P. Hagenmuller, On the preparation and characterization of a new polymorph of V₂O₅, *J. Solid State Chem.* 93 (1991) 497–502. doi:10.1016/0022-4596(91)90323-a.
- [19] R. Baddour-Hadjean, M.B. Smirnov, V.Y. Kazimirov, K.S. Smirnov, J.-P. Pereira-Ramos, The Raman spectrum of the γ' -V₂O₅ polymorph: a combined experimental and DFT study, *J. Raman Spectrosc.* 46 (2015) 406–412. doi:10.1002/jrs.4660.
- [20] C. Ho, I.D. Raistrick, R.A. Huggins, Application of A-C Techniques to the Study of Lithium Diffusion in Tungsten Trioxide Thin Films, *J. Electrochem. Soc.* 127 (1980) 343–350. doi:10.1149/1.2129668.
- [21] K. Zhu, C. Zhang, S. Guo, H. Yu, K. Liao, G. Chen, Y. Wei, H. Zhou, Sponge-like cathode material self-assembled from two-dimensional V₂O₅ nanosheets for sodium-ion batteries, *ChemElectroChem.* 2 (2015) 1660–1664.
- [22] D. Su, G. Wang, Single-Crystalline Bilayered V₂O₅ Nanobelts for High-Capacity Sodium-Ion Batteries, *ACS Nano.* 7 (2013) 11218–11226. doi:10.1021/nn405014d.
- [23] Y. Li, J. Ji, J. Yao, Y. Zhang, B. Huang, G. Cao, Sodium ion storage performance and mechanism in orthorhombic V₂O₅ single-crystalline nanowires, *Sci. China Mater.* (2020). doi:10.1007/s40843-020-1468-6.

CHAPTER 3

New $M_xV_2O_5$ bronzes as competitive cathode materials for sodium-ion batteries (M = Na, K)

3.1 Introduction

With the rapid development of renewable energy sources, the deployment of new Electrical Energy Storage solutions is highly desired. Lithium-ion batteries (LIBs), which dominate the portable electronic market, are expected to answer this requirement [1]. However, the use of Li is impeded by its high cost, limited reserves and uneven distribution [2]. As a result, research has turned to batteries composed of low-cost and earth-abundant elements, among them Na-ion batteries have been highlighted as one of the best alternatives to LIBs because their reaction mechanism is similar to that of LIBs and Na sources are essentially unlimited [3-13].

To date, a large variety of Na-insertion frameworks have been proposed as cathode materials [14-19]. Similar to LIBs, highly reversible cathode materials based upon the intercalation reaction are needed for high capacity and good cyclability of SIBs. These cathode materials are mainly categorized into oxides and polyanion types [14]. A major obstacle is the difficulty to get a sodium host material with comparable operating voltage and capacity to LIBs analogs. Among the transition metal oxides investigated as cathode materials the group of vanadium oxides and bronzes has been screened, most of them in the last years: V_2O_5 polymorphs [20-22], bilayered V_2O_5 [23, 24], $Na_{0.33}V_2O_5$ [25-27], Na_xVO_2 [28, 29], $NaVO_3$ [30], NaV_3O_8 [31]

In previous chapter we have reported the attractive electrochemical features exhibited by the γ' - V_2O_5 polymorph, prepared by the polyol process, as negative electrode material for LIBs and NIBs. This solution technique allows to get homogeneous nanoparticles 100-200 nm long. We outlined the high interest of the polyol- γ' - V_2O_5 host lattice in particular toward Na insertion. Indeed, this oxide can be considered as a high-performance cathode material working at high voltage 3.3 V vs Na^+/Na with a high capacity of 140 mAh g^{-1} , a high rate-capability, an excellent charge efficiency and good cycle life.

A few years ago, we described a novel Li intercalation compound, the potassium vanadium bronze $K_{0.5}V_2O_5$ (KVO) synthesized via a fast and facile solution route [32]. This cathode material was found to exhibit outstanding electrochemical performance, one of the best among the vanadium bronzes, with a specific capacity of 210 mAh g^{-1} at an average voltage of 2.9 V vs. Li^+/Li , without any significant structural changes after extended cycling experiments. An excellent capacity retention was also reported, with still 200 mAh g^{-1} at C/10 after 70 cycles and a good rate capability with 140 mAh g^{-1} at 1C. This attractive behaviour originates from the unusually large d -spacing of 7.7 \AA practically twice that of the parent oxide V_2O_5 , and the presence of interlayer K^+ ions that stabilize the stacking of double-sheet V_2O_5 layers.

Motivated by these two recent works, we put some efforts in two directions:

- 1- we decided to chemically synthesized the γ' - NaV_2O_5 bronze in order to have a positive active material directly usable in Na-ion batteries with the hope of keeping the attractive performances known for the γ' - V_2O_5 oxide.
- 2- we extended our study to the investigation of $K_{0.5}V_2O_5$ (named KVO) as a potential candidate for cathode material of SIBs.

3.2 The sodiated bronze γ - $Na_{0.96}V_2O_5$ as cathode material for Na-ion batteries

The stable high temperature phase γ - LiV_2O_5 , characterized by a puckered layered framework with Li ions located between the $(VO_5)_n$ layers [33, 34], was reported to exhibit a promising behavior as cathode material for LIBs [35-36]. The oxidation of γ - LiV_2O_5 leads to the γ' - V_2O_5 polymorph, which keeps the memory of the pristine γ - LiV_2O_5 structure [39, 40]. Electrochemical lithium insertion in γ' - V_2O_5 was reported to occur at a higher voltage (3.6-3.5 V vs. Li^+/Li) than in α - V_2O_5 (3.4-3.2 V vs. Li^+/Li) [35].

When $M = Na$ and $x = 1$, only the α' - NaV_2O_5 layered phase with an α - V_2O_5 isotype orthorhombic structure was obtained through solid-state reaction of $NaVO_3$ and VO_2 precursors around 600°C [41, 42]. More recently, this α' - NaV_2O_5 bronze was electrochemically prepared and investigated as a sodium intercalation compound. An interesting specific capacity of 120 mAh g^{-1} at C/10 rate near 1.6 V vs. Na^+/Na was reported [43]. A novel structural variety of sodium vanadium bronze belonging to the γ -system, namely γ - $Na_{0.97}V_2O_5$, was described as the discharge product of a

composite γ' -V₂O₅ electrode near 3.2 V vs. Na⁺/Na in a 1M NaClO₄ propylene carbonate electrolyte [44, 45]. However, this sodium bronze has never been synthesized as pure powder nor investigated as cathode material for SIBs. In spite of an interesting first discharge capacity of 145 mAh g⁻¹ reported for γ' -V₂O₅, a strong kinetic limitation was shown during the first charge limiting the cycling efficiency to only 60% even at a low rate of C/20 with merely 80 mAh g⁻¹ recovered [45]. The use of a polyol synthesis leading to nanosized particles allows to solve the poor charge/discharge efficiency. Another crucial drawback of γ' -V₂O₅ is that this Na-free material is not directly suitable as cathode in a SIB.

Herein, we present γ -Na_{0.96}V₂O₅ as a directly usable cathode material for sodium-ion batteries. This paper describes the first chemical synthesis of this sodium vanadium bronze, from chemical sodiation at room temperature of the γ' -V₂O₅ polymorph. We synthesize γ -Na_{0.96}V₂O₅ from a home-made α -V₂O₅ precursor obtained through a polyol process, leading easily to pure, fine and porous powders with homogeneous grain size distribution. As a result, a quantitative initial desodiation is obtained. The main electrochemical properties of γ -Na_{0.96}V₂O₅ as well as its structural behaviour upon the sodium insertion-extraction reactions are reported and discussed in details.

3.2.1 Synthesis

The polyol synthesis of γ -Na_{0.96}V₂O₅ consist of 4 steps illustrated in **Figure 1**.

Step 1. Synthesis of α -V₂O₅. Ammonium metavanadate (NH₄VO₃) and ethylene glycol (EG) were used without purification. NH₄VO₃ (7 gr) was dispersed in 500 ml of EG under stirring. The resulting mixture was heated to 110 °C under continuous stirring to obtain yellow colored solution, then refluxed at 340 °C for 3 hr until solution becomes blue color and cooled to room temperature. At the end of the reaction excess EG was removed and precipitant (vanadium ethyleneglycolate) was washed with ethanol and dried at 110 °C for 2 hr. To synthesize α -V₂O₅ powder, vanadium ethyleneglycolate was annealed at 490 °C for 3 hr in air.

Step 2. Synthesis of γ -LiV₂O₅. α -V₂O₅ was dispersed in 40 ml of acetonitrile under continuous stirring. Lithium iodide in excess (molar ratio 1:2) was slowly added to obtain δ -LiV₂O₅ and mixed for 4 hrs. The obtained powder was washed 4 times with acetonitrile and acetone to remove iodide.

After drying at 70 °C powder was heat-treated at 300 °C for 3 hrs under vacuum in Buchi furnace to form distorted γ -type layers (δ - $\text{LiV}_2\text{O}_5 \rightarrow \gamma$ - LiV_2O_5).

Step 3. Synthesis of γ' - V_2O_5 . γ' - V_2O_5 is obtained by chemical oxidation of γ - LiV_2O_5 . Deinsertion of lithium from γ - LiV_2O_5 was performed with strong oxidizing agent NO_2BF_4 (molar ratio 1:1.1) in acetonitrile. The solution was stirred at room temperature for 4 hrs. The obtained powder was washed 4 times with acetonitrile and acetone and dried at 80 °C. The color of powder changed from dark green to orange, which confirms complete delithiation of the product.

Step 4. Synthesis of γ - NaV_2O_5 . γ' - V_2O_5 was dispersed in 40 ml of acetonitrile under continuous stirring. Sodium iodide in excess (molar ratio 1:2) was slowly added and mixed for 4 hrs. The obtained powder was washed 4 times with acetonitrile and acetone to remove iodide. The obtained γ - NaV_2O_5 powder was dried at 70 °C.

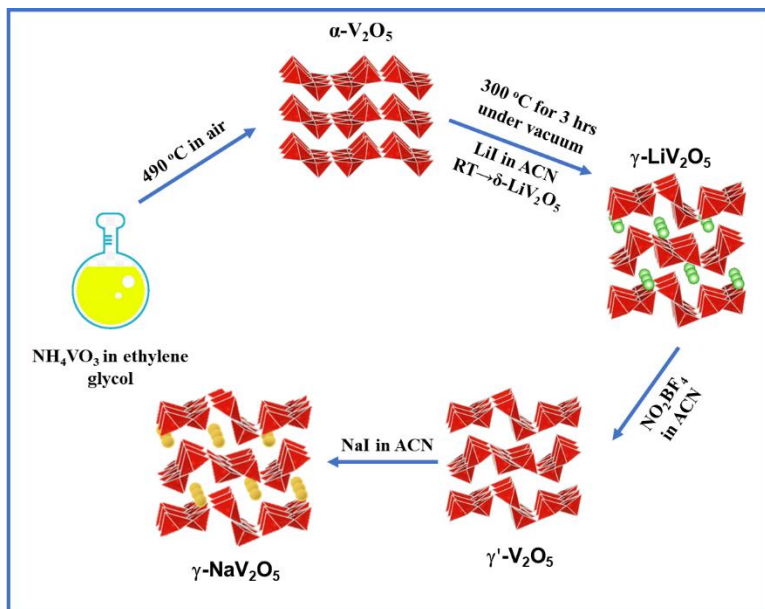


Figure 1. Scheme of polyol synthesis to obtain γ' - V_2O_5 and γ - NaV_2O_5

3.2.2 Structural characterization

The obtained powder after oxidation of γ - NaV_2O_5 has been examined by XRD and Raman spectroscopy. All the reflection lines in **Figure 2** can be indexed with expected orthorhombic symmetry of $Pnma$ space group (**Table 1**). Sharp and intense diffraction peaks illustrate high

crystallization degree. The Rietveld refinement does not reveal the presence of impurity and the calculated unit cell parameters are: $a=9.7806 \text{ \AA}$, $b=3.6299 \text{ \AA}$, $c=11.8872 \text{ \AA}$.

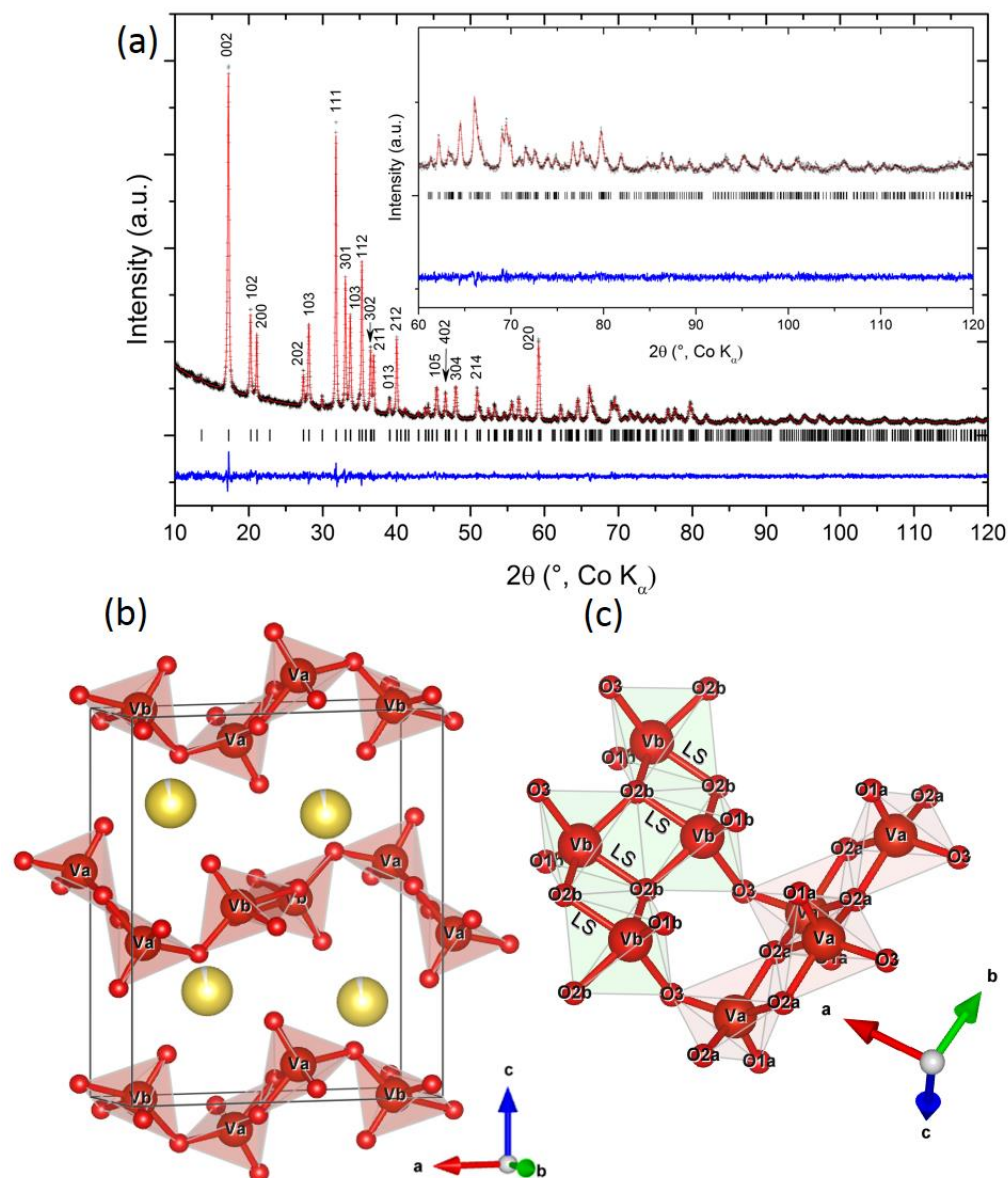


Figure 2. (a) X-ray diffraction pattern, (b) crystal structure, (c) local structure of $\gamma\text{-Na}_{0.96}\text{V}_2\text{O}_5$ powder

Table 1. Peak position, interplanar spacing, hkl indexes, FWHM, Crystallite size from XRD data of $\gamma\text{-NaV}_2\text{O}_5$

No.	Peak position		Interplanar spacing	Miller indices	FWHM	Crystallite size
	2 Theta ($^\circ$)	Theta ($^\circ$)	d (\AA)	(hkl)	(\circ)	nm

1	17.19122	8.59561	5.984561	002	0.21363	43.67
2	20.20105	10.10053	5.100192	102	0.19954	46.96
3	21.09154	10.54577	4.887146	200	0.16536	56.74
4	27.36424	13.68212	3.781471	202	0.21401	44.36
5	28.07536	14.03768	3.687542	103	0.21703	43.81
6	31.7304	15.8652	3.271879	111	0.18231	52.60
7	33.10029	16.55015	3.140025	301	0.20148	47.76
8	33.70553	16.85277	3.085233	203	0.21509	44.81
9	35.23118	17.61559	2.955597	112	0.19538	49.54
10	36.49104	18.24552	2.85685	302/104	0.21375	45.44
11	36.85969	18.42985	2.829255	211	0.19438	50.02
12	38.97902	19.48951	2.68093	013	0.20401	47.97
13	39.97083	19.98542	2.617027	212	0.20409	48.10
14	45.37053	22.68527	2.319218	105	0.24946	40.08
15	46.67079	23.3354	2.258069	402	0.22964	43.75
16	47.99869	23.99935	2.199145	304	0.24143	41.82
17	50.86149	25.43075	2.082927	214/403	0.29103	35.10
18	53.27013	26.63507	1.995176	411/015	0.26435	39.04

Similar to the γ' -V₂O₅ and γ -LiV₂O₅ lattices, γ -Na_{0.96}V₂O₅ structure consists of puckered layers stacked perpendicular to the c-axis. A common characteristic of these γ -type structures is that the layers are built of infinite V₂O₅ chains running in the b-direction and interconnected by the ladder step V–O₂ LS contact linkages (**Figure 2**).

The Raman spectrum of γ -Na_{0.96}V₂O₅ is consist of 15 peaks at 85, 110, 155, 191, 221, 250, 297, 323, 388, 470, 546, 655, 717, 959 and 1005 cm⁻¹ (**Figure 3**). The highest frequency bands at 1005 and 959 cm⁻¹ correspond to the stretching vibrations of the shortest V_a–O_{1a} and V_b–O_{1b} s bonds respectively; the bands at 717, 655 and 470 cm⁻¹ are due to the related to the stretching vibrations

within the $V_a-O_{2a}-V_a$, $V_b-O_{2b}-V_b$, and $V_a-O_3-V_b$ bridges respectively while the intense component observed at 546 cm^{-1} corresponds to the vibration of the $V-O_2$ LS bonds. The lower frequency modes at $85, 110, 155, 191, 221, 250, 297, 323, 388\text{ cm}^{-1}$ are assigned to the complex distortions of V_2O_5 ladders [46] Raman vibration and assignments have shown in **Table 3** can be found in [46].

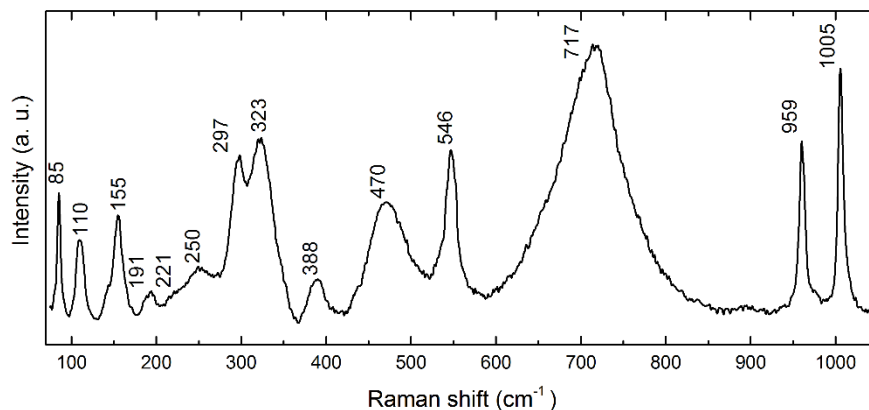


Figure 3. Raman spectra of $\gamma\text{-Na}_{0.96}\text{V}_2\text{O}_5$ powder

The morphology of the obtained powder was characterized by scanning electron microscopy (SEM) at different magnifications (**Figure 4**). It reveals that obtained product consists of agglomerated particles with uniform size. The average particles size is around $100\sim 200\text{ nm}$. On the basis of a Scherrer analysis of the XRD pattern (**Figure 2**), the average crystallite sizes were evaluated to $\sim 140\text{ nm}$ along the c -axis and $\sim 85\text{ nm}$ in the a - b plane.

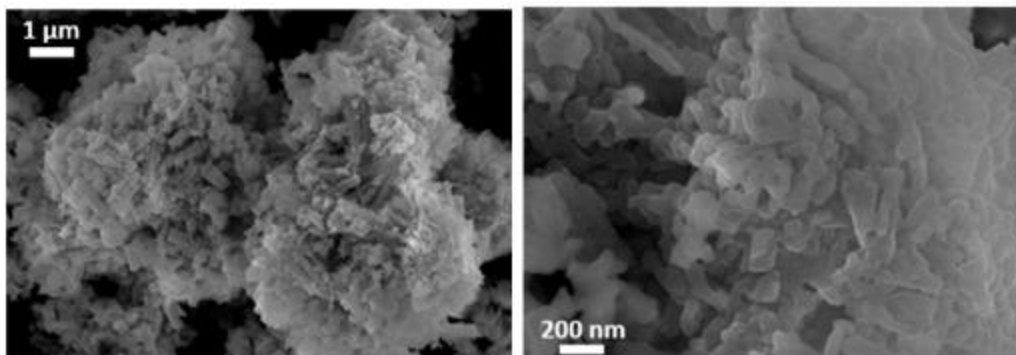


Figure 4. SEM micrographs of $\gamma\text{-Na}_{0.96}\text{V}_2\text{O}_5$ powder at different magnifications

3.2.3 Electrochemical study

The discharge/charge profile of γ -Na_{0.96}V₂O₅ at C/5 in voltage range of 4 – 1.75V is shown in **Figure 5**. From discharge/charge curve single plateau can be observed at 3.3/3.4V with total faradic yield 1 F/mol. The initial discharge/charge capacity exhibits 124 mAh g⁻¹, indicating reversible insertion/extraction process. The discharge capacity slightly decreased to 118 mAh g⁻¹ after 50 cycles with good capacity retention without impact on hysteresis of voltage profile shape (~100 mV).

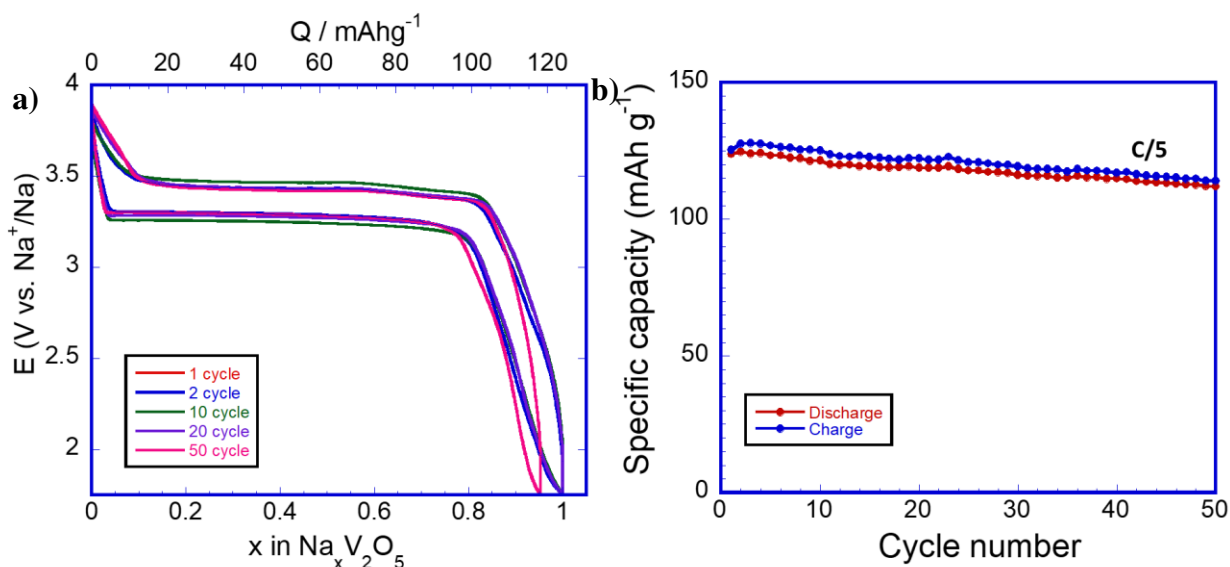


Figure 5. (a) Discharge/charge profile and (b) cycle performance of γ -Na_{0.96}V₂O₅ at C/5 in 4 - 1.75V voltage range

3.2.4 Structural investigation upon discharge-charge

The cycled electrode at C/5 after 50 cycles at voltage range of 4 – 1.75V has been examined by XRD and Raman (**Figure 6a**). It was found that after 1st oxidation XRD and Raman results show the typical fingerprint of γ -Na_{0.96}V₂O₅ with following unit cell parameters [$a=9.94$ Å, $b=3.58$ Å, $c=10.04$ Å], which is in a good agreement with the literature [47]. This reveals an efficient initial extraction process of sodium ions from the bronze structure. After 1 complete cycle, the initial γ -NaV₂O₅ structure is restored without additional peaks or bands. The unit cell parameters on discharged state [$a=9.75$ Å, $b=3.62$ Å, $c=11.95$ Å] fully agreed with that of sodiated γ -NaV₂O₅ phase [47] which is confirmed by Raman results (**Figure 6b**). The XRD pattern and Raman spectra of cycled electrode (after 50 cycles) illustrate the unchanged lattice parameters and completely

superimpose with initial γ - NaV_2O_5 , indicating a high stable structural stability upon electrochemical reaction.

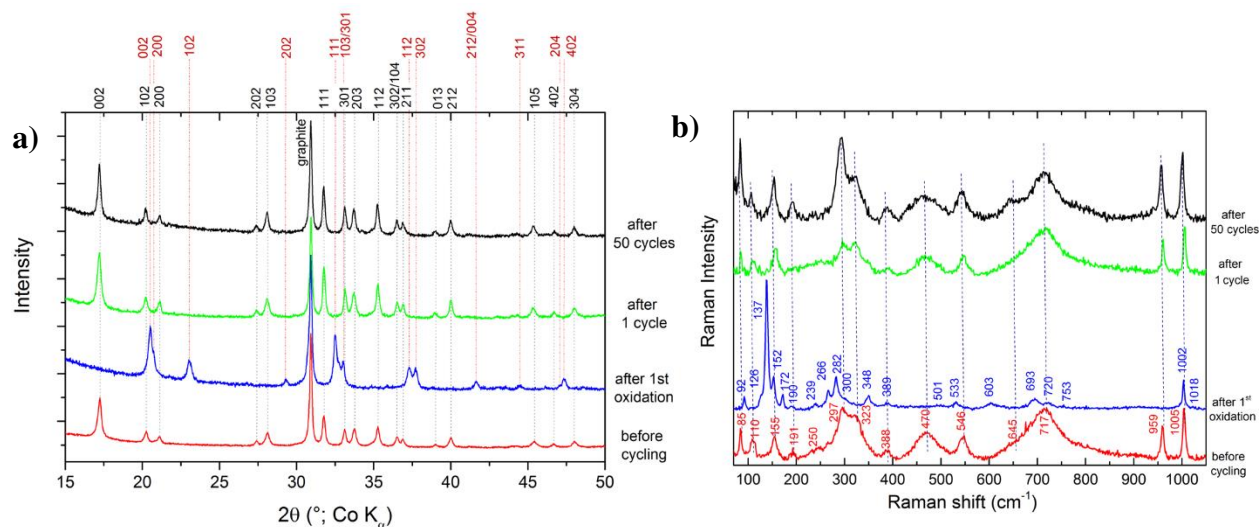


Figure 6. Ex-situ XRD and Raman study of γ - $\text{Na}_{0.96}\text{V}_2\text{O}_5$ electrode after 50 cycles at C/5 at 4.0 – 1.75 V voltage range

3.2.5 Cycling properties

The rate capability of γ - $\text{Na}_{0.96}\text{V}_2\text{O}_5$ is reported in **Figure 7a**. At C/10 and C/5, similar discharge capacities are achieved at 140 and 134 mAh g $^{-1}$, respectively, with stable hysteresis of 100 mV. The discharge capacities at C/2, 1C, 2C, 5C gain 122, 110, 91, 50 mAh g $^{-1}$, respectively. In addition, the charge capacity is systematically fully recovered with symmetric voltage shape at all C-rates (**Figure 7b**), indicating a high electrochemical reversibility of the cathode material. After high C-rate (5C), the discharge/capacity fully recovered to 137 mAh g $^{-1}$ at C/10 with stable cycling.

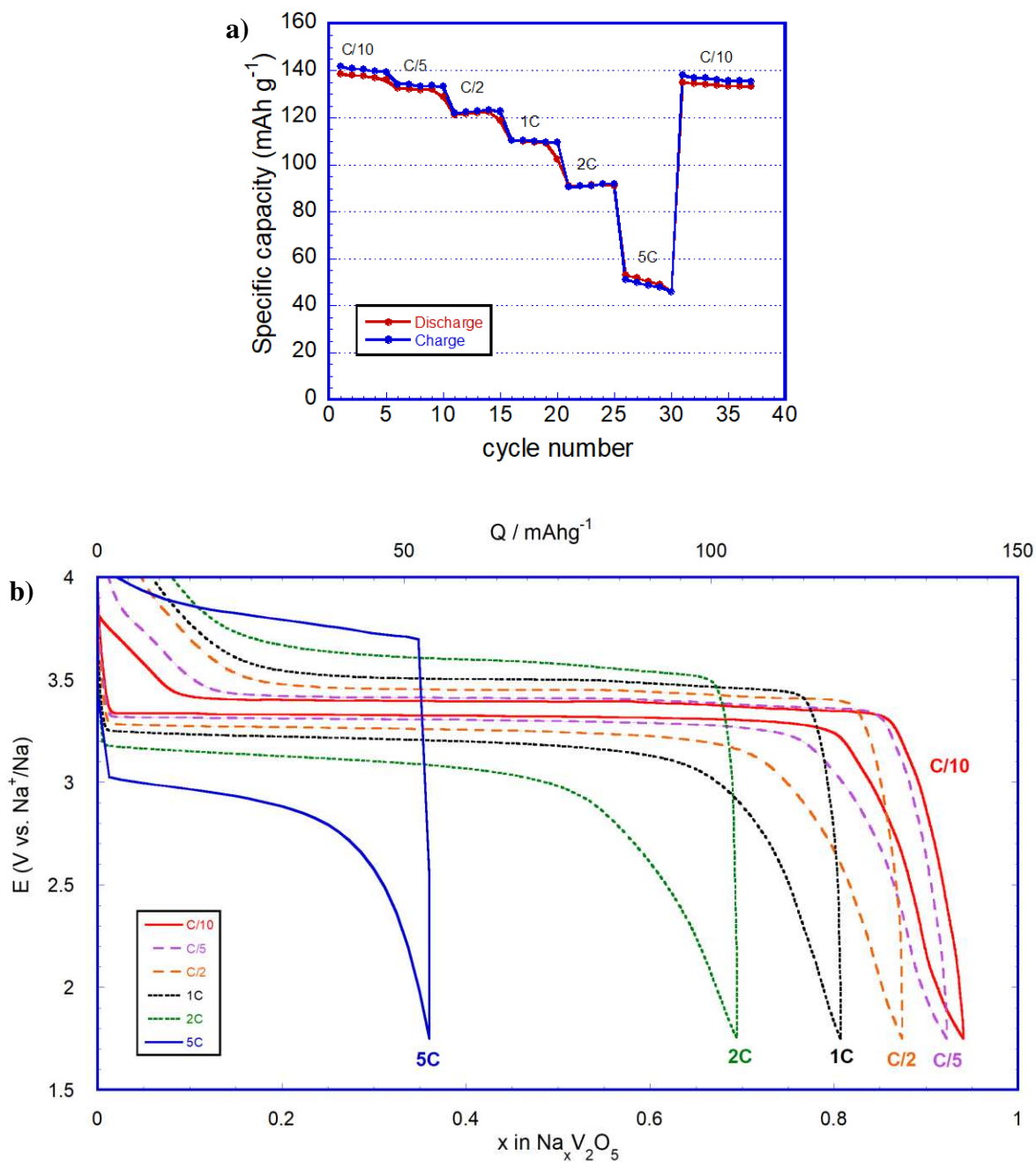


Figure 7: (a) Rate capability and (b) discharge/charge profile at different C-rate of $\gamma\text{-Na}_{0.96}\text{V}_2\text{O}_5$ at voltage range of 4 – 1.75V

3.2.6 Conclusion

In conclusion, a new sodium vanadium bronze (γ -Na_{0.96}V₂O₅) has been prepared by chemical sodiation using polyol synthesized γ' -V₂O₅ at room temperature. This low-cost soft chemistry route leads to fine particles with high purity and high crystallinity. The crystal features of the γ -Na_{0.96}V₂O₅ material upon charge and discharge have been characterized by X-ray diffraction and Raman spectroscopy. This sodiated bronze can be directly used as a high voltage positive electrode (3.4V) for Na-ion batteries with attractive attractive properties. A reversible specific capacity of 124 mAh g⁻¹ at C/5 is available at 3.4V vs. Na⁺/Na and still 112 mAh g⁻¹ after 50 cycles at C/5.

The high stability of the structure after charge and discharge has been shown from XRD and Raman spectroscopy which explains a good cycle life upon cycling. However it appears an improvement is still required in terms of rate capability especially at C rate higher than 2C

This work clearly confirms the interest exhibited by insertion properties of γ' -V₂O₅ toward Na insertion since the new γ -Na_{0.96}V₂O₅ vanadium bronze competes with the well-known cathode materials for sodium-ion batteries such as NaNi_{1/3}Mn_{1/3}Co_{1/3}O₂ and NaFePO₄

REFERENCES

- [1] D. Larcher, J. M. Tarascon, “Towards greener and more sustainable batteries for electrical energy storage”, *Nat. Chem.* 2015, 7, 19.
- [2] C. Grosjean, P. H. Miranda, M. Perrin, M. and P. Poggi, “Assessment of world lithium resources and consequences of their geographic distribution on the expected development of the electric vehicle industry”, *Renew. Sust. Energ. Rev.* 2012, 16 1735.
- [3] S. Komaba, W. Murata, T. Ishikawa, N. Yabuuchi, T. Ozeki, T. Nakayama, A. Ogata, K. Gotoh, K. Fujiwara, “Electrochemical Na Insertion and Solid Electrolyte Interphase for Hard-Carbon Electrodes and Application to Na-Ion Batteries”, *Adv. Funct. Mater.* 2011, 21, 3859.
- [4] B. L. Ellis, L. F. Nazar, “Sodium and sodium-ion energy storage batteries”, *Curr. Opinion Solid State Mater. Sci.* 2012, 16, 168.
- [5] V. Palomares, P. Serras, V. Villaluenga, K. B. Hueso, J. Carretero-González, T. Rojo, “Na-ion batteries, recent advances and present challenges to become low cost energy storage systems”, *Energy Environ. Sci.* 2012, 5, 5884.
- [6] S. W. Kim, D. H. Seo, X. Ma, G. Ceder, V. Kang, “Electrode Materials for Rechargeable Sodium-Ion Batteries: Potential Alternatives to Current Lithium-Ion Batteries”, *Adv. Energy Mater.* 2012, 2, 710.
- [7] V. Palomares, M. Casas-Cabanas, E. Castillo-Martinez, M.H. Han, T. Rojo, “Update on Na-based battery materials. A growing research path”, *Energy Environ. Sci.* 2013, 6, 2312.
- [8] H. Pan, Y. S. Hu, L. Chen, “Room-temperature stationary sodium-ion batteries for large-scale electric energy storage”, *Energy Environ. Sci.* 2013, 6, 2338.
- [9] M. D. Slater, D. Kim, V. Lee, C. S. Johnson, “Sodium-Ion Batteries”, *Adv. Funct. Mater.* 2013, 23, 947.
- [10] A. Ponrouch, A. R. Goni, M. R. Palacin, “High capacity hard carbon anodes for sodium ion batteries in additive free electrolyte”, *Electrochem. Comm.* 2013, 27, 85.
- [11] N. Yabuuchi, K. Kubota, M. Dahbi, S. Komaba, “Research Development on Sodium-Ion Batteries”, *Chem. Rev.* 2014, 114, 11636.
- [12] K. Kubota, S. Komaba, “Review—Practical Issues and Future Perspective for Na-Ion Batteries”, *J. Electrochem. Soc.* 2015, 162, A2538.
- [13] D. Kundu, E. Talaie, V. Duffort, L. F. Nazar, “The emerging chemistry of sodium ion batteries for electrochemical energy storage”, *Angew. Chem. Int. Ed. Engl.*, 2015, 54, 3431.
- [14] J. Y. Hwang, S. T. Myung, Y. K. Sun, “Sodium-ion batteries: present and future”, *Chem. Soc. Rev.* 2017, 46, 3529.
- [15] H. Kim, H. Kim, Z. Ding, M. H. Lee, K. Lim, G. Yoon, K. Kang, “Recent Progress in Electrode Materials for Sodium-Ion Batteries”, *Adv. Energy Mater.* 2016, 6, 1600943.
- [16] Z. Dai, U. Mani, H. T. Tan, Q. Yan, “Advanced Cathode Materials for Sodium-Ion Batteries: What Determines Our Choices?”, *Small Methods* 2017, 1, 1700098.
- [17] X. Xiang, K. Zhang, J. Chen, “Recent Advances and Prospects of Cathode Materials for Sodium-Ion Batteries”, *Adv. Mater.* 2015, 27, 5343.
- [18] C. Fang, Y. Huang, W. Zhang, J. Han, Z. Deng, Y. Cao, H. Yang, “Routes to High Energy Cathodes of Sodium-Ion Batteries”, *Adv. Energy Mater.* 2016, 6, 1501727.
- [19] Y. You, A. Manthiram, “Progress in High-Voltage Cathode Materials for Rechargeable Sodium-Ion Batteries”, *Adv. Energy Mater.* 2018, 8, 1701785.

- [20] K. West, B. Zachau-Christiansen, T. Jacobsen, S. Skaarup, "Sodium insertion in vanadium oxides", *Solid State Ion.* 1988, 28-30, 1128.
- [21] M. Safrany Renard, N. Emery, R. Baddour-Hadjean, J. P. Pereira-Ramos, " γ' -V₂O₅: A new high voltage cathode material for sodium-ion battery", *Electrochim. Acta* 2017, 252C, 4.
- [22] R. Baddour-Hadjean, M. Safrany Renard, N. Emery, L. T. N. Huynh, M. L. P. Le, J. P. Pereira-Ramos, *Electrochim. Acta* 2018, 270, 129.
- [23] S. Tepavcevic, H. Xiong, V.R. Stamenkovic, X. Zuo, M. Balasubramanian, V.B. Prakapenka, C.S. Johnson, T. Rajh, "Nanostructured Bilayered Vanadium Oxide Electrodes for Rechargeable Sodium-Ion Batteries", *ACS Nano* 2012, 6, 530.
- [24] D. Su, G. Wang, "Single-Crystalline Bilayered V₂O₅ Nanobelts for High-Capacity Sodium-Ion Batteries", *ACS Nano* 2013, 7, 11218.
- [25] S. Bach, N. Baffier, J. P. Pereira-Ramos, R. Messina, "Electrochemical sodium intercalation in Na_{0.33}V₂O₅ bronze synthesized by a sol-gel process", *Solid State Ionics* 1989, 37, 41.
- [26] J.P. Pereira-Ramos, R. Messina, S. Bach, N. Baffier, "Influence of the synthesis via a sol-gel process on the electrochemical lithium and sodium insertion in β -Na_{0.33}V₂O₅", *Solid State Ion.* 1990, 40-41, 970.
- [27] H. M. Liu, H. S. Zhou, L. P. Chen, Z. F. Tang, W. S. Yang, "Electrochemical insertion/deinsertion of sodium on NaV₆O₁₅ nanorods as cathode material of rechargeable sodium-based batteries", *J. Power Sources* 2011, 196, 814.
- [28] D. Hamani, M. Ati, J.-M. Tarascon, P. Rozier, "Na_xVO₂ as possible electrode for Na-ion batteries", *Electrochem. Commun.* 2011, 13, 938.
- [29] M. Guignard, C. Didier, J. Darriet, P. Bordet, E. Elkaim, C. Delmas, "P₂-Na_xVO₂ system as electrodes for batteries and electron-correlated materials", *Nat. Mater.* 2013, 12, 74.
- [30] G. Venkatesh, V. Pralong, O. I. Lebedev, V. Caignaert, P. Bazin, B. Raveau, "Amorphous sodium vanadate Na_{1.5} + yVO₃, a promising matrix for reversible sodium intercalation", *Electrochem. Comm.* 2014, 40, 100.
- [31] H. He, G. Jin, H. Wang, X. Huang, Z. Chen, D. Sun, Y. Tang, "Annealed NaV₃O₈ nanowires with good cycling stability as a novel cathode for Na-ion batteries", *J. Mater. Chem. A*, 2014, 2, 3563.
- [32] S. Bach, A. Boudaoud, N. Emery, R. Baddour-Hadjean, J. P. Pereira-Ramos, "K_{0.5}V₂O₅: A novel Li intercalation compound as positive electrode material for rechargeable lithium batteries", *Electrochim. Acta* 2014, 119, 38.
- [33] Galy, J.; Darriet, J.; Hagenmuller, P. LixV₂O₅ Bronzes- Structure of Beta'-Phase and Refinement of Gamma-Phase Structure. *Rev. Chim. Miner.* 1971, 8, 509–522.
- [34] Anderson, D. N.; Willett, R. D. Refinement of Structure of LiV₂O₅. *Acta Crystallogr., Sect. B: Struct. Crystallogr. Cryst. Chem.* 1971, 27, 1476–1477.
- [35] Cocciantelli, J. M.; Ménétrier, M.; Delmas, C.; Doumerc, J. P.; Pouchard, M.; Hagenmuller, P. Electrochemical and Structural Characterization of Lithium Intercalation and Deintercalation in the γ -LiV₂O₅ Bronze. *Solid State Ionics* 1992, 50, 99–105.
- [36] Dai, J. X.; Li, S. F. Y.; Gao, Z. Q.; Siow, K. S. Siow, Novel Method for Synthesis of γ -lithium vanadium oxide as cathode materials in lithium ion batteries. *Chem. Mater.* 1999, 11, 3086–3090.
- [37] Barker, J.; Saidi, M. Y.; Swoyer, J. L. Performance evaluation of the electroactive material γ LiV₂O₅ made by a carbothermal reduction method. *J. Electrochem. Soc.* 2003, 150, A1267–A1272.

- [38] Wang, W.; Wang, H.; Liu, S.; Huang, J. Synthesis of γ -LiV₂O₅ nanorods as a high-performance cathode for Li ion battery. *J. Solid State Electrochem.* 2012, 16, 2555–2561.
- [39] Cocciantelli, J. M.; Doumerc, J. P.; Pouchard, M.; Broussely, M.; Labat, J. Crystal chemistry of electrochemically inserted LixV₂O₅. *J. Power Sources* 1991, 34, 103–111.
- [40] Cocciantelli, J. M.; Graveriau, P.; Doumerc, J. P.; Pouchard, M.; Hagenmuller, P. On the preparation and characterization of a new polymorph of V₂O₅. *J. Solid State Chem.* 1991, 93, 497–502.
- [41] Pouchard, M.; Casalot, A.; Galy, J.; Hagenmuller, P. Vanadium bronzes with NaxV₂O₅ formula. *Bull. Soc. Chim. Fr.* 1967, 11, 4343–4348.
- [42] Carpy, A.; Galy, J. Refining crystal-structure of alpha-vanadium sodium oxybronze NaV₂O₅ alpha. *Acta Crystallogr., Sect. B: Struct. Crystallogr. Cryst. Chem.* 1975, 31, 1481–1482.
- [43] Muller-Bouvet, D.; Baddour-Hadjean, R.; Tanabe, M.; Huynh, L. T. N.; Le, L. M. P.; Pereira-Ramos, J. P. Electrochemically formed α' -NaV₂O₅: a new sodium intercalation compound. *Electrochim. Acta* 2015, 176, 586–593.
- [44] Safrany Renard, M.; Emery, N.; Roginskii, E.; Baddour-Hadjean, R.; Pereira-Ramos, J.-P. Crystal structure determination of a new sodium vanadium bronze electrochemically formed. *J. Solid State Chem.* 2017, 254, 62–68.
- [45] Safrany Renard, M.; Emery, N.; Baddour-Hadjean, R.; Pereira-Ramos, J.-P. γ' -V₂O₅: A new high voltage cathode material for sodium-ion battery. *Electrochim. Acta* 2017, 252, 4–11.7
- [46] Emery N.; Baddour-Hadjean, R; Batyrbekuly D, Laik B.; Bakenov Z.; Pereira-Ramos, J.-P. γ -Na_{0.96}V₂O₅: A New Competitive Cathode Material for Sodium-Ion Batteries Synthesized by a Soft Chemistry Route. *Chemistry of Mat.* 2018, 30, 5305 – 5314
- [47] Renard, Marianne. (2017). Propriétés électrochimiques et réponse structurale du polymorphe γ' -V₂O₅ vis-à-vis de l'insertion du lithium et du sodium

γ -Na_{0.96}V₂O₅: A New Competitive Cathode Material for Sodium-Ion Batteries Synthesized by a Soft Chemistry Route

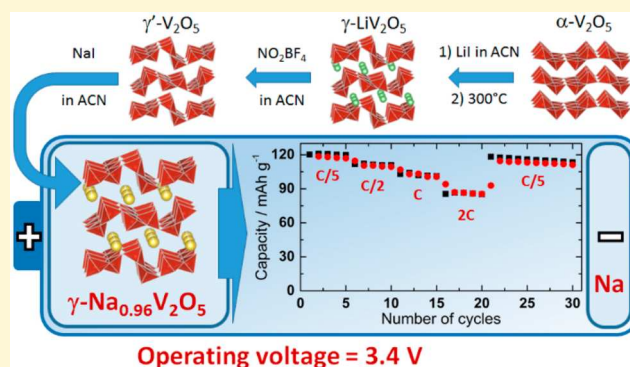
Nicolas Emery,^{*,†,‡} Rita Baddour-Hadjean,[†] Dauren Batyrbekuly,^{†,‡} Barbara Laik,^{†,‡} Zhumabay Bakenov,[‡] and Jean-Pierre Pereira-Ramos[†]

[†]Institut de Chimie et des Matériaux Paris Est, ICMPE/GESMAT, UMR 7182 CNRS-Université Paris Est Créteil, CNRS 2 rue Henri Dunant, 94320 Thiais, France

[‡]Institute of Batteries LLC, Nazarbayev University, 53 Kabanbay Batyr Avenue, Astana 010000, Kazakhstan

Supporting Information

ABSTRACT: A new cathode material for sodium-ion batteries, the sodium vanadium bronze γ -Na_{0.96}V₂O₅, is easily synthesized by chemical sodiation of the γ' -V₂O₅ polymorph at room temperature. This low-cost soft chemistry route leads to fine particles with high purity and high crystallinity. The crystal features and morphology of the γ -Na_{0.96}V₂O₅ material have been characterized by X-ray diffraction, Raman spectroscopy, and scanning electron microscopy. It exhibits a layered structure with orthorhombic symmetry (*Pnma* space group) isomorphic to that of the lithiated γ -LiV₂O₅ bronze. This cathode material is evaluated by charge–discharge experiments. Promising electrochemical performance is outlined. A quantitative Na extraction process is observed at a high voltage of 3.4 V versus Na⁺/Na, and a reversible electrochemical behavior is demonstrated with an initial specific capacity of 125 mAh g^{−1}, which remains at 112 mAh g^{−1} after 50 cycles at C/5. The structural reversibility of the sodium extraction–insertion reaction in γ -Na_{0.96}V₂O₅ is demonstrated upon cycling. This new vanadium bronze competes with the well-known cathode materials for sodium-ion batteries such as NaNi_{1/3}Mn_{1/3}Co_{1/3}O₂ and NaFePO₄.



INTRODUCTION

Worldwide large-scale integration of renewable energies will require the deployment of new electrical energy storage (EES) solutions. Lithium-ion batteries (LIBs), which dominate the portable electronic market, are now considered as a key energy storage technology for electric vehicles and, in parallel, are also evaluated for EES.^{1–5} However, large-scale applications of these batteries require that they be cost effective, sustainable, and environmentally friendly.⁶ In particular, concerns about the scarcity of Li and its uneven geographical distribution^{7–9} have prompted intense research activities beyond LIB technology. Room-temperature sodium-ion batteries (SIBs) are considered as promising alternatives to LIBs. Indeed, Na sources are practically inexhaustible and ubiquitous, which is extremely favorable for large-scale stationary EES.^{10–19} Hence, the discovery and development of new promising positive and negative electrode materials for SIBs are actively being pursued.^{11–25} To date, a large variety of Na insertion frameworks have been proposed as cathode materials.^{20–25} Similar to LIBs, highly reversible cathode materials based upon the intercalation reaction are needed for the high capacity and good cyclability of SIBs. These cathode materials are mainly categorized into oxides and polyanion types.²⁰ A major obstacle is the difficulty of obtaining a sodium host material

with an operating voltage and a capacity comparable to those of LIB analogues. Layered sodium transition metal oxides Na_xM_rO₂ (M_r = transition metal such as Co, Ti, V, Cr, Mn, Fe, or Ni) are regarded as promising candidates,^{25–31} and their electrochemical performance has been shown to depend largely on the structure and the transition metal chosen.³¹

Vanadium oxide bronzes of the general formula M_xV₂O₅ (M = Li, Na, etc.), with a mixed valence of vanadium ions (V⁵⁺ and V⁴⁺), are semiconductor or metallic conductor compounds that possess extended homogeneous composition ranges resulting from a nonstoichiometric intercalation of M cations within the [V₂O₅] network. These compounds have attracted much attention because of the great number of lamellar phases enabling accommodation of a large amount of guest cations.^{32–34}

When M = Li and *x* = 1, three orthorhombic ϵ -, δ -, and γ -LiV₂O₅ bronzes are found in the V₂O₅/Li phase diagram.^{32,35,36} The stable high-temperature phase γ -LiV₂O₅, characterized by a puckered layered framework with Li ions located between the (VO₅)_n layers,^{35,37} was reported to exhibit

Received: May 16, 2018

Revised: July 11, 2018

Published: July 11, 2018

promising behavior as a cathode material for LIBs.^{38–41} The oxidation of γ -LiV₂O₅ leads to the γ' -V₂O₅ polymorph, which retains the memory of the pristine γ -LiV₂O₅ structure.^{42,43} Electrochemical lithium insertion in γ' -V₂O₅ was reported to occur at a higher voltage (3.6–3.5 V vs Li⁺/Li) than in α -V₂O₅ (3.4–3.2 V vs Li⁺/Li).³⁸

When M = Na and $x = 1$, only the α' -NaV₂O₅ layered phase with an α -V₂O₅ isotype orthorhombic structure was obtained through solid-state reaction of NaVO₃ and VO₂ precursors around 600 °C.^{44,45} More recently, this α' -NaV₂O₅ bronze was electrochemically prepared and investigated as a sodium intercalation compound. An interesting specific capacity of 120 mAh g⁻¹ at a C/10 rate near 1.6 V versus Na⁺/Na was reported.⁴⁶ Another novel structural variety of sodium vanadium bronze belonging to the γ -system, namely γ -Na_{0.96}V₂O₅, was described as the discharge product of a composite γ' -V₂O₅ electrode near 3.2 V versus Na⁺/Na in a 1 M NaClO₄ propylene carbonate electrolyte.^{47,48} However, this sodium bronze has never been synthesized as pure powder or investigated as a cathode material for SIBs. In spite of the interesting first discharge capacity of 145 mAh g⁻¹ reported for γ' -V₂O₅, a strong kinetic limitation was shown during the first charge, with acycling efficiency of only 60% even at a low rate of C/20 with merely 80 mAh g⁻¹ recovered.⁴⁸ Another crucial drawback of γ' -V₂O₅ is that this Na-free material is not directly suitable as a cathode in a SIB.

Herein, we present γ -Na_{0.96}V₂O₅ as a directly usable cathode material for SIBs. This paper describes the first chemical synthesis of this sodium vanadium bronze, from chemical sodiation at room temperature of the γ' -V₂O₅ polymorph. We synthesize γ -Na_{0.96}V₂O₅ from a homemade α -V₂O₅ precursor obtained through a polyol process, leading easily to pure, fine, and porous powders with a homogeneous grain size distribution.⁴⁹ As a result, a quantitative initial desodiation is obtained electrochemically. Then, the γ -Na_{0.96}V₂O₅ cathode material exhibits a reversible electrochemical behavior and can deliver an interesting specific capacity of 125 mAh g⁻¹ at a high voltage of 3.4 V versus Na⁺/Na, with 112 mAh g⁻¹ still available after 50 cycles at C/5. Raman and X-ray diffraction (XRD) measurements of cycled electrodes demonstrate the high structural reversibility of the sodium insertion–extraction reactions in this new cathode material for SIBs.

EXPERIMENTAL SECTION

Synthesis. The synthesis pathway used to prepare the sodiated bronze is illustrated in Figure 1. The first step aimed to prepare the γ -LiV₂O₅ phase under mild-temperature conditions: the chemical lithiation of α -V₂O₅ was performed using lithium iodide in excess (molar ratio of 2:1) in acetonitrile at room temperature, leading to δ -LiV₂O₅.³⁶ The obtained powder was washed with acetonitrile before being dried at 70 °C and then heat-treated at 300 °C for 2 h under dynamic primary vacuum using a Büchi furnace. This heat treatment allowed the formation of the distorted γ -type layers via the δ -LiV₂O₅ → γ -LiV₂O₅ phase transition.³⁶ The second step consists of removing lithium ions from the interlayer spacing without altering the distorted framework, leading to the γ' -V₂O₅ polymorph. This chemical oxidation reaction was performed at room temperature in acetonitrile under continuous stirring, using NO₂BF₄ in molar excess (2:1). The obtained powder was dried at 80 °C. The last step consists of reducing chemically the γ' -V₂O₅ powder at room temperature in acetonitrile under continuous stirring without altering the distorted framework, leading to the γ -Na_{0.96}V₂O₅ polymorph. This chemical reduction reaction was performed at room temperature in acetonitrile under continuous stirring, using NaI in excess (2:1 molar excess). The resulting compound was washed with acetonitrile and then dried at 70 °C. The elemental analysis of the final compound, performed by ICP-OES measurements (PerkinElmer Optima 8300 DV), led to the γ -Na_{0.96(1)}V₂O₅ composition.

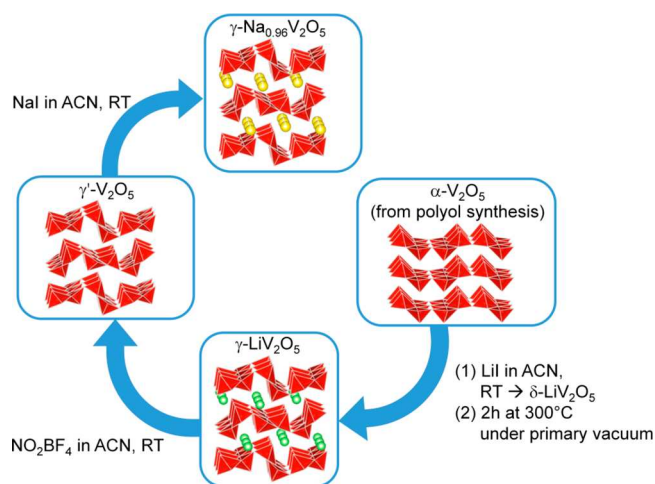


Figure 1. Scheme of the synthesis pathway leading to γ -Na_{0.96}V₂O₅ from α -V₂O₅.

The α -V₂O₅ precursor was prepared through the polyol method described in ref 49, which led to very fine powder with a narrow particle size distribution. Typically, NH₄VO₃ powder (Alfa Aesar, 99%) was slowly dissolved into ethylene glycol (Alfa Aesar, 99%) at 110 °C under continuous stirring. Once a yellow solution was formed, the temperature was increased to reach reflux conditions for 1 h. The vanadyl glycolate precipitate was then washed with ethanol and dried at 80 °C. A thermal treatment at 450 °C in air for 2 h was performed in a box furnace to obtain the V₂O₅ powder.

Structural Characterization. XRD patterns were collected using a Panalytical X'Pert pro diffractometer equipped with a Co K α X-ray source ($\lambda = 1.7889$ Å) and an X'celerator linear detector. Collected data were analyzed within the Rietveld method using the GSAS ExpGUI package.^{50,51} All the diffraction patterns were collected with a 2θ step of 0.0167°.

Valence states of the vanadium atoms using the bond valence sum (BVS) method and bond valence energy landscape (BVEL) maps were calculated with the BondStr program implemented in the FullProf Suite,^{52,53} using the soft bond valence parameters defined by Adams.⁵⁴ The BVEL method derives from the BVS method,⁵⁵ which is based on the analysis of the bond lengths extracted from the crystal structure. This approach usually gives coarse but reliable results compared to those of ab initio calculations on activation energies estimated for ionic conductors and energy storage materials.⁵⁶ It is recognized as a quick and simple tool for analyzing the possible shape and dimensionality of diffusion paths within the crystal structure for a given mobile ion and has been applied to estimate the Li and Na conduction paths in several cathode materials.^{57–59}

The Raman spectra were measured with a LaBRAM HR 800 (Jobin-Yvon-Horiba) Raman microspectrometer, including edge filters and equipped for signal detection with a back-illuminated charge-coupled device detector (Spex CCD) cooled by a Peltier effect to 200 K. A He:Ne laser (632.8 nm) was used as the excitation source. The spectra were measured in backscattering geometry. The resolution was ~ 0.5 cm⁻¹. A long distance 50 \times LWD objective was used to focus the laser light on the sample surface to a spot size of 1 μ m². To avoid local heating of the sample, the power of the laser beam was adjusted to 0.2–0.5 mW with neutral filters of various optical densities.

The powder morphology was investigated by using a field-emission scanning electron microscope (Zeiss, Merlin-type) operating at 5 kV.

Electrochemical Tests. Electrochemical experiments were conducted in sodium half-cells consisting of CR 2032 coin-type cells. The positive electrode was prepared by mixing γ -Na_{0.96}V₂O₅ as the active material, acetylene black, graphite, and PTFE as a binder [80:7.5:7.5:5 (w/w)]. Approximately 8 mg cm⁻² of this mix was pressed on a stainless steel grid current collector. A Na foil acted as both negative and reference electrodes. Consequently, all the potential

Table 1. Structural Parameters of α -V₂O₅, γ -LiV₂O₅, γ' -V₂O₅, and γ -Na_{0.96}V₂O₅^a

phase (space group)	<i>a</i> (Å)	<i>b</i> (Å)	<i>c</i> (Å)	unit cell volume (Å ³)	molar volume (cm ³ mol ⁻¹)
α -V ₂ O ₅ (<i>Pmmn</i>)	11.5054(3)	3.5563(1)	4.3765(2)	179.42(3)	54.00
γ -LiV ₂ O ₅ (<i>Pnma</i>)	9.6947(2)	3.6062(1)	10.6780(2)	373.32(2)	56.18
γ' -V ₂ O ₅ (<i>Pnma</i>)	9.9484(2)	3.5863(1)	10.0459(3)	358.42(2)	53.94
γ -Na _{0.96} V ₂ O ₅ (<i>Pnma</i>)	9.7806(3)	3.6299(1)	11.8872(5)	422.03(4)	63.52

^aUnit cell parameters and unit cell volumes.

values were expressed versus Na⁺/Na without further precision except when the reference was mentioned. The electrolyte was 1 M NaClO₄ in propylene carbonate (PC) containing a fluoroethylene carbonate (FEC) additive (2% by volume). The positive electrode was separated from the negative electrode by Whatman glass fiber disks soaked with the electrolyte. Coin-type cells were assembled in an argon-filled glovebox with controlled levels of oxygen and water of <1 ppm. After being cycled, the electrodes were removed from the coin-type cell in an argon-filled glovebox, rinsed with DMC, and further analyzed by X-ray diffraction and Raman spectroscopy, using specific airtight sample holders. Galvanostatic experiments were performed at room temperature in the voltage range of 1.75–4.00 V, using a VMP3 Bio-Logic apparatus.

RESULTS AND DISCUSSION

The chosen synthesis pathway lies on two singularities reported in the V₂O₅/Li system.^{38,43,62} (i) The reconstruction mechanism leading to γ -LiV₂O₅ from δ -LiV₂O₅ is irreversible; (ii) the γ -LiV₂O₅ phase can itself be oxidized into γ' -V₂O₅ while maintaining the γ -type structure.

Interestingly, electrochemical insertion of Na into γ' -V₂O₅ was recently reported to take place at nearly the same potential as Li insertion (−0.5/−0.6 V vs the normal hydrogen electrode).⁴⁸ Hence, the chemical reduction of γ' -V₂O₅ with sodium iodide in acetonitrile at room temperature is expected to be successful to produce a Na-intercalated bronze that maintains its γ -structure. The synthesis pathway leading to the new structural variety of sodium vanadium bronze belonging to the γ -system is illustrated in Figure 1. After synthesis of the α -V₂O₅ precursor through the polyol route, γ -LiV₂O₅ and γ' -V₂O₅ intermediates are successively prepared to obtain the final product γ -Na_{0.96}V₂O₅. As detailed below, this protocol interestingly retains the specific morphologic features of the α -V₂O₅ polyol precursor. The structural parameters of all the products, including lattice cell parameters, V–O, Li–O, and Na–O bond lengths, and the oxidation states of the vanadium atoms estimated from BVS, are listed in Tables 1 and 2.

Characterization of the α -V₂O₅ Precursor. α -V₂O₅ obtained through the polyol route⁴⁹ has been characterized by XRD (Figure S1a), Raman spectroscopy (Figure S2a), and scanning electron microscopy (SEM) (Figure 2a). Atomic positions, listed in Table S1, lead to the V–O bond lengths reported in Table 2. The Rietveld refinement of XRD data (Figure S1a) does not indicate the presence of any impurity, and the cell parameters [*a* = 11.5054(3) Å, *b* = 3.5563(1) Å, and *c* = 4.3765(2) Å (see Table 1)] are consistent with the expected orthorhombic structure of the *Pmmn* space group.^{60,61} The Raman spectrum of the obtained product (Figure S2a) fully agrees with the well-known fingerprint of α -V₂O₅,^{62,63} showing 10 bands at 103, 145, 195, 285, 304, 405, 482, 527, 701, and 994 cm⁻¹. The four highest-frequency modes above 450 cm⁻¹ correspond to the different V–O bond stretching vibrations in the α -V₂O₅ structure. Indeed, each vanadium atom in the chains forms four valence bonds (Figure S3 and Table 2): a vanadyl V=O₁ bond (*d*₁), a V–O₃ bond

Table 2. V–O Bond Lengths (in angstroms) in α -V₂O₅, γ -LiV₂O₅, γ' -V₂O₅, and γ -Na_{0.96}V₂O₅; Na–O and Li–O Bond Lengths (in angstroms) in γ -Na_{0.96}V₂O₅ and γ -LiV₂O₅, Respectively; V_a and V_b Valence States Estimated Using the BVS Approximation; and VO₅ Pyramid Volumes (in cubic angstroms)

	α -V ₂ O ₅	γ' -V ₂ O ₅	γ -LiV ₂ O ₅	γ -Na _{0.96} V ₂ O ₅
(V _a)O ₅				
V _a –O _{1a}	1.575(3)	1.560(6)	1.595(5)	1.548(7)
V _a –O ₃	1.763(2)	1.749(7)	1.737(5)	1.794(9)
V _a –O _{2a} (×2)	1.876(1)	1.893(2)	1.892(2)	1.909(3)
(V _a –O _{2a})LS	2.016(3)	1.968(6)	1.975(4)	1.970(7)
volume of (V _a)O ₅	4.423	4.461	4.675	4.649
BVS V _a	+5.17	+5.29	+5.15	+5.15
(V _b)O ₅				
V _b –O _{1b}		1.576(7)	1.576	1.587
V _b –O ₃		1.827(7)	1.961	1.882
V _b –O _{2b} (×2)		1.880(2)	1.937	1.953
(V _b –O _{2b})LS		2.028(6)	1.967	1.949
volume of (V _b)O ₅		4.531	5.114	5.042
BVS V _b		+4.99	+4.30	+4.37
(Na/Li)–O _{2b}	–	–	2.047	2.415
(Na/Li)–O _{1b}	–	–	2.044	2.275
(Na/Li)–O ₃ (×2)	–	–	2.226	2.425
(Na/Li)–O _{1a} (×2)	–	–	2.357	2.459

(*d*₂) in the V–O₃–V bridge lying in the *x*–*z* plane, and two V–O₂ bonds (*d*₃) resulting in the V–O₂–V bridges oriented along the *y*-axis. The chains in the layers are linked to each other by interchain V–O₂ contacts (*d*₄) named “ladder steps” (LS) and shown by dashed lines in Figure S3. As first noted by Abello and co-workers,⁶³ the frequency sequence ν (*d*₁) > ν (*d*₂) > ν (*d*₃) > ν (*d*₄) is in line with the relationship *d*₁ < *d*₂ < *d*₃ < *d*₄ (see Table 2). Peaks below 450 cm⁻¹ are due to angle bending vibrations. The peak at 405 cm⁻¹ is attributed to a mode consisting of a δ (V–O₃–V) angle bending vibration, whereas atomic displacements in modes below 400 cm⁻¹ are assigned to the LM ladder modes, mostly localized within the ladder steps, as detailed in ref 64.

SEM micrographs displayed in Figure 2a exhibit coral-like agglomerates of several micrometers composed of small rods, themselves made of small crystalline grains of 100–200 nm. The present crystallites are isotropic, as described in ref 49, with an average estimated size of ~85 nm from the diffraction peak width (Figure S1a).

Characterization of γ -LiV₂O₅. The chemical lithiation of α -V₂O₅ at room temperature using LiI as a reducing agent leads to the δ -LiV₂O₅ phase, as previously described by Murphy et al.³⁶ Then, the complete transformation of δ -LiV₂O₅ into γ -LiV₂O₅ involving a reorganization of the V₂O₅ layers themselves is achieved by a heat treatment at 300 °C under primary vacuum.^{36,65}

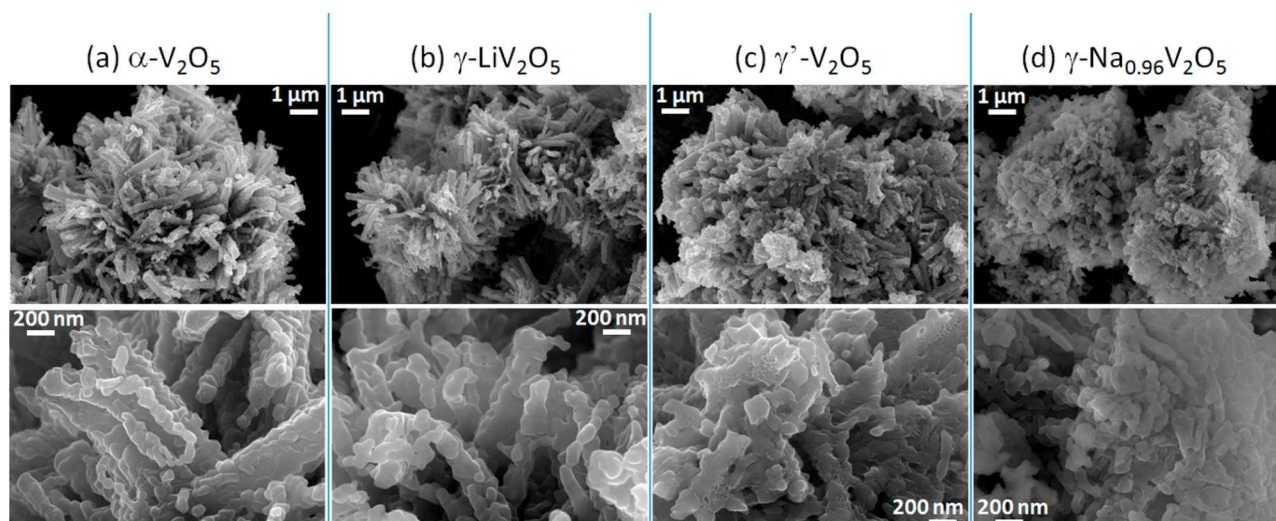


Figure 2. SEM micrographs of the obtained products: (a) α - V_2O_5 , (b) γ - LiV_2O_5 , (c) γ' - V_2O_5 , and (d) γ - $\text{Na}_{0.96}\text{V}_2\text{O}_5$.

Both the XRD pattern (Figure S1b) and the Raman spectrum (Figure S2b) of the resulting heat-treated product show the presence of a pure γ - LiV_2O_5 phase, which indicates a homogeneous chemical lithiation and a full subsequent $\delta \rightarrow \gamma$ phase transformation. Atomic positions, listed in Table S2, lead to the V–O bond lengths reported in Table 2. The cell parameters [$a = 9.6947(2)$ Å, $b = 3.6062(1)$ Å, and $c = 10.6780(2)$ Å (see Table 1)] are consistent with the expected orthorhombic structure of the $Pnma$ space group.^{35,37} The Raman spectrum of the obtained powder (Figure S2b) fully agrees with the previously reported fingerprint of γ - LiV_2O_5 ,^{64,66,67} showing 16 peaks at 99, 122, 171, 204, 254, 271, 311, 327, 374, 459, 532, 550, 643, 733, 964, and 988 cm^{-1} . Because two vanadium environments exist in the layered γ -type structures (see Table S2), the number of expected active modes is twice as large as that in the α -structure.^{64,66} Our previous vibrational dynamic analysis has allowed the assignment of the whole Raman spectrum of γ - LiV_2O_5 , corroborated by the computation of the Raman spectrum.⁶⁶ Then, the bands at 964 and 988 cm^{-1} correspond to the stretching vibrations of the two shortest $\text{V}_a\text{--O}_{1a}$ and $\text{V}_b\text{--O}_{1b}$ bonds (see Table 2); the peaks at 733, 643, and 459 cm^{-1} are due to the stretching vibrations within the $\text{V}_a\text{--O}_{2a}\text{--V}_a$, $\text{V}_b\text{--O}_{2b}\text{--V}_b$, and $\text{V}_a\text{--O}_3\text{--V}_b$ bridges, respectively, while the two components observed at 532 and 550 cm^{-1} are assigned to the vibrations localized in the V–O₂ ladder step bonds. Finally, peaks below 400 cm^{-1} have been described as distortions of the ladders.⁶⁶

SEM micrographs (Figure 2b) clearly show that the coral-like morphology of the α - V_2O_5 precursor is maintained, even after a complete reorganization of the layer shape, as shown by the schematic structure representations in Figure 1. Only smoother crystallite edges can be observed, suggesting limited sintering between particles. The crystallite size and shape were also estimated from the XRD pattern (Figure S1b) with the Scherrer formula. The mean crystallite size of ~ 100 nm is in line with that of the pristine α - V_2O_5 . A slight anisotropy of the crystallites can nevertheless be distinguished, with an average size of ~ 105 nm along the c -axis and ~ 95 nm in the a – b plane, probably because of the low-temperature heat treatment.

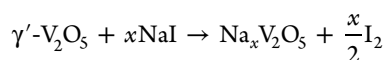
Characterization of γ' - V_2O_5 . The γ - LiV_2O_5 structure allows topotactic lithium removal. Indeed, chemical oxidation of γ - LiV_2O_5 at room temperature using a strong oxidizing

agent leads to the full leaching of Li ions and to the formation of γ' - V_2O_5 .^{43,48} The obtained product after oxidation by NO_2BF_4 is a fine orange powder, which provides evidence that all the vanadium ions are in the V^{5+} oxidation state. The resulting XRD pattern (Figure S1c) and Raman spectrum (Figure S2c) confirm the complete oxidation of γ - LiV_2O_5 into the metastable polymorph γ' - V_2O_5 . Atomic positions, listed in Table S3, lead to the V–O bond lengths reported in Table 2. The cell parameters [$a = 9.9484(2)$ Å, $b = 3.5863(1)$ Å, and $c = 10.0459(3)$ Å (see Table 1)] are consistent with the expected orthorhombic structure of the $Pnma$ space group.^{43,64} This phase is characterized by a c cell parameter (10.05 Å) that is smaller than that of the lithiated phase (10.68 Å). In addition, the Raman spectrum (Figure S2c) fully agrees with the newly reported fingerprint of γ' - V_2O_5 ,⁶⁴ composed of 21 peaks in the 90–1050 cm^{-1} wavenumber range. In the same manner as outlined above, all the vibrations of the chains can be identified: the stretching of the two vanadyl bonds at 1038, 1023, and 1004 cm^{-1} , the bond stretching vibrations localized within the $\text{V}_a\text{--O}_3\text{--V}_b$ bridges at 753 and 604 cm^{-1} , and those of the $\text{V}_a\text{--O}_{2a}\text{--V}_a$ and $\text{V}_b\text{--O}_{2b}\text{--V}_b$ bridges forming the rails of the ladders at 723 and 695 cm^{-1} . Modes involving the V–O₂ ladder step bonds are observed at 534 and 501 cm^{-1} , while lower-frequency modes observed at 93, 126, 138, 153, 172, 190, 239, 267, 282, 299, 349, and 392 cm^{-1} are related to the complex distortions of the ladders.⁶⁴

SEM micrographs show that the coral-like shape of the aggregates is still present but slightly less pronounced, composed of smoothed shorter sticks (Figure 2c). In addition, the mean grain size of 100–200 nm is maintained. The crystallite sizes estimated from diffraction peak widths (Figure S1c) remain almost constant after the oxidation process, with ~ 105 nm along the c -axis and ~ 85 nm in the a – b plane.

Characterization of the Final Sodiated Product. As detailed above, the chemical reduction of solid γ' - V_2O_5 with sodium iodide in acetonitrile at room temperature is expected to produce a Na-intercalated bronze that maintains its γ -structure.

NaI used as a reducing agent reacts with the powder dispersed in acetonitrile (2:1 molar excess) according to the following reaction with $x \sim 1$:



The reaction is rapid and spontaneous, leading to a dark blue powder. Elemental analysis of cationic species (ICP-OES) leads to an x content of 0.96(1) sodium ion for 2 vanadium atoms.

The XRD pattern and Raman spectrum of the obtained product are displayed in Figure 3a and 4, respectively. The Rietveld refinement of the XRD pattern indicates the presence of a pure and well-crystallized single phase, indexed using the same orthorhombic symmetry used for $\gamma\text{'-}$ and $\gamma\text{-LiV}_2\text{O}_5$ (space group $Pnma$). The sodium site occupation refinement

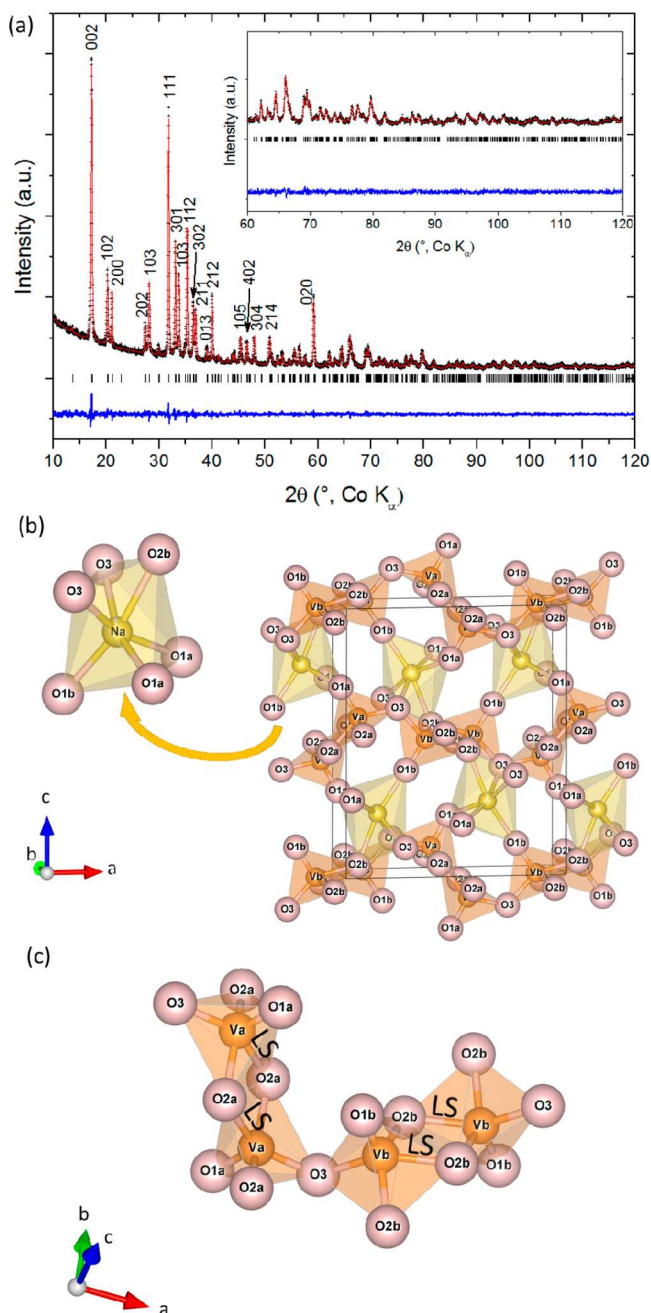


Figure 3. (a) Rietveld refinement of the X-ray diffraction pattern. (b) Crystal structure of $\gamma\text{-Na}_{0.96}\text{V}_2\text{O}_5$ and the Na octahedral site. (c) Local structure showing the two vanadium environments. Ladder step bonds are indicated by a LS label.

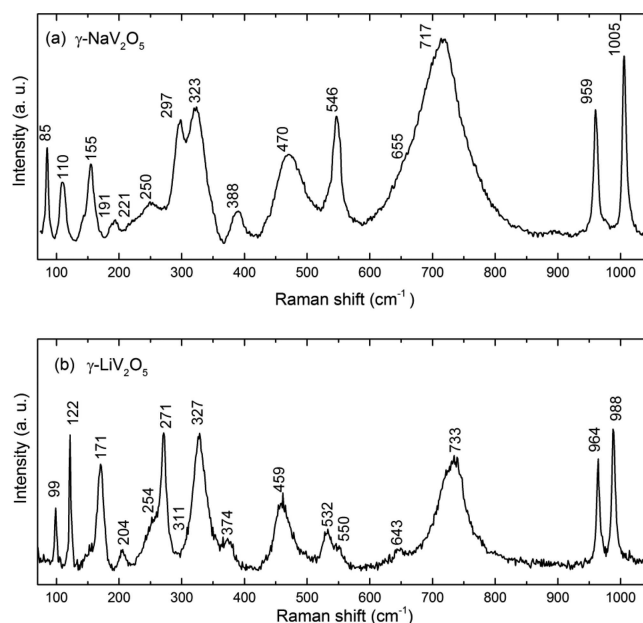


Figure 4. (a) Raman spectrum of $\gamma\text{-Na}_{0.96}\text{V}_2\text{O}_5$. (b) Raman spectrum of $\gamma\text{-LiV}_2\text{O}_5$ for comparison.

of diffraction data is in good agreement with the content of 0.96 sodium ion for 2 vanadium atoms.

Like the $\gamma\text{'-V}_2\text{O}_5$ and $\gamma\text{-LiV}_2\text{O}_5$ lattices, $\gamma\text{-Na}_{0.96}\text{V}_2\text{O}_5$ structure consists of puckered layers stacked perpendicular to the c -axis. A common characteristic of these γ -type structures is that the layers are built of infinite V_2O_5 chains running in the b -direction and interconnected by the ladder step V–O₂ LS contact linkages (Figure 3b,c; ladder step V_b–O_{2b} bonds are indicated by LS labels in Figure 3c).

Atomic positions, listed in Table 3, lead to the V–O and Na–O bond lengths listed in Table 2. The cell parameters [a =

Table 3. Atomic Positions and Thermal Motion Parameters Extracted from the Rietveld Refinement of $\gamma\text{-Na}_{0.96}\text{V}_2\text{O}_5$ (y = 0.25 for all positions)^a

atom type (label)	Wyckof position	x	z	U_{iso} (Å ²)
Na [occupancy of 0.96(1)]	4c	0.1578(5)	0.2302(4)	0.027(3)
V (V _a)	4c	0.0684(3)	0.5881(2)	0.011(1)
V (V _b)	4c	0.3759(2)	0.5011(2)	0.011(1)
O (O _{1a})	4c	0.4900(7)	0.7987(6)	0.029(1)
O (O _{1b})	4c	0.2873(8)	0.3892(7)	0.029(1)
O (O _{2a})	4c	0.4387(6)	0.0387(5)	0.029(1)
O (O _{2b})	4c	0.5685(7)	0.4591(5)	0.029(1)
O (O ₃)	4c	0.2479(9)	0.6193(6)	0.029(1)

^aOrthorhombic space group $Pnma$; a = 9.7806(4) Å, b = 3.6299(1) Å, and c = 11.8872(5) Å; χ^2 = 1.597; wR_p = 5.14%; R_p = 4.00%; R_F^2 = 3.77%; background, Shift Chebyshev 10 parameters.

9.7806(3) Å, b = 3.6299(1) Å, and c = 11.8872(5) Å (see Table 1)] are in fairly good agreement with those reported for the electrochemically formed $\gamma\text{-Na}_{0.97}\text{V}_2\text{O}_5$, the discharge product of a $\gamma\text{'-V}_2\text{O}_5$ electrode in a sodiated electrolyte.^{47,48} However, a thorough comparison reveals some differences in the atomic positions, leading to discrepancies in the bond lengths (Table S4). This is due to the quality of the employed data, i.e., to the fit accuracy. Indeed, the structural data

obtained for the present pure and isotropic γ -Na_{0.96}V₂O₅ powder are more precise than those collected on a highly oriented composite γ -Na_{0.97}V₂O₅ electrode. For the latest data, a preferential orientation correction was applied, implying the refinement of additional parameters.⁴⁷ Furthermore, the angular domain of data collection is extended in this case. As a result, the R_p^2 is greatly improved and reaches 3.77% compared to 9.1% in the case of the electroformed sample.

The comparison of γ' -V₂O₅, γ -LiV₂O₅, and γ -Na_{0.96}V₂O₅ unit cell parameters calls for comment (Table 1). Once the γ -type V₂O₅ layers are formed, the deformation induced by alkaline species intercalation (Li or Na) differs with the nature of the intercalated species. It is noteworthy that accommodation of Na in the interlayer spacing of γ' -V₂O₅ provokes a layer folding that is less important than Li insertion (−1.7% for γ -Na_{0.96}V₂O₅ vs −2.5% for γ -LiV₂O₅) but a larger increase in the c interlayer parameter (+18% for γ -Na_{0.96}V₂O₅ vs +6% for γ -LiV₂O₅).

The valence states of the vanadium ions have been estimated using the BVS approach. BVS values calculated for γ -Na_{0.96}V₂O₅ (Table 2) reach +5.15 and +4.37 for V_a and V_b valences, respectively. This result reveals a localized character comparable to that also observed for the lithiated analogue (+5.15 for V_a and 4.30 for V_b) and suggests that the V_b site is the redox center.

As determined by examination of the V_a–O_{1a} and V_b–O_{1b} bond lengths in the three γ -type structures (Table 2), it appears that they lie in the narrow range of 1.54–1.59 Å. It is noteworthy that the V_a–O_{1a} bond length is shorter in γ -Na_{0.96}V₂O₅ (1.548 Å) than in γ' -V₂O₅ (1.560 Å).

The comparison of the structural data obtained for lithiated and sodiated analogues calls for the following comments. Indeed, the effect of Na/Li intercalation on the (VO₅) polyhedral shape must be considered in light of the (Na/Li)–O interactions. In the interlayer space, Na/Li ions are located in octahedral sites, with two O_{1a} and two O₃ atoms forming the square basis and O_{1b} and O_{2b} in apical positions (Figure 3b). Because of a size effect, (NaO₆) and (LiO₆) sites exhibit quite different shapes (cf. the Na–O and Li–O distances in Table 2). As a consequence, VO₅ polyhedra present different charge distributions on V–O bonds, especially on the apical V–O₁ and bridge V–O₃ bonds. It is noteworthy that when the V_a–O_{1a} bond is shorter, the V_a–O₃ bridge is longer, because of a charge compensation effect. Indeed, in the V_aO₅ polyhedron, the V_a–O_{1a} bond length of the sodiated compound (1.548 Å) is shorter than that of the lithiated analogue (1.595 Å) but the bridging V_a–O₃ bond is longer (1.794 Å vs 1.737 Å). Conversely, in the V_bO₅ polyhedron, the bridging V_b–O₃ bond is shorter (1.882 Å vs 1.961 Å) while the V_b–O_{1b} bond is longer (1.587 Å vs 1.576 Å) than that of the lithiated analogue. These discrepancies do not affect the VO₅ polyhedral volumes that are similar in the Li and Na analogues (see Table 2). Volumes are linked to only the oxidation state of the vanadium ion according to the relationship (V⁵⁺O₅) volume < (V⁴⁺O₅) volume. These observations demonstrate the versatility of the γ -type V₂O₅ layers and their ability to accommodate intercalated species.

The Raman spectrum of γ -Na_{0.96}V₂O₅ is shown in Figure 4a, with that of γ -LiV₂O₅ also reported for comparison (Figure 4b). Figure 4 shows that the general shapes of both spectra are similar, with several band shifts reflecting the influence of the intercalated cation at the scale of the chemical bond. The Raman spectrum of γ -Na_{0.96}V₂O₅ is composed of 15 peaks at

85, 110, 155, 191, 221, 250, 297, 323, 388, 470, 546, 655, 717, 959, and 1005 cm^{−1}. Because of the similarity of the two spectra, one can propose a consistent assignment by relying on our previous vibrational dynamic analysis performed on γ -LiV₂O₅:⁶⁶ the two highest-frequency bands at 1005 and 959 cm^{−1} correspond to the stretching vibrations of the shortest V_a–O_{1a} and V_b–O_{1b} bonds, respectively, the peaks at 717, 655, and 470 cm^{−1} are due to the stretching vibrations within the V_a–O_{2a}–V_a, V_b–O_{2b}–V_b, and V_a–O₃–V_b bridges, respectively, while the intense component at 546 cm^{−1} should come from the vibration of the V–O₂ LS bonds. Finally, peaks below 400 cm^{−1} are assigned to the distortions of the ladders.

It is noteworthy the Raman fingerprints of the lithiated and sodiated analogues reveal some spectral changes that are in line with the bond length variations highlighted above. First, the ν (V_a–O_{1a}) stretching mode is observed at 988 cm^{−1} in γ -LiV₂O₅ versus 1005 cm^{−1} in γ -Na_{0.96}V₂O₅. This blue shift clearly indicates a strengthening of the V_a–O_{1a} bond in γ -Na_{0.96}V₂O₅, in line with a shortest bond length of 1.548 Å in γ -Na_{0.96}V₂O₅ versus 1.595 Å in γ -LiV₂O₅. Conversely, the ν (V_b–O_{1b}) component is observed at a lower wavenumber (959 cm^{−1} in γ -Na_{0.96}V₂O₅ vs 964 cm^{−1} in γ -LiV₂O₅), which is in agreement with the lengthening of the V_b–O_{1b} bond (1.587 in γ -Na_{0.96}V₂O₅ vs 1.576 Å in γ -LiV₂O₅). Another relevant spectral indicator of bond length variation between the lithiated and sodiated analogues is the pure ν (V_b–O₃) vibration, identified at 459 cm^{−1} in γ -LiV₂O₅.⁶⁶ A blue shift to 470 cm^{−1} is observed for γ -Na_{0.96}V₂O₅, in line with the shortest V_b–O₃ bond (1.882 in γ -Na_{0.96}V₂O₅ vs 1.961 Å in γ -LiV₂O₅).

As shown on the SEM micrographs (Figure 2d), the morphology is practically not modified by this additional chemical treatment. Indeed, the shape of the γ -Na_{0.96}V₂O₅ aggregates is similar to that found for the sodium-free γ' -V₂O₅ sample. Their size of a few micrometers is maintained as well as their porous character and the mean grain size of 100–200 nm. The surface of these aggregates seems to be affected little, even if the sodium intercalation in the interlayer spacing induces an 18% dilation along the c -axis. On the basis of a Scherrer analysis of the XRD pattern (Figure 3), the average crystallite sizes were evaluated to ~140 nm along the c -axis and ~85 nm in the a – b plane. The large expansion along the c -axis compared to sodium-free γ' -V₂O₅ is simply attributed to sodium intercalation because no granular growth is expected at room temperature. Then, using mainly redox reactions at room temperature combined with a moderate heat treatment, this multiple-step synthesis process keeps the initial interesting porous morphology of the α -V₂O₅ precursor (see Figure 2a–d).

Electrochemical Properties of Chemically Formed γ -Na_{0.96}V₂O₅. The electrochemical performance of γ -Na_{0.96}V₂O₅ has been investigated at a C/5 rate (i.e., one Na⁺ exchanged per formula unit in 5 h). Typical galvanostatic charge–discharge curves recorded in the potential window ranging from 1.75 to 4 V are presented in Figure 5. The sodium extraction process takes place at a high potential of 3.45 V along two voltage plateaus differing by a very small voltage. The subsequent Na insertion then proceeds at a slightly lower voltage of 3.35 V. In fact, low-scan rate cyclic voltammetry experiments performed at 10 μ V s^{−1} (not shown here) allow the discrimination of two steps separated by only 50 mV, both in oxidation and in reduction. Furthermore, it is remarkable that the Na extraction–insertion process occurs at the same

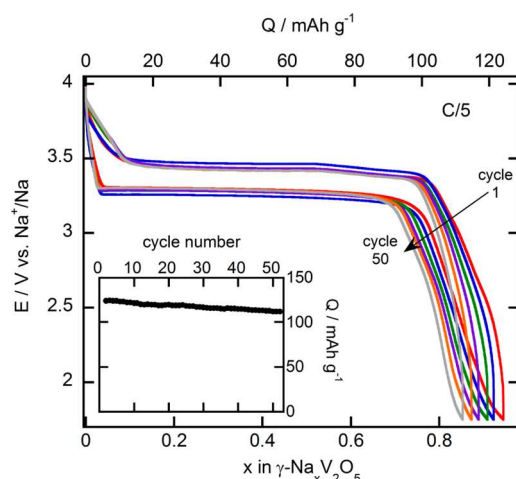


Figure 5. Charge–discharge cycles at a C/5 rate of γ - $\text{Na}_{0.96}\text{V}_2\text{O}_5$. Voltage window of 1.75–4 V vs Na^+/Na . Electrolyte of NaClO_4 1M/PC. The inset shows the evolution of the specific capacity vs cycles at a C/5 rate.

energy level as Li insertion in the γ' - $\text{V}_2\text{O}_5/\gamma$ - LiV_2O_5 system.^{38–41}

A specific capacity of 125 mAh g^{-1} (capacities expressed in milliamper hours per gram of γ - $\text{Na}_{0.96}\text{V}_2\text{O}_5$ in the composite electrode) is reached. It corresponds to the extraction of 0.95 Na^+ from the sodiated bronze whose formula has been determined by ICP-OES to be γ - $\text{Na}_{0.96}\text{V}_2\text{O}_5$, stating that a quantitative extraction takes place. The consecutive reduction engages the same specific capacity, highlighting an excellent electrochemical reversibility. This constitutes a great improvement if compared to the pioneering work on electrochemical sodium insertion in γ' - V_2O_5 ,⁴⁸ which reported a cycling efficiency limited to 46% at C/5 during the first cycle performed in the same potential range (Figure S4).

It is noteworthy that the shape of the galvanostatic curves is maintained over a few dozen cycles at C/5 (Figure 5). The hysteresis continuously decreases with cycles (from 220 to 125 mV), and a very small decrease in capacity is observed with a specific capacity of 112 mAh g^{-1} still available after 50 cycles (inset of Figure 5). These results confirm the present sodium vanadium bronze can accommodate consecutive sodium insertion–deinsertion reactions without a decrease in performance upon cycling. They significantly outperform the cycling properties achieved with the high-temperature γ' - V_2O_5 oxide.

We have also examined the structural reversibility of the material upon cycling. The X-ray diffraction pattern and the Raman spectrum of the charged electrode in the 1.75–4 V potential window at C/5 are shown in Figures 6b and 7b, respectively. They correspond to the typical XRD and Raman fingerprint of γ' - V_2O_5 described above (Figures S1c and S2c, respectively). The shift of the 002 line toward a larger 2θ angle is indicative of a smaller c parameter in γ' - V_2O_5 . Lattice parameters found for the charged material [$a = 9.946(1)$ Å, $b = 3.587(1)$ Å, and $c = 10.057(1)$ Å] are in good agreement with those cited above for the γ' - V_2O_5 phase (Table 1). Such findings demonstrate the complete electrochemical extraction of Na from the sodiated bronze lattice, leading to the Na-free γ' -polymorph.

After the consecutive reduction to 1.75 V, the XRD pattern and the Raman spectrum (Figures 6c and 7c, respectively) both indicate that the pristine sodiated phase is restored after

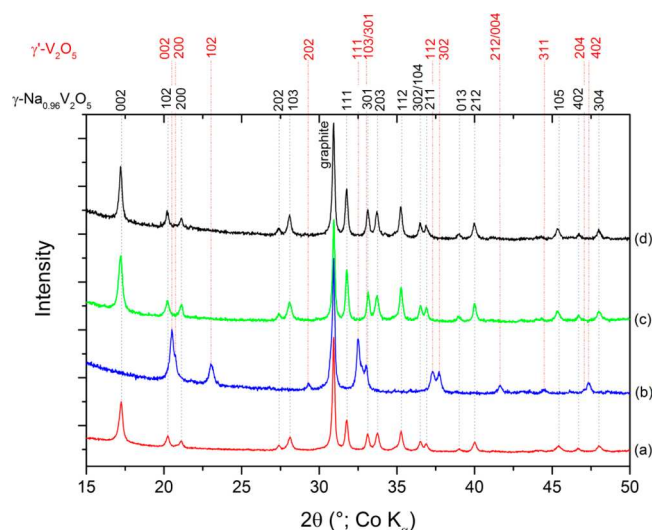


Figure 6. X-ray diffraction patterns of (a) the initial electrode, (b) after the first charge, (c) after one charge–discharge cycle, and (d) after 50 cycles.

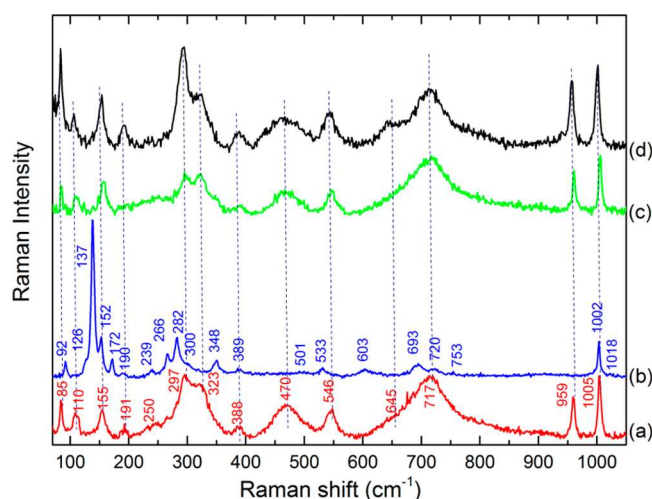


Figure 7. Raman spectra of (a) the initial electrode, (b) after the first charge, (c) after one charge–discharge cycle, and (d) after 50 cycles.

one cycle without a noticeable change in the lattice parameters [$a = 9.758(1)$ Å, $b = 3.627(1)$ Å, and $c = 11.954(1)$ Å]. These results prove the highly reversible character of the structural change, both in the long-range order and on an atomic scale.

An important issue to be addressed is the stability of the host lattice upon cycling. The XRD pattern and Raman spectrum obtained after 50 cycles at C/5 (Figures 6d and 7d, respectively) completely superimpose with those of the initial material (Figures 6a and 7a, respectively). This finding points to a high structural stability, which explains the good capacity retention described above for the present γ - $\text{Na}_{0.96}\text{V}_2\text{O}_5$ material.

The influence of the current density is illustrated in Figure 8. The recovered capacities at different increasing C rates (from C/5 to 2C) are reported as a function of cycle number. Whatever the C rate, the capacity is quite stable, ~ 120 mAh g^{-1} at C/5 and still 85 mAh g^{-1} at 2C. The specific capacity at C/5 can be fully recovered even after the application of higher current densities, which indicates that the γ - $\text{Na}_{0.96}\text{V}_2\text{O}_5$ structure is not damaged by the use of a 2C rate.

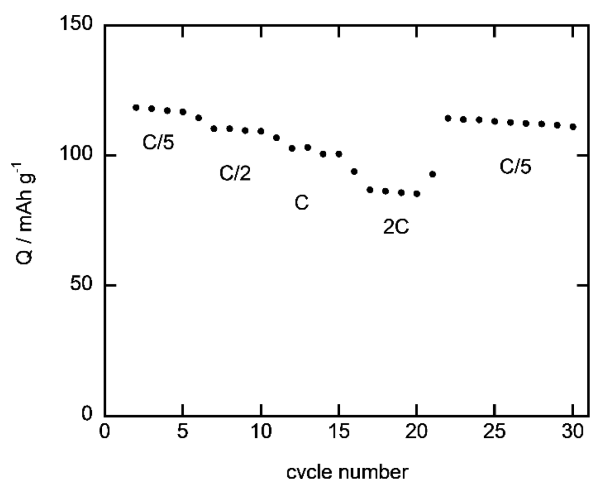


Figure 8. Rate capability performance of γ -Na_{0.96}V₂O₅. Voltage window of 1.75–4 V vs Na⁺/Na. Electrolyte of NaClO₄ 1M/PC.

This finding allows a considerable enhancement of the charge efficiency when starting from the chemically prepared γ -Na_{0.96}V₂O₅. In addition, this improvement is maintained upon cycling. These promoted performances compared to those of the γ' -V₂O₅ prepared via the high-temperature carboreduction route can be understood in terms of grain size and morphology. Indeed, using our soft chemistry synthesis process, porous coral-like aggregates made of small isotropic particles of 100–200 nm are obtained, as shown on SEM micrographs (Figure 2d). This is also consolidated by the Rietveld refinement performed on the XRD data (Figure 3a) because it was not necessary to introduce a preferential orientation correction function. Because of the specific atomic positions in the γ -Na_{0.96}V₂O₅ structure, the low I_{002}/I_{200} intensity ratio found (~ 5) reveals a lack of a preferred orientation. As a consequence, the high porosity of aggregates combined with isotropic nanometric particles allows all γ -Na_{0.96}V₂O₅ particles to homogeneously work, leading to an efficient extraction–insertion process.

Conversely, γ -Na_{0.97}V₂O₅ electrochemically formed from γ' -V₂O₅, itself synthesized through the high-temperature carboreduction route, is mainly composed of large and dense stacks of platelets several micrometers in length and a few hundred nanometers in thickness (in the c -axis direction). Such a morphology corresponds to a strong preferential orientation reflected by a significant enhancement of the 00 l reflections, with an I_{002}/I_{200} ratio reaching ~ 90 .^{47,48} This peculiar particle shape due to crystal growth in the a – b plane is detrimental to the electrochemical performance as it is responsible for a small electrochemical surface area and a lengthening of the sodium diffusion pathways. This point is exemplified well by the comparative discharge–charge curves of both sodium vanadium bronzes at C/5, with a 100% cycle efficiency for the γ -Na_{0.96}V₂O₅ prepared by the soft chemistry route versus a value of only 45% for the electrochemically formed compound⁴⁸ (Figure S4). Therefore, the present sodium vanadium bronze benefits from a larger electrochemical surface area and shorter diffusion pathways, promoting a more homogeneous and faster sodiation–desodiation process. This explains the good rate capability behavior (Figure 8) and the better charge efficiency systematically found for the present chemically synthesized γ -Na_{0.96}V₂O₅ bronze.

Expected Diffusion Pathways in γ -Na_{0.96}V₂O₅. On the basis of the crystallographic structure determined above, sodium diffusion pathways can be proposed for γ -Na_{0.96}V₂O₅ using the BVEL.^{54,55} Sodium ions are found to diffuse easily in the a – b plane within the interlayer space of γ -Na_{0.96}V₂O₅, with an activation energy evaluated to be 1.1 eV above the minimum energy. Indeed, a higher energy barrier of ~ 5 eV, calculated for diffusion of Na along the c -axis, hinders ionic movement in this direction. The isosurface at 1.2 eV above the minimum energy (Figure 9) illustrates the sodium diffusion

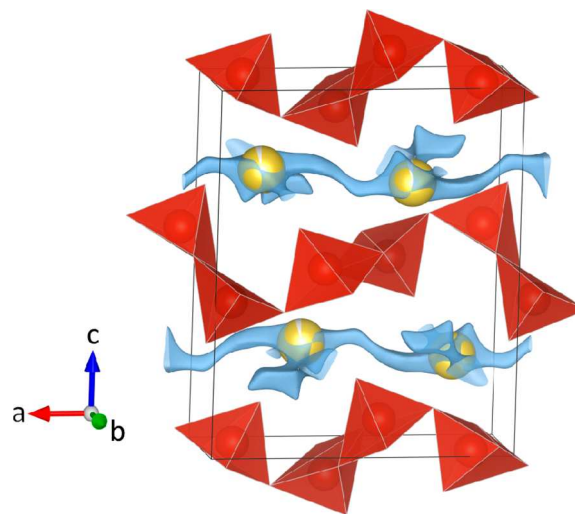


Figure 9. BVEL map with the isosurface plotted 1.2 eV above the maximum energy. Red polyhedra represent the VO₅ building blocks, and yellow spheres represent the sodium atoms in their crystallographic sites. The blue isosurface clearly shows possible diffusion paths along the a - and b -axes within the interlayer space.

pathway that clearly takes place in the interlayer spacing. This low-energy barrier is in line with values determined with the BVEL method for other attractive Na cathode materials like NaFePO₄ (1.25 eV), P2-NaCoO₂ (0.72 eV), or Na₃V₂(PO₄)₃ (1.25 eV).⁶⁸ These BVEL results account for the good rate capability of γ -Na_{0.96}V₂O₅ (Figure 8).

CONCLUSION

We have demonstrated that γ -Na_{0.96}V₂O₅ can be synthesized by chemical sodiation at room temperature of the γ' -V₂O₅ polymorph using a facile and low-cost soft chemistry route. To the best of our knowledge, this is the first example of sodiated material based on vanadium oxide that can be directly used as a high-voltage positive electrode for sodium-ion batteries, i.e., at 3.4 V versus Na⁺/Na. A thorough structural determination making use of X-ray diffraction and Raman spectroscopy reveals a corrugated orthorhombic layered structure, isomorphous to the lithiated analogue γ -LiV₂O₅. Because of the close resemblance between the two Raman spectra, a reliable assignment of the observed Raman peaks to the vibrations of specific structural units in the γ -Na_{0.96}V₂O₅ lattice is proposed. The electrochemical experiments clearly show a quantitative one-step sodium extraction–insertion process at a high potential of 3.4 V versus Na⁺/Na, i.e., at the same voltage as Li insertion in the γ' -V₂O₅/ γ -LiV₂O₅ system. A high reversible capacity of 125 mAh g^{−1} is available, and still 112 mAh g^{−1} is recovered after 50 cycles at C/5. The full reversibility of structural changes is demonstrated at the long-range and

atomic scale, which explains the good cycle life behavior. We demonstrate that the chosen synthesis pathway, leading to porous coral-like aggregates made of small γ - $\text{Na}_{0.96}\text{V}_2\text{O}_5$ particles, allows a remarkable improvement in the electrochemical efficiency in comparison with that of the high-temperature solid-state synthesized γ' - V_2O_5 material.

BVEL analysis reveals a low energy barrier of 1.1 eV, suggesting an easy Na diffusion in the a - b plane. Such a calculation accounts for the interesting rate capability reported here and provides evidence that these promising electrochemical features are favored by the corrugated lamellar structure of this cathode material for Na-ion batteries.

These findings open the way for the use of new high-performance V_2O_5 -based compounds as positive electrode materials for SIBs. The γ - $\text{Na}_{0.96}\text{V}_2\text{O}_5$ bronze reported here can be considered as one of the best cathode materials among the vanadate-based compounds. This material also competes with the well-known $\text{NaNi}_{1/3}\text{Mn}_{1/3}\text{Co}_{1/3}\text{O}_2$ and NaFePO_4 .

■ ASSOCIATED CONTENT

■ Supporting Information

The Supporting Information is available free of charge on the ACS Publications website at DOI: [10.1021/acs.chemmater.8b02066](https://doi.org/10.1021/acs.chemmater.8b02066).

Rietveld refinements of α - V_2O_5 , γ - LiV_2O_5 , and γ' - V_2O_5 X-ray diffraction patterns; Raman spectra of α - V_2O_5 , γ - LiV_2O_5 , and γ' - V_2O_5 ; representation of an isolated chain of the α - V_2O_5 structure; comparison of the first galvanostatic cycle of γ - $\text{Na}_{0.96}\text{V}_2\text{O}_5$ and γ' - V_2O_5 electrodes at a C/5 rate; atomic positions and thermal motion parameters extracted from the Rietveld refinement of α - V_2O_5 , γ - LiV_2O_5 , and γ' - V_2O_5 ; γ - $\text{Na}_{0.96}\text{V}_2\text{O}_5$ structural parameters compared to those previously reported for the γ - $\text{Na}_{0.97}\text{V}_2\text{O}_5$ electrochemically formed (PDF)

■ AUTHOR INFORMATION

Corresponding Author

*E-mail: emery@icmpe.cnrs.fr.

ORCID

Nicolas Emery: 0000-0003-2724-8789

Barbara Laïk: 0000-0001-5194-4210

Notes

The authors declare no competing financial interest.

■ REFERENCES

- (1) Diouf, B.; Pode, R. Potential of Lithium-ion batteries in renewable energy. *Renewable Energy* **2015**, *76*, 375–380.
- (2) Palizban, O.; Kauhaniemi, K. Energy storage systems in modern grids – matrix of technologies and applications. *J. Energy storage* **2016**, *6*, 248–259.
- (3) Hammond, G. P.; Hazeldine, T. Indicative energy technology assessment of advanced rechargeable batteries. *Appl. Energy* **2015**, *138*, 559–571.
- (4) Vetter, M.; Rohr, L. Lithium-ion batteries for storage of renewable energies and electric grid backup, book chapter in Lithium-ion Batteries. *Advances and Applications* **2014**, 293–309.
- (5) Yang, Z.; Zhang, J.; Kintner-Meyer, M. C. W.; Lu, X.; Choi, D.; Lemmon, J. P.; Liu, J. Electrochemical Energy storage for green grid. *Chem. Rev.* **2011**, *111*, 3577–3613.
- (6) Larcher, D.; Tarascon, J. M. Towards greener and more sustainable batteries for electrical energy storage. *Nat. Chem.* **2015**, *7*, 19–29.

(7) Tarascon, J. M. Is lithium the new gold? *Nat. Chem.* **2010**, *2*, 510–510.

(8) Grosjean, C.; Miranda, P. H.; Perrin, M.; Poggi, P. Assessment of world lithium resources and consequences of their geographic distribution on the expected development of the electric vehicle industry. *Renewable Sustainable Energy Rev.* **2012**, *16*, 1735–1744.

(9) The trouble with lithium 2, under the microscope. Meridian International Research: Martainville, France, 2008.

(10) Palomares, V.; Serras, P.; Villaluenga, I.; Hueso, K. B.; Carretero-Gonzalez, J.; Rojo, T. Na-ion batteries, recent advances and present challenges to become low cost energy storage systems. *Energy Environ. Sci.* **2012**, *5*, 5884–5901.

(11) Yabuuchi, N.; Kubota, K.; Dahbi, M.; Komaba, S. Research developments on sodium-ion batteries. *Chem. Rev.* **2014**, *114*, 11636–11682.

(12) Kim, S.-W.; Seo, D.-H.; Ma, X.; Ceder, G.; Kang, K. Electrode materials for rechargeable sodium-ion batteries: potential alternatives to current lithium-ion batteries. *Adv. Energy Mater.* **2012**, *2*, 710–721.

(13) Kubota, K.; Komaba, S. Practical issues and future perspective for Na-ion batteries. *J. Electrochem. Soc.* **2015**, *162*, A2538–A2550.

(14) Kundu, D.; Talaie, E.; Duffort, V.; Nazar, L. F. The emerging chemistry of sodium-ion batteries for electrochemical energy storage. *Angew. Chem., Int. Ed.* **2015**, *54*, 3431–3448.

(15) Palomares, V.; Casas-Cabanas, M.; Castillo-Martinez, E.; Han, M. H.; Rojo, T. Update on Na-based battery materials. A growing research path. *Energy Environ. Sci.* **2013**, *6*, 2312–2337.

(16) Slater, M. D.; Kim, D.; Lee, E.; Johnson, C. S. Sodium-ion batteries. *Adv. Funct. Mater.* **2013**, *23*, 947–958.

(17) Ellis, B. L.; Nazar, L. F. Sodium and sodium-ion energy storage batteries. *Curr. Opin. Solid State Mater. Sci.* **2012**, *16*, 168–177.

(18) Pan, H.; Hu, Y.-S.; Chen, L. Room-temperature stationary sodium-ion batteries for large-scale electric energy storage. *Energy Environ. Sci.* **2013**, *6*, 2338–2360.

(19) Nayak, K.; Yang, L.; Brehm, W.; Adelhelm, P. From lithium-ion to sodium-ion batteries: advantages, challenges and surprises. *Angew. Chem., Int. Ed.* **2018**, *57*, 102–120.

(20) Hwang, J. Y.; Myung, S. T.; Sun, Y. K. Sodium-ion batteries: present and future. *Chem. Soc. Rev.* **2017**, *46*, 3529–3614.

(21) Kim, H.; Kim, H.; Ding, Z.; Lee, M. H.; Lim, K.; Yoon, G.; Kang, K. Recent progress in electrode materials for sodium-ion batteries. *Adv. Energy Mater.* **2016**, *6*, 1600943.

(22) Dai, Z.; Mani, U.; Tan, H. T.; Yan, Q. Advanced cathode materials for sodium-ion batteries: what determines our choice. *Small Methods* **2017**, *1*, 1700098.

(23) Xiang, X.; Zhang, K.; Chen, J. Recent advances and prospects of cathode materials for sodium-ion batteries. *Adv. Mater.* **2015**, *27*, 5343–5364.

(24) Fang, C.; Huang, Y.; Zhang, W.; Han, J.; Deng, Z.; Cao, Y.; Yang, H. Routes to high energy cathodes of sodium-ion batteries. *Adv. Energy Mater.* **2016**, *6*, 1501727.

(25) You, Y.; Manthiram, A. Progress in high voltage cathode materials for rechargeable sodium-ion batteries. *Adv. Energy Mater.* **2018**, *8*, 1701785.

(26) Berthelot, R.; Carlier, D.; Delmas, C. Electrochemical Investigation of the $\text{P2-Na}_x\text{CoO}_2$ Phase Diagram. *Nat. Mater.* **2011**, *10*, 74–80.

(27) Yabuuchi, N.; Kajiyama, M.; Iwatate, J.; Nishikawa, H.; Hitomi, S.; Okuyama, R.; Usui, R.; Yamada, Y.; Komaba, S. P2-type $\text{Na}_x[\text{Fe}_{1/2}\text{Mn}_{1/2}]\text{O}_2$ made from earth-abundant elements for rechargeable Na batteries. *Nat. Mater.* **2012**, *11*, 512–517.

(28) Ma, X.; Chen, H.; Ceder, G. Electrochemical properties of monoclinic NaMnO_2 . *J. Electrochem. Soc.* **2011**, *158*, A1307–A1312.

(29) Komaba, S.; Takei, C.; Nakayama, T.; Ogata, A.; Yabuuchi, N. Electrochemical intercalation activity of layered NaCrO_2 vs. LiCrO_2 . *Electrochem. Commun.* **2010**, *12*, 355–358.

(30) Sabi, N.; Doubaji, S.; Hashimoto, K.; Komaba, S.; Amine, K.; Solhy, A.; Manoun, B.; Bilal, E.; Saadoun, I. Layered $\text{P2-Na}_{2/3}\text{Co}_{1/2}\text{Ti}_{1/2}\text{O}_2$ as a high-performance cathode material for sodium-ion batteries. *J. Power Sources* **2017**, *342*, 998–1005.

- (31) Kumakura, S.; Tahara, Y.; Sato, S.; Kubota, K.; Komaba, S. P'2-Na_{2/3}Mn_{0.9}Me_{0.1}O₂ (Me = Mg, Ti, Co, Ni, Cu and Zn): Correlation between orthorhombic distortion and electrochemical property. *Chem. Mater.* **2017**, *29*, 8958–8962.
- (32) Galy, J. Vanadium pentoxide and vanadium oxide bronzes-Structural chemistry of single (S) and double (D) layer M_xV₂O₅ phases. *J. Solid State Chem.* **1992**, *100*, 229–245.
- (33) Raistrick, I. D.; Huggins, R. A. Electrochemical studies of lithium insertion reactions of vanadium oxide bronzes. *J. Electrochem. Soc.* **1983**, *130*, C303–C308.
- (34) Raistrick, I. D. Lithium insertions reactions in tungsten and vanadium oxide bronzes. *Solid State Ionics* **1983**, *9-10*, 425–430.
- (35) Galy, J.; Darriet, J.; Hagenmuller, P. Li_xV₂O₅ Bronzes- Structure of Beta'-Phase and Refinement of Gamma-Phase Structure. *Rev. Chim. Miner.* **1971**, *8*, 509–522.
- (36) Murphy, D. W.; Christian, P. A.; Disalvo, F. J.; Waszczak, J. V. Lithium incorporation by vanadium pentoxide. *Inorg. Chem.* **1979**, *18*, 2800–2803.
- (37) Anderson, D. N.; Willett, R. D. Refinement of Structure of LiV₂O₅. *Acta Crystallogr., Sect. B: Struct. Crystallogr. Cryst. Chem.* **1971**, *27*, 1476–1477.
- (38) Cocciantelli, J. M.; Ménétrier, M.; Delmas, C.; Doumerc, J. P.; Pouchard, M.; Hagenmuller, P. Electrochemical and Structural Characterization of Lithium Intercalation and Deintercalation in the γ-LiV₂O₅ Bronze. *Solid State Ionics* **1992**, *50*, 99–105.
- (39) Dai, J. X.; Li, S. F. Y.; Gao, Z. Q.; Siow, K. S. Siow, Novel Method for Synthesis of γ-lithium vanadium oxide as cathode materials in lithium ion batteries. *Chem. Mater.* **1999**, *11*, 3086–3090.
- (40) Barker, J.; Saidi, M. Y.; Swoyer, J. L. Performance evaluation of the electroactive material γ LiV₂O₅ made by a carbothermal reduction method. *J. Electrochem. Soc.* **2003**, *150*, A1267–A1272.
- (41) Wang, W.; Wang, H.; Liu, S.; Huang, J. Synthesis of γ-LiV₂O₅ nanorods as a high-performance cathode for Li ion battery. *J. Solid State Electrochem.* **2012**, *16*, 2555–2561.
- (42) Cocciantelli, J. M.; Doumerc, J. P.; Pouchard, M.; Broussely, M.; Labat, J. Crystal chemistry of electrochemically inserted Li_xV₂O₅. *J. Power Sources* **1991**, *34*, 103–111.
- (43) Cocciantelli, J. M.; Gravereau, P.; Doumerc, J. P.; Pouchard, M.; Hagenmuller, P. On the preparation and characterization of a new polymorph of V₂O₅. *J. Solid State Chem.* **1991**, *93*, 497–502.
- (44) Pouchard, M.; Casalot, A.; Galy, J.; Hagenmuller, P. Vanadium bronzes with Na_xV₂O₅ formula. *Bull. Soc. Chim. Fr.* **1967**, *11*, 4343–4348.
- (45) Carpy, A.; Galy, J. Refining crystal-structure of alpha-vanadium sodium oxybronze NaV₂O₅ alpha. *Acta Crystallogr., Sect. B: Struct. Crystallogr. Cryst. Chem.* **1975**, *31*, 1481–1482.
- (46) Muller-Bouvet, D.; Baddour-Hadjean, R.; Tanabe, M.; Huynh, L. T. N.; Le, L. M. P.; Pereira-Ramos, J. P. Electrochemically formed α'-NaV₂O₅: a new sodium intercalation compound. *Electrochim. Acta* **2015**, *176*, 586–593.
- (47) Safrany Renard, M.; Emery, N.; Roginskii, E.; Baddour-Hadjean, R.; Pereira-Ramos, J.-P. Crystal structure determination of a new sodium vanadium bronze electrochemically formed. *J. Solid State Chem.* **2017**, *254*, 62–68.
- (48) Safrany Renard, M.; Emery, N.; Baddour-Hadjean, R.; Pereira-Ramos, J.-P. γ'-V₂O₅: A new high voltage cathode material for sodium-ion battery. *Electrochim. Acta* **2017**, *252*, 4–11.
- (49) Mjejri, I.; Rougier, A.; Gaudon, M. Low-cost and facile synthesis of the vanadium oxides V₂O₃, VO₂ and V₂O₅ and their magnetic, thermochromic and electrochromic properties. *Inorg. Chem.* **2017**, *56*, 1734–1741.
- (50) Larson, A. C.; Von Dreele, R. B. General Structure Analysis System (GSAS). Technical Report LAUR86-748; Los Alamos National Laboratory: Los Alamos, NM, 2004.
- (51) Toby, B. H. XPGUI, a graphical user interface for GSAS. *J. Appl. Crystallogr.* **2001**, *34*, 210–221.
- (52) Rodriguez-Carvajal, J. Recent advances in magnetic structure determination by neutron powder diffraction. *Phys. B* **1993**, *192*, 55–69.
- (53) Rodriguez-Carvajal, J. *FullProf suite*; <https://www.ill.eu/sites/fullprof/>.
- (54) Adams, S. From bond valence maps to energy landscapes for mobile ions in ion-conducting solids. *Solid State Ionics* **2006**, *177*, 1625–1630.
- (55) Brown, I. A. Recent developments in the methods and applications of the bond valence model. *Chem. Rev.* **2009**, *109*, 6858–6919.
- (56) Adams, S.; Prasada Rao, R. Understanding ionic conduction and energy storage materials with Bond-Valence-Based methods. *Struct. Bonding (Berlin, Ger.)* **2014**, *158*, 129–159.
- (57) Nikitina, V. A.; Fedotov, S. S.; Vassiliev, S. Yu.; Samarin, A. Sh.; Khasanova, N. R.; Antipov, E. V. Transport and kinetic aspects of alkali metal ions intercalation into AVPO₄F framework. *J. Electrochem. Soc.* **2017**, *164*, A6373–A6380.
- (58) Wong, L. L.; Chen, H. M.; Adams, S. Sodium-ion diffusion mechanisms in the low cost high voltage cathode material Na_{2+δ}Fe_{2-δ/2}(SO₄)₃. *Phys. Chem. Chem. Phys.* **2015**, *17*, 9186–9193.
- (59) Strauss, F.; Rousse, G.; Sougrati, M. T.; Alves Dalla Corte, D.; Courty, M.; Dominko, R.; Tarascon, J.-M. Synthesis, structure, and electrochemical Properties of Na₃MB₂O₁₀ (M = Fe, Co) containing M²⁺ in Tetrahedral Coordination. *Inorg. Chem.* **2016**, *55*, 12775–12782.
- (60) Enjalbert, R.; Galy, J. A refinement of the structure of V₂O₅. *Acta Crystallogr., Sect. C: Cryst. Struct. Commun.* **1986**, *42*, 1467–1469.
- (61) Bachmann, H. G.; Ahmed, F. R.; Barnes, W. H. The crystal structure of vanadium pentoxide. *Z. Kristallogr.* **1961**, *115*, 110–131.
- (62) Baddour-Hadjean, R.; Raekelboom, E.; Pereira-Ramos, J. P. New structural characterization of the Li_xV₂O₅ system provided by Raman spectroscopy. *Chem. Mater.* **2006**, *18*, 3548–3556.
- (63) Abello, L.; Husson, E.; Repelin, Y.; Lucazeau, G. Vibrational spectra and valence force field of crystalline V₂O₅. *Spectrochim. Acta Part A* **1983**, *39*, 641–651.
- (64) Baddour-Hadjean, R.; Smirnov, M. B.; Kazimirov, V. Y.; Smirnov, K. S.; Pereira-Ramos, J. P. The Raman spectrum of the γ'-V₂O₅ polymorph: A combined experimental and DFT study. *J. Raman Spectrosc.* **2015**, *46*, 406–412.
- (65) Satto, C.; Sciau, P.; Dooryhee, E.; Galy, J.; Millet, P. The δ-ε-γ LiV₂O₅ “High Temperature” phase transitions evidenced by Synchrotron X-ray powder diffraction analysis. *J. Solid State Chem.* **1999**, *146*, 103–109.
- (66) Smirnov, M.; Roginskii, E.; Kazimirov, V.; Smirnov, K.; Baddour-Hadjean, R.; Pereira-Ramos, J. P.; Zhandun, V. Spectroscopic and computational study of structural changes in γ-LiV₂O₅ cathodic material induced by lithium Intercalation. *J. Phys. Chem. C* **2015**, *119*, 20801–20809.
- (67) Popovic, Z.; Gajic, R.; Konstantinovic, M. J.; Provoost, R.; Moshchalkov, V. V.; Vasil'ev, A. N.; Isobe, M.; Ueda, Y. Infrared and Raman spectra of LiV₂O₅ single crystals. *Phys. Rev. B: Condens. Matter Phys.* **2000**, *61*, 11454–11459.
- (68) Fedotov, S. S.; Kabanova, N. A.; Kabanov, A. A.; Blatov, V. A.; Khasanova, N. R.; Antipov, E. V. Crystallochemical tools on the search for cathode materials of rechargeable Na-ion batteries and analysis of their transport properties. *Solid State Ionics* **2018**, *314*, 129–140.

Supporting Information

Title: γ -Na_{0.96}V₂O₅: a new competitive cathode material for sodium ion battery synthesized by a soft chemistry route

Nicolas Emery^{1,}, Rita Baddour-Hadjean¹, Dauren Batyrbekuly^{1,2}, Barbara Laik¹, Zhumabay Bakenov², Jean-Pierre Pereira-Ramos¹*

¹ Institut de Chimie et des Matériaux Paris Est, ICMPE/GESMAT, UMR 7182 CNRS-
Université Paris Est Créteil, CNRS 2 rue Henri Dunant, 94320 Thiais, France

² Institute of Batteries LLC, Nazarbayev University, 53 Kabanbay Batyr Avenue, Astana
010000, Kazakhstan

Table of content:

Figure S1. Rietveld refinements of α -V₂O₅ (a), γ -LiV₂O₅ (b) and γ' -V₂O₅ (c) X-Ray diffraction patterns.

Figure S2. Raman spectra of α -V₂O₅ (a), γ -LiV₂O₅ (b) and γ' -V₂O₅ (c).

Figure S3. Representation of an isolated chain of the α -V₂O₅ structure. White and grey circles represent the oxygen and vanadium atoms, respectively. Interchain contacts (ladder steps) are shown by dashed lines.

Figure S4. Comparison of the first galvanostatic cycle of γ -Na_{0.96}V₂O₅ and γ' -V₂O₅ electrodes. C/5 rate. Electrolyte NaClO₄ 1M/PC.

Table S1. Atomic positions and thermal motion parameters extracted from the Rietveld refinement of α -V₂O₅ (y = 0.25 for all positions).

Table S2. Atomic positions and thermal motion parameters extracted from the Rietveld refinement of γ -LiV₂O₅ (y = 0.25 for all positions).

Table S3. Atomic positions and thermal motion parameters extracted from the Rietveld refinement of γ' -V₂O₅ (y = 0.25 for all positions).

Table S4. Structural parameters for γ -Na_{0.96}V₂O₅ compared to those previously reported for the γ -Na_{0.97}V₂O₅ electroformed phase [47].

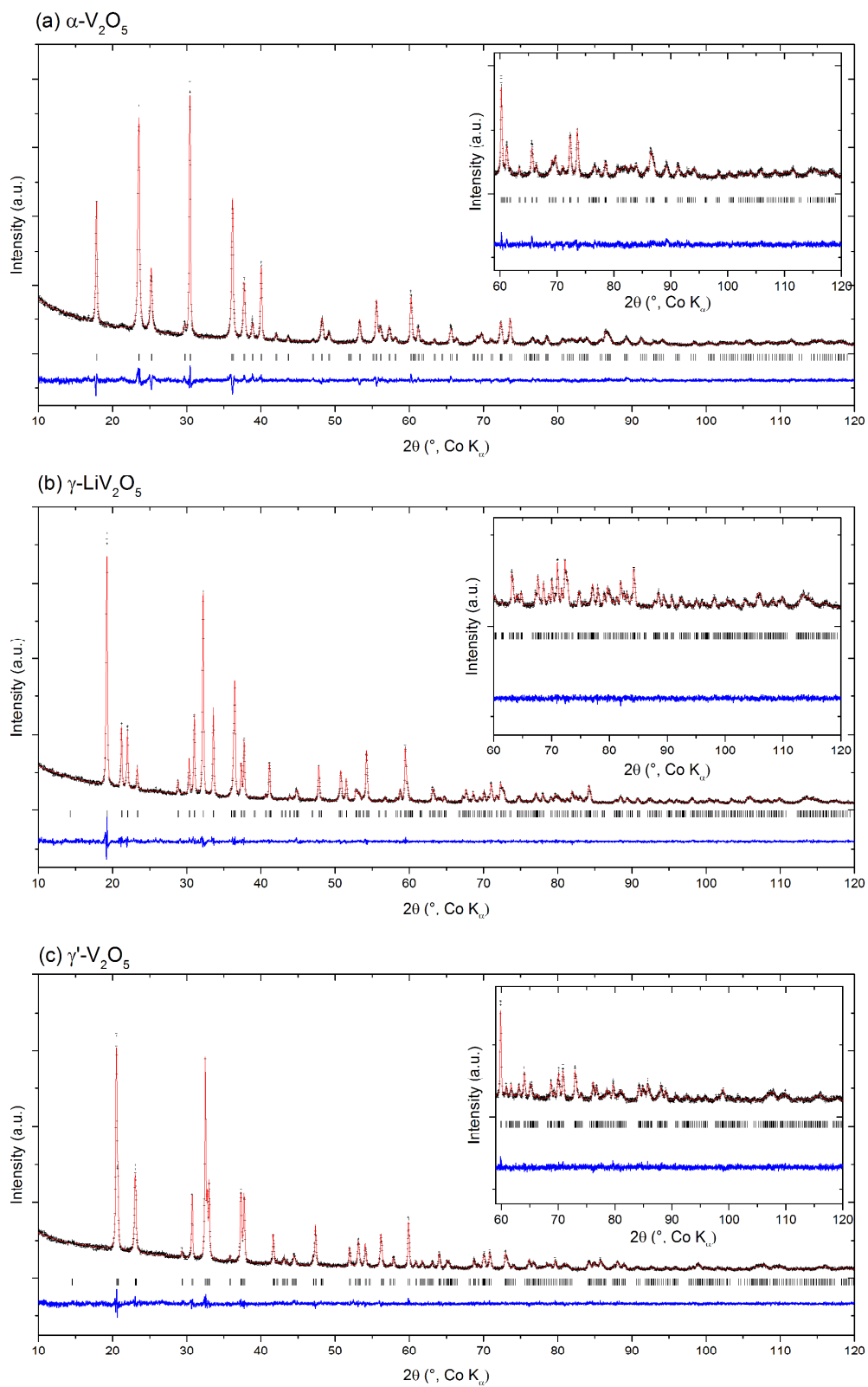


Figure S1. Rietveld refinements of (a) α -V₂O₅, (b) γ -LiV₂O₅ and (c) γ' -V₂O₅ X-ray diffraction patterns.

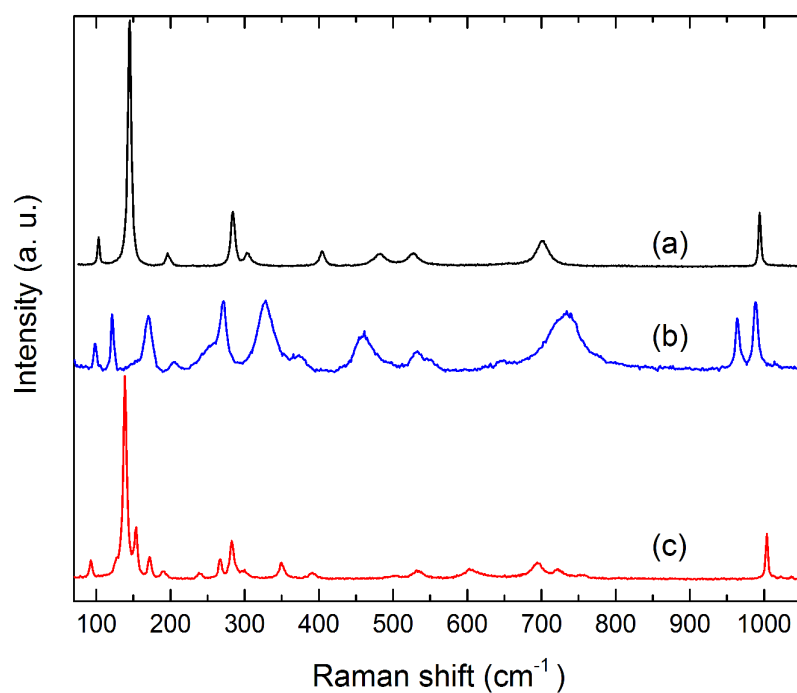


Figure S2. Raman spectra of (a) α - V_2O_5 , (b) γ - LiV_2O_5 and (c) γ' - V_2O_5 .

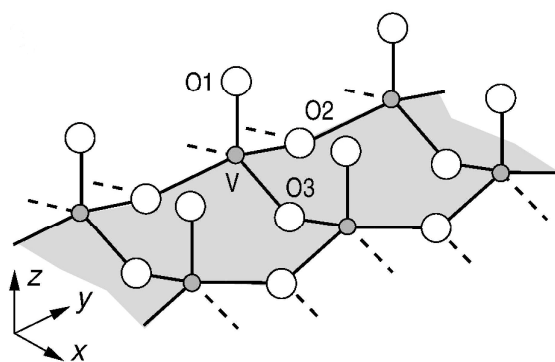


Figure S3. Representation of an isolated chain of the α - V_2O_5 structure. White and grey circles represent the oxygen and vanadium atoms, respectively. Interchain contacts (ladder steps) are shown by dashed lines.

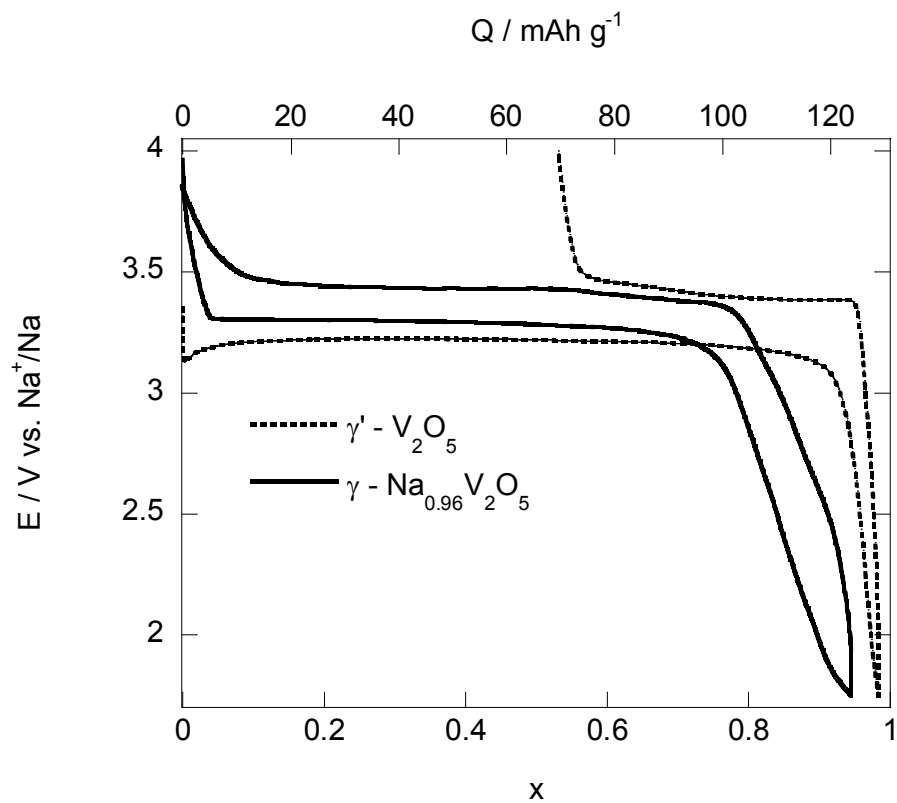


Figure S4. Comparison of the first galvanostatic cycle of $\gamma\text{-Na}_{0.96}\text{V}_2\text{O}_5$ and $\gamma'\text{-V}_2\text{O}_5$ electrodes. $C/5$ rate. Electrolyte NaClO_4 1M/PC. $\gamma'\text{-V}_2\text{O}_5$ first galvanostatic curve is taken from reference [1]

[1] M. Safrany Renard, N. Emery, R. Baddour-Hadjean, J. P. Pereira-Ramos, $\gamma'\text{-V}_2\text{O}_5$: A new high voltage cathode material for sodium-ion battery, *Electrochim. Acta* 252C (2017) 4-11.

Table S1. Atomic positions and thermal motion parameters extracted from the Rietveld refinement of α -V₂O₅ (y = 0.25 for all positions).

Atom type (label)	Wyckof pos.	x	z	U _{iso} (Å ²)
V (V)	4f	0.1013(1)	0.8956(3)	0.010(1)
O (O ₁)	4f	0.1046(3)	0.5358(7)	0.026(1)
O (O ₂)	4f	0.9307(2)	0.0002(7)	0.026(1)
O (O ₃)	2a	0.25	0.9936(9)	0.026(1)
Space group : <i>Pmmn</i> $a = 11.5054(3)$ Å, $b = 3.55631(1)$ Å, $c = 4.3765(2)$ Å $\alpha = \beta = \gamma = 90^\circ$ $\chi^2 = 1.878$, wR _p = 5.82%, Rp = 4.61%, Background: Shift Chebyshev 10 parameters.				

Table S2. Atomic positions and thermal motion parameters extracted from the Rietveld refinement of γ -LiV₂O₅ (y = 0.25 for all positions).

Atom type (label)	Wyckof pos.	x	z	U _{iso} (Å ²)
Li	4c	0.163(2)	0.221(2)	0.045(5)
V (V _a)	4c	0.0660(2)	0.5996(2)	0.013(1)
V (V _b)	4c	0.3766(2)	0.4984(2)	0.013(1)
O (O _{1a})	4c	0.4833(5)	0.7717(5)	0.030(1)
O (O _{1b})	4c	0.2817(5)	0.3791(5)	0.030(1)
O (O _{2a})	4c	0.4406(4)	0.0472(4)	0.030(1)
O (O _{2b})	4c	0.5734(4)	0.4527(4)	0.030(1)
O (O ₃)	4c	0.2415(5)	0.6347(4)	0.030(1)
Space group : <i>Pnma</i> $a = 9.6947(2)$ Å, $b = 3.6062(1)$ Å, $c = 10.6780(2)$ Å $\alpha = \beta = \gamma = 90^\circ$ $\chi^2 = 1.058$, wR _p = 4.87%, Rp = 3.78%, Background: Shift Chebyshev 10 parameters.				

Table S3. Atomic positions and thermal motion parameters extracted from the Rietveld refinement of γ' -V₂O₅ ($y = 0.25$ for all positions).

Atom type (label)	Wyckof pos.	x	z	U _{iso} (Å ²)
V (V _a)	4c	0.0713(2)	0.6018(2)	0.012(1)
V (V _b)	4c	0.3763(2)	0.5156(2)	0.012(1)
O (O _{1a})	4c	0.5005(6)	0.7597(6)	0.027(1)
O (O _{1b})	4c	0.2919(6)	0.3828(7)	0.027(1)
O (O _{2a})	4c	0.4368(6)	0.0418(6)	0.027(1)
O (O _{2b})	4c	0.5706(6)	0.4645(7)	0.027(1)
O (O ₃)	4c	0.2427(7)	0.6405(7)	0.027(1)
Space group : <i>Pnma</i> $a = 9.9484(2) \text{ \AA}$, $b = 3.5863(1) \text{ \AA}$, $c = 10.0459(3) \text{ \AA}$ $\alpha = \beta = \gamma = 90^\circ$ $\chi^2 = 1.316$, wR _p = 5.28%, Rp = 4.09%, Background: Shift Chebyshev 10 parameters.				

Table S4. Structural parameters for γ -Na_{0.96}V₂O₅ compared to those previously reported for the γ -Na_{0.97}V₂O₅ electroformed phase [47].

(Å)		γ - Na _{0.97} V ₂ O ₅ [47]	γ -Na _{0.96} V ₂ O ₅ [this work]
<i>a</i>		9.757	9.781
<i>b</i>		3.626	3.629
<i>c</i>		11.949	11.887
(V _a)O ₅	V _a -O _{1a}	1.672	1.548
	V _a -O ₃	1.740	1.794
	V _a -O _{2a} (x2)	1.893	1.909
	(V _a -O _{2a})LS	1.989	1.970
(V _a)O ₅			
Vol (Å ³)		4.885	4.649
BVS		+4.66	+5.15
(V _b)O ₅	V _b -O _{1b}	1.633	1.587
	V _b -O ₃	1.949	1.882
	V _b -O _{2b} (x2)	1.919	1.953
	(V _b -O _{2b})LS	1.921	1.949
(V _b)O ₅			
Vol (Å ³)		4.976	5.042
BVS		+4.35	+4.37
	(Na/Li)-O _{2b}	2.452	2.415
	(Na/Li)-O _{1b}	2.287	2.275
	(Na/Li)-O ₃ (x2)	2.518	2.425
	(Na/Li)-O _{1a} (x2)	2.346	2.459

3.3 Bilayered Potassium Vanadate $K_{0.5}V_2O_5$ as Superior Cathode Material for Na-ion Batteries

3.3.1 Introduction

Among the transition metal oxides investigated as cathode materials the group of vanadium oxides and bronzes has been screened, most of them in the last years: V_2O_5 polymorphs [1-3], bilayered V_2O_5 [4, 5], $Na_{0.33}V_2O_5$ [6-8], Na_xVO_2 [9, 10], $NaVO_3$ [11], NaV_3O_8 [12], γ - NaV_2O_5 [13].

Recently, we reported a novel Li intercalation compound, the potassium vanadium bronze $K_{0.5}V_2O_5$ synthesized via a fast and facile solution route [14]. This cathode material was found to exhibit outstanding electrochemical performance, one of the best among the vanadium bronzes, with a specific capacity of 210 mAh g^{-1} at an average voltage of 2.9 V vs. Li^+/Li , without any significant structural changes after extended cycling experiments. An excellent capacity retention was also reported, with still 200 mAh g^{-1} at C/10 after 70 cycles and a good rate capability with 140 mAh g^{-1} at 1C. This attractive behaviour originates from the unusually large d -spacing of 7.7 \AA practically twice that of the parent oxide V_2O_5 , and the presence of interlayer K^+ ions that stabilize the stacking of double-sheet V_2O_5 layers.

Such results prompted us to investigate in the present work $K_{0.5}V_2O_5$ (named KVO) as a potential candidate for cathode material of SIBs. Given the facile synthesis used in the case of KVO for LIBs, we have applied the same synthesis route in solution followed by an appropriate heat-treatment. Its electrochemical performance will be examined in the 1.5 - 4 V vs. Na^+/Na voltage range and discussed in relation with structural data obtained from XRD and Raman spectroscopy.

3.3.2 Synthesis

Potassium vanadate was synthesized by a solution route using 1 g of V_2O_5 (Alfa Aesar 99.995%) and stoichiometric amounts of KVO_3 dissolved in 10 cm^3 of an aqueous solution with 10 cm^3 H_2O_2 (30%). A fast and exothermic reaction takes place, leading to a fine precipitate. An appropriate heat treatment is then performed to obtain the potassium vanadate. The obtained compound was treated at $570 \text{ }^\circ\text{C}$ for 5 h under argon atmosphere. Elemental analysis by atomic absorption spectroscopy combined with redox titration have been carried out to determine the oxidation state of vanadium ions in the obtained product. This leads to the chemical composition $K_{0.5\pm 0.02}V_2O_5$.

3.3.3 Structural characterization

The obtained powder has been examined by XRD and Raman. All the reflection lines in **Figure 1** can be indexed with expected monoclinic $\delta\text{-K}_{0.486}\text{V}_2\text{O}_5$ structure $C2/m$ ($Z = 4$) [JCPDS 0860347] isomorphic to that of $\text{Na}_{0.56}\text{V}_2\text{O}_5$ and $\delta\text{-Ag}_{0.68}\text{V}_2\text{O}_5$, with lattice parameters $a = 11.659 \text{ \AA}$, $b = 3.668 \text{ \AA}$; $c = 9.469 \text{ \AA}$, $\alpha = \gamma = 90^\circ$, $\beta = 92.24^\circ$ are in a good agreement with the literature [14]. Sharp and intense diffraction peaks illustrate high crystallization degree. In addition, a high-preferred 00l orientation is seen from the high relative intensity of 001, 002, 003 and 004 lines.

All the useful data drawn from the XRD pattern of $\text{K}_{0.5}\text{V}_2\text{O}_5$ powder are summarized in **Table 1**. The structure of $\text{K}_{0.5}\text{V}_2\text{O}_5$ structure consists of double-sheet V_2O_5 layers built of (V1) O_6 and (V2) O_6 octahedra and interstitial K atoms, with V–O bond distances ranging from 1.60 to 2.52 \AA (**Figure 1 inset**). The calculation of crystallite size and average crystallite size from XRD by using Sherrer equation (see **Table 1**) for $\text{K}_{0.5}\text{V}_2\text{O}_5$ is $\sim 47 \text{ nm}$.

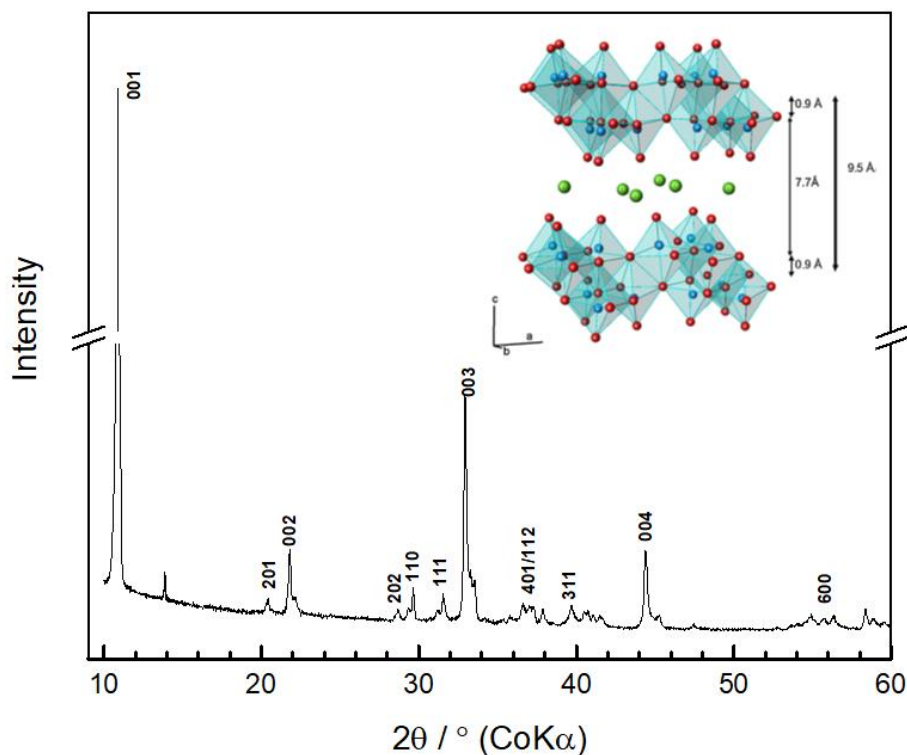
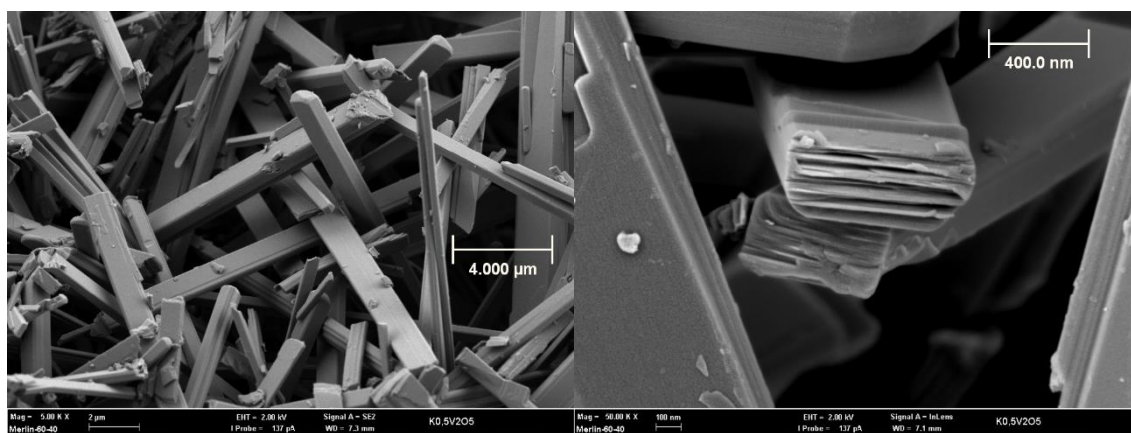


Figure 1. X-ray diffraction pattern of $\text{K}_{0.5}\text{V}_2\text{O}_5$ powder

Table 1. Peak positions, interplanar spacing, *hkl* indexes, FWHM, Crystallite size from XRD data of γ' -V₂O₅

No.	Peak position		Interplanar spacing	Miller indices	FWHM	Crystallite size
	2 Theta (°)	Theta (°)	<i>d</i> (Å)	(<i>hkl</i>)	(<i>o</i>)	<i>nm</i>
1	10.85823	5.429115	9.453655	001	0.20342	45.55
2	20.38	10.19	5.055876	201	N/A	-
3	21.79441	10.89721	4.73135	002	0.19312	48.64
4	28.66936	14.33468	3.612691	202	0.12682	75.08
5	28.66936	14.33468	3.612691	110	N/A	-
6	31.55622	15.77811	3.289476	111	0.23057	41.57
7	32.94692	16.47346	3.154235	003	0.23741	40.52
8	39.71242	19.85621	2.633362	311	0.44338	22.12
9	44.41479	22.2074	2.366518	004	0.27756	35.90

SEM images (**Figure 2**) show the KVO powder exhibits well-defined and regular platelets of about 10 μm long, 1 μm wide and 0.5 μm thick, with homogeneous distribution throughout the sample

**Figure 2.** SEM images of KVO at different magnifications

The Raman spectrum of K_{0.5}V₂O₅ exhibits 21 modes located at 96, 115, 165, 233, 271, 330, 347, 407, 431, 471, 509, 604, 702, 784, 850, 887, 946, 960, 980, 1008, and 1020 cm^{-1} (**Figure 3**). K_{0.5}V₂O₅ framework is made of VO₆ distorted units which are also involved to describe the structure of V₂O₅. In 200 – 900 cm^{-1} region corresponds to the $\delta(\text{V-O-V})$ bending and $\nu(\text{V-O})$

stretching vibrations in the (V1)O6 and (V2)O6 octahedra. In 900 – 1020 cm^{-1} region can be assigned to the stretching vibrations of the shortest V=O bonds of 1.6 Å (V1–O4 and V2–O5). Multiple features located at 946, 960, 980, 1008, and 1020 cm^{-1} related to the $\text{K}_{0.5}\text{V}_2\text{O}_5$ region. This multiplicity may be due to the presence of two short bonds in $\text{K}_{0.5}\text{V}_2\text{O}_5$ instead of a single one in V_2O_5 , combined with the existence of both $\text{V}^{4+}=\text{O}$ and $\text{V}^{5+}=\text{O}$ species in the bronze. Bands observed at 784 and 887 cm^{-1} can be assigned to the stretching vibrations of strongly asymmetric V1–O1–V2 and V1–O3–V2 bridges in the double-layer structure of $\text{K}_{0.5}\text{V}_2\text{O}_5$.

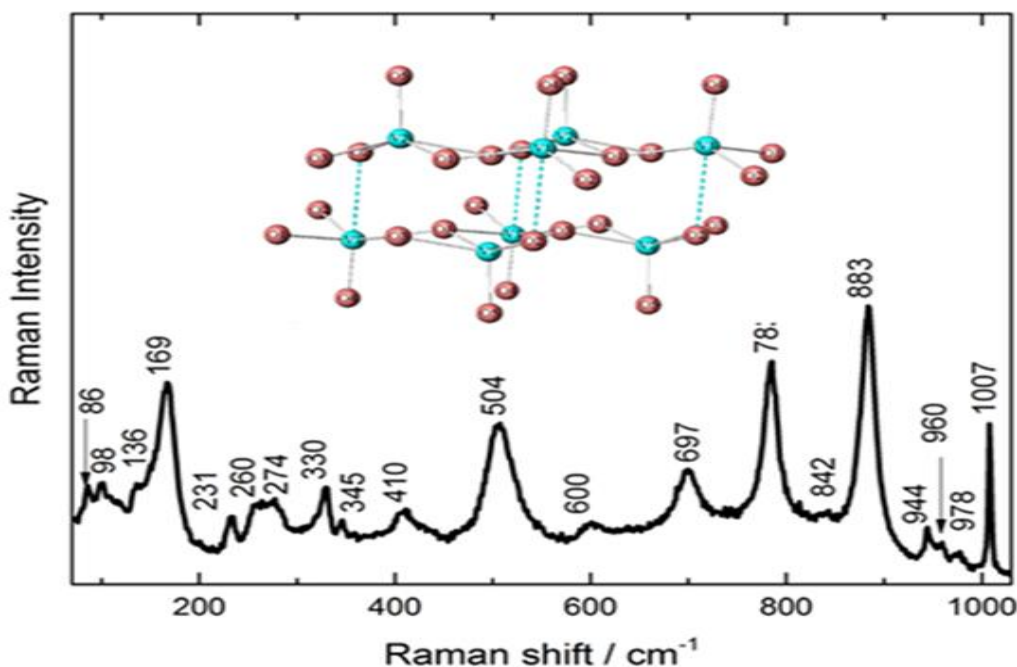


Figure 3. Raman spectrum and local structure (inset) of $\text{K}_{0.5}\text{V}_2\text{O}_5$ powder

3.3.4 Electrochemical study

The discharge/charge curves of $\text{K}_{0.5}\text{V}_2\text{O}_5$ investigated at C/10 at voltage range of 4 – 1.5V are presented in **Figure 4**. Starting from OCV voltage of 3.3V vs Na^+/Na , the working potential decreases along slope down to 1.5 V with total discharge capacity of 49 mAh g^{-1} (0.36 F/mol) (**Figure 4a**). After intercalating 0.36 sodium ions, two voltage plateaus can be observed at 2.71 and 3.6 V during the consecutive charge for total faradic yield of 0.62 F/mol (**Figure 4b**). These findings suggest the complete extraction of 0.36 Na^+ (~2.71V) and partial extraction of K^+ at higher voltage ~ 3.6V (0.26 F/mol) during oxidation. The second discharge exhibits a long sloping profile

down to 1.5V including numerous steps (**Figure 4b**). The discharge/charge capacity at 2nd cycle exhibits 140 mAh g⁻¹, indicating a reversible insertion/extraction process (**Fig 4c**). Interestingly, the specific capacity progressively increases from 140 mAh g⁻¹ (0.97 F/mol) to 160 mAh g⁻¹ (1.14F/mol) along the 20 cycles, then stabilizes at least over 80 cycles. The discharge/charge capacity after 80 cycles reaches 136 mAh g⁻¹ (**Figure 4d**).

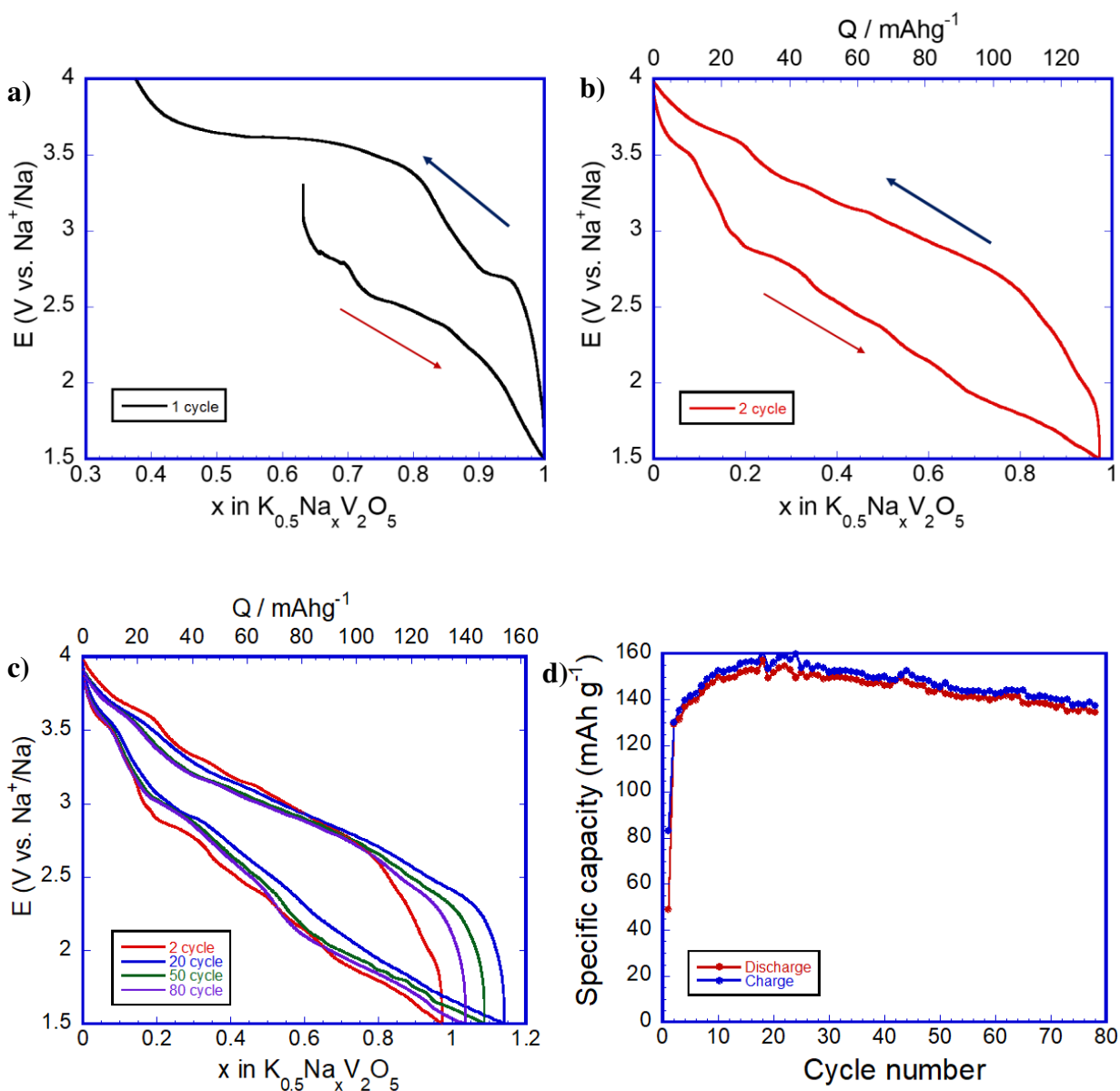


Figure 4. Electrochemical performance of $K_{0.5}V_2O_5$ at C/10 in voltage range of 4 – 1.5V. (a) First and (b) second discharge/charge. (c) discharge/charge profile (d) cycle performance

The rate-capability of $\text{K}_{0.5}\text{V}_2\text{O}_5$ is reported in **Figure 5**. The discharge capacity exhibits 140 mAh g^{-1} (1 F/mol) and decreases to 100 mAh g^{-1} (0.76 F/mol) at $\text{C}/10$ and $\text{C}/5$, respectively. $\text{K}_{0.5}\text{V}_2\text{O}_5$ intercalates 0.66Na/mol (95 mAh g^{-1}) at $\text{C}/2$, 0.6Na/mol (84 mAh g^{-1}) at 1C , 0.53 Na/mol (74 mAh g^{-1}) at 2C and 0.3 F/mol (38 mAh g^{-1}) at 5C . In addition, upon charge at various C-rates the capacity fully recovered with a symmetric voltage shape, indicates the electrochemical stability and reversibility of the potassium vanadium bronze. Even after switching from high rate (5C) to lower C-rate ($\text{C}/2$), a discharge/charge capacity of 95 mAh g^{-1} is recovered with stable cycling showing no structural damage for the host material. However the high 5C rate has a detrimental effect on the cathode properties with a capacity limited to only 40 mAh g^{-1} .

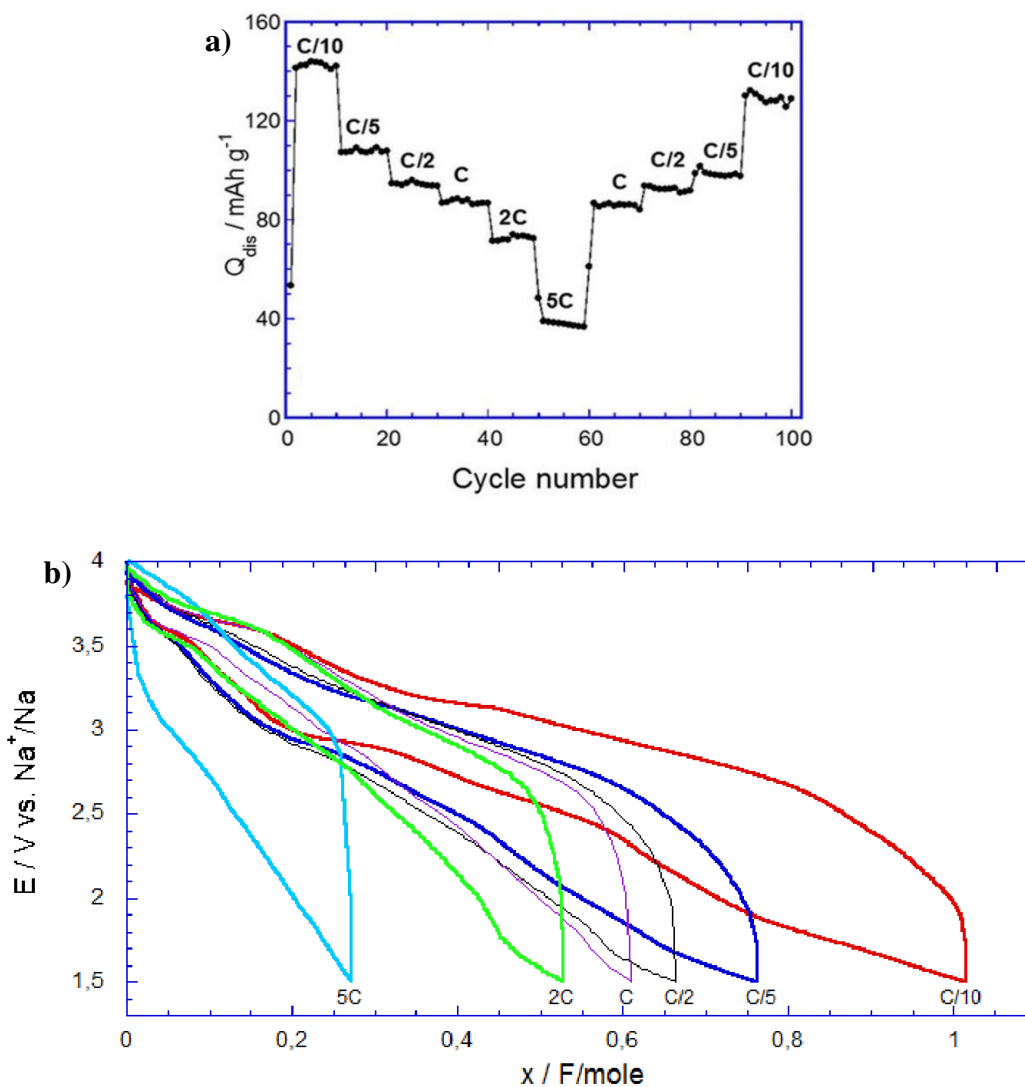


Figure 5. (a) Rate capability and (b) discharge/charge profile at different C-rate of $\text{K}_{0.5}\text{V}_2\text{O}_5$ at voltage range of 4 – 1.5V

3.3.5 Structural investigation upon discharge-charge

The structural evolution of $\text{K}_{0.5}\text{V}_2\text{O}_5$ at different states of discharge/charge during sodium extraction/insertion process was examined on 1st and 2nd cycles at C/10 (**Figure 6**). The Ex-situ XRD patterns and Raman spectra of the potassium bronze at different depths of charge and discharge are illustrated in **Figure 7** and **Figure 8**. Before discharge, the pristine electrode exhibits the typical XRD pattern of the monoclinic $\text{K}_{0.5}\text{V}_2\text{O}_5$ bronze ($C2/m$; $Z = 4$) with the following unit cell parameters [$a = 11.659 \text{ \AA}$, $b = 3.668 \text{ \AA}$; $c = 9.469 \text{ \AA}$] (**Figure 6 point a**). According to the obtained XRD results, $00l$ lines exhibit high relative intensities, which suggests a high-preferred orientation (**Figure 7**).

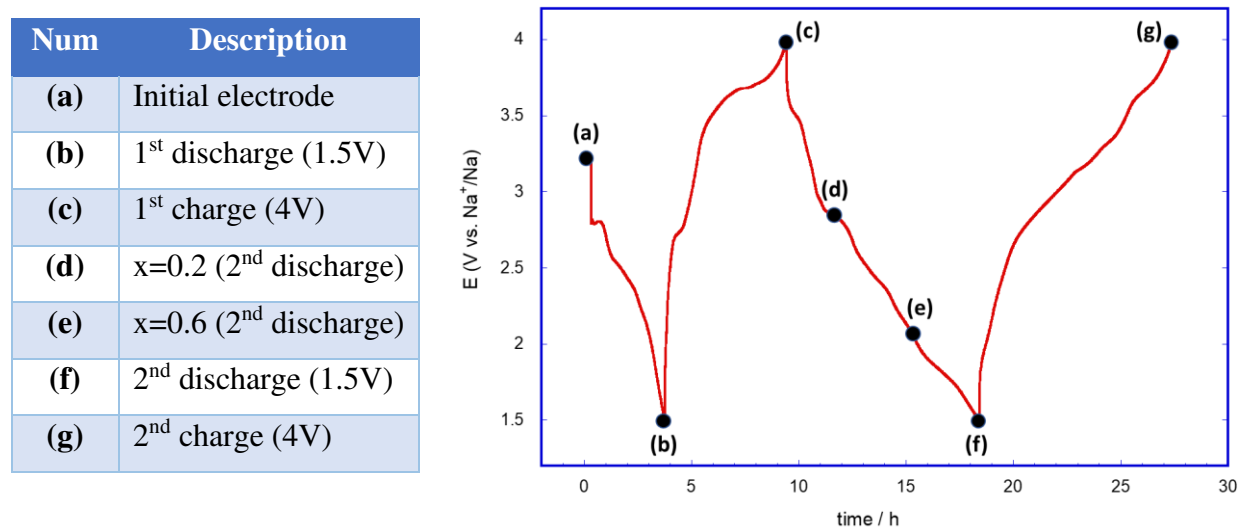


Figure 6. The 1st and 2nd cycle of $\text{K}_{0.5}\text{V}_2\text{O}_5$ at C/10 in 4 – 1.5V voltage range

The evolution of XRD patterns during discharge/charge process does not reveal strong modifications, indicating the structure of KVO material is maintained. During the 1st reduction to 1.5 V (**Figure 6 point b**), shift of 001 line to higher angle can be observed, indicating the decrease of inter-sheet distance c (from 9.469 \AA → to 9.07 \AA). After first discharge, a new $\text{Na}_{0.36}\text{K}_{0.5}\text{V}_2\text{O}_5$ composition is reached.

At subsequent charge to 4V (**Figure 6 point c**), an increase of the inter-sheet can be observed (shift of 001 main line toward lower angle). The c parameter increases from 9.07 \AA to 9.32 \AA . It demonstrates the extraction of large Na^+ and K^+ cations result in strong repulsion between negative

sheets of V_2O_5 . During the second discharge, for $x=0.2$ (**Figure 6 point d**), $x=0.6$ (**Figure 6 point e**) and after complete reduction $x=1$ (**Figure 6 point f**), a progressive shift of 001 line towards higher angle can be observed, indicating the decrease of interlayer distance. For fully reduced Na_1KVO composition the unit cell value $c=9.02$ Å (-3%).

Once again, a reverse trend is observed upon Na extraction (**Figure 6 point g**), with a c value of 9.30 Å recovered after the second cycle (**Figure 6 point g**).

Remarkably, the XRD pattern of an electrode after 50 cycles (**Figure 7**) is superimposable to the one after one cycle, showing the high stability of the structure upon cycling and no amorphization phenomenon. It can be indexed in the same monoclinic $C2/m$ symmetry, with unit cell parameters of $a = 11.54$ Å, $b = 3.47$ Å; $c = 9.30$ Å.

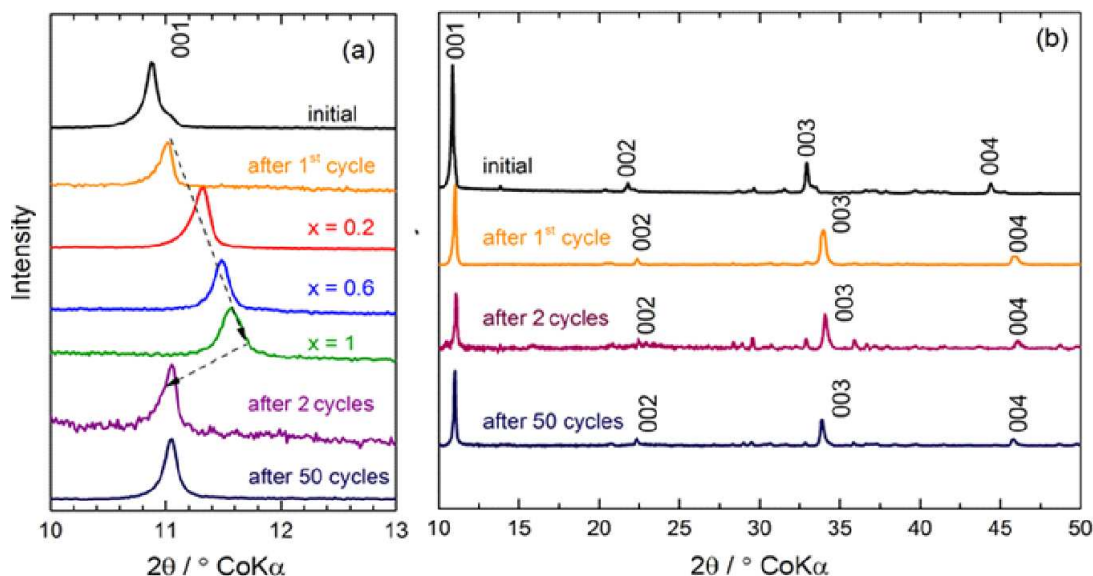


Figure 7. (a) Evolution of the 001 reflection of KVO electrodes: pristine electrode, electrode after one cycle, electrode during second discharge ($x = 0.2, 0.6$ and 1 in Na_xKVO), electrode after 2 and 50 cycles at C/10. (b) XRD patterns of initial and cycled KVO electrodes at C/10

The Raman spectra of KVO electrodes recording during discharge/charge process are shown in **Figure 8**. The Raman spectrum of the initial electrode exhibits typical fingerprint of KVO, which consist of 10 peaks located at 95, 169, 274, 330, 410, 504, 697, 781, 880 and 1007 cm^{-1} . It can be seen that the comparison of electrodes on charged state after 1st, 2nd and 50th cycle, demonstrate the total restoration of the host lattice of KVO without structural rearrangement. However, upon

discharge, broadening of Raman bands with an increase of x value ($0.2 \leq x \leq 1$) can be observed, indicating the increase in the electronic conductivity of the material during the sodiation process.

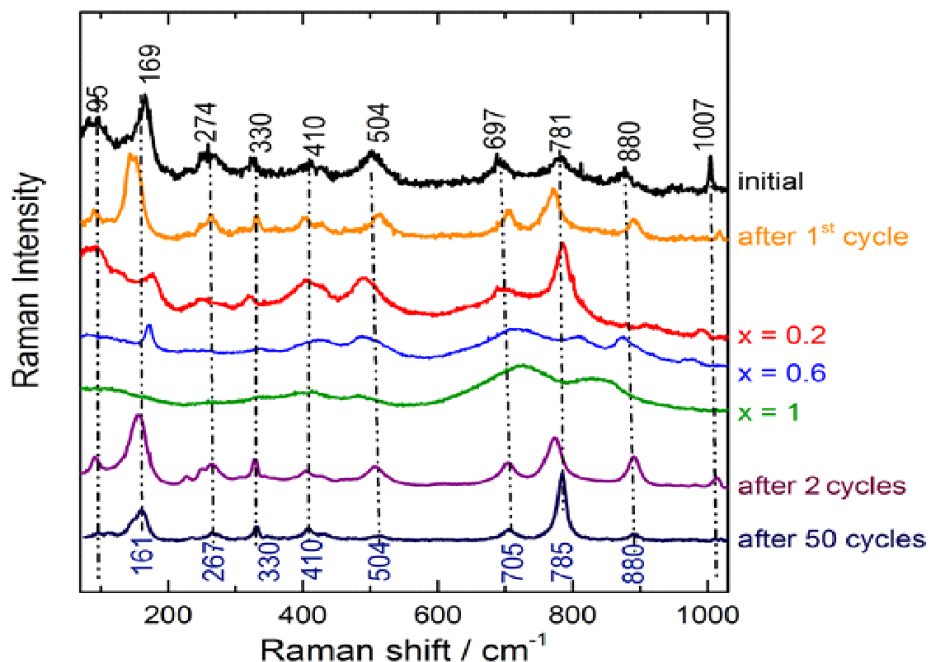


Figure 8. Raman spectra of KVO electrodes: pristine electrode, electrode after one cycle, electrode during second discharge ($x = 0.2, 0.6$ and 1 in Na_xKVO), electrode after 2 and 50 cycles at C/10.

3.3.6 Conclusion

In conclusion, $\text{K}_{0.5}\text{V}_2\text{O}_5$ material (KVO) has been synthesized through a fast and facile solution route and its structural and electrochemical behaviors toward Na insertion has been described. The bilayered potassium vanadate $\text{K}_{0.5}\text{V}_2\text{O}_5$ is characterized by a large interlayer parameter of 9.5 \AA . A first cycle in the 4 V - 1.5 V range at C/10 acts as an activation process, leading to a new KVO composition $\text{K}_{0.24}\text{V}_2\text{O}_5$ due to partial potassium extraction. KVO delivers a high reversible specific capacity of 160 mAh g^{-1} at C/10 with a good capacity retention leading to still 152 mAh g^{-1} after 50 cycles.

The XRD and Raman study was performed to investigate KVO crystal structure upon charge-discharge showing only small changes limited to expansion-contraction cycles of low magnitude (3%) in the distance between bilayers. In the same time no change was revealed in the layers plane.

Interestingly, an interesting rate-capability is shown up to 2C. The unique crystal structure of KVO with large interlayer space (9.5 Å), with pillaring K⁺ ions stabilizing the stacking of double-sheet V₂O₅ layers allows reaching high electrochemical properties as cathode material for Na-ion batteries.

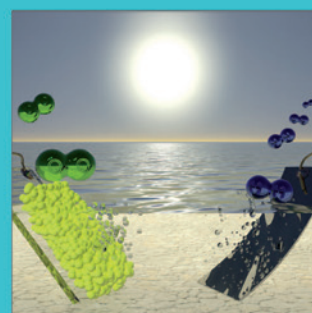
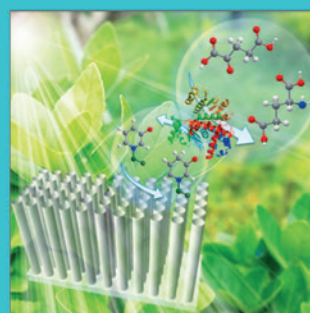
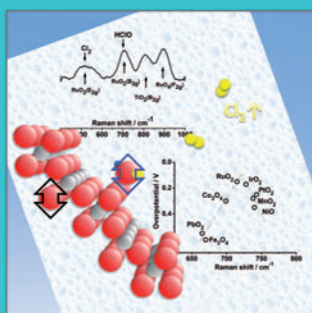
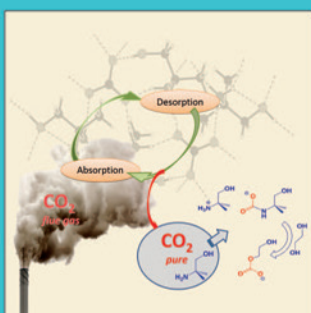
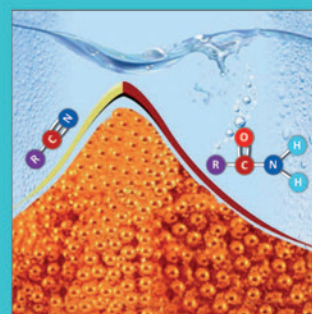
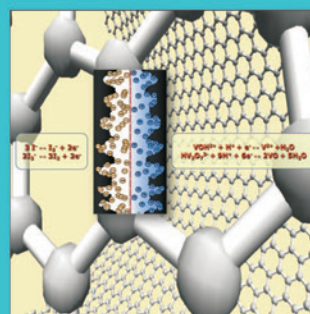
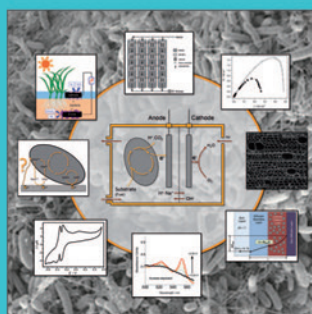
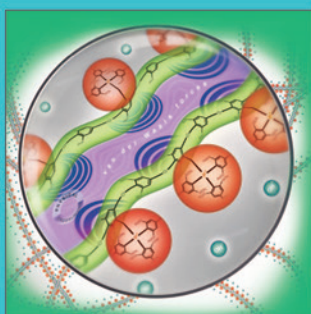
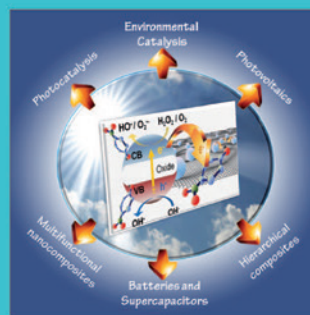
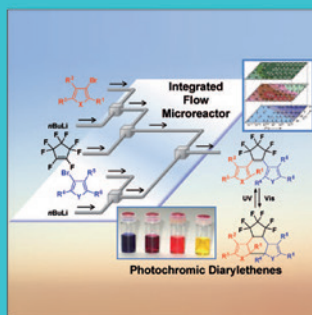
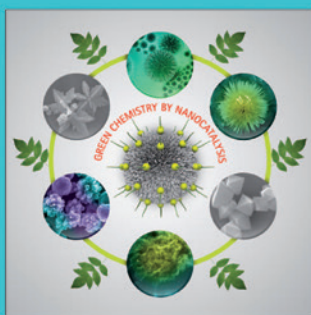
REFERENCES

- [1] K. West, B. Zachau-Christiansen, T. Jacobsen, S. Skaarup, "Sodium insertion in vanadium oxides", *Solid State Ion.* 1988, 28-30, 1128.
- [2] M. Safrany Renard, N. Emery, R. Baddour-Hadjean, J. P. Pereira-Ramos, " γ' -V₂O₅: A new high voltage cathode material for sodium-ion battery", *Electrochim. Acta* 2017, 252C, 4.
- [3] R. Baddour-Hadjean, M. Safrany Renard, N. Emery, L. T. N. Huynh, M. L. P. Le, J. P. Pereira-Ramos, *Electrochim. Acta* 2018, 270, 129.
- [4] S. Tepavcevic, H. Xiong, V.R. Stamenkovic, X. Zuo, M. Balasubramanian, V.B. Prakapenka, C.S. Johnson, T. Rajh, "Nanostructured Bilayered Vanadium Oxide Electrodes for Rechargeable Sodium-Ion Batteries", *ACS Nano* 2012, 6, 530.
- [5] D. Su, G. Wang, "Single-Crystalline Bilayered V₂O₅ Nanobelts for High-Capacity Sodium-Ion Batteries", *ACS Nano* 2013, 7, 11218.
- [6] S. Bach, N. Baffier, J. P. Pereira-Ramos, R. Messina, "Electrochemical sodium intercalation in Na_{0.33}V₂O₅ bronze synthesized by a sol-gel process", *Solid State Ionics* 1989, 37, 41.
- [7] J.P. Pereira-Ramos, R. Messina, S. Bach, N. Baffier, "Influence of the synthesis via a sol-gel process on the electrochemical lithium and sodium insertion in β -Na_{0.33}V₂O₅", *Solid State Ion.* 1990, 40-41, 970.
- [8] H. M. Liu, H. S. Zhou, L. P. Chen, Z. F. Tang, W. S. Yang, "Electrochemical insertion/deinsertion of sodium on NaV₆O₁₅ nanorods as cathode material of rechargeable sodium-based batteries", *J. Power Sources* 2011, 196, 814.
- [9] D. Hamani, M. Ati, J.-M. Tarascon, P. Rozier, "Na_xVO₂ as possible electrode for Na-ion batteries", *Electrochem. Commun.* 2011, 13, 938.
- [10] M. Guignard, C. Didier, J. Darriet, P. Bordet, E. Elkaim, C. Delmas, "P₂-Na(x)VO₂ system as electrodes for batteries and electron-correlated materials", *Nat. Mater.* 2013, 12, 74.
- [11] G. Venkatesh, V. Pralong, O. I. Lebedev, V. Caignaert, P. Bazin, B. Raveau, "Amorphous sodium vanadate Na_{1.5} + yVO₃, a promising matrix for reversible sodium intercalation", *Electrochem. Comm.* 2014, 40, 100.
- [12] H. He, G. Jin, H. Wang, X. Huang, Z. Chen, D. Sun, Y. Tang, "Annealed NaV₃O₈ nanowires with good cycling stability as a novel cathode for Na-ion batteries", *J. Mater. Chem. A*, 2014, 2, 3563.
- [13] N. Emery, R. Baddour-Hadjean, D. Batyrbekuly, B. Laïk, Z. Bakenov, J. P. Pereira-Ramos, γ -Na_{0.96}V₂O₅: A New Competitive Cathode Material for Sodium-Ion Batteries Synthesized by a Soft Chemistry Route, *Chem. Mater.* 2018, 30, 5305.
- [14] S. Bach, A. Boudaoud, N. Emery, R. Baddour-Hadjean, J. P. Pereira-Ramos, "K_{0.5}V₂O₅: A novel Li intercalation compound as positive electrode material for rechargeable lithium batteries", *Electrochim. Acta* 2014, 119, 38.

CHEMISTRY & SUSTAINABILITY

CHEMSUSCHEM

ENERGY & MATERIALS



Reprint

© Wiley-VCH Verlag GmbH & Co. KGaA, Weinheim

A Journal of



WILEY-VCH

www.chemsuschem.org

Bilayered Potassium Vanadate $K_{0.5}V_2O_5$ as Superior Cathode Material for Na-Ion Batteries

Rita Baddour-Hadjean,^{*,[a]} Le Thanh Nguyen Huynh,^[a] Daureen Batyrbekuly,^[a, b] Stéphane Bach,^[a, c] and Jean-Pierre Pereira-Ramos^{*,[a]}

A bilayered potassium vanadate $K_{0.5}V_2O_5$ (KVO) is synthesized by a fast and facile synthesis route and evaluated as a positive electrode material for Na-ion batteries. Half the potassium ions can be topotactically extracted from KVO through the first charge, allowing $1.14Na^+$ ions to be reversibly inserted. A good rate capability is also highlighted, with 160 mAh g^{-1} at C/10, 94 mAh g^{-1} at C/2, 73 mAh g^{-1} at 2C and excellent cycling stability with 152 mAh g^{-1} still available after 50 cycles at C/10. Ex situ X-ray diffraction reveals weak and reversible structural changes resulting in soft breathing of the KVO host lattice

upon Na extraction–insertion cycles ($\Delta V/V \approx 3\%$). A high structure stability upon cycling is also achieved, at both the long-range order and atomic scale probed by Raman spectroscopy. This remarkable behavior is ascribed to the large interlayer spacing of KVO ($\approx 9.5\text{ \AA}$) stabilized by pillar K ions, which is able to accommodate Na ions without any critical change to the structure. Kinetics measurements reveal a good Na diffusivity that is hardly affected upon discharge. This study opens an avenue for further exploration of potassium vanadates and other bronzes in the field of Na-ion batteries.

Introduction

With the rapid development of renewable energy sources, the deployment of new electrical energy storage solutions is highly desired. Lithium-ion batteries (LIBs), which dominate the portable electronic market, are expected to satisfy this requirement.^[1] However, the use of Li is impeded by its high cost, limited reserves and uneven distribution.^[2] As a result, research has turned to batteries composed of low-cost and earth-abundant elements; among them, Na-ion batteries (SIBs) have emerged as one of the best alternatives to LIBs because their reaction mechanism is similar to that of LIBs and Na sources are essentially unlimited.^[3–13]

To date, a large variety of Na-insertion frameworks have been proposed as cathode materials.^[14–19] Similar to LIBs, highly reversible cathode materials based on the intercalation reaction are needed for high capacity and good cyclability of SIBs. These cathode materials are mainly categorized into oxides and polyanion types.^[14] A major obstacle is the difficulty


to prepare a sodium host material with an operating voltage and capacity that is comparable to that of LIB analogs. Among the transition metal oxides investigated as cathode materials, a range of vanadium oxides and bronzes has been screened: V_2O_5 polymorphs,^[20–22] bilayered V_2O_5 ,^[23,24] $Na_{0.33}V_2O_5$,^[25–27] Na_xVO_2 ,^[28,29] $NaVO_3$,^[30] NaV_3O_8 ,^[31] $\gamma\text{-NaV}_2O_5$.^[32] More recently, we reported a novel Li intercalation compound, the potassium vanadium bronze $K_{0.5}V_2O_5$, which was synthesized through a fast and facile solution route.^[33] This cathode material exhibited outstanding electrochemical performance, one of the best among the vanadium bronzes, with a specific capacity of 210 mAh g^{-1} at an average voltage of 2.9 V versus (vs.) Li^+/Li , without any significant structural changes after extended cycling experiments. An excellent capacity retention of 200 mAh g^{-1} at C/10 after 70 cycles and a good rate capability of 140 mAh g^{-1} at 1C was also obtained. This attractive behavior originated from the unusually large interlayer spacing (d) of 7.7 \AA , which is nearly two times higher than that of the parent oxide V_2O_5 , and the presence of interlayer K^+ ions that stabilized the stacking of double-sheet V_2O_5 layers.

Motivated by the excellent electrochemical performance of vanadium oxides and bronzes in LIBs and NIBs, in the present work we investigated $K_{0.5}V_2O_5$ (KVO) as a potential cathode material for SIBs. Electrochemical studies showed that this material was capable of delivering a reversible Na-ion storage capacity of approximately 160 mAh g^{-1} at a current density of C/10 in the voltage range of 1.5–4 V vs. Na^+/Na . The material also demonstrated a good rate capability with a capacity of 94 mAh g^{-1} at C/2 and 73 mAh g^{-1} at 2C and excellent cycling stability with 158 mAh g^{-1} still available after 50 cycles at C/10. Ex situ XRD and Raman spectroscopy revealed a high structural stability of this layered potassium vanadate. A kinetic study of

[a] Dr. R. Baddour-Hadjean, Dr. L. T. N. Huynh, D. Batyrbekuly, Dr. S. Bach, Dr. J.-P. Pereira-Ramos
Institut de Chimie et des Matériaux Paris Est (ICMPE), GESMAT
UMR 7182 CNRS-Université Paris Est Créteil
2 rue Henri Dunant, 94320 Thiais (France)
E-mail: baddour@icmpe.cnrs.fr
pereira@icmpe.cnrs.fr

[b] D. Batyrbekuly
School of Engineering, National Laboratory Astana, Nazarbayev University
53 Kabanbay Batyr Avenue, Astana 010000 (Kazakhstan)

[c] Dr. S. Bach
Dept Chimie, Université d'Evry Val d'Essonne
Bd F. Mitterrand, 91000 Evry (France)

 The ORCID identification number(s) for the author(s) of this article can be found under:
<https://doi.org/10.1002/cssc.201902093>.

Na transport showed limited impact of the depth of discharge on the sodium diffusion rate. Given the facile synthesis and diversity of potassium vanadates, this study may stimulate further investigation of the insertion/deinsertion of guest species in this appealing family of compounds.

Results and Discussion

SEM images of the KVO powder indicated that it was composed of well-defined and regular platelets approximately 10 μm long, 1 μm wide and 0.5 μm thick, which were homogeneously distributed throughout the sample (Figure 1). The XRD

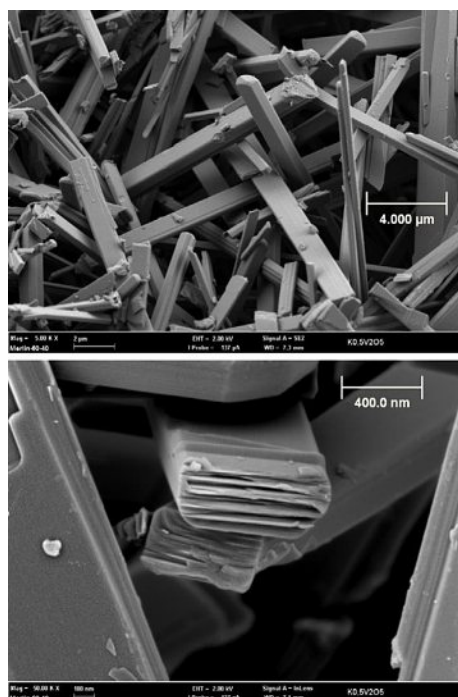


Figure 1. SEM images of KVO.

pattern of the KVO powder (Figure 2) was indexed to a monoclinic $\delta\text{-K}_{0.486}\text{V}_2\text{O}_5$ structure $C2/m$ ($Z=4$) [JCPDS 0860347] isomorphic to that of $\text{Na}_{0.56}\text{V}_2\text{O}_5$ and $\delta\text{-Ag}_{0.68}\text{V}_2\text{O}_5$, with lattice parameters $a=11.659 \text{ \AA}$, $b=3.668 \text{ \AA}$; $c=9.469 \text{ \AA}$, $\alpha=\gamma=90^\circ$, $\beta=92.24^\circ$. A small impurity of monoclinic $\text{K}_{0.25}\text{V}_2\text{O}_5$ was found (200 reflection at $\approx 14^\circ$). This result was consistent with previous studies performed on single crystals and powders.^[33–36] In our experiments, 00l lines exhibited high relative intensities, which suggested a highly preferred orientation, as previously observed for microwave-synthesized powders.^[35] However, in the latter case, larger particles with many defects and a heterogeneous size distribution were obtained. The crystal structure of KVO is illustrated in the inset of Figure 2: two single sheets made of octahedral VO_6 are alternately linked together by edge sharing to form the double-sheet V_2O_5 layered structure with K-ions lying between the layers, yielding a sandwiched structure. $\text{K}_{0.5}\text{V}_2\text{O}_5$ belongs to the $C2h$ point symmetry group. Factor group analysis yielded the allowed representations for

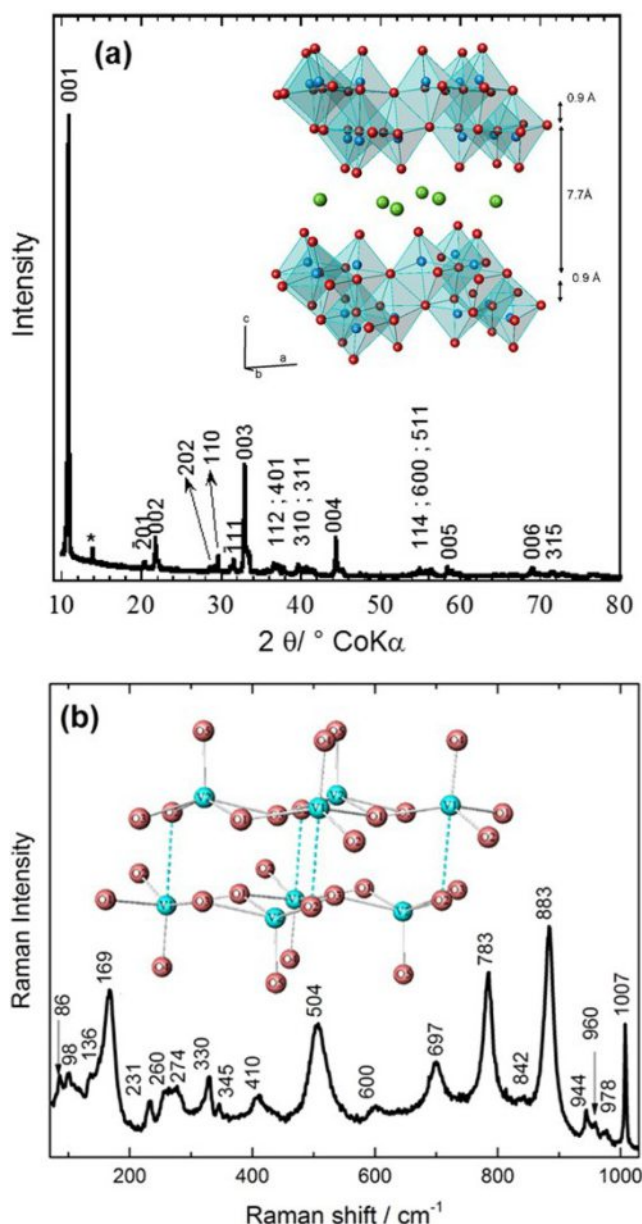


Figure 2. Structural characterizations of KVO. a) X-ray diffraction pattern. The * indicates $\text{K}_{0.25}\text{V}_2\text{O}_5$ impurity. Inset: Crystal structure. b) Raman spectrum. Inset: Schematic V–O polyhedra structure of the double layers.

each one of the selected Wyckoff positions (Table 1). By summing the overall contribution and subtracting the acoustic modes ($\Gamma_{ac} = A_u + 2B_u$), we obtain the following irreducible representations of $\text{K}_{0.5}\text{V}_2\text{O}_5$ vibrational modes [Equation (1)]:

$$\Gamma(\text{K}_{0.5}\text{V}_2\text{O}_5) = 16A_g + 8B_g + 7A_u + 14B_u \quad (1)$$

Table 1. Allowed representation for each atom in the $\text{K}_{0.5}\text{V}_2\text{O}_5$ crystal.

Atoms in $\text{K}_{0.5}\text{V}_2\text{O}_5$ unit cell	Wyckoff position	$\Gamma(i)$
V [1], V [2], K, O [1], O [2], O [3], O [4], O [5]	4i	$2A_g + B_g + A_u + 2B_u$

Therefore, 24 Raman active modes were expected to show up in the Raman spectrum of KVO. In this study, as in many spectroscopic studies of solids, the number of modes that were experimentally observed was significantly lower than that predicted by group theory methods. This situation occurs because of the low polarizability derivatives for many Raman-active modes and the small separation of their frequency shift, for example, B_g modes almost coincide with A_g modes. The Raman spectrum of the as-obtained powder (Figure 2b) shows the typical fingerprint previously reported for KVO, consisting of 20 bands located at 86, 98, 136, 169, 231, 260, 274, 330, 345, 410, 504, 600, 697, 783, 842, 883, 944, 960, 978 and 1007 cm^{-1} . A detailed assignment of this Raman spectrum can be found in Ref. [34]. Briefly, most of the observed modes correspond to the stretching and bending vibrations of the different V–O and V–O–V bonds. In the $200\text{--}900\text{ cm}^{-1}$ frequency region, the observed bands have their counterpart in the Raman spectrum of V_2O_5 crystal and are assigned to the $\delta(\text{V–O–V})$ bending and $\nu(\text{V–O})$ stretching vibrations in the $(\text{VO})_6$ octahedra.^[37,38] In the $900\text{--}1020\text{ cm}^{-1}$ range, the stretching vibrations of the two shortest apical V=O bonds ($d \approx 1.6\text{ \AA}$) are observed (see inset in Figure 2b). Multiple features (at 944, 960, 978 and 1007 cm^{-1}) are clearly evident in this region for KVO compared with two bands at 995 cm^{-1} and 976 cm^{-1} in V_2O_5 . This multiplicity is owing to the presence of two short bonds in KVO instead of a single one in V_2O_5 , combined with the existence of both $\text{V}^{4+}=\text{O}$ and $\text{V}^{5+}=\text{O}$ species in the potassium bronze. Intense Raman features at 783 and 883 cm^{-1} that correspond to the stretching

vibrations of strongly asymmetric $\text{V}_1\text{--O}_1\text{--V}_2$ and $\text{V}_1\text{--O}_3\text{--V}_2$ bridges in the double layer structure of KVO (see inset in Figure 2b). Finally, Raman features below 200 cm^{-1} are associated with the modes involving displacements of vanadium atoms.

The electrochemical properties of KVO were examined in a sodium half-cell. The first discharge–charge cycle of KVO at C/10 rate is shown in Figure 3a. Starting from the open-circuit voltage of 3.29 V vs. Na^+/Na , 0.36 Na^+ ions can be intercalated in KVO at an average potential of 2.45 V, corresponding to a specific capacity of 49 mAh g^{-1} . Then, the oxidation reaction proceeded along two plateaus at 2.71 and 3.57 V and involved a total capacity of 0.62 F mol^{-1} . This result indicates that not only 0.36 sodium ions can be reversibly extracted along the first plateau but additional potassium extraction takes place along the second plateau at 3.57 V (ca. $0.26\text{ K}^+\text{ mol}^{-1}$). The participation of a solid–electrolyte interface (SEI) can be excluded because it occurs at a higher voltage of 4.5 V. Therefore, after the first cycle, the composition of the oxidized electrode was $\approx \text{K}_{0.24}\text{V}_2\text{O}_5$. The subsequent discharge–charge cycles are shown in Figure 3b. The faradaic yield progressively increased with increasing cycles, from 0.96 Na^+ per mol (134 mAh g^{-1}) for cycle 2 to 1.14 Na^+ per mol (160 mAh g^{-1}) for cycle 10. A quantitative charge process was obtained, showing the excellent reversibility of the Na insertion–extraction process. Further cycling show the discharge–charge curves superimpose with an excellent capacity retention of 152 mAh g^{-1} and 140 mAh g^{-1} after 50 and 80 cycles, respectively, at C/10 (Figure 3c) and still 130 mAh g^{-1} after 100 cycles at various C-rates between C/10

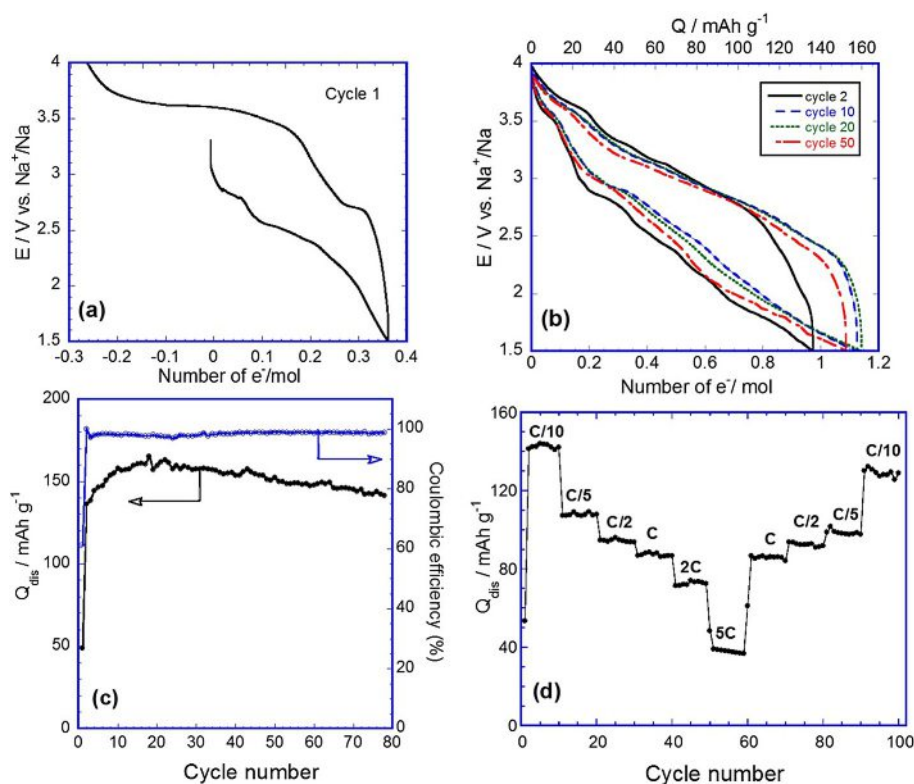


Figure 3. Electrochemical characterizations and performance of the KVO electrode as cathode material for SIBs. a) First discharge–charge cycle (C/10 rate). b) Extended galvanostatic discharge–charge cycles from the second cycle (C/10 rate). c) Discharge capacity as a function of the number of cycles (C/10 rate). d) Rate capability study in the C/10–5C range.

and 5C (Figure 3d). The results of the rate capability tests from C/10 to 5C are shown in Figure 3d.

A good stability was obtained regardless of the C rate. The capacity decreased from 144 mAh g^{-1} at C/10 to 106 mAh g^{-1} at C/5, 94 mAh g^{-1} at C/2 and 73 mAh g^{-1} at 2C. A significant drop in capacity was only observed for 5C ($\approx 40 \text{ mAh g}^{-1}$) but the same value of 94 mAh g^{-1} recovered at C/2 indicates that the structure can support high C-rate without irreversible damage. Except for the bilayered V_2O_5 nanobelts^[24] and the ϵ' - V_2O_5 phase^[22] delivering approximately 200 mAh g^{-1} , the present KVO exhibited the highest capacity with a maximum value of 160 mAh g^{-1} . Indeed, most of the capacity values obtained for V_2O_5 oxides, bronzes and derivatives do not exceed 120 – 150 mAh g^{-1} [20, 21, 25–32]

We investigated the structural changes during the Na insertion–extraction process in KVO. The XRD patterns and Raman spectra of the KVO electrodes are shown in Figure 4 and 5, respectively. For this highly oriented material, the evolution of the 001 reflection line (Figure 4a) is of particular interest. We checked if the structure of the pristine KVO material was re-

tained after the first reduction process involving the insertion of ≈ 0.36 Na ions in KVO (Figure 3a). Only a decrease in the c parameter was observed, from 9.49 \AA in the pristine material to 9.07 \AA for the reduced $\text{Na}_{0.36}\text{KVO}$ electrode. The reverse trend could be seen upon the oxidation involving sodium and potassium extraction. Indeed, the departure of large interlayer cations results in stronger repulsion between the negative V_2O_5 layers and consequently the corresponding interlayer c parameter increased from 9.07 to 9.32 \AA . Then, during the second discharge, further Na insertion in KVO induced a slight decrease in the interlayer spacing, as shown by the progressive shift toward higher angle observed in the $0.2 \leq x \leq 1$ composition range (Figure 4a), to reach $c = 9.02 \text{ \AA}$ for the fully reduced Na_1KVO composition ($\Delta c/c \approx 3\%$). Once again, the reverse trend was observed upon Na extraction, with a c value of 9.30 \AA recovered after the second cycle. Remarkably, the XRD pattern of an electrode after 50 cycles (Figure 4b) was superimposable to the one after one cycle, showing the high stability of the structure upon cycling and no amorphization phenomenon. It was indexed in the same monoclinic $C2/m$ symmetry, with unit cell parameters of $a = 11.54 \text{ \AA}$, $b = 3.47 \text{ \AA}$; $c = 9.30 \text{ \AA}$. The Raman spectra evolution during the second discharge (Figure 5) indicated progressive band broadening probably owing to an increase in the electronic conductivity of the material upon sodiation. However, a remarkable recovery of the KVO Raman fingerprint was observed after cycling, indicating the in-plane structural arrangement of KVO layers was not affected, even upon extended cycling. Furthermore, the Raman spectrum obtained after 50 cycles (Figure 5) does not show evidence of any secondary phase formed at the electrode surface during cycling.

These results demonstrate the high stability of the bilayered structure of KVO. The existence of a large interlayer spacing combined with the presence of K^+ ions, acting as pillar species, makes possible the reversible insertion of up to 1.14 sodium ions. As observed in the case of lithium insertion,^[33] the layered structure of KVO, characterized by a large interlayer spacing of 9.5 \AA , nearly twice that encountered in the V_2O_5 parent oxide ($\approx 4.37 \text{ \AA}$), probably explains the facile and reversible Na insertion–extraction process.

The electrochemical kinetics of Na insertion into KVO was investigated using impedance spectroscopy. The Nyquist diagrams obtained during the discharge are shown in Figure 6a. All the diagrams show a well-defined high frequency semi-circle centered at 125 – 200 Hz followed by a straight line with a phase angle of 45° corresponding to the Warburg region (when $\omega \gg 2D_{\text{Na}}/L^2$, L being the maximum length of the diffusion pathway) related to semi-infinite diffusion (see enlarged view in Figure 6b). Then, for the lowest frequencies, the impedance spectra show quasi-vertical lines corresponding to the finite diffusion process ($\omega \ll 2D_{\text{Na}}/L^2$). This behavior is consistent with that expected for a standard insertion compound.^[39] The systematic existence of a Warburg region allowed the calculation of the apparent Na chemical diffusion coefficient D_{Na} ac-

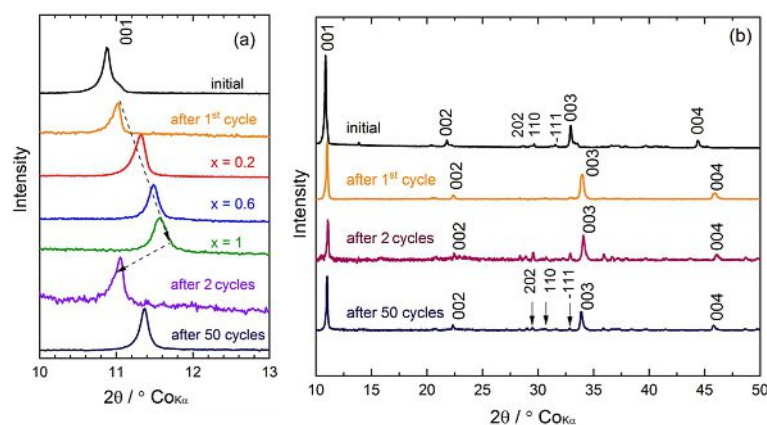


Figure 4. a) Evolution of the 001 reflection of KVO electrodes: pristine electrode, electrode after one cycle, electrode during second discharge ($x = 0.2, 0.6$ and 1 in Na_xKVO), electrode after 2 and 50 cycles at C/10. b) XRD patterns of initial and cycled KVO electrodes (after 1, 2 and 50 cycles at C/10).

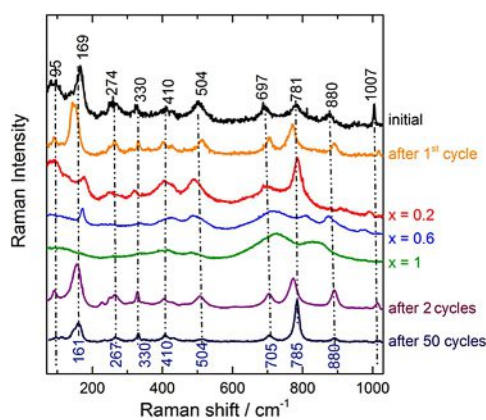


Figure 5. Raman spectra of KVO electrodes: pristine electrode, electrode after one cycle, electrode during second discharge ($x = 0.2, 0.6$ and 1 in Na_xKVO), electrode after 2 and 50 cycles at C/10.

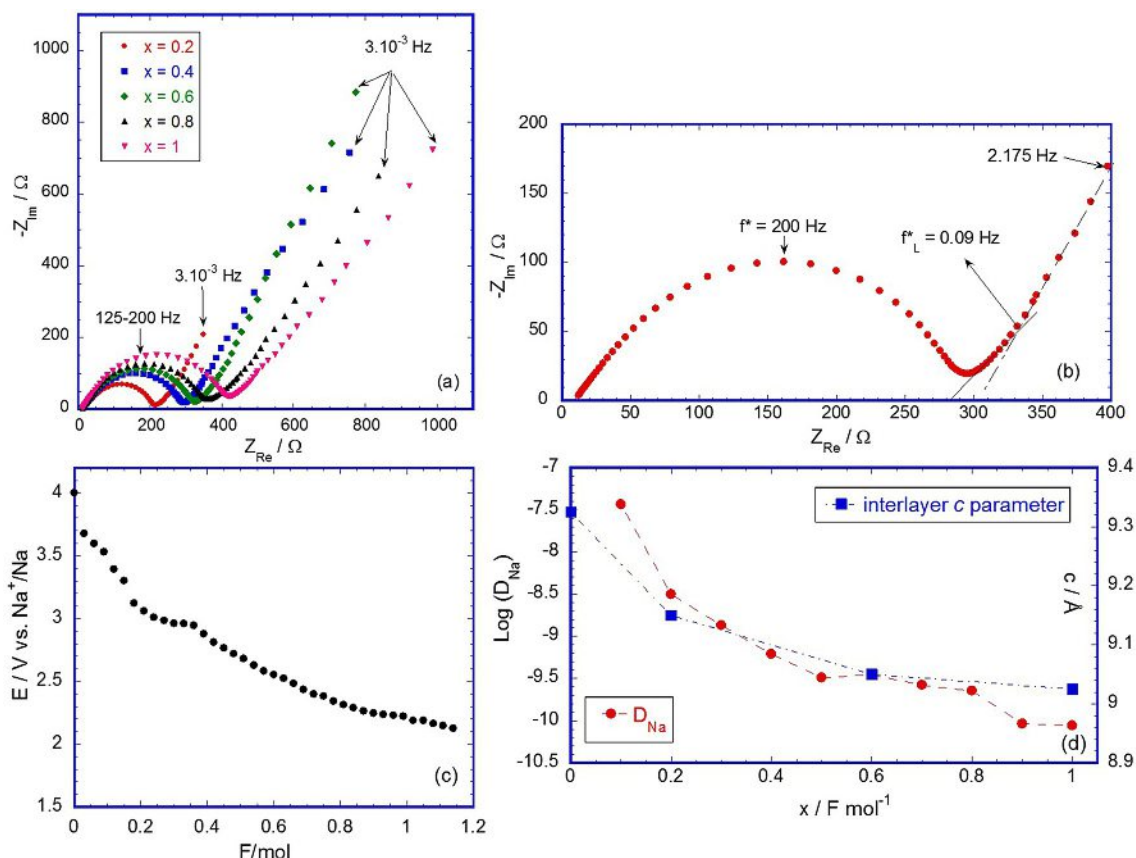


Figure 6. a) AC impedance diagrams of Na_xKVO electrodes. b) Enlarged view of the high frequency region for $x = 0.4$ c) Equilibrium open-circuit potential versus composition for Na-ion intercalation in KVO obtained from GITT measurements. d) Evolution of the apparent sodium coefficient D_{Na} and c parameter as a function of x in Na_xKVO (second discharge).

cording to Equation (2):^[39]

$$A_w = V_m \cdot (dE/dx)_x F \sqrt{2S} D_{\text{Na}}^{1/2} \quad \omega \gg 2D_{\text{Na}}/L^2 \quad (2)$$

in which A_w is the Warburg prefactor, V_m is the molar volume of the active material ($V_m = 61.223 \text{ cm}^3 \text{ mol}^{-1}$), S is the geometric surface area of the electrode (1 cm^2), $(dE/dx)_x$ is the slope, at fixed x , of the equilibrium potential composition curve (Figure 6c).

The evolution of the apparent chemical diffusion coefficient of sodium ions D_{Na} as a function of x in Na_xKVO ($0 < x \leq 1$) is shown in Figure 6d. The rate of sodium transport was higher at the beginning of the sodiation process, approximately $3.6 \cdot 10^{-8} \text{ cm}^2 \text{ s}^{-1}$ for $x = 0.1$, then it decreased by one order of magnitude for $x = 0.2$ ($D_{\text{Na}} \approx 3 \cdot 10^{-9} \text{ cm}^2 \text{ s}^{-1}$), and again by one order of magnitude between $x = 0.2$ and $x = 0.5$ ($D_{\text{Na}} \approx 3 \cdot 10^{-10} \text{ cm}^2 \text{ s}^{-1}$ for $x = 0.5$). In the $0.5 \leq x \leq 0.8$ composition range, D_{Na} remained constant then decreased again to a value of $10^{-10} \text{ cm}^2 \text{ s}^{-1}$ for the most sodiated compositions ($x = 0.9$ and 1). Therefore, the $\text{K}_{0.24}\text{V}_2\text{O}_5$ material obtained after the first cycle promoted fast transport of Na^+ ions in the large interlayer spacing of 9.32 \AA . The D_{Na} evolution is characterized by a moderate decrease limited to approximately one decade during discharge ($0.2 \leq x \leq 1$). This finding is in good correlation with the slight interlayer contraction combined with the

increasing amount of Na. Scarce data are available on Na^+ mobility in sodiated oxides and bronzes, with very close values in the range 10^{-12} – $10^{-10} \text{ cm}^2 \text{ s}^{-1}$ reported for $\text{Na}_{0.33}\text{V}_2\text{O}_5$,^[25,40] Na_xCoO_2 ,^[41] and $\text{P2-Na}_{0.67}\text{MnO}_2$.^[42]

Conclusions

This study shows that the structural richness of V_2O_5 -based compounds makes them promising cathode materials for Na-ion batteries. Bilayered potassium vanadate $\text{K}_{0.5}\text{V}_2\text{O}_5$ was successfully prepared through a reproducible, facile, and fast solution technique. The as-synthesized material had a large interlayer spacing of 9.5 \AA , which is two times higher than that reported for the $\text{Li}_{0.5-1}\text{V}_2\text{O}_5$ lithium vanadates.^[43] A first cycle in the 4 V – 1.5 V range at $C/10$ acted as an activation process, leading to a new KVO composition $\text{K}_{0.24}\text{V}_2\text{O}_5$ owing to partial potassium extraction. KVO delivered a high reversible specific capacity of 160 mAh g^{-1} at $C/10$ with a good capacity retention, maintaining 152 mAh g^{-1} after 50 cycles. A detailed XRD and Raman spectroscopy investigation provides evidence for weak structural changes upon discharge and charge: Electrochemical sodium insertion–extraction induced weak shrinking–swelling of the KVO host lattice ($\Delta c/c \approx 3\%$) and no significant structural change was detected inside the vanadium oxide slabs. The pillaring effect of K^+ ions probably ensures this par-

ticular and stable behavior upon cycling. Moreover, the apparent chemical sodium diffusion was not significantly affected during discharge, with values decreasing only by approximately one order of magnitude for $0.2 \leq x \leq 1$ in Na_xKVO . This work sheds light on the concept of pillaring species to stabilize host structures of cathode materials. In that way, soft breathing of the framework combined with a high cationic diffusivity results in stable cycling properties and good rate capability.

Experimental Section

Potassium vanadate $\text{K}_{0.5}\text{V}_2\text{O}_5$ was synthesized by a solution route using 1 g of V_2O_5 (Alfa Aesar 99.995%) and 0.5 g of KVO_3 (Alfa Aesar 99.99%) dissolved in 10 cm³ of an aqueous solution containing 30 cm³ H_2O_2 (30%). A fast and exothermic reaction occurred, leading to a fine precipitate. The solid compound was then heat-treated at 570 °C for 5 h under an argon atmosphere. Elemental analysis by atomic absorption spectroscopy combined with redox titration were performed to determine the oxidation state of vanadium ions in the obtained product. This led to the chemical composition $\text{K}_{0.5 \pm 0.02}\text{V}_2\text{O}_5$.

XRD experiments were performed using a Panalytical XPert pro apparatus equipped with a X'Celerator detector and using $\text{Co}_{\text{K}\alpha}$ radiation ($\lambda_{\text{K}\alpha} = 1.789 \text{ \AA}$). Data were then processed on Eva software to score peaks then CelRef to calculate the lattice parameters. The SEM experiments were performed using a LEO 1530 instrument. The Raman spectra were obtained with a LaBRAM HR 800 (Jobin-Yvon-Horiba) Raman micro-spectrometer including Edge filters and equipped for signal detection with a back-illuminated charge-coupled device detector (Spex CCD) cooled by Peltier effect to 200 K. A He:Ne laser (632.8 nm) was used as the excitation source. The spectra were measured in back-scattering geometry. The resolution was approximately 0.5 cm^{-1} . A 100× objective was used to focus the laser light on the sample surface to a spot size of 1 mm². To avoid local heating of the sample, the power of the laser beam was adjusted to 0.2–0.5 mW with neutral filters of various optical densities.

Electrochemical experiments were conducted in sodium half-cells consisting of 2032 coin-type cells with a Na foil as the negative electrode, an electrolyte of 1 M NaClO_4 in propylene carbonate (PC) containing fluoroethylene carbonate (FEC) additive (2% Vol.) and Whatman glass fiber separator. The KVO positive electrode was prepared by mixing 80 wt% of active material with 7.5 wt% of acetylene black, 7.5 wt% of graphite and 5 wt% of PTFE as binder. Approximately 8 mg of this mix was pressed on a stainless-steel grid current collector. The CR2032 coin-cell was assembled in argon-filled glovebox, in which the water and oxygen concentrations were kept to below 1 ppm. Galvanostatic experiments were performed at ambient temperature in the voltage range 1.50 to 4.00 V using a VMP3 Biologic apparatus. Impedance measurements were performed in the frequency range 10^5 Hz to $3 \times 10^{-3} \text{ Hz}$, using the same 2032 coin cell filled with 1 M NaClO_4 in PC. The excitation signal was 10 mV peak to peak. The positive electrode was made of the same composite electrode as the one used in the coin cells. The geometric surface area of the working electrode for impedance measurements was 1 cm². The working electrode composition was adjusted by coulometric titration using a low current density corresponding to a C/10 rate. Equilibrium was considered to have been reached when the open-circuit voltage remained stable ($< 0.2 \text{ mV}$ for 1 h). The open-circuit voltage curve was obtained by performing galvanostatic intermittent titration technique (GITT) measurements on the second discharge cycle, using a very low

current (C/40 rate) and composition steps of $\Delta x = 0.1$, i.e., current pulses of 100 μA for 30 min followed by a relaxation period of 5 h.

To investigate the sodium-driven structural changes in KVO, the cells were discharged to the required composition by galvanostatic reduction at C/10 rate. Equilibrium was considered to be reached when the drift in open-circuit voltage remained below 0.2 mV h^{-1} . After reaching equilibrium, the cell was opened in the glovebox and the positive electrode was removed, rinsed with dimethyl carbonate and placed in specifically designated airtight sample holders to be further analyzed by ex situ X-ray diffraction and Raman spectroscopy. To check the homogeneity, Raman spectra were recorded on 10 different spots of each sample.

Acknowledgements

The authors acknowledge the Agence Universitaire de la Francophonie (AUF), the Vietnam National University, Ho Chi Minh City (projects No. B2011-08-01TD and HS2013-76-01, the Ministry of Education and Science of Kazakhstan (grant number AP05136016-ZRABS) and Campus France for their financial support.

Conflict of interest

The authors declare no conflict of interest.

Keywords: bilayer • cathode material • $\text{K}_{0.5}\text{V}_2\text{O}_5$ • layered potassium vanadate • Na-ion battery

- [1] D. Larcher, J. M. Tarascon, *Nat. Chem.* **2015**, 7, 19.
- [2] C. Grosjean, P. H. Miranda, M. Perrin, P. Poggi, *Renewable Sustainable Energy Rev.* **2012**, 16, 1735.
- [3] S. Komaba, W. Murata, T. Ishikawa, N. Yabuuchi, T. Ozeki, T. Nakayama, A. Ogata, K. Gotoh, K. Fujiwara, *Adv. Funct. Mater.* **2011**, 21, 3859.
- [4] B. L. Ellis, L. F. Nazar, *Curr. Opin. Solid State Mater. Sci.* **2012**, 16, 168.
- [5] V. Palomares, P. Serras, V. Villaluenga, K. B. Hueso, J. Carretero-González, T. Rojo, *Energy Environ. Sci.* **2012**, 5, 5884.
- [6] S. W. Kim, D. H. Seo, X. Ma, G. Ceder, V. Kang, *Adv. Energy Mater.* **2012**, 2, 710.
- [7] V. Palomares, M. Casas-Cabanas, E. Castillo-Martinez, M. H. Han, T. Rojo, *Energy Environ. Sci.* **2013**, 6, 2312.
- [8] H. Pan, Y. S. Hu, L. Chen, *Energy Environ. Sci.* **2013**, 6, 2338.
- [9] M. D. Slater, D. Kim, V. Lee, C. S. Johnson, *Adv. Funct. Mater.* **2013**, 23, 947.
- [10] A. Ponrouch, A. R. Goni, M. R. Palacin, *Electrochem. Commun.* **2013**, 27, 85.
- [11] N. Yabuuchi, K. Kubota, M. Dahbi, S. Komaba, *Chem. Rev.* **2014**, 114, 11636.
- [12] K. Kubota, S. Komaba, *J. Electrochem. Soc.* **2015**, 162, A2538.
- [13] D. Kundu, E. Talaie, V. Duffort, L. F. Nazar, *Angew. Chem. Int. Ed.* **2015**, 54, 3431; *Angew. Chem.* **2015**, 127, 3495.
- [14] J. Y. Hwang, S. T. Myung, Y. K. Sun, *Chem. Soc. Rev.* **2017**, 46, 3529.
- [15] H. Kim, H. Kim, Z. Ding, M. H. Lee, K. Lim, G. Yoon, K. Kang, *Adv. Energy Mater.* **2016**, 6, 1600943.
- [16] Z. Dai, U. Mani, H. T. Tan, Q. Yan, *Small Methods* **2017**, 1, 1700098.
- [17] X. Xiang, K. Zhang, J. Chen, *Adv. Mater.* **2015**, 27, 5343.
- [18] C. Fang, Y. Huang, W. Zhang, J. Han, Z. Deng, Y. Cao, H. Yang, *Adv. Energy Mater.* **2016**, 6, 1501727.
- [19] Y. You, A. Manthiram, *Adv. Energy Mater.* **2018**, 8, 1701785.
- [20] K. West, B. Zachau-Christiansen, T. Jacobsen, S. Skaarup, *Solid State Ionics* **1988**, 28, 1128.
- [21] M. Safrany Renard, N. Emery, R. Baddour-Hadjean, J. P. Pereira-Ramos, *Electrochim. Acta* **2017**, 252, 4.

- [22] R. Baddour-Hadjean, M. Safrany Renard, N. Emery, L. T. N. Huynh, M. L. P. Le, J. P. Pereira-Ramos, *Electrochim. Acta* **2018**, *270*, 129.
- [23] S. Tepavcevic, H. Xiong, V. R. Stamenkovic, X. Zuo, M. Balasubramanian, V. B. Prakapenka, C. S. Johnson, T. Rajh, *ACS Nano* **2012**, *6*, 530.
- [24] D. Su, G. Wang, *ACS Nano* **2013**, *7*, 11218.
- [25] S. Bach, N. Baffier, J. P. Pereira-Ramos, R. Messina, *Solid State Ionics* **1989**, *37*, 41.
- [26] J. P. Pereira-Ramos, R. Messina, S. Bach, N. Baffier, *Solid State Ionics* **1990**, *40–1*, 970.
- [27] H. M. Liu, H. S. Zhou, L. P. Chen, Z. F. Tang, W. S. Yang, *J. Power Sources* **2011**, *196*, 814.
- [28] D. Hamani, M. Ati, J.-M. Tarascon, P. Rozier, *Electrochem. Commun.* **2011**, *13*, 938.
- [29] M. Guignard, C. Didier, J. Darriet, P. Bordet, E. Elkaim, C. Delmas, *Nat. Mater.* **2013**, *12*, 74.
- [30] G. Venkatesh, V. Pralong, O. I. Lebedev, V. Caignaert, P. Bazin, B. Raveau, *Electrochem. Commun.* **2014**, *40*, 100.
- [31] H. He, G. Jin, H. Wang, X. Huang, Z. Chen, D. Sun, Y. Tang, *J. Mater. Chem. A* **2014**, *2*, 3563.
- [32] N. Emery, R. Baddour-Hadjean, D. Batyrbekuly, B. Laïk, Z. Bakenov, J. P. Pereira-Ramos, *Chem. Mater.* **2018**, *30*, 5305.
- [33] S. Bach, A. Boudaoud, N. Emery, R. Baddour-Hadjean, J. P. Pereira-Ramos, *Electrochim. Acta* **2014**, *119*, 38.
- [34] R. Baddour-Hadjean, A. Boudaoud, S. Bach, N. Emery, J. P. Pereira-Ramos, *Inorg. Chem.* **2014**, *53*, 1764.
- [35] K. J. Rao, P. A. Ramankrishnan, R. Gadagkar, *J. Solid State Chem.* **1999**, *148*, 100.
- [36] Y. Oka, T. Yao, N. Yamamoto, *J. Mater. Chem.* **1995**, *5*, 1423.
- [37] R. Baddour-Hadjean, J. P. Pereira-Ramos, C. Navone, M. Smirnov, *Chem. Mater.* **2008**, *20*, 1916.
- [38] M. B. Smirnov, E. M. Roginskii, K. S. Smirnov, R. Baddour-Hadjean, J. P. Pereira-Ramos, *Inorg. Chem.* **2018**, *57*, 9190.
- [39] C. Ho, I. D. Raistrick, R. A. Huggins, *J. Electrochem. Soc.* **1980**, *127*, 343.
- [40] D. Jiang, H. Wang, G. Li, G. Li, X. Lan, M. H. Abib, Z. Zhang, Y. Jiang, *J. Electrochem. Soc.* **2015**, *162*, A697.
- [41] B. V. Rami Reddy, R. Ravikumar, C. Nithya, S. Gopukumar, *J. Mater. Chem. A* **2015**, *3*, 18059.
- [42] D. Tie, G. Gao, F. Xia, R. Yue, Q. Wang, R. Qi, B. Wang, Y. Zhao, *ACS Appl. Mater. Interfaces* **2019**, *11*, 6978.
- [43] R. Baddour-Hadjean, E. Raekelboom, J. P. Pereira-Ramos, *Chem. Mater.* **2006**, *18*, 3548.

Manuscript received: July 31, 2019

Revised manuscript received: October 1, 2019

Accepted manuscript online: October 9, 2019

Version of record online: October 30, 2019

CHAPTER 4

V₂O₅ polymorphs as cathode material in aqueous rechargeable Zinc batteries

4.1 Aqueous rechargeable Zinc batteries: a state of the art

4.1.1 Introduction

Energy-storage devices are now powering our world due to concerning the climate change. Sustainable energy resources such as solar and wind have entered the global spotlight, triggering the search for reliable, low-cost electrochemical energy storage. An ideal energy-storage device that is characterized by high capacity, fast charge/discharge capability, safety, environmental friendliness, and low cost is of vital important for today's society. Among the various options, lithium-ion batteries are currently the most attractive candidates due to their high energy density, and foothold in the marketplace [1], [2]. However, their toxicity, poor durability (≤ 5 years) and high cost ($\geq \text{USD}2.35/\text{Wh}$ every 25 years), along with the safety issues (very high degree of reactivity with water, flammable organic solvent) make them difficult to use in smart grids. In addition, LIBs have limited rate capability and power density due to the low ionic conductivity of organic electrolytes. Therefore, the development of high energy density and ecologically friendly rechargeable battery technology is crucial.

Aqueous rechargeable batteries (ARBs), which utilize low cost and safe water-based electrolytes, are promising alternatives. The high ionic conductivities of aqueous electrolytes (up to 1 S cm^{-1}) compared to non-aqueous electrolytes ($\sim 1\text{-}10 \text{ mS cm}^{-1}$) favor high rate capabilities suitable for emerging applications [3], [4].

4.1.2 Aqueous Rechargeable Li-ion batteries.

In 1994, Dahn et al. reported VO₂/LiMn₂O₄ rechargeable aqueous “rocking-chair” type battery (**Figure 1a**), in which metal-ions are inserted/extracted from the active material during the cycling [5]. 5M LiNO₃ and 0.001M LiOH used as electrolyte, the system delivers average voltage of 1.5 V, which is competitive with Pb-acid batteries. More recently, except traditional “rocking-chair” type battery, hybrid design with intercalation cathode with metal anode (**Figure 1b**) or combination of intercalation anode and metal oxide/sulphide (**Figure 1c**) was investigated (LiMn₂O₄//Zn [6], LiFePO₄//Zn [7], V₂O₅//Zn [8], Ni(OH)₂//TiO₂ [9], Co_xNi_{2-x}S₂//TiO₂ [10]). The main difference from “rocking-chair” type, these batteries operate based on two reversible redox processes on anode and cathode, separately. This reaction can be

zinc deposition/dissolution or proton-induced oxidation/reduction or lithium insertion-extraction reactions.

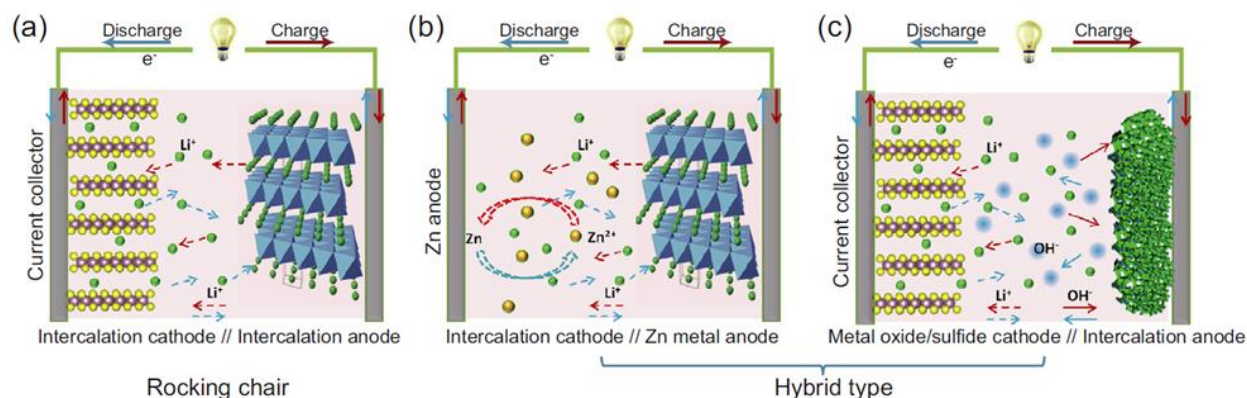


Figure 1. Schematic illustration of “rocking chair” and “hybrid type” aqueous rechargeable batteries [11].
Copyrights reserved

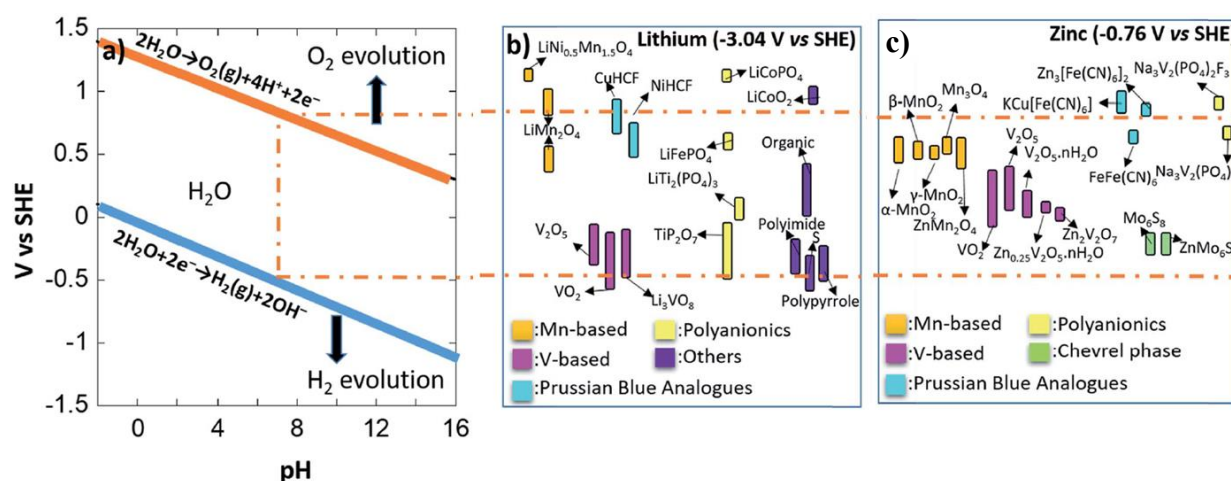


Figure 2. (a) Potential vs pH stability diagram. Main insertion materials studied as positive and negative electrodes in aqueous rechargeable lithium ion (b) and zinc ion batteries (c) [12]. Cpyrights reserved

The cathode materials exhibiting high operating voltage are more attractive, therefore most studies are devoted to LiMn_2O_4 or layered LiMO_2 (M: Ni, Co, Mn) or LiFePO_4 (lower working potential result on energy density). Together with low cost, abundant material source and environmentally benign making LiMn_2O_4 most promising cathode material in aqueous battery.

For Aqueous Rechargeable Li-ion batteries one of the attractive positive materials LiMn_2O_4 suffers from capacity limitation and degradation. At high pH value oxygen evolution occurs during the charge and H^+ or Li^+/H^+ co-insertion may occur at low pH [5], [13], [14], [15, Ch. 1]. In order to increase structural stability several strategies like morphological optimization [4], [16]–[18], metal ions doping [19], [20] have been proposed.

In addition, vanadium oxides [21]–[26], molybdenum oxide [27], titanium oxide [9], [28]–[30], polyanionic [31]–[36] and organic compounds [37] have been used as anode material for Aqueous Rechargeable Li-ion batteries with LiMn_2O_4 which are summarized in **Table 1**.

Table 1. Electrochemical properties of Full-Cell for ALIBs, adapted from [38]

Cathode	Anode	Electrolyte	Average voltage [V]	Capacity retention	Capacity [mAh g ⁻¹]	Ref
LiMn_2O_4	TiP_2O_7	5 M LiNO_3	1,35	35% (25) at C/10	42	[33]
LiMn_2O_4	$\text{LiTi}_2(\text{PO}_4)_3$	1 M Li_2SO_4	1,5	80% (200) at 10 mA cm ²	-	[31]
LiMn_2O_4	$\text{Li}_x\text{V}_2\text{O}_5$ -Ppy	5 M LiNO_3	1,0	86% (60) at C/5	43	[39]
LiMn_2O_4	TiO_2	3.5 M LiCl /0.25 M Li_2SO_4	1,9	90% (100) at 10 C	130	[30]
LiMn_2O_4	VO_2	5 M LiNO_3 /0.001 M LiOH	1,1	72% (50) at 0,01 A g ⁻¹	63	[25]
LiMn_2O_4	$\text{Na}_2\text{V}_6\text{O}_{16} \cdot 0.14\text{H}_2\text{O}$	satd Li_2SO_4	0,8	90% (200) at 0,3 A g ⁻¹	80	[40]
LiMn_2O_4	MoO_3 -Ppy	0,5M Li_2SO_4	1.2	90% (150) at 1 A g ⁻¹	90	[27]

Following the LiMn_2O_4 works above, $\text{LiMn}_2\text{O}_4//\text{TiO}_2$ in 3.5M LiCl and 0.25M Li_2SO_4 (pH=10) exhibits high operating voltage of 2V, high-rate discharge capability and excellent cyclability (**Figure 3**) [30].

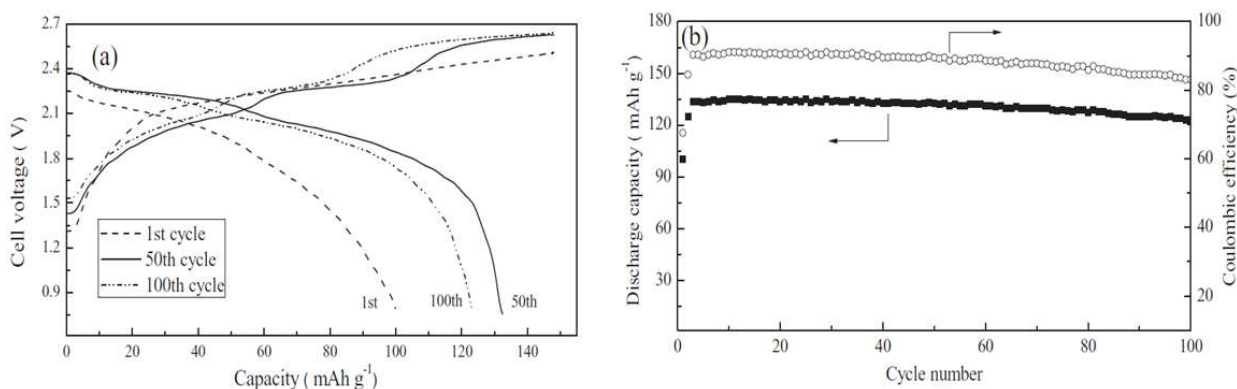


Figure 3. (a) The charge-discharge profile and (b) Cycle performance of TiO₂//LiMn₂O₄ at 10C in 3.5M LiCl and 0.25M Li₂SO₄ (pH=10) [30]

Since that, many aqueous systems have been studied by using different positive and negative electrodes [1], [33], [41]–[49]. Currently, the dissolution or reaction of electrode materials with water is challenge, which impacts on cycle performance of the battery systems. The main ways of solving this problem are: (i) use of high concentrated electrolytes [50]–[52]; (ii) control of pH in electrolyte [3], [13], [53]; (iii) remove of dissolved O₂ in electrolyte [3]; (iiii) surface coating of electrode [39], [54]–[57].

Recently, Tron et al reported AlF₃ coated LiFePO₄/Activated carbon cell with capacity of 120 mAhg⁻¹ at 1C in 1M Li₂SO₄ electrolyte [58]. The well designed and specially prepared spherical nano LiFePO₄/C anode and LiMn₂O₄ cathode are reported by Zeng [59]. The system exhibits 140 mAh g⁻¹ at 2C with working voltage of 0.4 V in 0.5 M Li₂SO₄ electrolyte.

Coating with conductive polypyrrole (Ppy) or carbon coating on LiV₃O₈ will enhance cycle properties in terms of capacity, rate capability and stability of electrode. These approaches could solve dissolution of vanadium ions, keep the initial crystal structure changes and reduce the amorphization upon the cycling. Liu et al. reported Ppy-coated LiV₃O₈/AC (activated carbon) cell using 0.5 M Li₂SO₄ electrolyte. Elemental analysis results show that in electrolyte with Ppy-coated electrode after 10 cycles has 10 times less dissolved vanadium than in pristine LiV₃O₈ [54]. Zhou et al. reported Ppy@MoO₃/LiMn₂O₄ system exhibits stable cycling with high rate capability [27].

The electrochemical performance of positive electrodes like LiCoO₂, LiNi_{1/3}Co_{1/3}Mn_{1/3}O₂ and LiMnPO₄ has been investigated in 3 electrode cells. It depends on electrolyte pH due to the possible proton (H⁺) intercalation in LiOH electrolyte [60], while with Li₂SO₄ or LiNO₃ it is

possible to insert/extract lithium. The possible proton intercalation can be solved by using concentrated electrolytes and high pH value.

Ruffo et al. reported LiCoO_2 positive electrode in different concentrations of LiNO_3 . At voltage window 0.55 – 1.55 V (vs. SHE) it delivers capacity of 100 -120 mAh g^{-1} [61]. Tang et al. in his work use crystalline nano- LiCoO_2 gains 140 mAh g^{-1} at 7C with 0.5 M Li_2SO_4 electrolyte (Figure 4) [62].

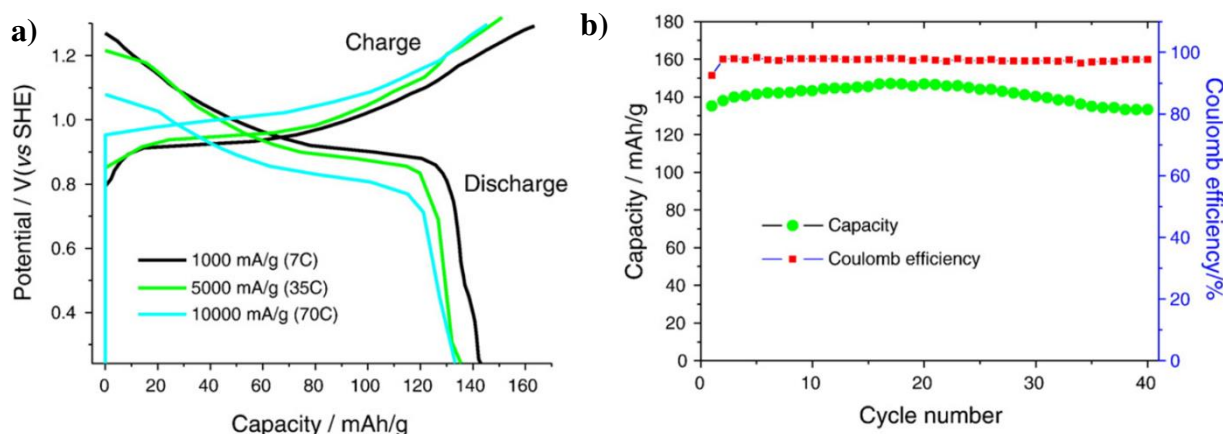


Figure 4. (a) Charge-discharge profile at different C-rate (b) Cycle performance at 7C of nano- LiCoO_2 in 0.5 M Li_2SO_4 [62].

Luo in his work, experimentally and theoretically demonstrates that most of discharged LIC negative electrodes in the presence of oxygen in electrolyte, could react with water and oxygen at any value of pH, which result on capacity fading [3]. Zhao et al. demonstrated that by O_2 elimination in electrolyte and use of high concentrated 9 M LiNO_3 $\gamma\text{-LiV}_3\text{O}_8//\text{LiFePO}_4$ system exhibits high capacity retention (90%) for 500 cycles [36].

ARLB demonstrates series advantages, however the low voltage window of water electrolysis effect on low energy density [63]–[65]. The water decomposition reaction includes overpotential on the surface of electrode materials, and absorption/desorption of water molecules on the electrode surface effect on electrolyte pH, which shifts the decomposition reaction at lower/higher voltage. In order to stabilize or widen the water stability window different salts and concentration can be used [12], [50], [52], [66].

Suo expanded the water stability window of aqueous electrolyte from 1.23 to >3 V by constructing $\text{LiMn}_2\text{O}_4/\text{Mo}_6\text{S}_8$ system (Figure 5), which demonstrated open-circuit voltage of 2.3 V by using “water-in-salt” electrolyte [50]. A “water in salt” electrolyte is obtained by dissolving lithium bis (trifluoromethane sulfonyl) imide (LiTFSI) at extremely high

concentrations (molality >20 m) in water (moles of LiTFSI in kilogram of solvent). The system exhibits 40 and 30 mAh g⁻¹ at 0.15 and 4.5 C, respectively.

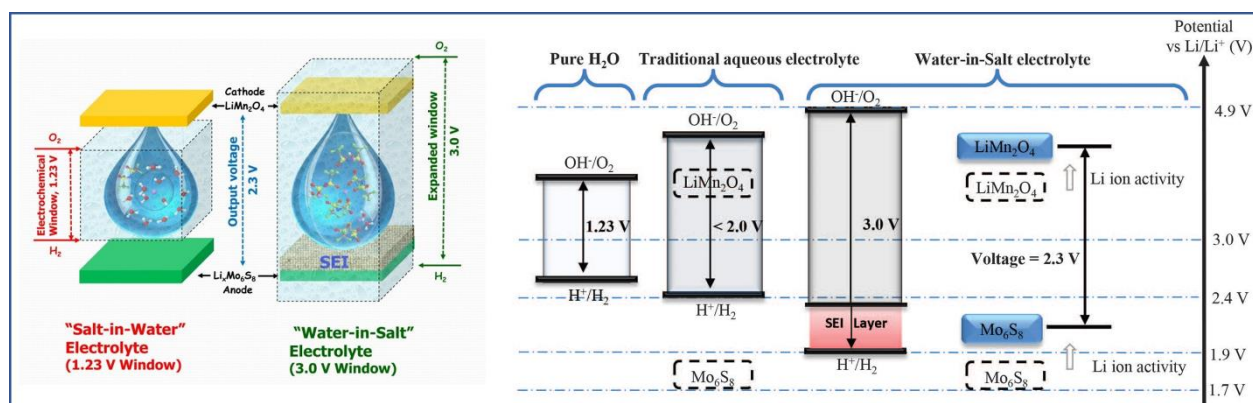


Figure 5. Schematic illustration of LiMn₂O₄/Mo₆S₈ system with “water-in-salt” electrolytes. Reprinted from ref. [50]

Though great progress has been achieved, there are still several points need to be solved. Typical anode materials like graphite or silicon can not be used in ARLBs due to the low operating voltage to be stable within the water stability window. Unfortunately, other anode materials with low ionic and electronic conductivity will affect on power density of ARLBs (**Figure 2**). Overall, the development of suitable negative material remains main challenge.

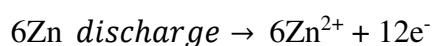
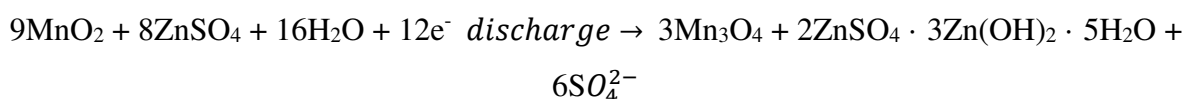
4.1.3 Rechargeable Aqueous Zinc-ion batteries

Besides the above-mentioned aqueous Li-ion battery systems, Aqueous Zinc-ion batteries (AZIB) are attracting key interest for grid-scale energy storage [12], [67]. Aqueous Zinc batteries are composed of zinc metal anode, mild neutral or acidic electrolyte, zinc-ion storage cathode. **Table 2** shows the ionic radius, standard potential, theoretical gravimetric and volumetric capacity, crustal abundance and cost of metallic cations. It is clear that zinc metal can be used as anode material in aqueous electrolyte due to the low cost and safe aqueous electrolytes related to the low oxidation/reduction potential (-0.76 V vs SHE). In addition, multivalent AZIB allows the multivalent electron transfers during the electrochemical reaction and could reach high energy and power density [68]. The ionic radius of Zn²⁺ ion is 0.74 Å which is close to the value of Li⁺ (0.76 Å), however the higher charge/radius ratio which cause polarizing character and may limit migration dynamics [68]. Therefore, many compounds with tunnel or layered type structure enable the insertion/extraction of zinc [69].

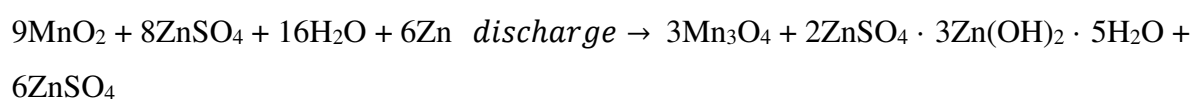
Table 2. A comparison of different ions in the ionic radius, standard potential, theoretical gravimetric and volumetric capacity, crustal abundance and cost, adapted from [69].

Characteristics	Li ⁺	Na ⁺	K ⁺	Zn ²⁺
Ionic radius [Å]	0,76	1,02	1,38	0,74
Standard potential [V] vs SHE	-3,05	-2,71	-2,93	-0,76
Theoretical gravimetric capacity (mAh g ⁻¹)	3829	1165	685	820
Theoretical volumetric capacity (mAh cm ⁻³)	2044	1128	610	5854
Crustal abundance [ppm]	18	23000	21000	79
Cost of metal anode (USD kg ⁻¹)	19,2	3,1	13,1	2,2

The first battery with metallic zinc as negative electrode was investigated by Volta in 1799 in different zinc batteries like, Zn-Mn, Ni-Zn, Zinc-air batteries due to the high capacity, redox potential [70]–[72]. Among them, rechargeable Zn-MnO₂ battery was investigated, however low cyclability and discharge capacity were observed due to the formation of zinc dendrites [73]–[75]. In 1988, the first investigation on aqueous ZIBs was investigated by Yamamotos group in Zn/MnO₂ system by replacing the alkaline electrolyte to zinc sulfate, which opened new direction in aqueous zinc-ion batteries [76]. According to the results overall chemical change at positive and negative electrode during the discharge in Zn/ZnSO₄/γ-MnO₂ cell is:



It gives the following overall reaction:



To date, various cathode materials for AZIB have been reported in the literature, including: Mn-based cathodes [67], [77]–[79], V-based cathodes [80]–[82], Prussian blue analogs [83], [84], polyanion compounds etc. [85], [86]. The reaction mechanisms in ZIB system are complicated and controversial in comparison to traditional lithium-based batteries. According to the literature, the redox reactions in ZIB system mainly involve three mechanisms: Zn²⁺ insertion/extraction [67], [80], [87], chemical conversion reaction [88] and H⁺/Zn²⁺ co-insertion/extraction [89], [90].

4.1.3-1 Mn-based cathode materials

Manganese oxide with multiple valence states have various crystal structures including α -, β -, γ -, δ -, λ - and R-types [91]. The main fundamental unit in MnO_2 polymorphs is $[\text{MnO}_6]$ octahedral, which is formed by hexagonal oxide ions and enable to accommodate zinc ions in tunnel or layer structure [92], [93]. The size of the tunnels determined by the number of $[\text{MnO}_6]$ octahedrons, wherein, α - MnO_2 has large $[2 \times 2]$ tunnel structure along the c -axis with four edge-sharing $[\text{MnO}_6]$ octahedral units, β - MnO_2 has $[1 \times 1]$ tunnels, todorokite MnO_2 has larger $[3 \times 3]$ tunnels and γ - MnO_2 has $[1 \times 1]$ and $[1 \times 2]$ hybrid tunnels along the b -axis, δ - MnO_2 has layered structure with larger interlayer space ($\sim 7 \text{ \AA}$) and λ - MnO_2 with spinel structure (**Figure 6**). The different types of crystal structure result in difference in electrochemical performance and structural evolution during cycling [67], [94].

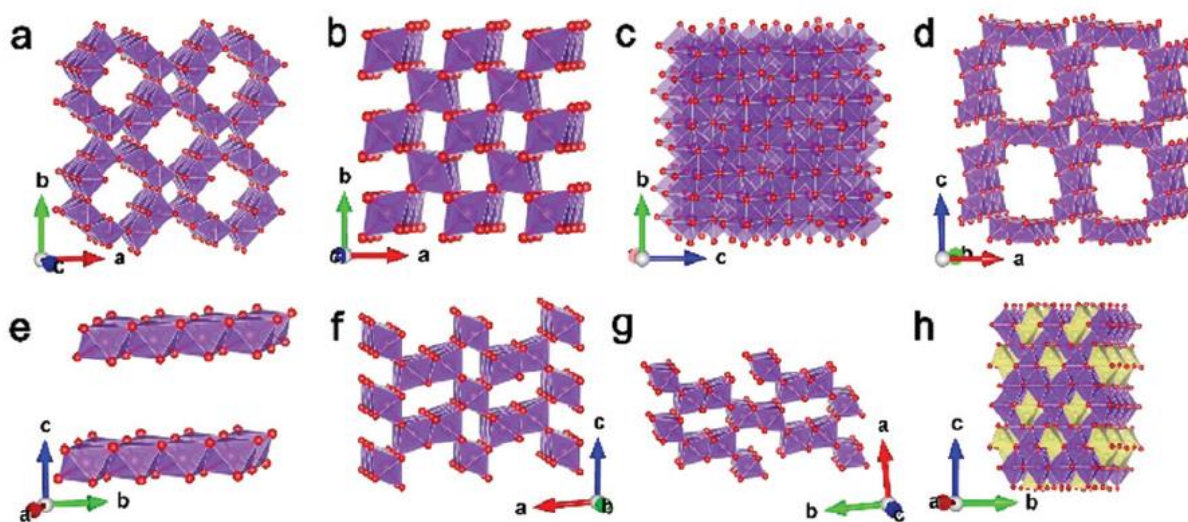


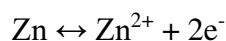
Figure 6. Schematic diagram of various crystal structures of manganese-based materials: (a) α - MnO_2 ; (b) β - MnO_2 ; (c) λ - MnO_2 ; (d) todorokite MnO_2 ; (e) δ - MnO_2 ; (f) γ - MnO_2 ; (g) R- MnO_2 ; (h) ZnMn_2O_4 . Reprinted from ref [91].

Zn^{2+} insertion/extraction mechanism

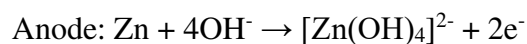
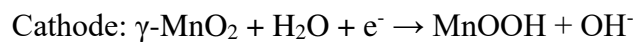
Kang reported $\text{Zn}/\alpha\text{-MnO}_2$ system (**Figure 7a**) with stable cyclability at 6C with capacity of 100 mAh g^{-1} in ZnSO_4 or $\text{Zn}(\text{NO}_3)_2$ electrolyte [67]. As shown in **Figure 7 b** there are two peaks at 1.3 V during reduction and 1.7 V during oxidation vs. Zn^{2+}/Zn . XRD analysis of MnO_2 electrode reveals that, ZnMn_2O_4 forms during the insertion of Zn^{2+} into $\alpha\text{-MnO}_2$, while during the extraction pure $\alpha\text{-MnO}_2$ was observed (**Figure 7 d**). The cathodic process can be described as:



And anodic process can be described as:



The working principle of ZIBs are very close to Zn/MnO₂ alkaline batteries, where γ - or δ -MnO₂ usually used as cathode in alkaline electrolyte (KOH or NaOH). However, the chemistry of these batteries is different. The first discharge of alkaline Zn/MnO₂ could be expressed as:



The second step which is irreversible with further discharge:

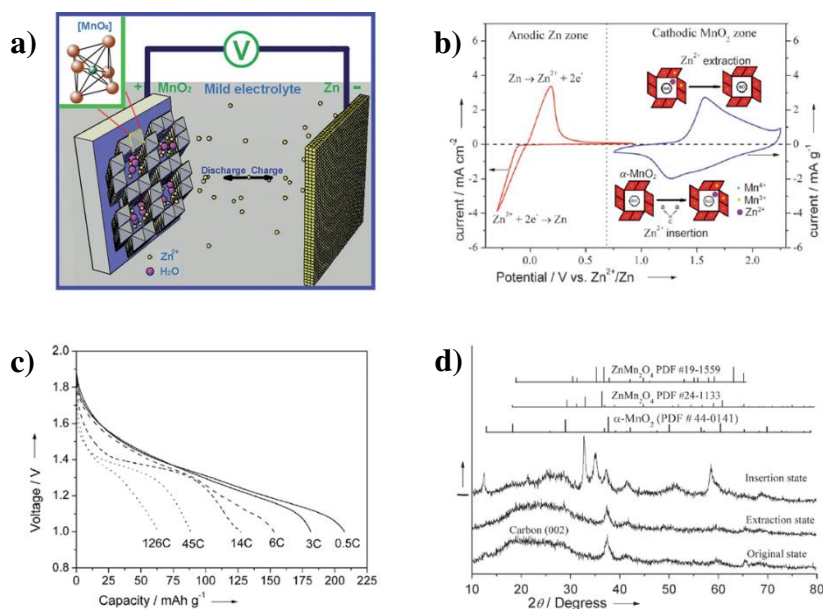
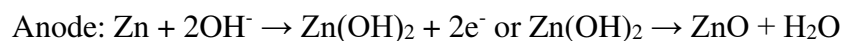
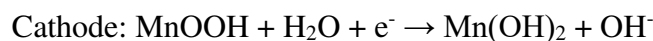


Figure 7. (a) Schematic illustration of zinc ion battery. (b) Cyclic voltammogram of zinc anode (red line) and α -MnO₂ cathode (blue line) in 0.1M Zn(NO₃)₂ (pH=5.2). (c) Discharge curves of Zn// α -MnO₂ system at various C-rate. (d) XRD patterns of α -MnO₂ electrode at different state. Copyrights reserved [67].

Kim et al. reported Zn/ γ -MnO₂ aqueous system with a phase transition of γ -MnO₂ to spinel ZnMn₂O₄ at initial stages of insertion with further transformation to γ -Zn_xMnO₂ phase (**Figure 8**). By continuous insertion of Zn²⁺ ions, layered L-Zn_yMnO₂ phase can be formed [87].

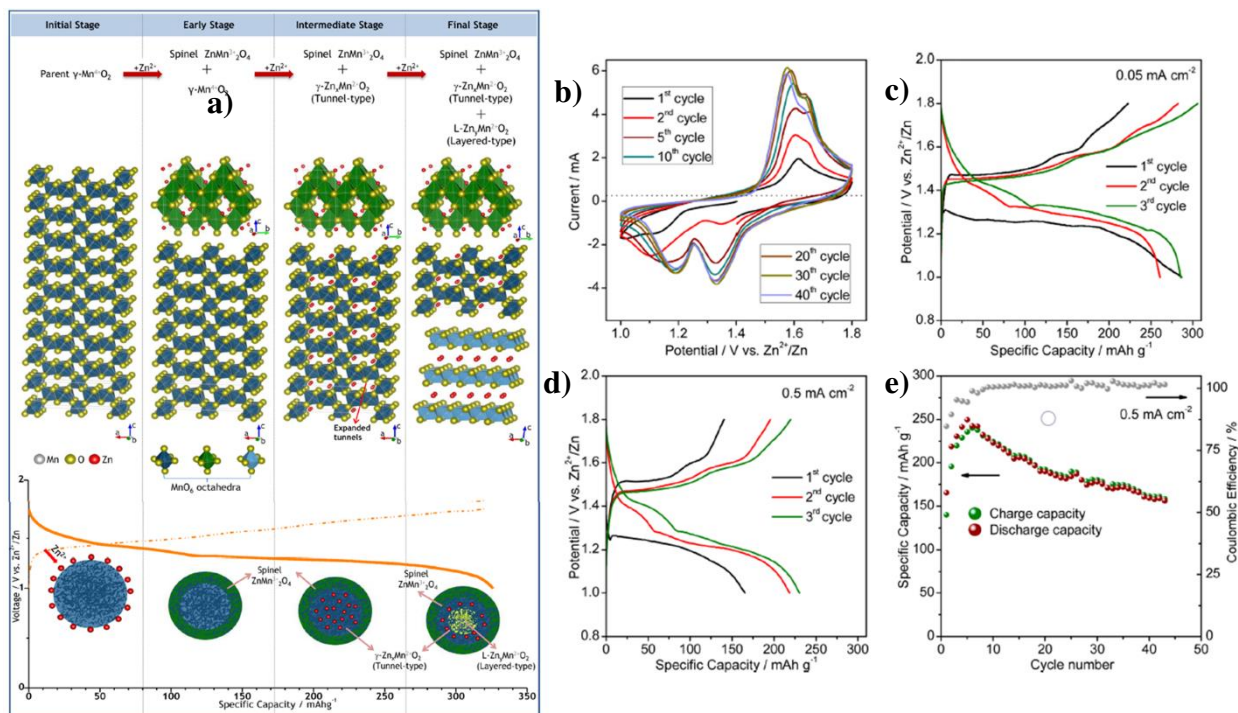


Figure 8. (a) Schematic illustration of Zinc insertion into $\gamma\text{-MnO}_2$ cathode. (b) CV curves until 40 cycles of Zn// $\gamma\text{-MnO}_2$ cell. The initial cycles at various C-rate (c) 0.05 mA cm^{-2} and (d) 0.5 mA cm^{-2} . (e) Cycle performance of the cell at 0.5 mA cm^{-2} at $0.8 - 1.8 \text{ V}$ range in 1M ZnSO_4 ($\text{pH}=4$). Copyrights reserved [87].

$\beta\text{-MnO}_2$ may not be desirable material for zinc insertion due to the narrow 1×1 tunnel structure [95]. However, the control of particle size and shape can influence on the electrochemical properties of $\beta\text{-MnO}_2$ [96].

Some investigations focused on Zn^{2+} insertion into the $\alpha\text{-MnO}_2$ host, have demonstrated phase transition from tunnel structure ($\alpha\text{-MnO}_2$) to layered Zn-buserite or birnessite [97], [98] which is different from spinel ZnMn_2O_4 mentioned above. It was found that almost 1/3 of the manganese of initial $\alpha\text{-MnO}_2$ structure is dissolved during discharge to form Zn-birnessite, nevertheless it is fully recovered to become initial $\alpha\text{-MnO}_2$ structure upon recharging.

The dissolution of manganese leads the formation of vacancies in the upper/underlying layers. The slight distortion of the structure results in Zn-birnessite with triclinic lattice. During the charge, Mn^{2+} ions are reversibly inserted back into the layers to reform tunnel structure. The $\alpha\text{-MnO}_2$ has one dimensional $[2 \times 2]$ and $[1 \times 1]$ tunnels, comprised of four identical cross-linking double chains of $[\text{MnO}_6]$ octahedra, that extend along c -axis, the edges are interconnected by corner-sharing MnO_6 octahedra, as shown in **Figure 9** [98]. Conversely, Zn-birnessite (P-1 space group) has layered structure with interlayer space of 7 \AA , similar to the size of $\alpha\text{-MnO}_2$ tunnel. **Figure 9c** exhibits discharge-charge profile of Zn/ $\alpha\text{-MnO}_2$ first two cycles and capacity

retention up to 30 cycles a C/20. During first discharge, a capacity around 194 mAh g⁻¹ was observed and increased to 205 mAh g⁻¹ for second cycle.

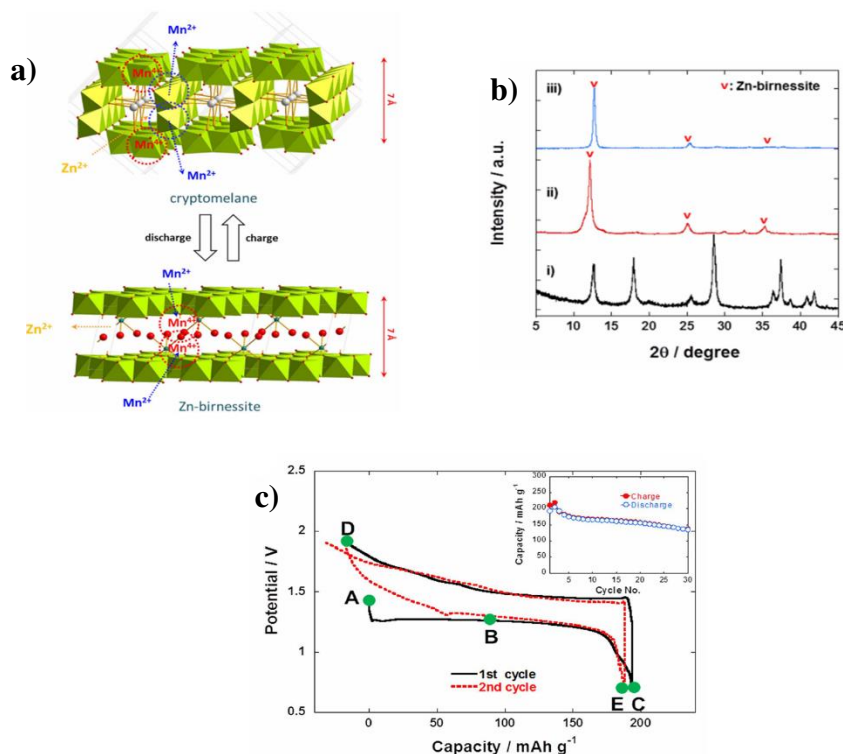


Figure 9. (a) Schematic illustration of zinc insertion into α -MnO₂. (b) X-ray diffraction patterns of i) as-prepared α -MnO₂ ii) hydrothermally prepared Zn-birnessite and iii) fully discharged electrode. (c) Discharge-charge profile of Zn/ α -MnO₂ and cycle performance at C/20 in 1M ZnSO₄ [98].

Cheng et al. demonstrated that tunnel structured MnO₂ polymorphs (α , β , γ) go through the phase transition to layered zinc-buserite during the first discharge in (Zn(CF₃SO₃)₂), which allows zinc insertion/extraction in the host lattice (**Figure 10**) [99]. The phase transformation, electrode pulverization and Mn dissolution lead to capacity fading. By formulating aqueous 3M Zn(CF₃SO₃)₂ + 0.1 M Mn(CF₃SO₃)₂ electrolyte, the Mn²⁺ dissolution can be solved and the electrode integrity can be maintained due to the in situ generated MnO_x layer. The system exhibits 225 mAh g⁻¹ and long-term cyclability over 2000 cycles with 94% capacity retention. The different inserted behaviors of Zn²⁺ in MnO₂ may be attributed to the difference in crystallographic polymorphs that change the insertion thermodynamics and kinetics [67].

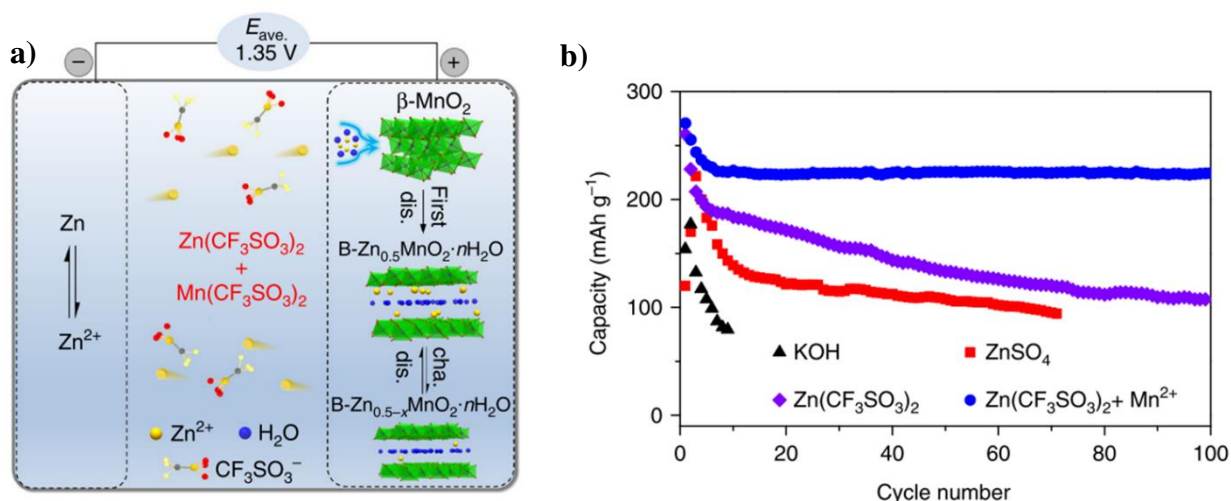


Figure 10. (a) Schematic illustration of Zn//MnO₂ cell using CF₃SO₃⁻ electrolyte. (b) Comparison of cycle performance of Zn//MnO₂ cell with electrolytes of 45wt.% KOH (at 0.32 C), 3M ZnSO₄, 3M Zn(CF₃SO₃)₂, and 3M Zn(CF₃SO₃)₂ with 0.1 M Mn(CF₃SO₃)₂ additive at 0.65 C at 0.65C. nC equals the rate to charge/discharge the theoretical capacity (308 mAh g⁻¹) of MnO₂ in 1/n hours [99].

Other types of Manganese based electrode materials have been reported including MnO₂-birnessite [100], MnO [101], Mn₂O₃ [79], Mn₃O₄ [102], [103], MgMn₂O₄ [104]. **Table 3** shows the typical Mn-based materials with electrochemical properties.

Table 3. Electrochemical performances of Mn-based electrodes, adapted from [68].

Material	Electrolyte	Potential window [V]	Specific capacity mAh g ⁻¹	Capacity retention	Ref
α-MnO ₂	1 M ZnSO ₄	1.0–1.8	233	65% (50) at 83 mA g ⁻¹	[105]
α-MnO ₂	2 M ZnSO ₄ + 0.1 M MnSO ₄	1.0–1.8	161	92% (5000) at 5C	[88]
α-MnO ₂ /CNT	2 M ZnSO ₄ + 0.5 M MnSO ₄	1.0–1.9	400	99% (500) at 1 A g ⁻¹	[106]
α-MnO ₂	1 M ZnSO ₄	0.8–2.0	120	66% (50) at 1C	[98]
β-MnO ₂	3 M Zn(CF ₃ SO ₃) ₂ + 0.1 M Mn(CF ₃ SO ₃) ₂	0.8–1.9	135	94% (2000) at 6.5 C	[99]
β-MnO ₂	1 M ZnSO ₄	1.0–1.8	135	75% (200) at 200 mA g ⁻¹	[96]
δ-MnO ₂	1 M ZnSO ₄	1.0–1.8	112	43% (100) at 83 mA g ⁻¹	[107]

Mn ₃ O ₄	2 M ZnSO ₄	0.8–1.9	106	72% (300) at 0.5 A g ⁻¹	[103]
Binder-free Mn ₃ O ₄	2 M ZnSO ₄ + 0.1 M MnSO ₄	1.0–1.8	~150	100% (500) at 500 mA g ⁻¹	[108]
α-Mn ₂ O ₃	2 M ZnSO ₄ + 0.1 M MnSO ₄	1.0–1.9	82.2	65% (2000) at 2000 mA g ⁻¹	[79]
Na _{0.44} MnO ₂	1 M Na ₂ SO ₄ + 0.5 M ZnSO ₄ + 0.05 M MnSO ₄	1.0–1.9	~340	100% (150) at 100 mA g ⁻¹	[109]
Na _{0.95} MnO ₂	0.5 M Zn(CH ₃ COO) ₂ + 0.5 M CH ₃ COONa	1.0–2.0	40	92% (1000) at 4C	[110]
KMn ₈ O ₁₆	1 M ZnSO ₄ + 0.3 M K ₂ SO ₄	0.8–1.8	77	50% (100) at 1C	[111]
ZnMn ₂ O ₄	1 M ZnSO ₄ + 0.05 M MnSO ₄	0.8–1.9	106.5	84% (300) at 100 mA g ⁻¹	[112]
ZnMn ₂ O ₄	3 M Zn(CF ₃ SO ₃) ₂ + 0.1 M Mn(CF ₃ SO ₃) ₂	0.8–2.0	150	94% (500) at 500 mA g ⁻¹	[77]

Chen et al. reported spinel ZnMn₂O₄ cathode for zinc insertion/extraction with good reversibility. Ex-situ XRD shows the shrink of the lattice space after zinc extraction when cell charged from 0.8 to 1.9 V by shifting of diffraction peak to higher angle [77]. After complete discharge all diffraction peaks are recovered, suggesting reversibility of ZnMn₂O₄ cathode.

While, Mn-based electrode materials suffer from limitation in electrochemical performance due to the poor electronic conductivity and Mn dissolution. High concentration of electrolyte [77], addition of Mn salts [79], doping [113], surface coating [114] could suppress the Mn dissolution.

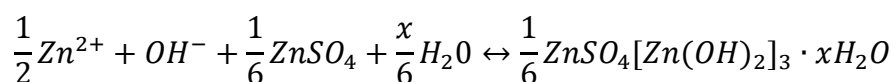
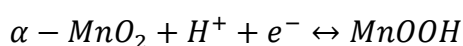
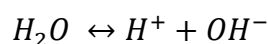
Khamsanga et al. proposed δ-MnO₂ nanoflower structure supported on graphite flake with high electrical conductivity and stable cyclability. The battery displayed initial discharge capacity of 235 mAh g⁻¹ at 200 mA g⁻¹ in comparison to pristine δ-MnO₂ (130 mAh g⁻¹) [115]. Zhu et al. adopted MnO with defects which provides accessible channels for insertion of zinc. The system delivers reversible capacity of 116 mAh g⁻¹ at 1 A g⁻¹ [101].

Chemical Conversion Reaction Mechanism

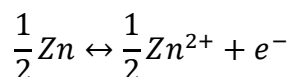
The redox reaction mechanism in Aqueous ZIBs is under investigation due to the side reactions involving proton/water insertion mentioned in ARLBs as a result of lower mobility of divalent

ion [116]. Liu et al. reported Zn/ α -MnO₂ system, in which MnOOH phase is observed at discharged state due to the reaction of MnO₂ with proton from water [88]. To reach a neutral charge in the system, OH⁻ ions will react with ZnSO₄ and H₂O in aqueous electrolyte to form ZnSO₄[Zn(OH)₂]₃·xH₂O phase. The STEM-EDS mapping of α -MnO₂ electrode on discharged state reveals that nanorods and nanoparticles consist of O and Mn, while Zn is distributed on the flakelike compounds. The reaction mechanism can be formulated as:

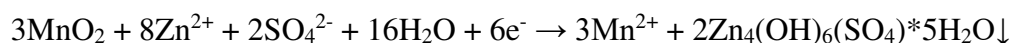
Cathode side:



Anode side:



The increase of Mn²⁺ concentration in electrolyte during the discharge is accompanied by a rise in pH value [MnO₂ + 2H₂O → Mn²⁺ + 4OH⁻] leading to the precipitation of zinc hydroxide sulfate Zn₄(OH)₆(SO₄)·5H₂O on the cathode:



The reaction mechanism of the active conversion reaction between MnO₂ and H⁺ is further confirmed by limited capacity in organic Zn²⁺-ion based electrolytes owing to the absence of H⁺ ion in organic electrolytes (**Figure 11b**). After adding H₂O into organic Zn-based electrolyte, the battery exhibits similar electrochemical performance than in aqueous electrolyte (**Figure 11a**). In addition the consequent formation of ZnSO₄[Zn(OH)₂]₃·xH₂O on the cathode side is also reversible and stable with hydrogenation/dehydrogenation of the MnO₂ cathode. According to the literature mentioned above, several different mechanisms are observed for α -MnO₂, suggesting more precise experiments and analysis methods are required to clarify the reaction mechanisms.

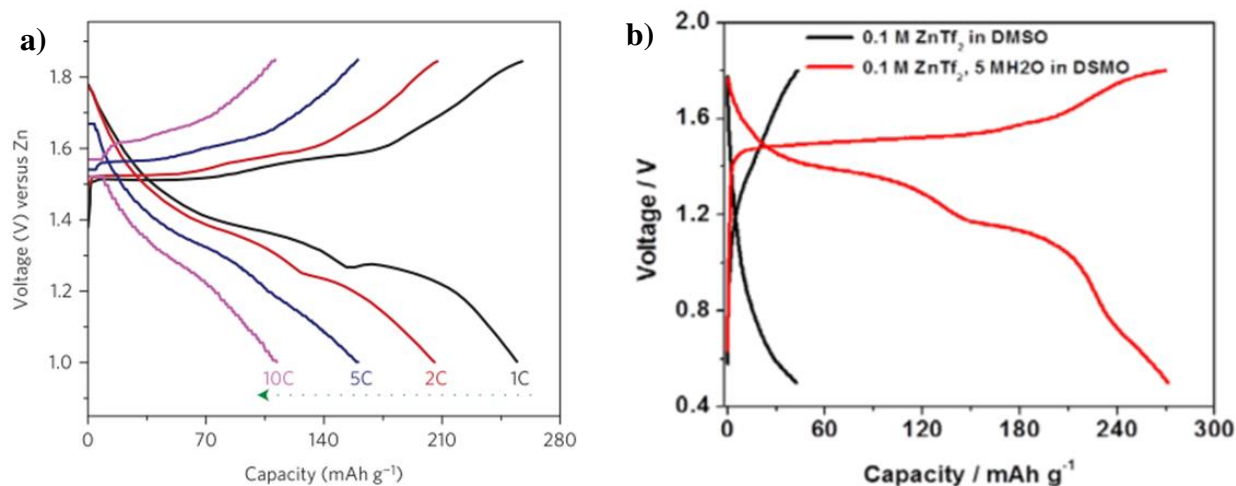


Figure 11. (a) Discharge-charge curves of Zn// α -MnO₂ system in 2M ZnSO₄ and 0.1M MnSO₄ at various C-rates. (b) The comparison of discharge-charge curves of α -MnO₂ electrode in organic 0.1 M ZnTf₂/DMSO electrolyte with and without adding H₂O (2nd cycle at 0.5 A g⁻¹) [88].

H⁺ and Zn²⁺ insertion/extraction mechanism

The electrode materials with tunnel or layered structure may enable co-insertion of H⁺/Zn²⁺. Sun et al. proposed H⁺ and Zn²⁺ insertion mechanism in Zn/ α -MnO₂ system [89]. Discharge galvanostatic intermittent titration technique (GITT) was used to identify the two different regions in profile of MnO₂ electrode, the overvoltage in region II (0.6 V) is larger than region I (0.08 V) (**Figure 12a**). This kind of difference may be attributed to the different ion insertion reactions. Divalent Zn²⁺ exhibits strong electrostatic interactions in host lattice which is related to region II, which is confirmed by electrochemical investigation of MnO₂ electrode in 0.2 M MnSO₄ with/without ZnSO₄ [89] (**Figure 12c**).

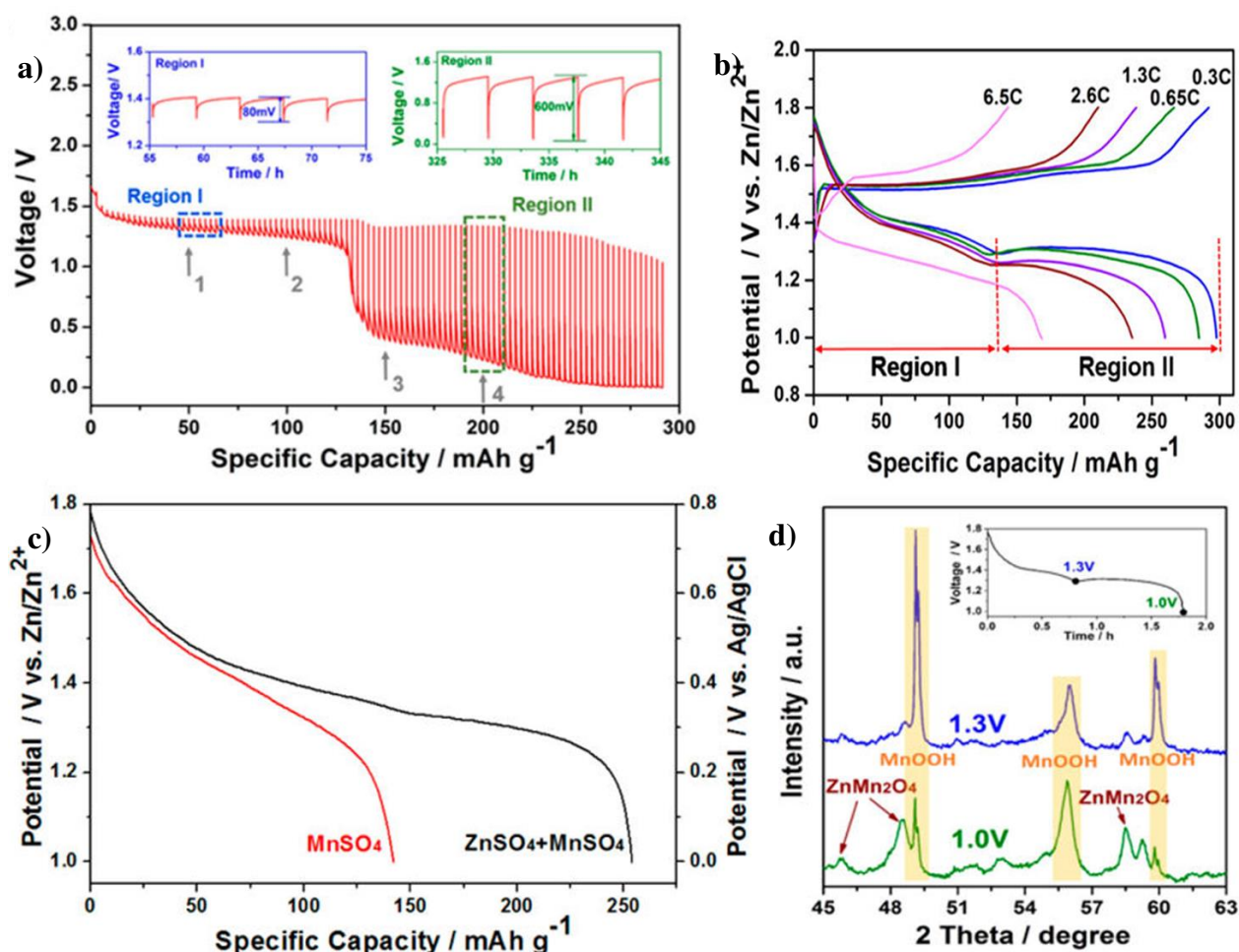


Figure 12. (a) GITT profiles of Zn/MnO₂@CFP cell (50 mA g⁻¹ for 120 s followed by 4 hr rest). (b) first discharge-charge curves of Zn/MnO₂@CFP in 2 M ZnSO₄+0.2 M MnSO₄ electrolyte at various C-rate. (c) Discharge curves of MnO₂@CFP cathode in 0.2 M MnSO₄ solution with or without ZnSO₄ as electrolytes at 0.3 C between 0 and 0.8 V (vs Ag/AgCl) in a three- electrode cell. The three-electrode cell use Pt metal as a counter and the Ag/AgCl electrode as a reference, and the potential has been converted to Zn/Zn²⁺ reference for convenience. (d) Ex-situ XRD of MnO₂@CFP cathode at depth of discharge at 1.3 and 1.0 V. Copyrights reserved [89]

Li et al. constructed Zn/ α -MnO₂ system using bi-cation (1 M Al(CF₃SO₃)₃/1 M Zn(CF₃SO₃)₂) electrolyte with operational potential around 1.7 V [117]. The cell demonstrated excellent cyclability with capacity of ~130 mAh g⁻¹ at 1C (**Figure 13**). The α -MnO₂ in the bi-cation electrolyte possesses the Zn²⁺ and H⁺ co-insertion during the discharge process. During the charge Al³⁺ and H₃O⁺ react with host material to form Al_xMnO₂·nH₂O during the extraction of Zn²⁺ and H⁺. After formation of Al_xMnO₂·nH₂O with layer structure contributes to the high discharge voltage. The 1 M Al(CF₃SO₃)₃ in electrolyte extends electrochemical stability window (from 1.7 to 1.9 V) with further suppression of hydrogen and oxygen evolution reaction.

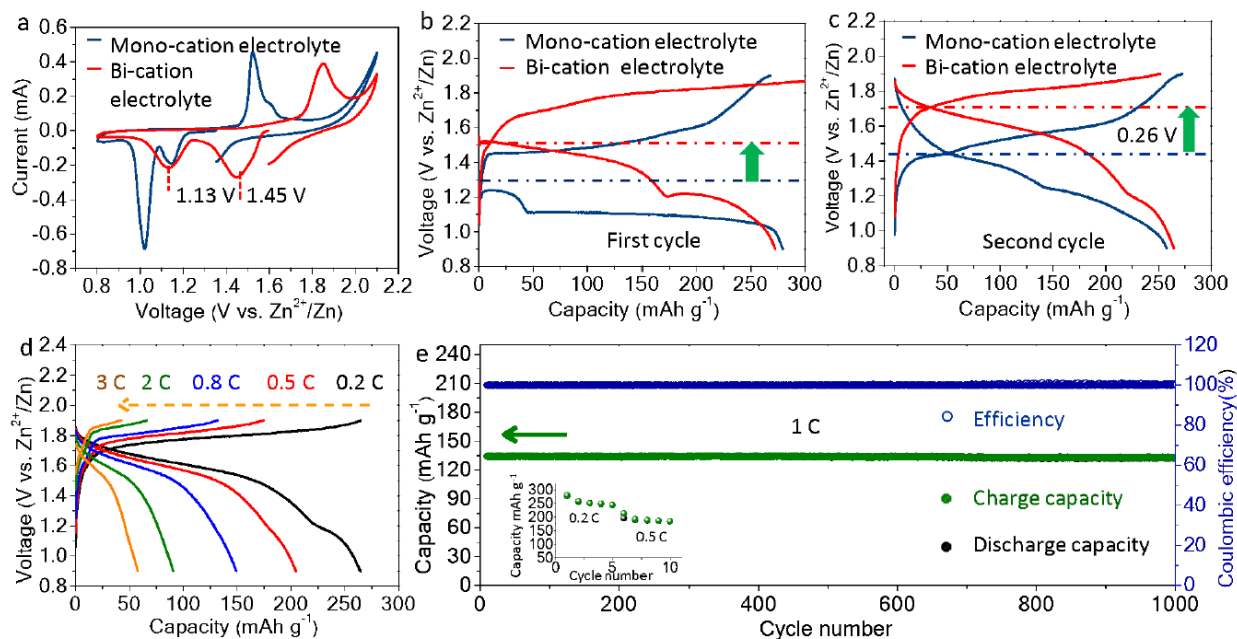


Figure 13. (a) Comparison of ZIBs with bi- and mono- cation electrolyte. (b) the initial CV curves. (c) Discharge-charge curve of 1st cycle. (d) Rate-capability (e) Cycle performance at 1C rate.
Copyrights reserved [117]

Moreover, pH value plays major role in term of understanding the mechanism during charge/discharge process. Pourbaix diagram shows the stability of materials depend on the pH value and working window [118]. Bischoff et al. reported Zn/MnO₂ cell with measuring the pH value during charge/discharge with 2M ZnSO₄ electrolyte and 0.1 M MnSO₄ additive [119]. It was shown that the initial pH value of 4.3 of the electrolyte increases during cycling and stabilizes at value of pH 5.2. According to the pH-diagram pH value above 5 leads to the passivation of zinc electrode. Low pH value is desirable to prevent the precipitation of zinc oxide on the negative electrode, while it can accelerate the dissolution of MnO₂, which can be prevented by addition of MnSO₄.

Prussian blue and analogs have also been investigated in aqueous ZIBs due to the three-dimensional framework and large intercalation sites. ZnHCF [83] and CuHCF [84], [120], [121] able to reach working potential of 1.6 V. However, important drawbacks like low capacity and uncontrolled phase transformation leading to fast capacity fading still remain [122].

Zhang et al. reported Zn/ZnHCF system which delivers capacity of 65.4 mAh g⁻¹ at voltage range of 0.8 – 2V at 1C in 1M ZnSO₄ electrolyte (**Figure 14**). The discharge capacities around 65, 60, 56, 52, 45, 39 and 32 mAh g⁻¹ can be reached at various C-rates [83].

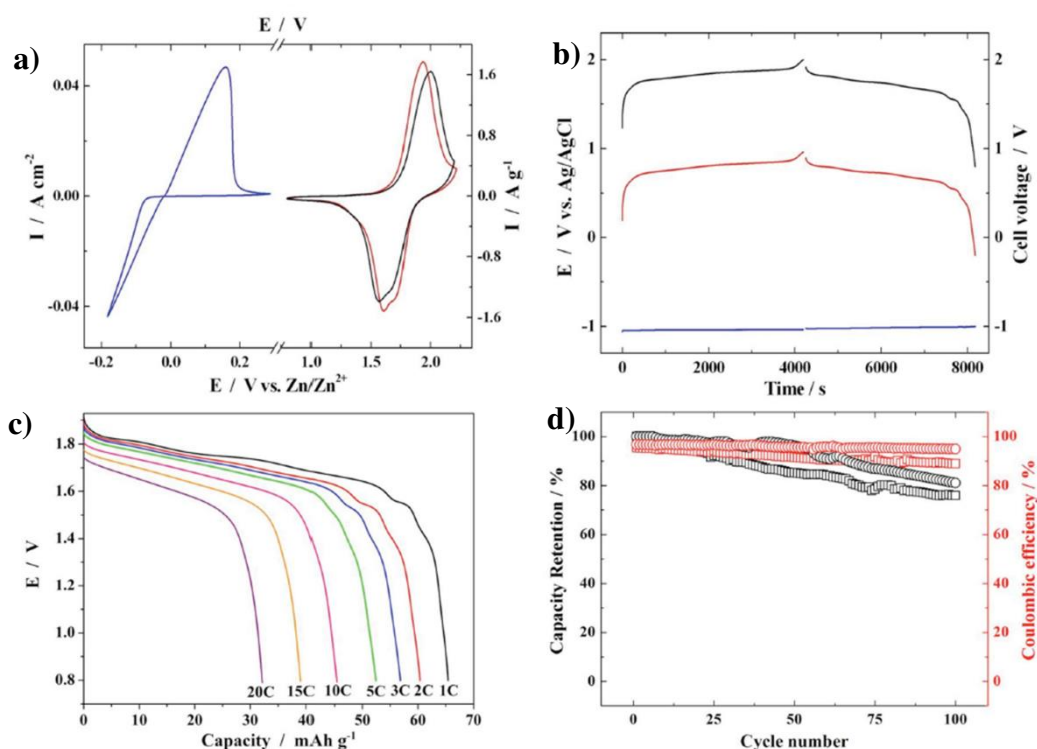


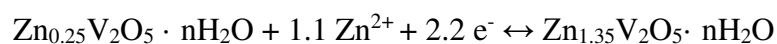
Figure 14. (a) CVs at a scan rate of 2 mV s^{-1} and (b) GCD profiles at a rate of 1 C for anode (blue), cathode (red) and full cell (black) in 1 M ZnSO_4 . (c) Rate capability of the battery. (d) Cycle life tests at a rate of 1 C (square) and 5 C (circle). $1 \text{ C} = 60 \text{ mA g}^{-1}$, $5 \text{ C} = 300 \text{ mA g}^{-1}$ [83].

4.1.3-2 Vanadium oxide -based cathode materials

Vanadium based materials (VO_2 [123]–[127], VS_2 [128], $\text{V}_3\text{O}_7 \cdot \text{H}_2\text{O}$ ($\text{H}_2\text{V}_3\text{O}_8$) [128]–[130], $\text{Zn}_{0.25}\text{V}_2\text{O}_5 \cdot n\text{H}_2\text{O}$ [80]) attracted attention for ZIB due to the tunnel-type and layered structure (Table 4). Vanadium has reach valence states (V^{2+} , V^{3+} , V^{4+} and V^{5+}) when used as electrode material, which means that multielectron transfer can be realized by achieving high capacity.

Nazar group reported $\text{V}_2\text{O}_5 \cdot n\text{H}_2\text{O}$ and $\text{Zn}_{0.25}\text{V}_2\text{O}_5 \cdot n\text{H}_2\text{O}$ electrode materials which exhibits 220 mAh g^{-1} at 15C in 1M ZnSO_4 [80]. The crystal structure of these compounds consist in vanadium pentoxide bilayers and water molecules allow for insertion/extraction of zinc (**Figure 15**). Co-insertion of Zn^{2+} and H_2O was proposed for $\text{V}_2\text{O}_5 \cdot n\text{H}_2\text{O}$ [81] and $\text{Zn}_{0.25}\text{V}_2\text{O}_5 \cdot n\text{H}_2\text{O}$ [80], in which H_2O molecules and/or $[\text{ZnO}_6]$ octahedra act as pillars to stabilize the structure of electrode material during the cycling.

The $\text{Zn}/\text{Zn}_{0.25}\text{V}_2\text{O}_5 \cdot n\text{H}_2\text{O}$ system exhibits capacity of 300 mAh g^{-1} with operating voltage of 0.9 V. The overall reaction in the system is:



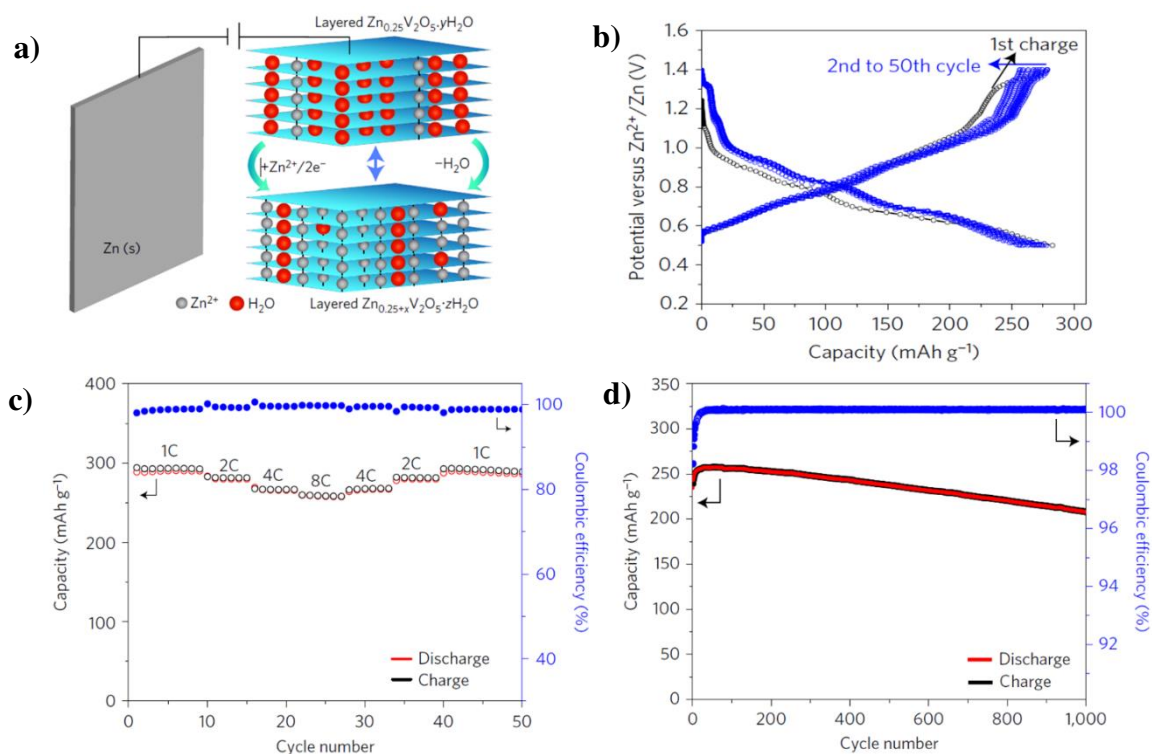


Figure 15. (a) Schematic illustration of Zn/Zn_{0.25}V₂O₅·nH₂O cell. (b) Discharge-charge profile of Zn_{0.25}V₂O₅ · nH₂O freestanding cathode at 1C in 1M ZnSO₄. (c) Rate capability (d) Cycle performance at 8C [80].

The structure of Zn_{0.25}V₂O₅·nH₂O shown in **Figure 16 b** and **Figure 16 c** consists of double-sheet-type two-dimensional (2D) V₂O₅ framework, similar to the V₂O₅ layers in δ -phase, extended in *a-b* plane [131]. The ordered interlayer ZnO₆ octahedra pin the 2D V₂O₅ layers into a framework enclosing intersecting paths in *a-b* plan along the [110] and [$\bar{1}\bar{1}0$] directions which accommodate additional Zn²⁺ on discharge. The spacious layered framework also permits insertion of water molecules from the electrolyte by expanding the interlayer space for facile Zn²⁺ intercalation, this occurs synergistically with the topotactic deintercalation of absorbed H₂O. According to the operando XRD structural modification of pristine Zn/Zn_{0.25}V₂O₅·nH₂O by immersion in aqueous electrolyte, the interlayer distance was increased from 10.8 Å to 12.9 Å. The increase of interlayer space related to the water insertion is in line with that the reported in layered oxides [132], [133] and double hydroxide [134]. The stable structural reversibility of the system is demonstrated by corresponding cell parameters of charged and discharged electrode after 50 cycles.

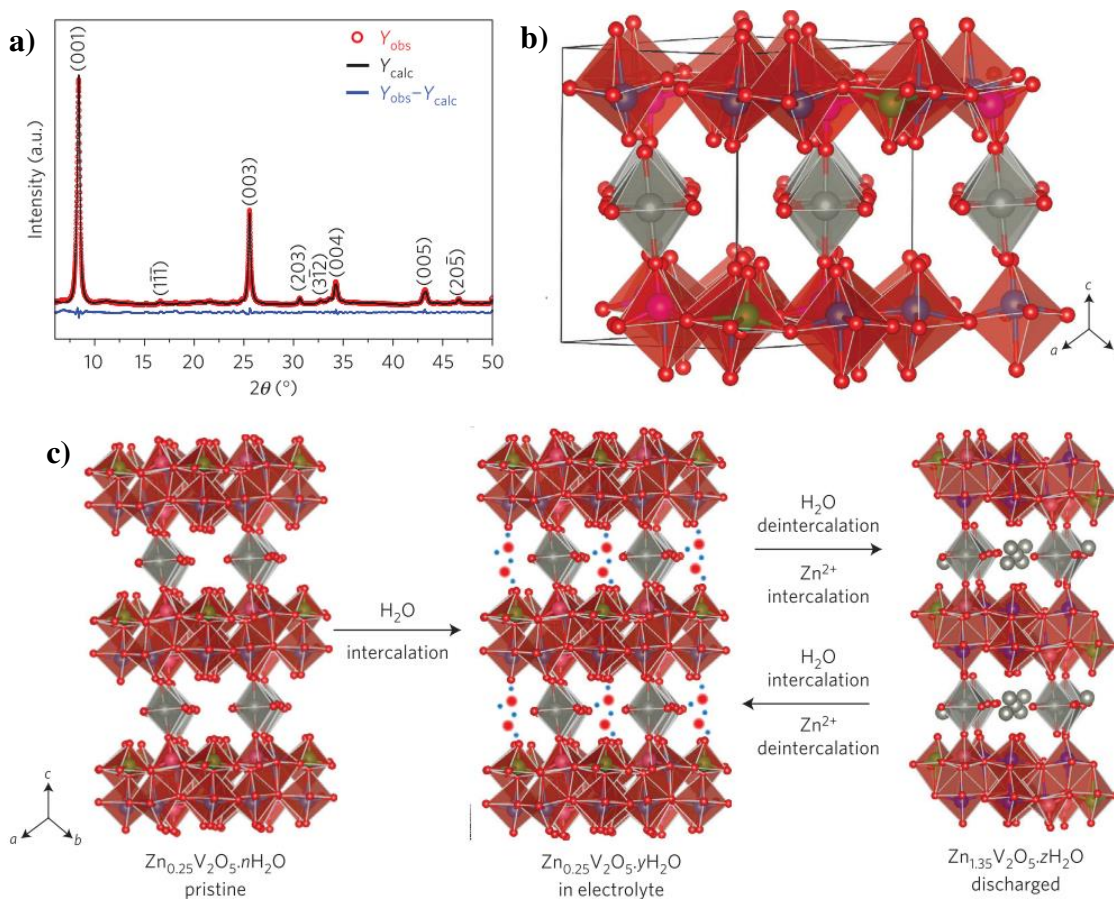


Figure 16. (a) Structural analysis of $\text{Zn}_{0.25}\text{V}_2\text{O}_5 \cdot n\text{H}_2\text{O}$ nanobelt. Unit cell parameters are $a = 10.75(2) \text{ \AA}$, $b = 7.77(1) \text{ \AA}$, $c = 10.42(4)$. (b) Crystal structure viewed along the $[110]$ direction. (c) Schematic illustration of reversible water intercalation into $\text{Zn}_{0.25}\text{V}_2\text{O}_5 \cdot n\text{H}_2\text{O}$ immersed in aqueous electrolyte and water deintercalation accompanying Zn^{2+} intercalation during discharge [80].

Yan et al. constructed $\text{V}_2\text{O}_5 \cdot n\text{H}_2\text{O}$ ($n \geq 1$) /graphene (VOG) cathode material, which delivers long-term cyclability and rate capability (248 mAh g^{-1} at 30 A g^{-1}) due to the effect of structural water on Zn^{2+} storage performance (**Figure 17**) [81].

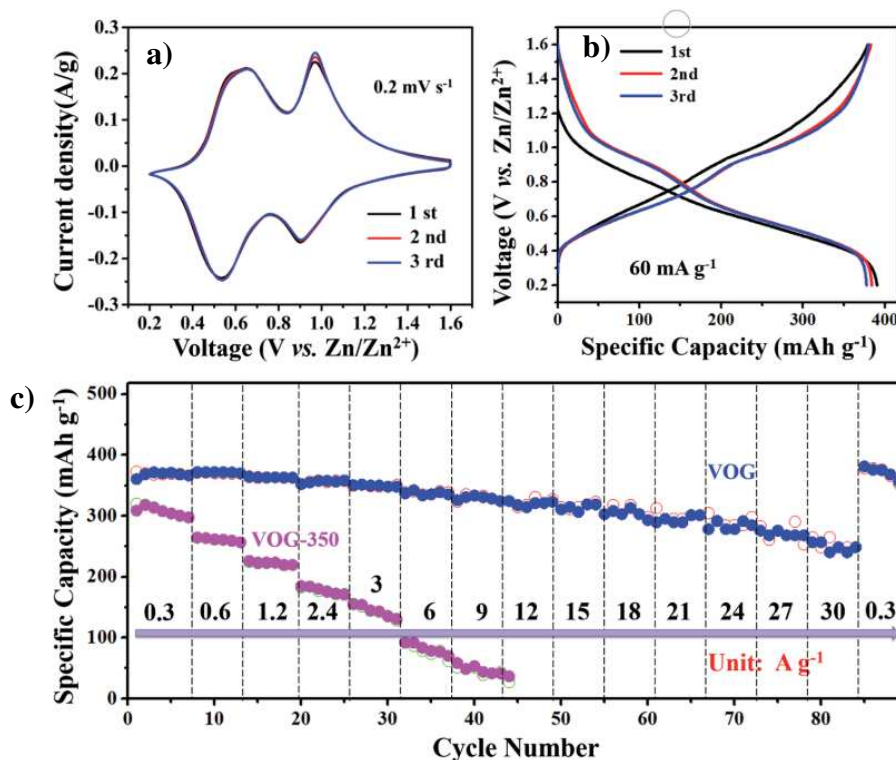


Figure 17. (a) CV and (b) charge-discharge curves for the first 3 cycles for V₂O₅·nH₂O/graphene. (c) Rate-capability of VOG and VOG-350 (without water in structure) at various C-rate in 3M of Zn(CF₃SO₃)₂ electrolyte with 0.1M of Vanadium sol as additive [81].

Magic-angle-spinning nuclear-magnetic-resonance (MAS NMR) was used to verify that structural H₂O molecules decrease the effective charge of Zn²⁺ by solvation and support for ion diffusion (**Figure 18**). The ¹H spectrum of pristine electrode show the broad resonance at 5.6 ppm, which is attributed to the trapped water in V₂O₅ bilayers. After charging to 1.3V ¹H peak slightly shifts to the 5.3 ppm with increasing intensity, accompanied with the decrease of interlayer distance (12.6 Å→10.4 Å), which is related to the formation of hydrogen bonds with Zn²⁺, CF₃SO₃⁻, H₂O by pulling the bilayers. After discharge ¹H peak separates to two peaks: sharp peak at 5.1 ppm (corresponding to water molecules, Zn²⁺ and CF₃SO₃⁻), while another peak at 2.9 ascribed to the water molecules associated with inserted Zn²⁺ by increasing interlayer space (10.4 Å→13.5 Å).

According to the XRD results the crystal structure of V₂O₅·nH₂O/graphene is completely reversible during charge and discharge. During the charge till 1.3V zinc ions are extracted from interlayer space of bilayer V₂O₅ (from 12.6 Å to 10.4 Å). During discharge till 0.8 V ~0.3 mol of zinc ion can be inserted without phase transformation. By continuous discharge till 0.4 V the unit cell parameters changed to $a=2.378(9)$ Å, $b=13.502(3)$ Å, $c=2.042(8)$ Å, which indicates formation of new phase. At 0.4V two-phase coexist: first phase similar to charged VOG charged to 1.3V, (space group of *C*/2 with lattice parameters of $a=9.403(3)$ Å, $b=3.367(6)$ Å,

$c=10.513(9)$ Å) and the second new formed phase with space group of Pc . New peaks at 6.53° , 13.14° and 19.73° are observed, which correspond to $(0\ 1\ 0)$, $(0\ 2\ 0)$ and $(0\ 3\ 0)$ planes, respectively. This phenomenon is different from XRD results obtained for $\text{Zn}_{0.25}\text{V}_2\text{O}_5 \cdot n\text{H}_2\text{O}$ [80], in which lattice interlayer decreases with Zn^{2+} intercalation.

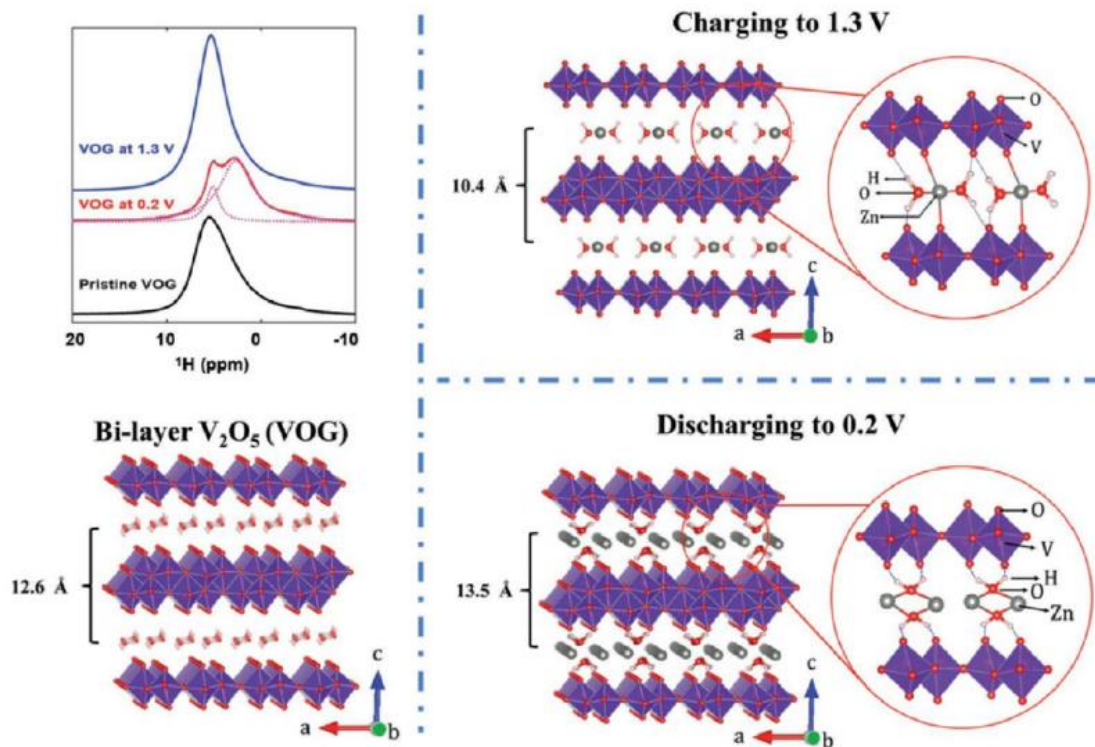


Figure 18. Ex-situ solid state ^1H NMR and the proposed crystal structure of $\text{V}_2\text{O}_5 \cdot n\text{H}_2\text{O}$ /graphene electrode after charging (till 1.3V) and discharging (till 0.2V) in 3M of $\text{Zn}(\text{CF}_3\text{SO}_3)_2$ electrolyte with 0.1M of Vanadium sol as additive [81].

The water-based shielding layer reduces the “effective charge” of Zn^{2+} , meanwhile, it is also increasing the distance between Zn^{2+} and neighboring oxygen ions (r_o). The electrostatic bond is $\propto \frac{1}{\epsilon_r r_0^2}$, where ϵ_r is the permittivity of water and r_o the distance between Zn^{2+} and the closest ions. Therefore, water-based shielding layer reduce electrostatic bond strength, which result on high diffusion coefficient of solvated Zn^{2+} .

Zhou et al. reported orthorhombic V_2O_5 cathode in aqueous zinc system with 3M ZnSO_4 electrolyte. The system shows 224 mAh g^{-1} at 0.1 A g^{-1} with coulombic efficiency of 67% [135].

Figure 19 shows cyclic voltammetry of $\text{Zn}/\text{V}_2\text{O}_5$ cells with multiple redox peaks, in good agreement with discharge/charge curves. The peak intensity reduction is related to the not fully extraction of Zn^{2+} ions from V_2O_5 structure. It can be explained by trapped Zn^{2+} ions acting as interlayer pillars to stabilize V_2O_5 structure, resulting good electrochemical performance.

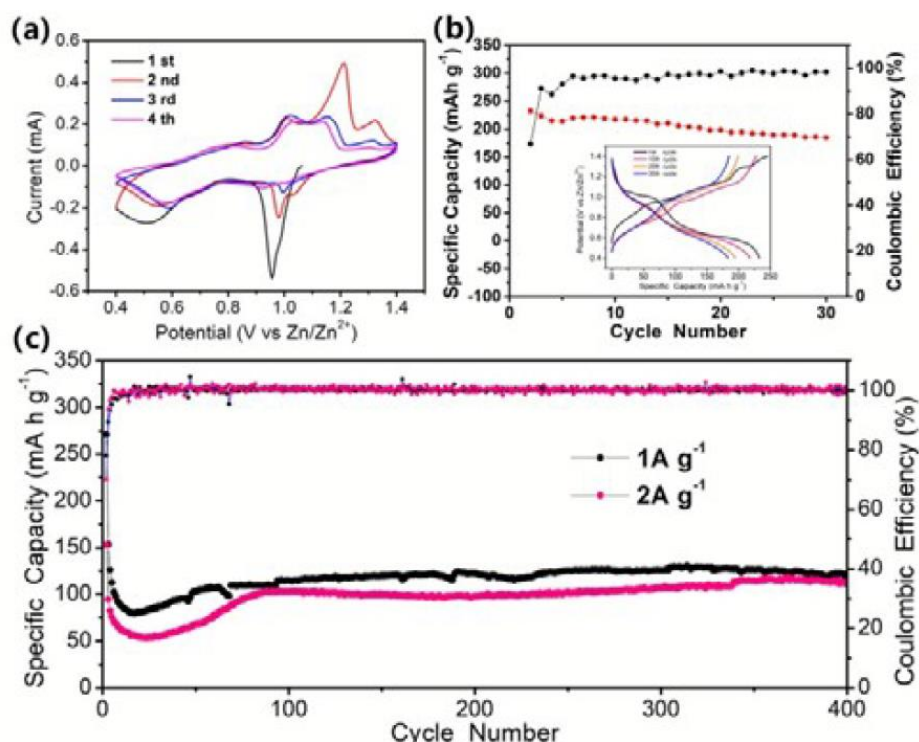


Figure 19. (a) The initial four cyclic voltammetry curves at a scan rate of 0.1 mV s⁻¹, (b) The cycling performance and coulombic efficiency of Zn/V₂O₅ cell at 100 mA g⁻¹, and the inset shows the charge/discharge profiles of selected cycles; (c) Cycling performances and coulombic efficiency at 1 A g⁻¹ and 2 A g⁻¹ of Zn-V₂O₅ cells in 3M ZnSO₄ [135].

Chen et al. developed V₂O₅ nanofibers with mesoporous structure to enhance electrochemical performance [136]. The electrochemical and structural investigations show that Zn/V₂O₅ system include two-step reaction. During the first discharge Zn_{3+x}(OH)₂V₂O₇ · 2H₂O (ZVO) is generated followed by reversible insertion/extraction of Zn²⁺ in open-structured host (**Figure 20**). ZVO adopts typical layered open structure consisting of ZnO₆ octahedral layers separated by double VO₄ tetrahedral interlayer pillars (**Figure 20a**). Water molecules randomly located in the large cavities. The high structural stability of ZVO is confirmed by XRD after 200 cycles. The galvanostatic intermittent titration technique (GITT) measurements have been applied to calculated Zn²⁺ diffusion coefficient (D_{Zn}). As shown in **Figure 20b** D_{Zn} values are in order of 10⁻⁹ – 10⁻¹¹ cm² s⁻¹, which is comparable to reported ZVO cathode and Li diffusion in vanadium oxides [82], [137].

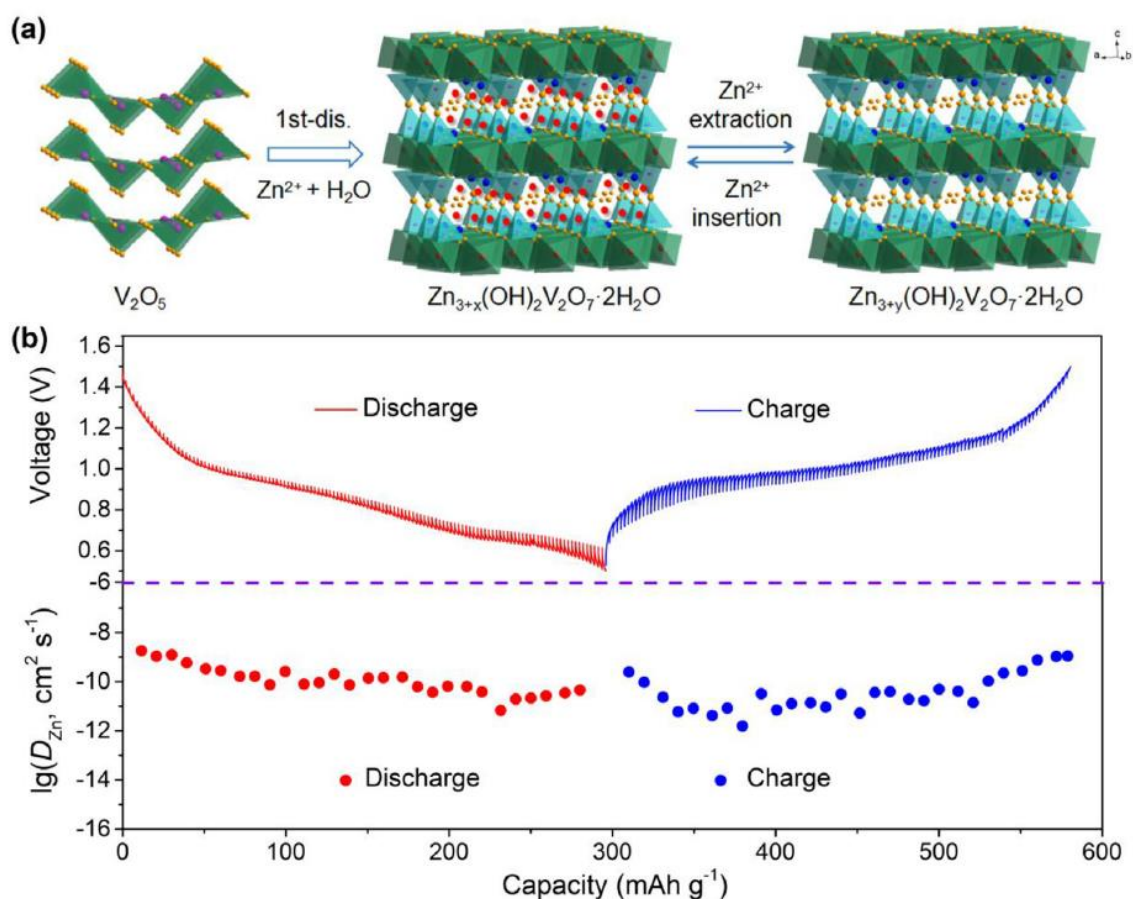


Figure 20. (a) Schematic illustration of reaction mechanism of V_2O_5 electrode. (b) GITT profiles at 5th cycle and calculated Zn^{2+} diffusion coefficient of the cathode in 3M of $Zn(CF_3SO_3)_2$ electrolyte.

Copyrights reserved [136]

As shown in **Figure 21** initial discharge capacity reaches 265 $mAh\ g^{-1}$, corresponding to the ~ 1.8 electron redox process at voltage range of 0.5 – 1.5V. The low Coulombic efficiency in first cycle is ascribed to the trapping of Zn^{2+} at the dead Zn^{2+} sites in the host structure [138], [139]. The specific capacity gradually increases with initial cycles, which is similar to the other vanadium oxide cathodes [80], [81]. The highest discharge capacity of 319 $mAh\ g^{-1}$ was obtained on fourth cycle. The change of the discharge/charge curves is related to the structural evolution upon cycling. The system exhibits good cycling stability at 2C with high reversible capacity of 166 $mAh\ g^{-1}$ after 500 cycles with 81% capacity retention.

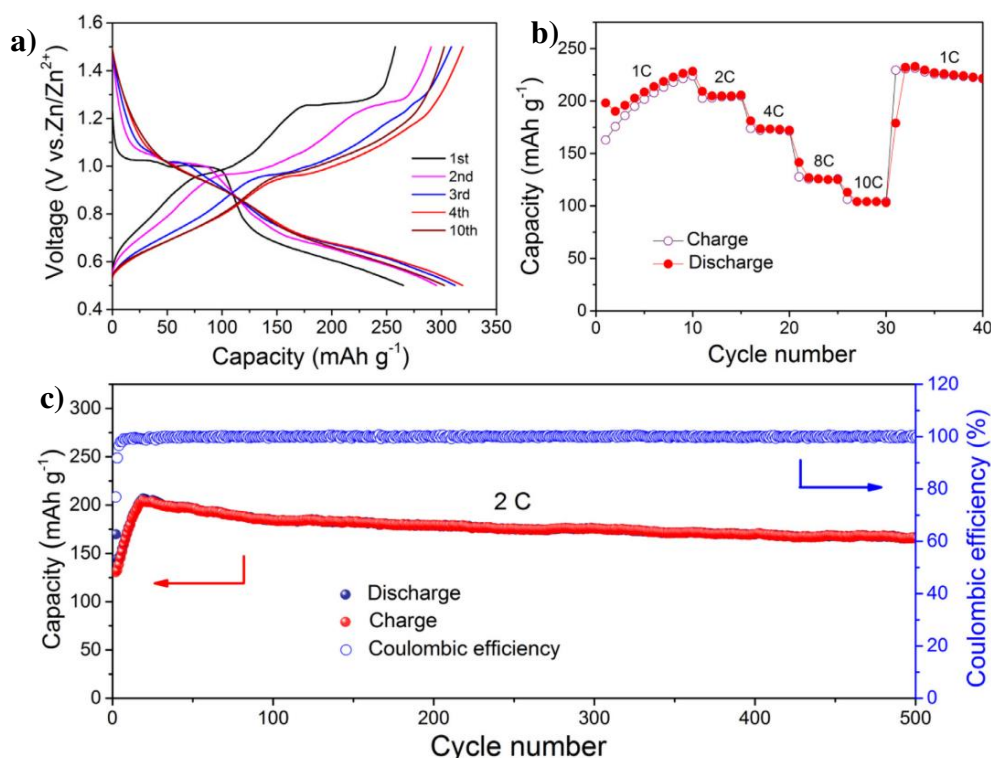
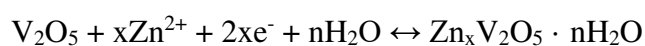


Figure 21. (a) Discharge/charge profile of V₂O₅ nanofibers at 20 mA g⁻¹. (b) Rate-capability at various C-rate. (c) Cycle performance at 2C in 3M of Zn(CF₃SO₃)₂ electrolyte [136].

Zhang et al. proposed Zn/V₂O₅ system with 3 M of Zn(CF₃SO₃)₂ electrolyte, which demonstrated capacity of 372 mAh g⁻¹ at 5 A g⁻¹ over 4000 cycles [140]. Upon the cycling the specific capacity increases and overpotential decreases due to the activation process of V₂O₅ electrode (**Figure 22**) evidenced by SEM/TEM and EIS observation. Ex-situ XRD shows that during the first discharge new layered Zn_xV₂O₅·nH₂O phase forms. The layered V₂O₅ undergoes structural evolution and transformation to Zn_xV₂O₅·nH₂O with enlarged interlayer space (4.4 to 13.4 Å) with co-insertion of Zn²⁺ and H₂O molecules. Furthermore, during the charging process hydrated Zn²⁺ are completely extracted. The reversible reaction of Zn//V₂O₅ battery can be as follows:



where x depends on the number of inserted Zn²⁺ which can reach up to 1.6.

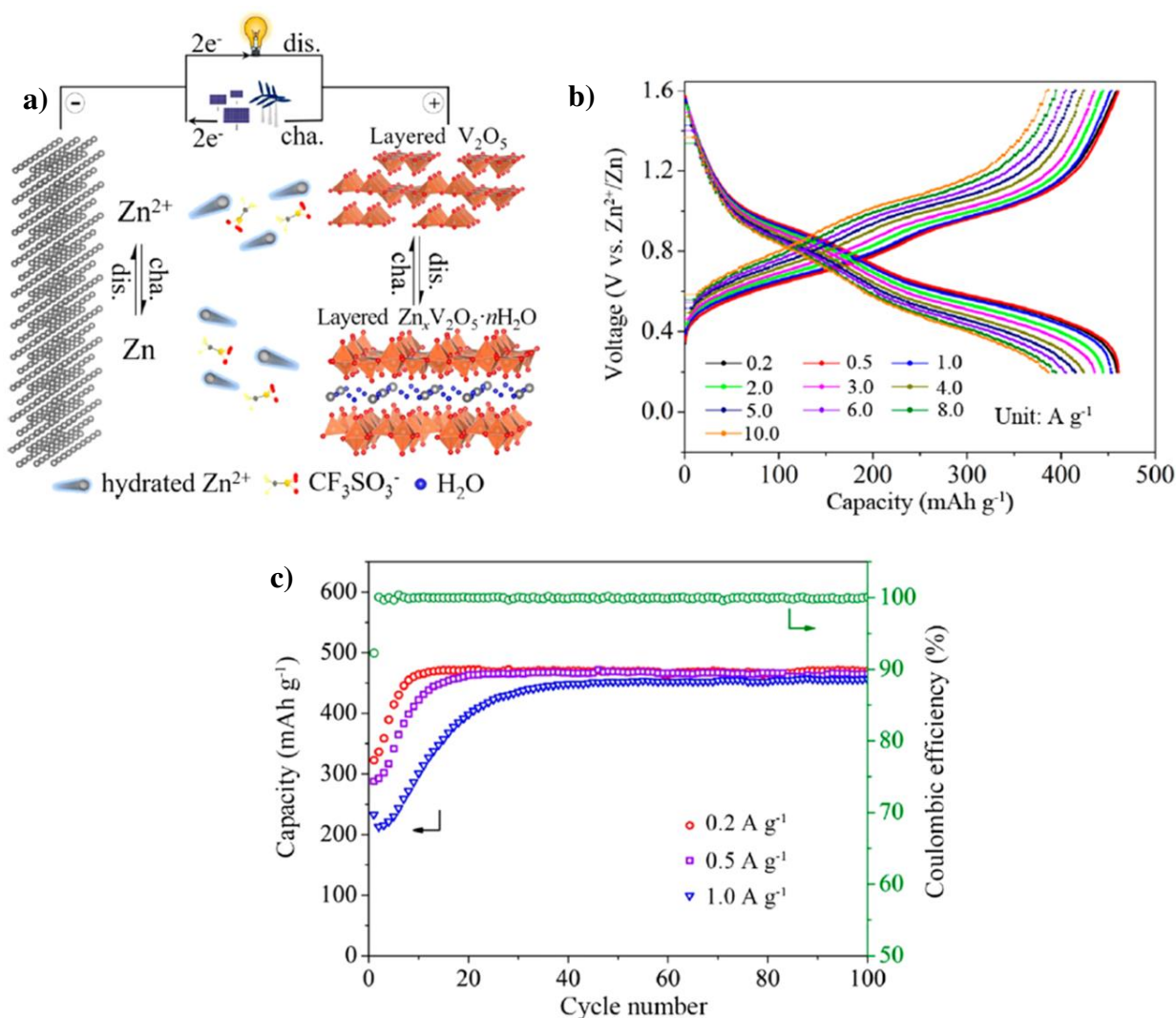


Figure 22. (a) Schematic illustration of Zn/V₂O₅ battery in 3 M of Zn(CF₃SO₃)₂ electrolyte. (b) Discharge-charge profile at various C-rate. (c) Cycle performance at various C-rate [140].

The electrochemical properties of V₂O₅ can be improved by mixing vanadium states of V⁴⁺/V⁵⁺, which leads to faster diffusion, lower polarization and higher electrochemical activity [141], [142]. V₃O₇·H₂O (H₂V₃O₈) in comparison with V₂O₅ has larger interlayer space and electronic conductivity (mixed valence of V⁵⁺/V⁴⁺) [129], [130], [143], [144]. V₃O₈ layer contains [VO₆] octahedrons and [VO₅] pyramids connected by corners and sharing edges.

He et al. adopted H₂V₃O₈ nanowires, which exhibits high capacity, however fast capacity fading can be observed due to the structure instability [129], [144]. The electrochemical performance could be improved by mixing with graphene to improve electronic conductivity and structure stability [130]. The battery delivers 240 mAh g⁻¹ at 5C (**Figure 23**). The results from DFT calculation demonstrates that vacancy sites in V-O octahedrons can accommodate zinc ions with small lattice deformation.

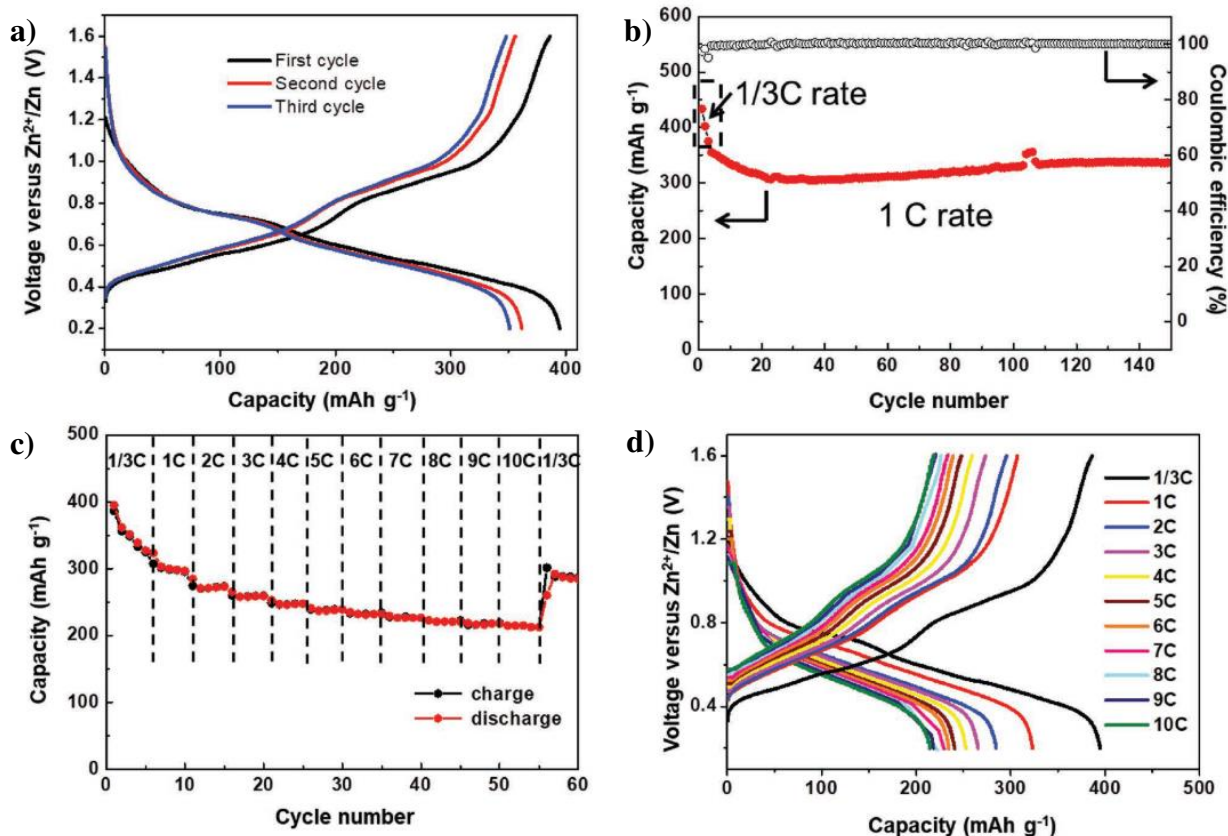


Figure 23. (a) Discharge/charge profile at 1/3. (b) Cycle performance at 1C. (c) Rate-capability at various C-rate. (d) Discharge/charge profile at various C-rate of H₂V₃O₈/graphene cathode in 3 M of Zn(CF₃SO₃)₂ electrolyte [130].

Nevertheless, the obtained complex and contradictory results on structure evolution of vanadium oxide during the discharge-charge process requires further detailed investigations. It is necessary to develop new strategies for vanadium oxide materials to reversibly insert/extract completely Zn²⁺ ions.

Researchers demonstrated that guest species like water molecules, relieves the structural deterioration of “pillar effect”, by stabilizing host structure during the cycling and enlarge crystal layer for more ion insertion. According to the results shown by researchers’ vanadium-based materials exhibits high capacity and rate capability and good cyclability.

Vanadium dioxide has different phases with several polymorphs like monoclinic VO₂ (M1), monoclinic VO₂ (M2), rutile VO₂ (R), tetragonal VO₂ (A), monoclinic VO₂ (B), VO₂ (D), BCC VO₂ etc (**Figure 24**) [145], [146].

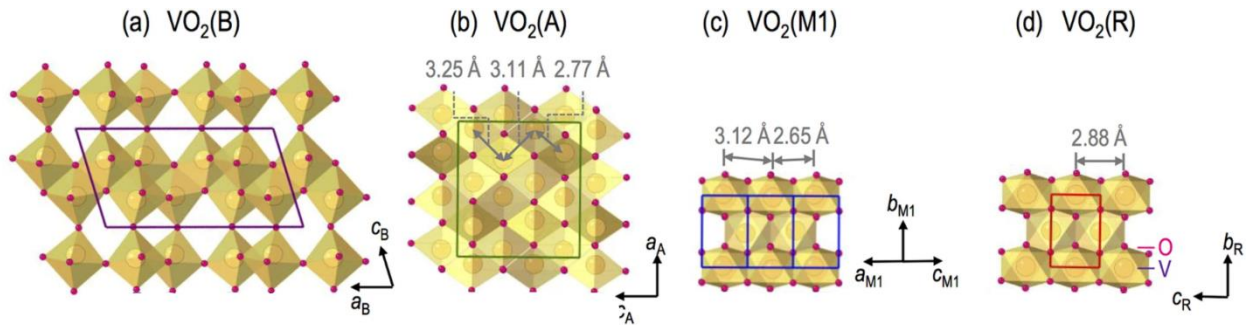


Figure 24. Schematics of (a) VO₂(B), (b) VO₂(A), (c) VO₂(M1) and (d) VO₂(R) phases [145]. Copyrights reserved.

Metastable VO₂ (B) due to the layered structure formed by [VO₆] octahedra, allows zinc insertion and reported by Ding et al [124]. By using VO₂ (B) nanofibers, capacity reaches 357 mAh g⁻¹ at 0.25C and long-term cyclability and excellent rate-capability (**Figure 25**). The XRD investigations of VO₂ (B) nanofibers before Zn²⁺ insertion three strong peaks can be observed at 45.1°, 49.2° and 59.1°, which indexed to (-601), (020), (-404) facets. After discharge to 0.3V (full zinc insertion) lattice spacing of (-601), (020), (-404) facets are slightly increased ($d_{-601} = 0.202 + 0.011$ nm, $d_{020} = 0.185 + 0.008$ nm and $d_{-404} = 0.156 + 0.003$ nm). At charged state of 1.5V (complete zinc extraction) the (-601), (020), (-404) peaks shift to initial locations revealing structure reversibility.

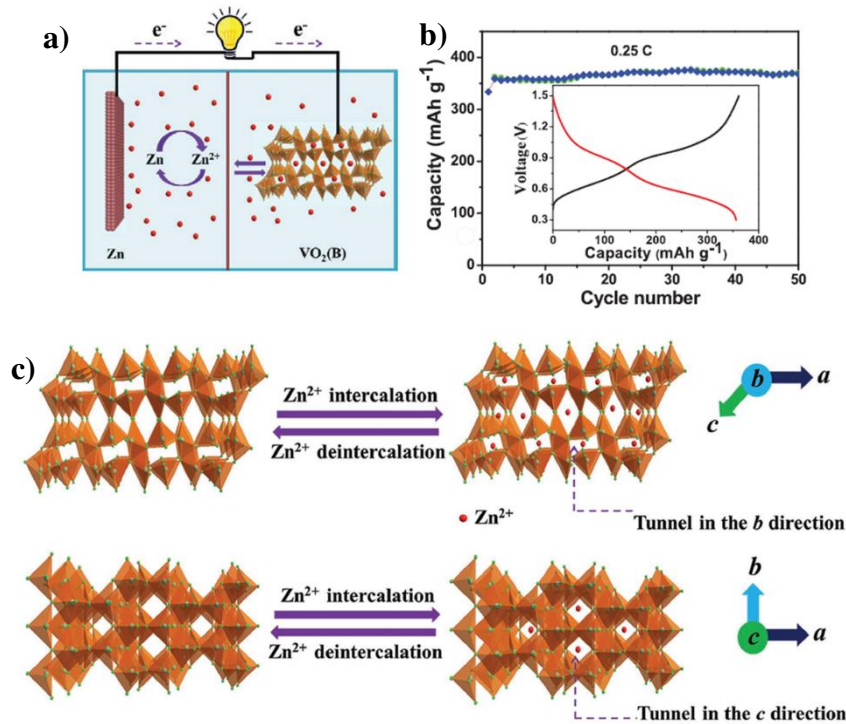
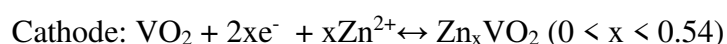
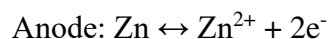


Figure 25. (a) (c) Schematic illustration of Zn//VO₂ (B) system. (b) Discharge/charge profile and cycle performance at voltage range of 0.3 – 1.5V at 0.25C in 3 M of Zn(CF₃SO₃)₂ electrolyte [124].

Dai et al. proposed VO₂ with free-standing reduced graphene oxide composite film [125]. Recently, the high reversible single-reaction mechanism of VO₂ nanorods has been revealed by

in situ monitoring and quantitative analysis [123]. The unit cell parameters (a , b , c) expand/shrink during charge/discharge with single-phase reaction with three stages, namely stage D1 and C1, stage D2 and C2, stage D3 and C3. (**Figure 26**). After full discharge the change ratios of a , b , c is 2.72%, 2.53% and 1.31%, respectively and volume expands by 6.69%. Based on the results, the overall reaction of the Zn//VO₂ system is:



In particular, the change of lattice parameter in D1 is opposite to C1, as same as D2 and C2, D3 and C3. In detail, D2 expands by 2.3% in a and 1.6% in c and D3 expands by 0.1% in a and 0.5% in c . The most noticeable changes can be observed in D2 with 4.5% volume expansion and C2 with 3.6%. Simultaneously, the expansion and shrinkage of unit cell parameters occurs along a and c directions, while b direction barely changes in both cases. It means that, the diffusion direction of Zn²⁺ is along the [010] orientation and edge-sharing [VO₆] octahedra expand along a and c directions. The DFT calculation model of Zn²⁺ ion insertion in VO₂ at different site is shown in **Figure 26d**. In the 2 x 2 x 2 k-points VO₂ crystal, the energy is – 205.87 eV after insertion of 4 zinc ions. The slightly changes in volume and total energy indicate the crystal stability of VO₂ structure with 0.5 Zn²⁺ insertion.

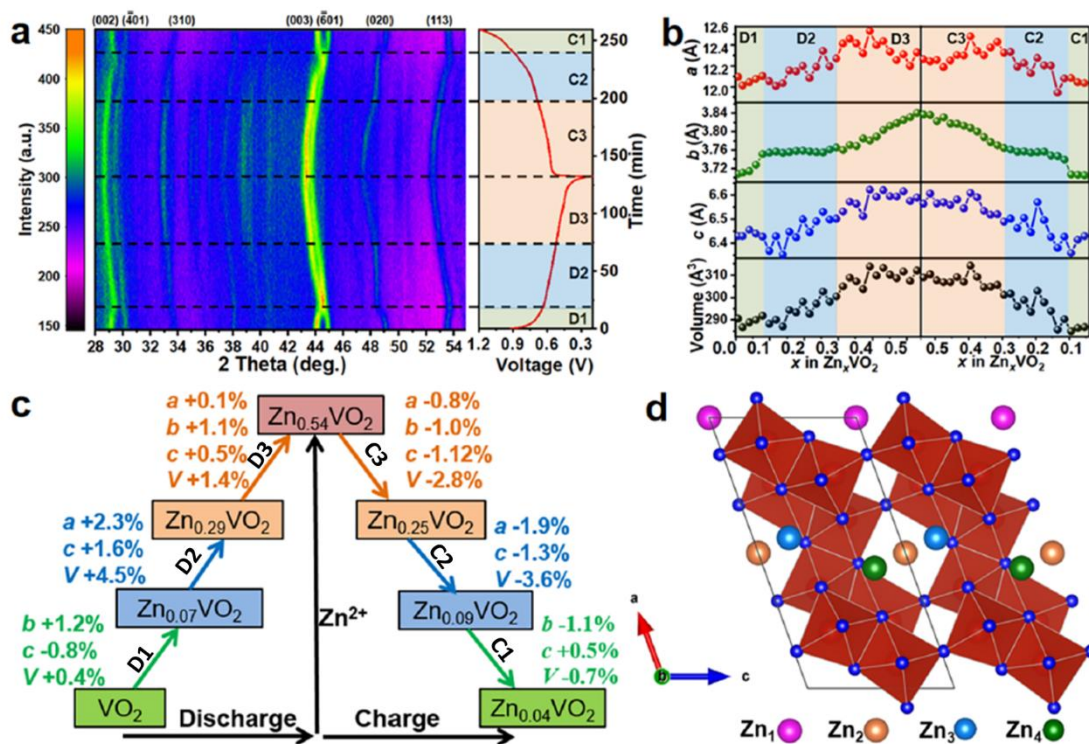
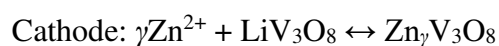
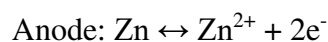


Figure 26. (a) 2D in-situ XRD patterns of 1st cycle in 1M ZnSO₄ (0.2 – 1.2V). (b) Evolution of lattice parameters during discharge and charge. (c) The change in unit cell parameters and volume expansion at different stages. (d) DFT calculation model of zinc insertion into VO₂ structure [123].

The monoclinic LiV_3O_8 (LVO) system is comprised from two edge-shared octahedra $[\text{VO}_6]$ and trigonal pyramid $[\text{VO}_5]$ units which form “string” and “ribbon” arrangement of $(\text{V}_3\text{O}_8)^-$ layers along (100) plane and layers linked by Li^+ ions in the octahedral and tetrahedral sites. Alfaruqi et al. displayed that layered LiV_3O_8 (LVO) had two-step reaction during discharge/charge process. On first step ZnLiV_3O_8 phase, further converted to solid-solution $\text{Zn}_\gamma\text{LiV}_3\text{O}_8$ ($\gamma > 1$), while during charge LiV_3O_8 a single-phase reaction observed (**Figure 27**) [138]. The electrochemical reactions can be written as:



The in-situ XRD investigation reveals that during discharge till 0.6V, the position in the (100) diffraction line is shifted to higher angle (from 14.06° to 14.82°) indicating the decrease of a parameter (by $\sim 0.3\text{\AA}$). Concordantly, shift of (003) peak to lower angle (from 23.14° to 22.31°) is related to the increase of c parameter (\sim by 0.11\AA). Similarly, the interplanar distance of the (-111) plane expands (from 3.25\AA to 3.40\AA). In initial discharge region (1.28 – 0.82V) the (100) diffraction peak shifts slightly (single phase domain displaying solid solution behavior), while in 0.81 – 0.7V significant shift by splitting the (100) diffraction peak (coexistence of LiV_3O_8 and ZnLiV_3O_8), ($1.5 < x < 3.2$). The continuous shift of (100) peak in final discharge (0.69 – 0.6V) represents single-phase domain. Nevertheless, during the charge the characteristic diffraction lines of LVO are restored via solid-solution behavior without peak-splitting feature.

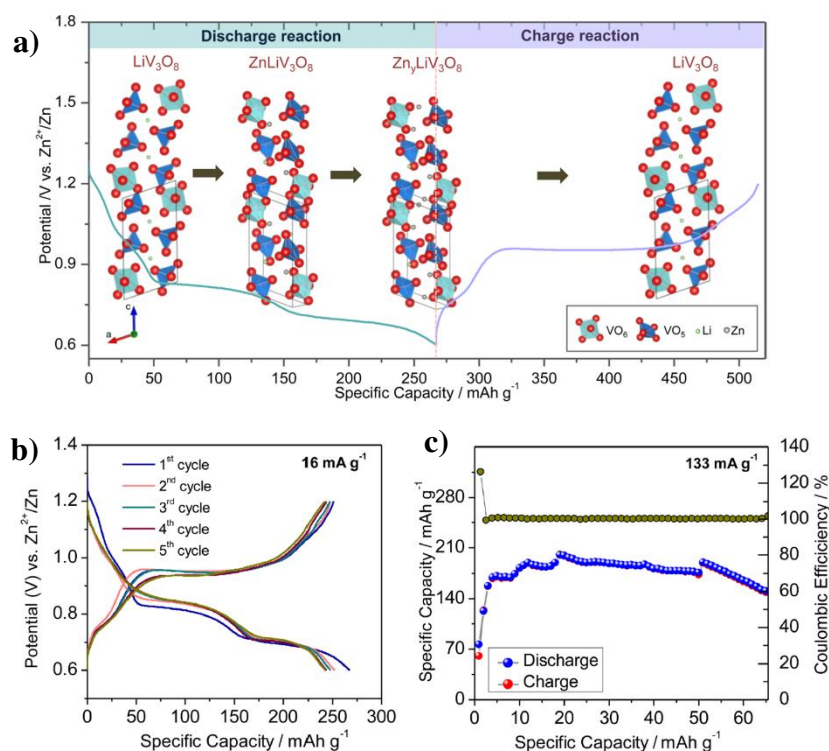


Figure 27. (a) Schematic illustration of Zn insertion mechanism in Zn//LiV₃O₈ system. (b) Discharge/charge profile and (c) Cycle performance at 133 mA g⁻¹ in 1M ZnSO₄ at voltage range of 1.2 – 0.6V [138].

In addition, different types of vanadates with/without water molecule, Zn₃V₂O₇(OH)₂·2H₂O [82], Ca_{0.25}V₂O₅·nH₂O [147], LiV₃O₈ [138], NaV₃O₈·1.5H₂O [90], Na₂V₆O₁₆·1.63H₂O [148], [149], Na_{1.1}V₃O_{7.9} [150], Na_{0.33}V₂O₅ [139], Na₅V₁₂O₃₂ [151], K₂V₈O₂₁ [152], Zn₂V₂O₇ [153], Mo_{2.5+y}VO_{9+z} [154], Li_xV₂O₅·nH₂O [155] and Ag_{0.4}V₂O₅ [156] are developed as cathode materials for aqueous ZIBs due to the layered and tunnel structure. The summary of V-based materials is shown in **Table 4**.

Table 4. Electrochemical performances of V-based electrodes, adapted from ref [68]

	Materials	Electrolyte	Working window [V]	Initial capacity [mAh g ⁻¹]	Capacity retention	Ref
Vanadium oxide	V ₂ O ₅	21 m LiTFSI+ 1 m Zn(CF ₃ SO ₃) ₂	0.2–1.6	238	80% (<i>n</i> = 2000) at 50 mA g ⁻¹	[157]
	V ₂ O ₅	3 M Zn(CF ₃ SO ₃) ₂	0.5–1.5	319	81% (<i>n</i> = 500) at 20 mA g ⁻¹	[136]
	V ₂ O ₅	3 M ZnSO ₄	0.4–1.4	224	67% (<i>n</i> = 400) at 100 mA g ⁻¹	[135]
	V ₂ O ₅ ·nH ₂ O/graphene	3 M Zn(CF ₃ SO ₃) ₂ + 0.1 M Vanadium sol	0.2–1.6	381	71% (<i>n</i> = 900) at 60 mA g ⁻¹	[81]

	VO ₂	1 M ZnSO ₄	0.2–1.3	325.6	86% (<i>n</i> = 5000) at 0.05 A g ⁻¹	[123]
	VO ₂	3 M Zn(CF ₃ SO ₃) ₂	0.2–1.2	357	91.2% (<i>n</i> = 300) at 0.25 C	[124]
	VO ₂ /graphene	3 M Zn(CF ₃ SO ₃) ₂	0.3–1.3	276	99% (<i>n</i> = 1000) at 0.1 A g ⁻¹	[125]
	V ₃ O ₇ ·H ₂ O	1 M ZnSO ₄	0.3–1.5	267	79% (<i>n</i> = 1000) at 1C	[143]
	H ₂ V ₃ O ₈	3 M Zn(CF ₃ SO ₃) ₂	0.2–1.6	423.8	94.3% (<i>n</i> = 1000) at 0.1 A g ⁻¹	[144]
	H ₂ V ₃ O ₈ /graphene	3 M Zn(CF ₃ SO ₃) ₂	0.2–1.6	394	87% (<i>n</i> = 2000) at 1/3C	[130]
	V ₃ O ₇ ·H ₂ O	1 M ZnSO ₄	0.4–1.1	375	80% (<i>n</i> = 200) at 1C	[129]
	V ₆ O ₁₃ · <i>n</i> H ₂ O	3 M Zn(CF ₃ SO ₃) ₂	0.2–1.4	395	87 (<i>n</i> = 1000) at 0.1 A g ⁻¹	[158]
	V ₁₀ O ₂₄ ·12H ₂ O	3 M Zn(CF ₃ SO ₃) ₂	0.7–1.7	165	80.1% (<i>n</i> = 3000) at 0.2 A g ⁻¹	[159]
Alkali metal vanadates	LiV ₃ O ₈	1 M ZnSO ₄	0.6–1.2	256	75% (<i>n</i> = 65) at 16 mA g ⁻¹	[138]
	Na _{0.33} V ₂ O ₅	3 M Zn(CF ₃ SO ₃) ₂	0.2–1.6	367	93% (<i>n</i> = 1000) at 0.1 A g ⁻¹	[139]
	Na _{1.1} V ₃ O _{7.9} /graphene	1 M Zn(CF ₃ SO ₃) ₂	0.4–1.4	191	84.8% (<i>n</i> = 100) at 50 mA g ⁻¹	[150]
	NaV ₃ O ₈	1 M ZnSO ₄ + 1 M NaSO ₄	0.2–1.2	380	82% (<i>n</i> = 1000) at 0.05 A g ⁻¹	[90]
	K ₂ V ₆ O ₁₆ ·2.7H ₂ O	3 M Zn(CF ₃ SO ₃) ₂	0.4–1.4	239.2	82% (<i>n</i> = 400) at 100 mA g ⁻¹	[160]
Alkali earth metal vanadates	CaV ₆ O ₁₆ ·3H ₂ O	3 m Zn(CF ₃ SO ₃) ₂	0.2–1.6	367	100% (<i>n</i> = 300) at 500 mA g ⁻¹	[161]
	Mg _{0.34} V ₂ O ₅ · <i>n</i> H ₂ O	3 M Zn(CF ₃ SO ₃) ₂	0.2–1.8	352	97% (<i>n</i> = 2000) at 5000 mA g ⁻¹	[162]
Transition metal vanadates	Zn ₃ V ₂ O ₇ (OH) ₂ ·2H ₂ O	1 M ZnSO ₄	0.2–1.8	213	68% (<i>n</i> = 300) 200 mA g ⁻¹	[82]
	Zn _{0.25} V ₂ O ₅ · <i>n</i> H ₂ O	1 M ZnSO ₄	0.5–1.4	300	80% (<i>n</i> = 1000) at 8C	[80]
	Fe ₅ V ₁₅ O ₃₉ (OH) ₉ ·9H ₂ O	0.3 M Zn(TFSI)	0.4–1.6	385	80% (<i>n</i> = 300) at 5 A g ⁻¹	[163]

Other vanadates	$\text{NH}_4\text{V}_4\text{O}_{10}$	3 M $\text{Zn}(\text{CF}_3\text{SO}_3)_2$	0.8–1.7	147	70.3% ($n = 5000$) at 5000 mA g^{-1}	[164]
	$(\text{NH}_4)_2\text{V}_{10}\text{O}_{25} \cdot 8 \text{H}_2\text{O}$	2 M ZnSO_4	0.7–1.7	228.8	90.1% ($n = 5000$) at 5 A g^{-1}	[165]
	$\text{Zn}_x\text{Mo}_{2.5+y}\text{VO}_{9+Z}$	0.5 M $\text{Zn}(\text{CH}_3\text{COO})_2$	0.01–1.6	180	66.6% ($n = 30$) at 20 mA g^{-1}	[154]
Vanadyl phosphates	$\text{Li}_3\text{V}_2(\text{PO}_4)_3/\text{C}$	4 M $\text{Zn}(\text{CF}_3\text{SO}_3)_2$	0.2–1.9	141	99% ($n = 4000$) at 20C	[166]
	$\text{Na}_3\text{V}_2(\text{PO}_4)_3$	0.5 M $\text{Zn}(\text{CH}_3\text{COO})_2$	0.8–1.6	97	74% ($n = 100$) at 0.5 C	[85]
	$\text{Na}_3\text{V}_2(\text{PO}_4)_3/\text{C}$	0.5 M CH_3COONa + 0.5 M $\text{Zn}(\text{CH}_3\text{COO})_2$	0.8–1.7	92	74% ($n = 200$) at 0.5 C	[78]
	$\text{Na}_3\text{V}_2(\text{PO}_4)_3/\text{graphene}$	2 M $\text{Zn}(\text{CF}_3\text{SO}_3)_2$	0.6–1.8	114	75% ($n = 200$) at 500 mA g^{-1}	[167]
	$\text{Na}_3\text{V}_2(\text{PO}_4)_2\text{F}_3$	2 M $\text{Zn}(\text{CF}_3\text{SO}_3)_2$	0.8–1.9	61.7	95% ($n = 4000$) at 1 A g^{-1}	[168]
	VS_2	1 M ZnSO_4	0.4–1.0	190	98% ($n = 200$) at 0.5 A g^{-1}	[128]
	$\text{VS}_4/\text{graphene}$	1 M $\text{Zn}(\text{CF}_3\text{SO}_3)_2$	0.3–1.8	180	93.3% ($n = 165$) at 1 A g^{-1}	[169]

Similar to manganese, vanadium dissolution occurs during the cycling by due to the solubility of vanadium ions in aqueous electrolyte [170]. Dissolution of vanadium-based materials lead to capacity fading and loss of active material, which may deposit on the surface of negative electrode (passivation) [171]. Moreover, the slow Zn^{2+} diffusion (high charge density) promotes the accumulation of zinc ions in host lattice [69], [172]. The accumulated zinc ions can interact with V-O layers and form $\text{Zn}_3\text{V}_2\text{O}_7(\text{OH})_2 \cdot 2\text{H}_2\text{O}$ phase, as a result of electrolytic decomposition and side reactions of active material with electrolyte [152], [158], [173]. This discharge product was found to be reversible in initial cycles in $\text{Zn}/\text{NH}_4\text{V}_4\text{O}_8$ system, however only after 30 cycles (**Figure 28**), due to the accumulation of Zn^{2+} ions and water molecules in the crystal lattice, which may account the capacity fading [174].

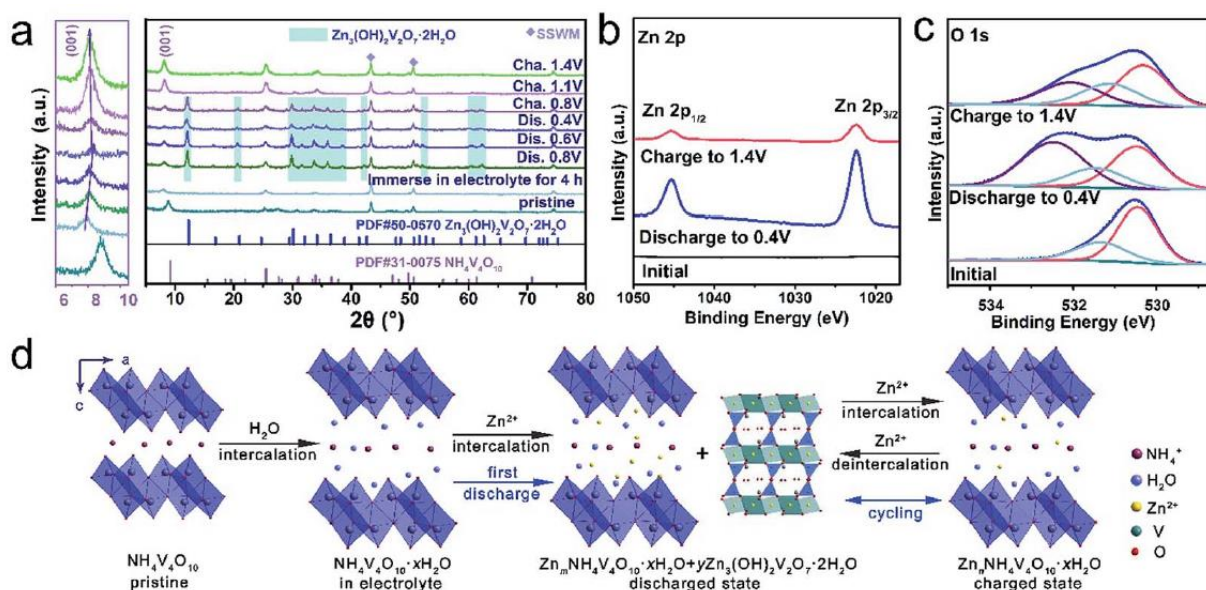


Figure 28. (a) Ex situ XRD patterns in different discharge/charge states; (b and c) ex situ high resolution XPS spectra of Zn 2p and O 1s at different discharge/charge states of the $\text{NH}_4\text{V}_4\text{O}_{10}$ electrode; (d) scheme showing the intercalation of H_2O molecules and the Zn^{2+} insertion/extraction process in $\text{NH}_4\text{V}_4\text{O}_{10}$ during cycling [174].

The strong electrostatic interaction with zinc and high charge density induce to bond with oxygen atoms in vanadate structure, thereby intercalated ions can be displaced from crystal lattice with further dissolution in electrolyte [90], [151], [164]. In addition during the cycling there is a possibility of formation $\text{Zn}_4(\text{SO}_4)(\text{OH})_6 \cdot n\text{H}_2\text{O}$ (ZHS) byproduct [104], [149], [175]. Nazar et al. reported that dissolved oxygen in electrolyte and existing Zn^{2+} , SO_4^{2-} and OH^- species can form ZHS [129]. The coated electrode materials and use of saturated electrolytes to reduce the amount water molecules could solve the problems with dissolution. The stability of VO_2 can be improved by carbon [21] or polypyrrole coating [27]. Zhang et al. demonstrated enhanced coulombic efficiency and exclude side reactions by using 30 m of ZnCl_2 [176]. It can be explained by reduced amount of water molecules and $[\text{Zn}(\text{OH})_2]^{2+}$ and $[\text{Zn}(\text{OH})_2\text{Cl}_4]^{2-}$ species.

Wang et al. proposed Carbon/vanadium dioxide (C/VO_2 (B)) core-shell microspheres prepared by hydrothermal process [21]. The electrochemical investigations of C/VO_2 (B) in LiCl aqueous electrolyte were evaluated by galvanostatic method and cyclic voltammetry. From **Figure 29** is shown that VO_2 (B) and C/VO_2 (B) two oxidation and one reduction peak are observed. The redox peaks of carbon coated sample slightly positively shifted due to the effect of carbon. After 17 cycles the redox peaks of bare VO_2 (B) completely disappeared suggesting poor cycle performance, while after 80 cycles, C/VO_2 (B) electrode has still distinct peaks.

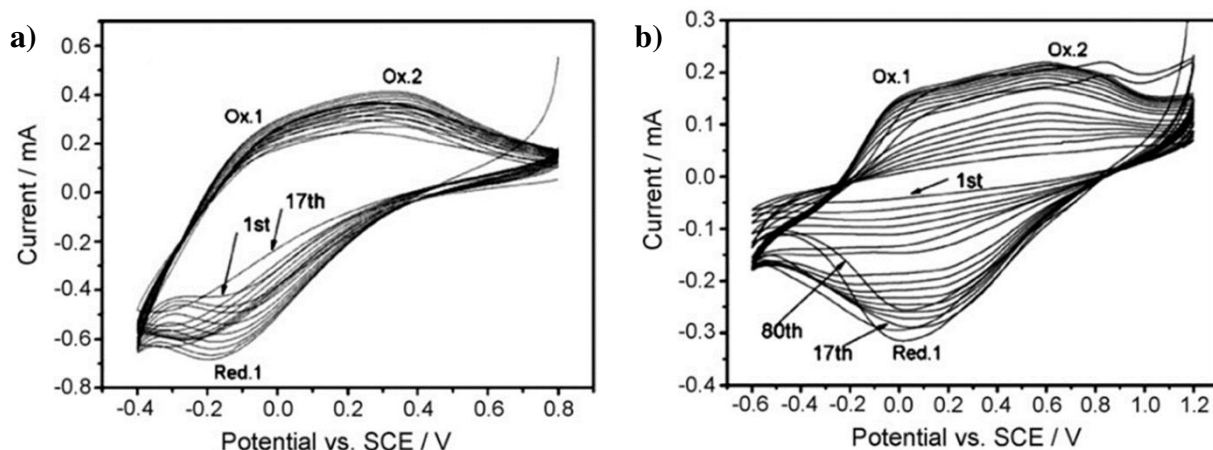


Figure 29. Cyclic voltammograms of (a) bare VO_2 (B) and (b) C/VO_2 (B) electrode in 2M LiCl with scan rate of 0.1 mV s^{-1} [21].

Liu et al. reported LiV_3O_8 -nanorod coated with conducting polypyrrole prepared by in-situ polymerization [54]. The prepared nanocomposite exhibits higher capacity and better rate capability in compare to pristine material, suggesting that Ppy works as conducting and coating agent inhibiting the dissolution of vanadium in aqueous electrolyte (**Figure 30**).

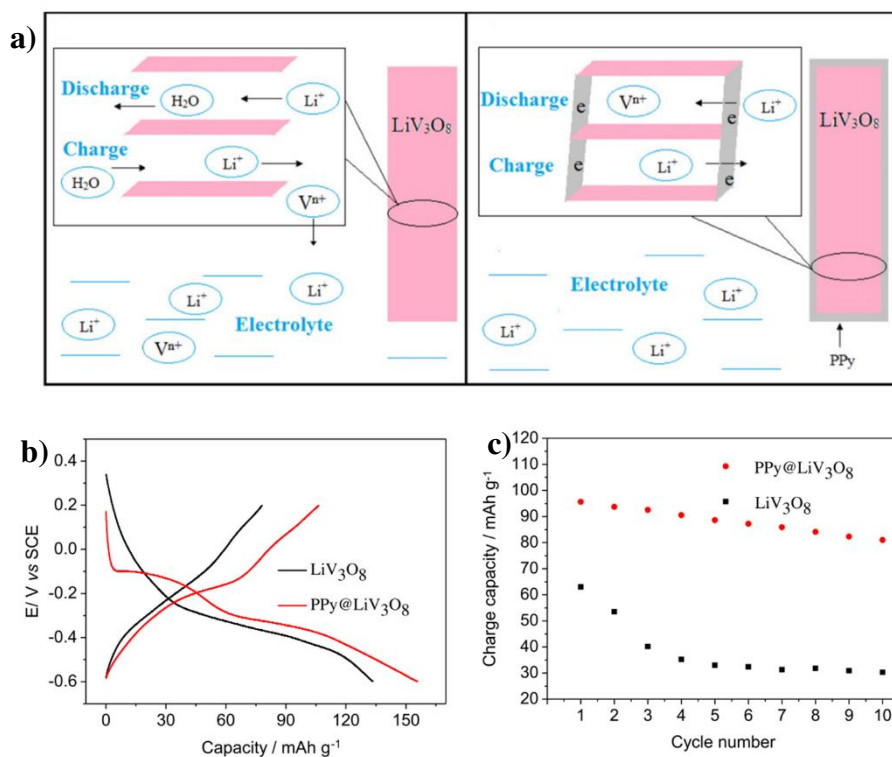


Figure 30. (a) Schematic illustration of lithium insertion/extraction for bare and coated LiV_3O_8 nanocomposite in aqueous electrolyte. (b) Charge/discharge profiles and (C) Cycle performance in 0.5M Li_2SO_4 using SCE as reference electrode [54].

Carbon modification also plays a vital role in alleviating the dissolution of Mn-based cathode materials in aqueous electrolytes [177], [178]. Wu et al. proposed $\alpha\text{-MnO}_2/\text{graphene}$ (MGO)

scrolls cathode material exhibiting highest energy value (406.6 Wh kg^{-1} at 0.3 A g^{-1}) among the reported cathode materials in AZIBs. The graphene scroll coating not only improve the electrical conductivity, it also reduces Mn dissolution and provide extra absorption sites for Zn^{2+} ions, resulting in high capacity, long-term cyclability and rate-capability (**Figure 31**). The overall reaction during discharge can be ascribed as following:

Cathode:

First discharge process: $2\text{x}\text{e}^- + \text{MnO}_2 + \text{xZn}^{2+} \leftrightarrow \text{Zn}_x\text{MnO}_2$ ($0 < x < 0.27$)

Second discharge process: $2(\text{x}-0.27) \text{e}^- + \text{Zn}_x\text{MnO}_2 + (\text{x}-0.27) \text{Zn}^{2+} \leftrightarrow \text{Zn}_x\text{MnO}_2$ ($0.27 < x < 0.59$)

Anode: $\text{Zn} - 2\text{e}^- \leftrightarrow \text{Zn}^{2+}$

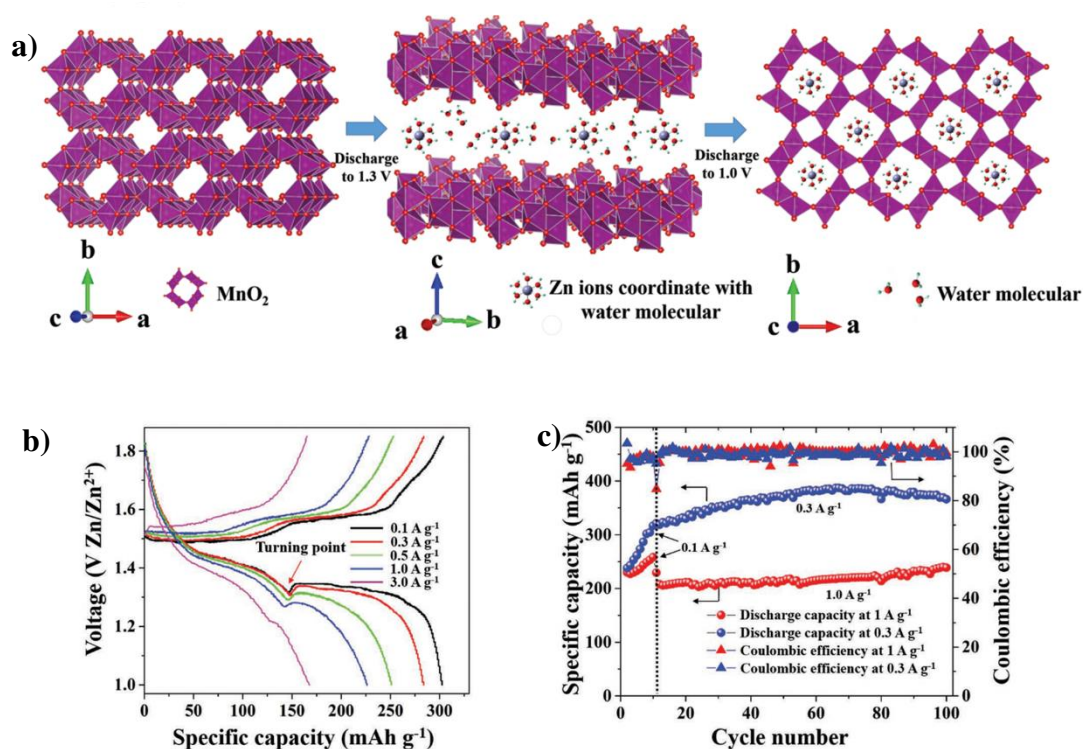


Figure 31. (a) Schematic illustration of two-step intercalation mechanism of MGO cathode. (b) Charge/discharge curves at various current density and (c) Cycle performance at 0.3 A g^{-1} and 1 A g^{-1} after activation process at 0.1 A g^{-1} in 2M ZnSO_4 electrolyte [177].

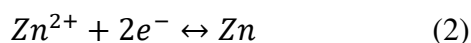
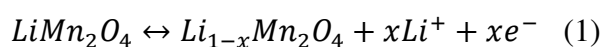
Several types of systems with various cathode materials have been already proposed for aqueous ZIBs, however several problems are existing like active material dissolution, sluggish diffusion, unexpected byproducts and contradictory results during the characterization of the insertion mechanisms. These problems make long-term cycling difficult to achieve, especially under low current density, which is not sustainable and practical for grid storage. Therefore,

more focused research solving these problems should be conducted to improve the capacity retention upon prolonged cycling and developed system to use in practical application.

4.1.4 Rechargeable Aqueous hybrid-ion batteries

The ideal battery could be one combining the stability and energy density of LIBs with the advantages of zinc aqueous batteries, which could remarkably reduce the cost of the energy storage. Therefore, the development of high energy density and ecologically friendly aqueous hybrid-ion battery technology is crucial.

More recently, Rechargeable Aqueous hybrid ion batteries (RAHBs) design (**Figure 32a**) attracted great interest due to the high operating voltage, low cost and high-power density compared to traditional Li and Zn aqueous batteries [11], [179]. The main difference from typical “rocking-chair” type, RAHBs operate based on two electrochemical redox processes separately on anode and cathode. Chen et al. proposed first hybrid Zn/ZnCl₂+LiCl/LiMn₂O₄ system operating in mild acidic electrolyte with high efficiency and long-term cyclability⁶. The electrolyte acts as conducting ions and cooperates with electrodes. The electrochemical reaction can be expressed as follows:



During the charge process, Li ions are extracted from LiMn₂O₄ at positive electrode (1.76–1.9 V vs Zn²⁺/Zn) and Zn²⁺ dissolution/deposition reaction at negative electrode (0 V vs. Zn²⁺/Zn). Upon discharge zinc metal loses electrons and dissolves in electrolyte, while on positive electrode Li ions insert into LiMn₂O₄ matrix. The two sets of reversible processes are observed at 0 and 1.76-1.9 V related to the deposition/dissolution of zinc and two-phase extraction/insertion process of lithium in spinel LiMn₂O₄, which is similar in organic electrolyte^{180–182}. XRD analysis confirms shifting characteristic peak of spinel LiMn₂O₄ toward higher angle during the charge, which indicates successful Li extraction. The reversible deposition/dissolution of zinc on the SS current collector during charge/discharge is also verified by XRD. The mechanism confirmed by electrochemical and structural investigations is illustrated in **Figure 32a**. Contrary to the “rocking-chair” type batteries, exchange of lithium and zinc ions in the aqueous electrolyte occurs during cycling. The electrolyte in the battery system is not only the conductive medium, it is also the source for zinc anode. The system

delivers high energy density of 50-80 Wh kg⁻¹ with excellent cyclability till 1000 cycles with 90% capacity retention (**Figure 32d**).

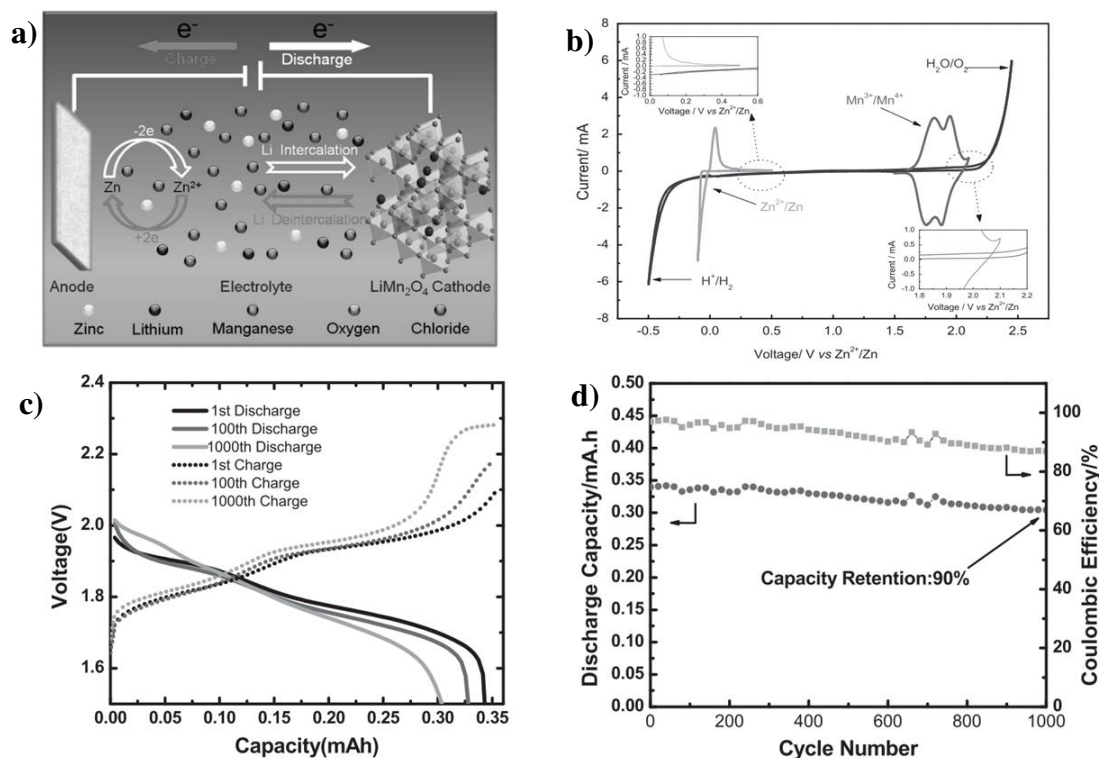


Figure 32. (a) Schematic illustration of Zn//LiMn₂O₄ in 4M ZnCl₂-3M LiCl hybrid electrolyte. (b) Cyclic voltammetry at scan rate of 0.5 mV s⁻¹. (c) Charge/discharge profiles and (d) Cycle performance at 4C [6].

However, the low conductivity and structural degradation of LiMn₂O₄ lead to poor rate capability [17], [180]. Chen et al. proposed LiMn₂O₄/porous graphene composite with significantly improved electrical conductivity and structure stability in 2M Li₂SO₄ + 1M ZnSO₄ electrolyte (pH=4) [181]. The system exhibits capacity 102.6 mAh g⁻¹ with 90% coulombic efficiency.

Similar to aqueous batteries, hybrid systems also face suffer from capacity fading resulting from change in pH value and concentration of electrolyte. Further improvements of electrochemical performance can be achieved by modifying electrolyte composition [182]–[184]. Chen et al. demonstrated thiourea (TU) as electrolyte additive in 2M ZnSO₄ + 1M Li₂SO₄ [182]. It was found that TU reduce voltage polarization and improve charge-discharge efficiency. Moreover, doping by SiO₂ in electrolyte (gel electrolyte) enhances the rate capability and high capacity by acceleration diffusion pathways for guest ions by reducing the polarization [183]. The highest capacity reaches 137.5 mAh g⁻¹ with 5% SiO₂. Hoang et al. developed new gelling system consist of β - cyclodextrin (CD) and fumes silica (FS) with hydroxyl groups on the surface [184]. The system Zn/LiMn₂O₄ with gel electrolyte delivers high discharge capacity retention (68%)

after 1000 cycles at 4C. The mixed gel electrolyte also suppresses the dendrite formation and corrosion on zinc electrode. The combination of pyrazole with fumes silica can act as corrosion inhibitor [185].

Furthermore, the pH value of hybrid electrolyte influence to the electrochemical performance of the battery. Chen et al. reported the regulation of pH value by dilute LiOH and H₂SO₄ to examine cycling properties of batteries [186]. It was found that at very low pH value of electrolyte increases the dissolution and at high pH makes OH⁻ concentration increase, resulting the Zn²⁺ precipitate by decreasing active material. Therefore, the control of pH value in zinc hybrid system plays major role on electrochemical performance.

In addition to LiMn₂O₄ other cathode materials like LiFePO₄ [7], [187], Li₃V₂(PO₄)₃ [186], LiVPO₄F [188], LiNi_{1/3}Co_{1/3}Mn_{1/3}O₂ [189], LiMn_{0.8}Fe_{0.2}PO₄ [190], V₂O₅ [8], [157] have been studied in aqueous hybrid batteries. However, the working potential of 4V materials in aqueous electrolyte is located close to the water decomposition potential (**Figure 33**) leading to the O₂ evolution resulting on the dissolution of metal ions in positive electrode.

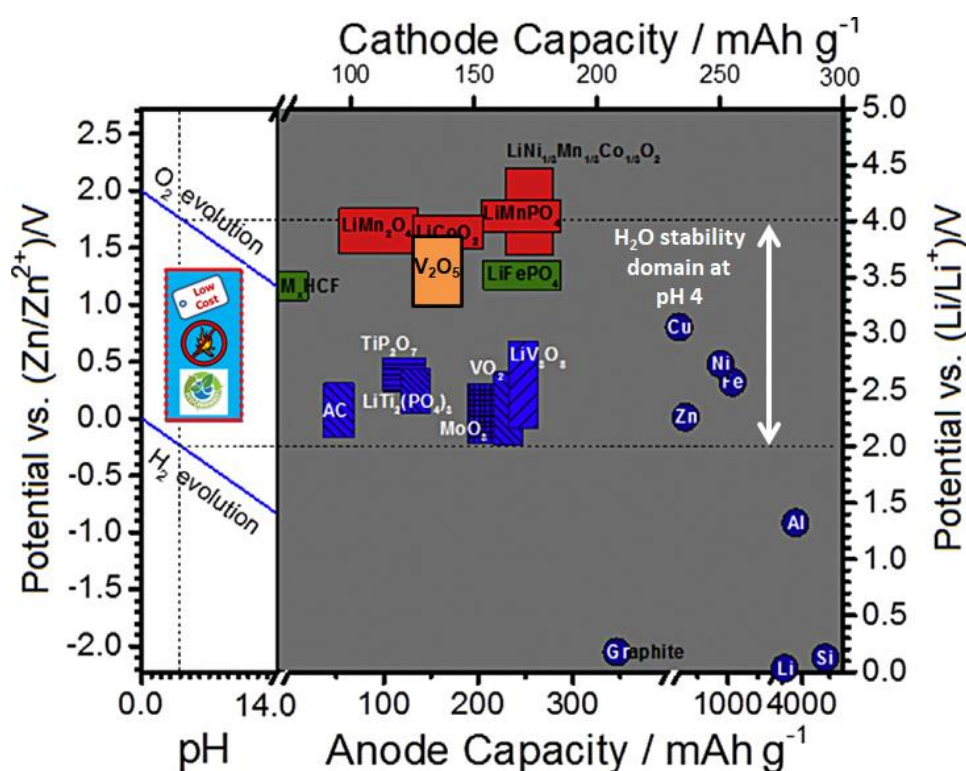


Figure 33. Electrochemical stability window of water and redox potential for negative and positive electrodes. Adapted from ref [7]

4.1.4-1 Water-is-salt hybrid electrolytes

Recently, new concept “water-in-salt” electrolytes have been developed for hybrid aqueous battery[8], [50], [157], [191]–[193]. High concentrations of salt widen the electrochemical stability window and enhance the cycling properties.

Zhang et al. reported that concentrated gelified electrolyte (21 m LiTFSI + 3 m ZnOTf₂) in polyvinyl alcohol (PVA) suppress side reactions and dendrite formation on the zinc surface (**Figure 34**)⁸. The shape of the CV curves between 0.2 – 1.6V demonstrates multistep insertion/extraction of Zn²⁺/Li⁺ with three pairs of redox peaks located at 0.66/0.57V, 0.89/0.8V and 1.45/1.2V which is similar to other works [155], [157]. Hybrid Zn/V₂O₅-GO system exhibits discharge capacity of ~180 mAh g⁻¹ and a capacity retention of 93% after 600 cycles at 500 mA g⁻¹. According to the in-situ XRD investigation, new reversible reflections observed at 16.9° and 33.1° in 0.7 – 0.2V range, attributed to Li_xZn_yV₂O₅ [139]. The capacity contribution above 1.9V can be attributed to oxygen redox chemistry or capacitive reaction without structural evolution (**Figure 34c**) [194].

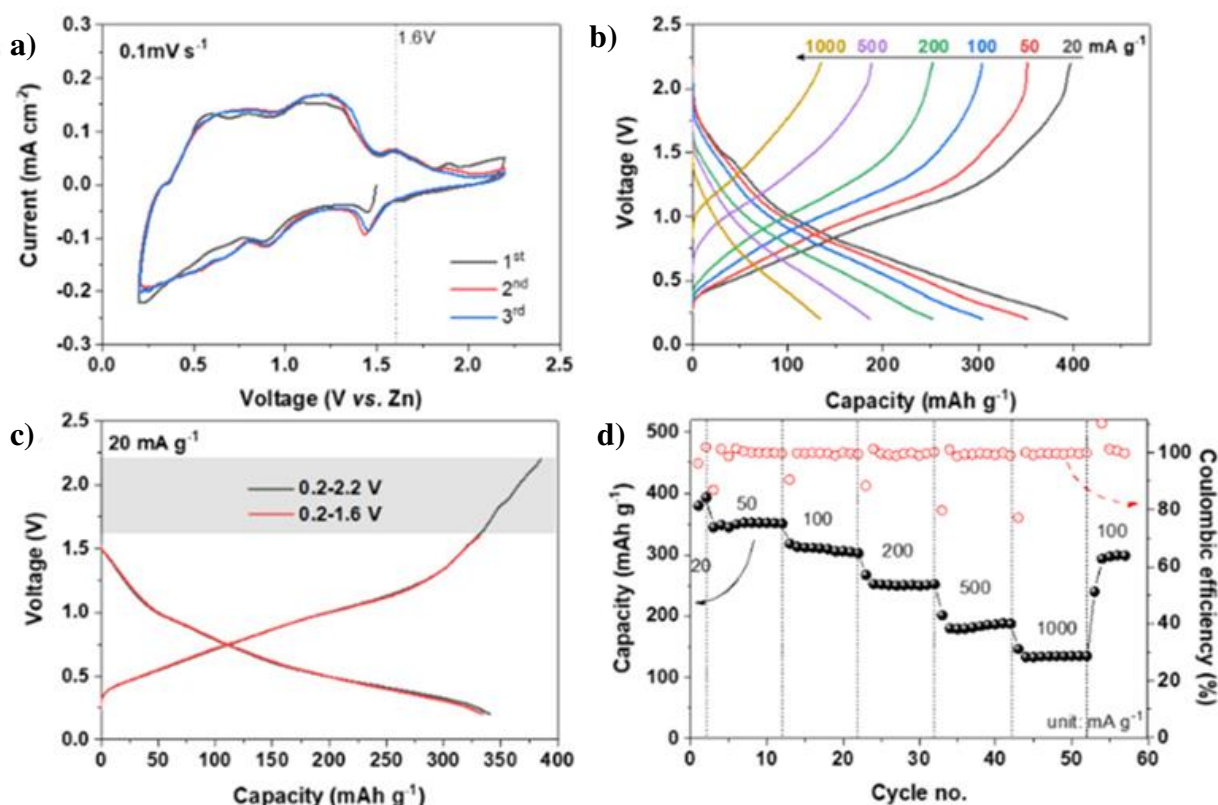


Figure 34. (a) Cyclic voltammetry of Zn//V₂O₅ cells at 0.1 mV s⁻¹ at voltage range of 0.2 – 2.2V in 21 m LiTFSI + 3 m ZnOTf₂ electrolyte. (b) Discharge/charge profiles at different C-rate. (c) 1st cycle at different voltage range. (d) Rate-capability [194].

Then Hu et al. reported Zn/V₂O₅ with 1m Zn(CF₃SO₃)₂ – 21 mLiTFSI water-in-salt electrolyte with outstanding cycle performance over 2000 cycles at 2 A g⁻¹ (**Figure 35**) [157].

In Zn(CF₃SO₃)₂ aqueous electrolyte three reduction peaks at 0.52, 0.93, 0.98V and four oxidation peaks at 0.71, 0.95, 1.22, 1.43V can be observed related to the zinc insertion/extraction process (**Figure 35a**).

In LiTFSI three reduction peaks at 0.56, 0.95, 1.17V and three oxidation peaks at 0.9, 1.08, 1.22V are associated with Li⁺ insertion/extraction reaction (**Figure 35b**).

In Zn(CF₃SO₃)₂-LiTFSI two redox peaks can be observed at 0.8/1.08V and 1.12/1.25V which probably corresponds to the intercalation/deintercalation of lithium ions with mixed Zn(CF₃SO₃)₂-LiTFSI electrolyte (**Figure 35**).

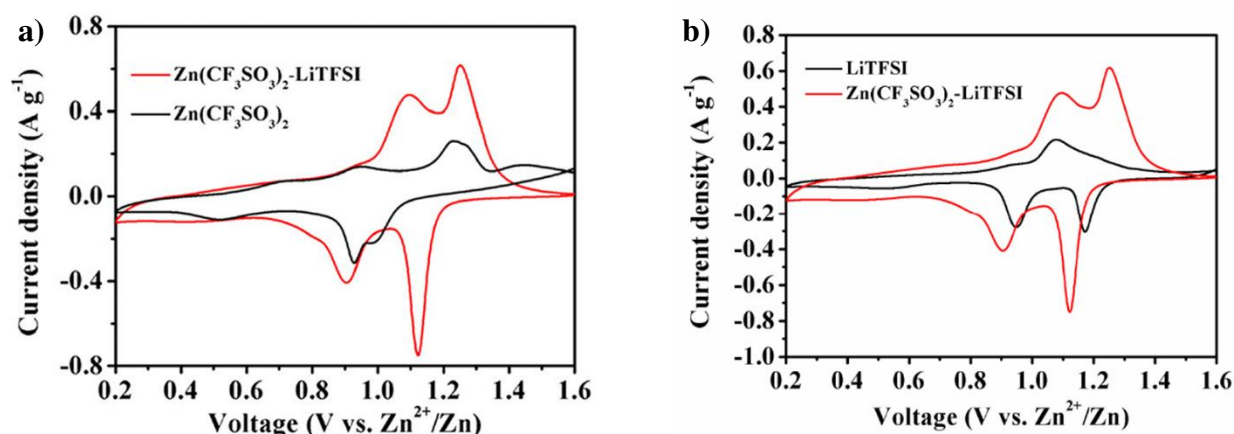


Figure 35. CV curves of Zn/V₂O₅ system with Zn(CF₃SO₃)₂-LiTFSI and (a) 1m Zn(CF₃SO₃)₂, (b) 21m LiTFSI aqueous electrolyte [157].

The Zn/V₂O₅ battery with Zn(CF₃SO₃)₂-LiTFSI electrolyte shows two discharge (1.1 and 0.9V) and two charge (1.23 and 1.06 V) plateaus which are higher than the plateau with Zn(CF₃SO₃)₂ (**Figure 36a**). The porous V₂O₅ electrode reaches initial capacity of 215 mAh g⁻¹ at 100 mA g⁻¹ in Zn(CF₃SO₃)₂-LiTFSI electrolyte and delivers 204 mAh g⁻¹ after 160 cycles demonstrating good cycling stability (**Figure 36b**).

In 1m Zn(CF₃SO₃)₂, V₂O₅ discharge capacity exhibits 201 mAh g⁻¹ with increasing capacity to 292 mAh g⁻¹ in initial 5 cycles, after retains capacity on 73 mAh g⁻¹ after 90 cycles.

In 21m LiTFSI, V₂O₅ reaches discharge capacity of 178 mAh g⁻¹ with rapid capacity fading after 50 cycles, due to the lack of Zn²⁺ ions, contributing on Zn deposition/dissolution process on the anode side. (**Figure 36b, c**).

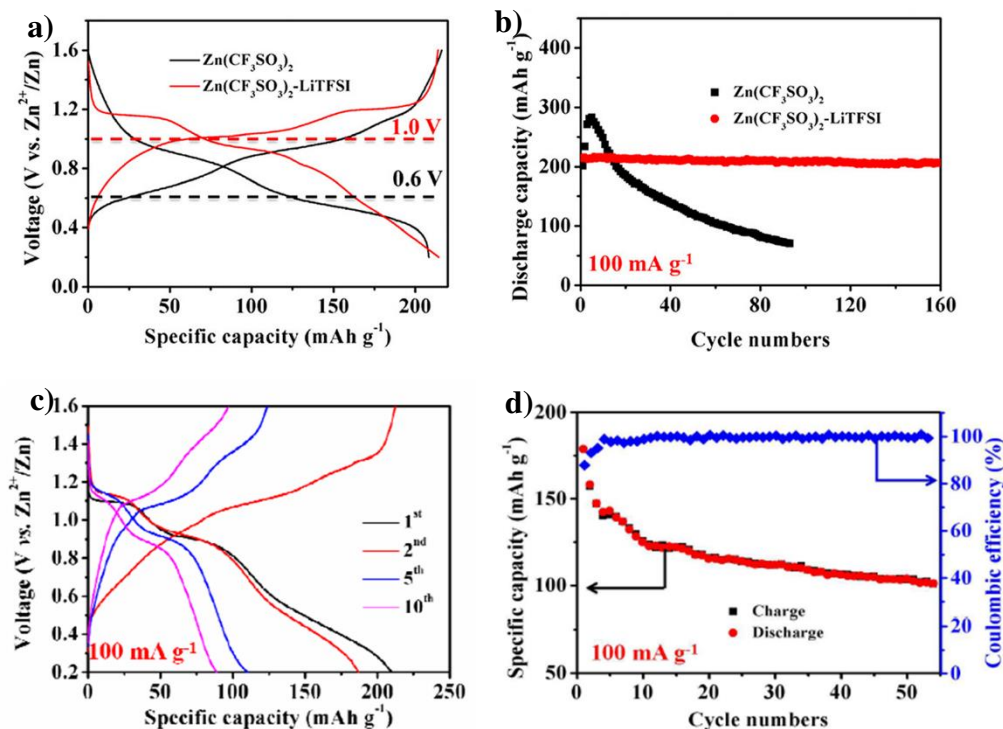


Figure 36. Electrochemical Investigation of Zn//V₂O₅ system (a) Discharge/charge profile and (b) cyclability with Zn(CF₃SO₃)₂-LiTFSI and (a) 1m Zn(CF₃SO₃)₂ electrolyte at 100 mA g⁻¹. (c) Discharge/charge and (d) Cycle performance with 21m LiTFSI electrolyte at 100 mA g⁻¹ [157].

XPS analysis of Zn//V₂O₅ system in Zn(CF₃SO₃)₂-LiTFSI electrolyte showed that during the discharge (at 0.2V), Zn²⁺ ions can intercalate into V₂O₅, however without complete extraction after charge to 1.6V due to the possible trapped Zn²⁺ ions, which may act as interlayer pillars and stabilize the structure of electrode material [80], [195]. In-situ XRD demonstrated that the (301) and (011) diffraction peaks merge into one peak during discharge and split during charge. These changes are completely reversible during the cycling, which reveals the structural stability of the system (**Figure 37**).

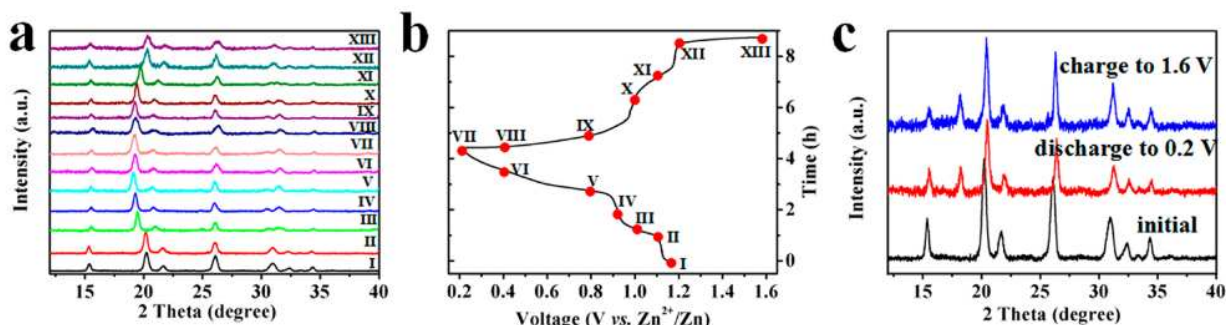


Figure 37. XRD patterns of V₂O₅ in Zn(CF₃SO₃)₂-LiTFSI electrolyte recorded at 100 mA g⁻¹ [157].

Wang et al. reported 1 m Zn(TFSI)₂ + 20m LiTFSI to reduce the presence of (Zn(H₂O)₆)²⁺ [193]. The pH value of electrolyte increases from 3 to ~7 with LiTFSI concentration, where

(Zn-TFSI)⁺ ion pairs forms which decrease the Zn²⁺ hydrolysis. Zn/LiMn₂O₄ system achieves energy density of 119 W h kg⁻¹ with long-term cycling over 4000 cycles at 4C and low specific capacity (30 mAh g⁻¹) (**Figure 38**).

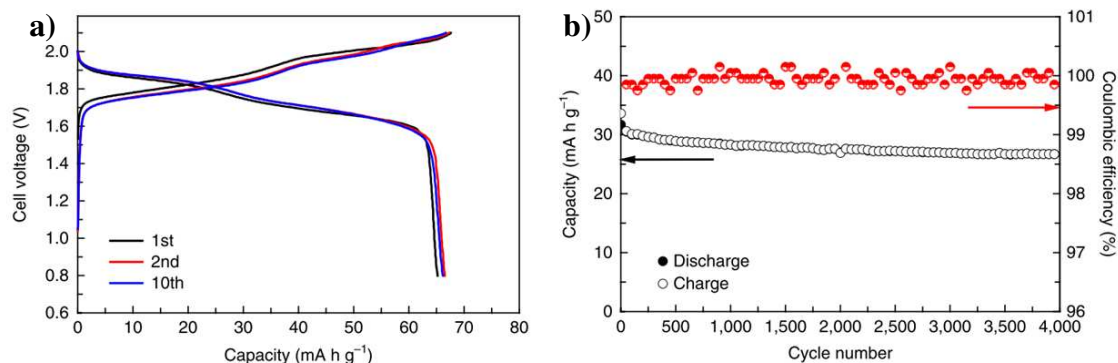


Figure 38. (a) Charge/discharge profile of Zn//LiMn₂O₄ system in 1 m Zn(TFSI)₂ + 20m LiTFSI electrolyte at 0.2C. (b) Cycle performance at 4C [193].

Chen et al. developed Zn/LiMn_{0.8}Fe_{0.2}PO₄ system with 21 m LiTFSI + 0.5 m ZnSO₄ (pH=4), which demonstrates 183 W h kg⁻¹ and a high operating voltage exceeding 1.8 V (**Figure 39**) [190]. However, the use of huge amount salts in electrolyte affects the cost of the battery and hinders practical application.

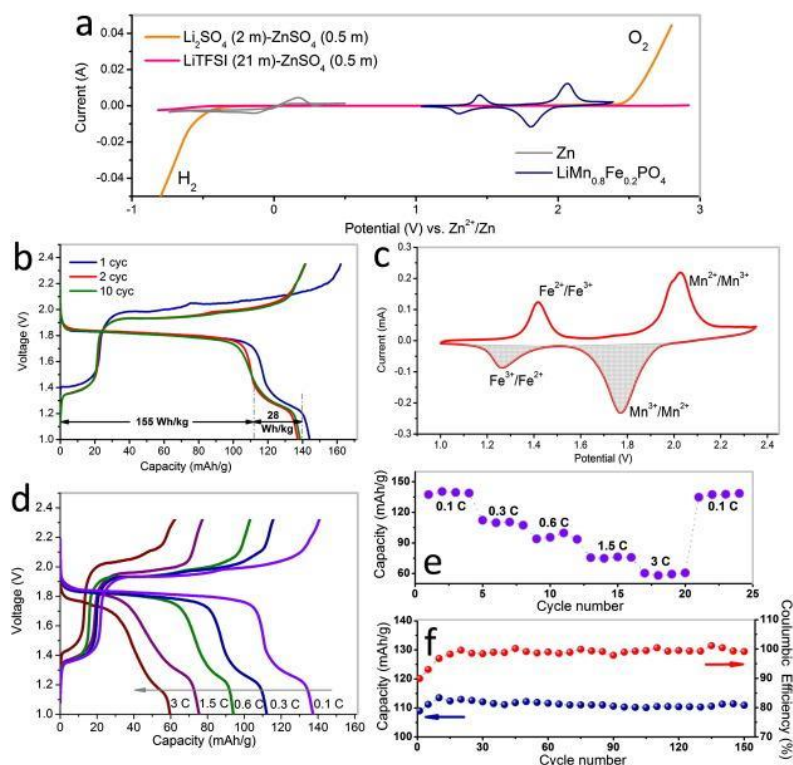
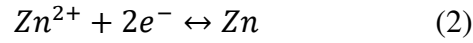
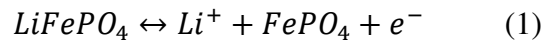


Figure 39. (a) CV curves of Zn at a scan rate of 0.2 mV/s and LiMn_{0.8}Fe_{0.2}PO₄ at 0.1 mV/s in 21 m LiTFSI + 0.5 m ZnSO₄ electrolyte in compare to 2m Li₂SO₄ + 0.5m ZnSO₄ (b) Charge/discharge curves of the

Zn/LiMn_{0.8}Fe_{0.2}PO₄ battery at 0.1 C rate (17 mA/g). (c) CV at a scan rate of 0.1 mV/s. (d) and (e) Rate capability of the battery. (f) Cycling stability of the battery at 0.3 C rate [190].

Yuan et al. proposed Zn/graphene coated LiFePO₄ in 0.5 M CH₃COOLi and 0.5 M Zn (CH₃COO)₂ electrolyte [187]. The battery delivers 145.8 mAh g⁻¹ at 0.2 C.

Bakenov group constructed Zn/LiFePO₄ system in 4M ZnCl₂ + 3M LiCl electrolyte (pH=4) [7]. At pH 4 the O₂ evolution reduced till 1.75 V vs. Zn/Zn²⁺, while H₂ evolution drops to -0.24 V vs. Zn/Zn²⁺. The system provides operating voltage of 1.2 V. During the charge LiFePO₄ is oxidized to FePO₄ and Li ions deintercalated from the matrix, while Zn ions deposits on the surface of zinc anode. Upon discharge Zn ions dissolves in electrolyte and Li ions intercalate into FePO₄ structure. The electrochemical reaction follows below:



Due to the deposition/dissolution process of zinc the concentration of electrolyte will increase/decrease respectively. Therefore, the amount of Zn²⁺ and Li⁺ should be enough for stable battery operation. The system exhibits 92 mAh g⁻¹ at 6C over 400 cycles with superior rate capability with capacity of 72 mAh g⁻¹ and 45 mAh g⁻¹ at 30 and 60 C respectively (**Figure 40**).

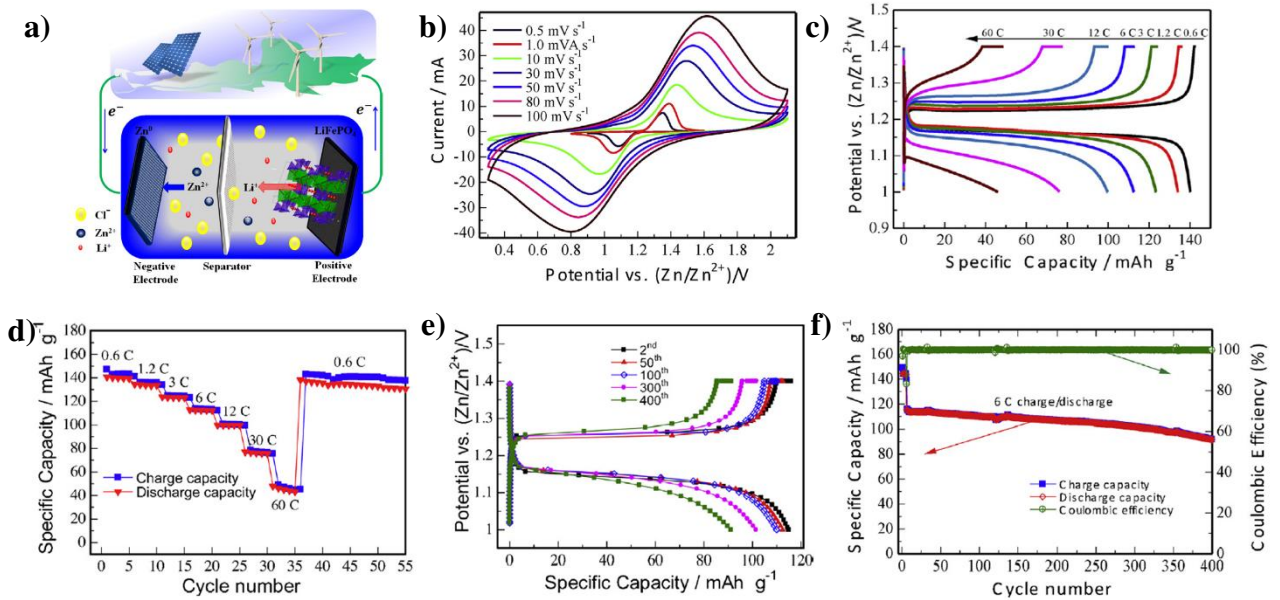


Figure 40. (a) Schematic illustration of Zn//LiFePO₄ with 4M ZnCl₂ + 3M LiCl. (b) Cyclic voltammetry at different scan-rates. (c) Charge/discharge at different C-rate. (d) Rate-capability. (e) Charge/discharge profile and (f) Cycle performance at 6C [7].

Table 5 demonstrates battery systems for Rechargeable Aqueous hybrid-ion batteries [63].

Table 5. Electrochemical performances of Rechargeable Aqueous hybrid-ion batteries, adapted from ref [63]

	Electrolyte	Average voltage [V]	Initial capacity [mAh g ⁻¹]	Cycle retention	Ref
LiMn ₂ O ₄ //Zn	3 M LiCl + 4 M ZnCl ₂ (pH=4)	1.8	-	1000 (90%)	[6]
CNT/AB/LiMn ₂ O ₄ //Zn	2 M Li ₂ SO ₄ + 1 M ZnSO ₄ (pH=4)	1.8	139	300 (66%) at 4C	[196]
LiMn ₂ O ₄ /PG//Zn	2 M Li ₂ SO ₄ + 1 M ZnSO ₄ (pH=4)	1.8	102.6	300 (74.2%) at 4C	[181]
LiMn ₂ O ₄ //Zn	2 M Li ₂ SO ₄ + 1 M ZnSO ₄ with 15 wt% fumed silica	1.8	96	800 (77.43%) at 4C	[197]
LiMn ₂ O ₄ //Zn	1 M Li ₂ SO ₄ + 2 M ZnSO ₄ with 0.14 wt% thiourea	1.8	-	300 (75%)	[182]
LiMn ₂ O ₄ //Zn	2 M Li ₂ SO ₄ + 1 M ZnSO ₄ with 5 wt% SiO ₂	1.8	122	700 (68.2%) at 4C	[183]
LiMn ₂ O ₄ //Zn	2 M Li ₂ SO ₄ + 1 M ZnSO ₄ with 4% fumed silica + 1% β -cyclodextrin	1.8	126	1000 (68%) at 4C	[184]
LiMn ₂ O ₄ //Zn	2 M Li ₂ SO ₄ + 1 M ZnSO ₄ with 5% fumed silica + 0.2% pyrazole	1.8	110	500 (85.2%) at 4C	[185]
LiMn ₂ O ₄ //Zn	2 M Li ₂ SO ₄ + 1 M ZnSO ₄ with 5% fumed silica + PbSO ₄	1.8	118	300 (74.4%) at 1C	[198]
LiMn ₂ O ₄ //Zn	1 m Zn(TFSI) ₂ + 20 m LiTFSI	1.8	34	4000 (85%) at 4C	[193]
LiMn ₂ O ₄ //Zn	“Water-in-deep eutectic solvent” electrolyte	1.92	110	300 (~90%) at 0.1C	[199]
LiMn ₂ O ₄ //Zn/AC	0.5 M Li ₂ SO ₄ + 1 M ZnSO ₄	1.8	150	210 (40%) at 240 mA g ⁻¹	[200]
LiMn ₂ O ₄ //Zn-TU	2 M Li ₂ SO ₄ + 1 M ZnSO ₄	1.8	96	1000 (80%)	[201]
LiNi _{1/3} Co _{1/3} Mn _{1/3} O ₂ @graphene@MWCNTs//Zn	0.25 M Li ₂ SO ₄ + 0.125 M Zn(CH ₃ COO) ₂	1.65	105	50 (99%) at 0.5C	[189]
LiMn _{0.8} Fe _{0.2} PO ₄ //Zn	21 m LiTFSI + 0.5 m ZnSO ₄ (pH=4)	1.8/1.3	137	150 (100%) at 0.1C	[190]
V ₂ O ₅ //Zn	4M ZnSO ₄ + 3M Li ₂ SO ₄ (pH=4)	1.12	80	300 (100%) at 1C	[202]
V ₂ O ₅ //Zn	1 m Zn(CF ₃ SO ₃) ₂ + 21 m LiTFSI	1.0	215	160 (95%) at 100 mA g ⁻¹	[157]

V ₂ O ₅ @GO//Zn	21 m LiTFSI + 3 m ZnOTf ₂ with 10 wt% PVA – Gel aqueous electrolyte	1.0	-	600 (93%) at 500 mA g ⁻¹	[8]
LiFePO ₄ //Zn	4M ZnSO ₄ + 3M Li ₂ SO ₄ (pH=4)	1.2	120	400 (100%) at 6C	[7]
LiFePO ₄ /graphene//Zn	0.5 M LiCH ₃ COO + 0.5 M Zn(CH ₃ COO) ₂	1.4	145.8	450 (78%) at 0.2C	[187]
Li ₃ V ₂ (PO ₄) ₃ //Zn	1 M Li ₂ SO ₄ + 2 M ZnSO ₄	1.4	128	200 (85.4%) at 0.2C	[186]

According to the literature review on hybrid electrolyte we can conclude that three main materials have been reported: spinel LiMnO₄, LiFePO₄, V₂O₅. Vanadium oxide (V₂O₅) material was widely investigated for aqueous zinc ion batteries, however according to the review, only few papers can be found related to the hybrid electrolyte system (water-in-salt). In addition, little attention has been paid to the structural behavior of cathode materials.

Therefore, our goal was to deeply examine the electrochemical properties of V₂O₅ polymorphs (α and γ' phases) in aqueous hybrid electrolyte (Li⁺, Zn²⁺) focusing on reaction mechanisms, structural evolution upon discharge/charge, and comparison with the obtained results in organic (non-aqueous) electrolyte.

Such approach is developed in the case of α -V₂O₅ and γ' -V₂O₅ phases in the following sub-chapters 4.2 and 4.3 respectively.

REFERENCES

- [1] P. Simon, Y. Gogotsi, and P. Simon, "08nature mater-Materials for electrochemical capacitors.PDF," *Nat. Mater.*, vol. 7, pp. 845–854, 2008.
- [2] L. ZUXIANG, Y. HUIJUN, L. SHICHUN, and T. SHUNBAO, "Phase relationship and electrical conductivity of $\text{Li}_{1+x}\text{Ti}_2-x\text{GaxP}_3\text{O}_{12}$ and $\text{Li}_{1+2x}\text{Ti}_2-x\text{MgxP}_3\text{O}_{12}$ systems," *Solid State Ionics*, vol. 18–19, no. PART 1, pp. 549–552, Jan. 1986, doi: 10.1016/0167-2738(86)90176-1.
- [3] J. Y. Luo, W. J. Cui, P. He, and Y. Y. Xia, "Raising the cycling stability of aqueous lithium-ion batteries by eliminating oxygen in the electrolyte," *Nat. Chem.*, vol. 2, no. 9, pp. 760–765, 2010, doi: 10.1038/nchem.763.
- [4] W. Tang *et al.*, "Aqueous rechargeable lithium batteries as an energy storage system of superfast charging," *Energy Environ. Sci.*, vol. 6, no. 7, pp. 2093–2104, 2013, doi: 10.1039/c3ee24249h.
- [5] W. Li, J. R. Dahn, and D. S. Wainwright, "Rechargeable Lithium Batteries with Aqueous Electrolytes," *Science (80-.)*, vol. 264, no. 5162, pp. 1115–1118, May 1994, doi: 10.1126/science.264.5162.1115.
- [6] J. Yan, J. Wang, H. Liu, Z. Bakenov, D. Gosselink, and P. Chen, "Rechargeable hybrid aqueous batteries," *J. Power Sources*, vol. 216, pp. 222–226, Oct. 2012, doi: 10.1016/j.jpowsour.2012.05.063.
- [7] N. Yesibolati *et al.*, "High Performance Zn/LiFePO₄ Aqueous Rechargeable Battery for Large Scale Applications," *Electrochim. Acta*, vol. 152, pp. 505–511, Jan. 2015, doi: 10.1016/j.electacta.2014.11.168.
- [8] H. Zhang, X. Liu, H. Li, B. Qin, and S. Passerini, "High-Voltage Operation of a V₂O₅ Cathode in a Concentrated Gel Polymer Electrolyte for High-Energy Aqueous Zinc Batteries," *ACS Appl. Mater. Interfaces*, vol. 12, no. 13, pp. 15305–15312, Apr. 2020, doi: 10.1021/acsami.0c02102.
- [9] S. Liu, G. L. Pan, N. F. Yan, and X. P. Gao, "Aqueous TiO₂/Ni(OH)₂ rechargeable battery with a high voltage based on proton and lithium insertion/extraction reactions," *Energy Environ. Sci.*, vol. 3, no. 11, pp. 1732–1735, 2010, doi: 10.1039/c0ee00170h.
- [10] J. Liu *et al.*, "Aqueous rechargeable alkaline Co_xNi_{2-x}S₂/TiO₂ battery," *ACS Nano*, vol. 10, no. 1, pp. 1007–1016, 2016, doi: 10.1021/acs.nano.5b06275.
- [11] J. Liu, C. Xu, Z. Chen, S. Ni, and Z. X. Shen, "Progress in aqueous rechargeable batteries," *Green Energy Environ.*, vol. 3, no. 1, pp. 20–41, 2018, doi: 10.1016/j.gee.2017.10.001.
- [12] R. Demir-Cakan, M. R. Palacin, and L. Croguennec, "Rechargeable aqueous electrolyte batteries: From univalent to multivalent cation chemistry," *J. Mater. Chem. A*, vol. 7, no. 36, pp. 20519–20539, 2019, doi: 10.1039/c9ta04735b.
- [13] W. Pie, Y. Hui, and Y. Huaquan, "Electrochemical behavior of Li-Mn spinel electrode material in aqueous solution," *J. Power Sources*, vol. 63, no. 2, pp. 275–278, 1996, doi: 10.1016/S0378-7753(96)02477-9.
- [14] M. M. Rao, M. Jayalakshmi, O. Schäf, H. Wulff, U. Guth, and F. Scholz, "Electrochemical behaviour of solid lithium cobaltate (LiCoO₂) and lithium manganate (LiMn₂O₄) in an aqueous electrolyte system," *J. Solid State Electrochem.*, vol. 5, no. 1, pp. 50–56, 2001, doi: 10.1007/pl00010801.
- [15] Y. Wang and Y. Xia, "Hybrid Aqueous Energy Storage Cells Using Activated Carbon and Lithium-Intercalated Compounds," *J. Electrochem. Soc.*, vol. 153, no. 2, p. A450, 2006, doi: 10.1149/1.2140678.
- [16] W. Tang *et al.*, "Nanochain LiMn₂O₄ as ultra-fast cathode material for aqueous rechargeable lithium batteries," *Electrochem. commun.*, vol. 13, no. 2, pp. 205–208, 2011, doi: 10.1016/j.elecom.2010.12.015.

- [17] W. Tang, Y. Hou, F. Wang, L. Liu, Y. Wu, and K. Zhu, "LiMn₂O₄ nanotube as cathode material of second-level charge capability for aqueous rechargeable batteries," *Nano Lett.*, vol. 13, no. 5, pp. 2036–2040, 2013, doi: 10.1021/nl400199r.
- [18] Q. Qu *et al.*, "Porous LiMn₂O₄ as cathode material with high power and excellent cycling for aqueous rechargeable lithium batteries," *Energy Environ. Sci.*, vol. 4, no. 10, pp. 3985–3990, 2011, doi: 10.1039/c0ee00673d.
- [19] P. He, J. L. Liu, W. J. Cui, J. Y. Luo, and Y. Y. Xia, "Investigation on capacity fading of LiFePO₄ in aqueous electrolyte," *Electrochim. Acta*, vol. 56, no. 5, pp. 2351–2357, 2011, doi: 10.1016/j.electacta.2010.11.027.
- [20] A. Yuan, L. Tian, W. Xu, and Y. Wang, "Al-doped spinel LiAl_{0.1}Mn_{1.9}O₄ with improved high-rate cyclability in aqueous electrolyte," *J. Power Sources*, vol. 195, no. 15, pp. 5032–5038, 2010, doi: 10.1016/j.jpowsour.2010.01.074.
- [21] F. Wang, Y. Liu, and C. yan Liu, "Hydrothermal synthesis of carbon/vanadium dioxide core-shell microspheres with good cycling performance in both organic and aqueous electrolytes," *Electrochim. Acta*, vol. 55, no. 8, pp. 2662–2666, 2010, doi: 10.1016/j.electacta.2009.12.017.
- [22] S. Zhang, Y. Li, C. Wu, F. Zheng, and Y. Xie, "Novel flowerlike metastable vanadium dioxide (B) micronanostructures: Facile synthesis and application in aqueous lithium ion batteries," *J. Phys. Chem. C*, vol. 113, no. 33, pp. 15058–15067, 2009, doi: 10.1021/jp903312h.
- [23] G. G. Amatucci *et al.*, "Investigation of Yttrium and Polyvalent Ion Intercalation into Nanocrystalline Vanadium Oxide," *J. Electrochem. Soc.*, vol. 148, no. 8, p. A940, 2001, doi: 10.1149/1.1383777.
- [24] C. Deng, S. Zhang, Z. Dong, and Y. Shang, "1D nanostructured sodium vanadium oxide as a novel anode material for aqueous sodium ion batteries," *Nano Energy*, vol. 4, pp. 49–55, 2014, doi: 10.1016/j.nanoen.2013.12.014.
- [25] C. Wu, Z. Hu, W. Wang, M. Zhang, J. Yang, and Y. Xie, "Synthetic paramontroseite VO₂ with good aqueous lithium-ion battery performance," *Chem. Commun.*, no. 33, pp. 3891–3893, 2008, doi: 10.1039/b806009f.
- [26] Y. Xu, L. Zheng, and Y. Xie, "From synthetic montroseite VOOH to topochemical paramontroseite VO₂ and their applications in aqueous lithium ion batteries," *Dalt. Trans.*, vol. 39, no. 44, pp. 10729–10738, 2010, doi: 10.1039/c0dt00715c.
- [27] W. Tang, L. Liu, Y. Zhu, H. Sun, Y. Wu, and K. Zhu, "An aqueous rechargeable lithium battery of excellent rate capability based on a nanocomposite of MoO₃ coated with PPy and LiMn₂O₄," *Energy Environ. Sci.*, vol. 5, no. 5, pp. 6909–6913, 2012, doi: 10.1039/c2ee21294c.
- [28] K. H. Reiman, K. M. Brace, T. J. Gordon-Smith, I. Nandhakumar, G. S. Attard, and J. R. Owen, "Lithium insertion into TiO₂ from aqueous solution - Facilitated by nanostructure," *Electrochem. commun.*, vol. 8, no. 4, pp. 517–522, 2006, doi: 10.1016/j.elecom.2006.01.017.
- [29] M. Manickam, P. Singh, T. B. Issa, and S. Thurgate, "Electrochemical behavior of anatase TiO₂ in aqueous lithium hydroxide electrolyte," *J. Appl. Electrochem.*, vol. 36, no. 5, pp. 599–602, 2006, doi: 10.1007/s10800-005-9112-9.
- [30] S. Liu, S. H. Ye, C. Z. Li, G. L. Pan, and X. P. Gao, "Rechargeable Aqueous Lithium-Ion Battery of TiO₂/LiMn₂O₄ with a High Voltage," *J. Electrochem. Soc.*, vol. 158, no. 12, p. A1490, 2011, doi: 10.1149/2.094112jes.
- [31] J. Y. Luo and Y. Y. Xia, "Aqueous lithium-ion battery LiTi₂(PO₄)₃/LiMn₂O₄ with high power and energy densities as well as superior cycling stability," *Adv. Funct. Mater.*, vol. 17, no. 18, pp. 3877–3884, 2007, doi: 10.1002/adfm.200700638.
- [32] M. Minakshi, P. Singh, S. Thurgate, and K. Prince, "Electrochemical behavior of

- olivine-type LiMnPO_4 in aqueous solutions,” *Electrochem. Solid-State Lett.*, vol. 9, no. 10, pp. 471–474, 2006, doi: 10.1149/1.2236379.
- [33] H. Wang, K. Huang, Y. Zeng, S. Yang, and L. Chen, “Electrochemical properties of TiP_2O_7 and $\text{LiTi}_2(\text{PO}_4)_3$ as anode material for lithium ion battery with aqueous solution electrolyte,” *Electrochim. Acta*, vol. 52, no. 9, pp. 3280–3285, 2007, doi: 10.1016/j.electacta.2006.10.010.
- [34] M. Zhao, G. Huang, W. Zhang, H. Zhang, and X. Song, “Electrochemical behaviors of $\text{LiMn}_{1-x}\text{Fe}_x\text{PO}_4/\text{C}$ cathode materials in an aqueous electrolyte with/without dissolved oxygen,” *Energy and Fuels*, vol. 27, no. 2, pp. 1162–1167, 2013, doi: 10.1021/ef301893b.
- [35] J. chao Zheng *et al.*, “Novel synthesis of $\text{LiFePO}_4\text{-Li}_3\text{V}_2(\text{PO}_4)_3$ composite cathode material by aqueous precipitation and lithiation,” *J. Power Sources*, vol. 195, no. 9, pp. 2935–2938, 2010, doi: 10.1016/j.jpowsour.2009.11.006.
- [36] M. Zhao, B. Zhang, G. Huang, H. Zhang, and X. Song, “Excellent rate capabilities of $(\text{LiFePO}_4/\text{C})//\text{LiV}_3\text{O}_8$ in an optimized aqueous solution electrolyte,” *J. Power Sources*, vol. 232, pp. 181–186, 2013, doi: 10.1016/j.jpowsour.2013.01.026.
- [37] G. Wang, Q. Qu, B. Wang, Y. Shi, S. Tian, and Y. Wu, “An aqueous electrochemical energy storage system based on doping and intercalation: $\text{Ppy}/\text{LiMn}_2\text{O}_4$,” *ChemPhysChem*, vol. 9, no. 16, pp. 2299–2301, 2008, doi: 10.1002/cphc.200800424.
- [38] H. Kim, J. Hong, K. Y. Park, H. Kim, S. W. Kim, and K. Kang, “Aqueous rechargeable Li and Na ion batteries,” *Chem. Rev.*, vol. 114, no. 23, pp. 11788–11827, 2014, doi: 10.1021/cr500232y.
- [39] H. Wang, Y. Zeng, K. Huang, S. Liu, and L. Chen, “Improvement of cycle performance of lithium ion cell $\text{LiMn}_2\text{O}_4/\text{Li}_x\text{V}_2\text{O}_5$ with aqueous solution electrolyte by polypyrrole coating on anode,” *Electrochim. Acta*, vol. 52, no. 15, pp. 5102–5107, 2007, doi: 10.1016/j.electacta.2007.02.004.
- [40] D. Zhou, S. Liu, H. Wang, and G. Yan, “ $\text{Na}_2\text{V}_6\text{O}_{16} \cdot 0.14\text{H}_2\text{O}$ nanowires as a novel anode material for aqueous rechargeable lithium battery with good cycling performance,” *J. Power Sources*, vol. 227, pp. 111–117, 2013, doi: 10.1016/j.jpowsour.2012.11.022.
- [41] V. A. Online, “Journal of Materials Chemistry A,” pp. 5423–5429, 2013, doi: 10.1039/c3ta01548c.
- [42] P. He, X. Zhang, Y.-G. Wang, L. Cheng, and Y.-Y. Xia, “Lithium-Ion Intercalation Behavior of LiFePO_4 in Aqueous and Nonaqueous Electrolyte Solutions,” *J. Electrochem. Soc.*, vol. 155, no. 2, p. A144, 2008, doi: 10.1149/1.2815609.
- [43] J. Köhler, H. Makihara, H. Uegaito, H. Inoue, and M. Toki, “ LiV_3O_8 : Characterization as anode material for an aqueous rechargeable Li-ion battery system,” *Electrochim. Acta*, vol. 46, no. 1, pp. 59–65, 2000, doi: 10.1016/S0013-4686(00)00515-6.
- [44] G. Wang, L. Fu, N. Zhao, L. Yang, Y. Wu, and H. Wu, “An aqueous rechargeable lithium battery with good cycling performance,” *Angew. Chemie - Int. Ed.*, vol. 46, no. 1–2, pp. 295–297, 2007, doi: 10.1002/anie.200603699.
- [45] H. Manjunatha, T. V. Venkatesha, and G. S. Suresh, “Electrochemical studies of LiMnPO_4 as aqueous rechargeable lithium-ion battery electrode,” *J. Solid State Electrochem.*, vol. 16, no. 5, pp. 1941–1952, 2012, doi: 10.1007/s10008-011-1593-3.
- [46] F. Wang, S. Xiao, Z. Chang, Y. Yang, and Y. Wu, “Nanoporous $\text{LiNi}_{1/3}\text{Co}_{1/3}\text{Mn}_{1/3}\text{O}_2$ as an ultra-fast charge cathode material for aqueous rechargeable lithium batteries,” *Chem. Commun.*, vol. 49, no. 80, pp. 9209–9211, 2013, doi: 10.1039/c3cc44360d.
- [47] C. D. Wessells, R. A. Huggins, and Y. Cui, “Copper hexacyanoferrate battery electrodes with long cycle life and high power,” *Nat. Commun.*, vol. 2, no. 1, pp. 550–

- 555, 2011, doi: 10.1038/ncomms1563.
- [48] C. D. Wessells, S. V. Peddada, R. A. Huggins, and Y. Cui, "Nickel hexacyanoferrate nanoparticle electrodes for aqueous sodium and potassium ion batteries," *Nano Lett.*, vol. 11, no. 12, pp. 5421–5425, 2011, doi: 10.1021/nl203193q.
 - [49] F. Sauvage, L. Laffont, J. M. Tarascon, and E. Baudrin, "Factors affecting the electrochemical reactivity vs. lithium of carbon-free LiFePO₄ thin films," *J. Power Sources*, vol. 175, no. 1, pp. 495–501, 2008, doi: 10.1016/j.jpowsour.2007.09.085.
 - [50] L. Suo *et al.*, "'Water-in-salt' electrolyte enables high-voltage aqueous lithium-ion chemistries," *Science (80-.)*, vol. 350, no. 6263, pp. 938–943, 2015, doi: 10.1126/science.aab1595.
 - [51] T. Fukutsuka, H. Miwa, K. Miyazaki, and T. Abe, "Electrochemical Behavior of Spinel Lithium Titanate in Ionic Liquid/Water Bilayer Electrolyte," *J. Electrochem. Soc.*, vol. 163, no. 13, pp. A2497–A2500, 2016, doi: 10.1149/2.0131613jes.
 - [52] F. Wang *et al.*, "Stabilizing high voltage LiCoO₂ cathode in aqueous electrolyte with interphase-forming additive," *Energy Environ. Sci.*, vol. 9, no. 12, pp. 3666–3673, 2016, doi: 10.1039/c6ee02604d.
 - [53] M. Jayalakshmi, M. M. Rao, and F. Scholz, "Electrochemical behavior of solid lithium manganate (LiMn₂O₄) in aqueous neutral electrolyte solutions," *Langmuir*, vol. 19, no. 20, pp. 8403–8408, 2003, doi: 10.1021/la0340448.
 - [54] L. L. Liu, X. J. Wang, Y. S. Zhu, C. L. Hu, Y. P. Wu, and R. Holze, "Polypyrrole-coated LiV₃O₈-nanocomposites with good electrochemical performance as anode material for aqueous rechargeable lithium batteries," *J. Power Sources*, vol. 224, pp. 290–294, 2013, doi: 10.1016/j.jpowsour.2012.09.100.
 - [55] R. B. Shivashankaraiah, H. Manjunatha, K. C. Mahesh, G. S. Suresh, and T. V. Venkatesha, "Electrochemical characterization of polypyrrole-LiNi_{1/3}Mn_{1/3}Co_{1/3}O₂ composite cathode material for aqueous rechargeable lithium batteries," *J. Solid State Electrochem.*, vol. 16, no. 3, pp. 1279–1290, 2012, doi: 10.1007/s10008-011-1520-7.
 - [56] A. Tron, H. Kang, J. Kim, and J. Mun, "Journal of Electrochemical Science and Technology Electrochemical Performance of AlF₃-Coated LiV₃O₈ for Aqueous Rechargeable Lithium Ion Batteries," vol. 9, no. 1, pp. 60–68, 2018.
 - [57] J. M. Chem, "A hybrid of V₂O₅ nanowires and MWCNTs coated with polypyrrole as an cycling performance †," pp. 20143–20145, 2012, doi: 10.1039/c2jm34563c.
 - [58] A. Tron, Y. N. Jo, S. H. Oh, Y. D. Park, and J. Mun, "Surface Modification of the LiFePO₄ Cathode for the Aqueous Rechargeable Lithium Ion Battery," *ACS Appl. Mater. Interfaces*, vol. 9, no. 14, pp. 12391–12399, 2017, doi: 10.1021/acsami.6b16675.
 - [59] X. Zeng *et al.*, "Electrochemical Behavior of Spherical LiFePO₄/C Nanomaterial in Aqueous Electrolyte, and Novel Aqueous Rechargeable Lithium Battery with LiFePO₄/C anode," *Electrochim. Acta*, vol. 177, pp. 277–282, 2015, doi: 10.1016/j.electacta.2014.12.088.
 - [60] X. Gu, J. L. Liu, J. H. Yang, H. J. Xiang, X. G. Gong, and Y. Y. Xia, "First-principles study of H⁺ intercalation in layer-structured LiCoO₂," *J. Phys. Chem. C*, vol. 115, no. 25, pp. 12672–12676, 2011, doi: 10.1021/jp202846p.
 - [61] R. Ruffo, C. Wessells, R. A. Huggins, and Y. Cui, "Electrochemistry Communications Electrochemical behavior of LiCoO₂ as aqueous lithium-ion battery electrodes," *Electrochem. commun.*, vol. 11, pp. 247–249, 2009, doi: 10.1016/j.elecom.2008.11.015.
 - [62] W. Tang *et al.*, "Electrochemistry Communications Nano-LiCoO₂ as cathode material of large capacity and high rate capability for aqueous rechargeable lithium batteries," vol. 12, pp. 1524–1526, 2010, doi: 10.1016/j.elecom.2010.08.024.

- [63] H. Ao *et al.*, “Rechargeable aqueous hybrid ion batteries: Developments and prospects,” *J. Mater. Chem. A*, vol. 7, no. 32, pp. 18708–18734, 2019, doi: 10.1039/c9ta06433h.
- [64] J. Park *et al.*, “A new water oxidation catalyst: Lithium manganese pyrophosphate with tunable mn valency,” *J. Am. Chem. Soc.*, vol. 136, no. 11, pp. 4201–4211, 2014, doi: 10.1021/ja410223j.
- [65] D. M. Robinson, Y. B. Go, M. Greenblatt, and G. C. Dismukes, “Water Oxidation by λ -MnO₂: Catalysis by the Cubical Mn₄O₄ Subcluster Obtained by Delithiation of Spinel LiMn₂O₄,” *J. Am. Chem. Soc.*, vol. 132, no. 33, pp. 11467–11469, 2010, doi: 10.1021/ja1055615.
- [66] S. L. Chou, Y. X. Wang, J. Xu, J. Z. Wang, H. K. Liu, and S. X. Dou, “A hybrid electrolyte energy storage device with high energy and long life using lithium anode and MnO₂ nanoflake cathode,” *Electrochem. commun.*, vol. 31, pp. 35–38, 2013, doi: 10.1016/j.elecom.2013.03.003.
- [67] C. Xu, B. Li, H. Du, and F. Kang, “Energetic zinc ion chemistry: The rechargeable zinc ion battery,” *Angew. Chemie - Int. Ed.*, vol. 51, no. 4, pp. 933–935, 2012, doi: 10.1002/anie.201106307.
- [68] L. Chen, Q. An, and L. Mai, “Recent Advances and Prospects of Cathode Materials for Rechargeable Aqueous Zinc-Ion Batteries,” *Adv. Mater. Interfaces*, vol. 6, no. 17, pp. 1–24, 2019, doi: 10.1002/admi.201900387.
- [69] B. Tang, L. Shan, S. Liang, and J. Zhou, “Issues and opportunities facing aqueous zinc-ion batteries,” *Energy Environ. Sci.*, vol. 12, no. 11, pp. 3288–3304, 2019, doi: 10.1039/c9ee02526j.
- [70] Y. Li and H. Dai, “Recent advances in Zinc-air batteries,” *Chem. Soc. Rev.*, vol. 43, no. 15, pp. 5257–5275, 2014, doi: 10.1039/c4cs00015c.
- [71] J. F. Parker *et al.*, “Rechargeable nickel–3D zinc batteries: An energy-dense, safer alternative to lithium-ion,” *Science (80-.)*, vol. 356, no. 6336, pp. 415–418, Apr. 2017, doi: 10.1126/science.aak9991.
- [72] P. Gu, M. Zheng, Q. Zhao, X. Xiao, H. Xue, and H. Pang, “Rechargeable zinc-air batteries: A promising way to green energy,” *J. Mater. Chem. A*, vol. 5, no. 17, pp. 7651–7666, 2017, doi: 10.1039/c7ta01693j.
- [73] X. Wang *et al.*, “An Aqueous Rechargeable Zn//Co₃O₄Battery with High Energy Density and Good Cycling Behavior,” *Adv. Mater.*, vol. 28, no. 24, pp. 4904–4911, 2016, doi: 10.1002/adma.201505370.
- [74] P. Senguttuvan *et al.*, “A High Power Rechargeable Nonaqueous Multivalent Zn/V₂O₅ Battery,” *Adv. Energy Mater.*, vol. 6, no. 24, 2016, doi: 10.1002/aenm.201600826.
- [75] Z. Liu *et al.*, “Dendrite-Free Nanocrystalline Zinc Electrodeposition from an Ionic Liquid Containing Nickel Triflate for Rechargeable Zn-Based Batteries,” *Angew. Chemie - Int. Ed.*, vol. 55, no. 8, pp. 2889–2893, 2016, doi: 10.1002/anie.201509364.
- [76] T. Shoji and T. Yamamoto, “Charging and discharging behavior of zinc-manganese dioxide galvanic cells using zinc sulfate as electrolyte,” *J. Electroanal. Chem.*, vol. 362, no. 1–2, pp. 153–157, 1993, doi: 10.1016/0022-0728(93)80016-B.
- [77] N. Zhang *et al.*, “Cation-Deficient Spinel ZnMn₂O₄ Cathode in Zn(CF₃SO₃)₂ Electrolyte for Rechargeable Aqueous Zn-Ion Battery,” *J. Am. Chem. Soc.*, vol. 138, no. 39, pp. 12894–12901, 2016, doi: 10.1021/jacs.6b05958.
- [78] G. Li, Z. Yang, Y. Jiang, W. Zhang, and Y. Huang, “Hybrid aqueous battery based on Na₃V₂(PO₄)₃/C cathode and zinc anode for potential large-scale energy storage,” *J. Power Sources*, vol. 308, pp. 52–57, 2016, doi: 10.1016/j.jpowsour.2016.01.058.
- [79] B. Jiang, C. Xu, C. Wu, L. Dong, J. Li, and F. Kang, “Manganese Sesquioxide as Cathode Material for Multivalent Zinc Ion Battery with High Capacity and Long Cycle

- Life,” *Electrochim. Acta*, vol. 229, pp. 422–428, 2017, doi: 10.1016/j.electacta.2017.01.163.
- [80] D. Kundu, B. D. Adams, V. Duffort, S. H. Vajargah, and L. F. Nazar, “A high-capacity and long-life aqueous rechargeable zinc battery using a metal oxide intercalation cathode,” *Nat. Energy*, vol. 1, no. 10, p. 16119, Oct. 2016, doi: 10.1038/nenergy.2016.119.
- [81] M. Yan *et al.*, “Water-Lubricated Intercalation in $V_2O_5 \cdot nH_2O$ for High-Capacity and High-Rate Aqueous Rechargeable Zinc Batteries,” *Adv. Mater.*, vol. 30, no. 1, p. 1703725, Jan. 2018, doi: 10.1002/adma.201703725.
- [82] C. Xia, J. Guo, Y. Lei, H. Liang, C. Zhao, and H. N. Alshareef, “Rechargeable Aqueous Zinc-Ion Battery Based on Porous Framework Zinc Pyrovanadate Intercalation Cathode,” *Adv. Mater.*, vol. 30, no. 5, pp. 1–7, 2018, doi: 10.1002/adma.201705580.
- [83] L. Zhang, L. Chen, X. Zhou, and Z. Liu, “Towards high-voltage aqueous metal-ion batteries beyond 1.5 V: The zinc/zinc hexacyanoferrate system,” *Adv. Energy Mater.*, vol. 5, no. 2, pp. 1–5, 2015, doi: 10.1002/aenm.201400930.
- [84] A. Widmann *et al.*, “Structure, insertion electrochemistry, and magnetic properties of a new type of substitutional solid solutions of copper, nickel, and iron hexacyanoferrates/hexacyanocobaltates,” *Inorg. Chem.*, vol. 41, no. 22, pp. 5706–5715, 2002, doi: 10.1021/ic0201654.
- [85] G. Li *et al.*, “Towards polyvalent ion batteries: A zinc-ion battery based on NASICON structured $Na_3V_2(PO_4)_3$,” *Nano Energy*, vol. 25, pp. 211–217, 2016, doi: 10.1016/j.nanoen.2016.04.051.
- [86] Y. Cheng *et al.*, “Highly Reversible Zinc-Ion Intercalation into Chevrel Phase Mo_6S_8 Nanocubes and Applications for Advanced Zinc-Ion Batteries,” *ACS Appl. Mater. Interfaces*, vol. 8, no. 22, pp. 13673–13677, 2016, doi: 10.1021/acsami.6b03197.
- [87] M. H. Alfaruqi *et al.*, “Electrochemically induced structural transformation in a γ - MnO_2 cathode of a high capacity zinc-ion battery system,” *Chem. Mater.*, vol. 27, no. 10, pp. 3609–3620, 2015, doi: 10.1021/cm504717p.
- [88] H. Pan *et al.*, “Reversible aqueous zinc/manganese oxide energy storage from conversion reactions,” *Nat. Energy*, vol. 1, no. 5, p. 16039, May 2016, doi: 10.1038/nenergy.2016.39.
- [89] W. Sun *et al.*, “Zn/ MnO_2 Battery Chemistry With H^+ and Zn^{2+} Coinsertion,” *J. Am. Chem. Soc.*, vol. 139, no. 29, pp. 9775–9778, Jul. 2017, doi: 10.1021/jacs.7b04471.
- [90] F. Wan, L. Zhang, X. Dai, X. Wang, Z. Niu, and J. Chen, “Aqueous rechargeable zinc/sodium vanadate batteries with enhanced performance from simultaneous insertion of dual carriers,” *Nat. Commun.*, vol. 9, no. 1, pp. 1–11, 2018, doi: 10.1038/s41467-018-04060-8.
- [91] T. R. Juran, J. Young, and M. Smeu, “Density Functional Theory Modeling of MnO_2 Polymorphs as Cathodes for Multivalent Ion Batteries,” *J. Phys. Chem. C*, vol. 122, no. 16, pp. 8788–8795, 2018, doi: 10.1021/acs.jpcc.8b00918.
- [92] M. Pourbaix, “Atlas of electrochemical equilibria in aqueous solutions. Houston:NACE International,” *Mater. Sci. Forum*, pp. 43–54, 1974, doi: 10.4028/www.scientific.net/msf.251-254.143.
- [93] L. M. Housel *et al.*, “Investigation of α - MnO_2 Tunneled Structures as Model Cation Hosts for Energy Storage,” *Acc. Chem. Res.*, vol. 51, no. 3, pp. 575–582, 2018, doi: 10.1021/acs.accounts.7b00478.
- [94] J. Lee, J. B. Ju, W. Il Cho, B. W. Cho, and S. H. Oh, “Todorokite-type MnO_2 as a zinc-ion intercalating material,” *Electrochim. Acta*, vol. 112, pp. 138–143, 2013, doi: 10.1016/j.electacta.2013.08.136.

- [95] C. Wei, C. Xu, B. Li, H. Du, and F. Kang, "Preparation and characterization of manganese dioxides with nano-sized tunnel structures for zinc ion storage," *J. Phys. Chem. Solids*, vol. 73, no. 12, pp. 1487–1491, 2012, doi: 10.1016/j.jpcs.2011.11.038.
- [96] S. Islam *et al.*, "Facile synthesis and the exploration of the zinc storage mechanism of β -MnO₂ nanorods with exposed (101) planes as a novel cathode material for high performance eco-friendly zinc-ion batteries," *J. Mater. Chem. A*, vol. 5, no. 44, pp. 23299–23309, 2017, doi: 10.1039/c7ta07170a.
- [97] B. Lee, H. R. Lee, H. Kim, K. Y. Chung, B. W. Cho, and S. H. Oh, "Elucidating the intercalation mechanism of zinc ions into α -MnO₂ for rechargeable zinc batteries," *Chem. Commun.*, vol. 51, no. 45, pp. 9265–9268, 2015, doi: 10.1039/c5cc02585k.
- [98] B. Lee, C. S. Yoon, H. R. Lee, K. Y. Chung, B. W. Cho, and S. H. Oh, "Electrochemically-induced reversible transition from the tunneled to layered polymorphs of manganese dioxide," *Sci. Rep.*, vol. 4, pp. 1–8, 2014, doi: 10.1038/srep06066.
- [99] N. Zhang *et al.*, "Rechargeable aqueous zinc-manganese dioxide batteries with high energy and power densities," *Nat. Commun.*, vol. 8, no. 1, pp. 1–9, 2017, doi: 10.1038/s41467-017-00467-x.
- [100] N. Qiu, H. Chen, Z. Yang, S. Sun, and Y. Wang, "Low-cost birnessite as a promising cathode for high-performance aqueous rechargeable batteries," *Electrochim. Acta*, vol. 272, pp. 154–160, 2018, doi: 10.1016/j.electacta.2018.04.012.
- [101] C. Zhu *et al.*, "Electrochemically induced cationic defect in MnO intercalation cathode for aqueous zinc-ion battery," *Energy Storage Mater.*, vol. 24, no. June, pp. 394–401, 2020, doi: 10.1016/j.ensm.2019.07.030.
- [102] M. Sun *et al.*, "Mn₃O₄@NC Composite Nanorods as a Cathode for Rechargeable Aqueous Zn-Ion Batteries," *ChemElectroChem*, vol. 6, no. 9, pp. 2510–2516, 2019, doi: 10.1002/celec.201900376.
- [103] J. Hao *et al.*, "Electrochemically induced spinel-layered phase transition of Mn₃O₄ in high performance neutral aqueous rechargeable zinc battery," *Electrochim. Acta*, vol. 259, pp. 170–178, 2018, doi: 10.1016/j.electacta.2017.10.166.
- [104] V. Soundharrajan *et al.*, "Aqueous Magnesium Zinc Hybrid Battery: An Advanced High-Voltage and High-Energy MgMn₂O₄ Cathode," *ACS Energy Lett.*, vol. 3, no. 8, pp. 1998–2004, 2018, doi: 10.1021/acsenergylett.8b01105.
- [105] M. H. Alfuruqi *et al.*, "Enhanced reversible divalent zinc storage in a structurally stable α -MnO₂ nanorod electrode," *J. Power Sources*, vol. 288, pp. 320–327, 2015, doi: 10.1016/j.jpowsour.2015.04.140.
- [106] D. Xu *et al.*, "Preparation and characterization of MnO₂/acid-treated CNT nanocomposites for energy storage with zinc ions," *Electrochim. Acta*, vol. 133, pp. 254–261, 2014, doi: 10.1016/j.electacta.2014.04.001.
- [107] M. H. Alfuruqi *et al.*, "A layered δ -MnO₂ nanoflake cathode with high zinc-storage capacities for eco-friendly battery applications," *Electrochem. commun.*, vol. 60, pp. 121–125, 2015, doi: 10.1016/j.elecom.2015.08.019.
- [108] C. Zhu *et al.*, "Binder-free stainless steel@Mn₃O₄ nanoflower composite: A high-activity aqueous zinc-ion battery cathode with high-capacity and long-cycle-life," *J. Mater. Chem. A*, vol. 6, no. 20, pp. 9677–9683, 2018, doi: 10.1039/c8ta01198b.
- [109] S. Bai *et al.*, "Effects of zinc and manganese ions in aqueous electrolytes on structure and electrochemical performance of Na_{0.44}MnO₂ cathode material," *RSC Adv.*, vol. 6, no. 47, pp. 40793–40798, 2016, doi: 10.1039/c6ra01768a.
- [110] B. Zhang *et al.*, "An aqueous rechargeable battery based on zinc anode and Na_{0.95}MnO₂," *Chem. Commun.*, vol. 50, no. 10, pp. 1209–1211, 2014, doi: 10.1039/c3cc48382g.

- [111] J. Cui *et al.*, “Cryptomelane-type $\text{KMn}_8\text{O}_{16}$ as potential cathode material - For aqueous zinc ion battery,” *Front. Chem.*, vol. 6, no. AUG, pp. 4–11, 2018, doi: 10.3389/fchem.2018.00352.
- [112] X. Wu *et al.*, “Green-low-cost rechargeable aqueous zinc-ion batteries using hollow porous spinel ZnMn_2O_4 as the cathode material,” *J. Mater. Chem. A*, vol. 5, no. 34, pp. 17990–17997, 2017, doi: 10.1039/c7ta00100b.
- [113] M. H. Alfaruqi *et al.*, “Applied Surface Science Ambient redox synthesis of vanadium-doped manganese dioxide nanoparticles and their enhanced zinc storage properties,” *Appl. Surf. Sci.*, vol. 404, pp. 435–442, 2017, doi: 10.1016/j.apsusc.2017.02.009.
- [114] H. Zhang *et al.*, “Extracting oxygen anions from ZnMn_2O_4 : Robust cathode for flexible all-solid-state Zn-ion batteries,” *Energy Storage Mater.*, vol. 21, pp. 154–161, 2019, doi: 10.1016/j.ensm.2018.12.019.
- [115] S. Khamsanga, P. Rojana, T. Yonezawa, and A. A. Mohamad, “ δ - MnO_2 nanoflower / graphite cathode for rechargeable aqueous zinc ion batteries,” no. March, pp. 1–9, 2019, doi: 10.1038/s41598-019-44915-8.
- [116] J. Huang, Z. Guo, Y. Ma, D. Bin, Y. Wang, and Y. Xia, “Recent Progress of Rechargeable Batteries Using Mild Aqueous Electrolytes,” *Small Methods*, vol. 3, no. 1, pp. 1–20, 2019, doi: 10.1002/smt.201800272.
- [117] C. Applications, “A Bi-Cation Electrolyte for a 1.7 V Aqueous Zn Ion Battery,” 2020, doi: 10.1021/acsami.9b20531.
- [118] B. Lee *et al.*, “Critical Role of pH Evolution of Electrolyte in the Reaction Mechanism for Rechargeable Zinc Batteries,” *ChemSusChem*, vol. 9, no. 20, pp. 2948–2956, 2016, doi: 10.1002/cssc.201600702.
- [119] C. F. Bischoff *et al.*, “Revealing the Local pH Value Changes of Acidic Aqueous Zinc Ion Batteries with a Manganese Dioxide Electrode during Cycling,” *J. Electrochem. Soc.*, vol. 167, no. 2, p. 020545, 2020, doi: 10.1149/1945-7111/ab6c57.
- [120] Z. Liu, G. Pulletikurthi, and F. Endres, “A Prussian Blue/Zinc Secondary Battery with a Bio-Ionic Liquid-Water Mixture as Electrolyte,” *ACS Appl. Mater. Interfaces*, vol. 8, no. 19, pp. 12158–12164, 2016, doi: 10.1021/acsami.6b01592.
- [121] R. Trócoli and F. La Mantia, “An aqueous zinc-ion battery based on copper hexacyanoferrate,” *ChemSusChem*, vol. 8, no. 3, pp. 481–485, 2015, doi: 10.1002/cssc.201403143.
- [122] G. Fang, J. Zhou, A. Pan, and S. Liang, “Recent Advances in Aqueous Zinc-Ion Batteries,” *ACS Energy Lett.*, vol. 3, no. 10, pp. 2480–2501, 2018, doi: 10.1021/acsenergylett.8b01426.
- [123] L. Chen *et al.*, “Ultrastable and High-Performance Zn / VO_2 Battery Based on a Reversible Single-Phase Reaction,” *Chem. Mater.*, vol. 31, pp. 699–706, 2019, doi: 10.1021/acs.chemmater.8b03409.
- [124] J. Ding *et al.*, “Ultrafast Zn^{2+} Intercalation and Deintercalation in Vanadium Dioxide,” *Adv. Mater.*, vol. 30, no. 26, p. 1800762, Jun. 2018, doi: 10.1002/adma.201800762.
- [125] X. Dai, F. Wan, L. Zhang, H. Cao, and Z. Niu, “Freestanding graphene/ VO_2 composite films for highly stable aqueous Zn-ion batteries with superior rate performance,” *Energy Storage Mater.*, vol. 17, pp. 143–150, 2019, doi: 10.1016/j.ensm.2018.07.022.
- [126] T. Wei, Q. Li, G. Yang, and C. Wang, “An electrochemically induced bilayered structure facilitates long-life zinc storage of vanadium dioxide,” *J. Mater. Chem. A*, vol. 6, no. 17, pp. 8006–8012, 2018, doi: 10.1039/c8ta02090f.
- [127] J. S. Park *et al.*, “Open-Structured Vanadium Dioxide as an Intercalation Host for Zn Ions: Investigation by First-Principles Calculation and Experiments,” *Chem. Mater.*, vol. 30, no. 19, pp. 6777–6787, 2018, doi: 10.1021/acs.chemmater.8b02679.

- [128] P. He *et al.*, “Layered VS₂ Nanosheet-Based Aqueous Zn Ion Battery Cathode,” *Adv. Energy Mater.*, vol. 7, no. 11, pp. 1–5, 2017, doi: 10.1002/aenm.201601920.
- [129] D. Kundu, S. Hosseini Vajargah, L. Wan, B. Adams, D. Prendergast, and L. F. Nazar, “Aqueous vs. nonaqueous Zn-ion batteries: consequences of the desolvation penalty at the interface,” *Energy Environ. Sci.*, vol. 11, no. 4, pp. 881–892, 2018, doi: 10.1039/C8EE00378E.
- [130] Q. Pang *et al.*, “H₂V₃O₈ Nanowire/Graphene Electrodes for Aqueous Rechargeable Zinc Ion Batteries with High Rate Capability and Large Capacity,” *Adv. Energy Mater.*, vol. 8, no. 19, pp. 1–9, 2018, doi: 10.1002/aenm.201800144.
- [131] T. Yao, Y. Oka, and N. Yamamoto, “Layered structures of vanadium pentoxide gels,” *Mater. Res. Bull.*, vol. 27, no. 6, pp. 669–675, 1992, doi: 10.1016/0025-5408(92)90073-9.
- [132] D. Buchholz, L. G. Chagas, C. Vaalma, L. Wu, and S. Passerini, “Water sensitivity of layered P2/P3-Na_xNi_{0.22}Co_{0.11}Mn_{0.66}O₂ cathode material,” *J. Mater. Chem. A*, vol. 2, no. 33, pp. 13415–13421, 2014, doi: 10.1039/c4ta02627f.
- [133] C. T. Lin, D. P. Chen, P. Lemmens, X. N. Zhang, A. Maljuk, and P. X. Zhang, “Study of intercalation/deintercalation of Na_xCoO₂ single crystals,” *J. Cryst. Growth*, vol. 275, no. 3–4, pp. 606–616, 2005, doi: 10.1016/j.jcrysgro.2004.12.021.
- [134] S. Radha, K. Jayanthi, J. Breu, and P. Vishnu Kamath, “Relative humidity-induced reversible hydration of sulfateintercalated layered double hydroxides,” *Clays Clay Miner.*, vol. 62, no. 1, pp. 53–61, 2014, doi: 10.1346/CCMN.2014.0620105.
- [135] J. Zhou, L. Shan, Z. Wu, X. Guo, G. Fang, and S. Liang, “Investigation of V₂O₅ as a low-cost rechargeable aqueous zinc ion battery cathode,” *Chem. Commun.*, vol. 54, no. 35, pp. 4457–4460, 2018, doi: 10.1039/C8CC02250J.
- [136] X. Chen, L. Wang, H. Li, F. Cheng, and J. Chen, “Porous V₂O₅ nanofibers as cathode materials for rechargeable aqueous zinc-ion batteries,” *J. Energy Chem.*, vol. 38, pp. 20–25, 2019, doi: 10.1016/j.jechem.2018.12.023.
- [137] Z. Tong, J. Hao, K. Zhang, J. Zhao, B. L. Su, and Y. Li, “Improved electrochromic performance and lithium diffusion coefficient in three-dimensionally ordered macroporous V₂O₅ films,” *J. Mater. Chem. C*, vol. 2, no. 18, pp. 3651–3658, 2014, doi: 10.1039/c3tc32417f.
- [138] M. H. Alfuruqi *et al.*, “Electrochemical Zinc Intercalation in Lithium Vanadium Oxide: A High-Capacity Zinc-Ion Battery Cathode,” *Chem. Mater.*, vol. 29, no. 4, pp. 1684–1694, Feb. 2017, doi: 10.1021/acs.chemmater.6b05092.
- [139] P. He *et al.*, “Sodium Ion Stabilized Vanadium Oxide Nanowire Cathode for High-Performance Zinc-Ion Batteries,” *Adv. Energy Mater.*, vol. 8, no. 10, p. 1702463, Apr. 2018, doi: 10.1002/aenm.201702463.
- [140] N. Zhang *et al.*, “Rechargeable Aqueous Zn–V₂O₅ Battery with High Energy Density and Long Cycle Life,” *ACS Energy Lett.*, vol. 3, no. 6, pp. 1366–1372, Jun. 2018, doi: 10.1021/acsenergylett.8b00565.
- [141] F. Liu *et al.*, “V₂O₅ Nanospheres with Mixed Vanadium Valences as High Electrochemically Active Aqueous Zinc-Ion Battery Cathode,” *Nano-Micro Lett.*, vol. 11, no. 1, pp. 1–11, 2019, doi: 10.1007/s40820-019-0256-2.
- [142] L. Shan *et al.*, “Highly Reversible Phase Transition Endows V₆O₁₃ with Enhanced Performance as Aqueous Zinc-Ion Battery Cathode,” *Energy Technol.*, vol. 7, no. 6, 2019, doi: 10.1002/ente.201900022.
- [143] C. Shen *et al.*, “Graphene-Boosted, High-Performance Aqueous Zn-Ion Battery,” *ACS Appl. Mater. Interfaces*, vol. 10, no. 30, pp. 25446–25453, 2018, doi: 10.1021/acsami.8b07781.
- [144] P. He *et al.*, “High-Performance Aqueous Zinc–Ion Battery Based on Layered

- H2V3O8 Nanowire Cathode,” *Small*, vol. 13, no. 47, pp. 1–7, 2017, doi: 10.1002/sml.201702551.
- [145] S. Lee, I. N. Ivanov, J. K. Keum, and H. N. Lee, “Epitaxial stabilization and phase instability of VO₂ polymorphs,” *Sci. Rep.*, vol. 6, no. November 2015, pp. 1–7, Sep. 2015, doi: 10.1038/srep19621.
- [146] S. R. Popuri, M. Miclau, A. Artemenko, C. Labrugere, A. Villesuzanne, and M. Pollet, “Rapid Hydrothermal Synthesis of VO₂ (B) and Its Conversion to Thermochromic VO₂ (M1),” *Inorg. Chem.*, vol. 52, no. 9, pp. 4780–4785, May 2013, doi: 10.1021/ic301201k.
- [147] C. Xia, J. Guo, P. Li, X. Zhang, and H. N. Alshareef, “Highly Stable Aqueous Zinc-Ion Storage Using a Layered Calcium Vanadium Oxide Bronze Cathode,” *Angew. Chemie - Int. Ed.*, vol. 57, no. 15, pp. 3943–3948, 2018, doi: 10.1002/anie.201713291.
- [148] P. Hu *et al.*, “Highly Durable Na₂V₆O₁₆·1.63H₂O Nanowire Cathode for Aqueous Zinc-Ion Battery,” *Nano Lett.*, vol. 18, no. 3, pp. 1758–1763, 2018, doi: 10.1021/acs.nanolett.7b04889.
- [149] V. Soundharrajan *et al.*, “Na₂V₆O₁₆·3H₂O Barnesite Nanorod: An Open Door to Display a Stable and High Energy for Aqueous Rechargeable Zn-Ion Batteries as Cathodes,” *Nano Lett.*, vol. 18, no. 4, pp. 2402–2410, 2018, doi: 10.1021/acs.nanolett.7b05403.
- [150] Y. Cai *et al.*, “Pilotaxitic Na_{1.1}V₃O_{7.9} nanoribbons/graphene as high-performance sodium ion battery and aqueous zinc ion battery cathode,” *Energy Storage Mater.*, vol. 13, pp. 168–174, 2018, doi: 10.1016/j.ensm.2018.01.009.
- [151] X. Guo *et al.*, “Mechanistic Insights of Zn²⁺ Storage in Sodium Vanadates,” *Adv. Energy Mater.*, vol. 8, no. 27, p. 1801819, Sep. 2018, doi: 10.1002/aenm.201801819.
- [152] B. Tang *et al.*, “Potassium vanadates with stable structure and fast ion diffusion channel as cathode for rechargeable aqueous zinc-ion batteries,” *Nano Energy*, vol. 51, pp. 579–587, Sep. 2018, doi: 10.1016/j.nanoen.2018.07.014.
- [153] B. Sambandam *et al.*, “Aqueous rechargeable Zn-ion batteries: An imperishable and high-energy Zn₂V₂O₇ nanowire cathode through intercalation regulation,” *J. Mater. Chem. A*, vol. 6, no. 9, pp. 3850–3856, 2018, doi: 10.1039/c7ta11237h.
- [154] W. Kaveevivitchai and A. Manthiram, “High-capacity zinc-ion storage in an open-tunnel oxide for aqueous and nonaqueous Zn-ion batteries,” *J. Mater. Chem. A*, vol. 4, no. 48, pp. 18737–18741, 2016, doi: 10.1039/C6TA07747A.
- [155] Y. Yang *et al.*, “Li⁺ intercalated V₂O₅·N H₂O with enlarged layer spacing and fast ion diffusion as an aqueous zinc-ion battery cathode,” *Energy Environ. Sci.*, vol. 11, no. 11, pp. 3157–3162, 2018, doi: 10.1039/c8ee01651h.
- [156] L. Shan *et al.*, “Observation of combination displacement/intercalation reaction in aqueous zinc-ion battery,” *Energy Storage Mater.*, vol. 18, pp. 10–14, 2019, doi: 10.1016/j.ensm.2018.08.008.
- [157] P. Hu *et al.*, “Zn/V₂O₅ Aqueous Hybrid-Ion Battery with High Voltage Platform and Long Cycle Life,” *ACS Appl. Mater. Interfaces*, vol. 9, no. 49, pp. 42717–42722, Dec. 2017, doi: 10.1021/acsami.7b13110.
- [158] J. Lai, H. Zhu, X. Zhu, H. Koritala, and Y. Wang, “Interlayer-Expanded V₆O₁₃·nH₂O Architecture Constructed for an Advanced Rechargeable Aqueous Zinc-Ion Battery,” *ACS Appl. Energy Mater.*, vol. 2, no. 3, pp. 1988–1996, 2019, doi: 10.1021/acsaem.8b02054.
- [159] T. Wei, Q. Li, G. Yang, and C. Wang, “High-rate and durable aqueous zinc ion battery using dendritic V₁₀O₂₄·12H₂O cathode material with large interlamellar spacing,” *Electrochim. Acta*, vol. 287, pp. 60–67, 2018, doi: 10.1016/j.electacta.2018.08.040.
- [160] B. Sambandam *et al.*, “K₂V₆O₁₆·2.7H₂O nanorod cathode: An advanced intercalation

- system for high energy aqueous rechargeable Zn-ion batteries,” *J. Mater. Chem. A*, vol. 6, no. 32, pp. 15530–15539, 2018, doi: 10.1039/c8ta02018c.
- [161] X. Liu *et al.*, “Calcium vanadate sub-microfibers as highly reversible host cathode material for aqueous zinc-ion batteries,” *Chem. Commun.*, vol. 55, no. 16, pp. 2265–2268, 2019, doi: 10.1039/c8cc07243d.
- [162] F. Ming, H. Liang, Y. Lei, S. Kandambeth, M. Eddaoudi, and H. N. Alshareef, “Layered $\text{Mg xV}_2\text{O}_5 \cdot \text{nH}_2\text{O}$ as Cathode Material for High-Performance Aqueous Zinc Ion Batteries,” *ACS Energy Lett.*, vol. 3, no. 10, pp. 2602–2609, 2018, doi: 10.1021/acsenergylett.8b01423.
- [163] Z. Peng *et al.*, “Novel layered iron vanadate cathode for high-capacity aqueous rechargeable zinc batteries,” *Chem. Commun.*, vol. 54, no. 32, pp. 4041–4044, 2018, doi: 10.1039/c8cc00987b.
- [164] G. Yang, T. Wei, and C. Wang, “Self-Healing Lamellar Structure Boosts Highly Stable Zinc-Storage Property of Bilayered Vanadium Oxides,” *ACS Appl. Mater. Interfaces*, vol. 10, no. 41, pp. 35079–35089, 2018, doi: 10.1021/acsami.8b10849.
- [165] T. Wei, Q. Li, G. Yang, and C. Wang, “Highly reversible and long-life cycling aqueous zinc-ion battery based on ultrathin $(\text{NH}_4)_2\text{V}_2\text{O}_5 \cdot 8\text{H}_2\text{O}$ nanobelts,” *J. Mater. Chem. A*, vol. 6, no. 41, pp. 20402–20410, 2018, doi: 10.1039/c8ta06626d.
- [166] F. Wang *et al.*, “A rechargeable aqueous Zn^{2+} -battery with high power density and a long cycle-life,” *Energy Environ. Sci.*, vol. 11, no. 11, pp. 3168–3175, 2018, doi: 10.1039/c8ee01883a.
- [167] P. Hu *et al.*, “Aqueous $\text{Zn} // \text{Zn}(\text{CF}_3\text{SO}_3)_2 // \text{Na}_3\text{V}_2(\text{PO}_4)_3$ batteries with simultaneous $\text{Zn}^{2+} / \text{Na}^+$ intercalation/de-intercalation,” *Nano Energy*, vol. 58, no. January, pp. 492–498, 2019, doi: 10.1016/j.nanoen.2019.01.068.
- [168] W. Li, K. Wang, S. Cheng, and K. Jiang, “A long-life aqueous Zn-ion battery based on $\text{Na}_3\text{V}_2(\text{PO}_4)_2\text{F}_3$ cathode,” *Energy Storage Mater.*, vol. 15, pp. 14–21, 2018, doi: 10.1016/j.ensm.2018.03.003.
- [169] H. Qin, Z. Yang, L. Chen, X. Chen, and L. Wang, “A high-rate aqueous rechargeable zinc ion battery based on the $\text{VS}_4@r\text{GO}$ nanocomposite,” *J. Mater. Chem. A*, vol. 6, no. 46, pp. 23757–23765, 2018, doi: 10.1039/c8ta08133f.
- [170] F. Wan and Z. Niu, “Design Strategies for Vanadium-based Aqueous Zinc-Ion Batteries,” *Angew. Chemie - Int. Ed.*, vol. 58, no. 46, pp. 16358–16367, 2019, doi: 10.1002/anie.201903941.
- [171] D. C. Bock, A. C. Marschilok, K. J. Takeuchi, and E. S. Takeuchi, “A kinetics and equilibrium study of vanadium dissolution from vanadium oxides and phosphates in battery electrolytes: Possible impacts on ICD battery performance,” *J. Power Sources*, vol. 231, pp. 219–225, 2013, doi: 10.1016/j.jpowsour.2013.01.012.
- [172] Q. Li, T. Wei, K. Ma, G. Yang, and C. Wang, “Boosting the Cyclic Stability of Aqueous Zinc-Ion Battery Based on Al-Doped $\text{V}_{10}\text{O}_{24} \cdot 12\text{H}_2\text{O}$ Cathode Materials,” *ACS Appl. Mater. Interfaces*, vol. 11, no. 23, pp. 20888–20894, 2019, doi: 10.1021/acsami.9b05362.
- [173] J. H. Jo, Y. K. Sun, and S. T. Myung, “Hollandite-type Al-doped $\text{VO}_{1.52}(\text{OH})_{0.77}$ as a zinc ion insertion host material,” *J. Mater. Chem. A*, vol. 5, no. 18, pp. 8367–8375, 2017, doi: 10.1039/c7ta01765k.
- [174] B. Tang *et al.*, “Engineering the interplanar spacing of ammonium vanadates as a high-performance aqueous zinc-ion battery cathode,” *J. Mater. Chem. A*, vol. 7, no. 3, pp. 940–945, 2019, doi: 10.1039/C8TA09338E.
- [175] I. Stoševski, A. Bonakdarpour, F. Cuadra, and D. P. Wilkinson, “Highly crystalline ramsdellite as a cathode material for near-neutral aqueous MnO_2 / Zn batteries,” *Chem. Commun.*, vol. 55, no. 14, pp. 2082–2085, 2019, doi: 10.1039/c8cc07805j.

- [176] C. Zhang *et al.*, “A ZnCl_2 water-in-salt electrolyte for a reversible Zn metal anode,” *Chem. Commun.*, vol. 54, no. 100, pp. 14097–14099, 2018, doi: 10.1039/c8cc07730d.
- [177] B. Wu *et al.*, “Graphene Scroll-Coated $\alpha\text{-MnO}_2$ Nanowires as High-Performance Cathode Materials for Aqueous Zn-Ion Battery,” *Small*, vol. 14, no. 13, p. 1703850, Mar. 2018, doi: 10.1002/sml.201703850.
- [178] S. Islam *et al.*, “Carbon-coated manganese dioxide nanoparticles and their enhanced electrochemical properties for zinc-ion battery applications,” *J. Energy Chem.*, vol. 26, no. 4, pp. 815–819, 2017, doi: 10.1016/j.jechem.2017.04.002.
- [179] X. Zeng, J. Hao, Z. Wang, J. Mao, and Z. Guo, “Recent progress and perspectives on aqueous Zn-based rechargeable batteries with mild aqueous electrolytes,” *Energy Storage Mater.*, vol. 20, no. December 2018, pp. 410–437, 2019, doi: 10.1016/j.ensm.2019.04.022.
- [180] X. Zhu, X. Wu, T. N. L. Doan, Y. Tian, H. Zhao, and P. Chen, “Binder-free flexible LiMn_2O_4 /carbon nanotube network as high power cathode for rechargeable hybrid aqueous battery,” *J. Power Sources*, vol. 326, pp. 498–504, 2016, doi: 10.1016/j.jpowsour.2016.07.029.
- [181] X. Zhu *et al.*, “Tuning Microstructures of Graphene to Improve Power Capability of Rechargeable Hybrid Aqueous Batteries,” *ACS Appl. Mater. Interfaces*, vol. 10, no. 43, pp. 37110–37118, 2018, doi: 10.1021/acsami.8b13744.
- [182] Z. He *et al.*, “The electrochemical performance improvement of LiMn_2O_4 /Zn based on zinc foil as the current collector and thiourea as an electrolyte additive,” *J. Power Sources*, vol. 300, pp. 453–459, 2015, doi: 10.1016/j.jpowsour.2015.09.096.
- [183] C. Lu *et al.*, “Rechargeable hybrid aqueous batteries using silica nanoparticle doped aqueous electrolytes,” *Appl. Energy*, vol. 170, pp. 58–64, 2016, doi: 10.1016/j.apenergy.2016.02.117.
- [184] T. K. A. Hoang, T. N. L. Doan, C. Lu, M. Ghaznavi, H. Zhao, and P. Chen, “Performance of thixotropic gel electrolytes in the rechargeable aqueous Zn/ LiMn_2O_4 battery,” *ACS Sustain. Chem. Eng.*, vol. 5, no. 2, pp. 1804–1811, 2017, doi: 10.1021/acssuschemeng.6b02553.
- [185] T. K. A. Hoang *et al.*, “Sustainable Gel Electrolyte Containing Pyrazole as Corrosion Inhibitor and Dendrite Suppressor for Aqueous Zn/ LiMn_2O_4 Battery,” *ChemSusChem*, vol. 10, no. 13, pp. 2816–2822, 2017, doi: 10.1002/cssc.201700441.
- [186] H. B. Zhao *et al.*, “Novel rechargeable $\text{M}_3\text{V}_2(\text{PO}_4)_3$ /Zinc (M = Li, Na) hybrid aqueous batteries with excellent cycling performance,” *Sci. Rep.*, vol. 6, no. May, pp. 1–10, 2016, doi: 10.1038/srep25809.
- [187] G. Yuan, J. Bai, T. N. L. Doan, and P. Chen, “Synthesis and electrochemical properties of LiFePO_4 /graphene composite as a novel cathode material for rechargeable hybrid aqueous battery,” *Mater. Lett.*, vol. 158, pp. 248–251, 2015, doi: 10.1016/j.matlet.2015.05.174.
- [188] Z. Liu *et al.*, “A Flexible Solid-State Aqueous Zinc Hybrid Battery with Flat and High-Voltage Discharge Plateau,” *Adv. Energy Mater.*, vol. 9, no. 46, pp. 1–12, 2019, doi: 10.1002/aenm.201902473.
- [189] F. Wang, Y. Liu, X. Wang, Z. Chang, Y. Wu, and R. Holze, “Aqueous Rechargeable Battery Based on Zinc and a Composite of $\text{LiNi}_{1/3}\text{Co}_{1/3}\text{Mn}_{1/3}\text{O}_2$,” *ChemElectroChem*, vol. 2, no. 7, pp. 1024–1030, 2015, doi: 10.1002/celec.201500033.
- [190] J. Zhao *et al.*, “High-voltage Zn/ $\text{LiMn}_{0.8}\text{Fe}_{0.2}\text{PO}_4$ aqueous rechargeable battery by virtue of ‘water-in-salt’ electrolyte,” *Electrochem. commun.*, vol. 69, pp. 6–10, 2016, doi: 10.1016/j.elecom.2016.05.014.
- [191] M. R. Lukatskaya *et al.*, “Concentrated mixed cation acetate ‘water-in-salt’ solutions as green and low-cost high voltage electrolytes for aqueous batteries,” *Energy Environ.*

- Sci.*, vol. 11, no. 10, pp. 2876–2883, 2018, doi: 10.1039/c8ee00833g.
- [192] D. P. Leonard, Z. Wei, G. Chen, F. Du, and X. Ji, “Water-in-Salt Electrolyte for Potassium-Ion Batteries,” *ACS Energy Lett.*, vol. 3, no. 2, pp. 373–374, 2018, doi: 10.1021/acsenerylett.8b00009.
- [193] F. Wang *et al.*, “Highly reversible zinc metal anode for aqueous batteries,” *Nat. Mater.*, vol. 17, no. 6, pp. 543–549, 2018, doi: 10.1038/s41563-018-0063-z.
- [194] F. Wan *et al.*, “Reversible Oxygen Redox Chemistry in Aqueous Zinc-Ion Batteries,” *Angew. Chemie Int. Ed.*, vol. 58, no. 21, pp. 7062–7067, May 2019, doi: 10.1002/anie.201902679.
- [195] Y. Zhao *et al.*, “Stable Alkali Metal Ion Intercalation Compounds as Optimized Metal Oxide Nanowire Cathodes for Lithium Batteries,” *Nano Lett.*, vol. 15, no. 3, pp. 2180–2185, Mar. 2015, doi: 10.1021/acs.nanolett.5b00284.
- [196] R. Djenadic, M. Botros, and H. Hahn, “Is Li-doped MgAl_2O_4 a potential solid electrolyte for an all-spinel Li-ion battery ?,” *Solid State Ionics*, vol. 287, pp. 71–76, 2016, doi: 10.1016/j.ssi.2016.02.008.
- [197] C. Lu *et al.*, “Journal of Industrial and Engineering Chemistry Influence of different silica gelling agents on the performance of aqueous gel electrolytes,” *J. Ind. Eng. Chem.*, 2016, doi: 10.1016/j.jiec.2016.07.036.
- [198] M. Rabe, D. Verdes, M. Rankl, G. R. J. Artus, and S. Seeger, “A Comprehensive Study of Concepts and Phenomena of the Nonspecific Adsorption of b -Lactoglobulin,” pp. 862–872, 2007, doi: 10.1002/cphc.200600710.
- [199] J. Zhao, J. Zhang, W. Yang, B. Chen, Z. Zhao, and H. Qiu, “Nano Energy ‘ Water-in-deep eutectic solvent ’ electrolytes enable zinc metal anodes for rechargeable aqueous batteries,” *Nano Energy*, vol. 57, no. December 2018, pp. 625–634, 2019, doi: 10.1016/j.nanoen.2018.12.086.
- [200] H. Tao, X. Tong, L. Gan, S. Zhang, X. Zhang, and X. Liu, “Effect of adding various carbon additives to porous zinc anode in rechargeable hybrid aqueous battery,” *J. Alloys Compd.*, vol. 658, pp. 119–124, 2016, doi: 10.1016/j.jallcom.2015.10.225.
- [201] K. E. K. Sun *et al.*, “Suppression of Dendrite Formation and Corrosion on Zinc Anode of Secondary Aqueous Batteries,” 2017, doi: 10.1021/acsami.6b16560.
- [202] D. Batyrbekuly *et al.*, “Mechanistic Investigation of a Hybrid $\text{Zn/V}_2\text{O}_5$ Rechargeable Battery with a Binary $\text{Li}^+/\text{Zn}^{2+}$ Aqueous Electrolyte,” *ChemSusChem*, vol. 13, no. 4, pp. 724–731, Feb. 2020, doi: 10.1002/cssc.201903072.

4.2 Electrochemical and structural investigation of α -V₂O₅ in hybrid Li⁺/Zn²⁺ aqueous electrolyte for rechargeable aqueous Zn batteries.

4.2.1 Introduction

The pioneering work of Bakenov's group in Astana on novel aqueous Zn/LiFePO₄ rechargeable battery using a binary concentrated electrolyte of 3 mol L⁻¹ LiCl and 4 mol L⁻¹ ZnCl₂ (pH 4) has shown remarkable cycling performance. Indeed, due to the use of hybrid electrolyte, a high capacity of 92 mAh g⁻¹ over 400 cycles at 6 C was reported as well as a high rate capability with still 72 mAh g⁻¹ available at 30 C. This original concept of binary electrolyte with both zinc and lithium ions has never been applied to the Zn/V₂O₅ system. It relies on a high ionic conductivity with sufficient amounts of zinc on one side for efficient cyclability of zinc anode and of lithium on the other side for reversible insertion/extraction in the host cathodic material. These appealing results prompted us to evaluate the Zn/V₂O₅ system in the binary lithium-zinc aqueous electrolyte at optimized pH 4.

In the present work, we report the electrochemical properties of V₂O₅ in 3 mol L⁻¹ Li₂SO₄ - 4 mol L⁻¹ ZnSO₄ electrolyte in the 1.6 V - 0.8 V vs. Zn²⁺/Zn voltage window (**Figure 1**) with special attention paid to the structural mechanism involved upon the discharge-charge process and cycling. X-ray diffraction and Raman spectroscopy will be used to study the discharged and charged electrodes to provide initial insights into the mechanism.

The expected electrochemical mechanism of Zn || Li₂SO₄-ZnSO₄ || α -V₂O₅ system is illustrated in **Figure 1**. During discharge process, on positive side Li inserts into the α -V₂O₅ host lattice (Eq. 1), while on negative side Zinc anode loses electrons and dissolves in electrolyte (Eq. 2). Upon charge Li ion extract from α -V₂O₅ and Zn²⁺ ions deposit on Zn anode. Due to the deposition/dissolution process of zinc the concentration of electrolyte will increase/decrease respectively. Therefore, the amount of Zn²⁺ and Li⁺ should be enough for stable battery operation [1].

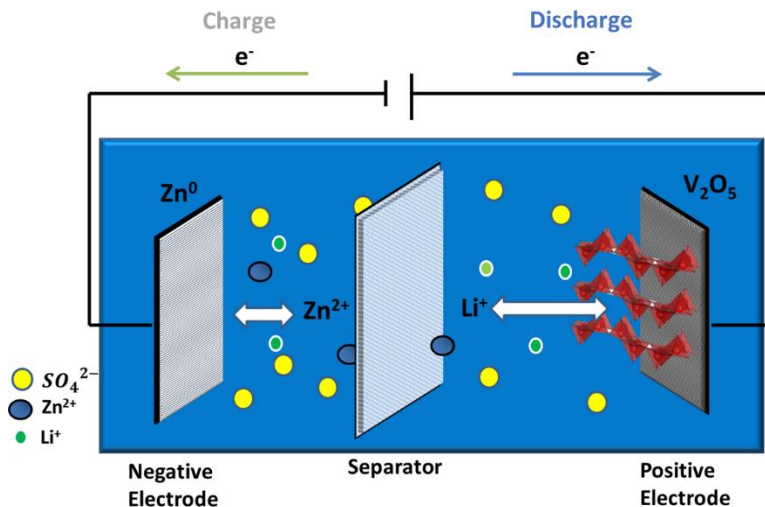


Figure 1. Schematic illustration of Zn || Li₂SO₄-ZnSO₄ || α-V₂O₅ system



4.2.2 Structural characterization of V₂O₅

The X-ray diffraction pattern of α-V₂O₅ powder (Alfa Aesar 99.5%) is shown in **Figure 2**. It can be indexed in orthorhombic cell (space group *Pmmn*) with the following unit cell parameters $a=11.5 \text{ \AA}$, $b=3.55 \text{ \AA}$, $c=4.37 \text{ \AA}$ calculated from Bragg's law ([see below](#)). **Table 1** gathers all the corresponding XRD data.

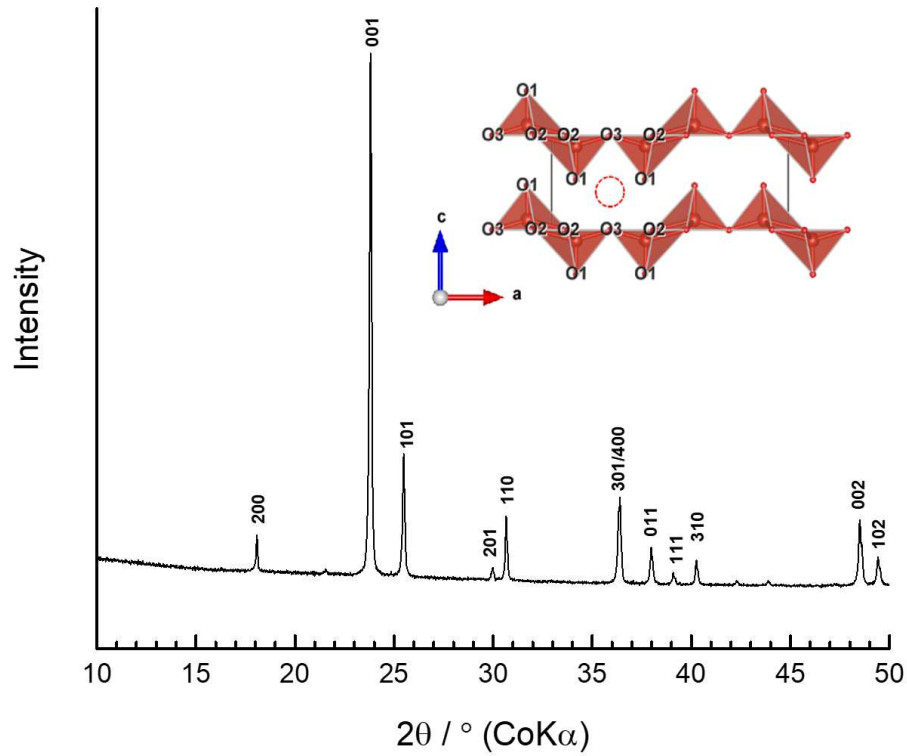


Figure 2. X-ray diffraction pattern, crystal structure (inset) of α -V₂O₅

For the calculation of d -spacing Bragg's law was used $dhkl = \frac{n\lambda}{2\sin\theta}$ where, $\lambda=1.7889$ Å (wavelength of X-ray Co source), θ = Peak position (in degree); $n=1$ (Order of diffraction); d = interplanar spacing (Å)

No.	Peak position		Interplanar spacing	Miller indices	FWHM
	2 Theta (°)	Theta (°)	d (Å)	(hkl)	
1	17,901	8,950	5,748	200	0,186
2	23,620	11,810	4,370	001	0,205
3	25,296	12,648	4,084	101	0,226
4	30,501	15,250	3,400	110	0,157
5	36,226	18,113	2,877	301/400	0,234
6	37,819	18,909	2,759	011	0,200
7	38,932	19,466	2,683	111	0,173

8	40,068	20,034	2,610	310	0,208
---	--------	--------	-------	-----	-------

$$\frac{1}{d^2} = \frac{h^2}{a^2} + \frac{k^2}{b^2} + \frac{l^2}{c^2}$$

To calculate a , b , c values the most intense hkl peaks will be chosen (200, 001, 110 peaks) in a first approach and a specific software (EVA software) is used for an accurate calculation of unit cell parameters using all the diffraction lines.

For instance: for calculation of a using the (200 peak) $\frac{1}{5.748^2} = \frac{2^2}{a^2}$; $a = 11.5 \text{ \AA}$

For calculation of lattice constant c (001 peak) $\frac{1}{4.37^2} = \frac{1^2}{c^2}$; $c = 4.37 \text{ \AA}$

For calculation of lattice constant b (110 peak) $\frac{1}{3.4^2} = \frac{1^2}{11.5^2} + \frac{1^2}{b^2}$; $b = 3.55 \text{ \AA}$

The structure of V_2O_5 consists of vanadium-centered $[VO_5]$ square pyramid building blocks where the vanadium is double-bonded with oxygen atom and single-bonded with other four oxygen atom forming square pyramid. The $[VO_5]$ polyhedral share edges along a-axis (up-up-down-down) and corner share along b-axis forming sheet-like structure, which are stacked upon each other and held by Van der Waals interactions. The atomic positions and characteristic bond lengths of α - V_2O_5 are shown in **Table2**.

Table 2. Atomic positions of V_2O_5 structure and V-O_x bond lengths of a square-based pyramid VO_5 . (y=0.25 for all positions)

Atoms	Wyckoff pos.	x	z	d _{v-o} polyhedra	
V	4f	0,101	0,892	-	
O ₁	4f	0,104	0,531	1,576 Å	vanadyl bond
				2,793 Å	inter-sheet bond
O ₂	4f	0,931	0,003	1,877 Å	x2, along b axis
				2,017 Å	x1, along c axis
O ₃	2a	0,25	0,001	1,778 Å	bridge link

Raman spectrum of α - V_2O_5 exhibits ten peaks at 105, 146, 199, 286, 305, 406, 483, 529, 703, 994 cm^{-1} (**Figure 3**). The Raman vibrational assignment is given Table 1. Most of low wavenumber modes can be described in terms of external modes of V_2O_5 units. They have been derived from the relative motions of two V_2O_5 units belonging to the unit cell, three of them generated by displacements of vanadium atoms along the x-axis (195 cm^{-1}), y-axis (145 cm^{-1}) and z-axis (105

cm^{-1}). The internal modes observed at medium and high frequency can be described in terms of O–V–O bending modes and V–O stretching modes. The band at 994 cm^{-1} is assigned to the V–O stretching vibration mode along z -axis (A_g symmetry), corresponding to the shortest V=O vanadyl bond oriented along c -axes. The V–O stretching modes along x - and y -axes are observed at 530 cm^{-1} (A_g) and 703 cm^{-1} (B_{1g}, B_{3g}), respectively.

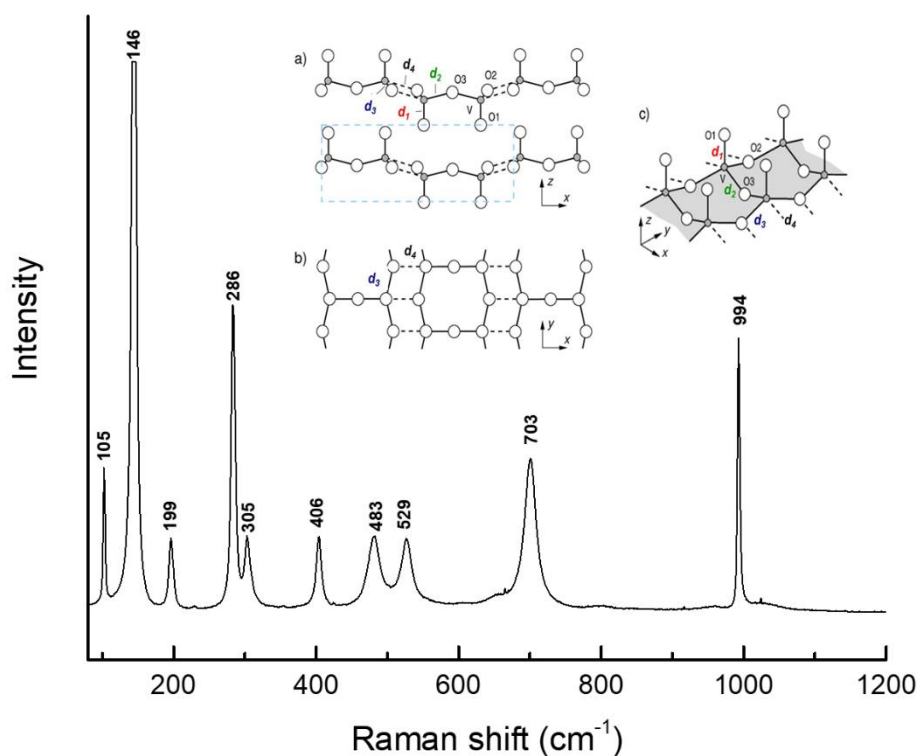


Figure 3. Raman spectrum and local structure (inset) of $\alpha\text{-V}_2\text{O}_5$

4.2.3 Electrochemical study

Figure 4a shows CV profiles of first 10 cycles at scan rate of 0.2 mV s^{-1} for $\alpha\text{-V}_2\text{O}_5$ in binary electrolyte. During reduction two cathodic peaks at 1.12 and 0.91V are observed. During oxidation anodic peaks at 1.21 and 1.33V are observed. The coulombic charge during cathodic and anodic scan corresponds to $\approx 0.75\text{ F/mol}$. After 10 cycles there is no substantial change in peak positions after first scan, indicating high reversibility of insertion/extraction reaction. Additional peaks were not detected, illustrating no side reactions (H_2 or O_2 evolution) or zinc (Zn^{2+}) co-insertion. For comparison the cyclic voltammetry was done with $3\text{M Li}_2\text{SO}_4$ (without zinc source in electrolyte) at scan rate of 0.2 mV s^{-1} (**Figure 4b**). Two reduction steps can be observed at 1.12V and 0.94 V

related to the lithium insertion. However, upon the cycles the intensity of peaks rapidly reduced indicating fast capacity decay related to loss of active material through dissolution and to the poor electrochemical behavior of Zn electrode. In addition, cyclic voltammograms was recorded with 4M ZnSO₄ (**Figure S1**). It was found that at lower potential (~0.92-0.94V) both lithium and zinc can be inserted at this potential.

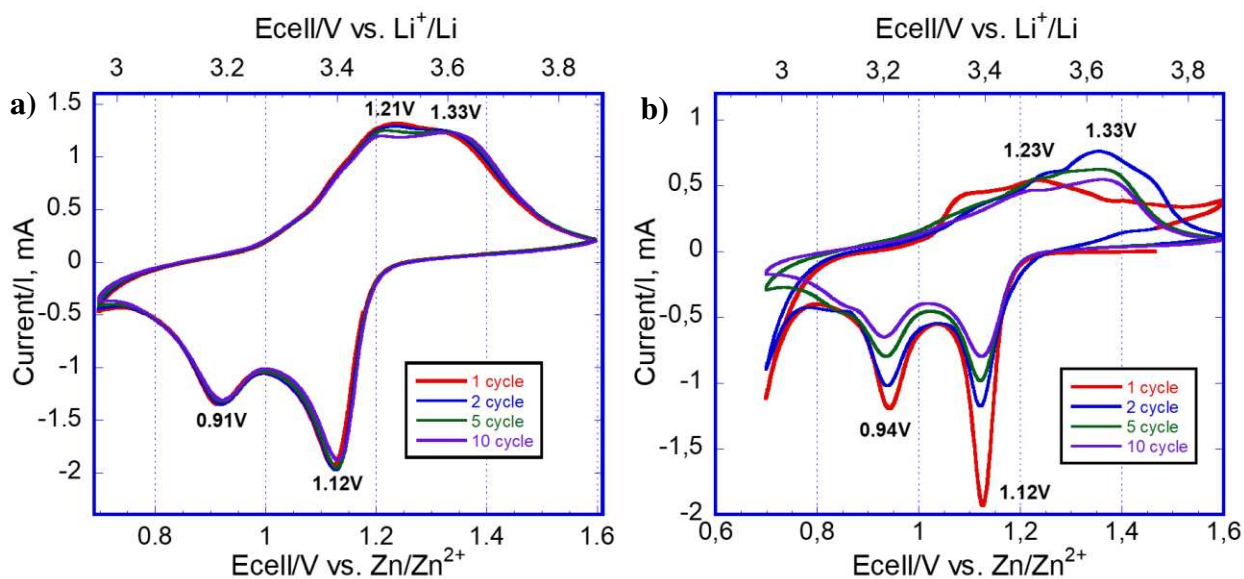


Figure 4. Cyclic voltammograms of Zn/ α -V₂O₅ system at scan rate of 0.2 mV s⁻¹ with (a) hybrid electrolyte and (b) 3M Li₂SO₄

The discharge/charge profile of α -V₂O₅ at C/5 in the 1.6-0.8V voltage range is shown in **Figure 5a**. From discharge curves two plateaus can be observed at 1.16 and 0.95V in good agreement with the reduction peaks from CV with a total faradaic experiments of 0.8 F/mol. A discharge/charge capacity of 120 mAh g⁻¹ is achieved indicating reversible insertion/extraction process. The obtained results show typical electrochemical fingerprint of α -V₂O₅ in organic lithiated electrolyte [2]–[5]. The Zn || Li₂SO₄-ZnSO₄ || α -V₂O₅ shows stable cycling stability properties (**Figure 5b**). The initial discharge capacity is only reduced to ~119 mAh g⁻¹ after 50 cycles with a good capacity retention up to 50 cycles.

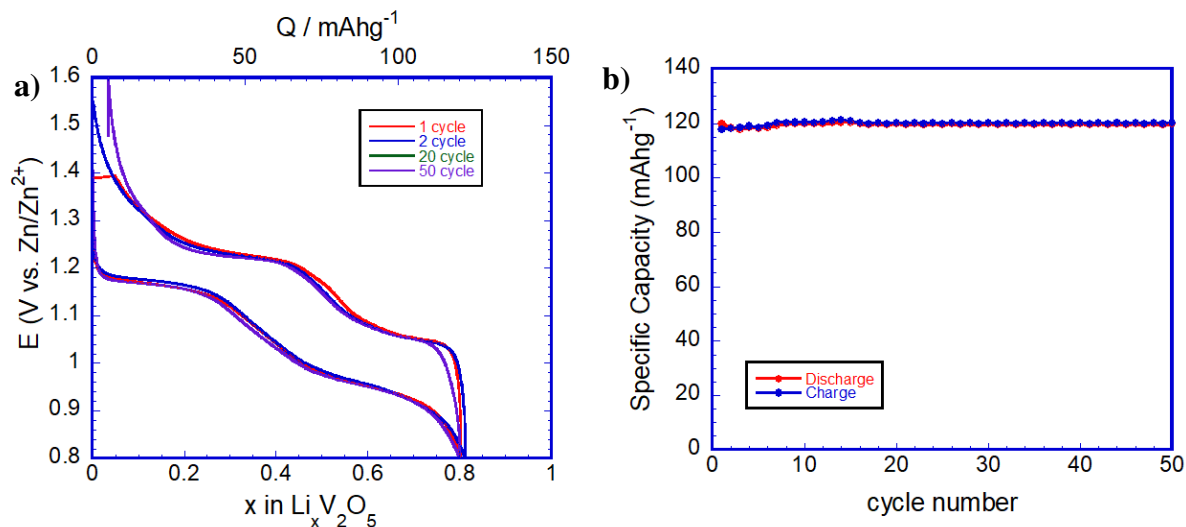


Figure 5. (a) Discharge-charge profile and (b) cyclability of $\text{Zn} \parallel \text{Li}_2\text{SO}_4\text{-ZnSO}_4 \parallel \alpha\text{-V}_2\text{O}_5$ system at C/5

4.2.4 Structural investigation upon discharge-charge

To clearly understand the insertion/extraction mechanisms the structural evolution of $\alpha\text{-V}_2\text{O}_5$ was investigated during first discharge/charge at C/5 in potential range of 0.8 – 1.6V (**Figure 6**) by using XRD and Raman spectroscopy.

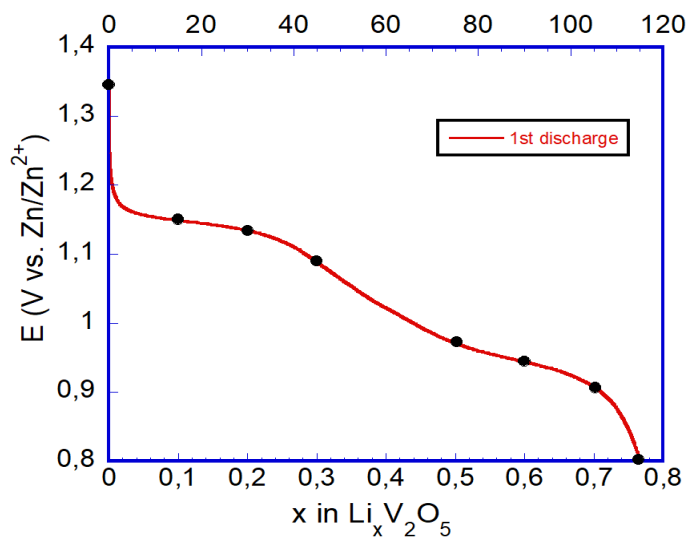


Figure 6. The first discharge of $\alpha\text{-V}_2\text{O}_5$ at C/5

The XRD patterns of discharged electrodes in function of faradaic yield $x \text{ F mol}^{-1}$ ($0 \leq x < 1$) are gathered in **Figure 7**. The low rate of C/20 was applied to reach maximum faradaic yield of $x=0.93$. The XRD pattern of initial electrode shows typical fingerprint of orthorhombic $\alpha\text{-V}_2\text{O}_5$ ($Pmmn$ space group) with unit cell parameters of: $a = 11.49$, $b = 3.56$ and $c = 4.36 \text{ \AA}$ [6]. From the first

reduction ($x=0.1$) shift of 0 0 1, 1 0 1, 0 1 1, 1 1 1 lines to lower angles can be observed, indicating the increase of c interlayer distance. While 2 0 0, 4 0 0, 3 1 0 lines slightly shift to higher angles due to the decrease of a parameter with increasing x values. From $x=0.1$ to $x=0.3$, the α phase ($a = 11.49$, $b = 3.56$, $c = 4.38$ Å) coexists with orthorhombic ϵ - $\text{Li}_{0.3}\text{V}_2\text{O}_5$ phase reported in organic electrolyte ($a = 11.42$, $b = 3.57$, $c = 4.47$ Å)[5]. For $0.3 < x \leq 0.93$ only the ϵ - $\text{Li}_x\text{V}_2\text{O}_5$ single phase can be observed. The interlayer c parameter of ϵ - $\text{Li}_x\text{V}_2\text{O}_5$ phase with lithium composition changes from 4.47 Å to 4.58 Å, which is in good agreement with previously reported data[7]. Finally, ϵ - $\text{Li}_{0.93}\text{V}_2\text{O}_5$ phase electrochemically formed with unit cell parameters $a=11.35$, $b=3.58$, $c=4.58$ Å without any further structural changes (**Figure 7**) The b parameter remains constant during discharge process which is consistent with Li diffusion along the b axis between layers. According to the **Figure 8** the formation of solid solution behavior ($x \geq 0.5$) is well illustrated by the linear expansion of unit cell volume vs. x and does not exceed 4%. This small volume change discards the insertion of water molecules into the structure of V_2O_5 . The obtained results were compared with organic system and general similarities can be seen, indicating the prove of lithium insertion (Fig. 8b). However, expected distorted δ - phase was not observed, due to the possibility of insertion of a few Zn^{2+} ions.

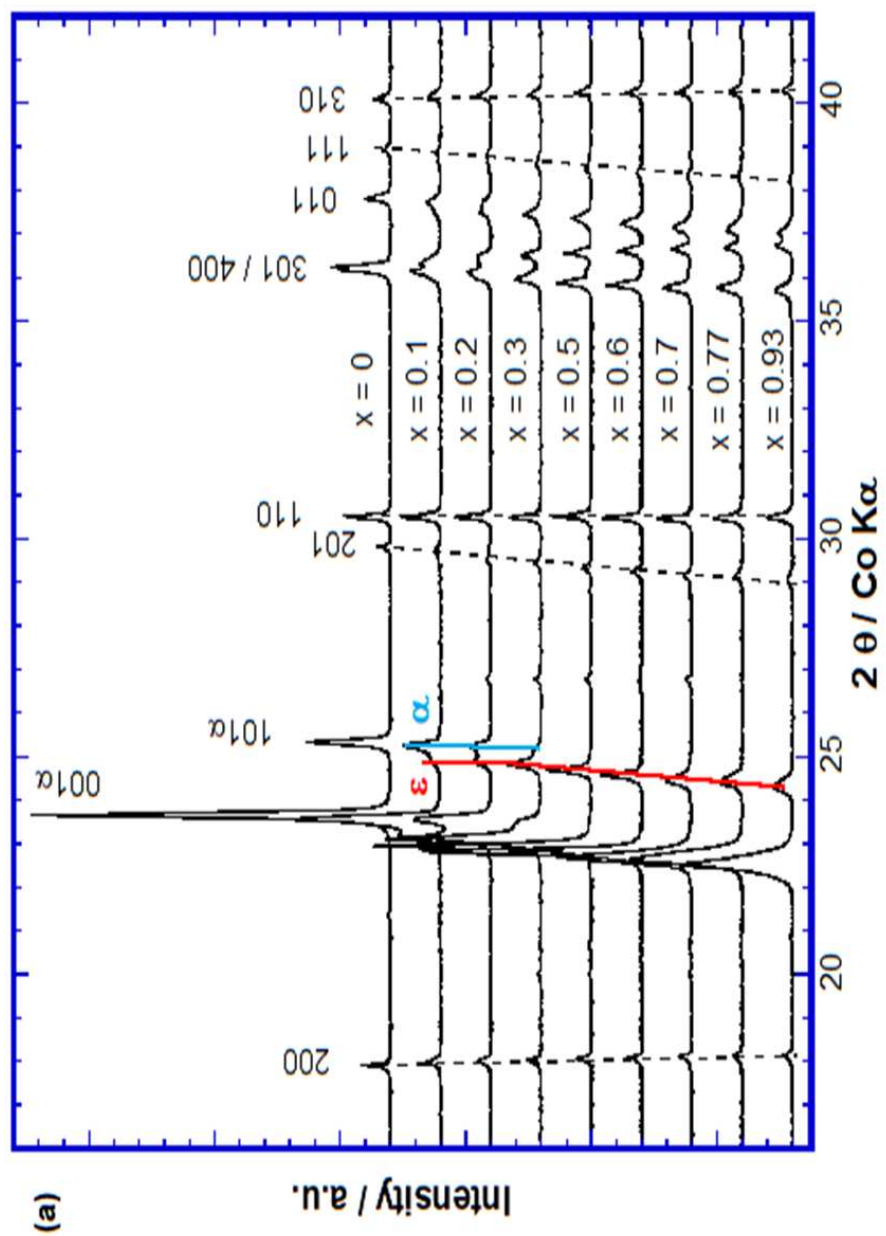


Figure 7. Ex-situ XRD pattern of Zn || ZnSO₄-Li₂SO₄ || α -V₂O₅ system during 1st discharge

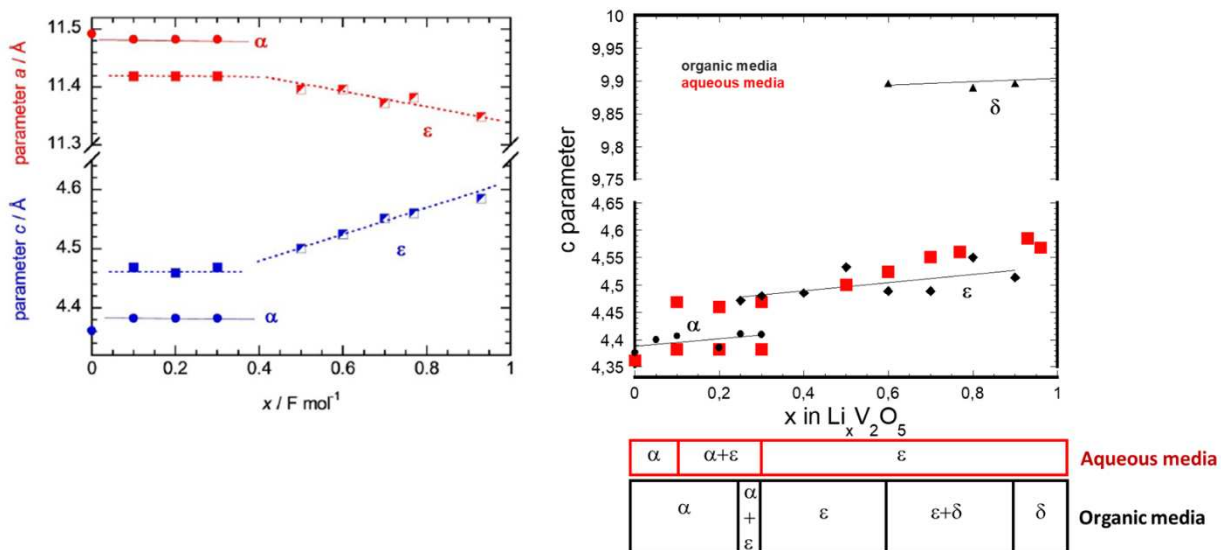


Figure 8. Evolution of unit cell parameters and unit cell volume as a function of x ($0 \leq x \leq 0.93$).

Raman spectroscopy was also carried out to identify the structural changes of V_2O_5 during 1st discharge. The Raman spectra series collected at different state of discharge in $0 \leq x \leq 0.93$ composition range are shown in **Figure 9**. The Raman spectrum of initial electrode agrees with well-known fingerprint of α - V_2O_5 showing 10 bands at 105, 146, 199, 286, 305, 406, 483, 529, 703 and 994 cm^{-1} . Most of low wavenumber modes can be described in terms of external modes of V_2O_5 units. They have been derived from the relative motions of two V_2O_5 units belonging to the unit cell, three of them generated by displacements of vanadium atoms along the x -axis (195 cm^{-1}), y -axis (145 cm^{-1}) and z -axis (105 cm^{-1}). The internal modes observed at medium and high frequency can be described in terms of O–V–O bending modes and V–O stretching modes. The band at 994 cm^{-1} is assigned to the V–O stretching vibration mode along z -axis (A_g symmetry), corresponding to the shortest V=O vanadyl bond oriented along c -axes. The V–O stretching modes along x - and y -axes are observed at 530 cm^{-1} (A_g) and 703 cm^{-1} (B_{1g} , B_{3g}), respectively.

At early stage of discharge ($x=0.1$), new band at 982 cm^{-1} is observed in the V–O stretching vibration mode, which is typical to the presence of V^{4+} ions. It can be assigned to the appearance of Li-poor ϵ - $\text{Li}_x\text{V}_2\text{O}_5$ phase [5]. Two weak features are detected at 995 and 1016 cm^{-1} , which related to the $V^{5+}=\text{O}$ stretching modes.

From $x \geq 0.1$ α -phase coexist with ϵ -phase up to $x=0.3$. Band at 146 shifts to higher frequency with decrease of intensity. The additional band shift can be determined: 406 to 418 cm^{-1} , 529 to 536 cm^{-1} , 703 to 707 cm^{-1} .

At $x=0.5$ the characteristic lines of pure ϵ - $\text{Li}_{0.5-0.6}\text{V}_2\text{O}_5$ at 158, 421, 475, 536, 707 and 983 cm^{-1} can be observed.

For $0.5 \leq x \leq 0.93$ following noticeable shifts can be observed: strong intensity decreases of 158 cm^{-1} , 475 to 438 cm^{-1} , 536 to 531 cm^{-1} , 707 to 712 cm^{-1} , 983 to 977 cm^{-1} and new band at 957 cm^{-1} . This trend is consistent with a solid solution behavior consisting in the Li enrichment of the ϵ -phase. These findings show similarities with previously reported for Li-rich LiV_2O_5 phase (denoted as ϵ'). The ϵ' phase was first reported in [7] and identified for chemically lithiated powders and electrochemically formed thin film electrodes. The new band at 957 cm^{-1} also observed in previous reports [5]. It is clear that on high values of x ($x > 0.5$) no biphasic region is found in binary electrolyte. Only the existence of ϵ -type phase in extended lithium composition range can be revealed. These findings are in good agreement with XRD results. In addition, δ -phase with well characteristic Raman features in organic electrolyte [7], [8] is not found in aqueous electrolyte. It can be explained by possible insertion of Zn^{2+} ions at potential range of ~ 0.9 V as shown in **Figure S1**. The presence of zinc cations between the oxide layers may acts as pillars to stabilize the structure upon the cycling [9].

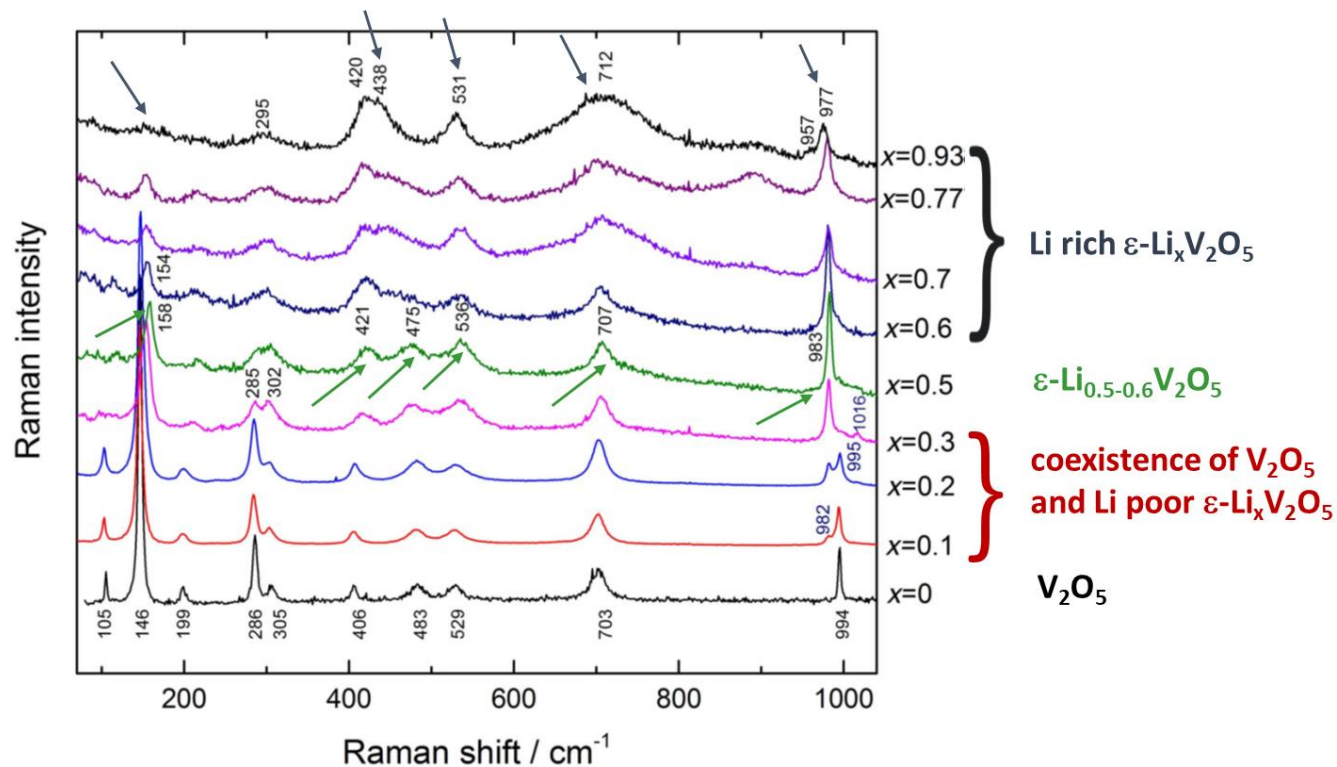


Figure 9. Raman spectra series collected at different stage of discharge $0 \leq x \leq 0.93$.

In order to check whether zinc is responsible of moderate structure change in α -V₂O₅, an electrode was discharged till $x=0.9$ F mol⁻¹ in 3M Li₂SO₄ (pH=4). The obtained XRD result reveals the formation of $\epsilon_{0.9-1}$ -LiV₂O₅ with unit cell parameters $a=11.38$, $b=3.57$, $c=4.59$ Å and δ -LiV₂O₅ (orthorhombic, *Amam* space group) with parameters $a=11.24$, $b=3.6$, $c=9.90$ Å as reported [10]. Raman spectroscopy confirmed the XRD results. The peaks of δ -LiV₂O₅ at 91, 152, 180, 252, 289, 420, 433, 631, 670 and 1007 cm⁻¹ and typical peaks of Li-rich ϵ -Li_{0.9-1}V₂O₅ at 708, 958, 978 cm⁻¹ were observed. This comparison of discharge products in hybrid and pure Lithium salt clearly indicates that in binary electrolyte, insertion of Zn²⁺ ions is probable which explains less severe structural changes.

4.2.5 Cycling properties

In order to improve the electrochemical behaviour of α -V₂O₅ described here, we decided to evaluate a nanosized oxide prepared by a solution technique briefly described in “supplementary file”. The *polyol* (*pol.*) synthesized α -V₂O₅ (nanosized, ~200 nm) was investigated and compared to the *commercial* (*com.*) α -V₂O₅ (microsized), in order to check the effect of morphology and particle size on electrochemical performance of the battery. The discharge/charge profile and cyclability at 1C in voltage range of 0.8 – 1.6V are shown in **Figure 10a**. For both materials during discharge two plateaus can be observed at 1.16 V and 0.95 V. The initial discharge capacity of *com.* α -V₂O₅ exhibits 80 mAh g⁻¹ and retains till 150 cycles without any capacity decay. The Ex-situ XRD and Raman results confirms the reversibility of structural rearrangement during the cycling **Figure S2**.

In comparison, the initial discharge capacity of *pol.* α -V₂O₅ exhibits ~120 mAh g⁻¹ decreases to 104 mAh g⁻¹ after 150 cycles (**Figure 10b**). The both materials show symmetric shape of complete cycle and stable cyclability over 150 cycles with 100% coulombic efficiency.

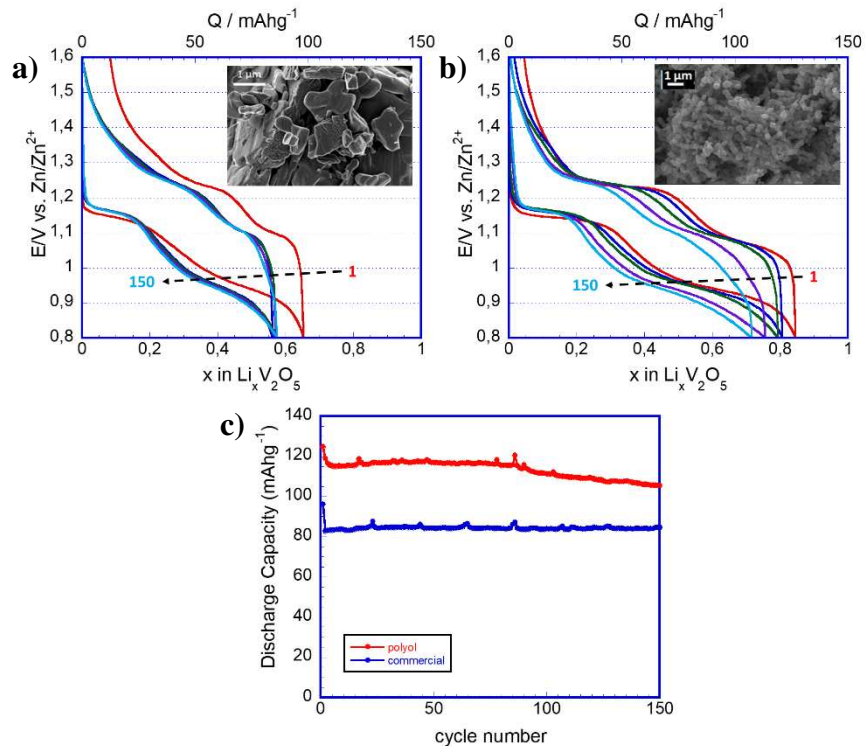


Figure 10. Discharge/charge profile of (a) *com.* and (b) *pol.* α -V₂O₅ (c) cycle performance at 1C at voltage range of 1.6 – 0.8V. inset SEM images of materials

The rate-capability of *com.* and *pol.* α -V₂O₅ is presented in **Figure 11**. The first discharge capacities of *com.* α -V₂O₅ at C/5, C/2, 1C, 2C, 5C, 10C, 20C are 110, 95, 85, 70, 45, 25, 15 mAh g⁻¹, respectively. Even after 20C the initial capacity of 110 mAh g⁻¹ can be recovered without capacity fading (**Figure 11a**).

In comparison the initial discharge capacities of *pol.* α -V₂O₅ at C/5, C/2, 1C, 2C, 5C, 10C, 20C are 140, 122, 110, 101, 82, 60, 36 mAh g⁻¹, respectively. After applying 20C and then C/5, the initial discharge capacity can be practically recovered to reach 128 mAh g⁻¹ with a stable capacity upon cycling. The higher specific capacity and lower polarization in discharge/charge curves of *pol.* α -V₂O₅ illustrates the beneficial effect of smaller particle sizes in electrochemical on the Zn/V₂O₅ system performances (**Figure 11b**).

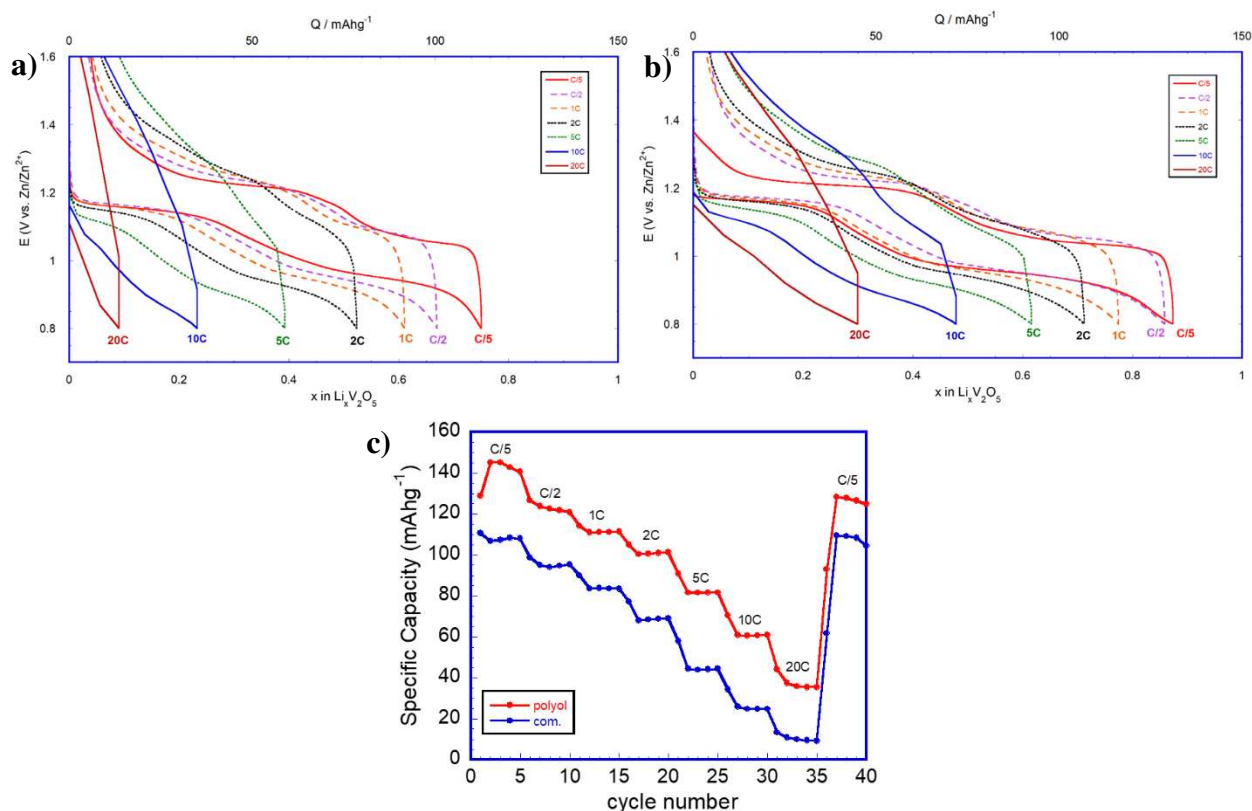


Figure 11. Discharge/charge profile at different C-rate (a) *com.* and (b) *pol.* $\alpha\text{-V}_2\text{O}_5$. (c) rate capability

Finally, long term cycling experiments have been performed even with micro-sized V_2O_5 over 300 cycles at 1C. A remarkable stable capacity of 80 mAh g^{-1} is achieved with no change in the discharge-charge profile suggesting the pristine orthorhombic structure of V_2O_5 is restored. This excellent structural reversibility has been demonstrated by XRD and Raman experiments of charged electrodes as a function of cycles (see paper; [11]). However, after 300 cycles a detailed examination of these data reveal the emergence of epsilon LiV_2O_5 with low lithium content and traces of $\text{Zn}_3(\text{VO}_4)_2 \cdot (\text{H}_2\text{O})$ phase

4.2.6 Conclusion

A novel Zn-V₂O₅ aqueous rechargeable battery has been proposed, using a Li⁺/Zn²⁺ binary electrolyte at pH 4. This cell exhibits a highly reversible capacity of 136 mAh g⁻¹ at C/20 and 125 mAh g⁻¹ at C/5 in the 1.6 V - 0.8 V range. The present investigation of α -V₂O₅ in hybrid Zn²⁺/Li⁺ electrolyte shows Li insertion can occur also in aqueous medium with similar discharge and charge profiles than in organic electrolyte. The system provides two working plateaus (1.12 – 0.9V vs. Zn/Zn²⁺) for a same maximum faradaic yield practically at the same energy level. **(Figure 12)** [2]–[5]. XRD and Raman spectroscopy confirm a high structural reversibility. However, we prove structure changes take place in hybrid electrolyte with an exclusive Li insertion in V₂O₅ up to mid-discharge followed by the co-insertion of a few zinc ions in the second part of the reduction. A pillaring effect of a few interlayer Zn²⁺ ions could explain the formation of the distorted δ -LiV₂O₅ phase expected in pure lithiated electrolyte is never observed in hybrid electrolyte. The high structural stability of V₂O₅ even after 300 cycles (80 mAh g⁻¹) makes this hybrid Zn/V₂O₅ system promising in aqueous binary electrolytes

Several questions still remain open. Indeed, the possible competitive insertion of protons cannot be completely discarded, this point has to be clarified in the future. Finally, the preliminary results achieved with polyol α -V₂O₅ indicate the nanosizing approach must be considered as a key factor to optimize electrochemical performance of the cathode material.

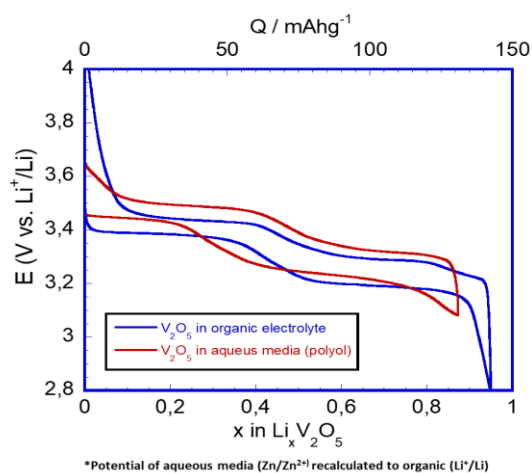


Figure 12. Comparison of discharge/charge curve of α -V₂O₅ in aqueous and organic electrolyte

SUPPORTING INFORMATION

Electrochemical characterization

α -V₂O₅ positive electrodes were prepared by mixing 90wt% of active material, 6wt% polyvinylidene fluoride (PVDF, Kynar, HSV900) as a binder, 4wt% ketjen black (Ketjen Black International Co., Japan) as conductive agent dissolved in 1-methyl-2-pyrrolidinone (NMP, Sigma-Aldrich). The prepared slurry was casted on carbon paper (Alfa Aesar Co.), vacuum dried at 70 °C for 3hr and punched into the disks of 8 mm in diameter. The mass loading of active material was around 5 mg/cm² (2.7-2.8 mg of active material). Zinc foil (Goodfellow, USA) was used as negative electrode. The electrolyte was prepared by dissolving 3.5 mole L⁻¹ of ZnSO₄ and 2.5 mole L⁻¹ of Li₂SO₄ in distilled water and pH was adjusted to 4 by titration with 0.5 mole L⁻¹ of H₂SO₄. Prepared electrolyte was bubbled with nitrogen gas (N₂) to remove dissolved oxygen. AGM (Absorptive Glass Mat NSG Corporation) was used as separator.

Structural characterization

XRD measurements were carried out using a Panalytical X'pert pro diffractometer equipped with an X'Celerator detector and a Co K α radiation (wavelength 1.7889 Å). All the diffraction patterns were collected with a 2 θ step of 0.0167°. The Raman spectra were measured with a LaBRAM HR 800 (Jobin-Yvon-Horiba) Raman micro-spectrometer including Edge filters and equipped for signal detection with a back illuminated charge coupled device detector (Spex CCD) cooled by Peltier effect to 200 K. A He:Ne laser (632.8 nm) was used as the excitation source. The spectra were measured in back-scattering geometry. The resolution was about 0.5 cm⁻¹. A 50X LWD objective was used to focus the laser light on sample surface to a spot size of 1 μ m². To avoid local heating of the sample, the power of the laser beam was adjusted to 0.2–0.5 mW with neutral filters of various optical densities. Raman spectra were recorded on ten different spots of each electrode to check the homogeneity. The powders were characterized by scanning electron microscopy (SEM), Zeiss, Merlin-type microscope. Energy Dispersive X-ray spectroscopy (EDS) was applied to determine the elemental composition with SEM an accelerating voltage of 10 – 15 kV.

Ex-situ structural investigations

The structural investigation of $\text{Zn} \parallel \text{Li}_2\text{SO}_4\text{-ZnSO}_4 \parallel \alpha\text{-V}_2\text{O}_5$ system was investigated by using two-electrode split cell (MTI company). The cells were discharged to the required composition by electrochemical reduction using VMP3 Biologic tester at C/5, C/20 rate. After reduction, cells were disassembled in air, electrodes were rinsed in distilled water in order to remove the traces of salt and separator. Cyclic voltammetry (CV) was performed with VMP3 potentiostat/galvanostat (Bio-Logic Science Instrument Co.)

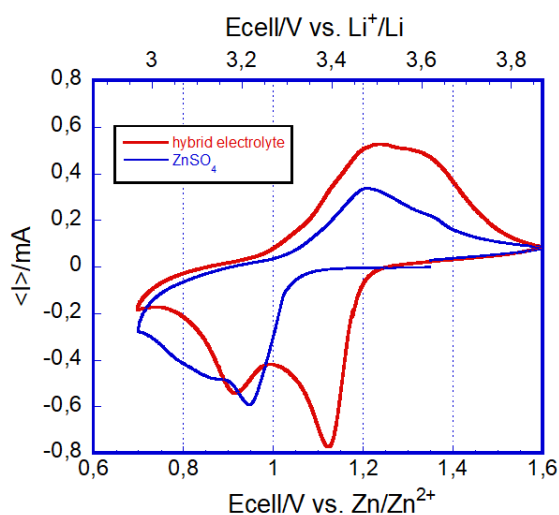


Figure S1. The cyclic voltammetry of $\text{Zn}/\alpha\text{-V}_2\text{O}_5$ on 1 cycle with hybrid and 4M ZnSO_4 electrolyte at scan rate of 0.2 mV/s in voltage range of 0.7 – 1.6 V.

The Raman results of electrodes before cycling, after 1 cycle, after 300 cycles demonstrate the stability of host lattice without any change of the bands to the presence of another phase (Fig. S2). XRD result of electrode after 1 cycle depicts that the structure of initial $\alpha\text{-V}_2\text{O}_5$ was completely restored after complete charge with 100% coulombic efficiency. However, after 300 cycles the peak of $\epsilon\text{-LiV}_2\text{O}_5$ with low Li content (unit cell parameters $a=11.46$, $b=3.56$, $c=4.46$ Å) remained. In addition, the presence of new diffraction peak at 14.23° , 24.5° , 34.5° , 35° , 39° corresponds to the trigonal $\text{Zn}_3\text{V}_2\text{O}_7(\text{OH})_2 \cdot 2\text{H}_2\text{O}$ pyrovanadate (ZVO, space group $P\bar{3}m1$) [12]. ZVO phase adopts typical layered structure consisting of ZnO_6 octahedra layers separated by double VO_4 tetrahedral interlayer pillars. Water molecules randomly located in large cavities [13]. According to the literature, $\text{Zn}_3\text{V}_2\text{O}_7(\text{OH})_2 \cdot 2\text{H}_2\text{O}$ phase forms on the surface of electrode as a result of electrolytic decomposition and side reaction of active material with electrolyte [14].

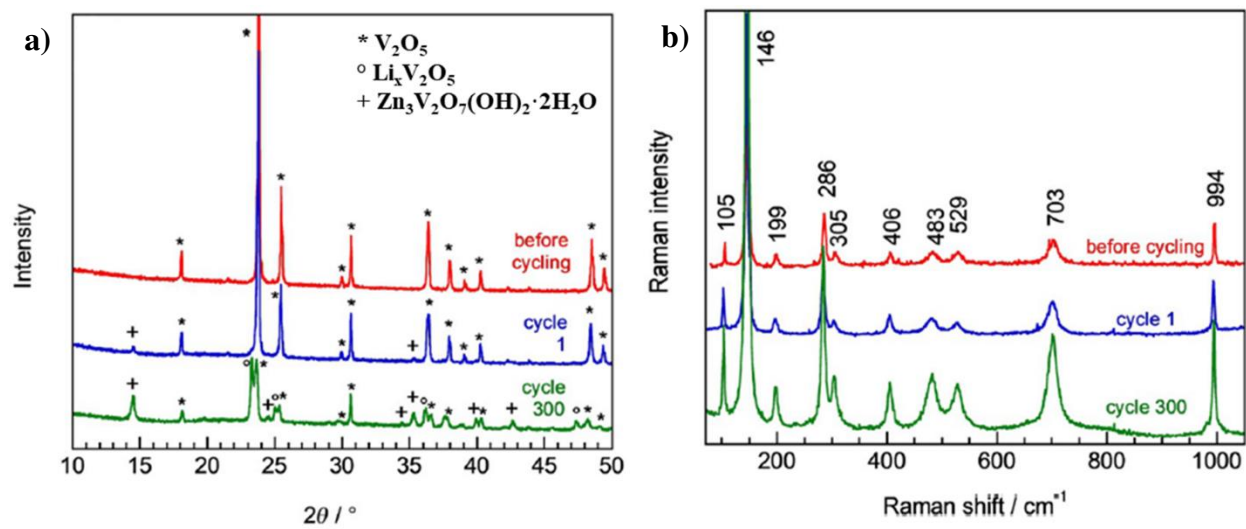


Figure S2. (a) XRD and (b) Raman spectra of Zn/α-V₂O₅ before and after cycling on charged state

REFERENCES

- [1] J. Yan, J. Wang, H. Liu, Z. Bakenov, D. Gosselink, and P. Chen, "Rechargeable hybrid aqueous batteries," *J. Power Sources*, vol. 216, pp. 222–226, Oct. 2012, doi: 10.1016/j.jpowsour.2012.05.063.
- [2] D. Huo *et al.*, "Understanding of the nanosize effect on the structure and electrochemistry of V₂O₅ obtained via fluorine chemistry," *Mater. Today Proc.*, vol. 5, no. 11, pp. 22850–22858, 2018, doi: 10.1016/j.matpr.2018.07.099.
- [3] C. Delmas, H. Cognac-Auradou, J. M. Cocciantelli, M. Ménétrier, and J. P. Doumerc, "The LixV₂O₅ system: An overview of the structure modifications induced by the lithium intercalation," *Solid State Ionics*, vol. 69, no. 3–4, pp. 257–264, 1994, doi: 10.1016/0167-2738(94)90414-6.
- [4] J. M. Cocciantelli, J. P. Doumerc, M. Pouchard, M. Broussely, and J. Labat, "Crystal chemistry of electrochemically inserted LixV₂O₅," *J. Power Sources*, vol. 34, no. 2, pp. 103–111, Mar. 1991, doi: 10.1016/0378-7753(91)85029-V.
- [5] R. Baddour-Hadjean, A. Marzouk, and J. P. Pereira-Ramos, "Structural modifications of LixV₂O₅ in a composite cathode (0 ≤ x < 2) investigated by Raman microspectrometry," *J. Raman Spectrosc.*, vol. 43, no. 1, pp. 153–160, Jan. 2012, doi: 10.1002/jrs.2984.
- [6] N. Emery, R. Baddour-Hadjean, D. Batyrbekuly, B. Laïk, Z. Bakenov, and J.-P. Pereira-Ramos, "γ-Na_{0.96}V₂O₅: A New Competitive Cathode Material for Sodium-Ion Batteries Synthesized by a Soft Chemistry Route," *Chem. Mater.*, vol. 30, no. 15, pp. 5305–5314, Aug. 2018, doi: 10.1021/acs.chemmater.8b02066.
- [7] R. Baddour-Hadjean, C. Navone, and J. P. Pereira-Ramos, "In situ Raman microspectrometry investigation of electrochemical lithium intercalation into sputtered crystalline V₂O₅ thin films," *Electrochim. Acta*, vol. 54, no. 26, pp. 6674–6679, Nov. 2009, doi: 10.1016/j.electacta.2009.06.052.
- [8] C. V. Ramana, R. J. Smith, O. M. Hussain, M. Massot, and C. M. Julien, "Surface analysis of pulsed laser-deposited V₂O₅ thin films and their lithium intercalated products studied by Raman spectroscopy," *Surf. Interface Anal.*, vol. 37, no. 4, pp. 406–411, Apr. 2005, doi: 10.1002/sia.2018.
- [9] D. Kundu, B. D. Adams, V. Duffort, S. H. Vajargah, and L. F. Nazar, "A high-capacity and long-life aqueous rechargeable zinc battery using a metal oxide intercalation cathode," *Nat. Energy*, vol. 1, no. 10, p. 16119, Oct. 2016, doi: 10.1038/nenergy.2016.119.
- [10] D. Huo *et al.*, "Evidence for a nanosize effect on the structural and high performance electrochemical properties of V₂O₅ obtained via fluorine chemistry," *Electrochim. Acta*, vol. 245, pp. 350–360, Aug. 2017, doi: 10.1016/j.electacta.2017.05.147.
- [11] D. Batyrbekuly *et al.*, "Mechanistic Investigation of a Hybrid Zn/V₂O₅ Rechargeable Battery with a Binary Li⁺/Zn²⁺ Aqueous Electrolyte," *ChemSusChem*, vol. 13, no. 4, pp. 724–731, Feb. 2020, doi: 10.1002/cssc.201903072.
- [12] Y. Lu, T. Zhu, W. Bergh, M. Stefik, and K. Huang, "A High Performing Zn-Ion Battery Cathode Enabled by In Situ Transformation of V₂O₅ Atomic Layers," *Angew. Chemie Int. Ed.*, vol. 59, no. 39, pp. 17004–17011, Sep. 2020, doi: 10.1002/anie.202006171.
- [13] C. Xia, J. Guo, Y. Lei, H. Liang, C. Zhao, and H. N. Alshareef, "Rechargeable Aqueous Zinc-Ion Battery Based on Porous Framework Zinc Pyrovanadate Intercalation Cathode," *Adv. Mater.*, vol. 30, no. 5, pp. 1–7, 2018, doi: 10.1002/adma.201705580.
- [14] J. H. Jo, Y. K. Sun, and S. T. Myung, "Hollandite-type Al-doped VO_{1.52}(OH)_{0.77} as a zinc ion insertion host material," *J. Mater. Chem. A*, vol. 5, no. 18, pp. 8367–8375, 2017,

doi: 10.1039/c7ta01765k.

Mechanistic Investigation of a Hybrid Zn/V₂O₅ Rechargeable Battery with a Binary Li⁺/Zn²⁺ Aqueous Electrolyte

Dauren Batyrbekuly,^[a, b] Sabrina Cajoly,^[a] Barbara Laïk,^{*,[a]} Jean-Pierre Pereira-Ramos,^[a] Nicolas Emery,^[a] Zhumabay Bakenov,^[b] and Rita Baddour-Hadjean^[a]

Low-cost, easily processable, and environmentally friendly rechargeable aqueous zinc batteries have great potential for large-scale energy storage, which justifies their receiving extensive attention in recent years. An original concept based on the use of a binary Li⁺/Zn²⁺ aqueous electrolyte is described herein for the case of the Zn/V₂O₅ system. In this hybrid, the positive side involves mainly the Li⁺ insertion/deinsertion reaction of V₂O₅, whereas the negative electrode operates according to zinc dissolution–deposition cycles. The Zn//3 mol L^{−1} Li₂SO₄–4 mol L^{−1} ZnSO₄//V₂O₅ cell worked in the narrow voltage range of 1.6–0.8 V with capacities of approximately 136–125 mAh g^{−1} at rates of C/20–C/5, respectively. At 1 C, the capacity of 80 mAh g^{−1} was outstandingly stable for more than 300 cycles with a capacity retention of 100%. A detailed structural study by XRD and Raman spectroscopy allowed the peculiar response of the V₂O₅ layered host lattice on discharge–

charge and cycling to be unraveled. Strong similarities with the well-known structural changes reported in nonaqueous lithiated electrolytes were highlighted, although the emergence of the usual distorted δ-LiV₂O₅ phase was not detected on discharge to 0.8 V. The pristine host structure was restored and maintained during cycling with mitigated structural changes leading to high capacity retention. The present electrochemical and structural findings reveal a reaction mechanism mainly based on Li⁺ intercalation, but co-intercalation of a few Zn²⁺ ions between the oxide layers cannot be completely dismissed. The presence of zinc cations between the oxide layers is thought to relieve the structural stress induced in V₂O₅ under operation, and this resulted in a limited volume expansion of 4%. This fundamental investigation of a reaction mechanism operating in an environmentally friendly aqueous medium has not been reported before.

Introduction

Since a few decades, annual global oil consumption has exceeded the discovery of new deposits. This energy crisis coupled with growing ecological concerns requires a rapid energy transition while meeting the ever-increasing demand for energy. Hence, research on renewable intermittent energies with special attention to safe and low-cost storage solutions is required.


Nonaqueous Li-ion batteries (LIBs) are the best technology for electrochemical energy storage owing to their high energy and power densities. As leaders in the portable electronics market, LIBs are also considered for large-scale applications such as electric vehicles and stationary grids combined with re-

newable energy.^[1] However, safety aspects owing to the flammability of the organic electrolyte and costs related to the need to use a clean room during the manufacturing process to remove all traces of water are among the crucial problems to be solved. In recent years, many efforts have been made to develop new concepts to overcome these critical issues. Among them, rechargeable batteries with aqueous electrolytes are attracting considerable attention for electrochemical energy storage.^[2] Indeed, besides the environmentally friendly aspect, the nonflammability of the solvent makes them safer. In addition, the use of water-based electrolytes instead of flammable organic electrolytes ensures high ionic conductivity promoting high rate capability. Moreover, because the total absence of oxygen or moisture is not necessary during preparation, the use of aqueous solvent leads to lower total cost. However, the narrow electrochemical stability window of water, which is limited to 1.23 V at 25 °C according to thermodynamic considerations, remains a major challenge.

In the last few years, research efforts have intensively focused on aqueous zinc batteries (AZBs).^[3–5] The reasons for this interest are the abundance, low cost, and low redox potential (−0.76 V vs. SHE) of Zn, as well as the wide potential range of approximately 2 V owing to the high overpotential for hydrogen evolution.^[6] Excellent reversibility and fast kinetics of Zn deposition/dissolution have been reported^[7] thanks to the use

[a] D. Batyrbekuly, S. Cajoly, Dr. B. Laïk, Dr. J.-P. Pereira-Ramos, Dr. N. Emery, Dr. R. Baddour-Hadjean
Institut de Chimie et des Matériaux Paris Est (ICMPE)
UMR 7182 CNRS-Université Paris Est Créteil
2 rue Henri Dunant, 94320 Thiais (France)
E-mail: laik@icmpe.cnrs.fr

[b] D. Batyrbekuly, Prof. Z. Bakenov
School of Engineering and Digital Sciences
National Laboratory Astana
Nazarbayev University
53 Kabanbay Batyr Avenue, Astana 010000 (Kazakhstan)

 The ORCID identification number(s) for the author(s) of this article can be found under:
<https://doi.org/10.1002/cssc.201903072>.

of aqueous electrolytes in neutral or slightly acidic pH preventing growth of Zn dendrites.^[8–10] On the cathode side, three main groups of active materials have been investigated: Prussian blue and its analogues, manganese compounds, and vanadium oxides as well as their derivatives.^[3,10,11] Vanadium-based cathodes have sparked great interest owing to the rich redox chemistry of vanadium, which enables high specific capacities to be reached, and to various open host structures promoting insertion reactions. Recently, attractive results have been achieved with the hydrated bronze $\text{Zn}_{0.25}\text{V}_2\text{O}_5 \cdot n\text{H}_2\text{O}$, which exhibits a capacity close to 300 mA h g^{-1} , fast rate capability, and long cycle life.^[4] On the basis of this pioneering work, studies have been extended to hydrated compounds such as $\text{V}_2\text{O}_5 \cdot n\text{H}_2\text{O}$,^[12] $\text{V}_3\text{O}_7 \cdot \text{H}_2\text{O}$,^[13] $\text{V}_{10}\text{O}_{24} \cdot 12\text{H}_2\text{O}$,^[14] $\text{Mg}_x\text{V}_2\text{O}_5 \cdot n\text{H}_2\text{O}$,^[15] $\text{K}_2\text{V}_6\text{O}_{16} \cdot 2.7\text{H}_2\text{O}$,^[16] $\text{Ca}_{0.25}\text{V}_2\text{O}_5 \cdot n\text{H}_2\text{O}$,^[17] $\text{Na}_2\text{V}_6\text{O}_{16} \cdot 3\text{H}_2\text{O}$,^[18] and $\text{Fe}_5\text{V}_{15}\text{O}_{39}(\text{OH}) \cdot 9.9\text{H}_2\text{O}$.^[19] Anhydrous phases such as VO_2 ,^[20] $\text{Zn}_2\text{V}_2\text{O}_7$,^[21] $\text{NH}_4\text{V}_4\text{O}_{10}$,^[22] potassium vanadates,^[23] and LiV_3O_8 ^[24] have also been investigated.

Surprisingly, the pristine conventional V_2O_5 oxide has received less attention than its derivatives. Mai and co-workers used water-free V_2O_5 microplates and, more recently, microspheres in a “water-in-salt” electrolyte mixture of 21 M lithium bis(trifluoromethanesulfonyl)imide (LiTFSI) and 1 M $\text{Zn}(\text{CF}_3\text{SO}_3)_2$,^[25,26] but insertion reactions of cations into this oxide are scarcely reported in conventional aqueous electrolytes,^[27,28] so that fundamental investigations of the reaction mechanism of AZBs must be intensified.^[3,10,11] The few papers already published only focused on the two-electron reaction in 3 mol L^{-1} ZnSO_4 or $\text{Zn}(\text{CF}_3\text{SO}_3)_2$ aqueous electrolyte and led to capacity values scattered in the range $220\text{--}470 \text{ mA h g}^{-1}$.^[27,28] Although the structural mechanism has not been completely elucidated, zinc and water insertion are thought to be responsible for the formation of a $\text{Zn}_x\text{V}_2\text{O}_5 \cdot n\text{H}_2\text{O}$ compound in the first discharge. After an activation process over a few or a few dozen cycles, a highly stable capacity can be reached.

Recently, some of us proposed the use of an aqueous Zn/LiFePO₄ rechargeable battery with a binary concentrated electrolyte consisting of 3 mol L^{-1} LiCl and 4 mol L^{-1} ZnCl_2 at an optimized pH of 4 to ensure high conductivity and electrode stability.^[29] Remarkable cycling performance was obtained with a capacity of 92 mA h g^{-1} over 400 cycles at 6 C and a high rate capability with retention of 72 mA h g^{-1} at 30 C. This concept of a binary electrolyte with both zinc and lithium ions has never been applied to the Zn/ V_2O_5 system. It relies on a high ionic conductivity with sufficient amounts of zinc for efficient cyclability of the zinc anode and lithium for reversible insertion/extraction in the host cathodic material. These appealing results prompted us to evaluate the Zn/ V_2O_5 system in the binary lithium–zinc aqueous electrolyte at optimized pH 4.

Herein, we report the electrochemical properties of V_2O_5 in 3 mol L^{-1} Li_2SO_4 – 4 mol L^{-1} ZnSO_4 electrolyte in the voltage window of 1.6–0.8 V versus Zn^{2+}/Zn , with special attention paid to the structural mechanism involved in the discharge–charge process and cycling. We show that V_2O_5 exhibits a similar discharge–charge profile in this binary aqueous electrolyte to that in nonaqueous lithiated electrolyte. Promising performance is demonstrated by highly reversible behavior and

capacities varying from 140 mA h g^{-1} at low rate to 80 mA h g^{-1} at 1 C. At 1 C, the capacity retention is excellent over more than 300 cycles, with a faradaic efficiency of 100%. XRD and Raman spectroscopy were performed on discharged and charged electrodes to provide initial insights into the mechanism: a highly reversible lithiation–delithiation process was revealed. Furthermore, we demonstrate that the structural changes of V_2O_5 in aqueous electrolyte have a smaller magnitude than those usually found in nonaqueous LIBs, which is probably owing to the co-insertion of zinc ions at the end of the reaction.

Experimental Section

V_2O_5 powder (Alfa Aesar, 99.5%) was used as received. Electrochemical studies were performed in two-electrode split cells (MTI Corporation) in which a zinc disk (Goodfellow) with 14 mm diameter acted as reference and auxiliary electrode. The positive electrode was prepared by mixing 90 wt% of V_2O_5 , 6 wt% of poly(vinylidene fluoride) (Kynar, HSV900) as binder, and 4 wt% of Ketjen black (Ketjen Black International Co., Japan) as conducting agent in 1-methyl-2-pyrrolidinone (Sigma–Aldrich). The resultant slurry was coated on carbon paper (Alfa Aesar Co.), vacuum-dried at 70°C for 2 h, and cut into disks 8 mm in diameter. The loading of active material in the electrodes was approximately 2.5–3.2 mg. The electrolyte was prepared by dissolving 3 mol L^{-1} Li_2SO_4 and 4 mol L^{-1} ZnSO_4 in deionized water and adjusting the pH to 4. An AGM (absorbent glass mat, NSG Corporation) separator was soaked with 80 μL of the resultant electrolyte and used in the battery. The two-electrode cells were tested galvanostatically at various C rates (1 C corresponds to 147 mA g^{-1}) and by cyclic voltammetry (sweep rate 0.2 mV s^{-1}) by using a VMP3 Bio-Logic apparatus. The test temperature was controlled and maintained at 20°C . All potentials are reported in volts versus Zn^{2+}/Zn and specific capacities per gram of active material.

To investigate the structural mechanism involved in the discharge–charge process of V_2O_5 in aqueous binary electrolyte, the cells were discharged to the required composition by galvanostatic reduction at C/5. A rate of C/20 was used to reach the highest depth of discharge. After 1 h equilibrium, the electrodes were removed from the cell in air and rinsed with water to remove all traces of salts. The XRD experiments were performed by using a PANalytical X-Pert Pro diffractometer equipped with a X'Celerator linear detector and CoK_α source. Data were then processed with Eva software to identify peaks and adjust the cell parameters of the identified phases. The Raman spectra were measured with a LaBRAM HR 800 (Jobin-Yvon-Horiba) Raman microspectrometer including edge filters and equipped for signal detection with a back-illuminated charge-coupled device detector (Spex CCD) cooled by Peltier effect to 200 K. An He:Ne laser (632.8 nm) was used as the excitation source. The spectra were measured in backscattering geometry. The resolution was approximately 0.5 cm^{-1} . A $100\times$ objective was used to focus the laser light on the sample surface to a spot size of $1 \mu\text{m}^2$. To avoid local heating of the sample, the power of the laser beam was adjusted to 0.2–0.5 mW with neutral filters of various optical densities. Raman spectra were recorded on ten different spots of each electrode to check the homogeneity. This led to similar spectra for all the investigated points, whatever the composition. Energy-dispersive X-ray spectroscopy (EDS, accelerating energy of 20 keV) was applied to determine the elements in the

electrodes together with electron microscopy (Zeiss, Merlin-type microscope).

Results and Discussion

The storage behavior of V_2O_5 in aqueous binary electrolyte ($3 \text{ mol L}^{-1} \text{ Li}_2\text{SO}_4$ and $4 \text{ mol L}^{-1} \text{ ZnSO}_4$) was investigated in the voltage window of 1.6–0.8 V (Figure 1a,b). The voltammetric curve recorded at 0.2 mV s^{-1} shows two well-defined cathodic peaks at 1.12 and 0.91 V. The anodic scan reveals quantitative rechargeability (Figure 1a). A broad current peak is observed with contributions at 1.21 and 1.33 V corresponding to the second and first cathodic peaks, respectively. The discharge–charge profile of V_2O_5 at C/5 (Figure 1b) shows two distinct reduction steps at 1.16 and 0.95 V involving a total faradaic yield of 0.87 F mol^{-1} . The symmetric charge process indicates a reversible mechanism with two steps at 1.03 and 1.21 V. This rechargeable behavior leads to a specific capacity of 128 mAh g^{-1} and calls for several comments. First, the electrochemical fingerprint in aqueous medium strongly resembles the typical V_2O_5 galvanostatic cycle in nonaqueous lithiated electrolyte with two well-defined plateaus separated by approximately 200 mV and involving the same reversible specific

capacity.^[30] Second, cyclic voltammograms recorded in aqueous electrolytes containing lithium salt alone, zinc salt alone, and both salts (Figure 2a) enlighten us regarding the electronic reactions that likely occur. Indeed, a first reduction step is observed at 1.12 V for the two electrolytes containing Li_2SO_4 , whereas it is not present when ZnSO_4 alone is used. Then, it is reasonable to assume that lithium ions are first selectively inserted in the binary electrolyte. At lower potential, reduction curves obtained with the three electrolytes exhibit a peak around 0.92–0.94 V, which evidences that both lithium and zinc insertion can take place at this potential. In addition, the comparison of cyclability during cycling in electrolytes containing only the lithium salt or containing both lithium and zinc salts (Figure 2b) highlights the merit of the hybrid electrolyte. Indeed, the available capacity decreases rapidly in the electrolyte without zinc but is stable over 300 cycles in the electrolyte containing both salts. These findings support the insertion of lithium ions previously suggested but lead us to also consider possible concomitant zinc insertion. This peculiar result prompted us to investigate the insertion mechanism of V_2O_5 in binary $\text{Li}^+/\text{Zn}^{2+}$ electrolyte by using XRD and Raman spectroscopy.

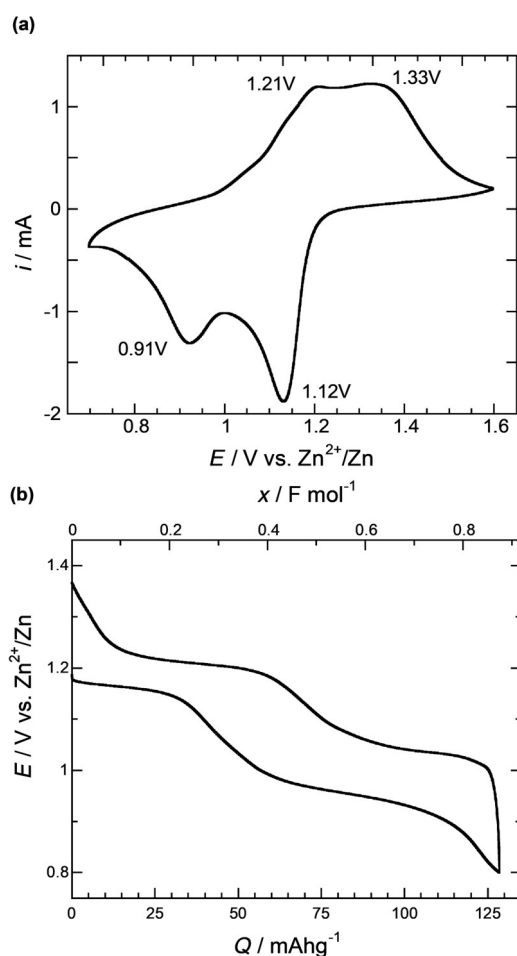


Figure 1. First a) voltammetric and b) galvanostatic cycles of a $\text{Zn}/\text{Li}_2\text{SO}_4\text{--ZnSO}_4/\text{V}_2\text{O}_5$ aqueous battery recorded at 0.2 mV s^{-1} and at C/5, respectively.

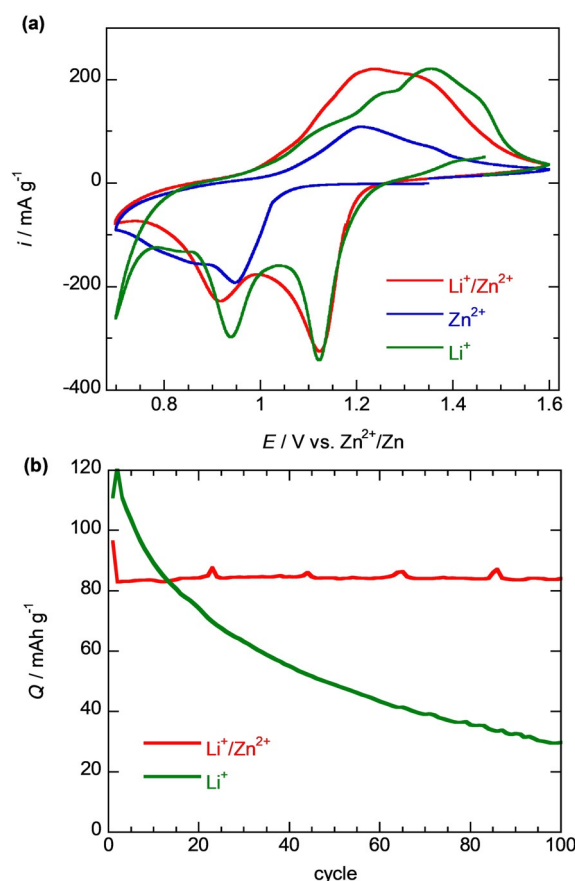


Figure 2. a) First voltammetric cycles of $\text{Zn}/3 \text{ mol L}^{-1} \text{ Li}_2\text{SO}_4\text{--}4 \text{ mol L}^{-1} \text{ ZnSO}_4/\text{V}_2\text{O}_5$ (red curve), $\text{Zn}/3 \text{ mol L}^{-1} \text{ Li}_2\text{SO}_4/\text{V}_2\text{O}_5$ (green curve), and $\text{Zn}/4 \text{ mol L}^{-1} \text{ ZnSO}_4/\text{V}_2\text{O}_5$ (blue curve) aqueous batteries recorded at 0.2 mV s^{-1} . b) Long-term cycling stability of $\text{Zn}/3 \text{ mol L}^{-1} \text{ Li}_2\text{SO}_4\text{--}4 \text{ mol L}^{-1} \text{ ZnSO}_4/\text{V}_2\text{O}_5$ (red curve) and $\text{Zn}/3 \text{ mol L}^{-1} \text{ Li}_2\text{SO}_4/\text{V}_2\text{O}_5$ (green curve) aqueous batteries at 1 C in the 1.6–0.8 V voltage range.

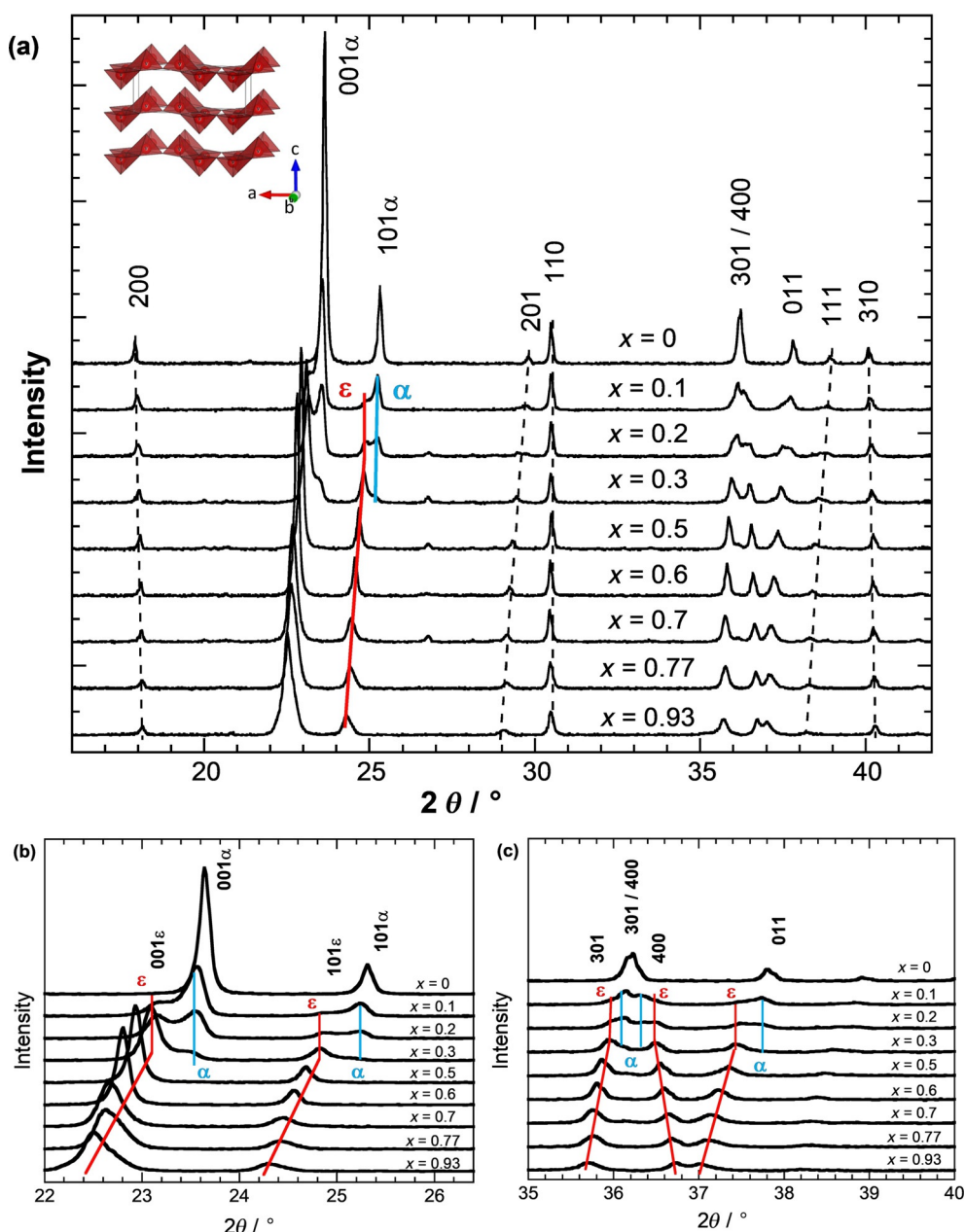


Figure 3. a) XRD patterns of reduced V_2O_5 electrodes for $0 \leq x \leq 0.93$. Zooms in the b) $22\text{--}26.4^\circ$ and c) $35\text{--}40^\circ$ 2θ ranges. $\alpha\text{-Li}_x\text{V}_2\text{O}_5$ and $\epsilon\text{-Li}_x\text{V}_2\text{O}_5$ peak displacements during the first reduction process are shown schematically by blue and red lines, respectively.

The XRD patterns of electrodes discharged at C/5 as a function of the faradaic yield x expressed in Fmol^{-1} ($0 \leq x < 1$) are shown in Figure 3. A lower rate of C/20 was applied to reach the highest depth of discharge of 0.93. Before discharge, the pristine electrode exhibited the typical XRD pattern of V_2O_5 , which can be indexed in an orthorhombic cell (space group $Pmmn$) with the following unit cell parameters: $a = 11.49$, $b = 3.56$, $c = 4.36$ Å (PDF 00-041-1426). Sharp and intense diffraction peaks indicate a high degree of crystallization. The evolution of XRD patterns during the reduction process did not reveal strong modification because all diffraction peaks of V_2O_5 are retained. However, examination of the enlarged views in Figure 3 b,c reveals a significant shift towards smaller angles of

the 001, 101, 011, and 111 lines, whereas the 200, 400, and 310 reflections shift slightly towards larger angles (Figure 3 a–c). These trends indicate a decrease in the a parameter on discharging, that is, a contraction of the V–V distances in the V_2O_5 layers while, at the same time, the c parameter, that is, the interlayer distance, increases. In addition to these changes, progressive broadening of the diffraction peaks gives evidence for a disordering process throughout the reduction. For $x \leq 0.3$, the enlarged views (Figures 3 b,c) reveal a diphasic domain with two sets of 001, 101, 301, and 400 lines. The unit-cell parameters reported in Figure 4 confirm the coexistence of the $\alpha\text{-Li}_x\text{V}_2\text{O}_5$ phase ($a = 11.49$, $b = 3.56$, $c = 4.38$ Å) with a reduced phase ($a = 11.42$, $b = 3.57$, $c = 4.47$ Å) that can be assigned, con-

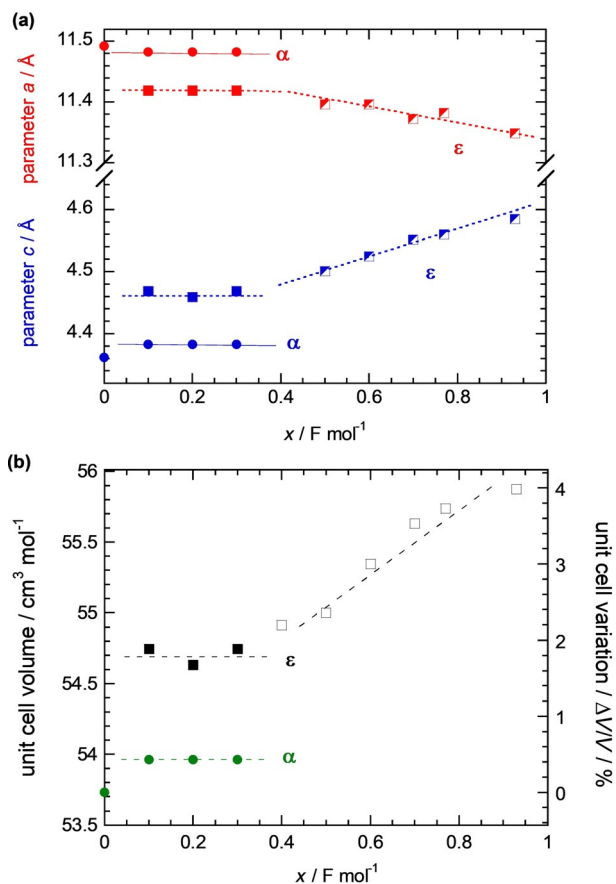


Figure 4. Evolution a) of the unit-cell parameters a (red) and c (blue) and b) of the unit-cell volume as a function of x for $0 \leq x \leq 0.93$ (circles and squares for α and ϵ phases, respectively).

sidering the cell-parameter values, to the lithiated $\epsilon\text{-Li}_{0.3}\text{V}_2\text{O}_5$ phase found in usual organic electrolytes.^[29] This assignment to a lithiated V_2O_5 phase is perfectly consistent with the involved redox process previously proposed. Indeed, in the $0 \leq x \leq 0.3$ composition domain, the potential remains higher than 1.05 V, at which only the lithium ions are likely to be inserted into the material. For $0.3 < x \leq 0.93$, a single set of diffraction lines is observed, corresponding to solid-solution behavior with a continuous contraction in a parameter and increase in c parameter to reach $a=11.35$ and $c=4.58$ Å for the fully discharged electrode ($x=0.93$). This corresponds to continuous lithium enrichment of $\epsilon\text{-Li}_x\text{V}_2\text{O}_5$ up to the composition $\epsilon\text{-Li}_{0.93}\text{V}_2\text{O}_5$. The unit-cell parameters found for $\epsilon\text{-Li}_{0.93}\text{V}_2\text{O}_5$ are in good accord with those previously reported for $\epsilon\text{-Li}_{0.95}\text{V}_2\text{O}_5$.^[31] At this point, several findings are noteworthy: 1) the b parameter remains largely constant ($b=3.56\text{--}3.57$ Å); 2) the composition range observed for the α - ϵ diphasic region matches that reported for nonaqueous electrolytes;^[30,32] 3) the single-phase $\epsilon\text{-Li}_x\text{V}_2\text{O}_5$ behavior strongly contrasts with the diphasic $\epsilon\text{-Li}_{0.5}\text{V}_2\text{O}_5/\delta\text{-LiV}_2\text{O}_5$ region usually reported in organic electrolytes.^[30,32] In the present case, the structural impact of the reduction process leads to a very

moderate increase in the unit-cell volume that does not exceed 4% (Figure 4b). This small magnitude of variations rules out any hypothesis of water insertion, and the insertion reaction of lithium ions is highlighted. However, at this stage of the study, possible involvement of a few Zn^{2+} ions to explain the peculiar structural response of V_2O_5 on discharging cannot be definitively excluded.

Raman spectroscopy was used to investigate the structural impact of the reduction at the scale of the chemical bond. Raman spectra obtained at different depths of discharge are shown in Figure 5. From a spectroscopic viewpoint, the point symmetry group of V_2O_5 crystal is D_{2h}^{13} , and the Raman spectrum of the pristine material exhibits the typical V_2O_5 fingerprint, consisting of ten peaks located at 105, 146, 199, 286, 305, 406, 483, 529, 703, and 994 cm^{-1} . Most of the low-wavenumber peaks can be assigned to external modes of V_2O_5 units. They are derived from relative motions of two V_2O_5 units belonging to the unit cell, three of which generate displacements of vanadium atoms along the x axis (199 cm^{-1}), y axis (146 cm^{-1}), and z axis (105 cm^{-1}). Internal modes, however, which are observed in the medium- and high-wavenumber regions, can be described in terms of V–O–V stretching modes. The band at 994 cm^{-1} is assigned to the V–O stretching vibration along the z axis, corresponding to the shortest V=O vanadyl bond oriented along the c axis. The V–O–V stretching modes along the x and y axes are observed at 529 and 703 cm^{-1} , respectively.^[30,31,33] For $x=0.1$, a new band at 982 cm^{-1} is observed in the region of V–O stretching vibrations, typical of the presence of V^{4+} ions. This band belongs to the Li-poor $\epsilon\text{-Li}_{0.5-0.6}\text{V}_2\text{O}_5$ phase that coexists with V_2O_5 in the $0.1 \leq x \leq 0.3$ composition domain and is pure for $x=0.5$. Indeed, the Raman spectrum recorded for $x=0.5$ exhibits the characteristic lines of $\epsilon\text{-Li}_{0.5-0.6}\text{V}_2\text{O}_5$ at 158, 475, 421, 536, 707, and 983 cm^{-1} .^[34] For $0.5 \leq x \leq 0.93$, further Li accommodation in the

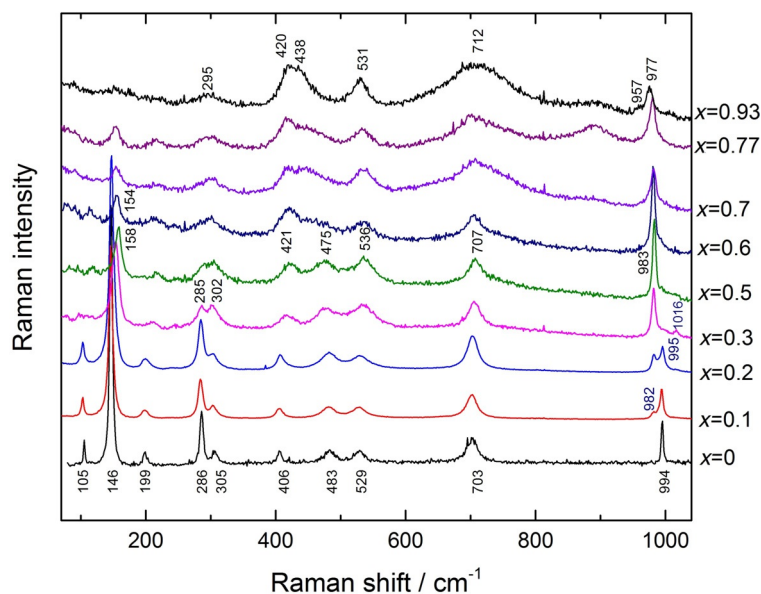


Figure 5. Series of Raman spectra collected on reduced V_2O_5 electrodes for $0 \leq x \leq 0.93$ during the first discharge.

ϵ phase induces a strong intensity decrease in the band at 158 cm^{-1} as well as progressive broadening and shifts of typical bands: 475 to 438, 707 to 712, 536 to 531, and 983 to 977 cm^{-1} . In addition, a new feature at 957 cm^{-1} can be detected for $x=0.93$. The Raman spectrum of the fully discharged electrode ($x=0.93$) matches that previously reported for the Li-rich $\epsilon\text{-LiV}_2\text{O}_5$ phase.^[28,33] It is noteworthy that the typical fingerprint of the $\delta\text{-LiV}_2\text{O}_5$ phase, characterized in particular by a sharp Raman band at 1008 cm^{-1} ,^[30,34] is not observed.

These findings are in good agreement with those deduced from the XRD study and outline a specific structural behavior in binary aqueous electrolytes. Indeed, both XRD and Raman investigations do not detect formation of the folded $\delta\text{-LiV}_2\text{O}_5$ phase in $\text{Li}^+/\text{Zn}^{2+}$ electrolyte. Therefore, minor participation of zinc ions must be considered, in accordance with EDS analysis giving approximately 0.02Zn per V_2O_5 , because the zinc-insertion reaction into V_2O_5 is reported to occur in the potential range of 0.9–1 V (Figure 2a). In this scenario, the inserted Zn^{2+} cations located between the oxide layers would act as pillar species, which hinder gliding of one layer over another in the b direction and lead to the corrugated δ -phase.

However, the stabilization of the architecture afforded by the presence of Zn^{2+} ions is not a mandatory condition for the δ -phase not to appear. Indeed, another example of mitigated structural changes was recently reported for nanosized V_2O_5 .^[35] In that case, it was demonstrated that the nanosize effect prevents the emergence of the distorted $\delta\text{-LiV}_2\text{O}_5$ phase to the benefit of a solid-solution behavior throughout the reduction process ($0 < x < 1$).^[35] Conversely, Dickens et al. claimed that $\delta\text{-LiV}_2\text{O}_5$ is formed as the final product of V_2O_5 reduction in an aqueous LiCl electrolyte but without the corresponding XRD pattern.^[36] To check whether zinc is responsible for the moderate structural changes of the V_2O_5 host lattice highlighted herein, a V_2O_5 electrode was deeply discharged at $x=0.9$ in a single-salt aqueous electrolyte ($3\text{ mol L}^{-1}\text{ Li}_2\text{SO}_4$). In this case, the corresponding XRD pattern (Figure 6a) and the Raman spectrum (Figure 6b) show unambiguously the formation of the $\delta\text{-LiV}_2\text{O}_5$ phase. Indeed, the XRD pattern exhibits two sets of peaks: those characteristic of $\epsilon\text{-LiV}_2\text{O}_5$, with parameters $a=$

11.38 , $b=3.57$, and $c=4.59\text{ \AA}$, and a second set ascribed to the $\delta\text{-LiV}_2\text{O}_5$ phase (orthorhombic cell, $Amam$ space group) with parameters $a=11.24$, $b=3.60$, and $c=9.90\text{ \AA}$ (JCPDS file 04-010-2882^[35]). Consequently, in the $\delta\text{-LiV}_2\text{O}_5$ phase, the interlayer distance corresponds to $c/2$, that is, 4.95 as opposed to 4.58 \AA for the present fully discharged compound $\epsilon\text{-Li}_{0.93}\text{V}_2\text{O}_5$ (Figure 4a).

Raman spectroscopy confirmed the formation of $\delta\text{-LiV}_2\text{O}_5$ at the atomic scale in Li_2SO_4 single-salt electrolyte. Indeed, the Raman spectrum (Figure 6b) exhibits the characteristic bands of the δ -phase at 91, 152, 180, 252, 289, 420, 433, 631, 670, and 1007 cm^{-1} ^[30,34] in a mixture with the Li-rich $\epsilon\text{-Li}_{0.93}\text{V}_2\text{O}_5$ phase (bands at 708, 958, and 978 cm^{-1}).

These findings together demonstrate that the V_2O_5 discharge process in the $\text{Li}_2\text{SO}_4\text{-ZnSO}_4$ binary electrolyte involves a lithiation mechanism that is likely associated with the co-insertion of a few Zn^{2+} ions. Zinc cations would act as pillar species preventing important structural changes usually observed at the end of the discharge in nonaqueous electrolyte, such as gliding of one oxide layer over another in the b direction.

Figure 7a shows the cycling performance of a $\text{V}_2\text{O}_5\text{-Zn}$ battery with binary electrolyte at 1C in the 1.6–0.8 V voltage window. An attractive capacity of 80 mAh g^{-1} is obtained in this narrow voltage range without any capacity fading over 300 cycles (inset in Figure 7a). In addition, the voltage profile is almost unaffected upon cycling. These results suggest excellent structural reversibility, high stability of the cathode material in the binary electrolyte, and no dissolution process. Figure 7b,c gives evidence for the high reversibility of the structural mechanism described above. Comparison of Raman spectra of the cathode material before cycling, after one cycle, and after 300 cycles at 1C clearly demonstrates total restoration of the host lattice at the atomic scale because the Raman spectra of cycled electrodes perfectly match that before cycling. Examination of the XRD patterns (Figure 7b) shows that the structure of the pristine material is fully recovered at the end of the first cycle. In addition, the symmetric charge profile associated with 100% coulombic efficiency leaves no doubt that the same electrochemical and structural mechanism is involved in

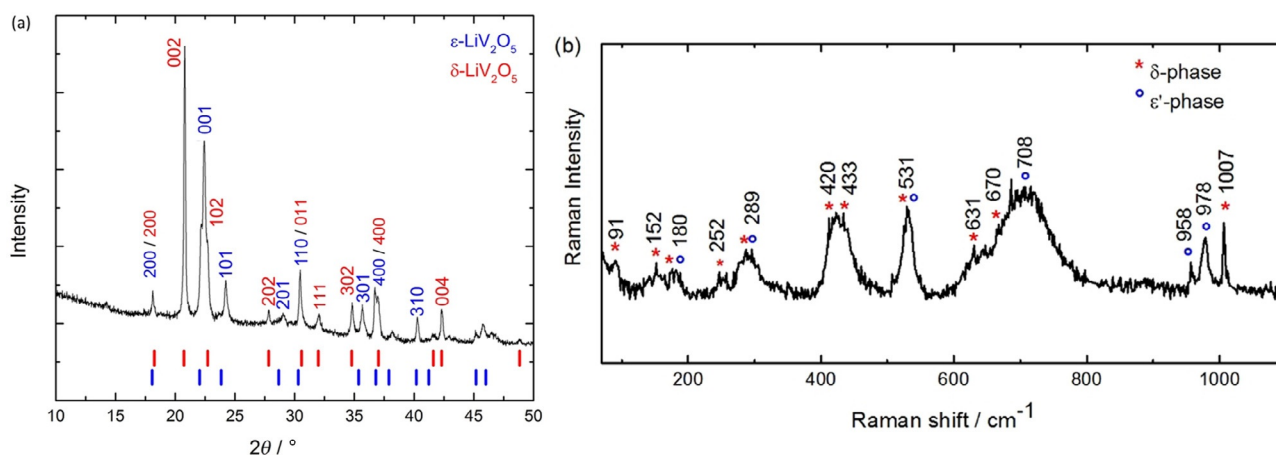


Figure 6. a) XRD pattern and b) Raman spectrum of a V_2O_5 electrode reduced in $3\text{ mol L}^{-1}\text{ Li}_2\text{SO}_4$ electrolyte. C/20 rate, cutoff voltage $E=0.8\text{ V}$ versus Zn/Zn^{2+} ($x=0.9\text{ F mol}^{-1}$).

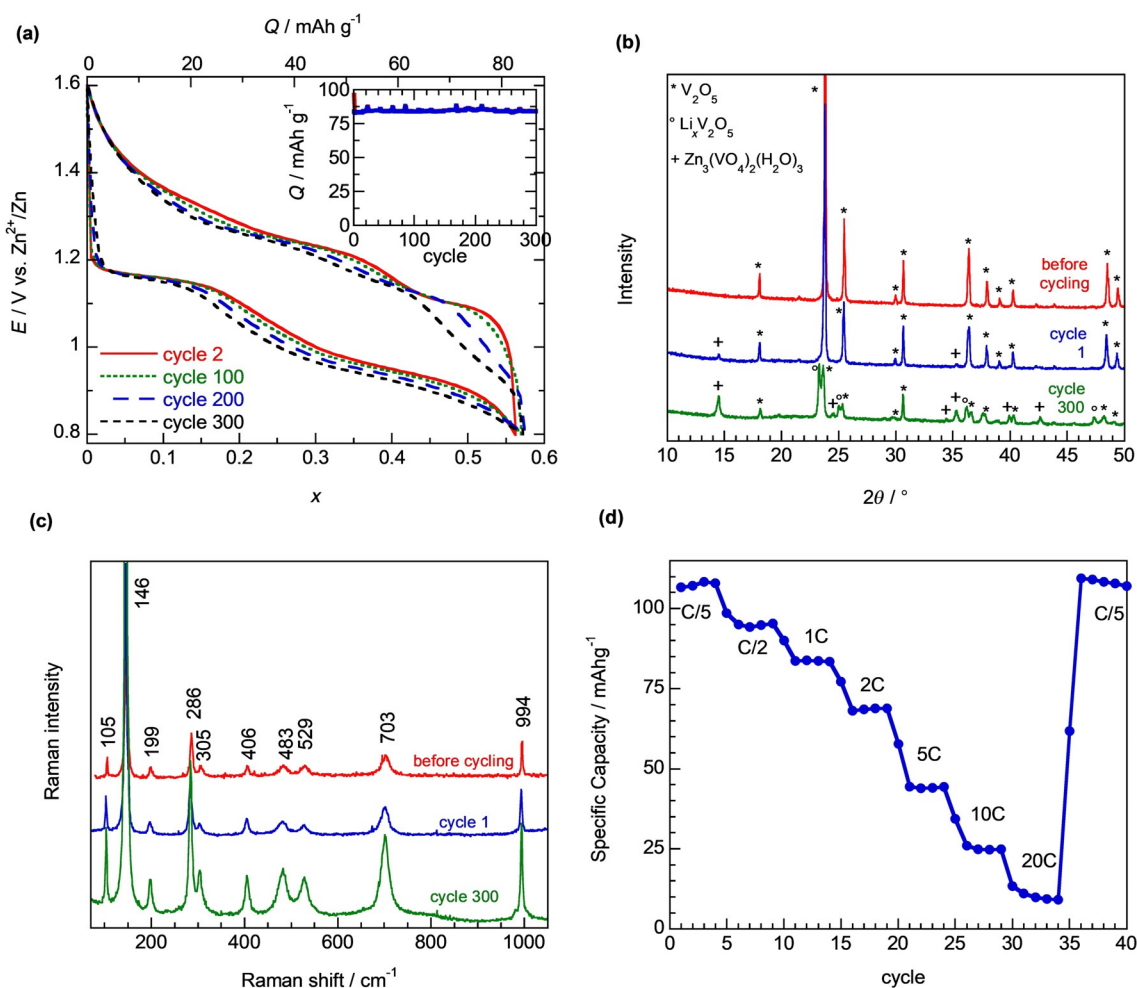


Figure 7. a) Cycling performance and long-term cycling stability (inset) of V_2O_5 in the $Zn/Li_2SO_4-ZnSO_4/V_2O_5$ aqueous battery at 1 C in the 1.6–0.8 V voltage range. b) XRD patterns and c) Raman spectra of the positive V_2O_5 electrode before cycling and after a complete cycle. d) Rate capability at various current densities.

discharge and charge. However, after 300 cycles, α - V_2O_5 is found to coexist with traces of ϵ - $Li_xV_2O_5$ and an additional $Zn_3(VO_4)_2(H_2O)_3$ phase (JCPDS 04-018-46-01).^[37] The cell parameters of the ϵ - $Li_xV_2O_5$ phase ($a=11.46$, $b=3.56$, $c=4.46$ Å) correspond to a low lithium content in the ϵ -phase (Figure 4a). This result proves that most of the lithium ions have been extracted from the interlayer spacing. In contrast, the structure of the $Zn_3(VO_4)_2(H_2O)_3$ phase does not correspond to an insertion compound to the vanadium oxide family. This result highlights that the mechanism occurring on cycling in the binary aqueous electrolyte is far from that described when single zinc salt is used, which leads to the formation of layered $Zn_xV_2O_5 \cdot nH_2O$,^[4, 27] nor is it that occurring in pure aqueous Li electrolyte, which involves the δ - LiV_2O_5 phase. Further work is required to examine in detail the reaction mechanism upon long-term cycling.

The rate capability of the system was also evaluated (Figure 7d). The specific capacity of $110\ mAh\ g^{-1}$ delivered by commercial V_2O_5 in a $Zn-V_2O_5$ hybrid battery at C/5 decreases to 95, 85, 70, 45, and 25 $mAh\ g^{-1}$ at C/2, 1C, 2C, 5C, and 10C respectively. However, after cycling at a high rate of 10 or 20C,

the initial capacity of $110\ mAh\ g^{-1}$ can be recovered at C/5 with no irreversible damage and excellent structural stability.

Conclusions

A Zn/V_2O_5 aqueous rechargeable battery with an Li^+/Zn^{2+} binary electrolyte at pH 4 has been reported. This cell exhibits highly reversible capacities of $136\ mAh\ g^{-1}$ at C/20 and $125\ mAh\ g^{-1}$ at C/5 in the 1.6–0.8 V range. In addition, outstanding stability of the rechargeable capacity is observed, with $80\ mAh\ g^{-1}$ available at 1C and 100% capacity retention over 300 cycles. The discharge–charge profile achieved in aqueous medium is similar to that observed for the analogous reaction in organic lithiated electrolyte. However, an original reversible insertion mechanism was revealed by XRD and Raman spectroscopy. Exclusive Li insertion into V_2O_5 occurs up to mid-discharge, but the co-insertion of a few zinc ions is likely involved in the second part of the reduction. Moderate expansion of the interlayer spacing and limited layer puckering point to much lower structural stress in the aqueous binary electrolyte. A pillaring effect of a few interlayer Zn^{2+} ions is

suggested, which hinders the formation of the distorted δ - LiV_2O_5 phase. The final discharge product corresponds unambiguously to the Li-rich ε - LiV_2O_5 phase, and the charge process ensures quantitative extraction of cations, leading back to the pristine host lattice. The high structural stability of V_2O_5 even after 300 cycles makes this hybrid $\text{Zn}/\text{V}_2\text{O}_5$ system promising in aqueous binary electrolytes. Moreover, a significant improvement in rate capability has already been evidenced using the same cathode material prepared by a nanosizing approach, which will be reported elsewhere.

Acknowledgements

One of the authors wishes to thank the Ministry of Education and Science of Kazakhstan (grant number AP05136016-ZRABS), French Embassy in Astana, Kazakhstan, and Campus France for financial support.

Conflict of interest

The authors declare no conflict of interest.

Keywords: aqueous zinc batteries • binary electrolytes • electrochemistry • reaction mechanisms • vanadium

- [1] J.-M. Tarascon, M. Armand, *Nature* **2001**, 414, 359–367.
- [2] H. Kim, J. Hong, K.-Y. Park, H. Kim, S.-W. Kim, K. Kang, *Chem. Rev.* **2014**, 114, 11788–11827.
- [3] A. Konarov, N. Voronina, J. H. Jo, Z. Bakenov, Y.-K. Sun, S.-T. Myung, *ACS Energy Lett.* **2018**, 3, 2620–2640.
- [4] D. Kundu, B. D. Adams, V. Duffort, S. H. Vajargah, L. F. Nazar, *Nat. Energy* **2016**, 1, 16119.
- [5] C. Xu, B. Li, H. Du, F. Kang, *Angew. Chem. Int. Ed.* **2012**, 51, 933–935; *Angew. Chem.* **2012**, 124, 957–959.
- [6] X. G. Zhang, *Corrosion and Electrochemistry of Zinc*, Springer Science & Business Media, New York, **2013**.
- [7] N. Zhang, F. Cheng, Y. Liu, Q. Zhao, K. Lei, C. Chen, X. Liu, J. Chen, *J. Am. Chem. Soc.* **2016**, 138, 12894–12901.
- [8] F. W. T. Goh, Z. Liu, T. S. A. Hor, J. Zhang, X. Ge, Y. Zong, A. Yu, W. Khoo, *J. Electrochem. Soc.* **2014**, 161, A2080–A2086.
- [9] H. Pan, Y. Shao, P. Yan, Y. Cheng, K. S. Han, Z. Nie, C. Wang, J. Yang, X. Li, P. Bhattacharya, *Nat. Energy* **2016**, 1, 16039.
- [10] J. Ming, J. Guo, C. Xia, W. Wang, H. N. Alshareef, *Mater. Sci. Eng. R* **2019**, 135, 58–84.
- [11] G. Fang, J. Zhou, A. Pan, S. Liang, *ACS Energy Lett.* **2018**, 3, 2480–2501.
- [12] M. Yan, P. He, Y. Chen, S. Wang, Q. Wei, K. Zhao, X. Xu, Q. An, Y. Shuang, Y. Shao, *Adv. Mater.* **2018**, 30, 1703725.
- [13] P. He, Y. Quan, X. Xu, M. Yan, W. Yang, Q. An, L. He, L. Mai, *Small* **2017**, 13, 1702551.
- [14] T. Wei, Q. Li, G. Yang, C. Wang, *Electrochim. Acta* **2018**, 287, 60–67.
- [15] F. Ming, H. Liang, Y. Lei, S. Kandambeth, M. Eddaoudi, H. N. Alshareef, *ACS Energy Lett.* **2018**, 3, 2602–2609.
- [16] B. Sambandam, V. Soundharajan, S. Kim, M. H. Alfaruqi, J. Jo, S. Kim, V. Mathew, Y. Sun, J. Kim, *J. Mater. Chem. A* **2018**, 6, 15530–15539.
- [17] C. Xia, J. Guo, P. Li, X. Zhang, H. N. Alshareef, *Angew. Chem. Int. Ed.* **2018**, 57, 3943–3948; *Angew. Chem.* **2018**, 130, 4007–4012.
- [18] V. Soundharajan, B. Sambandam, S. Kim, M. H. Alfaruqi, D. Y. Putro, J. Jo, S. Kim, V. Mathew, Y.-K. Sun, J. Kim, *Nano Lett.* **2018**, 18, 2402–2410.
- [19] Z. Peng, Q. Wei, S. Tan, P. He, W. Luo, Q. An, L. Mai, *Chem. Commun.* **2018**, 54, 4041–4044.
- [20] T. Wei, Q. Li, G. Yang, C. Wang, *J. Mater. Chem. A* **2018**, 6, 8006–8012.
- [21] B. Sambandam, V. Soundharajan, S. Kim, M. H. Alfaruqi, J. Jo, S. Kim, V. Mathew, Y. Sun, J. Kim, *J. Mater. Chem. A* **2018**, 6, 3850–3856.
- [22] G. Yang, T. Wei, C. Wang, *ACS Appl. Mater. Interfaces* **2018**, 10, 35079–35089.
- [23] B. Tang, G. Fang, J. Zhou, L. Wang, Y. Lei, C. Wang, T. Lin, Y. Tang, S. Liang, *Nano Energy* **2018**, 51, 579–587.
- [24] M. H. Alfaruqi, V. Mathew, J. Song, S. Kim, S. Islam, D. T. Pham, J. Jo, S. Kim, J. P. Baboo, Z. Xiu, *Chem. Mater.* **2017**, 29, 1684–1694.
- [25] P. Hu, M. Yan, T. Zhu, X. Wang, X. Wei, J. Li, L. Zhou, Z. Li, L. Chen, L. Mai, *ACS Appl. Mater. Interfaces* **2017**, 9, 42717–42722.
- [26] P. Hu, T. Zhu, J. Ma, C. Cai, G. Hu, X. Wang, Z. Liu, L. Zhou, L. Mai, *Chem. Commun.* **2019**, 55, 8486–8489.
- [27] N. Zhang, Y. Dong, M. Jia, X. Bian, Y. Wang, M. Qiu, J. Xu, Y. Liu, L. Jiao, F. Cheng, *ACS Energy Lett.* **2018**, 3, 1366–1372.
- [28] J. Zhou, L. Shan, Z. Wu, X. Guo, G. Fang, S. Liang, *Chem. Commun.* **2018**, 54, 4457–4460.
- [29] N. Yesibolati, N. Umirov, A. Koishybay, M. Omarova, I. Kurmanbayeva, Y. Zhang, Y. Zhao, Z. Bakenov, *Electrochim. Acta* **2015**, 152, 505–511.
- [30] R. Baddour-Hadjean, A. Marzouk, J. P. Pereira-Ramos, R. Baddour-Hadjean, A. Marzouk, J. P. Pereira-Ramos, *J. Raman Spectrosc.* **2012**, 43, 153–160.
- [31] R. Baddour-Hadjean, C. Navone, J. P. Pereira-Ramos, *Electrochim. Acta* **2009**, 54, 6674–6679.
- [32] C. Delmas, H. Cognac-Auradou, J. M. Cocciantelli, M. Menetrier, J. P. Doumerc, *Solid State Ionics* **1994**, 69, 257–264.
- [33] M. B. Smirnov, E. M. Roginskii, K. S. Smirnov, R. Baddour-Hadjean, J.-P. Pereira-Ramos, *Inorg. Chem.* **2018**, 57, 9190–9204.
- [34] R. Baddour-Hadjean, E. Raekelboom, J. P. Pereira-Ramos, *Chem. Mater.* **2006**, 18, 3548–3556.
- [35] D. Huo, A. Contreras, B. Laik, P. Bonnet, K. Guérin, D. Muller-Bouvet, C. Cenac-Morthe, R. Baddour-Hadjean, J. P. Pereira-Ramos, *Electrochim. Acta* **2017**, 245, 350–360.
- [36] P. G. Dickens, S. J. French, A. T. Hight, M. F. Pye, *Mater. Res. Bull.* **1979**, 14, 1295–1299.
- [37] D. A. Hoyos, A. Echavarría, C. Saldarriaga, *J. Mater. Sci.* **2001**, 36, 5515–5518.

Manuscript received: November 8, 2019

Revised manuscript received: December 2, 2019

Accepted manuscript online: December 4, 2019

Version of record online: January 21, 2020

4.3 Electrochemical and structural investigation of γ' -V₂O₅ in hybrid Li⁺/Zn²⁺ aqueous electrolyte for rechargeable aqueous Zn batteries Chapter 4.3

4.3.1 Introduction

In previous chapter, hybrid system Zn/ α -V₂O₅ in 4M ZnSO₄ + 3M Li₂SO₄ (pH=4) was reported with investigation of structural mechanisms upon discharge/charge process. The Zn / 3M Li₂SO₄ + 4M ZnSO₄ /V₂O₅ cell demonstrated capacity values about 136-125 mAh g⁻¹ at C/20-C/5 rates respectively at 0.8 – 1.6 V range. At 1C, a capacity of 80 mAh g⁻¹ is outstandingly stable over more than 300 cycles with a capacity retention of 100 %. A detailed structural study by XRD and Raman spectroscopy allows unravelling the peculiar response of the V₂O₅ layered host lattice. Strong similarities with the well-known structural changes reported in nonaqueous lithiated electrolytes are highlighted, although the emergence of the usual distorted δ -Li V₂O₅ phase is not detected upon discharge to 0.8 V. The pristine host structure is restored and maintained along cycling with mitigated structural changes leading to the high capacity retention. The present electrochemical and structural findings reveal a reaction mechanism mainly based on Li⁺ intercalation, however co-intercalation of a few Zn²⁺ ions cannot be completely dismissed. The presence of zinc cations between the oxide layers may act as pillars to stabilize the structure upon the cycling [1].

Besides stable α -V₂O₅ phase another metastable γ' -V₂O₅ polymorph exists [2], [3]. The puckered layers of γ' -V₂O₅ allow reversible Li insertion in higher voltage window (3.6/3.5 V vs. Li⁺/Li) than α -V₂O₅ (3.4/3.2 V vs. Li⁺/Li) (**Figure 1**). The layered structure of γ' -V₂O₅ consists of infinite ribbons made of VO₅ edge-sharing distorted pyramids leading larger interlayer spacing enables to accommodate large amount of guest cations (5.02 Å in γ' -V₂O₅ against 4.37 Å). Therefore, it attracts the current attention as cathode material for Li, Na-ion batteries in organic electrolyte [4], [5].

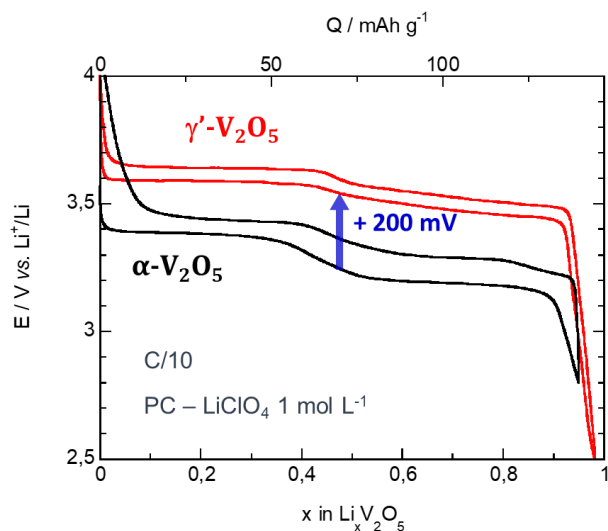


Figure 1. Discharge-charge curves of α - V_2O_5 and γ' - V_2O_5 in organic electrolyte at C/10

However, in spite of attractive structural features, γ' - V_2O_5 phase has been never studied in aqueous batteries with hybrid electrolyte. In this work, for the first time the electrochemical and structural investigations will be provided in $\text{Zn}/2.5\text{M Li}_2\text{SO}_4 + 3.5\text{M ZnSO}_4/\gamma'$ - V_2O_5 system (**Figure 2**).

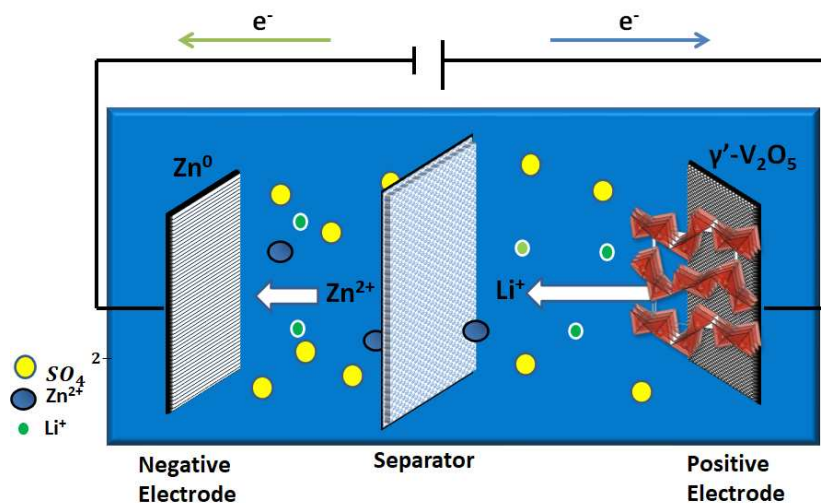


Figure 2. Schematic mechanism of $\text{Zn}/2.5\text{ M Li}_2\text{SO}_4 + 3.5\text{ M ZnSO}_4/\gamma'$ - V_2O_5 system

4.3.2 Synthesis

The synthesis of γ' - V_2O_5 *pol.* developed in the laboratory is already described in **Chapter 2**.

4.3.3 Structural characterization

The obtained powder after oxidation of γ -LiV₂O₅ has been examined by XRD and Raman spectroscopy. All the reflection lines in **Figure 3** can be indexed with expected orthorhombic symmetry of *Pnma* space group and calculated unit cell parameters using Bragg's law [$a=9.94$ Å, $b=3.58$ Å, $c=10.05$ Å] are in a good agreement with the literature [3]. Sharp and intense diffraction peaks illustrate high crystallization degree. The Rietveld refinement does not reveal the presence of impurity. (**Figure S1**)

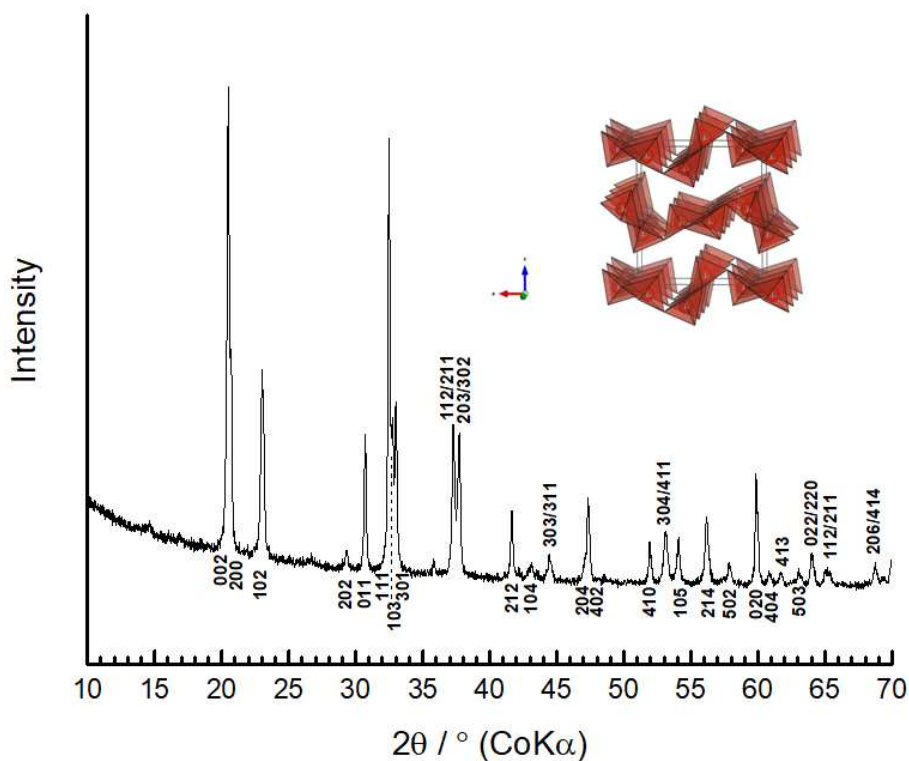


Figure 3. X-ray diffraction pattern of γ' -V₂O₅ powder

Table 1. The calculation of Peak position, interplanar spacing, *hkl* indexes, FWHM, Crystallite size from XRD data of γ' -V₂O₅

No.	Peak position		Interplanar spacing	Miller indices	FWHM	Crystallite size
	2 Theta (°)	Theta (°)				
1	20,493	10,246	5,028	002	0,23984	39,085
2	20,727	10,363	4,972	200	0,13165	71,232

3	23,036	11,518	4,479	102	0,29284	32,148
4	29,323	14,661	3,533	202	0,16776	56,838
5	30,711	15,355	3,377	011	0,18548	51,575
6	32,476	16,238	3,198	111	0,14759	65,099
7	32,668	16,334	3,180	103	0,61662	15,589
8	33,018	16,509	3,147	301	0,14349	67,052
9	35,803	17,901	2,909	210	0,00632	37,040
10	37,286	18,643	2,798	112/211	0,26262	37,071
11	37,700	18,850	2,768	203/302	0,2633	37,020
12	41,636	20,818	2,516	212	0,22336	44,184
13	47,335	23,667	2,228	402	0,27842	36,175
14	51,938	25,969	2,042	410	0,22971	44,668
15	53,123	26,561	2,000	304/411	0,33246	31,021
16	54,055	27,027	1,968	105	0,27272	37,972
17	56,174	28,087	1,899	214	0,30788	33,962
18	59,888	29,944	1,791	020	0,25538	41,686

The layered γ' -V₂O₅ structure consists of infinite ribbons with VO₅ edge-sharing distorted pyramids oriented alternatively up and down. The following ribbons are connected each other along the a-direction by one pyramid corner oxygen, which leads to formation of puckered layers located perpendicular to the c-axis. The average crystallite size of γ' -V₂O₅ is ~ 45 nm, which is calculated by the Sherrer equation ([see below](#)). The atomic positions and characteristic bond lengths of α -V₂O₅ are shown in **Table 2**.

The calculation of **crystallite size** and average crystallite size from XRD by using Sherrer equation ([see Table 1](#))

$$D = \frac{k\lambda}{\beta \cos\theta}$$

where, D = crystallite size (nm), $K = 0.9$ (Sherrer constant), $\lambda = 0.17889$ nm (wavelength of Co X-ray source), β = FWHM, θ = Peak position

Table 2. Atomic positions of γ' -V₂O₅ structure and V-O_x bond lengths of a square-based pyramid VO₅. ($y=0.25$ for all position)

Atoms	Wyckoff pos.	x	z	dv.o polyhedra	
V (Va)	4c	0.0713(2)	0.6018(2)	-	
V (Vb)	4c	0.3763(2)	0.5156(2)	-	
O (O1a)	4c	0.5005(6)	0.7597(6)	1.587 Å	<i>V_a-O_{1a} vanadyl bond</i>
O (O1b)	4c	0.2919(6)	0.3828(7)	1.545 Å	<i>V_b-O_{1b} vanadyl bond</i>
O (O2a)	4c	0.4368(6)	0.0418(6)	1.894 Å 1.972 Å	<i>x2, V_a-O_{2a} along b axis x1, V_a-O_{2a}</i>
O (O2b)	4c	0.5706(6)	0.4645(7)	1.890 Å 1.985 Å	<i>V_b-O_{2b} along b axis x1, V_a-O_{2a}</i>
O (O3)	4c	0.2427(7)	0.6405(7)	1.846 Å 1.731 Å	<i>V_a-O₃ bridge link V_b-O₃ bridge link</i>

The Raman spectrum of γ' -V₂O₅ fully agrees with reported work [3] is shown in **Figure 4**. All vibrations of the chains can be identified: bands at 1037, 1021 and 1003 cm⁻¹ correspond to the shortest V_a-O_{1a} and V_b-O_{1b} stretching bonds, bands at 752 and 603 cm⁻¹ related to the bond stretching vibrations localized within the V_a-O₃-V_b bridges, additionally V_a-O_{2a}-V_a and V_b-O_{2b}-V_b forming the rails of ladders at 722 and 694 cm⁻¹. Band observed at 532 and 500 cm⁻¹ correspond to the V_a-O_{2a} and V_b-O_{2b} ladder step bonds. The lower frequency modes at 92, 126, 138, 153, 171, 190, 238, 266, 282, 299, 349, 390 cm⁻¹ are corresponded to the complex distortions of V₂O₅ ladders. Raman vibration and assignments have shown in **Table 3**.

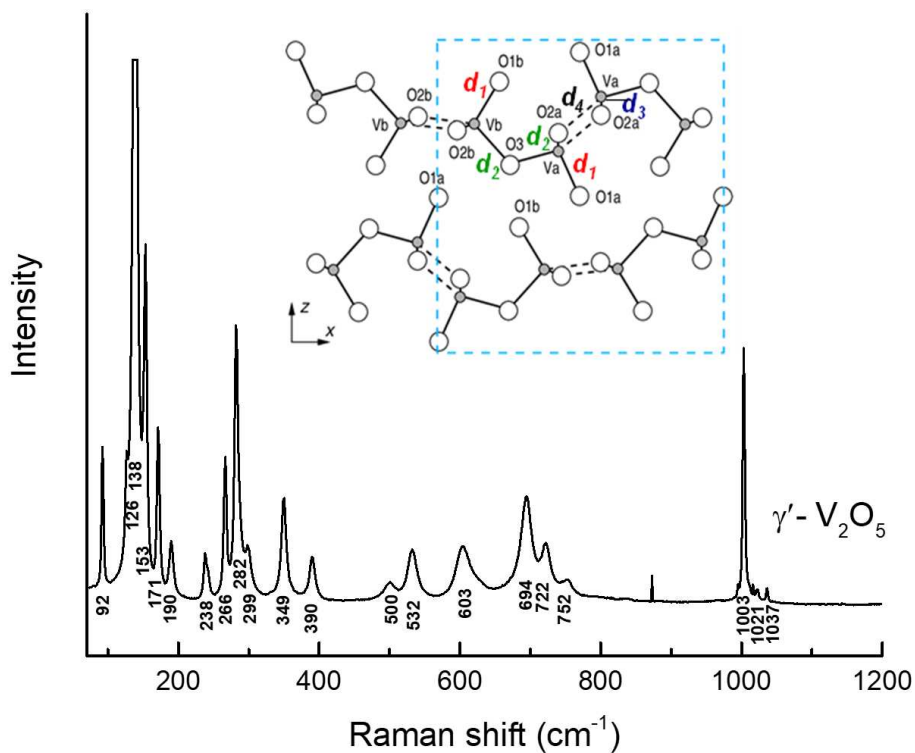


Figure 4. Raman spectrum and local structure (inset) of γ' - V_2O_5 powder

The **Figure 5** demonstrates the morphology of synthesized powder by scanning electron microscopy (SEM). It reveals that obtained product consists of agglomerated particles with uniform size. The average particles size is around 200~500 nm. The high sharp intensity from XRD indicates the good crystallinity of the γ' - V_2O_5 powder.

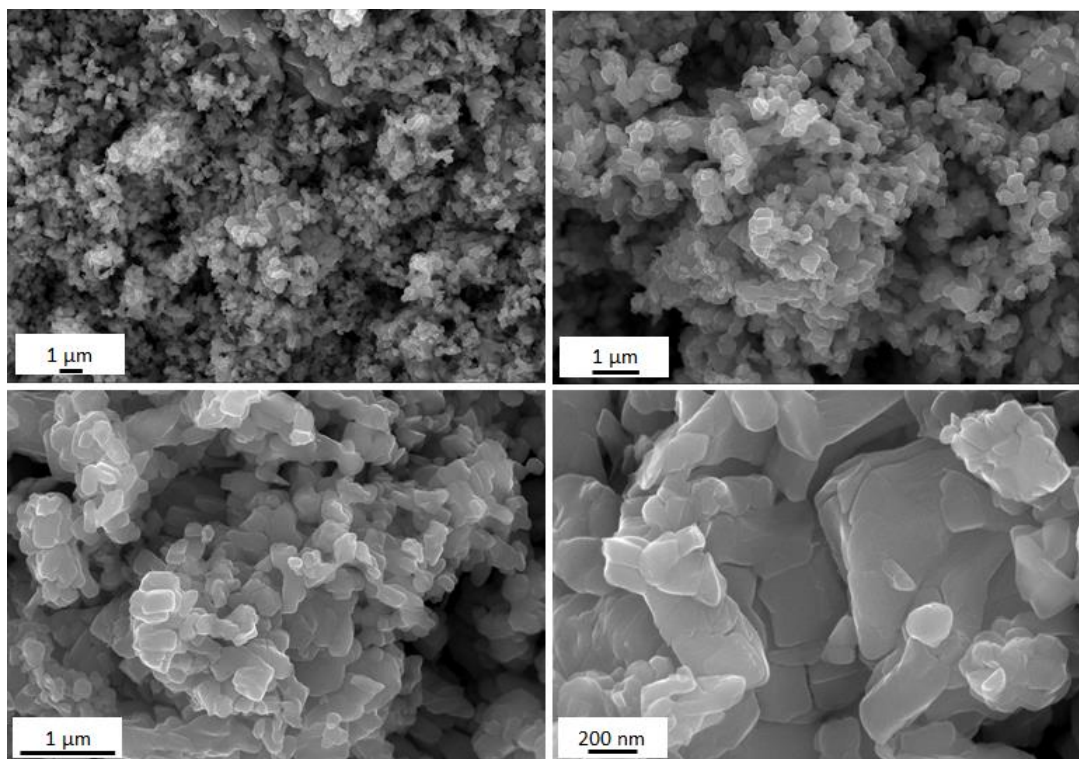


Figure 5. SEM micrographs of γ' -V₂O₅ powder at different magnifications.

4.3.4 Electrochemical study in the 1.6-1V voltage range

CV was performed to determine the optimal battery voltage window with scanning rate of 0.2 mV s⁻¹. From CV experiments, the lithium insertion/extraction is seen to be characterized by two separate reversible processes with two well-defined cathodic peaks located at 1.32 V and 1.22 V and two anodic peaks at 1.31 V and 1.46 V (**Figure 6a**). During the reduction, the sharp peak at 1.32V is related to the two-phase behavior ($0 \leq x < 0.4$), while the relatively broad peak at 1.22V indicates the lithiation process corresponds to a single-phase region ($0.4 \leq x \leq 1$). The intensities of peaks are nearly same showing the reversibility of γ' -V₂O₅ as shown from 1 cycle at C/5 (**Figure 6b**). The two well-defined plateaus during discharge/charge, assume that lithium ions are inserted into the structure, which are in good agreement with previously reported works on Li/ γ' -V₂O₅ system in organic electrolyte [4], [6]–[8]. Additional peaks were not detected, indicating no side reactions (H₂ or O₂ evolution) or zinc (Zn²⁺) co-insertion. However, upon cycling, from cyclic voltammetry curves it can be seen that the intensity of peaks is rapidly reduced, which can be related to the dissolution of active material. The CV results were confirmed by discharge/charge cycling at C/5.

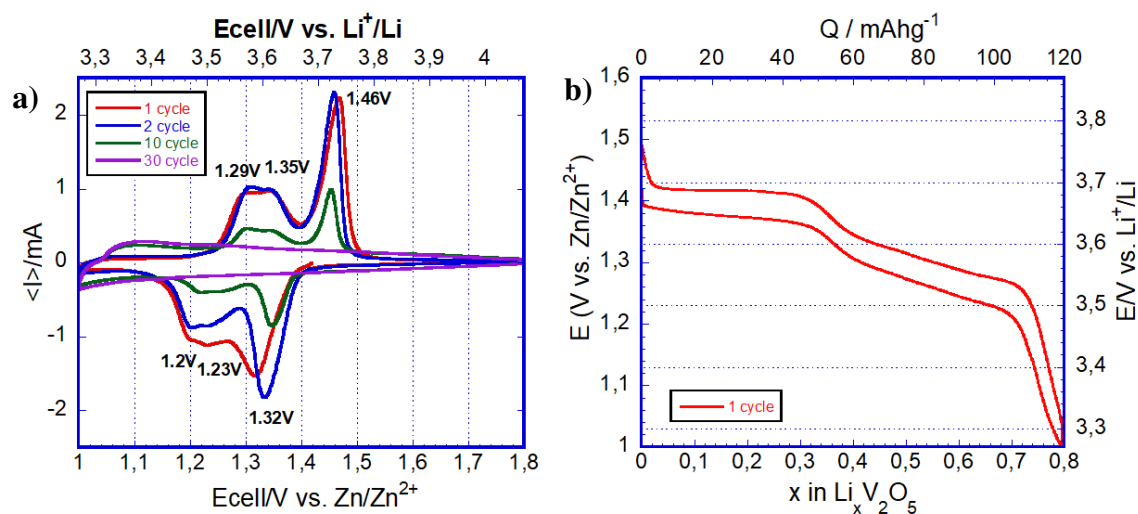


Figure 6. (a) Cyclic voltammogram at 0.2 mV s $^{-1}$ and (b) initial cycle of Zn/Li₂SO₄-ZnSO₄/γ'-V₂O₅ system at C/5 rate

The discharge-charge profile of γ'-V₂O₅ at C/5 rate is illustrated in **Figure 7**. From discharge curve two plateaus can be observed at 1.38 V (Step I) and 1.27 V (Step II) involving faradic yield of 0.8 F mol $^{-1}$ and consistent with the two major peaks in the cyclic voltammogram of the cell. **Figure 7** indicates the discharge and charge capacity reaches 120 mAh g $^{-1}$, and illustrates the reversibility of lithium insertion/extraction process. However, the discharge capacities decreases with cycles and exhibit only 60 mAh g $^{-1}$ and 40 mAh g $^{-1}$ after 10 and 100 cycles, respectively.

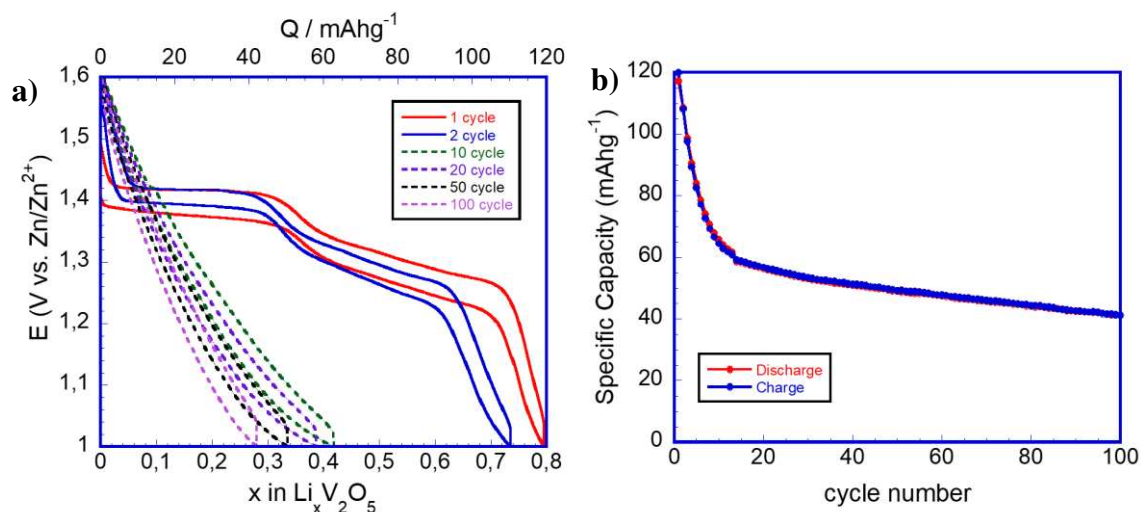


Figure 7. (a) Discharge/charge curves and (b) cyclability of Zn/Li₂SO₄-ZnSO₄/γ'-V₂O₅ system at C/5 rate

To grasp insights into the structural modifications associated to electrochemical lithium insertion and extraction mechanisms in γ' -V₂O₅ structure, ex-situ XRD and Raman spectroscopy experiments have been performed during the first discharge and further cycles.

4.3.5 Structural investigation upon discharge-charge

The XRD patterns of electrodes during the first discharge at C/5 (**Figure 8**) as a function of faradic yield x in F mol⁻¹ ($0 \leq x < 1$) are shown in **Figure 9**. Before discharge, the pristine electrode shows typical fingerprint of γ' -V₂O₅ of orthorhombic system (*Pnma* space group) with following unit cell parameters: $a=9.94$ Å, $b=3.58$ Å, $c=10.043$ Å.

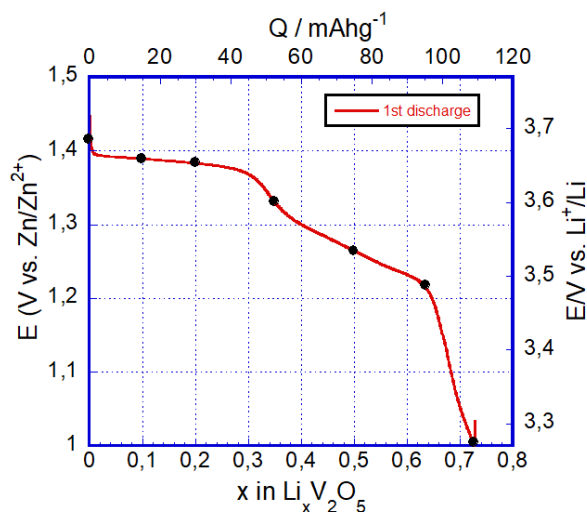


Figure 8. The first discharge of Zn/ γ' -V₂O₅ system at C/5

For the early Li content $x=0.1$, several new *hkl* lines can be observed at 20°, 22.5°, 32.5°, which coexist with initial lithium free γ' -V₂O₅ material. The new set of lines are indexed as orthorhombic system (*Pnma* space group) which belongs to lithiated γ -LiV₂O₅ phase. The unit cell parameters shown in **Figure 10** confirm the coexistence of γ' -V₂O₅ phase [$a=9.94$ Å, $b=3.58$ Å, $c=10.04$ Å] and reduced γ -Li_{0.1}V₂O₅ phase [$a=9.83$ Å, $b=3.59$ Å, $c=10.34$ Å] considered as usual in organic electrolyte system [4].

In the $0.1 \leq x < 0.35$ composition range, the main *hkl* lines of the pristine structure progressively decreases to the benefit of the new lines and completely disappeared for $x=0.35$ with strong shift 002 reflection line. The position at 19.6° instead of 20.5° indicates the increase of interlayer distance, i.e. c parameter (10.3 Å against 10.0 Å of γ' -V₂O₅). This indicates the existence of a diphasic domain.

In the $0.35 \leq x \leq 0.72$ composition range, the diffraction patterns are indexed related to the single orthorhombic lithiated phase of $Pnma$ space group. As shown in **Figure 9**, the shift of the most reflections are observed. These phenomena are typical for solid solution behavior with continuous decreasing of a parameter and increasing of c parameter with progressive enrichment of lithium from $\gamma\text{-Li}_{0.35}\text{V}_2\text{O}_5$ to $\gamma\text{-Li}_{0.72}\text{V}_2\text{O}_5$ composition. The unit cell parameters for $\gamma\text{-Li}_{0.72}\text{V}_2\text{O}_5$ [$a=9.69$ Å, $b=3.60$ Å, $c=10.67$ Å] match with previously reported works in non- aqueous lithium electrolytes[4], [9]–[11]. The obtained results refute the insertion of water molecules into host lattice. The detailed evolution of lattice parameters as a function of x in $\gamma\text{-Li}_x\text{V}_2\text{O}_5$ during first discharge ($0 \leq x \leq 0.72$) is shown in **Figure 10**.

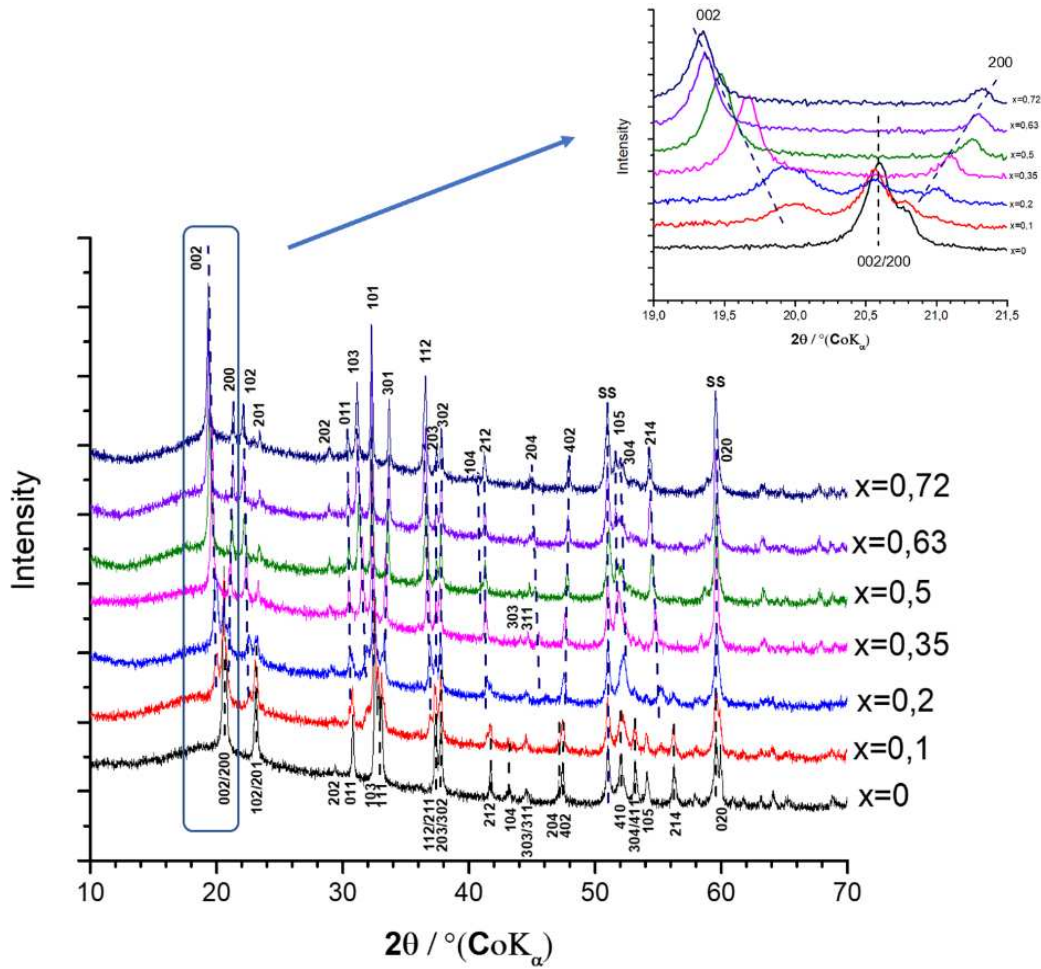


Figure 9. X-ray diffraction pattern of reduced γ' - V_2O_5 electrodes for $0 \leq x \leq 0.72$ at C/5 rate

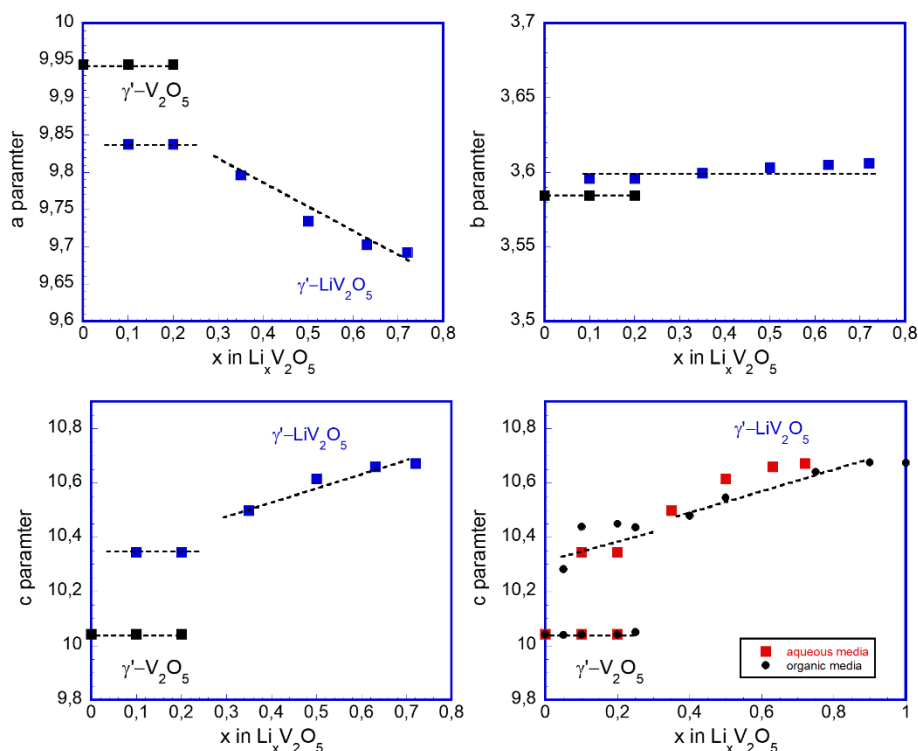


Figure 10. Evolution of the unit cell parameters a , b , c and unit cell volume as a function of x in reduced γ' - V_2O_5 electrodes for $0 \leq x \leq 0.72$ at C/5 rate and comparison with organic medium

Raman spectroscopy experiments of reduced γ' - V_2O_5 $0 \leq x \leq 0.72$ are illustrated on **Figure 11**. During the lithium insertion following modifications appears:

For $x=0.1$, the typical fingerprint of γ' - V_2O_5 is observed, while slight shift of the bands to lower wavenumber are detected: 349 to 343 cm^{-1} , 390 to 380 cm^{-1} , 1002 to 993 cm^{-1} . In addition, new bands arise at 990 and 1017 cm^{-1} . (blue dashed)

From $x=0.2$, new bands not related to the γ' - V_2O_5 appear at 272 , 300 , 340 , 462 and 642 cm^{-1} .

Up to $x=0.35$ these bands become more intense compare to the bands at 138 , 153 , 171 , 266 , 282 , 299 , 349 , 532 , 694 , and 722 cm^{-1} , only several bands remain until this composition located at 138 , 171 , 1015 cm^{-1} .

For $x=0.5$, no vibrational band corresponding to the initial γ' - V_2O_5 phase detected. The bands at 299 and 349 cm^{-1} disappeared and new band at 331 cm^{-1} appeared. The band at 722 cm^{-1} shifted to 727 cm^{-1} .

For $x=0.63$, new vibration bands at 101 , 171 , 272 , 462 , 531 , 642 , 990 and 966 cm^{-1} are largely dominating without any progressive change until final composition $x=0.72$. The Raman fingerprint matches to the previously reported works in organic system[4].

The evolution of Raman spectra provides complimentary picture of phase diagram obtained from XRD measurements. For $0.1 \leq x \leq 0.35$ a diphasic domain is well identified due to the presence of γ' - V_2O_5 and $\gamma\text{-Li}_{0.35}\text{V}_2\text{O}_5$. For $0.35 < x \leq 0.72$ only the fingerprint of $\gamma\text{-Li}_x\text{V}_2\text{O}_5$ is observed showing the existence of a solid solution region.

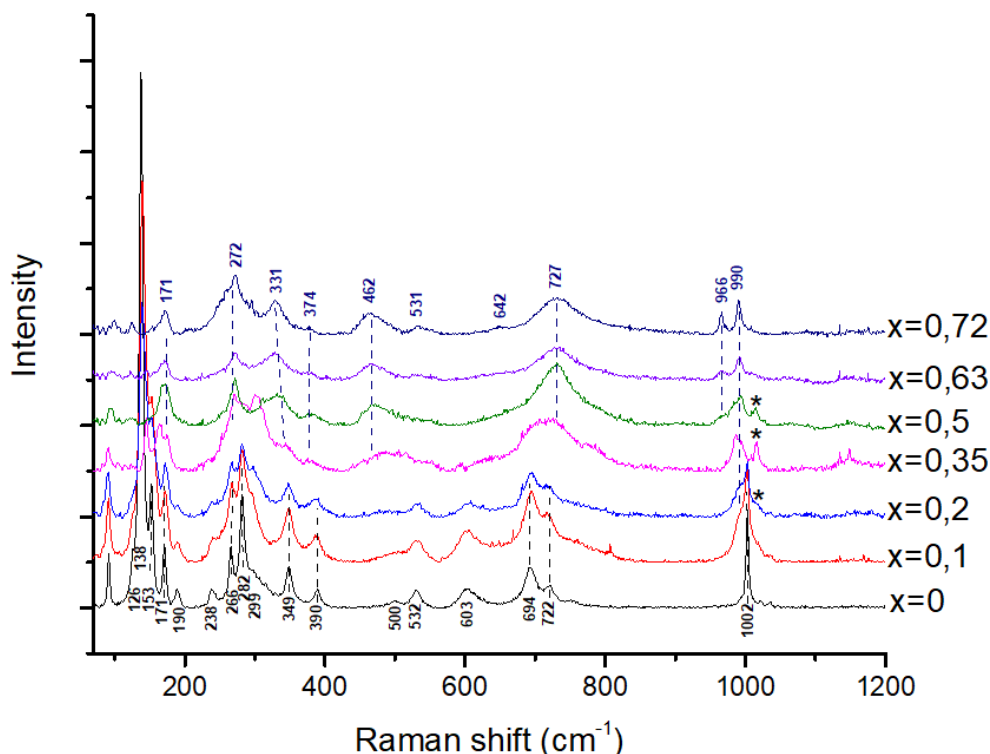


Figure 11. Raman spectra of reduced γ' - V_2O_5 for $0 \leq x \leq 0.72$ at C/5 rate

According to the obtained results from Ex-situ XRD and Raman spectroscopy measurements, it was found that during discharge-charge Li^+ intercalate/deintercalate from γ' - V_2O_5 structure. The evolution of unit cell parameters during first discharge illustrated strong similarities with previous data obtained in organic electrolyte (**Figure 10**). These findings can exclude the possible co-insertion of Zn^{2+} , H^+ or water molecules.

In addition, the structural reversibility of the γ' - V_2O_5 material was examined after 1 cycle. The Ex-situ XRD pattern and Raman spectrum of charged electrode in potential range 1-1.6V at C/5 is shown in **Figure 12**. The obtained results correspond to the initial γ' - V_2O_5 , demonstrating the complete Li insertion/extraction from the γ' - V_2O_5 structure.

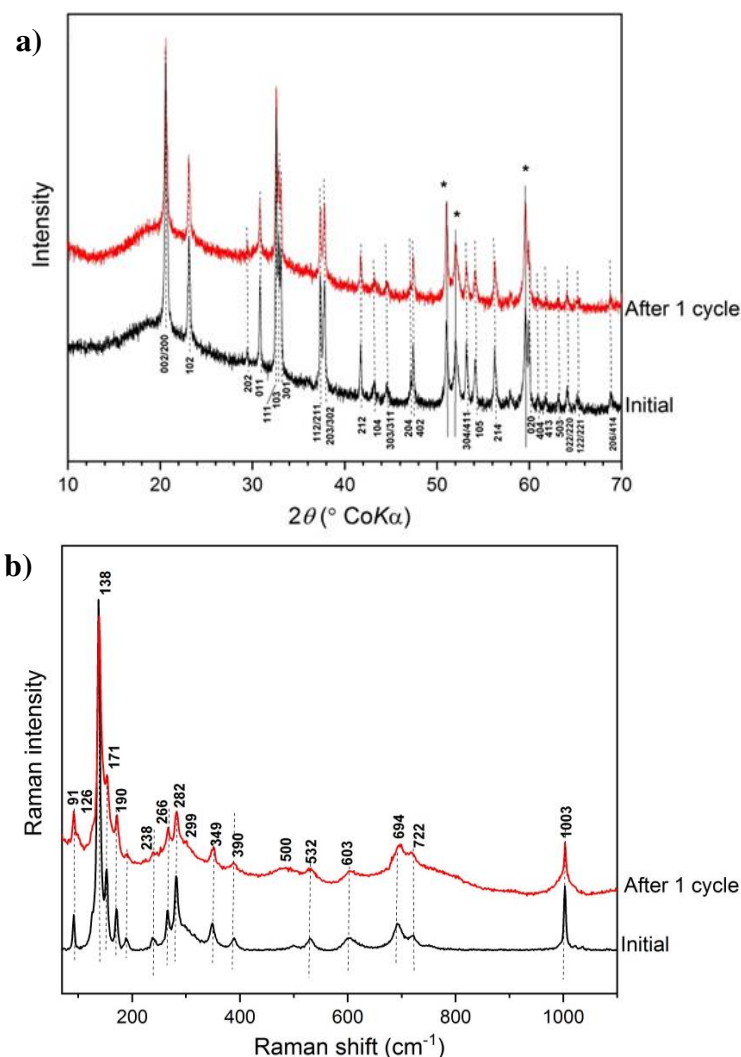
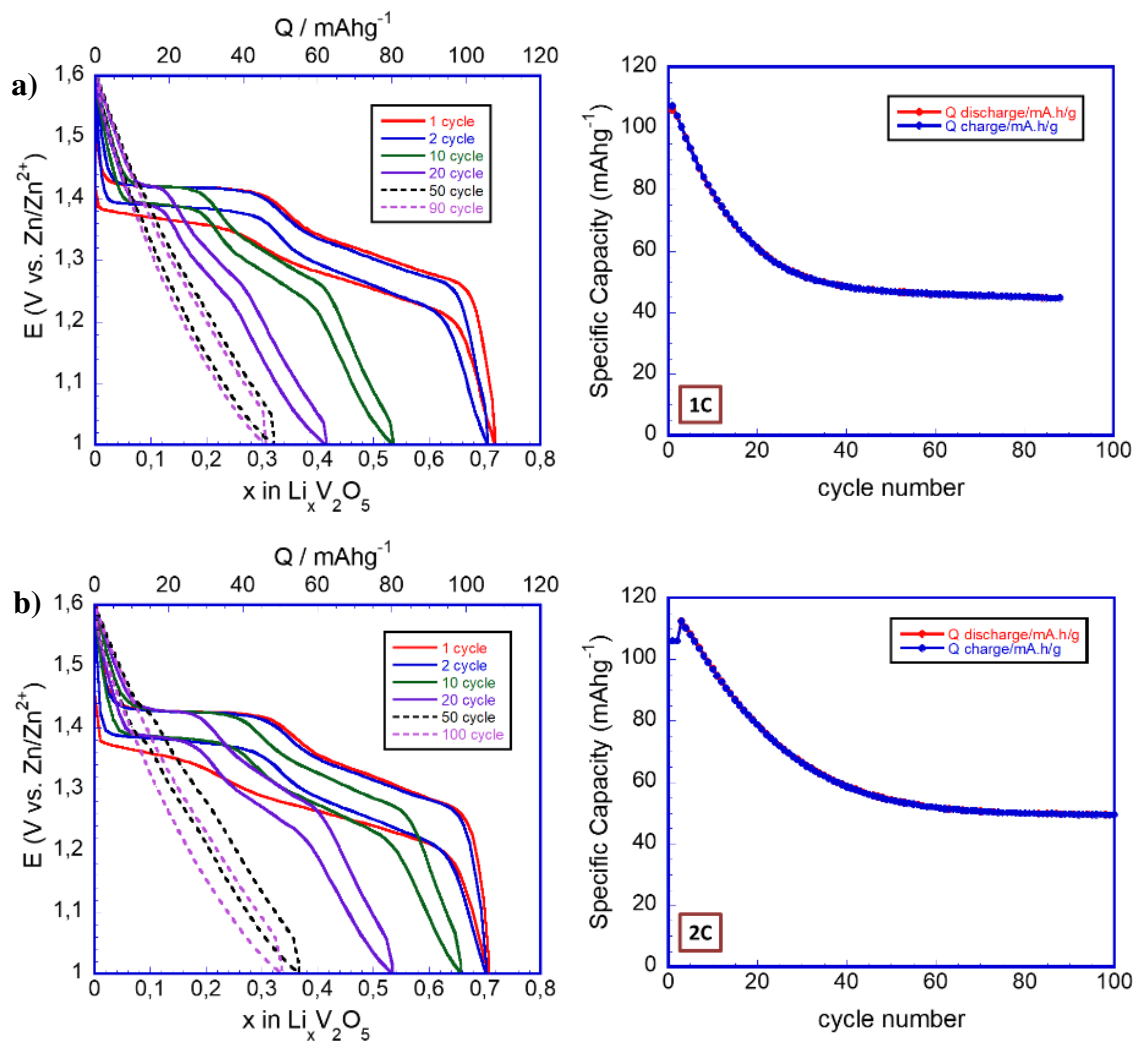


Figure 12. Ex-situ (a) XRD and (b) Raman for Zn/ γ' -V₂O₅ after 1 cycle at C/5 in potential range of 1-1.6V

4.3.6 Cycling properties in the 1.6-1V

Figure 13 shows the rate-capability of Zn/Li₂SO₄-ZnSO₄/ γ' -V₂O₅ system (1C, 2C, 5C). The first discharge capacity reaches ~114 mAh g⁻¹ at 1C (**Figure 13a**) and 2C (**Figure 13b**) and ~100 mAh g⁻¹ at 5C (**Figure 13c**) and the typical two working plateaus located at 1.38V and 1.27V are maintained at initial cycles. The polarization is slightly increased from ~40 mV to ~100 mV at lower C-rates (1C-2C) and 5C, respectively. The cyclability shows that C-rate has no effect on specific capacity. The rapid capacity loss (from 114 to 50 mAh g⁻¹) can be explained by dissolution of active material in electrolyte. Hence, the fastest capacity fading occurs at low C-rate, due to the longer time for each cycle. On the contrary, high C-rates favors relatively slow vanadium dissolution, resulting in better cycle performance. In order to check the dissolution of active

material, γ' -V₂O₅ electrode was kept in 3.5M ZnSO₄+2.5M Li₂SO₄ electrolyte for two weeks. As seen from **Figure S2**, the initial electrolyte with γ' -V₂O₅ electrode was colorless, after 1 day it becomes light green and after two weeks the color becomes greener which reveals the dissolution of active material. After two weeks stored in electrolyte, γ' -V₂O₅ electrode was assembled by using two-electrode split cell and galvanostatically studied at C/5. The assembled cell exhibits a very low initial discharge capacity of 58 mAh g⁻¹ and reaches 55 mAh g⁻¹ after 10 cycles (**Figure S3**). The typical two working plateaus at 1.38 and 1.27V were no more observed, demonstrating the amorphization of active material (material dissolution).



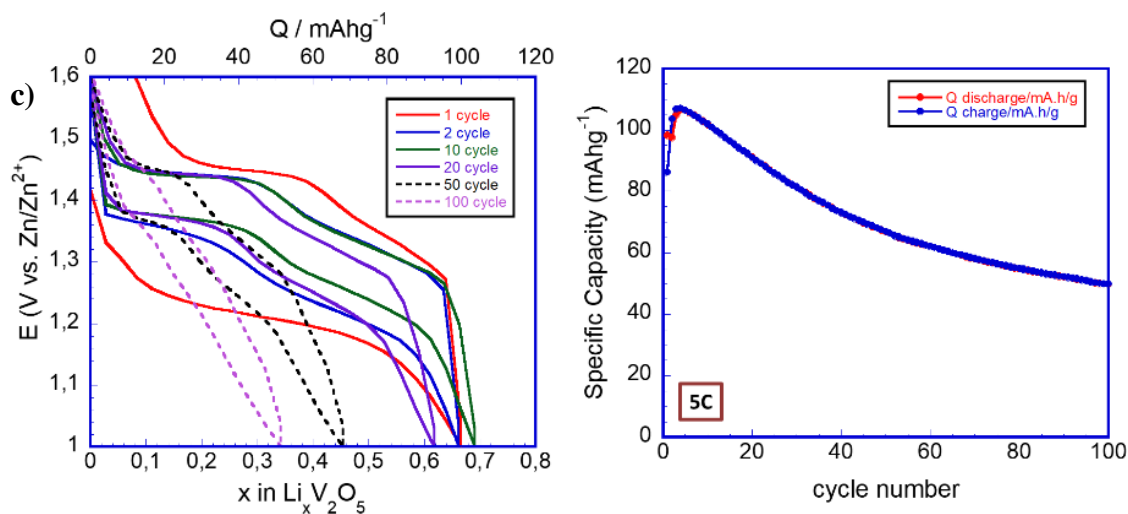


Figure 13. Discharge-charge and cyclability of Zn/Li₂SO₄-ZnSO₄/γ'-V₂O₅ system at (a) 1C, (b) 2 C and (c) 5C.

An ex-situ XRD study was carried out to investigate γ'-V₂O₅ electrodes after 100 cycles at different C-rates. The corresponding XRD pattern after 1 cycle demonstrates the total reversibility of the structure without any peak shift. The unit cell parameters are $a=9.94 \text{ \AA}$, $b=3.58 \text{ \AA}$, $c=10.04 \text{ \AA}$ (**Figure 14**). As seen from **Figure 14**, the characteristic peaks of γ'-V₂O₅ can be observed for a sample cycled at 5C with lower intensity of peaks in comparison to the sample after 1 cycle. For samples cycled at 1C and 2C most of the peaks of γ'-V₂O₅ completely disappeared resulting from a dissolution of active material.

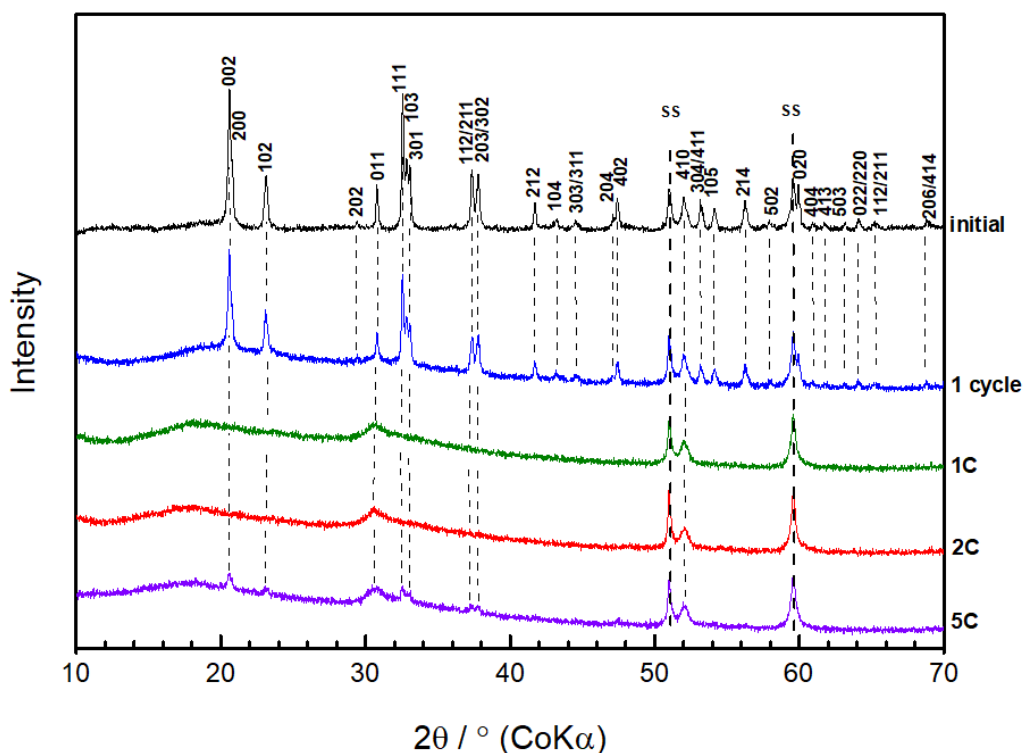


Figure 14. Ex-situ XRD of γ' -V₂O₅ electrodes cycled at different C-rate.

4.3.7 Optimization of the specific capacity

According to the literature review on hybrid electrolyte, the α -V₂O₅ material was investigated in the wide voltage range (0.2 – 1.6V) using “water-in-salt” electrolyte with discharge capacity of 215 mAh g⁻¹ at current density of 100 mA g⁻¹. [12]

In order to increase the specific capacity of γ' -V₂O₅, the Zn/Li₂SO₄-ZnSO₄/ γ' -V₂O₅ system was investigated in the extended voltage range (0.7 – 1.6V) by decreasing the lower cutoff voltage from 1V to 0.7V.

As described above, in narrow voltage range, lithium intercalation/deintercalation process occurs, however with rapid capacity fading resulting in active material loss (dissolution of vanadium) after 29 cycles (**Figure 15**). However, by enlarging the voltage range an additional reduction/oxidation process can be observed from cyclic voltammetry curve with a simplified shape: one very broad cathodic peak observed at 0.8V during reduction and one corresponding anodic peak at 1V during oxidation. This redox peak could suggest the co-insertion of Zn²⁺ ions as reported by *Hu et al.* [12], therefore some experiments we performed in pure Zn²⁺ electrolyte.

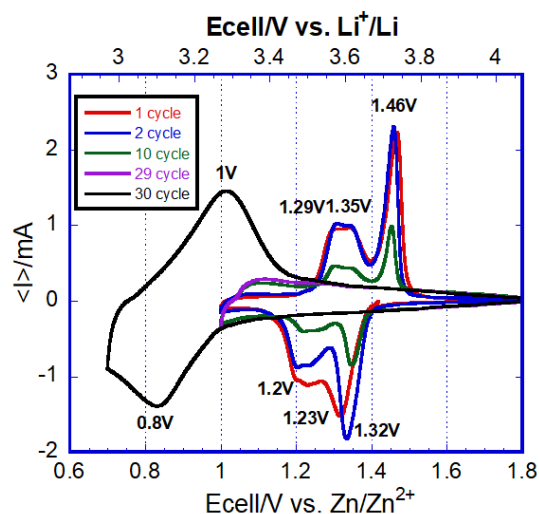


Figure 15. CV of Zn/Li₂SO₄-ZnSO₄/γ'-V₂O₅ system at 0.2 mV s⁻¹ in voltage range of 0.7-1.8V

Figure 16 shows the discharge/charge cycles of Zn/ γ'-V₂O₅ system at 1C in 0.7-1.6V voltage range. From initial cycles the typical two working plateaus located at 1.37V and 1.27V can be observed. The initial discharge capacity of the Zn/ γ'-V₂O₅ system gains ~144 mAh g⁻¹ with total faradic yield of 0.96 F mol⁻¹. An additional step can be seen at ~0.9V with contribution of ~0.13 F mol⁻¹ for the first two cycles. After 4 cycles the capacity increases from 144 mAh g⁻¹ to 186 mAh g⁻¹). The contribution of new step at lower voltage (~0.9V) increases from 0.13 F mol⁻¹ to 0.65 F mol⁻¹ (4th cycle). In the same time the two working plateaus disappear in first 10 cycles with the complete change in discharge/charge profile. This phenomenon can be explained by a phase transformation and activation of new phases upon cycling. The further lithiation at wide voltage range is expected to appear around 1V lower than high voltage steps (**Figure S5**), i.e., around 0.4V. This indicates a possible Zn²⁺/H₂O insertion into γ'-V₂O₅ structure.

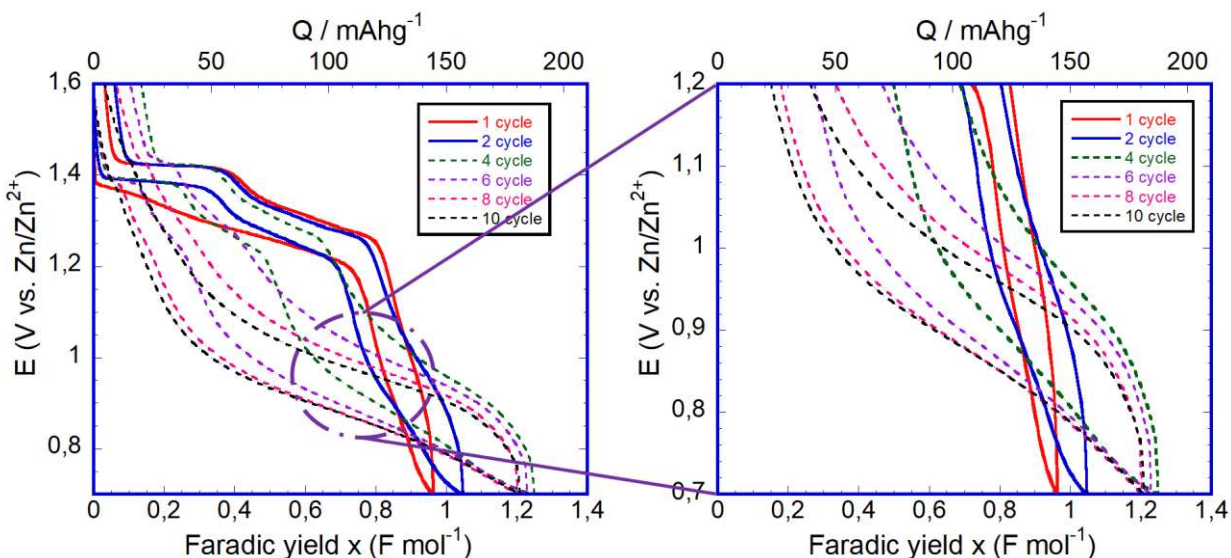


Figure 16. Discharge/charge profiles of Zn/ γ' -V₂O₅ system at initial 10 cycles at 1C at voltage range of 0.7-1.6V

4.3.8 Structural Investigation of Zn || Li₂SO₄-ZnSO₄ || γ' -V₂O₅ system at wide voltage range

In order to understand the corresponding insertion/extraction mechanism, the structural evolution of γ' -V₂O₅ was investigated in the 0.7-1.6V voltage range at 1st cycle (**Figure 17**). As shown from Ex-situ XRD and Raman results, after complete cycle at C/5, the total restoration of initial γ' -V₂O₅ structure is observed without additional peaks or bands. The unit cell parameters at discharged state [$a=9.69$ Å, $b=3.6$ Å, $c=10.67$ Å] fully agree with those of lithiated γ -LiV₂O₅ phase. After 1 complete cycle the unit cell parameters [$a=9.94$ Å, $b=3.58$ Å, $c=10.04$ Å] correspond to the initial γ' -V₂O₅. From Ex-Raman results illustrates that, the initial structure of γ' -V₂O₅ is complete restored after 1 cycle, no extra band related to the presence of another phase is detected (**Figure 18**).

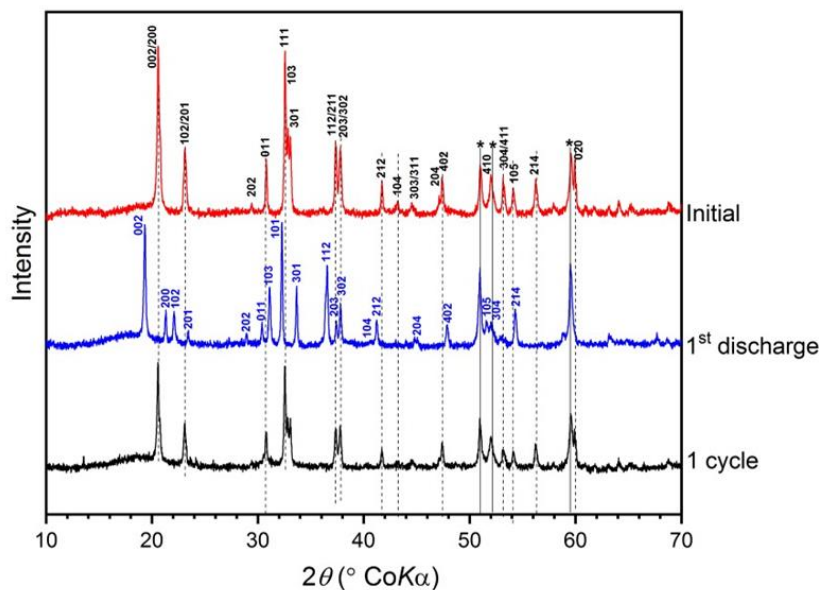


Figure 17. Ex-situ XRD pattern of γ' -V₂O₅ after 1 cycle at C/5

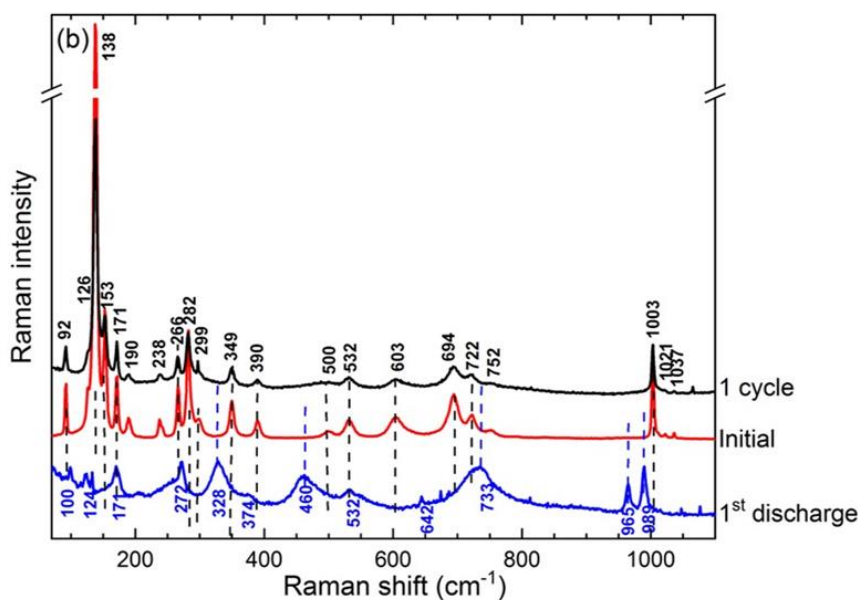


Figure 18. Ex-situ Raman results of γ' -V₂O₅ after 1 cycle at C/5

However, upon cycling, ex-situ XRD and Raman results show the intensity decrease and broadening of the bands related to a disordering process. Only few reflection lines (002/200, 102/201, 011, 111, 301) can be observed after 6 cycles. Despite, after 50 cycles (**Figure 19a** and **Figure S6a**) characteristic peaks of initial γ' -V₂O₅ do not exist, indicating a deep structural rearrangement during cycling. Noteworthy, on discharged state after 50 cycles a peak at 14.23° is detected, which corresponds to formation of new phase Zn₃V₂O₇(OH)₂·2H₂O pyrovanadate (ZVO, P3m1, JCPDS 50-0570). ZVO consists of zinc oxide layers pillared by (V₂O₇) groups and

water molecules along the z-axis. The Zn atoms occupy three of four octahedral sites in close-packed O atoms [13]. The open-framework of ZVO has large interlayer spacing of 7.19 Å, which is favorable for Zn²⁺ insertion/extraction. The most intense peak of ZVO located at 14.23 (001 line) showing the *c* interlayer space of 7.3Å. [14].

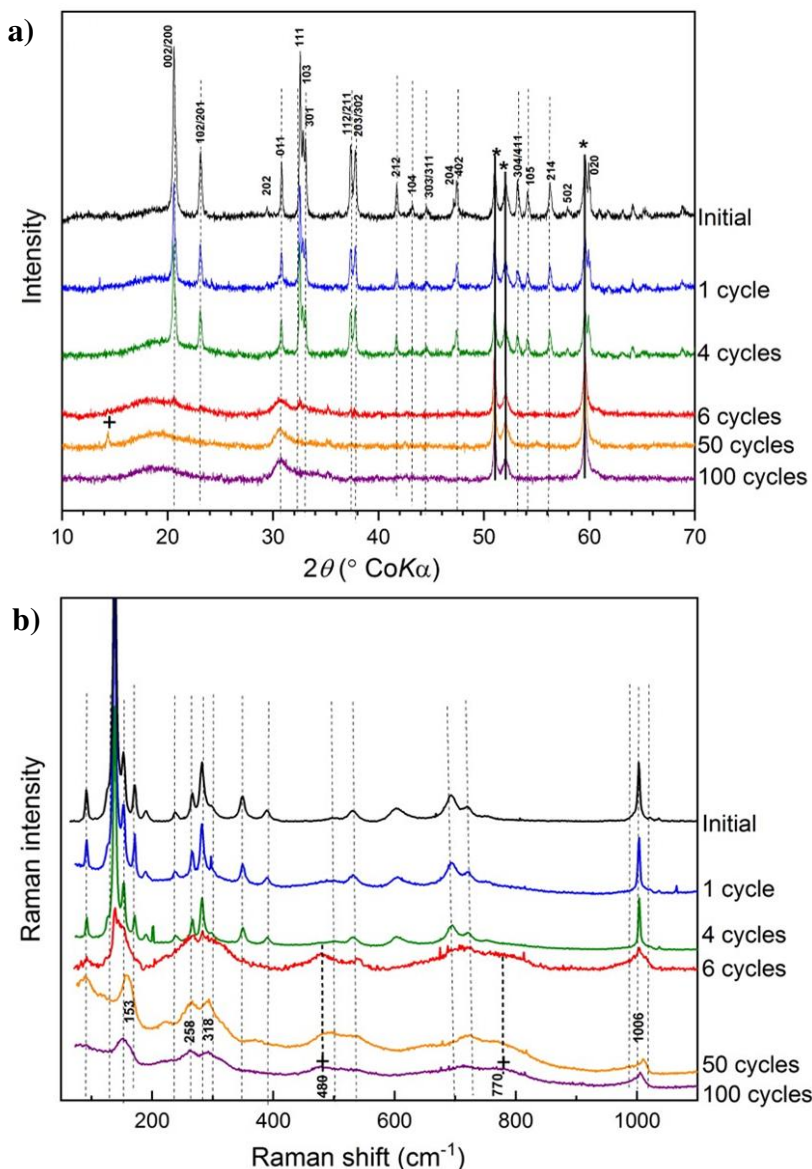


Figure 19. Ex-situ XRD and Raman on cycled electrodes at 1C in 0.7-1.6V range

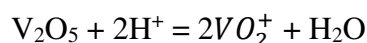
The obtained results from ex-situ XRD have been confirmed by the Raman study on same samples (**Figure 19b** and **Figure S6b**). The typical band of initial γ' -V₂O₅ can be still detected at 4th cycle but from the 6th cycle broad bands at 153, 258, 318, 1006 cm^{-1} with additional bands at 480 cm^{-1} , 770 cm^{-1} can be ascribed to the ZVO [14], [15].

During discharge from 6th cycle the broad bands at 460, 530, 730 and 996 cm⁻¹ correspond to the disordered γ -LiV₂O₅ with the presence of the new additional bands at 480, 770 and 860 cm⁻¹ related to the ZVO [14], [15]. The band at 480 cm⁻¹ is related to the Zn-O vibration bond, while bands at 770 and 860 cm⁻¹ correspond to the V-O vibration bond. The broad band at 460 cm⁻¹ accords to the ν (V_b-O₃) mode of γ -LiV₂O₅ [11].

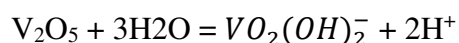
From the present structural data, it can be concluded that a significant phase transformation occurs in the 0.7-1.6V voltage range. It was found that, in narrow range till 1V Li⁺ intercalation/deintercalation was the reaction mechanism while enlarging the voltage window γ '-V₂O₅ undergoes structural evolution and transforms into ZVO during discharge.

Myung et al. reported VO_{1.52}(OH)_{0.77} material [[16]], which gradual dissolution of Vanadium species in acidic electrolyte might be responsible for the formation of Zn₃V₂O₇(OH)₂*2H₂O phase. It was found that on the surface for the cycled electrode Zn₄SO₄(OH)₆*0.5H₂O and Zn₃V₂O₇(OH)₂*2H₂O were found as a result of electrolytic decomposition and side reaction of active material with electrolyte.

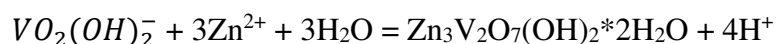
Lu et al. [[13]] found the strong dependence between V₂O₅ dissolution and pH value of electrolyte. At pH < 3.2 and [V⁵⁺] < 10⁻¹ M, the most stable form of V-species in aqueous solution is VO₂⁺:



which leads to an increase in pH by consuming protons. In addition, at 3.8 ≤ pH ≤ 7.8 and [V⁵⁺] < 10⁻⁴ M, the most stable V-species is VO₂(OH)₂⁻ (or H₂VO₄⁻) and V₂O₅ dissolution follows:

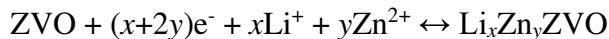


resulting in pH decrease by releasing the protons. The formed VO₂(OH)₂⁻ further reacts with Zn²⁺ in zinc salts, forming ZVO with following reaction:



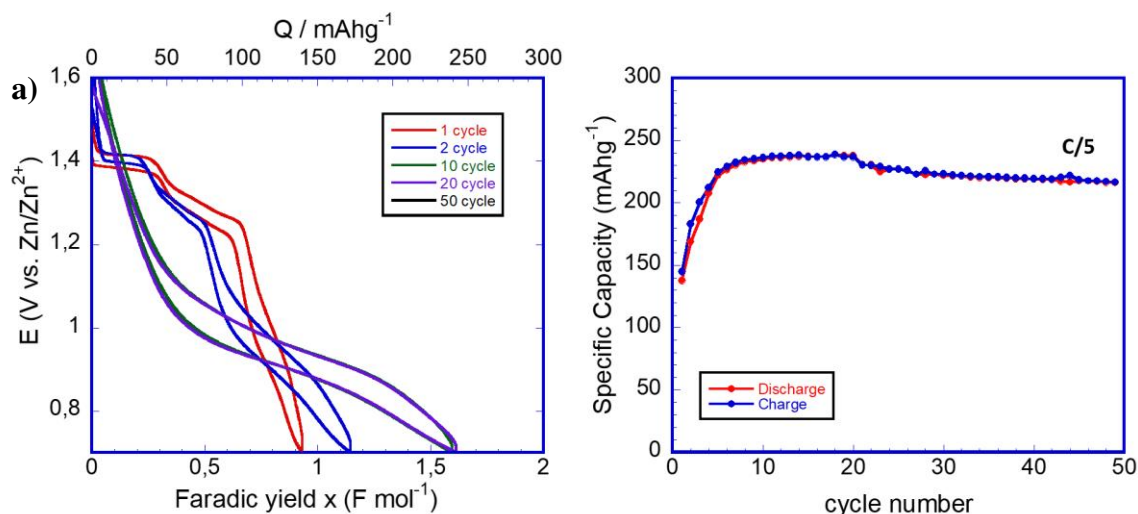
As seen in SEM-EDS image, it is clear that Zn elements can be observed for γ '-V₂O₅ electrode discharged to 0.7 V at different cycles. On the 1st discharge (**Figure S7**). The Zn/V ratio was 0.16 and significantly increased to 0.62 after 50 cycles. A high capacity of 180 mAh g⁻¹ is delivered on cycling at 1C, corresponding to the ~1.2 electron redox process. However, the EDS results completely eliminate the traditional Zn²⁺ insertion mechanism by forming Zn_xV₂O₅ bronze [17].

Indeed, the obtained Zn/V ratio (0.62) from EDS is far from the value of ~1.5 in ZVO (**Figure S7**). It rather indicates the co-existence of disordered γ' -V₂O₅ and ZVO, with the possibility of lithium insertion even after phase transformation. The possible reaction mechanism is following:



4.3.9 Cycling properties in the 1.6-0.7V

The electrochemical performance of Zn/ γ' -V₂O₅ system with 3.5M ZnSO₄+2.5M Li₂SO₄ investigated at C/5–1C are shown in **Figure 20**. As mentioned above, after 10 cycles (activation process), the discharge capacity increases from 147 mAh g⁻¹ to 240 mAh g⁻¹ at C/5 and is maintained over 50 cycles with an excellent capacity retention (**Figure 20a**). According to the discharge/charge shape the typical two voltage plateaus completely disappear after cycle 10, to the benefit of a new plateau at ~ 0.9 V demonstrating an important structural rearrangement of the cathode material. At 1C, the same activation process is revealed since the discharge capacity gains 144 mAh g⁻¹ at 1st cycle, reaches 180 mAh g⁻¹ after 10 cycles without further decay after 100 cycles (**Figure 20b**).



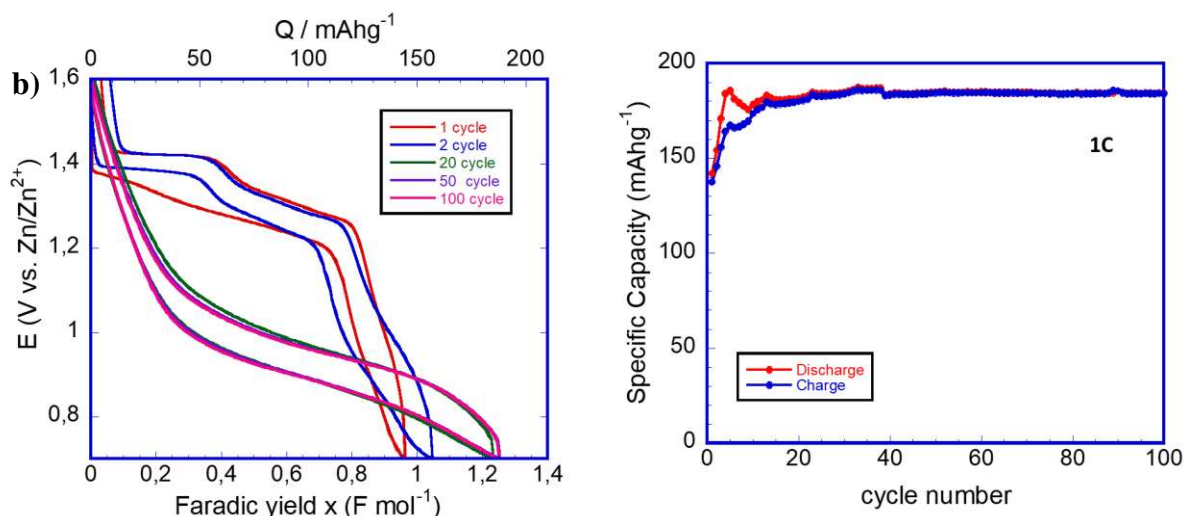


Figure 20. Discharge/charge profiles and cycle performance of Zn/ γ' -V₂O₅ system at (a) C/5 – (b) 1C in voltage range of 0.7-1.6V

For comparison, the Zn/γ'-V₂O₅ cell with 4M ZnSO₄ electrolyte was investigated in 0.7-1.6V voltage range at C/5 (**Figure 21**). A drastic capacity decay was observed from 250 mAh g⁻¹ to 75 mAh g⁻¹ in 50 cycles, which reveals a better cyclability can be achieved with hybrid electrolyte (3.5M ZnSO₄ + 2.5M Li₂SO₄).

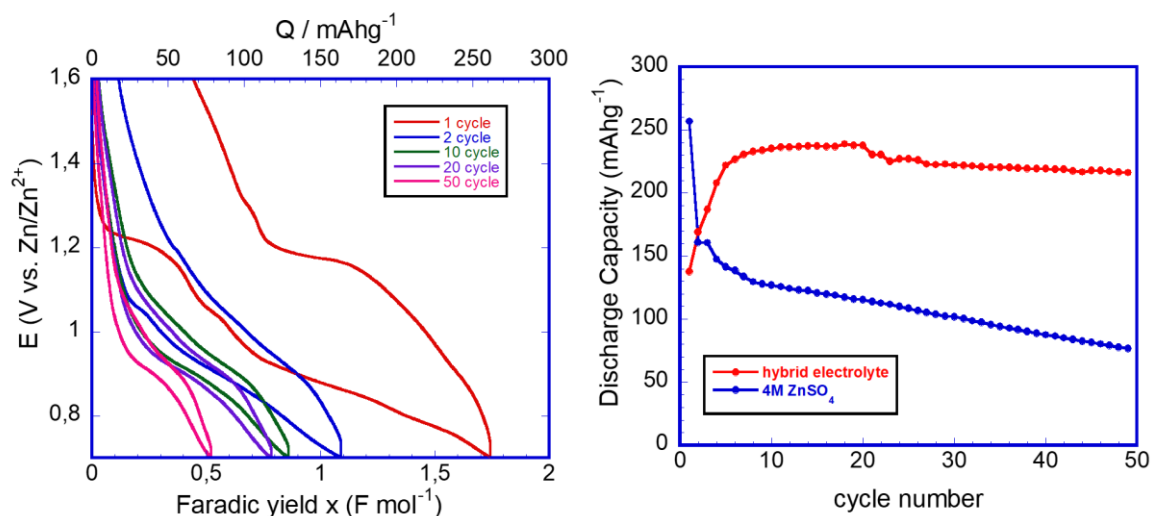


Figure 21. Discharge/charge profile and cycle performance of Zn/ γ' -V₂O₅ system with hybrid and 4M ZnSO₄ in voltage range of 0.7-1.6V at C/5

The rate-capability of Zn/ γ'-V₂O₅ system at 0.7-1.6 V is illustrated in **Figure 22**. After the activation process of first 10 cycles at 1C, the discharge capacity increased from 135 mAh g⁻¹ to 190 mAh g⁻¹. The discharge capacity decreases in the 2C-10C range, with 170 mAh g⁻¹ at 2C, 130

mAh g^{-1} at 5C and 65 mAh g^{-1} at 10C, without impacting in charge efficiency. After extremely high 20C-50C C-rate, the discharge capacity of 190 mAh g^{-1} is recovered at 1C, indicating the stable rate-capability of the system. This last clearly shows no dissolution process takes place as soon as ZVO is electrochemically formed.

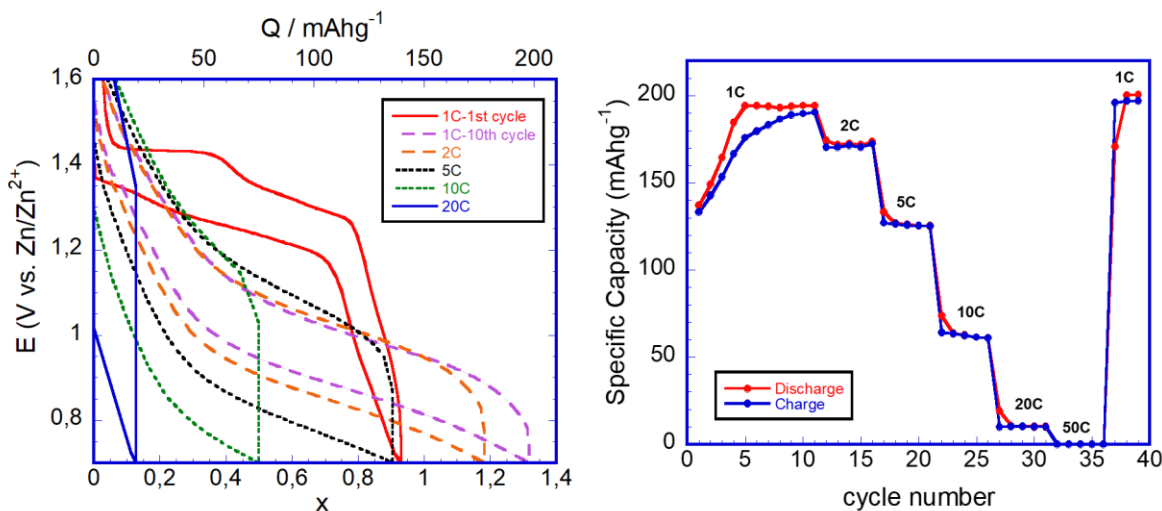


Figure 22. The rate-capability of Zn/ γ' -V₂O₅ system.

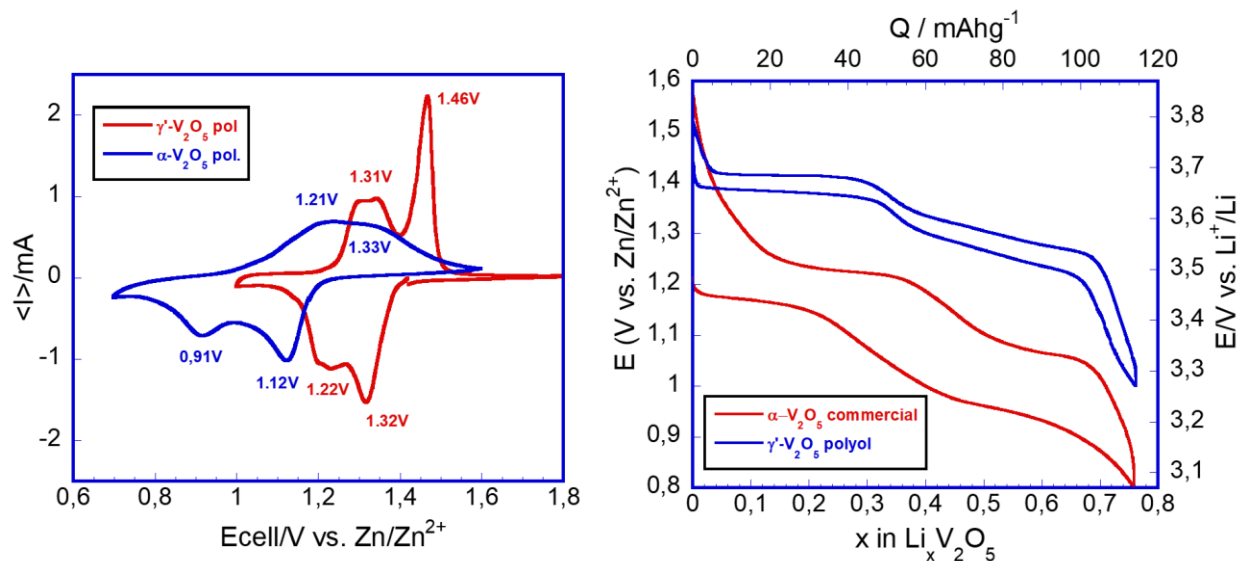


Figure 23. The comparison of cyclic voltammetry and first discharge/charge profile of α -V₂O₅ and γ' -V₂O₅ at C/5.

4.3.10 Conclusion

The electrochemical and structural behaviour of γ' -V₂O₅ as cathode in the Zn/3.5M ZnSO₄ + 2.5M Li₂SO₄/ γ' -V₂O₅ system was investigated. The battery exhibits 114 mAh g⁻¹ at C/5 in voltage range of 1–1.6V. The operating voltage of γ' -V₂O₅, similar to organic electrolyte, exhibits ~200mV higher than α -V₂O₅ in same aqueous hybrid electrolyte (**Figure 23**).

During the first cycle, ex-situ XRD and Raman studies demonstrated a similar structural behavior than in organic lithium electrolyte. The insertion of zinc ions can be completely excluded due to the high operational voltage of γ' -V₂O₅ [4], [9]–[11]. However, a significant vanadium oxide dissolution occurs upon cycling. Hence, a huge capacity fading is observed at low current densities while high current density favors slow vanadium oxide dissolution [18]–[20]. Therefore, poor capacity values around 50 mAh g⁻¹ can be achieved.

Improvement in specific capacity and cycle stability can be achieved by enlarging the voltage window to 0.7V. The main difference from narrow voltage window (1-1.6V) is the shape change in voltage profile in initial 10 cycles, which can be explained by phase transformation of γ' -V₂O₅ to ZVO. This finding is supported by ex-situ XRD and Raman analysis. After activation process, a specific capacity gains 240 mAh g⁻¹ at C/5 and 180 mAh g⁻¹ at 1C with excellent cyclability and good rate capability. The main interest offered by this phase transformation leading to a ZVO-type phase is its high stability in the hybrid electrolyte showing the key point of dissolution can be overcome with the choice of an appropriate host lattice.

SUPPORTING INFORMATION

Electrochemical characterization

γ' -V₂O₅ positive electrodes were prepared by mixing 90wt%% of active material, 6wt% polyvinylidene fluoride (PVDF, Kynar, HSV900) as a binder, 4wt% ketjen black (Ketjen Black International Co., Japan) as conductive agent dissolved in 1-methyl-2-pyrrolidinone (NMP, Sigma-Aldrich). The prepared slurry was casted on carbon paper (Alfa Aesar Co.), vacuum dried at 70 °C for 3hr and punched into the disks of 8 mm in diameter. The mass loading of active material was around 5 mg/cm² (2.7-2.8 mg of active material). Zinc foil (Goodfellow, USA) was used as negative electrode. The electrolyte was prepared by dissolving 3.5 mole L⁻¹ of ZnSO₄ and 2.5 mole L⁻¹ of Li₂SO₄ in distilled water and pH was adjusted to 4 by titration with 0.5 mole L⁻¹ of H₂SO₄. Prepared electrolyte was bubbled with nitrogen gas (N₂) to remove dissolved oxygen. AGM (Absorptive Glass Mat NSG Corporation) was used as separator. The structural investigation of Zn/Li₂SO₄-ZnSO₄/ γ' -V₂O₅ system was investigated by using two-electrode split cell (MTI company). The cells were discharged to the required composition by electrochemical reduction using VMP3 Biologic tester at C/5 rate. After reduction, cells were disassembled in air, electrodes were rinsed in distilled water in order to remove the traces of salt and separator. Cyclic voltammetry (CV) was performed with VMP3 potentiostat/galvanostat (Bio-Logic Science Instrument Co.)

Structural investigations

XRD measurements were carried out using a Panalytical X'pert pro diffractometer equipped with an X'celerator detector and a Co K α radiation (wavelength 1.7889 Å). All the diffraction patterns were collected with a 2 θ step of 0.0167°. The Raman spectra were measured with a LaBRAM HR 800 (Jobin-Yvon-Horiba) Raman micro-spectrometer including Edge filters and equipped for signal detection with a back illuminated charge coupled device detector (Spex CCD) cooled by Peltier effect to 200 K. A He:Ne laser (632.8 nm) was used as the excitation source. The spectra were measured in back-scattering geometry. The resolution was about 0.5 cm⁻¹. A 50X LWD objective was used to focus the laser light on sample surface to a spot size of 1 μ m². To avoid local heating of the sample, the power of the laser beam was adjusted to 0.2–0.5 mW with neutral filters of various optical densities. Raman spectra were recorded on ten different spots of each electrode

to check the homogeneity. The powders were characterized by scanning electron microscopy (SEM), Zeiss, Merlin-type microscope.

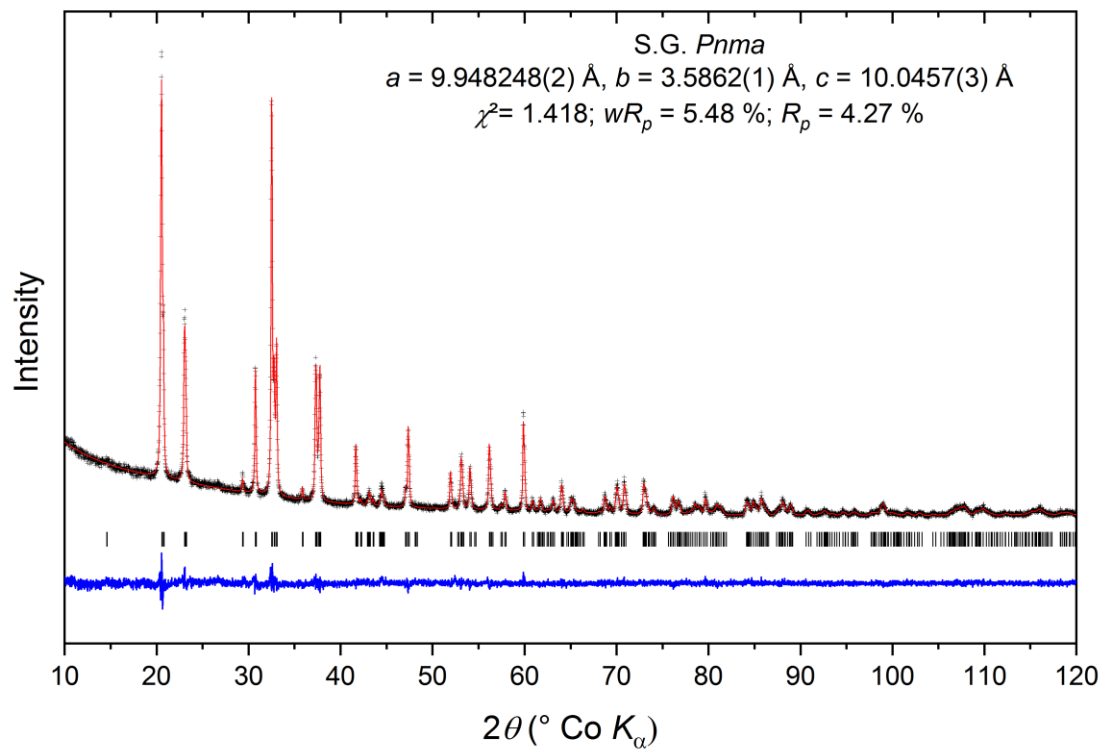


Figure S1. Rietveld refinement of γ' - V_2O_5 XRD pattern

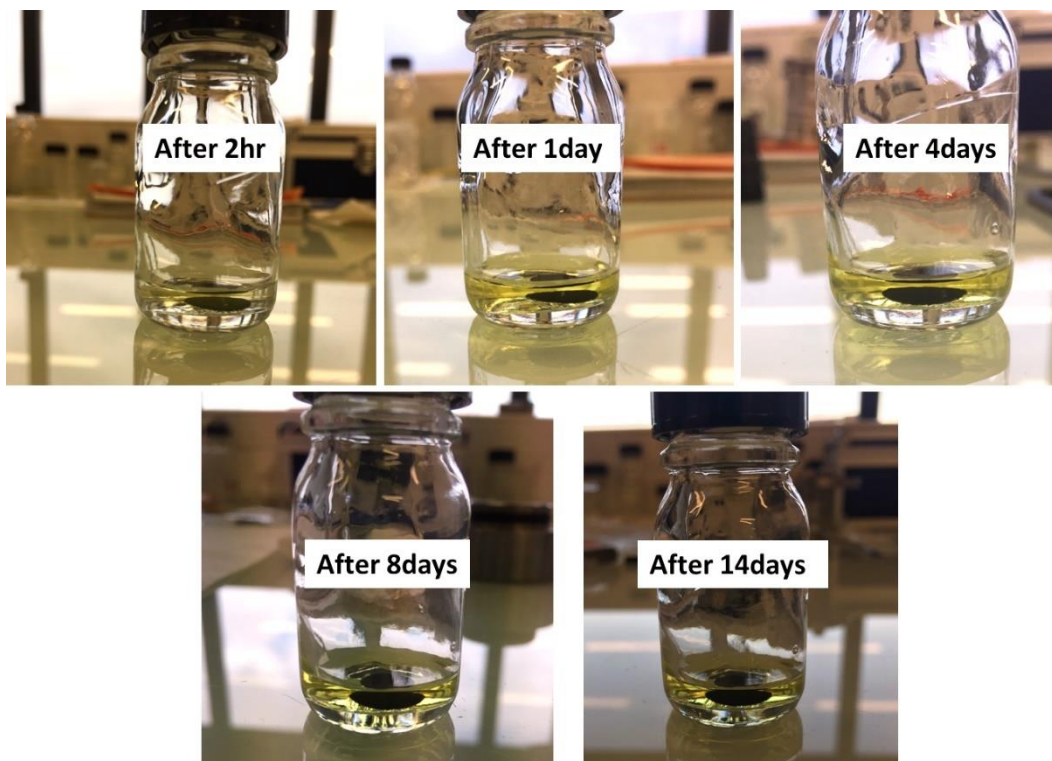


Figure S2. The γ' - V_2O_5 electrode stored in 3.5M ZnSO_4 + 2.5M Li_2SO_4 electrolyte

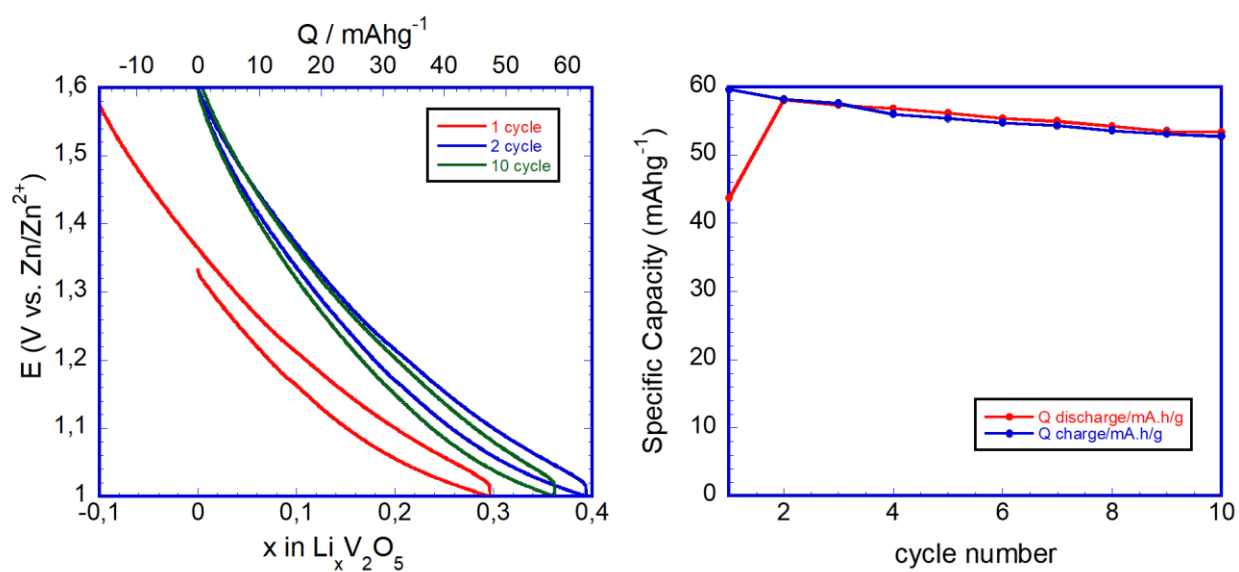


Figure S3. The assembled 2 electrode split cell with stored γ' - V_2O_5 electrode in electrode and tested at C/5

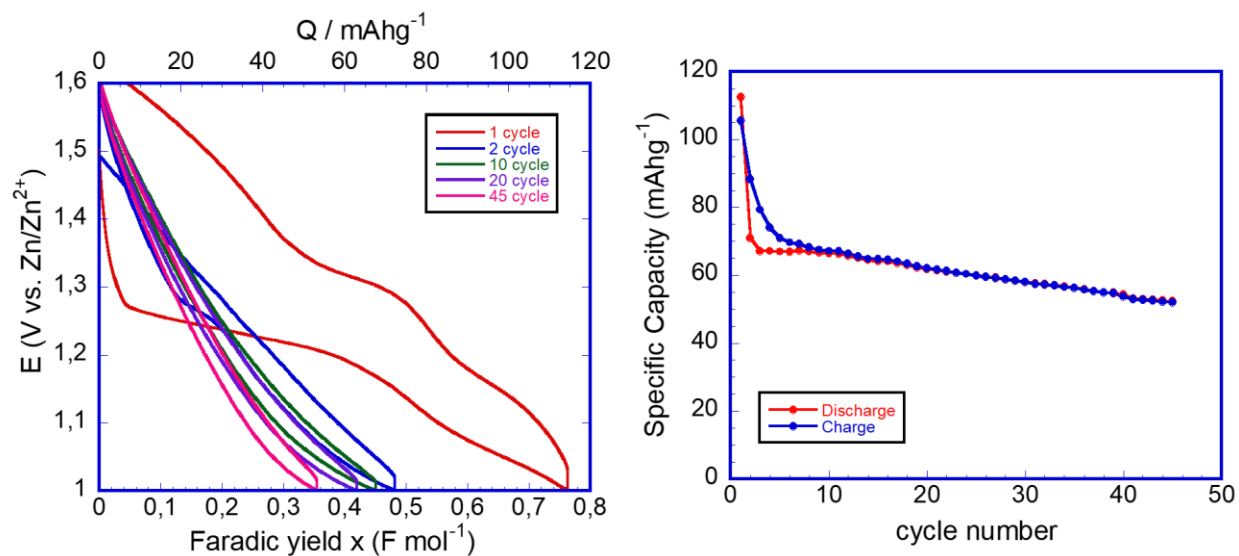


Figure S4. The discharge/charge profile and cycle performance of $\text{Zn}/\gamma'-\text{V}_2\text{O}_5$ system in 4M ZnSO_4 in 1.6V – 1V voltage range at C/5

Wide voltage range (0.7 – 1.6V)

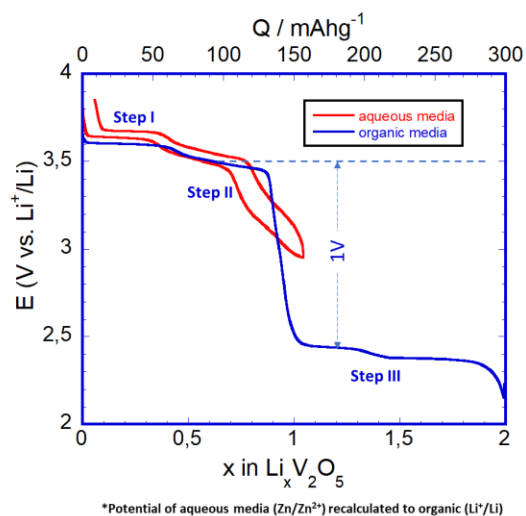


Figure S5. The comparison of discharge-charge curves of $\gamma'-\text{V}_2\text{O}_5$ in aqueous ($3.5\text{M ZnSO}_4 + 2.5\text{M Li}_2\text{SO}_4$) and organic electrolyte (1M LiClO_4 in PC)

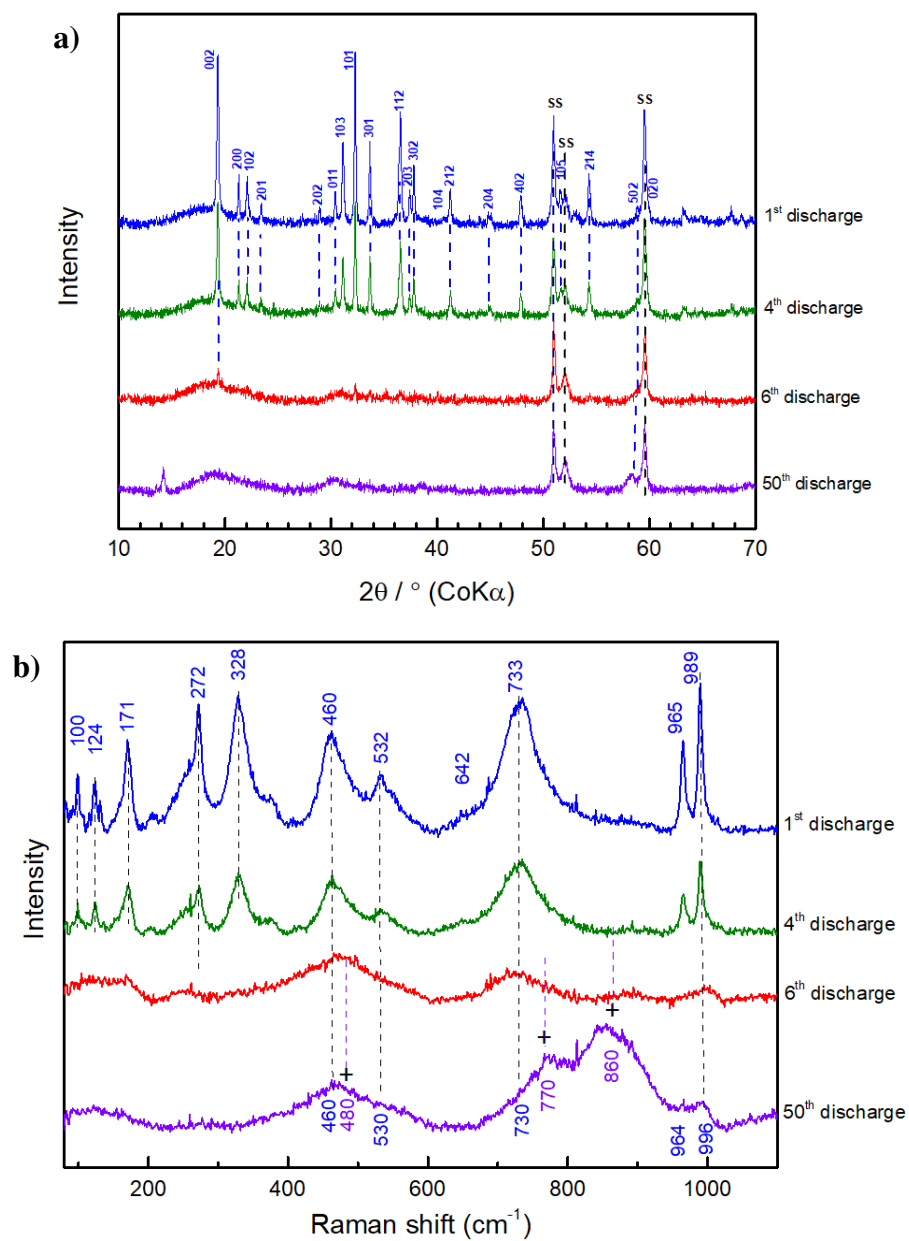


Figure S6. Ex-situ XRD ana Raman results at different cycles at discharged state

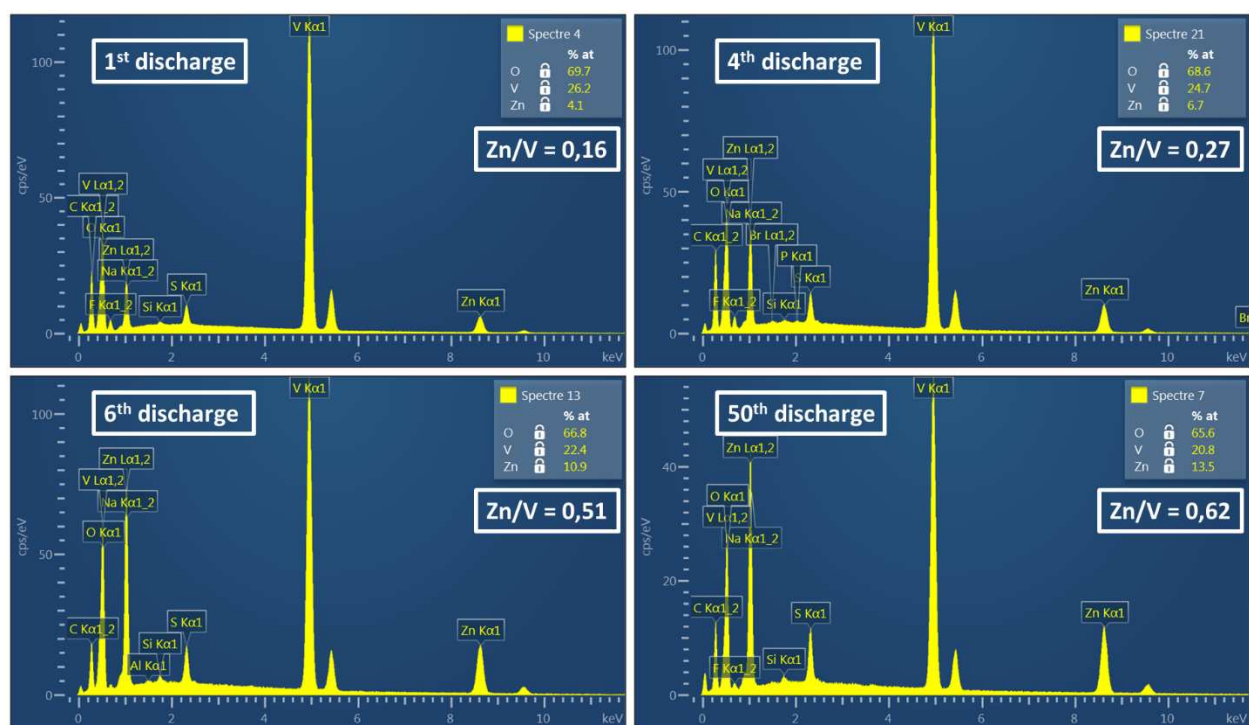


Figure S7. SEM-EDS results of cycled electrodes at discharged state

REFERENCE

- [1] D. Batyrbekuly *et al.*, “Mechanistic Investigation of a Hybrid Zn/V 2 O 5 Rechargeable Battery with a Binary Li + /Zn 2+ Aqueous Electrolyte,” *ChemSusChem*, vol. 13, no. 4, pp. 724–731, Feb. 2020, doi: 10.1002/cssc.201903072.
- [2] R. Baddour-Hadjean, M. B. Smirnov, V. Y. Kazimirov, K. S. Smirnov, and J. P. Pereira-Ramos, “The Raman spectrum of the γ -V2O5 polymorph: A combined experimental and DFT study,” *J. Raman Spectrosc.*, vol. 46, no. 4, pp. 406–412, 2015, doi: 10.1002/jrs.4660.
- [3] N. Emery, R. Baddour-Hadjean, D. Batyrbekuly, B. Laïk, Z. Bakenov, and J.-P. Pereira-Ramos, “ γ -Na 0.96 V 2 O 5 : A New Competitive Cathode Material for Sodium-Ion Batteries Synthesized by a Soft Chemistry Route,” *Chem. Mater.*, vol. 30, no. 15, pp. 5305–5314, Aug. 2018, doi: 10.1021/acs.chemmater.8b02066.
- [4] R. Baddour-Hadjean, M. Safrany Renard, and J. P. Pereira-Ramos, “Unraveling the structural mechanism of Li insertion in γ' -V2O5 and its effect on cycling properties,” *Acta Mater.*, vol. 165, pp. 183–191, 2019, doi: 10.1016/j.actamat.2018.11.043.
- [5] M. S. Renard, N. Emery, R. Baddour-Hadjean, and J. P. Pereira-Ramos, “ γ' -V2O5: A new high voltage cathode material for sodium-ion battery,” *Electrochim. Acta*, vol. 252, pp. 4–11, 2017, doi: 10.1016/j.electacta.2017.08.175.
- [6] J. M. Cocciantelli, J. P. Doumerc, M. Pouchard, M. Broussely, and J. Labat, “Crystal chemistry of electrochemically inserted LixV2O5,” *J. Power Sources*, vol. 34, no. 2, pp. 103–111, Mar. 1991, doi: 10.1016/0378-7753(91)85029-V.
- [7] J. Barker, M. Y. Saidi, and J. L. Swyer, “Performance Evaluation of the Electroactive Material, γ -LiV[sub 2]O[sub 5], Made by a Carbothermal Reduction Method,” *J. Electrochem. Soc.*, vol. 150, no. 9, p. A1267, 2003, doi: 10.1149/1.1600462.
- [8] S. Caes *et al.*, “Mesoporous lithium vanadium oxide as a thin film electrode for lithium-ion batteries: Comparison between direct synthesis of LiV2O5 and electrochemical lithium intercalation in V2O5,” *J. Mater. Chem. A*, vol. 2, no. 16, pp. 5809–5815, 2014, doi: 10.1039/c4ta00090k.
- [9] R. Baddour-Hadjean, A. Marzouk, and J. P. Pereira-Ramos, “Structural modifications of LixV2O5 in a composite cathode ($0 \leq x < 2$) investigated by Raman microspectrometry,” *J. Raman Spectrosc.*, vol. 43, no. 1, pp. 153–160, Jan. 2012, doi: 10.1002/jrs.2984.
- [10] C. Delmas, S. Brèthes, and M. Ménétrier, “ ω -LixV2O5 - a new electrode material for rechargeable lithium batteries,” *J. Power Sources*, vol. 34, no. 2, pp. 113–118, 1991, doi: 10.1016/0378-7753(91)85030-Z.
- [11] M. B. Smirnov *et al.*, “Spectroscopic and Computational Study of Structural Changes in γ -LiV2O5 Cathodic Material Induced by Lithium Intercalation,” *J. Phys. Chem. C*, vol. 119, no. 36, pp. 20801–20809, 2015, doi: 10.1021/acs.jpcc.5b05540.
- [12] P. Hu *et al.*, “Zn/V 2 O 5 Aqueous Hybrid-Ion Battery with High Voltage Platform and Long Cycle Life,” *ACS Appl. Mater. Interfaces*, vol. 9, no. 49, pp. 42717–42722, Dec. 2017, doi: 10.1021/acsami.7b13110.
- [13] Y. Lu, T. Zhu, W. Bergh, M. Stefik, and K. Huang, “A High Performing Zn-Ion Battery Cathode Enabled by In Situ Transformation of V 2 O 5 Atomic Layers,” *Angew. Chemie Int. Ed.*, vol. 59, no. 39, pp. 17004–17011, Sep. 2020, doi: 10.1002/anie.202006171.
- [14] C. Xia, J. Guo, Y. Lei, H. Liang, C. Zhao, and H. N. Alshareef, “Rechargeable Aqueous Zinc-Ion Battery Based on Porous Framework Zinc Pyrovanadate Intercalation Cathode,” *Adv. Mater.*, vol. 30, no. 5, pp. 1–7, 2018, doi: 10.1002/adma.201705580.

- [15] S. Ni *et al.*, “Hydrothermal synthesis of $\text{Zn}_3(\text{OH})_2\text{V}_2\text{O}_7 \cdot n\text{H}_2\text{O}$ nanosheets and its application in lithium ion battery,” *Mater. Lett.*, vol. 63, no. 28, pp. 2459–2461, Nov. 2009, doi: 10.1016/j.matlet.2009.07.070.
- [16] J. H. Jo, Y. K. Sun, and S. T. Myung, “Hollandite-type Al-doped $\text{VO}_{1.52}(\text{OH})_{0.77}$ as a zinc ion insertion host material,” *J. Mater. Chem. A*, vol. 5, no. 18, pp. 8367–8375, 2017, doi: 10.1039/c7ta01765k.
- [17] N. Zhang *et al.*, “Rechargeable Aqueous $\text{Zn-V}_2\text{O}_5$ Battery with High Energy Density and Long Cycle Life,” *ACS Energy Lett.*, vol. 3, no. 6, pp. 1366–1372, Jun. 2018, doi: 10.1021/acsenenergylett.8b00565.
- [18] M. H. Alfaruqi *et al.*, “Electrochemical Zinc Intercalation in Lithium Vanadium Oxide: A High-Capacity Zinc-Ion Battery Cathode,” *Chem. Mater.*, vol. 29, no. 4, pp. 1684–1694, Feb. 2017, doi: 10.1021/acs.chemmater.6b05092.
- [19] F. Wan and Z. Niu, “Design Strategies for Vanadium-based Aqueous Zinc-Ion Batteries,” *Angew. Chemie - Int. Ed.*, vol. 58, no. 46, pp. 16358–16367, 2019, doi: 10.1002/anie.201903941.
- [20] P. He *et al.*, “Layered VS_2 Nanosheet-Based Aqueous Zn Ion Battery Cathode,” *Adv. Energy Mater.*, vol. 7, no. 11, pp. 1–5, 2017, doi: 10.1002/aenm.201601920.



A porous puckered V_2O_5 polymorph as new high performance cathode material for aqueous rechargeable zinc batteries

Dauren Batyrbekuly^{a,b}, Barbara Laïk^a, Jean-Pierre Pereira-Ramos^a, Zhumabay Bakenov^b, Rita Baddour-Hadjean^{a,*}

^aInstitut de Chimie et des Matériaux Paris Est (ICMPE), UMR 7182 CNRS et Université Paris Est Créteil, 2 rue Henri Dunant, 94320 Thiais, France

^bSchool of Engineering, National Laboratory Astana, Nazarbayev University, 53 Kabanbay Batyr Avenue, Astana 010000, Kazakhstan

ARTICLE INFO

Article history:

Received 21 December 2020

Revised 22 January 2021

Accepted 27 January 2021

Available online 12 February 2021

Keywords:

Vanadium pentoxide

γ' - V_2O_5

Cathode

Aqueous zinc battery

High performance

Layered structure

Energy storage

Renewable energy

ABSTRACT

Aqueous rechargeable zinc batteries are getting increasing attention for large-scale energy storage owing to their advantages in terms of cost, environmental friendliness and safety. Here, the layered puckered γ' - V_2O_5 polymorph with a porous morphology is firstly introduced as cathode for an aqueous zinc battery system in a binary Zn^{2+}/Li^+ electrolyte. The $Zn||\gamma'$ - V_2O_5 cell delivers high capacities of 240 and 190 mAh g^{-1} at current densities of 29 and 147 mA g^{-1} , respectively, and remarkable cycling stability in the 1.6 V–0.7 V voltage window (97% retention after 100 cycles at 0.15 A g^{-1}). The detailed structural evolution during first discharge-charge and subsequent cycling is investigated using X-ray diffraction and Raman spectroscopy. We demonstrate a reaction mechanism based on a selective Li insertion in the 1.6 V–1.0 V voltage range. It involves a reversible exchange of 0.8 Li^+ in γ' - V_2O_5 and the same structural response as the one reported in lithiated organic electrolyte. However, in the extended 1.6 V–0.7 V voltage range, this work puts forward a concomitant and gradual phase transformation from γ' - V_2O_5 to zinc pyrovanadate $Zn_3V_2O_7(OH)_2 \cdot 2H_2O$ (ZVO) during cycling. Such mechanism involving the *in-situ* formation of ZVO, known as an efficient Zn and Li intercalation material, explains the high electrochemical performance here reported for the $Zn||\gamma'$ - V_2O_5 cell. This work highlights the peculiar layered-puckered γ' - V_2O_5 polymorph outperforms the conventional α - V_2O_5 with a huge improvement of capacity of 240 mAh g^{-1} vs 80 mAh g^{-1} in the same electrolyte and voltage window.

© 2021 Science Press and Dalian Institute of Chemical Physics, Chinese Academy of Sciences. Published by ELSEVIER B.V. and Science Press. All rights reserved.

1. Introduction

Lithium ion batteries (LIBs) are known to provide the best option in terms of energy density and technical maturity to store renewable energy. However, LIBs large-scale energy storage systems have great limitations such as high cost and insufficient safety. In search of alternative batteries, aqueous rechargeable Zn-based batteries (ARZB) are attractive due to their low cost, safety and moderate toxicity. In addition, the high conductivity of the aqueous electrolyte made of Zn salts (e.g. 1 M–3 M $ZnSO_4$) allows a substantial gain on rate performance. While traditional alkaline electrolytes induce dendrite formation and byproducts, recent works have demonstrated the use of mild acidic electrolytes (pH \approx 4) significantly improves the stability of metallic Zn anode [1–3].

Finding suitable cathode materials for ARZBs with high capacity, high operating voltage and long cycle life is actually a great challenge. Previous explorations of cathode materials mostly concern three main groups [4–6]: Prussian blue and analogues, manganese oxides and vanadium-based compounds that have been extensively investigated owing to the richness of layered structures in that family combined to the multiple oxidation states of vanadium [1,7–27]. Fast rate capability and good capacity retention of 80–95% over a few hundred cycles with specific capacities mostly in the range 100–300 mAh g^{-1} have been reported for hydrated V-based compounds such as $Zn_{0.25}V_2O_5 \cdot nH_2O$ [1], $V_2O_5 \cdot nH_2O/ RGO$ [7], V_2O_5 xerogel flakes [8], $V_3O_7 \cdot H_2O$ nanowires [9], $V_{10}O_{24} \cdot 12H_2O$ [10], $Mg_xV_2O_5 \cdot nH_2O$ [11], $K_2V_6O_{16} \cdot 2.7H_2O$ [12], $Ca_{0.25}V_2O_5 \cdot nH_2O$ [13], $Na_2V_6O_{16} \cdot 3H_2O$ [14], $Fe_5V_{15}O_{39}(OH)_{0.9} \cdot 9H_2O$ nanosheets [15], $Zn_3V_2O_7(OH)_2 \cdot 2H_2O$ [16] and hydrated porous δ - $Ni_{0.25}V_2O_5 \cdot nH_2O$ nanoribbons [17]. Anhydrous vanadium-based phases have also been investigated like VO_2 [18], $Zn_2V_2O_7$ [19], $NH_4V_4O_{10}$ [20], KV_3O_8 , $K_2V_8O_{21}$ [21] and LiV_3O_8 [22].

* Corresponding author.

E-mail address: baddour@icmpe.cnrs.fr (R. Baddour-Hadjean).

In contrast to the abundant literature devoted to the vanadium oxide derivatives, very few works concern the conventional anhydrous α - V_2O_5 oxide. The reported papers [23–29] focus on the wide operating voltage windows 1.6 V–0.5 V, 1.5 V–0.3 V or 1.4 V–0.4 V involving the 2-electron reaction or more. From a mechanistic point of view, zinc and water insertion are thought to be responsible for the formation of a $\text{Zn}_x\text{V}_2\text{O}_5 \cdot n\text{H}_2\text{O}$ compound [25,27] or a zinc pyrovanadate [27,28] upon cycling. After an activation process over several cycles (fewer than ten, to a few dozen at most), highly stable capacities with scattered values in the range 220–470 mAh g^{-1} are achieved.

Recently, the use of a binary electrolyte of Li and Zn salts in mild acidic electrolyte attracted great interest, leading to the concept of rechargeable aqueous hybrid electrolyte, which involves two separate electrochemical redox processes on Zn anode and cathode, respectively. The electrolyte acts as conducting ions and cooperates with electrodes, ensuring efficient cyclability of Zn anode as well as reversible lithium insertion-extraction in the host cathodic material. Chen et al. proposed the first hybrid $\text{Zn}||\text{ZnCl}_2 + \text{LiCl}||\text{LiMn}_2\text{O}_4$ system operating with high efficiency and long-term cyclability [30]. In addition to LiMn_2O_4 , other cathode materials like LiFePO_4 [31,32], $\text{Li}_3\text{V}_2(\text{PO}_4)_3$ [33], LiVPO_4F [34], $\text{LiNi}_{1/3}\text{Co}_{1/3}\text{Mn}_{1/3}\text{O}_2$ [35], $\text{LiMn}_{0.8}\text{Fe}_{0.2}\text{PO}_4$ [36] have been investigated. High capacities in the range 100–130 mAh g^{-1} have been reported with good capacity retention upon cycling near 1.6/1.8 V. A high rate capability is a common feature of such hybrid batteries with a 70–80% capacity retention at 4C.

We newly applied this concept of rechargeable aqueous hybrid batteries, using the conventional pristine α - V_2O_5 oxide as cathode material and Zn as anode in 2.5 M $\text{Li}_2\text{SO}_4 + 3.5$ M ZnSO_4 (pH = 4) binary electrolyte with a special emphasis on the structural mechanism involved upon discharge/charge process in the 1.6 V–0.8 V potential range (corresponding to the transfer of one-electron) [37]. The $\text{Zn}||2.5$ M $\text{Li}_2\text{SO}_4 + 3.5$ M $\text{ZnSO}_4||\alpha$ - V_2O_5 cell delivered capacity values about 136–125 mAh g^{-1} at C/20–C/5 rates (7.35–29.4 mA g^{-1}), respectively. At 1C (147 mA g^{-1}), a capacity of 80 mAh g^{-1} was outstandingly retained over more than 300 cycles. A detailed structural study by X-ray diffraction (XRD) and Raman spectroscopy allowed unravelling the peculiar response of the α - V_2O_5 layered host lattice. Strong similarities with the well-known structural changes reported in non-aqueous lithiated electrolytes were highlighted. The mitigated structural findings revealed a reaction mechanism mainly based on Li^+ intercalation but also suggested a possible cointercalation of Zn^{2+} cations or protons by the end of the discharge. The presence of a few zinc cations between the oxide layers was suggested, which act as pillars stabilizing the structure upon cycling [37].

An exploratory approach for finding new advanced cathode materials in the vanadium oxide family consists in considering the interest of the various V_2O_5 polymorphs. Among them, γ' - V_2O_5 was recently proved to be of great interest as an insertion compound, with attractive electrochemical features for Li and Na-ion batteries [38–41]. In particular, the puckered layered lattice of γ' - V_2O_5 allows reversible Li insertion in a higher voltage window by about 200 mV than α - V_2O_5 (3.6/3.5 V vs. 3.4/3.2 V vs. Li^+/Li). The structure of this polymorph consists of infinite ribbons made of VO_5 edge-sharing distorted pyramids leading to larger interlayer spacing (5.02 Å in γ' - V_2O_5 vs. 4.37 Å in α - V_2O_5), which enables an easier accommodation of guest cations.

However, in spite of such remarkable structural features, γ' - V_2O_5 phase has never been studied in an aqueous battery. In this work, the electrochemical and structural behaviour of γ' - V_2O_5 are depicted for the first time in an aqueous $\text{Zn}||\gamma'$ - V_2O_5 battery using a binary 2.5 M $\text{Li}_2\text{SO}_4 + 3.5$ M ZnSO_4 electrolyte. Electrochemical performances are investigated in two different voltage ranges

(1.6 V–1.0 V and 1.6 V–0.7 V) and the structural response of the cathode material is investigated by XRD and Raman spectroscopy.

2. Experimental

2.1. Synthesis

γ' - V_2O_5 was obtained by chemical oxidation of γ - LiV_2O_5 prepared by chemical lithiation of α - V_2O_5 under mild-temperature conditions. Further details can be found in [39]. A very fine powder of α - V_2O_5 with narrow particle size distribution was used as precursor, prepared using the polyol route [42]. The chemical reaction of α - V_2O_5 with LiI in excess (molar ratio 2:1) in acetonitrile leads to δ - LiV_2O_5 . After drying at 70 °C, the δ - LiV_2O_5 powder was heat-treated at 300 °C for 3 h under vacuum in a Büchi furnace to form the distorted layered γ - LiV_2O_5 structure. The last step consists in extracting lithium ions from the interlayer spacing of γ - LiV_2O_5 by keeping the distorted γ -type host structure. This chemical oxidation reaction requires the use of the strong oxidizing agent NO_2BF_4 (molar ratio 1:4) in acetonitrile. The solution was stirred at room temperature for 4 h. The obtained powder was washed 4 times with acetonitrile and acetone and then dried at 80 °C. The powder color changed from dark green to orange, which confirms the complete delithiation of the product. Electrochemical titration using galvanostatic oxidation and chemical redox titration confirmed the 5 + oxidation state of vanadium in γ' - V_2O_5 .

2.2. Electrochemical tests

γ' - V_2O_5 positive electrodes were prepared by mixing 90 wt% of active material, 6 wt% polyvinylidene fluoride (PVDF, Kynar, HSV900) as a binder, 4 wt% carbon black (Ketjen Black International Co., Japan) as conductive agent dissolved in N-methyl-2-pyrrolidone (NMP, Sigma-Aldrich). The prepared slurry was casted on carbon paper (Alfa Aesar Co.), vacuum dried at 70 °C for 3 h and punched into disks of 8 mm in diameter. The mass loading of active material was around 6 mg cm^{-2} . Zinc foil (Goodfellow, USA) was used as both negative and reference electrodes. The electrolyte was prepared by dissolving 3.5 M $\text{ZnSO}_4 \cdot 7\text{H}_2\text{O}$ and 2.5 M Li_2SO_4 in distilled water and according to previous pH optimizations [31], the pH was adjusted to 4 by titration with 0.5 mol L^{-1} H_2SO_4 . Prepared electrolyte was bubbled with nitrogen gas (N_2) to remove dissolved oxygen. AGM (Absorptive Glass Mat NSG Corporation) was used as separator. The two-electrode cells were tested galvanostatically at various C rates (1C corresponds to 147 mA g^{-1}) and by cyclic voltammetry (sweep rate 0.2 mV s^{-1}), using a VMP3 potentiostat/galvanostat (Bio-Logic Science Instrument Co.). The tests temperature was controlled at 20 °C. All potentials are reported in V vs. Zn/Zn^{2+} . The structural investigation of the $\text{Zn}||\text{Li}_2\text{SO}_4\text{-ZnSO}_4||\gamma'$ - V_2O_5 system was investigated by using a two-electrode split cell (MTI company). The cells were discharged or charged to the required composition at C/5 rate (29.4 mA g^{-1}). Then after disassembling the cell, the positive electrodes were rinsed in distilled water in order to remove the traces of salt and separator, and then analyzed by XRD and Raman spectroscopy.

2.3. Characterizations

XRD measurements were carried out using a Panalytical X'pert pro diffractometer equipped with an X'celerator detector and a $\text{Co K}\alpha$ radiation (wavelength 1.7889 Å). All the diffraction patterns were collected with a 2θ step of 0.0167°. The Raman spectra were measured with a LaBRAM HR 800 (Jobin-Yvon-Horiba) Raman micro-spectrometer including Edge filters and equipped for signal

detection with a back illuminated charge coupled device detector (Spex CCD) cooled by Peltier effect to 200 K. A He:Ne laser (632.8 nm) was used as the excitation source. The spectra were measured in back-scattering geometry. The resolution was about 0.5 cm^{-1} . A 50X LWD objective was used to focus the laser light on sample surface to a spot size of $1\text{ }\mu\text{m}^2$. To avoid local heating of the sample, the power of the laser beam was adjusted to 0.2–0.5 mW with neutral filters of various optical densities. Raman spectra were recorded on ten different spots of each electrode to check the homogeneity. The pristine powder and the electrodes were characterized by scanning electron microscopy (SEM), Zeiss, Merlin-type microscope. Energy Dispersive X-ray spectroscopy (EDS) was applied to determine the elemental composition together with SEM with an accelerating voltage of 10–15 kV

3. Results and discussion

3.1. Structural characterization of γ' - V_2O_5

SEM micrographs of the as-synthesized γ' - V_2O_5 powder (Fig. 1) reveal a homogeneous grain size distribution made of porous aggregates of small platelets in the range 100–500 nm. The XRD pattern of the as-synthesized γ' - V_2O_5 powder is shown in Fig. 2a. All the reflection lines can be indexed in an orthorhombic symmetry (JCPDS Card No. 01–085–2422, $Pnma$ space group) leading to the following unit cell parameters: $a = 9.93(9)\text{ }\text{\AA}$, $b = 3.58(3)\text{ }\text{\AA}$, $c = 10.04(0)\text{ }\text{\AA}$ in agreement with literature data [41]. The Rietveld refinement of the XRD pattern (Fig. S1) confirms the presence of a pure and well-crystallized single phase. The layered structure of γ' - V_2O_5 is composed of infinite ribbons parallel to the b axis made of VO_5 edges-sharing distorted pyramids oriented alternatively up and down (inset in Fig. 2a). These ribbons are linked to each other along the a -direction by one pyramid corner oxygen forming puckered layers perpendicular to the c -axis. The mean crystallite size estimated from diffraction peaks width is 90–100 nm.

The Raman spectrum of γ' - V_2O_5 is shown in Fig. 2b. The projection of the γ' - V_2O_5 structure along the b -crystallographic direction showing all the V–O contacts in the two non-equivalent vanadium environments (V_a , V_b) is shown in inset of Fig. 2b. This Raman fingerprint fully agrees with previous study [38]. The whole vibrations of the chains are identified as follows: bands at 1037, 1021 and 1003 cm^{-1} correspond to the stretching modes of the shortest $V_a\text{--O}_{1a}$ and $V_b\text{--O}_{1b}$ bonds, bands at 752 and 603 cm^{-1} are related to the bond stretching vibrations localized within the $V_a\text{--O}_3\text{--}V_b$ bridges. The stretching modes of the $V_a\text{--O}_{2a}\text{--}V_a$ and $V_b\text{--O}_{2b}\text{--}V_b$ bridges forming the rails of the ladders are observed at 722 and 694 cm^{-1} . Modes involving the $V_a\text{--O}_{2a}$ and $V_b\text{--O}_{2b}$ ladder step

bonds (indicated by dashed line) are seen at 532 and 500 cm^{-1} . The lower frequency modes at 92, 126, 138, 153, 171, 190, 238, 266, 282, 299, 349 and 390 cm^{-1} correspond to the complex distortions of the V_2O_5 ladders [38].

3.2. Electrochemical study and structural mechanism in the 1.6 V–1.0 V potential range

The first cyclic voltammetric curve of γ' - V_2O_5 (black curve in Fig. 3a) indicates an electrochemical reaction characterized by two distinct redox processes. Indeed, two cathodic peaks are observed at 1.32 V and 1.22 V, with their corresponding reversible anodic peaks at 1.46 V and 1.31 V, respectively. The coulombic charge involved upon cathodic scan corresponds to $\approx 0.8\text{ F/mol}$ of oxide and the same amount of electricity is engaged during the reverse anodic process, showing the excellent reversibility of the electrochemical reaction. The first discharge–charge profile of γ' - V_2O_5 at C/5 rate in the 1.6 V–1.0 V potential range is shown in Fig. 3b. Similarly, the discharge curve exhibits two steps involving a total faradaic yield of 0.8 F mol^{-1} (specific capacity of 120 mAh g^{-1}). The voltage plateau at 1.38 V is related to the two sharp voltammetric peaks at 1.32/1.46 V and suggests a two-phase behavior, while the sloping curve centered near 1.27 V seems to indicate a single-phase redox process. A quantitative charge is achieved, with only 30 mV hysteresis between discharge and charge, i.e. half that observed for $\alpha\text{-V}_2\text{O}_5$. It is worth noting the higher operating voltage ($\approx 200\text{ mV}$) of γ' - V_2O_5 compared with $\alpha\text{-V}_2\text{O}_5$ (red dotted curves in Fig. 3), as observed in organic lithiated electrolyte [40], which outlines the interest of the puckered polymorph as cathode material in aqueous electrolyte. In addition, the present electrochemical fingerprint of γ' - V_2O_5 closely resembles that known in non-aqueous lithiated electrolyte [40]. This suggests a similar reaction mechanism is involved in binary $\text{Li}_2\text{SO}_4/\text{ZnSO}_4$ electrolyte.

To address this issue, we have investigated the structural response of γ' - V_2O_5 during the first discharge–charge cycle at C/5 in the 1.6 V–1.0 V potential range, using XRD and Raman spectroscopy. The XRD patterns of reduced electrodes as a function of the faradaic yield x (in F mol^{-1}), $0 \leq x \leq 0.72$, are shown in Fig. 4. The XRD pattern of the pristine electrode ($x = 0$) shows the typical fingerprint of orthorhombic γ' - V_2O_5 ($Pnma$ space group) with the unit cell parameters of the pristine powder ($a = 9.94\text{ }\text{\AA}$, $b = 3.58\text{ }\text{\AA}$, $c = 10.04\text{ }\text{\AA}$). From the very first reduction rate ($x = 0.1$), a new set of 002, 102, 103 and 214 diffraction lines are detected at 19.95 , 22.5 , 32.0 and 55.3° , respectively, that coexist with those of the initial γ' - V_2O_5 material. This new set of lines is indexed in an orthorhombic symmetry ($Pnma$ space group) and

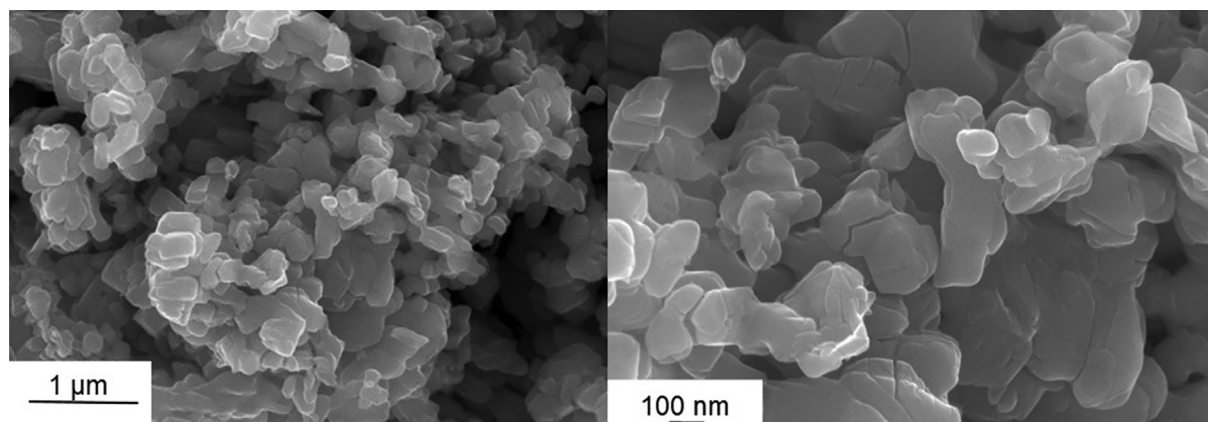


Fig. 1. SEM micrographs of as-prepared γ' - V_2O_5 powder.

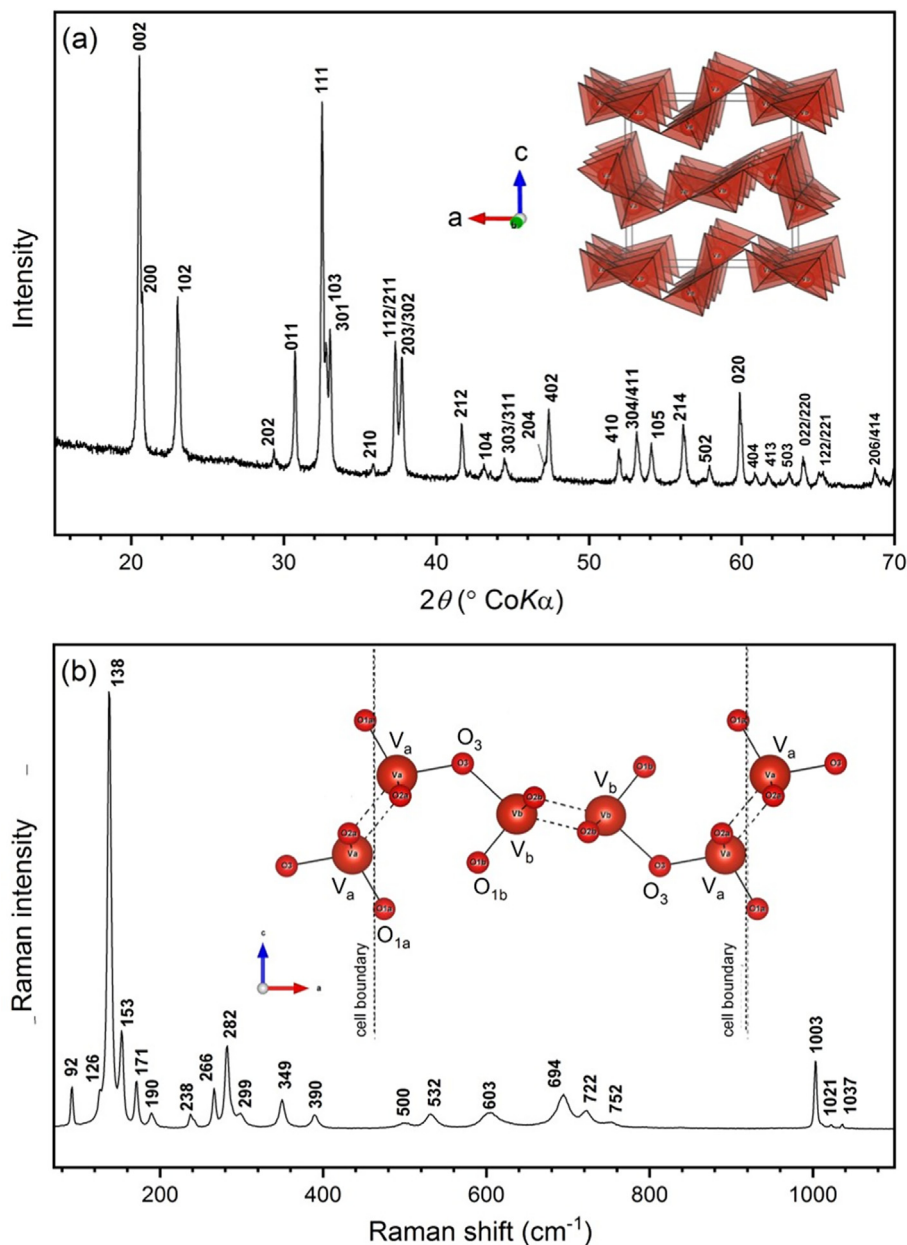


Fig. 2. (a) X-ray diffraction pattern of γ' - V_2O_5 powder. Inset: crystal structure of γ' - V_2O_5 . (b) Raman spectrum of γ' - V_2O_5 powder. Inset: projection of the structure of γ' - V_2O_5 along the b -crystallographic direction showing all the V-O contacts. Dashed lines show V-O interchain contacts (ladder-step bonds).

reveals the emergence of a lithiated $\gamma\text{-Li}_x\text{V}_2\text{O}_5$ phase. The same comment can be made for $x = 0.2$, with the new lines increasing at the expense of those related to the pristine compound. The shifts toward lower 2θ values for the 002, 102, 103, 104, 204, 105 and 214 reflections and to higher 2θ one for the 200 line clearly indicate an expansion in the c interlayer distance and a contraction in the a parameter, respectively. Indeed, the unit cell parameters calculated for the reduced $\gamma\text{-Li}_x\text{V}_2\text{O}_5$ phases ($x = 0.1$; 0.2) are $a = 9.83$ Å, $b = 3.59$ Å, $c = 10.34$ Å. From $x = 0.35$, this trend is maintained: all the diffraction lines belong to the lithiated phase with a continuous shift of the 002 and 200 reflection lines toward higher and lower 2θ values, respectively, indicating a continuous expansion of the c interlayer parameter and shrinkage in the a parameter. In the $0.35 \leq x \leq 0.72$ composition range, the diffraction patterns show the existence of a single phase with cell parameters changing linearly with the depth of discharge. The unit cell

parameters for the fully reduced $\gamma\text{-Li}_{0.72}\text{V}_2\text{O}_5$ electrode ($a = 9.69$ Å, $b = 3.60$ Å, $c = 10.67$ Å) match very well those reported for $\gamma\text{-Li}_1\text{V}_2\text{O}_5$ formed during electrochemical lithiation of $\gamma'\text{-V}_2\text{O}_5$ in non-aqueous lithiated electrolyte ($a = 9.71$ Å, $b = 3.61$ Å and $c = 10.67$ Å) [40]. It is also worth noting the similarity of the unit cell variations vs. composition in aqueous and non-aqueous electrolytes [40]. Such findings are well consistent with a pure Li insertion reaction and enable us to rebut the hypothesis of water molecules, zinc or proton insertion into the $\gamma'\text{-V}_2\text{O}_5$ host lattice.

The detailed lattice parameters evolutions as a function of x in $\gamma\text{-Li}_x\text{V}_2\text{O}_5$ during the first discharge ($0 \leq x \leq 0.72$) are depicted in Fig. 5. Two main domains clearly appear. First, a diphasic region for $0 < x < 0.35$ where $\gamma'\text{-V}_2\text{O}_5$ coexists with a lithiated phase $\gamma\text{-Li}_x\text{V}_2\text{O}_5$ characterized by a slight interlayer expansion of 3% (Fig. 5c) and a very low contraction of 1% along the a direction (Fig. 5a). On further reduction ($0.35 \leq x \leq 0.72$), a single-phase

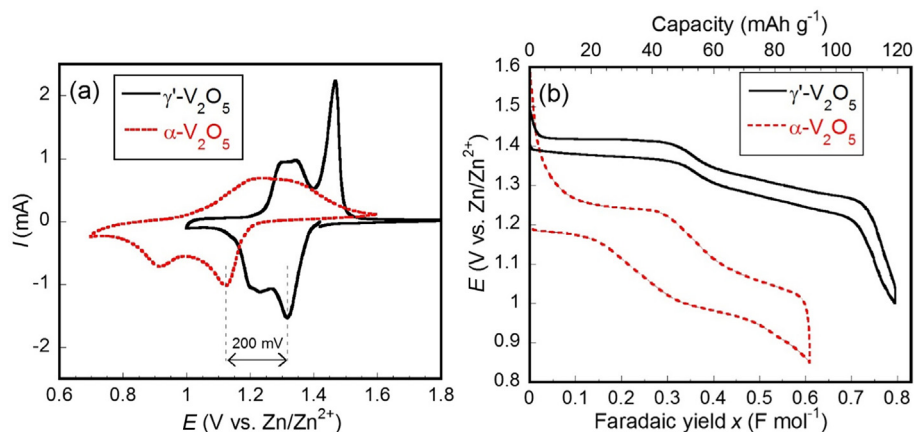


Fig. 3. (a) Cyclic voltammograms (scanning rate 0.2 mV s^{-1}) and (b) first galvanostatic cycles at C/5 rate of γ' - V_2O_5 (black curves) and α - V_2O_5 (red dotted curves). (For interpretation of the references to colour in this figure legend, the reader is referred to the web version of this article.)

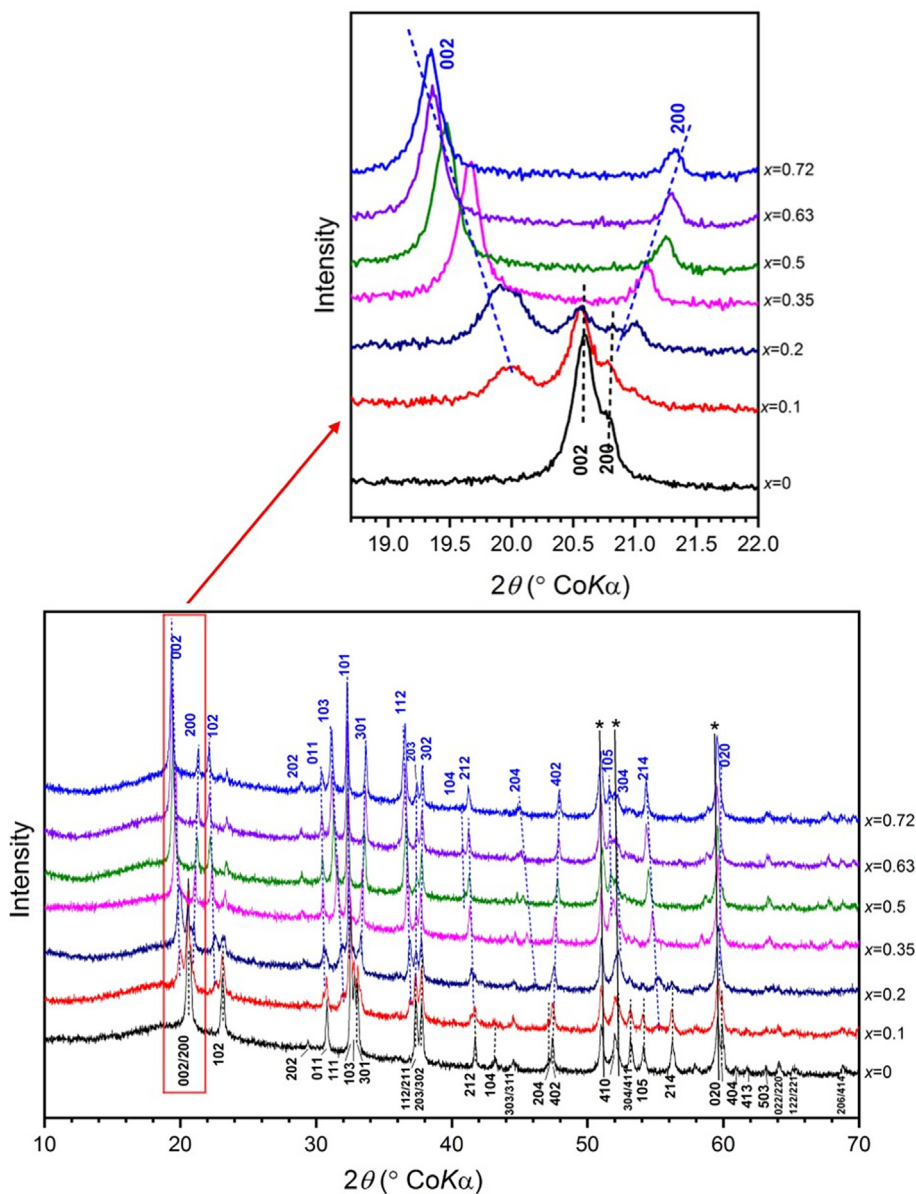


Fig. 4. X-ray diffraction patterns of γ' - V_2O_5 electrodes during the first discharge at C/5 as a function of the faradaic yield x (F mol^{-1}), $0 \leq x \leq 0.72$. *: sample holder (stainless steel) reflections. 1.6 V–1.0 V voltage window.

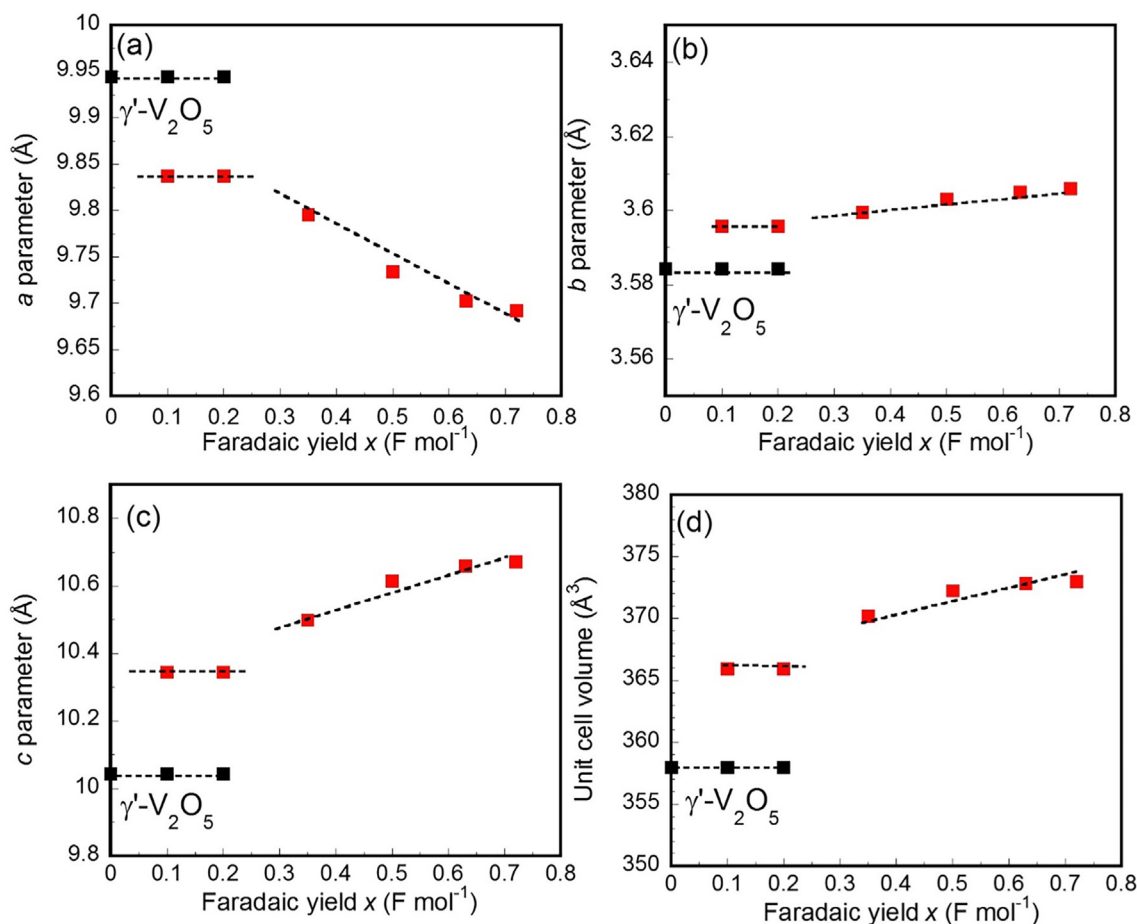


Fig. 5. Evolution of the unit cell parameters a , b , c and unit cell volume of γ' -V₂O₅ electrodes during the first discharge at C/5 as a function of the faradaic yield x (F mol⁻¹). $0 \leq x \leq 0.72$. Black squares: γ' -V₂O₅; red squares: new phase.

region is evidenced with a negligible b variation of 0.3% (Fig. 5b), a minor contraction in a parameter (1%) and a moderate expansion in c parameter (3%), showing the puckered layered arrangement of γ' -V₂O₅ is not altered upon Li insertion. The small change in b parameter is consistent with a Li diffusion occurring along the b direction.

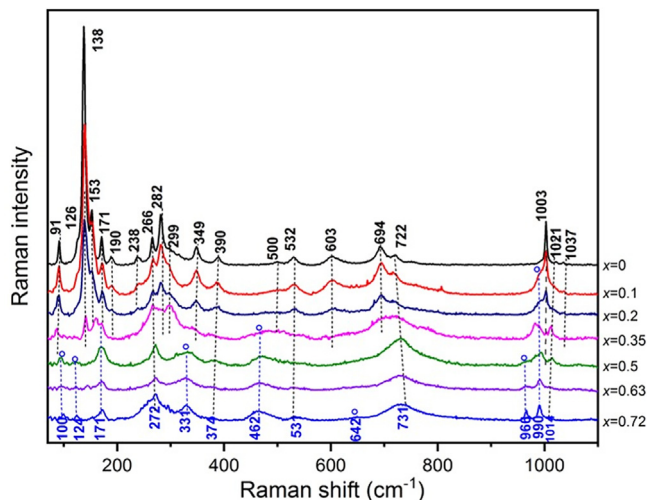


Fig. 6. Raman spectra of V₂O₅ electrodes during the first discharge at C/5 as a function of the faradaic yield x (F mol⁻¹). $0 \leq x \leq 0.72$. 1.6 V–1.0 V voltage window.

The Raman spectra of reduced electrodes as a function of the faradaic yield x , $0 \leq x \leq 0.72$, are gathered in Fig. 6. As the reduction rate increases in the $0 < x \leq 0.5$ composition range, the Raman spectra undergo progressive changes in intensity or position while new bands are observed. These changes can be depicted as follows: the relative intensity of bands belonging to the pristine γ' -V₂O₅ material, at 91, 138, 153, 190, 238, 282, 299, 349, 500, 603, 694, 1003 and 1037 cm⁻¹ gradually decreases up to their total disappearance for $x = 0.5$. At the same time, new peaks (indicated by blue open circles) belonging to the electroformed phase are detected, with increasing relative intensity as the reduction rate increases: at 990 cm⁻¹ (from $x = 0.1$), 462 cm⁻¹ (from $x = 0.35$), 100, 124, 331 and 966 cm⁻¹ (from $x = 0.5$). Finally, three bands belonging to both systems are kept all along the reduction process but undergo continuous wavenumber shifts: 266 to 272 cm⁻¹, 722 to 731 cm⁻¹, 1021 to 1014 cm⁻¹. For $x = 0.35$, the Raman spectrum is modified, showing mostly the bands of the electroformed phase with only traces of the pristine oxide through the presence of low features at 138, 159, 171, 266, 282, 299 and 694 cm⁻¹. This is due to the high Raman scattering cross section of γ' -V₂O₅ [38]. For $x = 0.5$, the Raman spectrum is characteristic of the pure new system with bands at 100, 124, 171, 272, 331, 374, 462, 531, 642, 731, 966, 990 and 1014 cm⁻¹. For $0.5 \leq x \leq 0.72$, the fingerprint of the new phase dominates the Raman spectrum. An ultimate feature appears at 642 cm⁻¹ for the fully reduced sample while the 966 cm⁻¹ peak increases in intensity. Such trends indicate the existence of a diphasic region in the composition range $0 < x < 0.35$, in which the pristine γ' -V₂O₅ phase disappears progressively while a

new system emerges, followed by a single-phase region of the pure new system for $x \geq 0.35$. The Raman fingerprint of the electroformed phase matches perfectly that reported for γ - $\text{Li}_x\text{V}_2\text{O}_5$ formed during electrochemical lithiation of γ' - V_2O_5 in non-aqueous lithiated electrolyte [40] as well as chemically synthesized γ - LiV_2O_5 [43]. The whole assignment of the Raman spectrum of the γ - LiV_2O_5 bronze can be found in [43]. Examination of the charged electrodes by XRD and Raman spectroscopy (Fig. S2) shows the complete restoration of the γ' - V_2O_5 host lattice after one discharge–charge cycle, both at the long-range order and atomic scale, with no extra peak or band related to the presence of another phase. Such findings explain the good electrochemical reversibility displayed in Fig. 3.

These structural data drawn from XRD and Raman spectroscopy reveal that γ' - V_2O_5 electrodes selectively intercalate Li^+ ions upon discharge in the 1.6 V–1.0 V potential range. The nature of structural changes of the γ' - V_2O_5 host lattice as well their magnitude exclude any participation of proton, zinc ions or water molecules. Instead, we highlight a reversible reaction mechanism, very similar to that reported in non-aqueous electrolyte [40], involving a diphasic domain for $0 < x < 0.35$ with coexistence of γ' - V_2O_5 and γ - $\text{Li}_{\approx 0.3}\text{V}_2\text{O}_5$, followed by a solid solution region γ - $\text{Li}_x\text{V}_2\text{O}_5$ for $0.35 \leq x \leq 0.72$.

Preliminary rate capability study indicates a promising behaviour since the specific capacity is little affected with increasing C rate (Fig. S3). Indeed the discharge capacity decreases from 120 mAh g^{-1} at C/5 to 105 and 95 mAh g^{-1} at 1C and 5C, respectively. In addition, the low hysteresis achieved between the charge and discharge, 60 mV at 1C and 100 mV at 5C, are quite remarkable. In spite of these promising performances, electrochemical experiments in the 1.6 V–1.0 V voltage window do not allow to reach a specific capacity larger than 120 mAh g^{-1} , value that is much less than those usually reported for vanadium-based cathode materials [7–29]. In order to increase the available capacity, we have extended the voltage window by lowering the cutoff voltage to 0.7 V and investigated the electrochemical properties and related structural changes of γ' - V_2O_5 in this enlarged voltage range.

3.3. Electrochemical study and structural mechanism in the enlarged 1.6 V–0.7 V potential range

The successive discharge–charge cycles of γ' - V_2O_5 at 1C rate in the 1.6 V–0.7 V window are displayed in Fig. 7a. The first cycle exhibits the typical reversible fingerprint of γ' - V_2O_5 with two high voltage discharge steps at 1.36 V and 1.25 V followed by a potential drop, a total faradaic yield of 0.96 F mol^{-1} being involved. A careful examination of the first cycle shows however the presence of an additional ill-defined step near 0.9 V. The contribution of this lower voltage contribution increases with cycles, from about 0.13 F mol^{-1} for the first cycle to 0.3 F mol^{-1} for the second one and 0.65 F mol^{-1} for cycle 4, the total discharge capacity increasing significantly from 143 to 187 mAh g^{-1} . At the same time, the contribution of the two high voltage steps decreases progressively to completely disappear for cycle 10, which exhibits a sloping voltage profile involving a capacity value of 185 mAh g^{-1} .

Cycling tests (Fig. 7b) show a remarkable capacity retention of 97% at least over 100 cycles. A similar activation process is observed at C/5 rate (Fig. S4). Indeed, the capacity increases from 140 to 240 mAh g^{-1} along the ten first cycles, then stabilizes at 240 mAh g^{-1} over at least 50 cycles. This high stable capacity of 240 mAh g^{-1} competes very well with previous values reported for V_2O_5 using only a Zn salt [23,26,28]. It is noteworthy the reproducible discharge profile displayed from cycle 10, with completely superimposed reversible charge process, does not exhibit anymore the typical Li insertion steps of γ' - V_2O_5 . This suggests the lowering

of the voltage window at 0.7 V induces a strong structural rearrangement. The redox process below 1 V involves a capacity that increases from 20 to 90 mAh g^{-1} during the five first cycles at 1C while the capacity contribution related to Li insertion in the upper voltage window (1.6 V–1.0 V) decreases from 123 to 97 mAh g^{-1} . This trend is then confirmed up to cycle 10 with the 1.6 V–1.0 V contribution still decreasing to only 50 mAh g^{-1} for the benefit of the low voltage part that reaches 120 mAh g^{-1} after the activation process. Since further lithiation is expected to occur around 1 V lower than the high voltage steps, i.e. at about 0.4 V [40], Zn^{2+} and/or proton insertion is probably involved below 1 V, leading to a progressive capacity gain and change in the discharge–charge profile during the first activation cycles.

The rate capability behaviour of γ' - V_2O_5 in the 1.6 V–0.7 V window has been investigated in the C/5–10C range, after performing an activation process of 10 cycles at C/5 (Fig. 7c and S5). Interesting capacities are reached: the stabilized capacity of 235 mAh g^{-1} at C/5 decreases moderately to 190 mAh g^{-1} at 1C, 170 mAh g^{-1} at 2C, still 130 mAh g^{-1} at 5C and 65 mAh g^{-1} at 10C. Even after sustaining high 10C rate, the cathode material is not damaged since the high capacity of about 200 mAh g^{-1} is recovered at 1C (Fig. 7c). Far superior cycling performance are found here for γ' - V_2O_5 compared to those recently reported for the conventional α - V_2O_5 form in the same binary Li/Zn electrolyte and same voltage range. Indeed, a stable capacity of 80 mAh g^{-1} was achieved upon cycling α - V_2O_5 at 1C [37] against 180–190 mAh g^{-1} here for γ' - V_2O_5 . This huge improvement in capacity value shows the porous puckered polymorph γ' - V_2O_5 exhibits a more suitable structure towards zinc insertion, promoting then the electrochemical reaction. The beneficial effect of the binary electrolyte on electrochemical performance of γ' - V_2O_5 in a Zn battery is highlighted in Fig. S6 showing a sharp capacity decrease in the pure ZnSO_4 electrolyte, with an available discharge capacity of only 50 mAh g^{-1} after 50 cycles while a fast capacity stabilization around 240 mAh g^{-1} over at least 50 cycles is observed using our hybrid electrolyte (Fig. 7b and S4).

The present capacities compete also well with those reported for α - V_2O_5 in binary $\text{Zn}(\text{CF}_3\text{SO}_3)_2$ -LiTFSI “water in salt” electrolyte in the wider 1.6 V–0.3 V voltage window [23]. A detailed comparison of γ' - V_2O_5 cycling behaviour with α - V_2O_5 properties is a difficult task. Indeed, the latter has been mainly investigated in Zn (CF_3SO_3)₂ or ZnSO_4 aqueous electrolytes, in various and larger cycling limits, using different electrode technologies and material morphologies, which may explain that scattered capacity values and occasionally contradictory data can be found in the range 200–400 mAh g^{-1} [24–26,28,29]. For instance, a comparable capacity of 240 mAh g^{-1} was reported in 3 M ZnSO_4 in the wide 1.4 V–0.4 V potential window [26] while higher values of 300–400 mAh g^{-1} were achieved in the 1.6 V–0.2/0.5 V potential range using porous nanofibers [28], ball-milled [25] and α - V_2O_5 microspheres [24]. Outstanding values of 400–500 mAh g^{-1} can be reached with ALD-deposited V_2O_5 layers on carbon paper but the mass loading is limited to 0.1 mg cm^{-2} [27].

To understand the peculiar electrochemical storage mechanism underlined by the discharge–charge profiles changes, we have carried out a structural study to provide information on the nature of the electroformed phases upon cycling of γ' - V_2O_5 in the 1.6 V–0.7 V range. As shown by the XRD patterns in Fig. S7, the γ -type structure of the initial host lattice is kept on first discharge at 0.7 V. The shift toward lower 2θ of the 001 reflections (Fig. S7a) for the electrode discharged at 0.7 V reveals once again an expanded c interlayer parameter (10.67 Å vs. 10.03 Å for the initial material). On the other hand, the Raman spectrum of the discharged electrode displays also the characteristic bands of the lithiated γ - LiV_2O_5 structure (Fig. S7b). After one cycle, the initial structure of γ' - V_2O_5 is completely restored, both at the long range

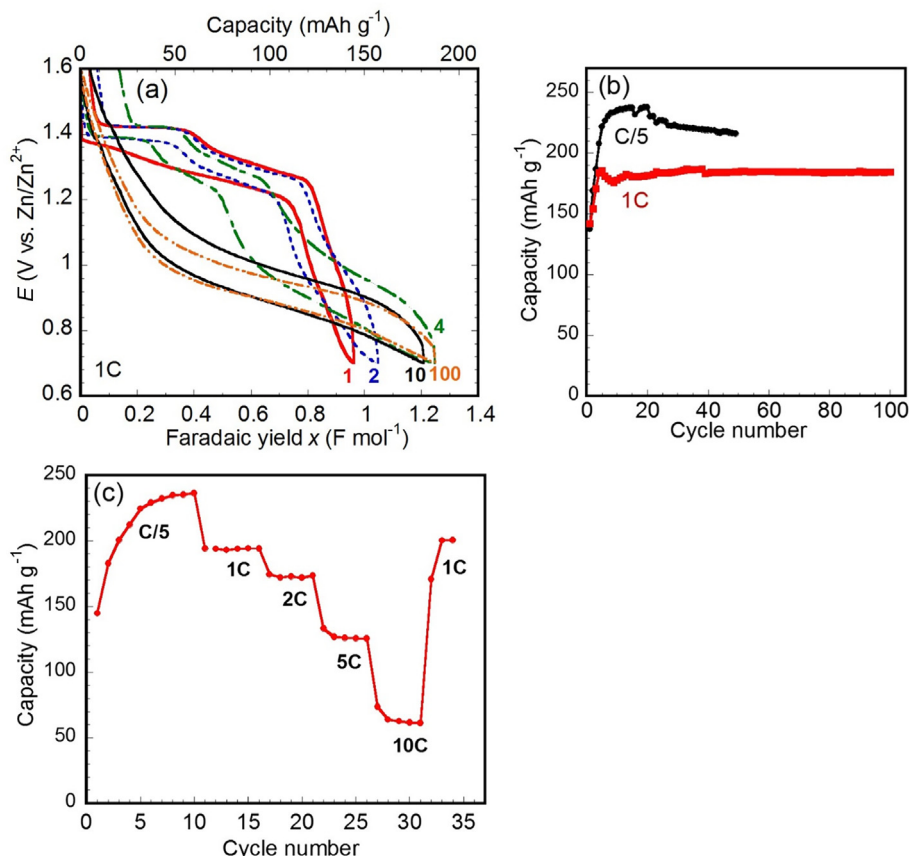


Fig. 7. Electrochemical performance of γ' - V_2O_5 in the extended 1.6 V–0.7 V voltage window: (a) discharge-charge cycles at 1C rate; (b) evolution of the specific capacity as a function of the number of cycles at C/5 and 1C rates; (c) rate capability study.

order (Fig. S7a) and at the scale of the chemical bond (Fig. S7b). Furthermore, no extra peak or band related to the presence of another phase is detected. Such observations are consistent with the high electrochemical reversibility exhibited by the first cycle.

However, upon successive cycling tests, the structural analysis indicates the occurrence of an increasing disordering process and suggests a deep structural rearrangement upon cycling (Fig. 8), in line with the changes observed in the cycling curves profiles (Fig. 7a and S4). Indeed, the XRD patterns (Fig. 8a) and Raman spectra (Fig. 8b) of discharged electrodes show a huge peak intensity decrease and Raman bands broadening with increasing cycling. This phenomenon takes place rapidly as only the 002, 102, 101, 301, 112 reflection lines of γ - $\text{Li}_x\text{V}_2\text{O}_5$ are still visible for the 6th discharge (Fig. 8a) whereas none of them can be detected for the 50th discharge. The presence of a new diffraction peak at 14.23° after 50 cycles (indicated by a cross in Fig. 8a) points to the formation of a new ill-crystallized phase that could correspond to trigonal $\text{Zn}_3\text{V}_2\text{O}_7(\text{OH})_2 \cdot 2\text{H}_2\text{O}$ pyrovanadate (ZVO, space group $P\bar{3}m1$, JCPDS 50-0570) [44,45]. Similar to V_2O_5 , ZVO phase exhibits a layered structure built of zinc oxide layers separated by V–O–V pillars ($\text{V}_2\text{O}_7^{4-}$ groups), the water molecules randomly filling the large cavities [44,45]. The characteristic peak at 14.23° observed for the 50th discharge would then correspond to the most intense 001 reflection of ZVO, giving an interlayer c parameter of 7.3 Å, in good accord with the values reported in previous studies [16,44–46].

The Raman spectra of discharged electrodes also point to a significant amorphization process with cycling (Fig. 8b). While the typical fingerprint of γ - LiV_2O_5 is nicely distinguished for the 4th discharge, a low intensity spectrum is displayed for the 6th dis-

charge, with broad features centered at 460, 530, 730 and 996 cm^{-1} indicating the presence of disordered γ - LiV_2O_5 . For the 50th discharge, the Raman spectrum still points to the presence γ - LiV_2O_5 (characteristic peaks at 460, 964 and 996 cm^{-1} indicated in blue color), however coexisting with a new phase giving well visible bands at 770 and 860 cm^{-1} . Such phase is likely to correspond to ZVO, characterized by Raman modes at 482, 791 and 876 cm^{-1} [46]. Hence, the bands observed at 770 and 860 cm^{-1} after 50 cycles (see crosses in Fig. 8b) probably correspond to the most intense V–O stretching vibrations localized in VO_4 and VO_3 polyhedra in ZVO. The lower intensity Zn–O vibration expected at 482 cm^{-1} is barely visible in the wide intense 460 cm^{-1} broad feature of A_g symmetry assigned to the stretching $\nu(\text{V}_b\text{O}_3)$ mode localized within the $\text{V}_a\text{O}_3\text{V}_b$ bridges in γ - $\text{Li}_x\text{V}_2\text{O}_5$ [43].

The increasing disordering process upon cycling is also observable on the charged electrodes. Indeed, the typical hkl reflections of γ' - V_2O_5 have practically disappeared after 6 cycles and are no more discernable after 50 cycles (Fig. S8a) while the occurrence of electroformed ZVO manifests itself again through the observation of a 001 reflection at 14.4° . At the level of the chemical bond, the well-defined Raman bands of γ' - V_2O_5 merge into broad bands after 6 cycles, located at ca. 150, 300, 750 and 1000 cm^{-1} (Fig. S8b) while new components at 480 and 770 cm^{-1} (indicated by crosses) arise from cycle 6, revealing the presence of ZVO phase coexisting with disordered γ' - V_2O_5 .

This electrochemical and structural study suggests deep structural changes take place upon cycling γ' - V_2O_5 in the 1.6 V–0.7 V voltage range. While an exclusive Li insertion process is clearly demonstrated when the discharge is limited to 1 V, another mechanism responsible for a fast disordering process and involving Zn

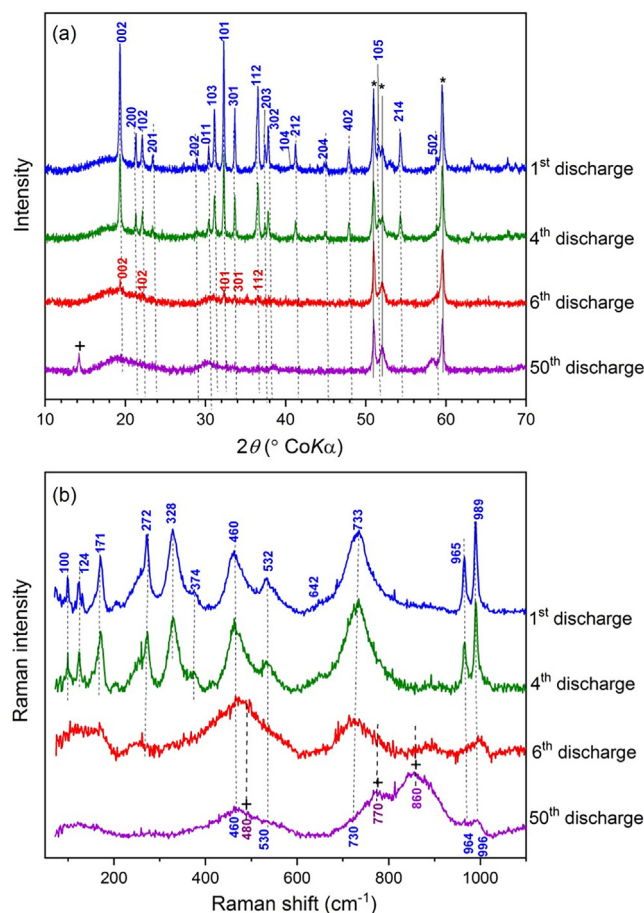
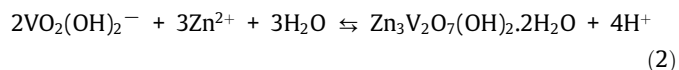
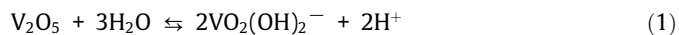


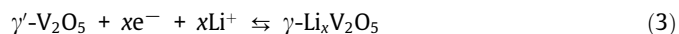
Fig. 8. (a) XRD patterns and (b) Raman spectra of γ' -V₂O₅ discharged electrodes upon cycling. *: sample holder (stainless steel) reflections. +: new phase. 1C rate. 1.6 V–0.7 V voltage window.

participation is observed in the lower 1 V–0.7 V voltage range. XRD and Raman analysis both converge toward the formation of ZVO as new electroactive phase responsible for the capacity gain, the high capacity and the excellent cyclability highlighted in this work. This gradual phase transformation from γ' -V₂O₅ to ZVO is probably promoted by a chemical reaction between the positive electrode and the aqueous hybrid electrolyte according to Eqs. (1) and (2) [27]:

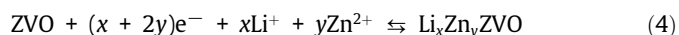


Hence, the mechanism involved during discharge–charge in the present binary electrolyte is illustrated in Eqs. (3) and (4):

In the 1.6 V – 1.0 V voltage range ($x < 1$):



In the 1 V–0.7 V voltage range (after activation):



Previous works have reported ZVO as promising intercalation cathode for aqueous ZIB [16] and non-aqueous Li-ion battery [46]. Such findings are ascribed to the open framework with large interlayer spacing of ZVO (0.74 nm vs 0.43 nm for hydrated ionic radius of Zn²⁺), providing an ideal pathway for guest species intercalation.

Table 1

Zn/V ratios determined from EDS in discharged γ' -V₂O₅ electrodes at 0.7 V. Cycle rate 1C.

Discharge number	Zn/V
1	0.16
4	0.27
6	0.51
50	0.62

Even when all structural data on V₂O₅ derived electrodes deal with cycling properties obtained in wider voltage ranges using a lower cutoff voltage (0.2 V–0.4 V) and only a Zn salt (3 M ZnSO₄ or Zn(CF₃SO₃)₂), some common features exist with the present study. Indeed, a phase transformation is often reported upon successive discharge–charge cycles involving the hydrated layered phases H₂V₃O₈ [26] or Zn_xV₂O₅ · nH₂O [25] while other studies indicate the predominant role of Zn₃V₂O₇(OH)₂ · 2H₂O [27,28]. The present structural analysis clearly demonstrates a fast transformation of γ' -V₂O₅ from the first cycle. XRD and Raman data show a more complex mechanism than in pure Zn based electrolytes since Li ions can still participate to the electrochemical process of layered ZVO phases whatever their composition. However, the active material obtained after capacity stabilization is made of disordered γ' -V₂O₅ and ZVO. It can be argued that longer cycling experiments would allow a complete conversion of the initial crystalline γ' -V₂O₅ phase into ZVO.

Additional supporting evidence to the phase transformation is provided by EDS analysis performed for electrodes discharged to 0.7 V (1st, 4th, 6th and 50th discharge). Table 1 shows that the discharged product continuously enriches itself with Zn ions with cycling, as revealed by the significant increase of the Zn/V ratio. Such a finding supports a phase transformation from γ' -V₂O₅ to ZVO, as recently evidenced in 3 M Zn(CF₃SO₃)₂ electrolyte for Atomic Layer Deposited derived α -V₂O₅ [27] and α -V₂O₅ nanofibers [28]. The maximum Zn/V value of 0.62 associated to a faradaic yield of 1.2 e[−]/mol of V₂O₅ discards a pure Zn insertion reaction leading to the Zn_xV₂O₅ bronze. Moreover, this value does not meet either the expected Zn/V ratio of 1.5 in ZVO, which can be understood assuming the coexistence of disordered γ' -V₂O₅ with ZVO in the electrodes, in which Li ions can still be reversibly inserted.

4. Conclusions

In this work, we present the layered-puckered γ' -V₂O₅ as a prospective cathode for zinc-ion batteries in a binary 3.5 M ZnSO₄ + 2.5 M Li₂SO₄ electrolyte. After an activation process of a few cycles, high and stable capacities of 240 mAh g^{−1} and 190 mAh g^{−1} are achieved in the 1.6 V–0.7 V potential window at C/5 and 1C rate, respectively. These capacities outperform those reported for the conventional α -V₂O₅ oxide in the same electrolyte. The detailed structural evolution during first discharge–charge and subsequent cycling in two different voltage ranges (1.6 V–1.0 V and 1.6 V–0.7 V) is investigated using XRD and Raman spectroscopy. We show the occurrence of selective lithium intercalation in the 1.6 V–1.0 V voltage window, with a reversible exchange of 0.8 Li⁺ in γ' -V₂O₅ inducing the same structural response as the one reported in lithiated organic electrolyte while a concurrent reaction involving zinc ions takes place concomitantly in the extended 1.6 V–0.7 V range.

A gradual phase transformation from γ' -V₂O₅ to zinc pyrovandate Zn₃V₂O₇(OH)₂ · 2H₂O during cycling is strongly supported by XRD, Raman and EDS analysis. This work highlights the benefit provided by the peculiar layered-puckered γ' -V₂O₅ compared to the conventional α -V₂O₅ oxide, with a huge improvement of capac-

ity of 240 mAh g⁻¹ vs 80 mAh g⁻¹ at C/5 in the same voltage window. Further optimization of cycling properties are under investigation by lowering the cut-off voltage to 0.3 V.

Declaration of Competing Interest

The authors declare that they have no known competing financial interests or personal relationships that could have appeared to influence the work reported in this paper.

Acknowledgments

One of the authors wishes to thank the Ministry of Education and Science of Kazakhstan (grant number AP05136016-ZRABS), French Embassy in Astana, Kazakhstan and Campus France for financial support. All the authors thank Dr. Nicolas Emery (ICMPE-CNRS) for assistance in refinement of XRD data.

Appendix A. Supplementary data

Supplementary data to this article can be found online at <https://doi.org/10.1016/j.jechem.2021.01.042>.

References

- [1] D. Kundu, B.D. Adams, V. Duffort, S.H. Vajargah, L.F. Nazar, *Nat. Energy* 1 (2016) 16119.
- [2] H. Pan, Y. Shao, P. Yan, Y. Cheng, K.S. Han, Z. Nie, C. Wang, J. Yang, X. Li, P. Bhattacharya, *Nat. Energy* 1 (2016) 16039.
- [3] F. Wan, L. Zhang, X. Dai, X. Wang, Z. Niu, J. Chen, *Nat. Commun.* 9 (2018) 1656.
- [4] A. Konarov, N. Voronina, J.H. Jo, Z. Bakenov, Y.-K. Sun, S.-T. Myung, *ACS Energy Lett.* 3 (2018) 2620–2640.
- [5] J. Ming, J. Guo, C. Xia, W. Wang, H.N. Alshareef, *Mater. Sci. Eng.: R: Reports* 135 (2019) 58–84.
- [6] G. Fang, J. Zhou, A. Pan, S. Liang, *ACS Energy Lett.* 3 (2018) 2480–2501.
- [7] M. Yan, P. He, Y. Chen, S. Wang, Q. Wei, K. Zhao, X. Xu, Q. An, Y. Shuang, Y. Shao, *Adv. Mater.* 30 (2018) 1703725.
- [8] Y. Li, P. Xu, J. Jiang, J. Yao, B. Huang, J. Yang, *Mater. Today Commun.* (2020) 101849.
- [9] P. He, Y. Quan, X. Xu, M. Yan, W. Yang, Q. An, L. He, L. Mai, *Small* 13 (2017) 1702551.
- [10] T. Wei, Q. Li, G. Yang, C. Wang, *Electrochim. Acta* 287 (2018) 60–67.
- [11] F. Ming, H. Liang, Y. Lei, S. Kandambeth, M. Eddaoudi, H.N. Alshareef, *ACS Energy Lett.* 3 (2018) 2602–2609.
- [12] B. Sambandam, V. Soundharajan, S. Kim, M.H. Alfaruqi, J. Jo, S. Kim, V. Mathew, Y.-K. Sun, J. Kim, *J. Mater. Chem. A* 6 (2018) 15530–15539.
- [13] C. Xia, J. Guo, P. Li, X. Zhang, H.N. Alshareef, *Angew. Chem. Int. Ed.* 57 (2018) 3943–3948.
- [14] V. Soundharajan, B. Sambandam, S. Kim, M.H. Alfaruqi, D.Y. Putro, J. Jo, S. Kim, V. Mathew, Y.-K. Sun, J. Kim, *Nano Lett.* 18 (2018) 2402–2410.
- [15] Z. Peng, Q. Wei, S. Tan, P. He, W. Luo, Q. An, L. Mai, *Chem. Commun.* 54 (2018) 4041–4044.
- [16] C. Xia, J. Guo, Y. Lei, H. Liang, C. Zhao, H.N. Alshareef, *Adv. Mater.* 30 (2017) 1705580.
- [17] J. Li, K. McColl, X. Lu, S. Sathasivam, H. Dong, L. Kang, Z. Li, S. Zhao, A.G. Kafizas, R. Wang, D.J.L. Brett, P.R. Shearing, F. Corà, G. He, C.J. Carmalt, I.P. Parkin, *Adv. Energy Mater.* 10 (2020) 2000058.
- [18] T. Wei, Q. Li, G. Yang, C. Wang, *J. Mater. Chem. A* 6 (2018) 8006–8012.
- [19] B. Sambandam, V. Soundharajan, S. Kim, M.H. Alfaruqi, J. Jo, S. Kim, V. Mathew, Y.-K. Sun, J. Kim, *J. Mater. Chem. A* 6 (2018) 3850–3856.
- [20] G. Yang, T. Wei, C. Wang, *ACS Appl. Mater. Interfaces* 10 (2018) 35079–35089.
- [21] B. Tang, G. Fang, J. Zhou, L. Wang, Y. Lei, C. Wang, T. Lin, Y. Tang, S. Liang, *Nano Energy* 51 (2018) 579–587.
- [22] M.H. Alfaruqi, V. Mathew, J. Song, S. Kim, S. Islam, D.T. Pham, J. Jo, S. Kim, J.P. Baboo, Z. Xiu, *Chem. Mater.* 29 (2017) 1684–1694.
- [23] P. Hu, M. Yan, T. Zhu, X. Wang, X. Wei, J. Li, L. Zhou, Z. Li, L. Chen, L. Mai, *ACS Appl. Mater. Interfaces* 9 (2017) 42717–42722.
- [24] P. Hu, T. Zhu, J. Ma, C. Cai, G. Hu, X. Wang, Z. Liu, L. Zhou, L. Mai, *Chem. Commun.* 55 (2019) 8486–8489.
- [25] N. Zhang, Y. Dong, M. Jia, X. Bian, Y. Wang, M. Qiu, J. Xu, Y. Liu, L. Jiao, F. Cheng, *ACS Energy Lett.* 3 (2018) 1366–1372.
- [26] J. Zhou, L. Shan, Z. Wu, X. Guo, G. Fang, S. Liang, *Chem. Commun.* 54 (2018) 4457–4460.
- [27] Y. Lu, T. Zhu, W. van den Bergh, M. Stefik, K. Huang, *Angew. Chem. Int. Ed.* 59 (2020) 17004–17011.
- [28] X. Chen, L. Wang, H. Li, F. Cheng, J. Chen, *J. Energy Chem.* 38 (2019) 20–25.
- [29] W. Zhou, J. Chen, M. Chen, X. Xu, Q. Tian, J. Xu, C.P. Wong, *RSC Adv.* 9 (2019) 30556–30564.
- [30] J. Yan, J. Wang, H. Liu, Z. Bakenov, D. Gosselink, P. Chen, *J. Power Sources* 216 (2012) 222–226.
- [31] N. Yesibolati, N. Umirov, A. Koishybaya, M. Omarova, I. Kurmanbayeva, Y. Zhang, Y. Zhao, Z. Bakenov, *Electrochim. Acta* 152 (2014) 505–511.
- [32] G. Yuan, J. Bai, T.N.L. Doan, P. Chen, *Mater. Lett.* 158 (2015) 248–251.
- [33] H.B. Zhao, C.J. Hu, H.W. Cheng, J.H. Fang, Y.P. Xie, W.Y. Fang, T.N.L. Doan, T.K.A. Hoang, J.Q. Xu, P. Chen, *Sci. Rep.* 6 (2016) 1–10.
- [34] Z. Liu, Q. Yang, D. Wang, G. Liang, Y. Zhu, F. Mo, Z. Huang, X. Li, L. Ma, T. Tang, Z. Lu, C. Zhi, *Adv. Energy Mater.* 9 (2019) 1–12.
- [35] F. Wang, Y. Liu, X. Wang, Z. Chang, Y. Wu, R. Holze, *ChemElectroChem* 2 (2015) 1024–1030.
- [36] J. Zhao, Y. Li, X. Peng, S. Dong, J. Ma, G. Cui, L. Chen, *Electrochem. Commun.* 69 (2016) 6–10.
- [37] D. Batyrbekuly, S. Cajoly, B. Laïk, J.-P. Pereira-Ramos, N. Emery, Z. Bakenov, R. Baddour-Hadjean, *ChemSusChem* 13 (2020) 724–731.
- [38] R. Baddour-Hadjean, M.B. Smirnov, V.Y. Kazimirov, K.S. Smirnov, J.-P. Pereira-Ramos, *J. Raman Spectrosc.* 46 (2015) 406–412.
- [39] N. Emery, R. Baddour-Hadjean, D. Batyrbekuly, B. Laïk, Z. Bakenov, J.-P. Pereira-Ramos, *Chem. Mater.* 30 (2018) 5305–5314.
- [40] R. Baddour-Hadjean, M. Safrany Renard, J.-P. Pereira-Ramos, *Acta Mater.* 165 (2019) 183–191.
- [41] M. Safrany Renard, N. Emery, R. Baddour-Hadjean, J.-P. Pereira-Ramos, *Electrochim. Acta* 252 (2017) 4–11.
- [42] I. Mjejri, A. Rougier, M. Gaudon, *Inorg. Chem.* 56 (2017) 1734–1741.
- [43] M.B. Smirnov, E.M. Roginskii, V.Y. Kazimirov, K.S. Smirnov, R. Baddour-Hadjean, J.-P. Pereira-Ramos, V.S. Zhandun, *J. Phys. Chem. C* 119 (2015) 20801–20809, <https://doi.org/10.1021/acs.jpcc.5b05540>.
- [44] P.Y. Zavalij, F. Zhang, M.S. Whittingham, *Acta Cryst. C* 53 (1997) 1738–1739.
- [45] T. Chirayil, P.Y. Zavalij, M.S. Whittingham, *Chem. Mater.* 10 (1998) 2629–2640.
- [46] S. Ni, G. Zhou, S. Li, X. Wang, Q. Pan, F. Yang, D. He, *Mater. Lett.* 63 (2009) 2459–2461.

Supplementary data

A porous puckered V_2O_5 polymorph as new high performance cathode material for aqueous rechargeable zinc batteries

Figure S1. Rietveld refinement of γ' - V_2O_5 XRD pattern

Figure S2. (a) XRD patterns and (b) Raman spectra of initial γ' - V_2O_5 electrode and after one discharge-charge cycle. C/5 rate. 1.6 V - 1 V voltage window. Stars correspond to the sample holder (stainless steel) reflections

Figure S3. Influence of the C rate on discharge-charge curves of γ' - V_2O_5 . 1.6 V - 1 V voltage window. 2.5M Li_2SO_4 -3.5M $ZnSO_4$ electrolyte

Figure S4. Discharge-charge curves of γ' - V_2O_5 during cycling at C/5 rate. 1.6 V - 0.7 V voltage window. 2.5M Li_2SO_4 -3.5M $ZnSO_4$ electrolyte

Figure S5. Typical discharge-charge curves of γ' - V_2O_5 at different C-rates after 10 activation cycles at C/5. 1.6 V - 0.7 V voltage window. 2.5M Li_2SO_4 -3.5M $ZnSO_4$ electrolyte

Figure S6. Discharge-charge curves of γ' - V_2O_5 during cycling at C/5 rate. 1.6 V - 0.7 V voltage window. 3.5M $ZnSO_4$ electrolyte

Figure S7. (a) XRD patterns and (b) Raman spectra of initial γ' - V_2O_5 electrode, after the first discharge and after the first discharge-charge cycle. Stars correspond to the sample holder (stainless steel) reflections. 1C rate. 1.6 V - 0.7 V voltage window

Figure S8. (a) XRD patterns and (b) Raman spectra of initial γ' - V_2O_5 and after cycle tests. *: sample holder (stainless steel) reflections. +: new phase. 1C rate. 1.6 V - 0.7 V voltage window

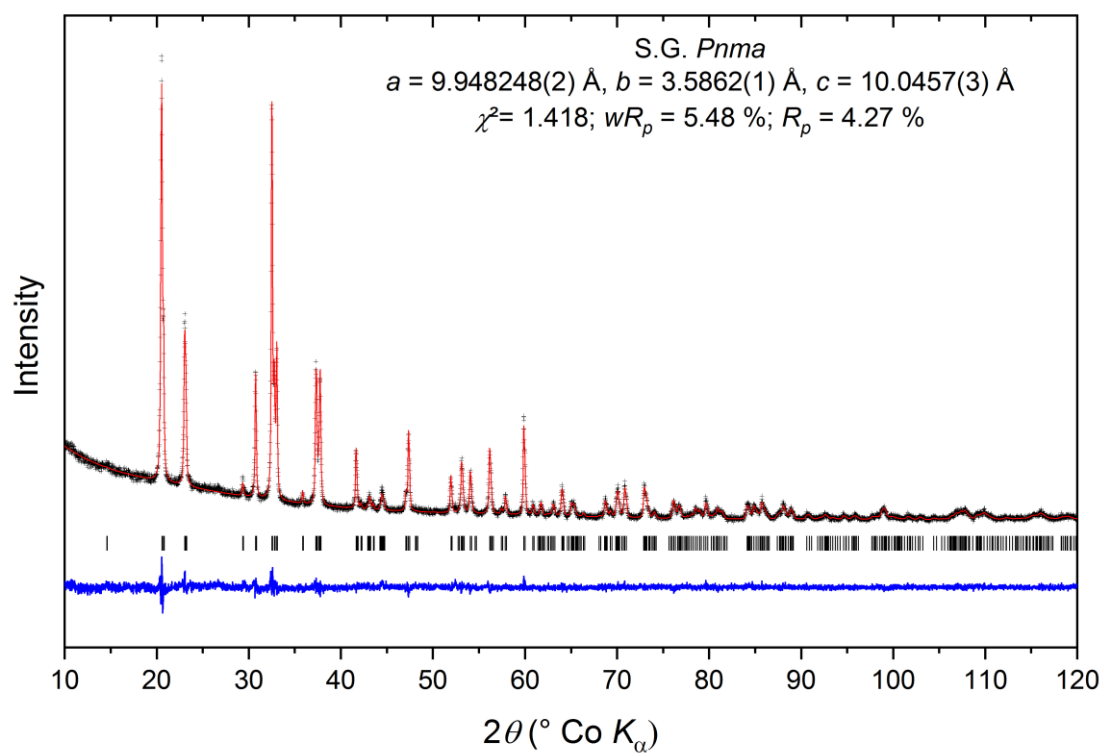


Fig. S1. Rietveld refinement of γ' -V₂O₅ XRD pattern

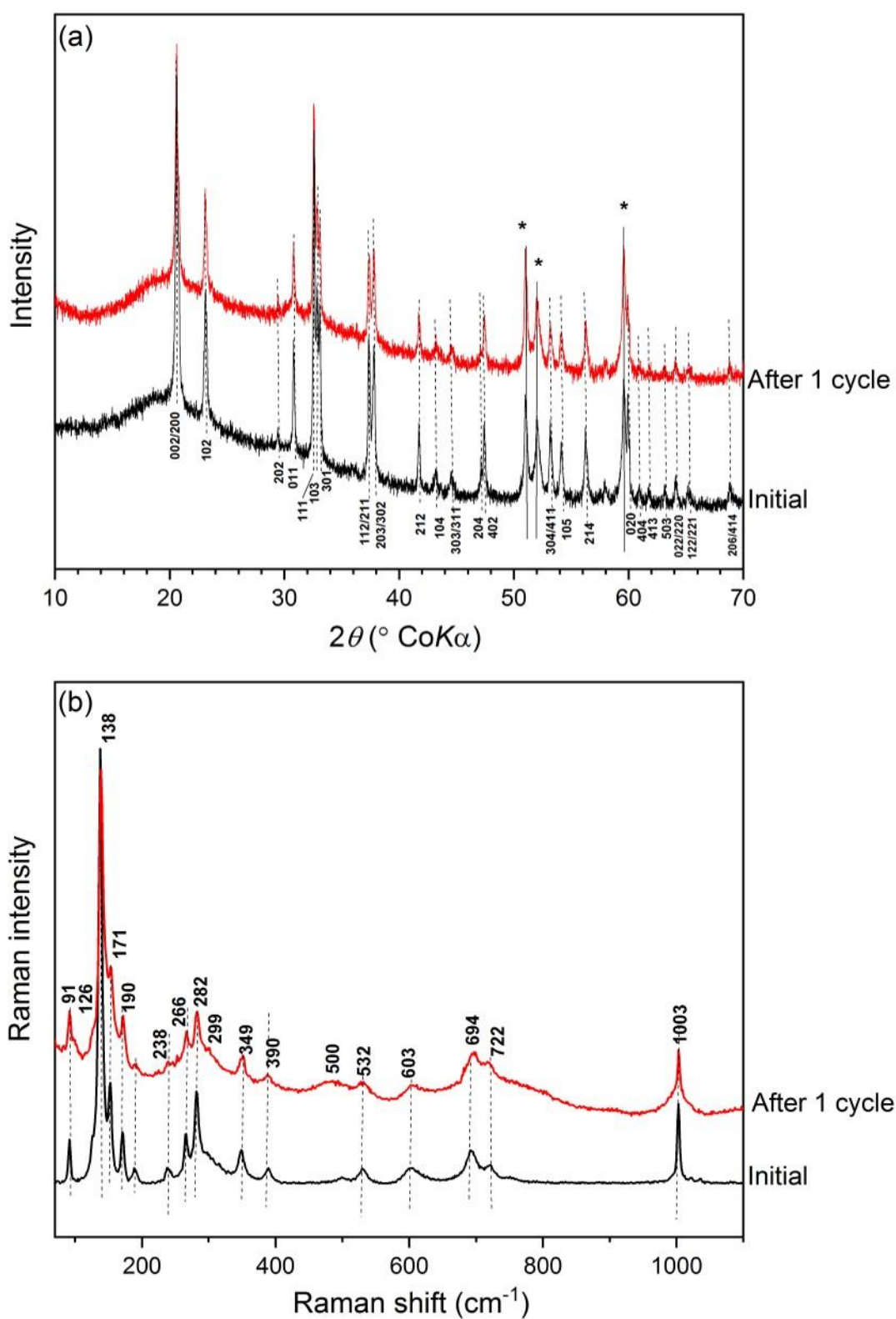


Fig. S2. (a) XRD patterns and (b) Raman spectra of initial γ' - V_2O_5 electrode and after one discharge-charge cycle at C/5 rate. 1.6 V - 1 V voltage window. *: sample holder (stainless steel) reflections

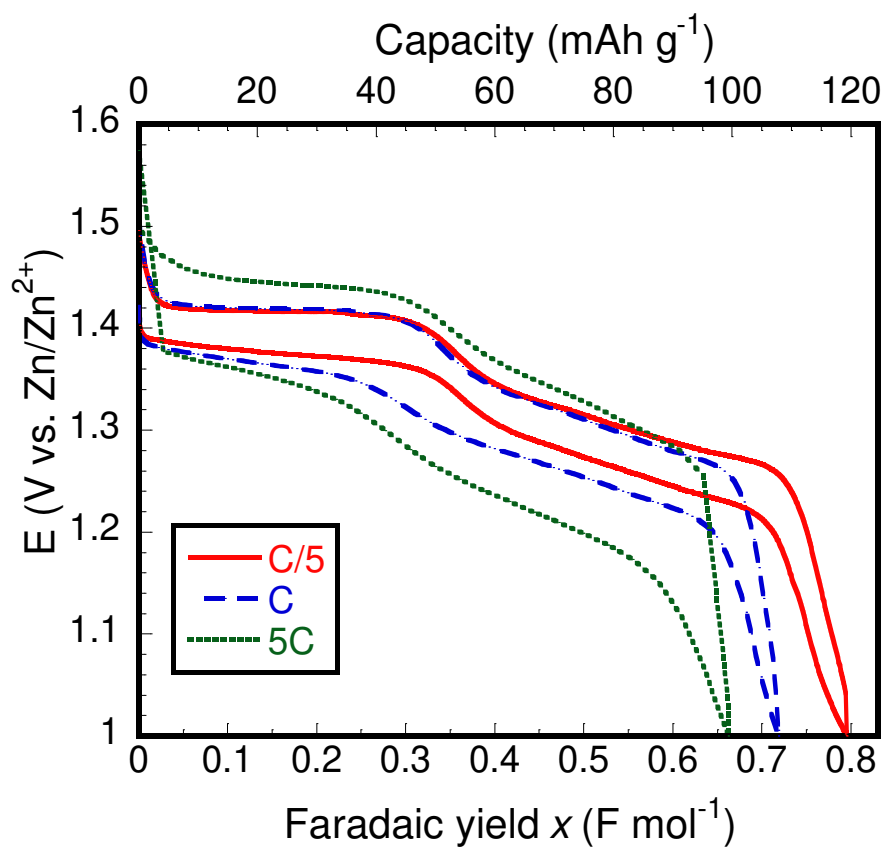


Fig. S3. Influence of the C rate on discharge-charge curves of γ' - V_2O_5 . 1.6 V - 1 V voltage window. 2.5M Li_2SO_4 -3.5M ZnSO_4 electrolyte

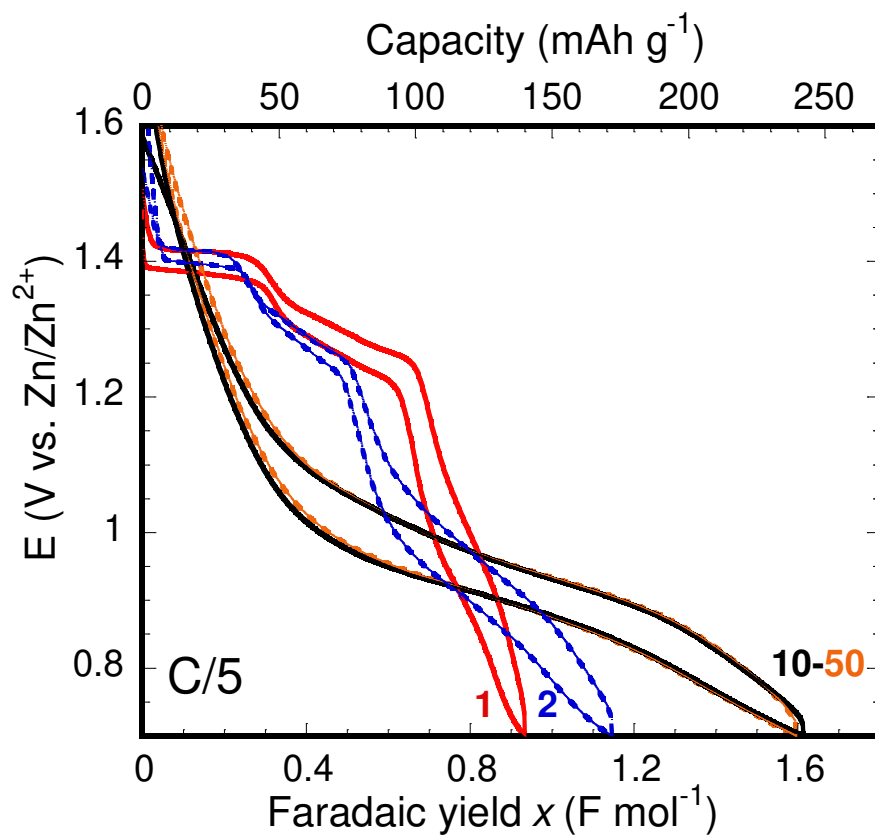


Fig. S4. Discharge-charge curves of γ' -V₂O₅ during cycling at C/5 rate. 1.6 V - 0.7 V voltage window. 2.5M Li₂SO₄-3.5M ZnSO₄ electrolyte

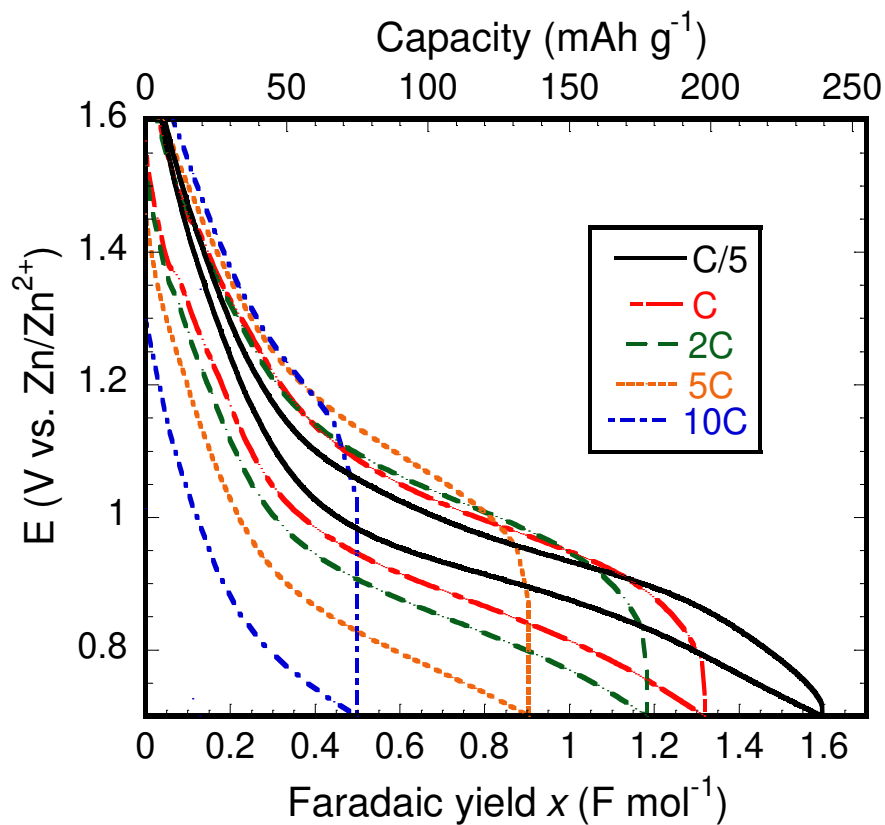


Fig. S5. Typical discharge-charge curves of γ' -V₂O₅ at different C-rates after 10 activation cycles at C/5. 1.6 V - 0.7 V voltage window. 2.5M Li₂SO₄-3.5M ZnSO₄ electrolyte

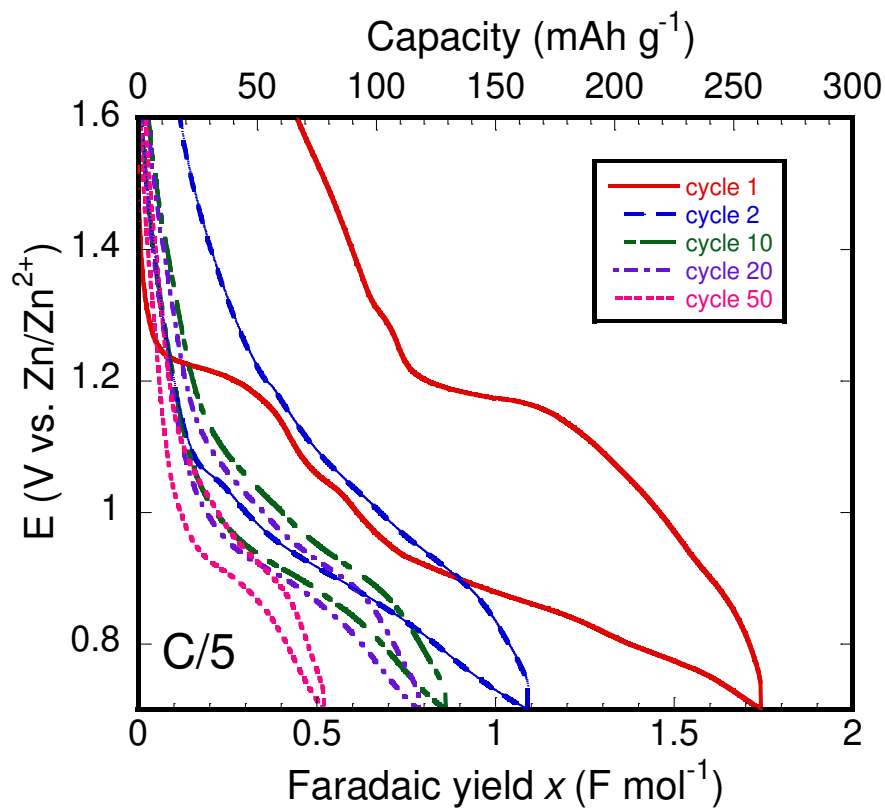


Fig. S6. Discharge-charge curves of γ' - V_2O_5 during cycling at C/5 rate. 1.6 V - 0.7 V voltage window. 3.5M ZnSO_4 electrolyte

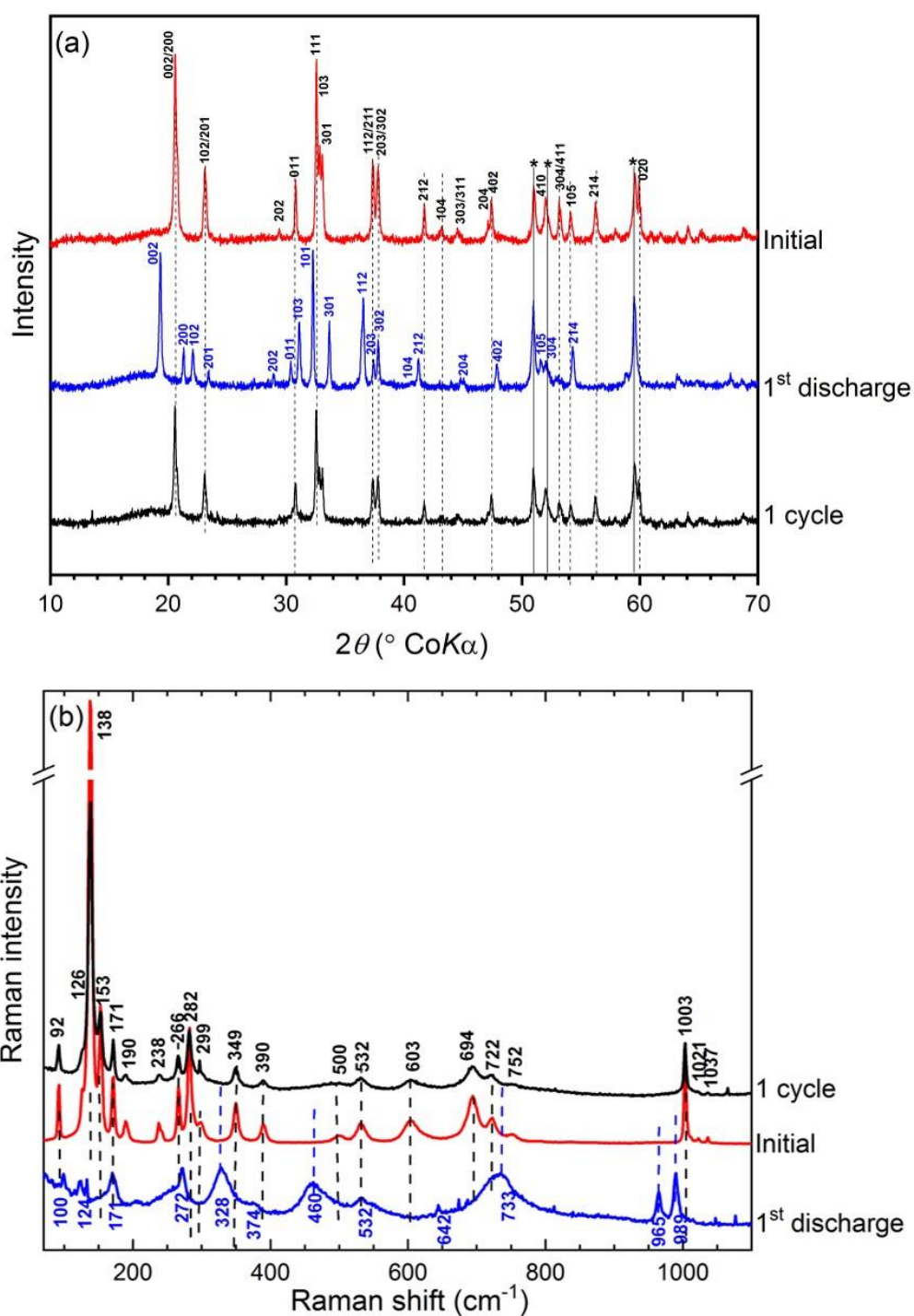


Fig. S7. (a) XRD patterns and (b) Raman spectra of initial γ' - V_2O_5 electrode, after the first discharge and after the first discharge-charge cycle. *: sample holder (stainless steel) reflections. 1C rate. 1.6 V - 0.7 V voltage window

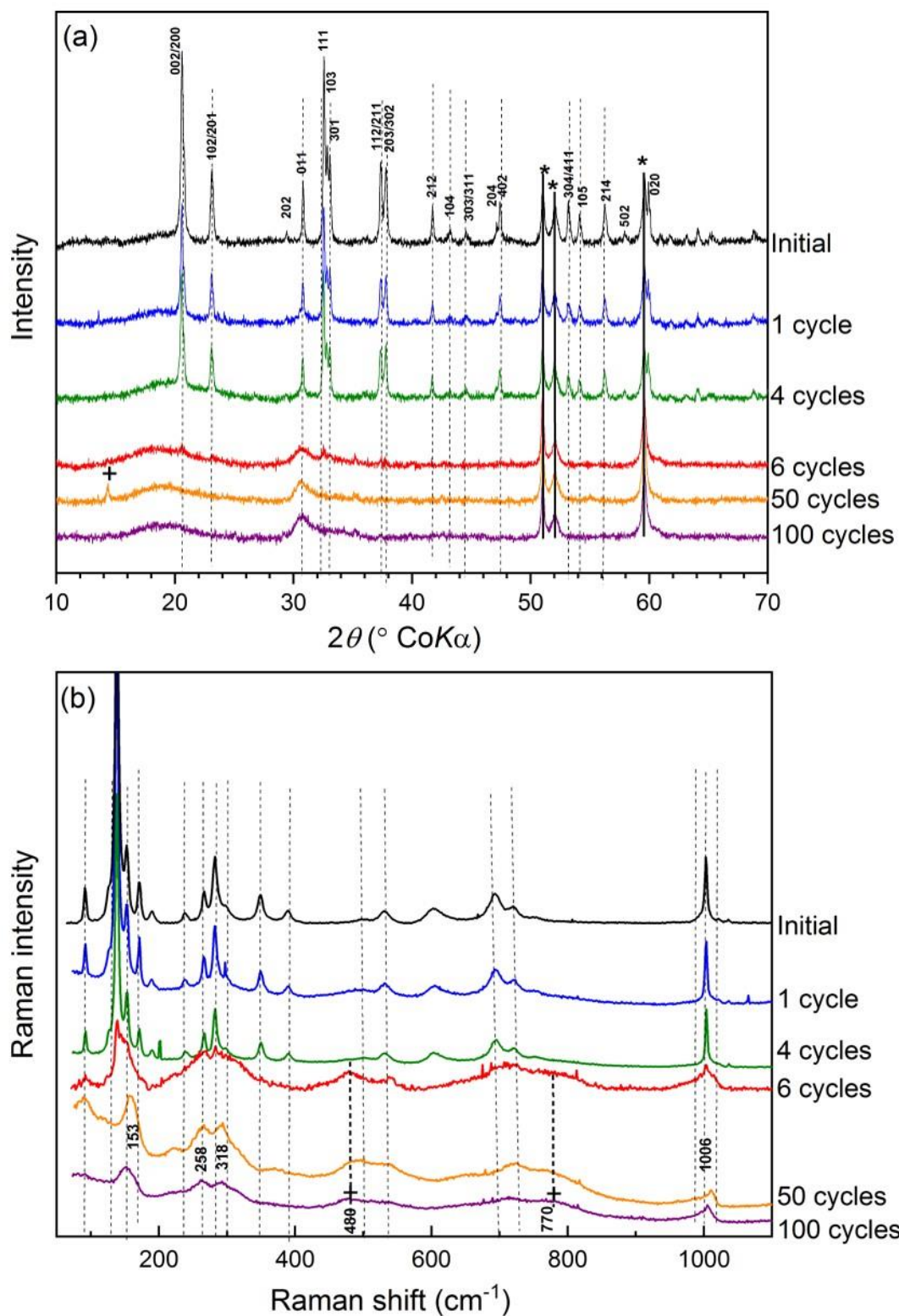


Fig. S8. (a) XRD patterns and (b) Raman spectra of initial γ' - V_2O_5 and after cycle tests. *: sample holder (stainless steel) reflections. +: new phase. 1C rate. 1.6 V - 0.7 V voltage window

General Conclusion

The results achieved in the present work have enriched the knowledge on the electrochemical and structural data of the γ' -V₂O₅ polymorph as Lithium, Sodium and Zinc insertion compound. Our findings usefully complete data of the V₂O₅ family including the most stable phase, i.e. α -V₂O₅, but also the double-layered ε' -V₂O₅ phase and the high pressure β -V₂O₅ oxide. This has been performed through the study of γ' -V₂O₅ prepared by a solution technique (polyol synthesis) allowing to get nanosized particles investigated as positive electrode material for Lithium and Sodium-ion non aqueous batteries and for aqueous Zinc batteries.

The puckered layers of γ' -V₂O₅ allow reversible Li insertion in higher voltage window (3.6/3.5 V vs. Li⁺/Li) than α -V₂O₅ (3.4/3.2 V vs. Li⁺/Li). The structural evolution of γ' -V₂O₅ was investigated by ex-situ XRD and Raman spectroscopy during first discharge and one complete cycle showing the existence of a diphasic region for the first half discharge while the second part corresponds to a single phase whose interlayer distance increases with Li content. A high structural reversibility explains its good cycle life with a stable capacity of 130 mAh g⁻¹ available at a high voltage of 3.5V (50 cycles; 1C).

The obtained results on the rate capability of *pol.* and *carbo.* synthesized γ' -V₂O₅ illustrate the correlation between particle size, morphology and electrochemical performance of the material (Table 1 and Table 2). The smaller particle size (~200 nm) against micrometric pellets, leads to the enhancement of rate capability of material with minimized hysteresis.

Table 1. The rate-capability of γ' -V₂O₅ in Li-ion battery

Material	Discharge capacity (mAh g ⁻¹) at various C-rate						
	C/10	C/5	C/2	1C	2C	5C	10C
γ' -V ₂ O ₅ <i>pol</i>	145	138	134	130	127	123	106
γ' -V ₂ O ₅ <i>carbo.</i>	145	140	130	100	80	40	5

Table 2. The rate-capability of γ' -V₂O₅, γ -Na_{0.96}V₂O₅ and K_{0.5}V₂O₅ in Na-ion battery

Material	Discharge capacity (mAh g ⁻¹) at various C-rate						
	C/10	C/5	C/2	1C	2C	5C	10C

γ' -V ₂ O ₅ <i>pol</i>	140	140	129	119	105	69	29
γ' -V ₂ O ₅ <i>carbo.</i>	75	63	-	47	-	-	-
γ -Na _{0.96} V ₂ O ₅	140	134	122	110	91	50	-
K _{0.5} V ₂ O ₅	140	100	95	84	74	38	-

Optimized electrochemical properties can be achieved using polyol- γ' -V₂O₅ to produce a high-performance cathode material for Na-ion batteries. This polyol- γ' -V₂O₅ is working at a high voltage of 3.3 V vs Na⁺/Na with a high capacity of 140 mAh g⁻¹, a high rate-capability, an excellent charge efficiency and good cycle life.

From a detailed picture of structure changes upon electrochemistry we show the nanosizing approach has induced a significant shortening of the diphasic region ($0 < x \leq 0.4$) and an expansion of the single-phase region γ -Na_xV₂O₅ ($0.4 < x \leq 1$).

Impedance spectroscopy data reveal a moderate change in electrode impedance upon sodiation and illustrates the significant nanosize effect with a surface enhancement by a factor 4-5 of the electrochemical surface area compared to micro-sized oxide. The evolution of the chemical diffusion coefficient D_{Na} shows a faster diffusion in the single-phase region than in diphasic domain.

The drawback of γ' -V₂O₅ *pol* is that this Na-free material is not directly suitable as cathode in a Sodium-ion batteries. Therefore, we successfully prepared γ -Na_{0.96}V₂O₅ as a directly usable cathode material for sodium-ion batteries. The novel sodium vanadium bronze γ -Na_{0.96}V₂O₅ has been prepared by chemical sodiation of γ' -V₂O₅ *pol* polymorph at room temperature for the first time. The γ -Na_{0.96}V₂O₅ has layered structure with orthorhombic symmetry (*Pnma* space group) isomorphic to the lithiated γ -LiV₂O₅ bronze.

A reversible specific capacity of 124 mAh g⁻¹ at C/5 is available at 3.4V vs. Na⁺/Na and still 112 mAh g⁻¹ after 50 cycles at C/5. The high stability of the structure after charge and discharge has been shown from XRD and Raman spectroscopy which explains a good cycle life upon cycling. However, an improvement is still required in terms of rate capability (2C-5C) in comparison to sodium-free γ' -V₂O₅ *pol* (**Table 2**).

Further optimization of electrochemical properties and structural investigations of this new high voltage sodiated γ -Na_{0.96}V₂O₅ cathode material will be studied in the future; in particular specific

surface coating by oxides (TiO_2 , SiO_2) or the use of conductive materials like rGO, CNT, and conducting polymers could greatly improve the cycle life.

We extended our study by preparing $\text{K}_{0.5}\text{V}_2\text{O}_5$ (KVO) through a fast and facile solution route as a potential candidate for cathode material of SIBs. The bilayered potassium vanadate $\text{K}_{0.5}\text{V}_2\text{O}_5$ is characterized by a large interlayer parameter of 9.5 Å. A first cycle in the 4 V-1.5 V range at C/10 acts as an activation process, leading to a new KVO composition $\text{K}_{0.24}\text{V}_2\text{O}_5$ due to partial potassium extraction. KVO delivers a high reversible specific capacity of 160 mAh g⁻¹ at C/10 with a good capacity retention leading to still 152 mAh g⁻¹ after 50 cycles. Its good capacity retention is explained by a limited expansion-contraction of 3% in the distance between bilayers during cycling with pillaring K^+ ions stabilizing the stacking of double-sheet V_2O_5 layers. The KVO also exhibits attractive rate-capability up to 2C (**Table 2**).

We have also addressed the interest of $\alpha\text{-V}_2\text{O}_5$ and $\gamma'\text{-V}_2\text{O}_5$ polymorphs as cathode materials in Zn- V_2O_5 aqueous rechargeable batteries using a hybrid $\text{Li}^+/\text{Zn}^{2+}$ binary electrolyte at pH 4.

In the case of $\alpha\text{-V}_2\text{O}_5$ a highly reversible capacity of 136 mAh g⁻¹ at C/20 and 125 mAh g⁻¹ at C/5 is achieved in the 1.6 V - 0.8 V range. Li insertion occurs in aqueous medium with similar discharge and charge profiles than in organic electrolyte which has been confirmed by XRD and Raman spectroscopy.

However, at the stage of the study, a possible involvement of a few Zn^{2+} ions cannot be definitively excluded to explain the peculiar structural response of V_2O_5 upon discharging with mitigated structure changes near the end of discharge. In this scenario, a few inserted Zn^{2+} cations located between the oxide layers would act as pillar species, then hindering the gliding of one layer over two in the b direction to produce the expected corrugated δ -phase.

To date, the exact electrochemical reaction mechanism in pure zinc electrolytes is still an open question especially if we enlarge the potential window. A competitive Zn^{2+} and/or H^+ species should be taken into account especially at low potential (<0.8V). The identification of the charge carriers cation is a crucial point which is rarely considered in literature. Their different insertion thermodynamics and kinetics must be deeply investigated as a function of electrolytes, pH, along with detailed operando XRD and Raman spectroscopy as well as a modeling approach.

Calculations are urgently needed for further investigation and prediction to accelerate the understanding of currently unclear reaction mechanism in aqueous ZIBs.

In the case of γ' -V₂O₅ as cathode in the ZnSO₄ + Li₂SO₄ electrolyte, the cathode exhibits 114 mAh g⁻¹ at C/5 in voltage range of 1–1.6V. The operating voltage of γ' -V₂O₅, similar to organic electrolyte, is higher by ~200mV than α -V₂O₅ in same aqueous hybrid electrolyte.

If a similar structural behavior than in organic lithium electrolyte is revealed then excluding any competitive zinc insertion in the 1V-1.6V range, a significant phase transformation takes place upon cycling at lower voltage with the progressive formation of ZVO pyrovanadate responsible of strong modifications in discharge-charge profiles.

Our studies point the important issue due to cathode dissolution which could be solved by different approaches including surface coating with carbon or polymers.

The advances in aqueous ZIBs are supposed to be attached to the optimization of novel types of cathodes and electrolytes. Importantly, developing solid-state/gel polymer electrolytes is one promising route toward solving cathode dissolution. Considering their distinctive merits of low-cost, environmentally benign, and high security, it is strongly believed that aqueous ZIBs possess enormous prospects and will be taken into application in the near future.